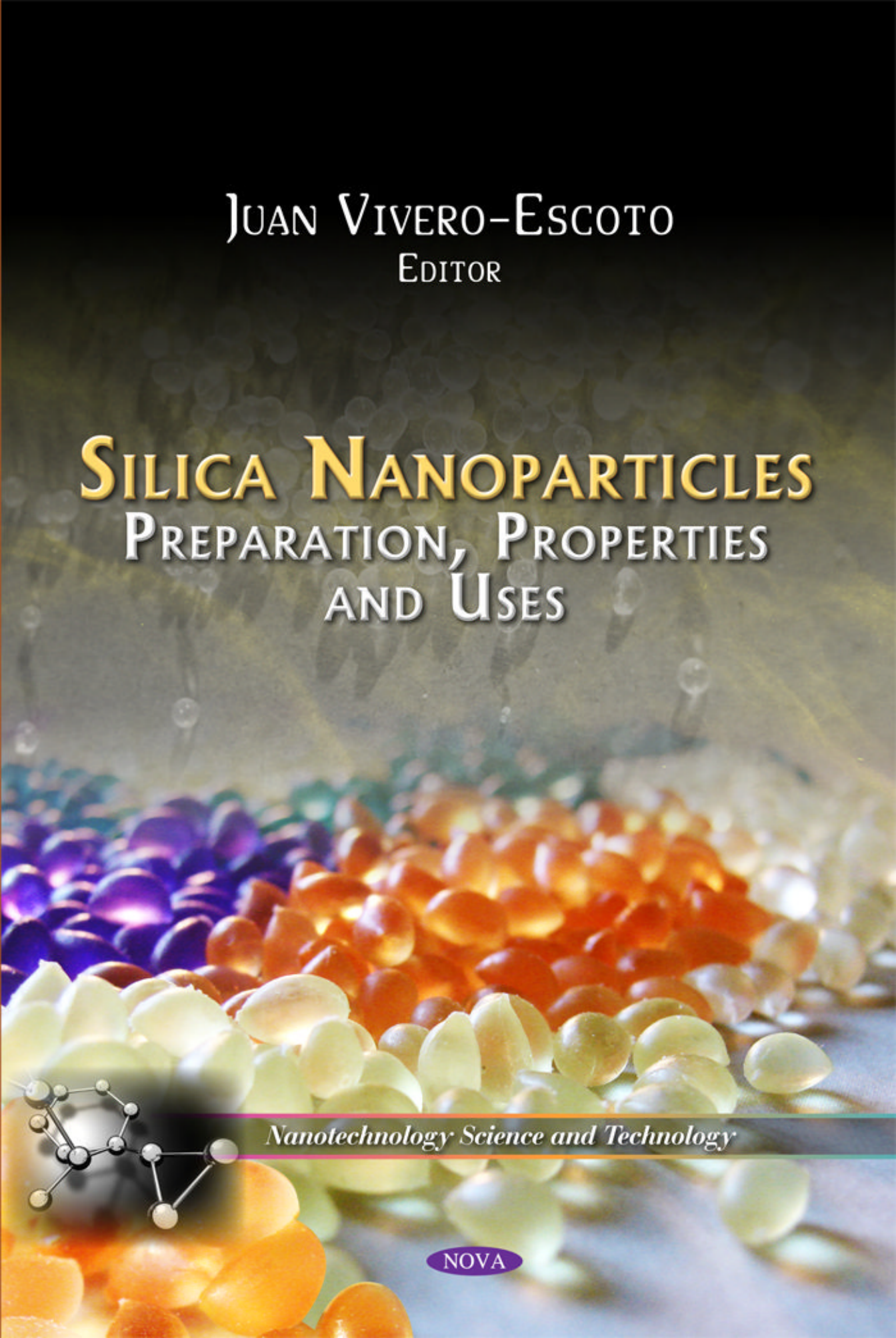
Juan Vivero-Escoto
Editor

Silica Nanoparticles
Preparation, Properties and Uses



Nanotechnology Science and Technology

NOVA

NANOTECHNOLOGY SCIENCE AND TECHNOLOGY

SILICA NANOPARTICLES

PREPARATION, PROPERTIES AND USES

No part of this digital document may be reproduced, stored in a retrieval system or transmitted in any form or by any means. The publisher has taken reasonable care in the preparation of this digital document, but makes no expressed or implied warranty of any kind and assumes no responsibility for any errors or omissions. No liability is assumed for incidental or consequential damages in connection with or arising out of information contained herein. This digital document is sold with the clear understanding that the publisher is not engaged in rendering legal, medical or any other professional services.

NANOTECHNOLOGY SCIENCE AND TECHNOLOGY

Additional books in this series can be found on Nova's website under the Series tab.

Additional E-books in this series can be found on Nova's website under the E-books tab.

CHEMICAL ENGINEERING METHODS AND TECHNOLOGY

Additional books in this series can be found on Nova's website under the Series tab.

Additional E-books in this series can be found on Nova's website under the E-books tab.

NANOTECHNOLOGY SCIENCE AND TECHNOLOGY

SILICA NANOPARTICLES

PREPARATION, PROPERTIES AND USES

JUAN VIVERO-ESCOTO
EDITOR

Nova Science Publishers, Inc.
New York

Copyright © 2012 by Nova Science Publishers, Inc.

All rights reserved. No part of this book may be reproduced, stored in a retrieval system or transmitted in any form or by any means: electronic, electrostatic, magnetic, tape, mechanical photocopying, recording or otherwise without the written permission of the Publisher.

For permission to use material from this book please contact us:
Telephone 631-231-7269; Fax 631-231-8175
Web Site: http://www.novapublishers.com

NOTICE TO THE READER

The Publisher has taken reasonable care in the preparation of this book, but makes no expressed or implied warranty of any kind and assumes no responsibility for any errors or omissions. No liability is assumed for incidental or consequential damages in connection with or arising out of information contained in this book. The Publisher shall not be liable for any special, consequential, or exemplary damages resulting, in whole or in part, from the readers' use of, or reliance upon, this material. Any parts of this book based on government reports are so indicated and copyright is claimed for those parts to the extent applicable to compilations of such works.

Independent verification should be sought for any data, advice or recommendations contained in this book. In addition, no responsibility is assumed by the publisher for any injury and/or damage to persons or property arising from any methods, products, instructions, ideas or otherwise contained in this publication.

This publication is designed to provide accurate and authoritative information with regard to the subject matter covered herein. It is sold with the clear understanding that the Publisher is not engaged in rendering legal or any other professional services. If legal or any other expert assistance is required, the services of a competent person should be sought. FROM A DECLARATION OF PARTICIPANTS JOINTLY ADOPTED BY A COMMITTEE OF THE AMERICAN BAR ASSOCIATION AND A COMMITTEE OF PUBLISHERS.

Additional color graphics may be available in the e-book version of this book.

Library of Congress Cataloging-in-Publication Data

Silica nanoparticles : preparation, properties, and uses / editor, Juan Vivero-Escoto.
p. cm.
Includes index.
ISBN: 978-1-62257-030-0 (eBook)
1. Nanosilicon. 2. Nanoparticles. 3. Biotechnology--Materials. 4. Silica dust--Industrial applications. I. Vivero-Escoto, Juan.
TA418.9.N35S55 2011
620.1'93--dc23
2011014205

Published by Nova Science Publishers, Inc. †New York

CONTENTS

Preface		**vii**
Chapter 1	Silica Nanoparticle as Carrier for Biosensing *Jing Qian and Songqin Liu*	**1**
Chapter 2	Reactivity of Inorganic Radicals and Excited Triplet States in Colloidal Silica Suspensions *Valeria B. Arce, Paula Caregnato, Mónica C. Gonzalez and Daniel O. Mártire*	**39**
Chapter 3	Multifunctional Mesoporous Silica Nanoparticles for Controlled Drug Delivery, Multimodal Imaging and Simultaneous Imaging and Drug Delivery *Juan L. Vivero-Escoto*	**81**
Chapter 4	Mesoporous Silica Nanoparticles as a Drug Delivery System *Dennis Douroumis, Ichioma Onyesom, Mohammed Maniruzzaman and Mark Edwards*	**115**
Chapter 5	Silica-Based Hybrid Nanomaterials with Well-Defined Architectures *Haiqing Li and Il Kim*	**147**
Chapter 6	Functional Silica Nanoparticles Synthesized by Water-in-Oil Microemulsion *Tangi Aubert, Stéphane Cordier and Fabien Grasset*	**179**
Chapter 7	Biomedical Applications of Nanosilica *Seyed Shahabeddin Mirsasaani, Maedeh Hajipour Manjili, Farhad Ghomi, Seyed Mohammadreza Mousavi, Nasimsadat Mousavi and Masoud Mozafari*	**205**
Chapter 8	Monodisperse Luminescent Silica Nanoparticles: Synthesis, Characterization and Application to the DNA Microarray Technology *F. Enrichi*	**225**

Chapter 9 Degree of Dispersion and Coagulation of Silica Nanoparticles Determined by Using an Electric Field **249**
Akira Otsuki

Chapter 10 Temperature-Responsive DNA-Capped Mesoporous Silica Nanoparticles Based Delivery System **2611**
Juan L. Vivero-Escoto and Victor S.-Y. Lin

Index **2733**

PREFACE

In this book, the authors present topical research in the study of the preparation, properties and use of silica nanoparticles. Topics discussed include the reactivity of inorganic radicals and excited triplet states in colloidal silica suspensions; multifunctional mesoporous silica nanoparticles for controlled drug delivery, multimodal imaging and simultaneous imaging and drug delivery; monodisperse luminescent silica nanoparticles and their application to DNA microarray technology.

Chapter 1 - Recently, silica nanoparticles (NPs) have attracted considerable attention because of their tunble properties and composition in a very predictable manner to meet the needs of many specific applications. The silica shells facilitate a wide variety of powerful novel surface modification and bioconjugation. Although the pure silica itself cannot be regarded as a versatile label, new technologies can provide efficient means to prepare a silica-based three-dimensional network suitable for encapsulation of a variety of molecules or particles. An extensive amount of work has been done in aim to synthesize doped-silica NPs based on luminophore and nanosized particles such as quantum dots, magnetic particles, noble metal or metal oxide particles with unique optical, magnetic, or raman-active properties. Recent research activities have focused on possible applications of silica-based NPs as carriers in a multitude of selective and ultrasensitive bioassays, such as biosensors, immunoassay, biolabelling, bioimaging, and cell targeting. In this chapter, the authors first describe recent advances in silica-based NPs, various process to synthesize silica or doped-silica NPs. The functionalization of silica-based NPs with various chemicals and biomolecules and the biological applications of functional and biifunctional silica-based NPs with respect to biosensing are also described.

Chapter 2 - Aquatic photochemistry studies the degradation of contaminants induced by light (either terrestrial sunlight or artificial light used in engineered water treatment systems). In addition to the “direct photolysis” or “direct phototransformation” route there exist a variety of photochemical reactions involving chromophores already present in natural waters and producing reactive species that initiate the degradation of the target contaminant (“indirect phototransformation”). Since the main absorber of light in natural waters is colored dissolved natural organic matter (CDOM), the excited triplet states of CDOM are involved in the indirect phototransformation of contaminants. However, irradiation of CDOM leads to the formation of other species, such as singlet molecular oxygen, solvated electrons, hydrogen peroxide, and hydroxyl radicals among others. Most of these species are able to initiate

chemical reactions in which undesirable organic components are attacked and ultimately destroyed, thus providing a mechanism for self-cleansing of the water sources.

Silica is a ubiquitous material in the environment, which is present in great amounts in natural waters. This material is an excellent sorbent of contaminants, as well as reactive species involved in their degradation. Thus, it is relevant to know the mechanisms of the reactions that take place at the silica/water interfaces.

Because colloidal silica has a very high specific surface area and is optically transparent in the near-infrared, visible and ultraviolet regions, it is very appropriate for investigating interfacial reaction kinetics involving photochemically generated species.

This chapter reviews recent research concerned with the kinetic behavior of two kinds of reactive species in colloidal silica suspensions. On one hand, excited triplet states, mainly those of benzophenone, and on the other hand inorganic radicals, such as $SO_4^{\bullet-}$, $Cl^{\bullet}$, $Cl_2^{\bullet-}$, $HPO_4^{\bullet-}$, $(SCN)_2^{\bullet-}$.

Chapter 3 - The application of nanotechnology in the field of biomedicine has received enormous attention in the latest decades. Recent breakthroughs on the morphology control and surface functionalization of inorganic-based imaging/delivery vehicles, such as mesoporous silica nanoparticles (MSNs), have brought new possibilities to this burgeoning area of research. The ability to functionalize the surface of mesoporous-silica-based nanocarriers with stimuli responsive groups, nanoparticles, polymers, optical and MR imaging agents that work as caps and gatekeepers for controlled release of various cargos and multimodal imaging probes is just one of the exciting results reported in the literature that highlights MSNs as a promising platform for various biotechnological and biomedical applications. This chapter focuses on the most recent progresses in the application of MSNs in the areas of controlled drug delivery and biomedical imaging. The versatility of MSNs as controlled drug delivery system is shown, with special emphasis given to stimuli-responsive nanodevices containing nanoparticles as gatekeepers. The latest research on the development of mesoporous multimodal nanoparticles is described. In addition, the current research progress on the biocompatibility of this material *in vivo* is discussed. Finally, the latest breakthroughs in the simultaneous application of MSNs as therapeutic and diagnostic (theranostic) agents *in vivo* are presented.

Chapter 4 - During the last decade a substantial progress in utilizing mesoporous silica nanoparticles (MSNs) has taken place. These nanosized inorganic materials can be synthesized to act as imaging, targeting and drug delivery systems. The surface area and the pore size can be tailored to selectively encapsulate the desired molecules, the shape and the size can be tuned to enhance cellular uptake, while the surface can be functionalized for active targeting. In the current chapter the authors discuss the MSNs preparation methods, uses and biological applications both *in vit*ro and *in vivo*.

Chapter 5 - Silica nanomaterials with well-defined architectures exhibit low cytotoxicity, uniform size, and excellent chemical stability, which in addition to their low-cost, versatile functionalization chemistry and relative ease of large-scale preparation make them very suited to the role of host material for the development of novel silica-based nanoarchitectures targeted to biomedical, catalytic and photoelectronic applications. This chapter surveys the recent research progresses on the fabrication strategies and the corresponding applications of silica and silica-based hybrid nanostructures: 1) silica nanostructures with varied morphologies such as silica solid spheres, capsules, wires, tubes and novel multilevel interior structures; 2) silica-based hybrid nanostructures with various compositions such as

silica/polymer hybrids obtained by “grafting from” approach or templating methods, silica/metal nanoparticles achieved by “surface deposition”, “matrix entrapping” and templating strategies, silica/carbon nanotubes hybrids achieved on the basis of covalent and non-covalent surface-modified carbon nanotubes, as well as other hierarchical complex structures; 3) silica-based Janus spheres. In the last section of this chapter, the perspectives and outlook of the current research challenges and future research directions in the related fields are presented.

Chapter 6 - The elaboration of monodisperse and size-controlled silica nanoparticles has already been perfectly mastered for years. However, creating functional nanoparticles with sophisticated structural designs is still an open challenge and offers the scientific community a wide range of possibilities and opportunities. Among the different techniques available for the elaboration of such materials, the water-in-oil (w/o) microemulsion appears as a particularly dedicated tool. Indeed, the aqueous inverted micelles that constitute the w/o microemulsion is a well-suitable confined reacting medium for the synthesis of structured functional nanoparticles with controlled size and shape. This process allows the encapsulation in silica nanoparticles of different type of core elements (nanocrystals, molecules, etc.) with a high control on the structure of the obtained nanoparticles and on the concentration of the encapsulated elements. In this chapter will be presented the synthesis via microemulsion processes of different functional silica nanoparticles. The obtained materials exhibit interesting properties such as optical properties (photoluminescence, UV absorption, etc.) and/or magnetic properties. They should therefore find numerous applications in a broad range of technologies, such as biotechnologies, photonics, cosmetics, etc.

Chapter 7 - Application of nanotechnology to biomedical has increased over the years. There is a great deal of interest in investigating controlling the size and the shape of silica nanoparticles, understanding the overall, and applications of these particles in medicine.

Silica particles have received much attention in biomedical area because of their applications in new drug delivery systems, tissue engineering, dental materials, etc.

In recent decades, significant advances in drug delivery systems have enabled more effective drug administration. For example, nanosilica is used for cancer treatment.

Addition of nanosilica can improve the bioactivity and biocompatibility of scaffolds which are used in bone tissue engineering applications.

Silica is also used in preparation of dental nanomaterials. Most of the fillers which are used to reinforce dental cements and composites are silicate glasses. These materials with nanosilica fillers provide materials with high mechanical properties and low polymerization shrinkage.

In this chapter, three mentioned applications of silica nanoparticles in biomedical are presented.

Chapter 8 - The ability to modify the properties of materials by controlling their structure at nanoscale makes them extremely attractive for many applications: from fundamental scientific studies to commercially realizable technologies. In the biological context a variety of nanomaterials promise to offer sensitive, rapid and cost-effective solutions for modern clinical laboratory. In particular, dye-doped silica nanoparticles (NPs) have been demonstrated to be sensitive labeling markers for biosensing and bioimaging. Their flexible conjugation, excellent photostability, and ultrasensitivity make them a powerful tool in bioanalysis. Indeed luminescent dye-doped nanoparticles are excellent candidates for biological applications because (1) they can be analyzed with the standard existing tools

(microarray scanners, optical fluorescence microscopes), which are fitted for standard fluorophore excitation and emission curves, (2) a large number of dye molecules can be incorporated in a single particle, increasing the optical signal and (3) the silica matrix provides a protective barrier minimizing photobleaching and photodegradation.

A very efficient synthesis strategy for silica nanoparticles is the Stöber method, which has the advantage that it can be easily scaled up for commercial production and the possibility to effortlessly transfer the nanoparticles into aqueous solutions (typically required for bioanalysis applications). However, modifications on the synthesis process are required to obtain luminescent particles and proper investigation on the particles size control and on the dye-doping process are needed. In this chapter the authors describe a modifyedStöber synthesis which is based on the use of 3-Aminopropyl-triethoxysilane (APTES) for the efficient incorporation of dye molecules into the silica NPs. The parameters of the modified synthesis have been systematically investigated in order to optimize their morpho-optical properties and to maximize their optical efficiency.

Moreover the application of these luminescent silica nanoparticles to DNA microarray technology is also reported for a specific case study: the detection of carcinogenic risky Human Papilloma Virus, which is one of the primary causes for cervical cancer in women worldwide. In particular, DNA microarray is a powerful tool for the parallel, high-throughput detection and quantification of many nucleic acids and other biologically significant molecules. The authors show that the luminescent silica nanoparticles in comparison to conventional dye labelling or commercial quantum dots allow achieving a significant tenfold increase in the optical signal, and a related decrease of the limit of detection, thus giving a remarkable improvement in this technique towards early diagnosis of the disease. It is worth noticing the fact that this result can be easily transferred to other pathologies and to other fields like for example trace level detection of dangerous biological contaminants in food or in the environment.

Chapter 9 - It is important to manipulate the degree of dispersion and coagulation of fine particles in various media for many industrial processes. Therefore, understanding those characteristics of fine particles in the specific media is of great importance. Many techniques have been developed for evaluating them by measuring size, turbidity, contact angle, zeta potential, force between particles and combination of these techniques. However, these techniques usually are not suitable for evaluating those characteristics of particles in highly concentrated suspensions and non transparent suspensions. On the other hand, these kinds of suspensions are commonly used in the many industrial procedures, such as selective separation and flocculation of fine particles.

Chapter 10 - Recent developments in designing mesoporous silica nanoparticles (MSNs) based delivery systems using “caps and gatekeepers” able to selectively release entrapped guest molecules by specific triggers have attracted a great deal of attention. For example; inorganic nanoparticles, large molecules, biomolecules, and polymers have been used to block the pore openings and prevent guest molecules from leaving the system. The release mechanisms in these platforms include changes in pH, redox potential, UV irradiation or temperature for uncapping the pores. Herein, the authors report on the synthesis of an organically functionalized MSN material functionalized with an oligonucleotide intercalating phenanthridinium functionality (PAP-MSN). The working principle of this MSN delivery system is based on the strong binding affinity of thephenanthridinium group toward double-stranded oligonucleotides (ds-oligo) to block the pore openings. The release of the guest

molecules is achieved once the melting temperature of the ds-oligo has been reached breaking the non-covalent interaction between the complementary oligonucleotide strands and the phenanthridium moeity. To prove this hypothesis, PAP-MSNs were loaded with guest molecules, $[Ru(bipy)_3]^{2+}$ complex. The temperature-dependent release profile showed the successful performance of the ds-oligo (36 mers; melting temperature = 67 ºC) as stimuli-responsive cap. In addition, the control sample under similar conditions did not show a considerable release of guest molecule after several hours. In summary, the authors have shown how the incorporation of ds-oligo into a novel cap system can impart temperature-responsive release behavior. The possibility of expanding the scope of this system based on different supports and tailor-made oligonucleotides makes this approach of interest for a wide variety of biomedical and biotechnological applications.

In: Silica Nanoparticles
Editor: Juan Vivero-Escoto
ISBN 978-1-61324-452-4
© 2012 Nova Science Publishers, Inc.

Chapter 1

SILICA NANOPARTICLE AS CARRIER FOR BIOSENSING

Jing Qian[1] and Songqin Liu[2]
School of Chemistry and Chemical Engineering, Southeast University,
Nanjing, P. R. China

ABSTRACT

Recently, silica nanoparticles (NPs) have attracted considerable attention because of their tunble properties and composition in a very predictable manner to meet the needs of many specific applications. The silica shells facilitate a wide variety of powerful novel surface modification and bioconjugation. Although the pure silica itself cannot be regarded as a versatile label, new technologies can provide efficient means to prepare a silica-based three-dimensional network suitable for encapsulation of a variety of molecules or particles. An extensive amount of work has been done in aim to synthesize doped-silica NPs based on luminophore and nanosized particles such as quantum dots, magnetic particles, noble metal or metal oxide particles with unique optical, magnetic, or raman-active properties. Recent research activities have focused on possible applications of silica-based NPs as carriers in a multitude of selective and ultrasensitive bioassays, such as biosensors, immunoassay, biolabelling, bioimaging, and cell targeting. In this chapter, we first describe recent advances in silica-based NPs, various process to synthesize silica or doped-silica NPs. The functionalization of silica-based NPs with various chemicals and biomolecules and the biological applications of functional and biifunctional silica-based NPs with respect to biosensing are also described.

[1]Corresponding Author: Email-Address: qianjing16@126.com.
[2]Corresponding Author: Tel.: +86-25-52090613; Fax: +86-25-52090618,
E-mail Address: liusq@seu.edu.cn.

1. INTRODUCTION

The rapid evolving fields of nanotechnology and the versatile processes used to generate, manipulate and utilize nanomaterials, have attracted a considerable attention in recent years and opened up a promising era in bioanalytical, biotechnological, and biomedical applications [1-4]. A burst of research activity has focused on the synthesis and functionalization of the nanoparticles (NPs), owing to their unique physical (structural, electronic, magnetic, and optical, compatible), chemical (catalytic), and electrochemical properties [5–7]. NPs of many types, from a diversity of metal NPs to types of semiconducting NPs, and so on, have emerged to satisfy a wide range of specific applications [8-11]. Particularly, the use of functionalized NPs as carriers, or labels, markers, and probes has shown great success in bioimaging, biolabeling, and biosensing as well as for diagnostic and therapeutic purposes because their tunable and tailored properties [12-15]. For example, functionalized gold NPs have been used to develop DNA and protein biosensors combination with colorimetric [16, 17], scanometric [18], and electrochemical techniques [19]. Quantum dots (QDs) have been already used to develop various optical [20], electrochemical [21], electrochemiluminescence (ECL) [22], chemiluminescence (CL) [23] bioassays. With manipulated composition and surface modification, these nanoparticle carriers, or labels, markers, probes have enhanced the detection signal, increased sensitivity, reduced detection time, generated better reproducibility, and lead to an array of new applications.

Silica-based NPs are robust inorganic materials, which have high specific surface area, a three-dimensional (3D) structure with highly open spaces interconnected to each other, and, especially, a high surface silanol concentration, which makes it facile to introduce functional groups, such as aminos, mercaptos and carboxyls, to the surface of the silica NPs for the further binding of biomolecules [24]. Owing to their promising properties such as good biocompatibility, non-toxicity, thermal stability, electroinactive in aqueous media, and suitability for many surface immobilization mechanisms, silica-based NPs have been considered as excellent substrate suitable for many biomolecule conjugatation including biotin–avidin, antigen–antibodies, peptides, proteins, and DNA [25]. The resultant "nanocomposition" determines both the compatibility and the suitability of the carriers towards the analyte, which has provided new opportunities for their effective applications in a wide variety of fields [26].

Although the pure silica itself cannot be regarded as a versatile label, new technologies can provide efficient means to prepare a silica-based 3D network suitable for encapsulation of a variety of molecules or NPs. An extensive amount of work has been done in aim to synthesize doped-silica NPs based on luminophore [27, 28] and nanosized particles such as QDs, magnetic particles, noble metal or metal oxide particles with unique optical, magnetic, or raman-active properties [28-33]. The typical preparation process involves chemical synthesis of monodisperse NPs, water solubilization, and functionalization with targeting ligands. Numerous works have been published on the use of silica-based NPs as effective carriers for proteins, gene transport and expression, bioseparation/purification of nucleic acids, bio-signal probing, and many other important biological applications [34-38]. The 3D network structure of silica shell can protect the entrapped molecules or particles from the surrounding environment, increase photostability, and provide signal enhancement due to an increase of the number of the functional molecules or particles doped within per silica NP,

which prompt the researchers to investigate them in various bioapplications. The emerging applications of silica-based NPs would also lead to a variety of essential tools in medical diagnostics.

This chapter focuses on recent advances in silica-based NPs, various process to synthesize silica or doped-silica NPs. Then, the functionalization of silica-based NPs with various chemicals and biomolecules and the biological applications of functional and biifunctional silica-based NPs with respect to biosensing are also described.

2. SYNTHESIS OF SILICA-BASED NPS

A variety of techniques are available for the preparation of NPs. Typically, two general routes can be followed to prepare silica-based NPs. One is the Stöber technique, which is mainly used for synthesizing pure silica NPs and hydrophobic organic dye-doped NPs [39-41]. In a typical Stöber-based protocol, a silica alkoxide precursor (such as tetraethoxysilane, TEOS) is hydrolyzed in an ethanol and ammonium hydroxide mixture. The hydrolysis of TEOS produces silicic acid, which then undergoes a condensation process to form amorphous silica particles.The NP diameter can be controlled through the parameters involved in the process, i.e., temperature and concentration. This method is relatively simple but limited by the non-uniformity of the particles obtained, and further filtration and separation are needed to isolate different size fractions. Another significant limitation of the conventional Stöber procedure is that it is inherently incompatible with proteins. To overcome these shortcomings, so-called “sol–gel” processing conditions can be adopted to prepare silica-based biocomposites at low temperatures under mild chemical conditions [42-45]. The other is reverse micelle or water-in-oil (W/O) microemulsion system, primarily for the dye and the magnetic NPs doped SNPs [46-48]. In a typical W/O microemulsion system, water droplets are stabilized by surfactant molecules and remain dispersed in bulk oil. The nucleation and growth kinetics of the silica are highly regulated in the water droplets of the microemulsion system, and the dye molecules or particles are physically encapsulated in the silica network, resulting in the formation of highly monodisperse doped silica NPs. The diameter of the NPs can be tuned by controlling the size of the water cores and the water-to-surfactant molar ratio. Compared with the Stöber process, this method has been shown to be highly efficient for the fabrication of highly spherical and monodispersed NPs.

3. DOPED SILICA NPS

Uniform doped silica NPs have attracted a great deal of attention recently, both for their fundamental scientific interest and their potential biological applications. This section will present the current preparation methods, practical features, and diverse potential applications of doped silica NPs based on luminophore, QDs, magnetic particles, and noble metal particles.

3.1. Luminophore-Doped Silica NPs

Fluorescence-based detection techniques have been used extensively for a wide range of applications in biochemical research and disease diagnosis. To detect trace levels of analytes, fluorophores are commonly exploited as signal transduction tools. Otheriwise, only a limited number of fluorophores can be linked to a biomolecule without interfering with its binding specificity or causing it to precipitate, which makes analyses more complicated because signal amplification is needed when targeting trace amounts of analytes. All of these limitations have greatly hindered the use of fluorophores for modern bilogical development while the luminophore-doped silica NPs has initiating a promising era. Furthermore, these NPs have high fluorescence intensity for their containing of a large quantity of fluorescent molecules housed inside the silica matrix, good photostability duing to the exclusion of oxygen by the silica encapsulation, and good potential for surface modification with various biomolecules [49, 50]. The as prepared dye-doped silica NPs demonstrated similar absorption and emission spectra to native dye molecules. While the Stöber process is commonly used for the preparation of hydrophobic dye-doped NPs, hydrophilic dyes tend to be encapsulated using the microemulsion method [7].

Various diameters of dye-doped silica NPs, which include tris (2,2′-bipyridyl)-dichlororuthenium(II) hexahydrate (Ru(bpy)), Rhodamine 6G, tetramethylrhodamine (TMR), TMR-dextran (TMR-Dex), fluorescein 5-isothiocyanate (FITC), and Cy5-NHS were reported [46, 51-53]. Except for a slight red-shift in the emission of Ru(bpy)-doped NPs, no other significant changes in the absorption and emission properties of the other dye-doped NPs were observed [53]. Compared to the pure dye, the dye-doped NPs did not suffer from photobleaching over a long period of continuous intensive light exposure.

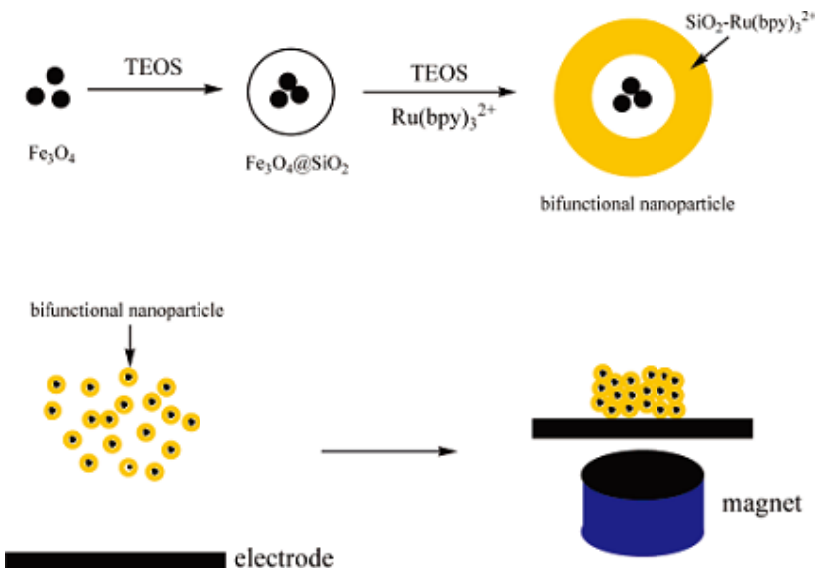


Figure 1. Scheme for the preparation of magnetic, luminescent nanoparticles, and fabrication of a bifunctional nanoparticle-modified electrode (from Ref. [56] reproduced by permission of American Chemical Society, https://s100.copyright.com/CustomerAdmin/PLF.jsp?lID=2011041_1303267153056).

The preparation, characterization and application of dye-doped NPs have been extensively studied by Tan's group [54]. For example, they have reported the preparation of monodispersed luminescent NPs composed of an metalorganic luminescent dye Ru(bpy) physically doped inside silica using controlled ammonia-catalyzed hydrolysis of TEOS in a W/O microemulsion method as shown in Fig. 1 [55,56]. The doped silica NPs with different sizes were shown an excellent uniformity by transmission electron microscopy (TEM) images, i.e., 5±1 nm for small, 63±4 nm for medium, and 400±10 nm for large size particles. There were also recent reports on the ECL of Ru(bpy) -encapsulated silica NPs, which served as tri-*n*-propylamine (TPA) or polyamine sensors [56-59]. In those studies, Ru(bpy) could be directly oxidized on the electrode surface to produce an ECL signal. The physical encapsulation of tris (1, 10-phenanthroline) ruthenium (II) chloride [$Ru(phen)_3Cl_2$] by the Stöber method was reported by Rosenzweig et al [60]. Interestingly, the bright and photostable luminescent silica NPs showed quite a narrow size distribution with negligible leakage of dye molecules. To demonstrate the utility of the NPs in bioassays, they further modified their surface with streptavidin and demonstrated their binding to biotinylated glass slides.

The organic dye TMR was made water soluble by linking it with a hydrophilic dextran molecule, then particle synthesis was performed under acidic conditions and showed reduced leakage because of the electrostatic attraction to the silica matrix [61]. Using a modified Stöber method, Wiesner [62] also described the synthesis of highly fluorescent monodisperse tetramethylrhodamine isothiocyanate (TRITC) doped silica NPs in the 20–30nm size range with core/shell architecture. These NPs were 20 times brighter, more photostable than their constituent fluorophore, and were amenable to specific labeling of biological macromolecules for bioimaging experiments. The fabrication of near-infrared (NIR) cyanine fluorophore doped silica NPs was also described using a modified Stöber synthesis [63]. Using this approach, multiple fluorophores can be loaded into a single particle, allowing the light absorption and emission properties of the particle to be controlled independent of particle size.

Accordingly, lanthanide-doped silica NPs which have unique luminescence properties such as high quantum yields, sharp absorption and emission lines, and superior photostability, may also have very interesting biological applications [64-66]. Reverse microemulsions were used by Trindade's group [67] to encapsulate 3-hydroxypicolinate complexes of Eu(III) and/or Tb(III) complexes in silica NPs. the preparation of particles with an average diameter of 45 nm and below confirmed that reverse micelles were useful for producing such NPs that are less than 100 nm in diameter. Their earlier work [68] to prepare silica NPs by encapsulating Eu (III) complex with coordinated 3-hydroxypicolinate ligands, $[Eu(H_2O)\text{-}(picOH)_2(\mu\text{-}HpicO)]\cdot 3H_2O$ using the sol-gel method led to particles with an average diameter above 100 nm. Recently, Lanthanide (III) (Eu and Tb)-imidazoledicarboxylic acid complexes were immobilized on colloidal mesoporous silica by Huo' team with diameter less than 100 nm by covalent bond grafting technique [69], the uniform and monodisperse lanthanide(III) complexes-functionalized mesoporous silica NPs show strong photoluminescence upon irradiation with ultraviolet light and exhibit long lifetimes. Ultrafine, pure cubic polyvinylpyrrolidone (PVP)/$NaYF_4$ nanocrystals co-doped with lanthanide ions such as Yb/Er or Yb/Tm were synthesized using PVP as stabilizer by Li and Zhang [70] with strong multicolor upconversion fluorescence under excitation from a 980-nm NIR laser, which were then coated by a uniform layer of silica to form a core–shell structure, with the silica

thickness adjustable down to 1-3 nm. The combination of two luminescent centers within silica enables dual visible and NIR-emitting spectra have been reported. There's report introduced heterometallic silica NPs with dual NIR-visible luminescence with $[Ru(dipy)_3]Cl_2$ and $[YbHL]Na_4$ (H_4LNa_4 is *p*-sulfonatothiacalix[4]arene) complexes visible -NIR luminescent centers [71].

3.2. Quantum Dots-Doped Silica NPs

Semiconductor nanocrystals (NCs) or QDs are a new generation of nanostructured materials used as fluorescent labels due to their numerous advantageous features, such as broad excitation spectra for multicolor imaging, robust and narrowband emissions [72]. Possible application areas for QDs include assay labelling, fluorescence resonance energy transfer (FRET) biosensing, optical barcoding and *in vivo* imaging [73, 74]. Nonetheless, QDs cannot be used directly in most cases because of certain limitations in practical application such as toxicity, hydrophobicity, and interactions with oxygen. Extensive research efforts have been under way to overcome these disadvantages and silica coating is one of the significant attempts.

Silica-capped QDs have been achieved using alkoxysilane with a silica shell thickness ranging from 2-5 nm [75] to 40-80 nm [76]. Recently, a series of QDs-doped silica NPs have been obtained including CdSe/ZnS@SiO_2[75], CdSe/ZnS@SiO_2[77], CdSe/ZnSe/ZnS@SiO_2 [77]and $CdSe_xTe_{1-x}$/ZnS@SiO_2 [78] with single QDs core and ZnO@SiO_2[79], ZnO@SiO_2[80,81] with multiple QDs core based on the Stöber sol-gel chemistry and CdSe@SiO_2[82], PbSe@SiO_2 [82], InP/ZnS@SiO_2 [83], CdSe/ZnS@SiO_2[84], CdS@SiO_2[85], CdSe/ZnS@SiO_2[84,86,87], ZnS:Mn@SiO_2[88] with single QDs as the core and CdTe/CdSe/ZnS@SiO_2[86]with multiple QDs in the center based on the microemulsion systems. Selvan [89] also demonstrated that the PbSe QDs could be encapsulated as a single core within a spherical silica shell or multiple cores within ～40-160 nm shells using a simple silica coating method in a reverse microemulsion.Various others techniques such as spray drying [90], RF sputtering [91,92] have also been demonstrated for ZnO QDs@SiO_2 composite formation.

Torimoto's group reported a novel synthesis of silica-coated CdS QDs with a void space, in which a CdS core was incorporated in hollow SiO_2 shell particles to form a ''jingle-bell''-shaped nanocomposite, using a size-selective photoetching technique [93-95]. The size of the CdS core was adjusted from 3.7 to 2.8 nm with a relatively narrow size distribution by changing the wavelength of the monochromatic light used for the size-selective photoetching (letch) from 514 to 458 nm [94].

Ying et al. [96] described a simple strategy for making plain CdSe QDs or ZnS-capped CdSe QDs water soluble by coating with silica using the revrse-microemulsion approach. Single QDs or multiple QDs were encapsulated within each silica nanosphere and the thickness of the silica shell could be controlled by varying the TEOS concentration.

Yang demonstrated aqueous colloidal CdTe QDs could be incorporated in silica with single CdTe QD cores by microemulsion method. Further experiments demonstrated photostability of the CdTe QDs greatly increased after silica coating, and the number of CdTe QDs could be tuned by manipulating the electrostatic interactions between the negatively

charged CdTe QDs and the negatively charged silica intermediates within the micro water droplets [97, 98]. To solve the problem of large loss in fluorescence, Gao et al. optimized the preparation by incubating the CdTe QDs in an alkaline solution for a certain time prior to the reverse microemulsion process [99].

A facile method for the preparation of CdSe/ZnS@SiO_2 NPs has been developed using a reverse microemulsion system by Darbandi [100] and a time interval addition of silica precursor method has been used to tune the size and photoluminescence property. By a similar method, Borri [101] demonstrated the fabrication of CdSe/ZnS@SiO_2 with single QDs in the center of a thin silica shell. Spherical particles of <20 nm diameter had good morphology, small size distribution and up to 15% quantum yield, which paved the way for the exploitation of silica-coated QDs in biophotonics applications such as FRET.

Gao and Hu [102] have developed a surprising method for preparation of ultrastable CdSe/ZnS QDs based on silica shells and amphiphilic polymers (Fig. 2). Amazingly, this synergistic combination yields QDs with significantly improved resistance to harsh chemical treatment including strong acids, which has never been achieved previously using either coating material alone. They further demonstrated the resultant doped silica NPs for pH sensing and applications of this new class of QDs in quantitative imaging, their *in vivo* behaviors, and long-term toxicity are currently under investigation.

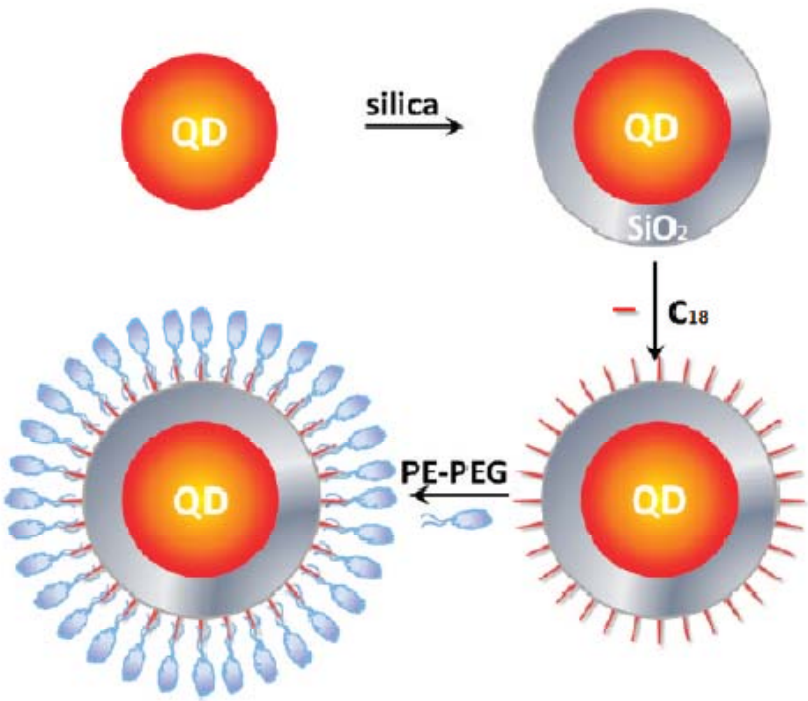


Figure 2. Schematic illustration of a double-phase transfer procedure for QD@SiO2@PE-PEG synthesis. Single hydrophobic QDs are encapsulated within a layer of hydrophilic silica, followed by surface modification with a hydrophobic silane, OTMS. The hydrophobic QD@SiO_2-C18 is then solubilized with PE-PEG (from Ref. [102] reproduced by permission of American Chemical Society, https://s100.copyright.com/CustomerAdmin/PLF.jsp?lID=2011041_1303267971274).

A new generation of silica encapsulated single CdSe/ZnS QDs was synthesized based on the surfactant templated mesoporous silica coating [103]. The cationic surfactant molecule, cetyltrimethylammonium bromide (CTAB), played two important roles in this process, solubilization of hydrophobic QDs into aqueous solutions and templating the nanometer-sized pore formation.

3.3. Magnetic Particles-Doped Silica NPs

Magnetic NPs have attracted a lot of interests devoted to their unique properties and potential applications. However, for bio-related applications, the pure magnetic NPs might possess some obvious shortcomings associated with the formation of large aggregates, alteration of magnetic properties and their toxicity in the biological system. Therefore, it is necessary to coat a protective layer to ensure their chemical stability and improve their biocompatibility. Hence, the magnetic NPs coated with a silica surface are perhaps one of the most ideal options [104,105].

Magnetic NPs-doped silica can be obtained by various techniques including mechanical process [106] and embedding/fumigating porous silica into the solution/steam of precursors such as M(II/III) solutions (M = Fe, Co, Ni, Zn, Mn, etc.) and some volatile M(II/III) compounds [107-109]. These methods, however, only provide products with a low content of inclusion (less than 10 wt.%) and weak magnetic response. Electrodeposition technique has also been used to prepare multi-layer $Fe/Fe_2O_3@SiO_2$ NPs [110,111], which still require improvement in the homogeneity and dispersion of NPs.

Several research groups have synthesized magnetic NPs-doped silica relied on the common Stöber process [112-117]. For example, Im and co-workers[114] have prepared silica colloids loaded with superparamagnetic iron oxide NPs using this process, their study showed that the final size of silica colloids depended upon the concentration of iron oxide NPs and the type of solvent because the size of silica was closely related to the number of seeds in the emulsion drops. Larger colloids were obtained at lower concentrations of iron oxide NPs and in alcohols with higher molecular weights.

Ohmor and Matijevic [118] prepared spindle-type hematite particles with length of about 400 nm, and coated them directly with silica. Using surfactant stabilized magnetite NPs as seeds, Philipse [112] and Lu [115] respectively prepared silica-coated magnetite particles. A systematic investigation of the formation of silica-coated magnetite particles via sol–gel approach was conducted by Fu [116]. They demonstrated that the size of the particles could be controlled by changing the SiO_2/Fe_3O_4 ratio.

Ammar [119] made use of the Stöber method—to encapsulate FeNi NPs within a silica shell. Followed by the same process, monodispersed, amorphous cobalt NPs coated with silica in aqueous/ethanolic solution was obtained [120]. Both the initial, amorphous NPs and their crystalline counterpart were magnetic, which promised important applications for ferrofluid preparation and for magnetic recording media. More recently, novel cubic nanocapsules consisting of metallic iron core and amorphous silica shell were fabricated by Ni et al. [121] through a simple chemical reduction route.

Microemulsion synthesis of magnetic NPs-doped silica is another popular method [122-130]. A systematic study of the formation of silica-coated Fe_3O_4 particles via a modified reverse microemulsion approach has been described by Zhang and co-workers [131]. Based

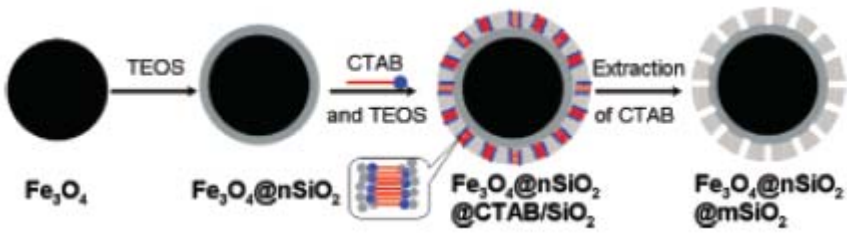


Figure 3. The formation of Fe_3O_4@$nSiO_2$@$mSiO_2$ microspheres (from Ref. [137] reproduced by permission of American Chemical Society, https://s100.copyright.com/CustomerAdmin/PLF.jsp ?lID=2011041_1303269731071).

on the same system, Tago [132] have synthesized ferrite NPs (Fe_3O_4 and $Co_xFe_{3-x}O_4$) coated with silica. Shi et al. [133] reported a novel scheme to fabricate uniform magnetic nanospheres with a magnetic core/mesoporous silica shell structure, and its drug storage and in vitro release property were also demonstrated.

The aim of Lee's work [134] was to propose a new reaction pathway to synthesize magnetic core/shell type silica NPs with improved homogeneity, monodispersity, and a magnetic property close to that of the core. Core/shell type silica NPs with an average diameter of 11 nm were synthesized by coating Fe_3O_4 core in an alkyl alcohol (octanol) with amorphous silica shell. The synthesized NPs were calcined under various conditions to produce different types of core/shell particles. The saturation magnetization of the particles calcined for 5 h was found to be higher than those of the other particles.

Recently, a novel procedure on coating magnetic NPs and their clusters with mesoporous silica was developed by Hyeon [135,136] based on a surfactant-templating approach. Using a similar procedure, Zhao's group [137] reported the synthesis of sandwich structured mesoporous silica microspheres (～500 nm) with a silica-coated magnetite core and ordered mesoporous silica shell with perpendicularly oriented channels (Fig. 3).

3.4. Noble Metal Particles-Doped Silica NPs

Surface-enhanced Raman spectroscopy (SERS) leads to an increase in signal intensity of several orders of magnitude, making it a fascinating method for sensitive biological detection. Meanwhile, noble metal NPs such as gold (Au) and silver (Ag) are considered to be promising materials and are emerging as effective SERS substrates. Recently, several groups have reported on research using SERS and nanotagging of materials using Raman active NPs [138,139]. In order to prepare more robust Raman based tags and create consistent surface chemistry, novel synthesis methods to prepare Au@SiO_2 or Ag@SiO_2 core-shell NP-based SERS tags have received considerable interest in recent years [140].

Gold colloids have been homogeneously coated with silica using the silane coupling agent (3-aminopropyl)-trimethoxysilane as a primer to render the gold surface vitreophilic. After the formation of a thin silica layer in aqueous solution, the particles were transferred into ethanol for further growth using the Stöber method [141]. Mine [142] have prepared silica-coated gold NPs through a conventional citrate-reduction method without surface

modification for gold NPs, by means of a seeded polymerization technique following the same method. Based the modified Stöber method, silica-coated gold NPs were successfully produced by a number of groups [143-147].

A general method to coat Au colloids with silica was described by Blaaderen [148]. After the absorption of PVP, the stabilized particles could be transferred to a solution of ammonia in ethanol and directly coated with smooth and homogeneous silica shells of variable thickness by addition of TEOS in a seeded growth process.This method is especially useful for colloidal particles that cannot be covered directly with SiO_2 by a Stöber-like growth process.

A reverse microemulsion method was reported by Ying's group [149] for preparing monodispersed silica-coated gold (or silver) NPs without the use of a silane coupling agent or polymer as the surface primer. This method enabled a fine control of the silica shell thickness with nanometer precision. As compared to the Stöber method reported for direct silica coating, which can only coat large gold particles (～50 nm in diameter) at low concentrations ($<1.5 \times 10^{10}$ particles mL^{-1}), this new approach is capable of coating gold particles of a wide range of sizes (from 10 to 50 nm) at a much higher concentration ($\sim 1.5 \times 10^{13}$ particles mL^{1}).

A synthesis method was described by Xu and Perry [150] to prepare $Au@SiO_2$ core-shell spheres, using a commercial gold colloid and tetraethyl orthosilicate as the precursors. Based on their synthesis concept, the Au@silica coreshell spheres, each containing a single gold nanoparticle or an aggregate of several gold NPs at the center, have been successfully prepared.

Recently, a convenient methodology to fabricate silver-coated $Au@SiO_2$ core/shell nanomaterials ($Au@SiO_2@Ag$ nanostructures) was developed by cyclic electroplating and stripping of $AgNO_3$ on the surface of $Au@SiO_2$ core/shell NPs, and the $Au@SiO_2@Ag$ NPs served as sensitive and reproducible SERS substrates [151].

Recently, a novel approach was reported by Brioude [152] using the Stöber method allowed breaking of the symmetry of core–shell systems based on metallic core and metal oxide shell. By adjusting the proportion of the TiO_2 precursor with regard to the silica precursor, different morphologies of the $Au@(TiO_2, SiO_2)$ NPs have been obtained displacing the gold particle from center to eccentric positions leading to acorn-like and raspberry-like structure.

The $Ag@SiO_2$ core-shell NPs can also be synthesized by the common Stöber method [153-159] or in reverse microemulsion [160,161]. For example, Natan and co-workers have prepared glass-coated, analyte-tagged nanoparticle Raman tags, where a nanometer-scale Au or Ag core is functioned by Raman dye and encapsulated with a silica layer [162]. Yu's group[163,164] have reported a novel simplified method based on reverse micelle technique for synthesis of surface-enhanced Raman scattering tags which were composed of silver core, Raman active molecules and silica shell. The Raman active molecules absorbed on the silver surface could yield strong SERS.

Zhao's group[165] have developed $SiO_2@Au@SiO_2$ sandwich nanoaggregates constructed with one, two, and three SiO_2-Au building blocks. The irregular polycore aggregates were greatly eliminated through adsorption of PVP molecules on the surface of the building block. Different sized aggregates exhibited distinct surface enhancement for amplifying near-infrared (NIR) signals when an NIR dye was placed in the electromagnetic

field of the nanostructures, which may open a new door for applications of surface enhancement in the sensitive detection of biological samples in the NIR region.

Monodisperse Au@SiO_2 NPs were prepared by vortex mixing technique [166] and linear assemblies of silica-coated gold NPs were obtained using carbon nanotubes as templates [167]. Additionally, silica shells were directly coated onto surfactant-capped gold nanorods by a simple one-step method, which required no intermediate coating of the gold nanorod prior to the formation of the smooth silica shell and the thickness of the shell could be accurately controlled [168].

3.5. Bifunctional Silica-Based NPs

Nano-scale composites having bifunctional properties, which construct materials possessing desirable properties in a single entity, are gaining tremendous interest largely due to their unique coupled behaviours. Silica-based NPs with bifunction could be used in a wide range of applications in biological systems because such NPs possess a combination of properties [169-171].

Generally, a lot of work has been focused on fabricating bifunctional nanoarchitecture by combining the magnetic NPs with the luminescent reagents [172-175]. Advantages of the bifunctional NPs are two-fold: one is the simple detection of the NPs by conventional optical means and the other is the easy manipulation by an external magnetic field. For example, Dong [56] synthesized a new kind of nanoarchitecture containing a magnetic Fe_3O_4 core and a luminescent Ru(bpy)-encapsulated silica shell. They further explored these bifunctional NPs to fabricate an efficient ECL sensor, which based on the multilayer films of the as-prepared NPs stimulated by an external magnet (Fig. 1). For the longstanding interest in luminescent metalbased materials, Zu's group [176] reported the synthesis and investigation of multifunctional core-shell magnetic silica nanocomposites, with the Fe_3O_4 core coated with a silica shell, to which luminescent ruthenium(II) complexes were covalently attached and further encapsulated with an additional layer of silica shell. The magnetic, luminescent, and ECL behavior of these nanocomposites were studied in their research.

Hur et al. [177] have reported the fabrication of silica-coated magnetic ferrite NPs functionalized by luminescent Ln ions in which the Ln ions were attached to the silica surface through the 2,29-bipyridine-4,49-dicarboxylic acid (BDA)molecule. The biocompatible luminescent/magnetic NPs, in which Ln ions act as luminescent markers and silica-coated magnetic NPs serve as cores, show a significantly enhanced luminescence due to the ligand-to-metal energy transfer.

Until recently, Zhang [178] reported the fabrication and characterization of magnetic mesoporous silica nanospheres covalently bonded with NIR luminescent lanthanide complexes, in which Fe_3O_4 magnetic NPs were embedded in the mesoporous silica nanospheres and $Ln(DBM)_3$phen complexes were covalently bonded to the framework of mesoporous silica based on the modified 1,10-phenanthroline (phen-Si). These novel nanospheres had magnetic separability and NIR luminescent properties.

Similarly, the core-shell structure Fe_3O_4@SiO_2-doped with Tb-complex bifunctional nanocomposites with emitting green fluorescence and magnetic behavior reported by Yu et al. [179], which only exhibited a low value (7.44 emu g^{-1}) at room temperature.

Bifunctional doped silica NPs consisting of QDs and magnetic NPs, are emerging as a versatile system for both fluorescence- and magnetic-based applications. Hyeon et al. [135] reported a synthetic procedure for the fabrication monodisperse magnetite (Fe_3O_4) nanocrystals and CdSe/ZnS QDs embedded in uniform pore-sized mesoporous silica spheres with an average size of 150 nm. These mesoporous silica spheres were further applied to the uptake and controlled release of drugs. The encapsulation of both QDs and magnetic NPs in micelles, microemulsion, and finally in silica was illustrated by Ying et al.[180] A two step synthesis was used to derive CdSe/γ-Fe_2O_3@SiO_2 nanocomposites: magnetic NPs and QDs were prepared separately, prior to their introduction into the reverse microemulsion medium for silica coating. This direct silica-coating approach has enabled a wide variety of bifunctional NPs to be encapsulated within spherical silica particles [181].

Bifunctional magnetic-luminescent Fe_3O_4@SiO_2/Y_2O_3:Tb nanocomposite was obtained by assembling Y_2O_3:Tb nanorods onto the surface of Fe_3O_4@SiO_2 core-shell nanostructures. The results showed that the nanocomposite displayed a strong green emission and superparamagnetic behavior at room temperature; therefore, the nanocomposite is expected to find many potential applications in biomedical fields [182].

Yamashita [163] have prepared a new class of nanosized photocatalysts composed of core/shell Ag@SiO_2 NPs with an anchored Ru(bpy) dye. The enhanced electromagnetic field in the vicinity of the Ag NPs due to localized surface plasmon resonance (LSPR) significantly enhances emission intensity of the dye, which ultimately results in the enhanced catalytic activity for photooxidation with O_2.

4. CONJUGATION OF SILICA-BASED NPS WITH DESIRED BIOMOLECULES

The linking of biomolecules to silica-based NPs is very challenging and requires an appropriate bioconjugation strategy. Various surface modifications and immobilization procedures such as physical absorption, affinity interaction, covalent conjugation, and entrapment in sol-gel matrices, have been explored [183]. These strategies have been applied to the conjugation of silica-based NPs to different biomolecules, antibodies, aptamers, DNA, proteins, phospholipids, and cells are examples of such biomolecules.

4.1. Physisorption of Biomolecules

Many of the biomolecules can be physically adsorbed onto the surface of silica NPs. For example, electrostatic adsorption of antisense oligonucleotides on poly(l-lysine) modified silica surfaces was described by Zhu [184]. Likewise, disposition of biomolecules, and polyelectrolytes, and poly(ethyleneimine), and negatively charged poly(styrenesulfonate) on Ru(bpy)-doped silica NPs by electrostatic layer-by-layer self-assembly was reported by Wei et al. [185]. A novel glucose biosensor based on the platinum and SiO_2-sol-glucose oxidase (GOD) biomimetic membrane was developed by Tang et al. [186], the SiO_2 NPs in reverse micelles could strongly adsorb many active GOD molecules, and enhance the current response of the electrode. A highly hydrophobic and non-toxic colloidal silica NPs/polyvinyl

butyral sol-gel composite membrane was prepared on a platinum wire electrode [187]. With diphtheria-toxoid (D-Ag) as a model antigen and encapsulation of diphtheria antibody (D-Ab) in the composite architecture, this membrane could be used for reagentless electrochemical immunoassay. Liang and Wang [188] have synthesized two kinds of pH-dependent magnetic nanoadsorbent based on silica-coated $MnFe_2O_4$ NPs (SMNPs) and amino-modified silica-coated $MnFe_2O_4$ NPs (AS-MNPs), and then used them to adsorb bovine serum albumin (BSA). The adsorption capacity of BSA largely depended on the pH and ionic strength of solution, BSA was adsorbed on AS-MNPs and SMNPs at the value of 164 mg g^{-1} and 100 mg g^{-1}, which attridued to the increased surface amino could be conjugated to BSA. This strategy is simple to perform, but limitation must be mentioned that physical absorption of biological targets can lead to subsequent dissociation of biomolecules and may interfere with proper folding.

4.2. Entrapment of Biomolecules by the Sol-Gel Method

Beyond physisorption, the entrapment of biomolecules by the sol-gel method may be a useful substitute for certain bioapplications. Some papers have reported the physical encapsulation of biomolecules within a porous matrix using either the Stöber method [189-191], the reverse microemulsion system [192-196], or a special one-step process under 'protein friendly' conditions [197,198].

The use of a two-step Stöber method for the preparation of biomolecule-doped silica NPs was reported recently by Luckarift and co-workers [189,190]. After prehydrolysis of TMOS in 1mM hydrochloric acid, the antibacterial enzyme lysozyme was added in phosphate buffer to form the NPs. An appreciable retention of the antimicrobial activity was observed; and similarly, butyrylcholinesterase was also successfully entrapped [191].

Jain et al. [192] have described the successful encapsulation of horseradish peroxidase (HRP) into silica NPs using TMOS, Triton X-100 and a reverse micellar method. Highly monodispersed enzyme-doped particles with an average diameter less than 100 nm were obtained. Recently, a novel nanoparticle-based electrochemical immunoassay of carbohydrate antigen 125 (CA125) was designed to couple with a microfluidic strategy using anti-CA125-functionalized magnetic beads as immunosensing probes [199]. Thionine-HRP conjugation was initially doped into silica NPs using the reverse micelle method, and then HRP-labeled anti-CA125 antibodies (HRP-anti-CA125) were bound onto the surface of the synthesized NPs, which were then used as recognition elements. The assay was evaluated for clinical serum samples, receiving in excellent accordance with results obtained from the standard enzyme-linked immunosorbent assay (ELISA) method (Fig. 4).

Based on earlier work involving the preparation of protein-doped, macroporous, monolithic silica materials under 'protein friendly' conditions using a series of sugarsilanes, HRP-doped NPs were synthesized in a one-step process in Brennan's group [198]. One merit of this study was that these precursors could be used in water or buffer under alcohol-free neutral conditions, which permitted a rather mild incorporation of the biomolecules. The encapsulated enzyme was observed to remain its activity for more than 3 months.

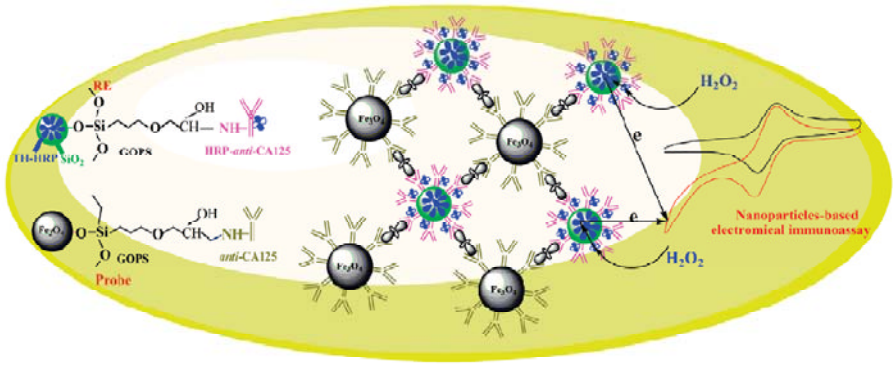


Figure 4. Construction of the Immunosensing Probe and Recognition Element (RE) and Measurement Protocol of the Nanoparticle-Based Electrochemical Immunoassay with a Sandwich-Type Format (from Ref. [199] reproduced by permission of American Chemical Society, https://s100.copyright.com /CustomerAdmin/PLF.jsp?lID=2011041_1303269984290).

4.3. Affinity-Based Interactions

The avidin/streptavidin-biotin interaction is the strongest noncovalent receptor-ligand interaction and cannot be affected by most extreme entironments. Hence, avidin/streptavidin linkage is a very practical conjugation approach to attach recognition agents onto silica-based NPs, which was utilized by many groups [57, 195,198,200-203].

For example, Tan's group [203] used this approach to immobilize avidin on rhodamine 6G-doped silica NPs, and then applied these to the determination of biotinylated BSA. Furthermore, the immobilization of the biotinylated glutamate dehydrogenase on the surfaceof the avidin-coated silica, enabled NPs to be used as a biosensor for glutamate determination. Ying's group recently introduced a silica-coating procedure for various hydrophobic NPs, including Au, Ag, Fe_3O_4, and ZnS:CdSe using commercially available silanes to create water-soluble NPs of 20–30nm in size, which were further functionalized directly with biotin [204]. These particles had a positive or negative surface charge which depended on the surface functional group and the solution pH. When 2-aminoethyl-aminopropyltrimethoxysilane (AEAPTMS) was used as the silane monomer, the silica coating presented surface primary amino groups which were used for biofunctionalization to create biotinylated NPs using *N*-hydroxysuccinimide (NHS)-polyethylene glycol (PEG)-biotin. In Smith's study, various conjugation chemistries were evaluated along with different levels of groups of various fluorophore-doped silica NPs. The results of the labeling step for the various doped silica NPs with the target and control aptamer showed the avidin-coated magnetic NPs and biotinylated aptamers fluorescent NPs had the highest selectivity, which also showing the ability to discriminate between target and control cells [51].

4.4. Covalent Binding

Covalent attachment of biorecognition elements to the silica-based NPs surface is commonly preferred, since this method not only decreases desorption from the particle

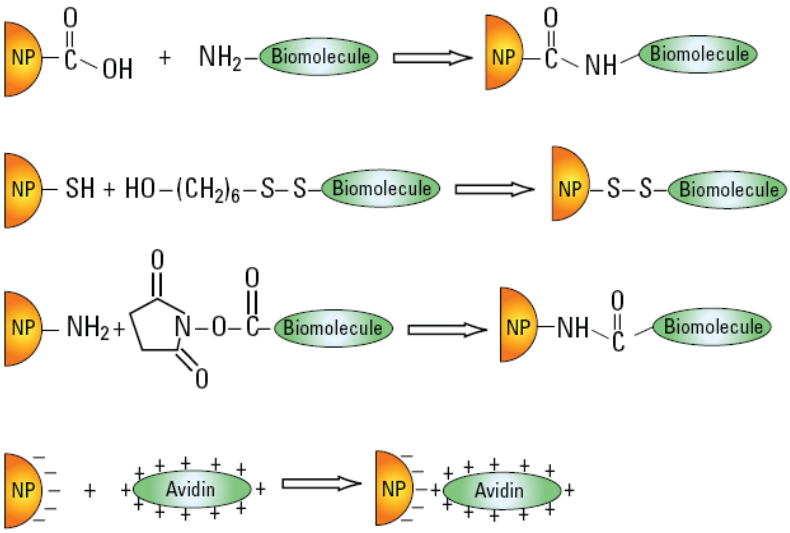


Figure 5. Representative bioconjugation schemes for attaching biomolecules to silica-based NPs for bioanalysis (from Ref. [205] reproduced by permission of American Chemical Society, https://s100 .copyright.com/CustomerAdmin/PLF.jsp?lID=2011041_1303198170814).

surface, but also leads to the production of stoichiometrically defined NPs with correctly oriented immobilized biorecognition elements. For covalent attachment, the particle surface first needs to be modified with suitable functional groups, then they can act as a scaffold for the grafting of biological moieties (DNA oligonucleotides, aptamers, antibodies, proteins, etc.) by means of standard covalent bioconjugation schemes (Fig. 5) [205].

For example, Available hydroxyl residues on silica surfaces may be activated by cyanogen bromide (CNBr) to form a very reactive cyanate ester [206]. Carboxyl-terminated silica-based NPs have pendent carboxylic acids, making them suitable for covalent coupling of oligonucleotide or other amine-containing biomolecules via carbodiimide coupling [207].

Amine-terminated silia-based NPs can be coupled to a wide variety of amine-oligonucleotides and antibodies via succinimidyl esters and iso(thio)cyanates. Otherwise, it is well known that the reaction between amine groups and aldehyde groups proceeds easily under moderate conditions with no contamination or significant deactivation of the enzyme. Based on this Schiff-base reaction, periodate oxidized GOD could be covalently attached to aminated silica NPs [208].

Disulfide-modified biomolecules can also be conjugated onto thiol-functionalized silica-based NPs through thiol/disulfide exchange reactions without any pretreatment [209]. After the bioconjugation step, the NPs can be separated from unbound biomolecules by centrifugation, dialysis, filtration, or other laboratory techniques.

5. Silica-Based NPs as Carriers for Biosensing

There are a great many potential applications of silica-based NPs in biosensing and bioanalytical applications. They have made advances in bioimaging, biolabeling, and biosensors, rational cells targeting and immunoassays.

5.1. Targeting of Cells

One of the emerging applications of silica-based NPs is to recognise, label and image specific target cells. Diverse strategies have been explored for using these NPs to target cell surface proteins to understand the complex dynamics of intracellular networks, signal transduction, and cell-cell interplay.

Recently, uniform Ru(bpy) doped silica NPs were first exploited to conjugate with mouse anti-human CD10 antibodies through silica chemistry and then applied successfully for leukemia cell identification by an optical microscopy imaging technique. [210].

Tan et al. [211] have developed a novel two-nanoparticle assay with aptamers as the molecular recognition element. Aptamer-modified Fe_3O_4@SiO_2 magnetic NPs were used as nanoharvesting agents, while aptamer-modified Ru(bpy)@SiO_2 fluorescent NPs were simultaneously added for sensitive cell detection. Combining two types of NPs, intact human leukemia cells (CCRF-CEM cells) were isolated from mixed cell batches (Bcell, human Burkitt's lymphoma cells) and whole-blood samples as little as 5min. Thy have further developed the same aptamer-conjugated NPs protocols to perform the extraction of multiple cancer cell targets using additional high-affinity DNA aptamers for recognition [212]. Aptamer-modified fluorescent Ru(bpy)-doped NPs were also used for sensitive cell detection. Ow et al. have synthesized bright, stable, core/shell fluorescent silica NPs functionalized with immunoglobulin E (IgE), to label rat basophilic leukemia (RBL) mast cells [62].

Due to the importance of QDs in current and future biomedical and clinical applications, Chen et al. [213] believe it is essential to more completely understand and verify this negative global response from cells treated with silica-coated CdSe/ZnS QDs terminated with both thiol and PEG functional groups (PEG-silane-QDs). Then, they examined the molecular and cellular response of cells treated with two different dosages of PEG-silane-QDs. Human fibroblasts were exposed to 8 and 80 nM of these QDs, and both phenotypic as well as whole genome expression measurements were made. The experimental evidence shows PEG-silane-QDs, unlike carbon nanotubes, do not activate genes indicative of a strong immune and inflammatory response or heavy-metal-related toxicity. This study also indicates that PEG-coated silanized QDs pose minimal impact to cells and are a very promising alternative to uncoated QDs.

Bardi [214] developed NH_2-functionalized CdSe/ZnS QDs-doped SiO_2 NPs with both imaging and gene carrier capabilities. They showed that QDs-doped SiO_2 NPs were internalized by primary cortical neural cells without inducing cell death *in vitro* and *in vivo*. Moreover, the ability to bind, transport and release DNA into the cell allows GFP-plasmid transfection of NIH-3T3 and human neuroblastoma SH-SY5Y cell lines.

In Xue's work [215], ZnO QDs with various emission colors were synthesized and then encapsulated within silica to form ZnO@SiO_2 core shell NPs. The *in vitro* cell culture experiments indicated that the as prepared core-shell NPs exhibited low cytotoxicity and could be promised in cell labeling applications.

A simple method for synthesis of silica coated CdSe/CdS/ZnS quantum rods (QRs) and their use as probes for *in vitro* and *in vivo* optical bioimaging was presented [216]. Confocal bioimaging of different cell lines, labeled with silica-coated QRs, showed robust uptake and good fluorescence from the NPs with low cytoxicity. The fluorescence from the tumor with no visible toxicity to the experimental animal showed the potential of these silica-coated QRs

in various biological labeling applications, including whole body *in vivo* optical imaging involving tumor targeting and diagnosis.

Sha and co-workers [217] have synthesized CdSeS QDs@SiO_2 NPs, which exhibits excellent properties. By coupling with folic acids, the CdSeS QDs@SiO_2 conjugates were successfully used for live tumor cell (HepG2 and Hela cells) imaging.

The effect of applying an alternating magnetic field (AMF) to HeLa cells after incubation with silica-coated manganese oxide perovskites NPs has been studied by Rivero [218]. The induced cellular damage or cell death mechanism had been also analyzed. Magnetic manganese oxide NPs have been coated with a silica shell achieving high water stability and biocompatibility, i.e., large cell survival after 24 h.

Monodisperse silica-coated manganese oxide NPs were synthesized and aminated through silanization by Shi et al. [219], which enabled further covalent conjugation of a fluorescent dye, Rhodamine B isothiocyanate (RBITC), and folate (FA) onto their surface for targeted imaging of cancer cells. Studies showed that the Mn_3O_4@SiO_2(RBITC)–FA NPs could specifically target HeLa cells, a human cervical carcinoma cell line overexpressing FA receptors, which suggested that the as prepared NPs could be used as a platform for bimodal imaging in various biological systems.

Li et al. [220] report a novel and simple strategy to produce fluorescent NPs by self-assembly of a conjugated polymer onto the core-shell NPs Ag@SiO_2. The NPs exhibited good monodispersity and low cytotoxicity, which promote their application in cellular imaging. Murphy et al. [221] have demonstrated the synthesis of silica coated, silver-containing tracer particles with magnetic, light scattering and SERS properties. The cytotoxic study on HT29 human colon adenocarcinoma cells by using the MTT assay showed lower cytotoxicity compared to free silver NPs. These tracer particles coud be used for bio-separations, SERS sensing and bio-imaging by fluorescence and darkfield light scattering techniques, thus making them truly multifunctional tracer particles that hold promise for different biomedical applications.

The core-shell structured luminomagnetic microsphere Fe_3O_4@SiO_2@Eu-$(DBM)_3 \cdot 2H_2O$@SiO_2 was fabricated by a modified Stöber method combined with a layer-by-layer assembly technique [222]. The luminomagnetic microspheres could be uptaken by HeLa cells and there was no adverse cell reaction. These results suggest that the luminomagnetic microspheres with magnetic resonance response and fluorescence probe property may be useful in biomedical imaging and diagnostic applications.

Ying et al. [181] described a facile synthesis of a bifunctional nanocomposite system consisting of Fe_2O_3 magnetic NPs and CdSe QDs. The resulting magnetic QDs exhibited superparamagnetism and tunable optical emission properties and were further coated with a thin silica shell and used for the labeling of different live cell membranes through a simple bioconjugation method.

The rhodamine B (RhB) covalently grafted SBA-15-structured mesoporous silica NPs (MSNs-RhB) with positively charged surface, has been developed as a drug delivery system (SAB@MSNs-RhB) for anti-ROS (reactive oxygen species)/hepatic fibrosis by loading a negatively charged drug salvianolic acid B (SAB) [223]. The results showed that the inhibiting effect of SAB@MSNs-RhB on the ROS level and proliferative activity of LX-2 cells was more remarkable than free SAB in a long term (72 h), and became more intensive with the increase of the sample concentration and the incubation time. SAB@MSNs-RhB

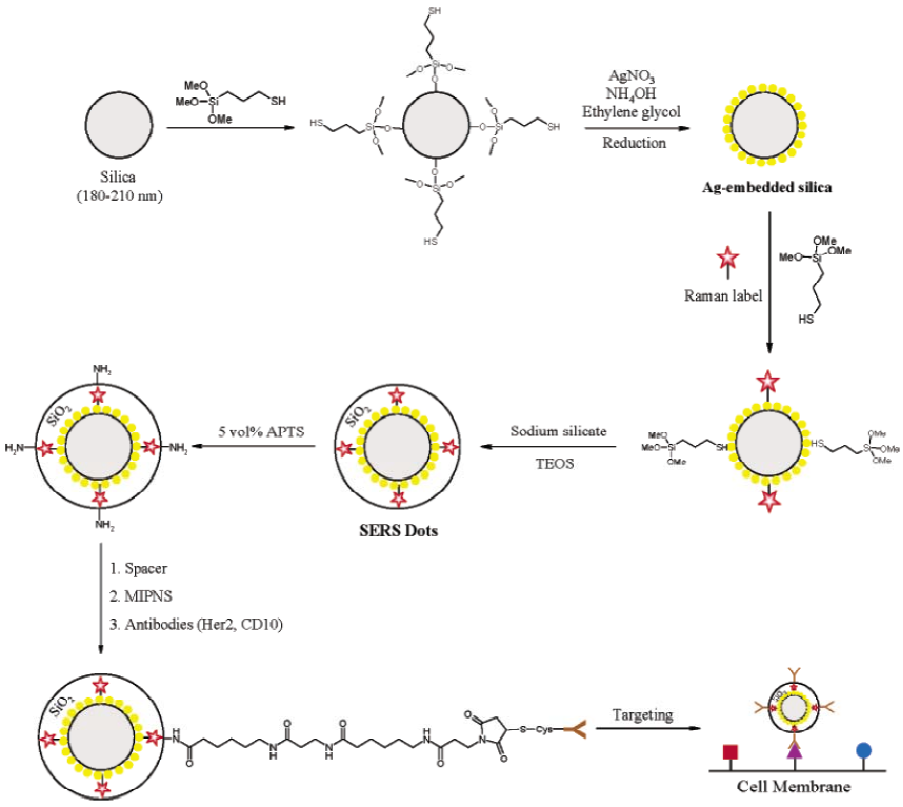


Figure 6. Schematic illustration of SERS dots synthesis and targeting of cellular cancer markers (from Ref. [225] reproduced by permission of American Chemical Society, https://s100.copyright.com /CustomerAdmin/PLF.jsp?lID=2011041_1303271444946).

enhanced the cellular drug uptake, the drug bioaccessability and efficacy for anti-ROS/hepatic fibrosis via the NPs-mediated endocytosis and the sustained release of the drug.

Zhao prepared Ru(bpy)@SiO_2 fluorescent silica NPs, which were then used for the cage of an analgesic and anti-inflammatory drug, ibuprofen, which contains one carboxylic group [224]. The drug-carrying silica NPs were incubated with RAW 264.7 cells for 24 h on plate and then washed with phosphate buffered saline to remove the non-internalized NPs. Significant fluorescence was observed inside the cells, indicating that drug-carrying silica NPs functionalized with fluorescent properties can be optically monitored inside cells with confocal fluorescence microscopy.

Kim [225] have further reported on the development and application of functionalized SERS dots composed of silver nanoparticle-embedded silica spheres and organic Raman labels for cellular targeting of cancer cells (such as breast cancer cells (MCF-7), and floating leukemia cells (SP2/0)). The particles were functionalized with antibodies against the cellular cancer markers HER2 and CD10 with a good specificity towards the targets (Fig. 6).

Fabricated multimodal NPs containing gadolinium and Ru(bpy) dye (providing for both optical and magnetic resonance imaging (MRI), detection) have also been conjugated to FA and then incubated with human cancer cells (A-549) [226].Ying et al.[181] have used silica-coated QDs and magnetic QDs for live cell imaging. Silanization in a reverse microemulsion

produced a thin silica coating on bare CdSe QDs or magnetic QDs with amine groups on the surface. The reaction between the amine group and the NHS ester resulted in covalent amide bond formation, leaving the exposed oleyl group for the effective targeting of cell membranes. The specific labeling of live cell membranes (HepG2 human liver cancer cells and NIH-3T3 mouse fibroblast cells) indicates the successful conjugation of silica-coated QDs and magnetic QDs with BAM.

Recently, a Stöber synthesis of multifluorescent silica NPs using more reactive and stablechemical residues, succinimidyl esters conjugated with fluorescent dyes was reported [64]. The as prepared NPs are suitable for flow cytometry and fluorescence microscopy analyses, also exhibited no toxicity on in vivo injection or in labeled cells, which can be employed in many areas of in *vitro* and in *vivo* biological and medical analysis.

In cell biology, the cell membrane acts as the defining principle for many biological processes. Significant efforts have been devoted towards understanding the mechanisms used by cells to allow proteins, DNA, and ions to directly traverse biological membranes. Ying [181] described a facile synthesis of a bifunctional nanocomposite system by growing CdSe QDs onto Fe_2O_3 magnetic NPs. Then were coated with a thin silica shell and used for the labeling of different live cell membranes. This study describes a new bioconjugation approach for the bifunctional NPs to target the cell membrane for the imaging of live cells.

5.2. Ultrasensitive DNA Detection

The intense fluorescence signal of one nanoparticle can be effectively used in DNA hybridization analysis and offers a distinct advantage over traditional fluorescence-based techniques. Silica NPs, doped with either magnetic materials or pigment molecules, have been widely exploited for the collection, purification and detection of DNA/RNA.

A sandwich DNA assay is presented in Fig. 7: Capture DNA is immobilized onto a solid surface and hybridized with unlabeled target DNA complementary to both the capture and probe DNA sequences. Probe DNA attached to dye-doped silica NPs is then added. One probe DNA hybridizes one target DNA and thus immobilizes one dye-doped nanoparticle to the surface, bringing many dye molecules for signaling. With the monitoring of fluorescence intensity or counting the number of fluorescent spots from the surface-bound TMR-doped NPs, DNA target molecules have been detected down to subpicomolar levels; single

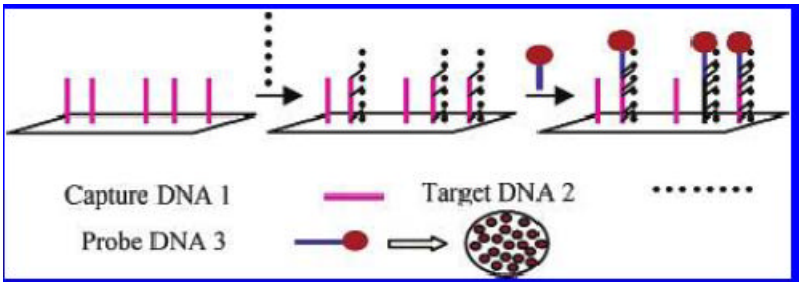


Figure 7. Schematic representation of a sandwich DNA assay based on bioconjugated silica NPs (from Ref. [227] reproduced by permission of American Chemical Society, https://s100.copyright.com /CustomerAdmin/PLF.jsp?lID=2011041_1303262595399).

nucleotide polymorphism analysis is also feasible [227]. This strategy could be extended to the use of NPs as fluorescent labels for DNA and protein microarray technology to meet the critical demand for enhanced sensitivity.

A new and sensitive electrochemical DNA hybridization detection assay, using tris 2, 2'-bipyridyl)cobalt(III) (Co(bpy))-doped silica NPs as the oligonucleotide labeling tag was described by Fang [228].The Co(bpy) labeled DNA probe was used to hybridize with target DNA immobilized on the surface of glassy carbon electrode. Due to the large number of Co(bpy) molecules inside silica NPs linked to oligonucleotide DNA probe, the assay showed a high sensitivity with a detection limit of 2.0×10^{-10} mol L^{-1} for the target oligonucleotides.

Wang' group [202] reported an improved recovery method for target ssDNA using amino-modified silica-coated magnetic NPs. A linear DNA probe was then immobilized onto NPs through streptavidin conjugation using covalent bonds. A target single-stranded DNA (ssDNA) had been successfully recovered from a crude sample under a magnet field through their special recognition and hybridization. This method has also been successfully used to recover trace concentrations of target ssDNA fragment of sever acute respiratory syndrome (SARS) virus with high efficiency and good selectivity.

Yu and co-workers [229] described a novel analytical technique, which combined the $Ag@SiO_2$ nanoparticle-based Raman tags with silica-coated magnetic nanoparticle-based separation technology for detection of DNA sequences related to HIV. The utilization of magnetic NPs not only possesses the advantage of superparamagnetism, but also preconcentrates the analyte thus efficiently amplifying the Raman signal.

Plasmid DNA could be isolated from the crude bacteria efficiently by use of amino-modified silica coated magnetic NPs (ASMNPs) through the formation of plasmid DNA-ASMNPs complexes and released easily with 3M NaCl [230]. From the downstream application of the isolated plasmid DNA, it can be seen that the isolated plasmid DNA retains biological activity with all of the operation under the external magnetic fields.

Recently, Chang's group [231] reported the feasibility of chemically functionalized magnetic silica NPs for high-throughput magnetic DNA separation process using electrostatic interaction with a negative phosphate backbone of DNA. However, the results had a lack of systematic investigation to elucidate the magnetic separation process due to the ill-defined morphology and dispersion. In the further work [232], they prepared well-defined magnetic NPs and demonstrated magnetic DNA separation as a function of the Si-magnetic NPs' particle sizes as well as control of the electrostatic strength according to various amino groups. It is expected that the aminofunctionalized silica-coated magnetic NPs described here will be useful for magnetic DNA separation methods using a simple treatment and a high-throughput process involving selective interaction, replacing conventional silica-based processes.

In Vallet-Regí's system [233], oligonucleotide-modified mesoporous silica, encapsulating iron oxide superparamagnetic NPs, was loaded with fluorescein and subsequently capped with magnetic nanocrystals functionalized with the complementary DNA strand. Ultrasmall and uniform silica-coated magnetic NPs were first treated with (3-mercaptopropyl) trimethoxysilane. The mercaptosilane-activated NPs were then allowed to react with 5-prime disulfidemodified oligonucleotides. The attachment of oligonucleotides onto the solid support was based on the thiol/disulfide exchange reaction. Oligonucleotides attached by this method provided a highly efficient substrate for nucleic acid hybridization and primer extension assays. The successful attachment of disulfide modified oligonucleotide

to the nanoparticle's surface was tested by double-stranded DNA intercalator reagent ithidium bromide (EtBr). The formation of the double-stranded hybrid was detected by using an intercalation reagent, EtBr; and a clear fluorescence signal from the hybrid was detected. This strategy is being employed to make useful magnetic probes for the separation of target oligonucleotides, such as cellular m-RNA [234].

A novel method for preparing gold nanorods that were first coated with a thin silica film and then functionalized with ssDNA was presented [235]. Amine-modified ssDNA is attached to the silica-coated gold nanorods via a reductive amination reaction with an aldehyde trimethoxysilane monolayer. The nanorods exhibit an intense absorption band at 780 nm, and were used to enhance the sensitivity of surface plasmon resonance imaging (SPRI) measurements on DNA microarrays.

The infrared emissivity of silica-coated Au NPs deposited on indium tin oxide substrates was investigated by Franzen [236]. Silica-coated Au NPs were then coated with DNA and tested as labels for two types of hybridization detection assays (direct and sandwich assay). Target DNA concentrations as low as 100 pM were achieved for both assays with the Au NPs as labels and as low as 10 pM in the sandwich assay when silica-coated Au NPs were used. These results show that thermographic detection of blackbody radiation emitted by Au NPs can be successfully used to develop a sensitive detection assay and that the detection limit can be lowered by coating the Au NPs with a silica layer.

A direct silica-coating method has been developed for the gram-scale synthesis of well-dispersed $Ag@SiO_2$ NPs [237]. Subsequent surface functionalization via the well established silica surface chemistry provided arching points for straightforward bioconjugation with aminoterminated oligonucleotides. Fast hybridization kinetics of the resulting robust oligo-modified $Ag@SiO_2$ nanoprobes with complementary target oligonucleotides render themselves very useful for the fast colorimetric DNA detection based on the sequence-specific hybridization properties of DNA.

Han and co-workers [238] have reported monodisperse $Au@SiO_2$ NPs functionalized with carboxylic groups for further bioconjugation with amino-terminated oligonucleotides. The oligonucleotide-modified $Au@SiO_2$ nanoprobes have been applied in the fast colorimetric DNA based on the sequence specific hybridization properties of DNA. Simple diagnostic process could be achieved by simply heating the solution of DNA attached $Au@SiO_2$ NPs to a temperature higher than melting point, and the following cooling process could lead to the obvious aggregates/precipitates for the fast colorimetric DNA detection. Liu and Han [239] reported an enfficient process for preparing monodisperse $Au@SiO_2$ NPs using homogeneous shaking without the use of surface-coupling silan agents or large stabilizers. Subsequent covalent bioconjugation of the aldehyde- functionalized $Au@SiO_2$ NPs with various biomolecules was successfully employed to make robust nanoprobes for fast, colorimetric DNA and proteins detection based on the sequence-specific hybridization properties of DNA and specific binding affinity between proteins.

A time-resolved fluorescence assays based on a two-probe tandem DNA hybridization assay including capture DNA1, probe DNA2, and target DNA3 was prepared with long-lived luminescent europium complex doped silics NPs as the biomarker [240]. This approach was successfully employed for preliminary application in the detection of pure cultured E. coli, it might be an effective tool for pathogen DNA monitoring.

Ru(bpy)-doped silica NPs have been used in a one-color microarray system that has shown good correlation with the phycoerythrin labeling method, with better photostability

and a 20×lower detection limit [241]. Cy3- and Cy5-doped silica NPs have also been used for two-color microarray detection in a sandwich assay format and exhibited 10×higher sensitivity than the conventional cyanine dyes. Although the technology of nanoparticle-based microarrays is still in its infancy, these advances showed the great potential of NPs for microarray analysis in genetic screening, proteomics, and medical diagnostics.

5.3. Biosenors

Biosensor developers utilize advanced biotechnology to create state of the art products for the detection and quantification of analytes in clinical settings. Such devices must link high sensitivity and selectivity with miniaturization, high speed, and low cost. Nanostructures have been used extensively as immobilized materials for the fabrication of biosensor [242]. Recently, many groups have been reported to immobilize and stabilize biomolecules for application in biosensors based on silica-based NPs. By immobilizing biomolecules in silica-based nanospheres developers can provide systems with high loading capacities for biomolecular immobilization, which have high volumetric activity and enhanced mechanical stability [183,243]. In addition to sol-gel-based entrapment of biomolecules, covalent conjugation has also been extensively used for the preparation of biosensors [183].

Wang and Zhang [244] have constructed a H_2O_2 biosensor using HRP-encapsulated silica colloids. The HRP based hybrid material was prepared from natural chitosan and tetrakis(2-hydroxyethyl)orthosilicates (THEOS), and provided a fast amperometric response towards H_2O_2. To monitor the loading capacity of the silica NPs towards biomolecules, Tang et al. compared the effect of various NPs (such as nanogold, nanosilver and nanosilica) on the properties of the electrochemical immunosensor using a polyvinyl butyral-based sol–gel technique [245].

Experimental results indicated that the silica-based immunosensor exhibited higher sensitivity and a lower LOD compared to the nanosilver or nanogold-based sensors. Various hybrid materials, for example, PEG [246] and hydroxyapatite [247] have also been doped into silica sol–gel for the fabrication of biosensors. β-lactamase doped silica by the water-in-oil microemulsion technique which displays a comparable activity as free enzyme but with magnetic recoverability[37]. In Habulin's study [248], superparamagnetic silica NPs of maghemite, additionally functionalized with amino silane organic molecules, were prepared for the immobilization of cholesterol oxidase.

A novel amperometric biosensor for glucose was developed by entrapping GOD in a chitosan composite doped with ferrocene monocarboxylic acid-aminated silica NPs conjugate (FMC-ASNPs) and multiwall carbon nanotubes (MWNTs) [249]. This matrix showed a biocompatible microenvironment for retaining the native activity of the entrapped GOD and was in favor of the accessibility of substrate to the active site of GOD, thus the affinity to substrates wass improved greatly. Under optimal conditions this biosensor was able to detect glucose with a detection limit of 10 mM (S/N=3) in the linear range of 0.04 to 6.5 mM.

Di et al. [250] proposed a novel approach to developing a H_2O_2 sensor based on the HRP enzyme and gold NPs simultaneously embedded in silica sol–gel network. The immobilized HRP exhibited direct electrochemical behavior toward the reduction of hydrogen peroxide. The resulted biosensor displayed an excellent elctrocatalytic response to the reduction of

H_2O_2 without any mediator. The calibration range of H_2O_2 was from 1.6 μmol L^{-1} to 3.2 mmol L^{-1} and a detection limit of 0.5 μmol L^{-1} at a signal-to-noise ratio of 3.

A novel amperometric glucose biosensor based on ferrocene-doped silica (FcDS) NPs conjugated with a biopolymer chitosan (CHIT) membrane was developed [251]. The nanosilica surface exhibited high biocompatability and the ferrocene doped inside maintained its high electron-transfer efficiency as a mediator. The glucose biosensor showed a detection limit of 2.0×10^{-6} mol L^{-1} with a linear range from 5.0×10^{-6} to 1.2×10^{-2} mol L^{-1}. Coupled to microdialysis, it was used to determine the glucose concentration in rat brain.

Platinum NPs could enhance the electrode conductivity and SiO_2 NPs could provide a biocompatible environment for enzyme. They have been used as the matrix for the immobilization of enzyme to retain the protein bioactivity and enhance the sensitivity of the biosensors [252,253]. Tang [254] used these two kinds of NPs in the immobilization of GOD to form one enzyme electrode that could make full use of the advantage of both materials. The enzyme electrode containing platinum and silica NPs significantly enhanced the response current compared with the electrode containing only platinum NPs and with the electrode containing only silica NPs.

An ethanol biosensor, based on the ECL of Ru(bpy)-doped silica NPs, was investigated by Chen [255]. The biosensor was a modified glassy carbon electrode, where alcohol dehydrogenase was crosslinked to Ru(bpy)-doped silica NPs, and then immobilized on the electrode surface using chitosan. The results indicated that the biosensor exhibited excellent performance during ethanol determination with a wide linear range (10^{-7} to 10^{-2} M), low detection limit (5.0×10^{-8} M) and good stability.

A new glucose biosensor was developed based on the signal-enhanced effect of chitosan, PtNP and sol–gel of chitosan/silica organic–inorganic hybrid composite film [256]. The resulting biosensor exhibited several advantages, such as high sensitivity at a low potential, good stability, and easy fabrication at room temperature and encapsulation for nanomaterials and biocatalysts. Furthermore, the biosensor was applied for the determination of glucose in human serum sample.

A feasible approach to construct multilayer films of aminated silica NPs/GOD (ASNPs/GOD) on the Au electrode surface using a glutaraldehyde as a covalent attachment cross-linker was described [257]. From the analysis of voltammetric signals, the coverage of active enzyme on the electrode was estimated, which showed a linear relationship with the number of ASNPs/GOD bilayers. This suggested that the analytical performance such as sensitivity, detection limit could be tunable by controlling the number of attached bilayers. The linear response range of the biosensor constructed with four bilayers of ASNPs/GOD to the concentration of glucose can extend at least to 8 mM and reached 95% of the steady-state current in less than 4 s with the detection limit of 9 μM.

A one-step method has been developed for the fabrication of superoxide dismutase (SOD) based biosensor [258]. This method was used to form a silica sol–gel thin film and to immobilize SOD and gold NPs (GNPs) in silica sol-gel network for the fabrication of biosensor. The immobilized SOD realized direct electron transfer between the enzyme and electrode surface. The resulting biosensor exhibited fast amperometric response to superoxide anion with calibration range of superoxide anion was from 0.05 to 0.4 μmol L^{-1}.

Pod-shaped gold/silica NPs (PGSNPs) were prepared using perfluorooctanoic acid (PFOA) and cetyltrimethylammonium bromide (CTAB) as cotemplates [259]. Then the PGSNPs were utilized to explore a novel biosensor through coupling myoglobin (Mb) with

chitosan (Chi). Compared with Mb–Chi-PSNPs (pod-shaped silica NPs)/GC modified electrode, Mb–Chi-PGSNPs/GC electrode exhibited a pair of much stronger redox peaks at -0.28 V (vs. Ag/AgCl). Moreover, facilitated direct electron transfer of the metalloenzymes with smaller peak-to-peak separation (ΔEp) of about 46 mVwas acquired on the PGSNPs-based enzyme electrode. The PGSNPs-based biosensor demonstrated significant electrocatalytic activity for the reduction of hydrogen peroxide with a wide linear range and high sensitivity.

A sensitive amperometric sensor for hemoglobin (Hb) biomolecules based on Toluidine blue (TB)@SiO_2 NPs conjugated with a biopolymer chitosan membrane was developed [260]. The electrocatalytic reduction of Hb was observed at the modified electrode with high sensitivity, stability, and long-term usage life. Electroanalysis of Hb in clinical blood was achieved by use of the resulting sensor, with satisfactory results.

An electrochemical method suitable for the simultaneous measurement of cerebral glucose, lactate, Lglutamate and hypoxanthine concentrations from in vivo microdialysis sampling has been successfully performed for the first time using a neutral red-doped silica (NRDS) nanoparticle-derived enzyme sensor system [261]. These NPs were then mixing with the GOD, lactate oxidase (LOD), L-glutamate oxidase (L-GLOD) or xanthine oxidase (XOD), and immobilized on four glassy carbon electrodes, respectively. A thin Nafion film was coated on the enzyme layer to prevent interference from molecules such as ascorbic acid and uric acid in the dialysate. The high sensitivity of the NRDS modified enzyme electrode system enables the simultaneous monitoring of trace levels of glucose, L-glutamate, lactate and hypoxanthine in diluted dialysate samples from a rat striatum.

A systematic approach towards the fabrication of highly amino silane molecules functionalized maghemite doped-silica NPs presently used for cholesterol oxidase (COD) immobilization with glutaraldehyde as bifunctional crosslinker. Compared to the free enzyme, the covalently bound cholesterol oxidase retained 50% of its activity [262].

5.4. Immunoassay

An immunoassay is based on the reaction between the antigen and a selective antibody. The reaction may be visualized with different labels, e.g., with enzymes and fluorophores. To develop a sensitive assay, highly affine antibodies and appropriate labels are indispensable.

Recently, Ru(bpy)-encapsulated silica NPs were also synthesized by Liu et al. [263] using a modified a reverse microemulsion procedure, where, after conjugation with α-fetoprotein (AFP) antibody on the silica surface with glutaraldehyde as linkage, the antigen could be determined by a sandwich type ECL immunoassay. Ru(bpy)-encapsulated silica NPs were also synthesized using a similar procedure, where, after conjugation with recombinant human interleukin-6(IL-6) antibody, the antigen could be determined by a sandwich type fluoroimmunoassay [264].

A new approach was established to construct a sandwich-type ECL immunosensor by using Ru(bpy)-doped silica (abbreviated as Ru@SiO_2) NPs to label secondary antibody[265]. Firstly, carboxylate-terminated MWCNTs were modified on the electrode to bond with avidin. Subsequently, biotinylated antibodies were immobilized on the surface of the electrode by employing the specific interaction of biotin/avidin and the non-covalent and covalent conjugation function of MWCNTs. Later, the electrode was incubated with antigen

of mouse immunoglobulin G (IgG) and then reacted with the secondary antibody which was labeled by Ru@SiO_2. Accordingly, through the ECL response of Ru@SiO_2 and TPA, a strong ECL signal was obtained and an amplification analysis of protein interaction was achieved. The present immunosensor showed a wide linear range of 0.05–200 ng mL^{-1} for detecting mouse IgG with a low detection limit of 17 pg mL^{-1}.

A sensitive sandwich-type ECL immunosensor for AFP on nano-gold modified glassy carbon electrode (GCE) was developed by using Ru-silica (Ru(bpy)-doped silica) doped Au (Ru-silica@Au) composite as labels [266]. The primary antibody, anti-AFP was first immobilized on the gold NPs modified electrode due to the covalent conjugation, then the antigen and the Ru-silica@Au composite NPs labeled secondary antibody was conjugated successively to form a sandwich-type immunocomplex through the specific interaction. The immunosensor performed high sensitivity and wide liner for detection AFP in the range of 0.05–50 ng mL^{-1} with a detection limit of 0.03 ng mL^{-1}.

In an effort to make ultrasmall, coated, and uniform size magnetic NPs, Tan et al. [128] presented a W/O microemulsion mediated sonochemical synthesis of superparamagnetic iron oxide NPs, which were then coated with a thin layer of silica to protect the core. The silica-coated NPs could be easily immobilized with the antibody to deliver them into a specific target via the antibody-antigen recognition.

Yu's group described a sensitive method combining the Ag@SiO_2 nanoparticle-based Raman tags as the detection probe and the amino group functionalized silica-coated magnetic NPs as immobilization matrix and separation tool for immunoassay of AFP [267]. In the proposed system, a sandwich-type immunoassay was performed between polyclonal antibody functionalized Ag@SiO_2 nanoparticle-based Raman tags and monoclonal antibody modified silica-coated magnetic NPs. Using this strategy, concentration of human AFP up to 0.12 μg mL^{-1} was detected with a detection limit of 11.5 pg mL^{-1}.

Ma [268] described an efficient silica coating process to prepare silica-coated gold nanorods (Aurod@SiO_2) and the subsequent covalent bioconjugation of amino-functionalized Aurod@SiO_2 films with goat anti-human-IgG (anti-h-IgG) was successfully employed for the colorimetric detection of h-IgG in a model reaction based on the specific binding affinity between the proteins. Significantly, the protein-recognition event on the Aurod@SiO_2 films could not only be monitored by changes in the absorption of light, but was also observable by the naked eye.

Chu et al. reported the combination of alkaline phosphatase (ALP) and antibody-cofunctionalized silica NPs and biocatalytic deposition of silver for an amplified electrochemical immunoassay of prostate specific antigen (PSA) in human serum [269]. They synthesized the functionalized silica NPs carried with ALP and detection antibody through the1-Ethyl-3-(3-dimethylaminopropyl) carbodiimide hydrochloride (EDC)/NHS crosslink. After the formation of sandwich type immunocomplex of capture antibody, antigen and functionlized silica NPs on the electrode surface, the ALP carried on the silica NPs converted the ascorbic acid 2-phosphate (AA-P) into ascorbic acid. The later reduced the Ag (I) ions in the solution, leading to the deposition of silver onto the electrode surface. The amount of deposited silver was then determined by linear sweep voltammetry (LSV).

A simple piezoelectric immunoagglutination assay technique with antibody-modified NPs has been developed for direct quantitative detection of protein. The proposed technique was based on the specific agglutination of goat anti-hIgG-coated silica (or gold) NPs in the presence of human IgG (hIgG), which caused a frequency change and was monitored by a

piezoelectric device. The antibody modified on the probe surface would combine with antibody-coated NPs in the presence of antigen (hIgG) when the surface agglutination reaction took place, which coupled both the mass effect and viscoelastic effect acting on the probe. The frequency responses of the immunoagglutination assay were found to correlate well with the hIgG concentration with a detection limit of 84 ng mL^{-1}[270].

The "electroactive" silica NPs label was prepared by covalently binding poly (guanine) (poly[G]) and antibodies to the silica NP surface by using the conventional coupling reagent EDC/NHS was reported [271]. The ease of functionalization and stability of the silica NPs rendered the poly[G]-functionalized NPs very suitable as electroactive labels for amplified electrochemical detection of proteins.

A highly hydrophilic and nontoxic colloidal silica nanoparticle/titania sol-gel composite membrane was prepared on a gold electrode via a chemical vapor deposition method. With carcinoembryonic antigen (CEA) as a model antigen and encapsulation of carcinoembryonic antibody (anti-CEA) in the composite architecture, this membrane could be used for reagentless electrochemical immunoassay [272]. The formation of immunoconjugate by a simple one-step immunoreaction between CEA in sample and the immobilized anti-CEA introduced the change in the potential wide linear range from 1.5 to 240 ng mL^{-1}, with a detection limit of 0.5 ng mL^{-1}.

Amino-group functionalized mesoporous silica NPs were prepared and used to immobilize Au NPs, which was further utilized for the adsorption of HRP and the secondary antibody (Ab2). The resulting NPs, Au-silica/HRP-Ab2 were used as labels for immunosensors to detect norethisterone antigen. A sandwich-type protocol was used to prepare the immunosensor with the primary antibody (Ab1) immobilized onto thionine and graphene sheet modified glassy carbon electrode surface [273]. The sensitivity of the sandwich-type immunosensor using Au-MSN-HRP-Ab2 as labels for norethisterone antigen detection was much higher than that using either Au-MSN-Ab2 or MSN-HRP-Ab2 as labels. Within norethisterone concentration range (0.01–10 ng mL^{-1}), a linear calibration plot with a coefficient of 0.9993 was obtained with a detection limit of 3.58 pg mL^{-1} under optimal conditions. Recently, Yang et al. [274] have also used mesoporous silica NPs as label for the preparation of immunosensor for the detection of human IgG, which exhibited high sensitivity and low detection limit.

Rusling [275] have combined Ru(bpy)@silica-Ab_2 labels with a single-wall carbon nanotube (SWCNT) forest platform in a sandwich immunoassay procedure for PSA detection. A sandwich immunoassay was designed for PSA by first chemically attaching capture antibodies (Ab1) for PSA on SWCNT forests on pyrolytic graphite disks. This immunosensor was then incubated with 10 mL serum or a standard in calf serum, and PSA was captured on the sensor surface. After washing with nonspecific binding blockers, the Ru(bpy)@silica-Ab2 nanoparticle bioconjugate was added, followed by a second washing cycle.

To further improve their biocompatibility, the silica-capped QDs have been functionalized with PEG and thiol-terminated biolinkers. Through the use of these linkers, antibody proteins were successfully conjugated as confirmed by agarose gel electrophoresis [276].

Pan and Yang [277] presented the preparation and functionalization of magnetic (Fe_3O_4)core–(SiO_2)shell NPs, and the covalent conjugation of anti-CEA to an epoxysilane-modified nanoparticle surface. The activity of the immobilized-antibody coated magnetic NPs was monitored using electrochemical impedance spectroscopy (EIS). The resistance response

depended linearly on the CEA concentration over the range 1.5-60 ng mL^{-1} with a detection limit of 0.5 ng mL^{-1}. The magnetic NPs were used not only as carriers for numerous antibody tags, but also as electrode linkers in their study.

A effective approach was developed to synthesize amino functionalized Fc-COOH-doped SNPs. Based on its features of excellent biocompability and easy modification to couple with biomolecules, an amperometric immunosensor for fast detection of cancer antigen 15-3 (CA 15-3) was constructed [242]. Under optimal conditions, the developed immunosensor showed good linearity at the studied concentration range of 2.0–240 U mL^{-1} with a coefficient 0.9986 and a detection limit of 0.64 U mL^{-1}.

Novel fluorescent europium(III) chelate-doped silica NPs were prepared by Yuan et al. by using W/O microemulsions system. Nanoparticle-labelled streptavidin was then used in a highly sensitive time-resolved fluoroimmunoassay (TR-FIA) test for the human hepatitis B surface antigen [278]. These authors further prepared silica-coated Tb^{3+} chelate fluorescent NPs using a similar synthesis technique. After labelling with streptavidin, their use in a sandwich-type TR-FIA test for a prostatespecific antigen (PSA) was presented [279].

A unique lanthanide chelate capable of binding both Eu(III) and Tb(III) was successfully covalently encapsulated into silica NPs [280]. Single wavelength excitation with dual emission endows the NPs with optical encoding capability for multiplexed detection. Typically, as a model of application, a sandwich TR-FIA for human hepatitis B surface antigen (HBsAg) was developed on the basis of Tb(III)-incorporated silica NPs.

A W/O microemulsion was employed to synthesize gold-deposited fluorescent silica NPs with three different colors, red (R), green (G) and blue (B), using ultrasound irradiation [281]. Specific target protein was also adopted for the biomolecular separation using a magnet. GBP-fused avian influenza viral surface antigen (AIa) protein was employed and immobilized onto the gold NPs to detect its specific antibody and a magnet, which is a portable tool for biomolecular separation, was used to separate the conjugated fluorescent NPs.

The biocompatible silica shell coated on the surface of the magnetic cores has become a good solution by incorporating the hydrophobic rare earth fluorescent complex molecules into the SiO_2 shell. For example, Yuan's group has synthesized many silica-based functionalized Eu and Tb fluorescent NPs for the fluoroimmunoassay and the time-resolved fluorescence imaging and actualized the sensitive homogeneous TR-FIA and the fluorescence imaging detection of the cells [282-285].

We have also provided several strategies to construct sensitive and reusable immunosensors [286-289]. The silica nanoparticles was functionalized by coimmobilization of horseradish peroxidase and α-fetoprotein antibody onto the surface of SiO_2 nanoparticles using γ-glycidoxypropyltrimethoxysilane as the linkage. Through "sandwiched" immunoreaction, the enzyme-functionalized silica nanoparticle labels were brought close to the surface of gold substrates. Enhanced detection sensitivity was achieved where the large surface area of SiO_2 nanoparticle carriers increased the amount of HRP bound per sandwiched immunoreaction. The electrochemical and chemiluminescence measurement showed 29.5- and 61-fold increases in detection signals, respectively, in comparison with the traditional sandwich immunoassay (Fig. 8). Silica nanospheres were also employed as the carrier for immobilization of QDs and antibodies. Goat antirabbit IgG antibody was covalently bound to CdTe QDs on the surface of silica nanospheres. CdTe QDs coated with a

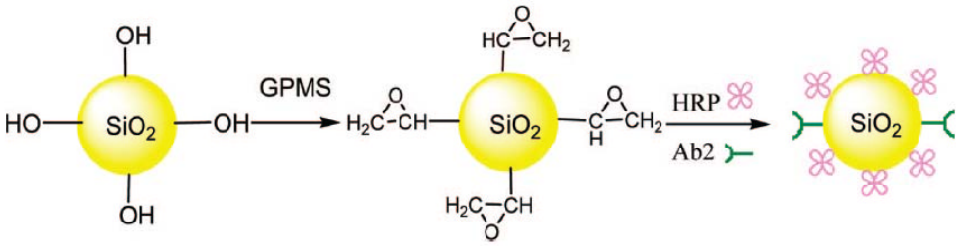


Figure 8. Coimmobilization of HRP and Anti-AFP on Monodisperse SiO_2 Spheres (from Ref. [286] reproduced by permission of American Chemical Society, https://s100.copyright.com/CustomerAdmin/PLF.jsp?lID=2011041_1303270877149).

silica nanosphere label were attached onto the gold electrode surface through a subsequent "sandwich" immunoreaction. Due to signal amplification from the high loading of CdTe QDs, 6.6- and 5.9-fold enhancements in electrochemiluminescent (ECL) and square-wave voltammetric (SWV) signals for IgG detection were achieved compared to the unamplified method. The resulting versatile immunosensor possesses high sensitivity, satisfactory reproducibility and regeneration, and good precision. This simple and specific strategy has vast potential to be used in other biological assays.

CONCLUSION

We have described a variety of functionalized silica-based NPs consisting of a silica shell and various encapsulated molecular or particles with tunble properties and composition for use in advanced bioanalytical detection, bioimaging, cell targeting, and bioseparation applications. These tailored silica-based NPs can pave the way of conjugating of biomolecule recognition events with signal amplification and optical-encoded spectroscopic labels. High selectivity and ultrasensitive detection is one of the most fascinating and challenging aspects of this field. To achieve the ultrasensitive analysis, great efforts will be needed to understand the fabrication process, control particle aggregation, and develop powerful surface interactions. Although considerable advances have been obtained in recent years, the application of silica-based NPs in i*n vivo* imaging is still in its infancy. This invites the development of more functional systems with less-toxic carriers. Additionally, developing uses for a variety of silica-based nanomaterials coupled with new detection technologys will offer advanced miniaturized high-throughput and cost-effective multiplex assays for tagging of a wide variety of biological entities in a single run. With further developments, silica-based NPs will become increasingly accepted as carrier reagents in bioanalytical and biotechnological applications owing to their unique physicochemical properties.

REFERENCES

[1] Ionita P.; Volkov A.; Jeschke G.; Chechik V. *Anal Chem*. 2008, *80*, 95-106.
[2] Daniel, M. C.; Astruc, D. *Chem. Rev.* 2004, *104*, 293-346.
[3] Katz, E.; Willner, I. *Angew. Chem. Int. Ed.* 2004, *43*, 6042-6108.
[4] Wang, J.; *Small* 2005, *1*, 1036-1043.

[5] Zhang, F.; Skoda, M. W. A.; Jacobs, R. M. J.; Zorn, S.; Martin, R. A.; Martin, C. M.; Clark, G. F.; Goerigk, G.; Schreiber, F. *J. Phys. Chem. A* 2007, *111*, 12229-12237.
[6] Zotti, G.; Vercelli, B.; Berlin, A. *Chem. Mater.* 2008, *20*, 397-412.
[7] Lee, M.; Amaratunga, P.; Kim, J.; Lee, D. *J. Phys. Chem. C* 2010, *114*, 8366-18371.
[8] Taton, T. A.; Mirkin, C. A.; Letsinger,R. L. *Science* 2000, *289*, 1757-1760.
[9] Deng, C. M.; He, Q. G.; He, C.; Shi, L. Q.; Cheng, J. G.; Lin, T. *J. Phys. Chem. B* 2010, *114*, 4725-4730.
[10] Trewyn, B. G.; Giri, S.; Slowing, I. I.; Lin, V. S. Y. *Chem. Commun.* 2007, *31*, 3236-3245.
[11] Sun, Y.; Yan, F.; Yang, W.; Zhao, S.; Yang, W.; Sun, C. *Anal. Bioanal. Chem.* 2007, *387*, 1565-1572.
[12] Andrew, B.; Prabuddha, S.; Tara Z.; Barbara B.; Ulrich, W. *small* 2006, *2*, 723-726.
[13] Cao,Y. W. C.; Jin, R. C.; Mirkin, C. A. *Science* 2002, *297*, 1536-1540.
[14] Huang, C. C.; Huang, Y. F.; Cao, Z. H.; Tan, W. H.; Chang, H. T. *Anal. Chem.* 2005, *77*, 5735-5741.
[15] Nam, J. M.; Stoeva, S. I.; Mirkin, C. A. *J. Am. Chem. Soc.* 2004, *126*, 5932-5933.
[16] Shi, H.Y.; Yuan, L.; Wu, Y. F.; Liu, S. Q. *Biosens. Bioelectron.* 2011, in press.
[17] Zhao, W.; Ali, M. M.; Aguirre, S. D.; Brook, M. A.; Li Y. F. *Anal. Chem*. 2008, *80*, 8431-8437.
[18] Kim, D.; Daniel, W. L.; Mirkin, C. A. *Anal. Chem*. 2009, *81*, 9183-9187.
[19] Wang, J.; Li, J. H.; Baca, A. J.; Hu, J. B.; Zhou, F. M.; Yan, W.; Pang, D. W. *Anal. Chem.* 2003, *75*, 3941-3945.
[20] Kuo, Y. C.; Wang, Q.; Ruengruglikit, C.; Yu, H.; Huang, Q. *J. Phys. Chem. C* 2008, *112*, 4818-4824.
[21] Pinwattana, K.; Wang, J.; Lin, C. T.; Wu, H.; Du, D.; Lin, Y.; Chailapakul, O. *Biosens. Bioelectron.* 2010, *26,* 1109-1113.
[22] Liu, X.; Ju, H. X. *Anal. Chem.* 2008, *80*, 5377-5382.
[23] Wang, Z.; Li, J.; Liu, B.; Li, J. *Talanta* 2009*, 77*, 1050-1056.
[24] Liu, M.; Shi, G.; Zhang, L.; Zhao, G.; Jin, L. *Anal. Bioanal. Chem.* 2008*, 391*, 1951-1959.
[25] Webster, A.; Compton, S. J.; Aylott, J.W. *Analyst* 2005, *130*, 163-170.
[26] Qhobosheane, M.; Santra, S.; Zhang, P.; Tan, W. *Analyst* 2001, *126*, 1274-1278.
[27] Roy, I.; Ohulchanskyy, T. Y.; Pudavar, H. E.; Bergey, E. J.; Oseroff, A. R.; Morgan, J.; Dougherty, T. J.; Prasad, P. N. *J. Am. Chem. Soc.* 2003, *125*, 7860-7865.
[28] Ren, T.; Erker, W.; Basché, T.; Schärtl, W. *Langmuir* 2010, 26*,* 23, 17981-17988.
[29] Gerion, D.; Herberg, J.; Bok, R.; Gjersing, E.; Ramon, E.; Maxwell, R.; Kurhanewicz, J.; Budinger, T. F.; Gray, J. W.; Shuman, M. A.; Chen, F. *J. Phys. Chem. C* 2007, *111,* 12542-12551.
[30] Li, D.; Teoh, W. Y.; Selomulya, C.; Woodward, R. C. *Chem. Mater.* 2006**,** *18,* 6403-6413.
[31] Tada, D. B.; Vono, L. L. R.; Duarte, E. L.; Itri, R.; Kiyohara, P. K.; Baptista, M. S.; Rossi, L. M. *Langmuir* 2007, *23*, 8194-8199.
[32] Dembski, C. G. S.; Hofmann, A.; Ruehl, E. *Langmuir* 2006, *22*, 5604-5610.
[33] Gao, L.; Peay, M. A.; Gray, T. G. *Chem. Mater*. 2010, *22*, 6240-6245.
[34] Liu, X.; Ma, Z.; Xing, J.; Liu, H. *J. Magn. Magn. Mater.* 2004, *270*, 1-6

[35] Liu, X.; Xing, J.; Guan, Y.; Shan, G.; Liu, H. *Colloid. Surface. A* 2004, *238*, 127-131.
[36] Bruce, I.J.; Taylor, J.; Todd, M.; Davies, M.J.; Borioni, E.; Sangregorio, C.; Sen, T. *J. Magn. Magn. Mater.* 2004, *284*, 145-160.
[37] Gao, X.; Yu, K. M. K.; Tam, K. Y.; Tsang, S. C. *Chem. Commun.* 2003*, 24*, 2998-2999.
[38] Santra, S. *J. Nanosci. Nanotechnol*. 2005, *5*, 899-904.
[39] Shibata, S.; Taniguchi, T.; Yano, T.; Yamane, M. *J. Sol-Gel Sci. Technol*. 1997, *10*, 263-268.
[40] Stöber, W.; Fink, A.; Bohn, E. *J. Colloid Interf. Sci.* 1968, *26*, 62-69.
[41] Shibata, S.; Yano, T.; Yamane, M. *Jpn. J. Appl. Phys*. 1998, *1*, 37-41.
[42] Hu, S. H.; Liu, T. Y.; Huang, H. Y.; Liu, D. M.; Chen, S. Y. *Langmuir* 2008, *24*, 239-244.
[43] Gupta, R.; Chaudhury, N.K. *Biosens. Bioelectron.* 2007, *22*, 2387-2399.
[44] Verónica, S. M.; Miguel, A. C.; Michael, F.; Arturo, L. Q.; Karl, S.; Rodolfo, D. *Chem. Mater.* 2006, *18*, 2701-2706.
[45] Cho, E. J.; Jung, S.; Lee, K.; Lee, H. J.; Nam, C.; Bae, H. J. *Chem. Commun.*, 2010, *46*, 6557-6559
[46] Zhao, X.; Tapec, D. R.; Tan, W. *J. Am. Chem. Soc.* 2003, *125*, 11474-11475.
[47] Cannas, C.; Musinu, An.; Ardu, A.; Orrù, F.; Peddis, D.; Casu, M.; Sanna, R.; Angius, F.; Diaz, G.; Piccaluga, G. *Chem. Mater*. 2010, *22*, 3353-3361.
[48] Yu, C. H.; Al-Saadi, A.; Shih, S. J.; Qiu, L.; Tam, K. Y.; Tsang, S. C. *J. Phys. Chem. C* 2009, *113*, 537-543.
[49] Lian, W.; Litherland, S.; Badrane,H.; Tan, W.; Wu, D.; Baker, H.; Gulig, P.; Lim, D.; Jin, S. *Anal. Biochem.* 2004, *334*, 135-144.
[50] Bringley, J.; Penner, T.; Wang, R.; Harder, J.; Harrison, W.; Buonemani, L. *J. Colloid Interf. Sci.* 2008, *320*, 132-139.
[51] Medley, C. D.; Bamrungsap, S.; Tan, W.; Smith, J. E. *Anal. Chem.* 2011, *83*, 727-734.
[52] Hartlen, K. D.; Athanasopoulos, A. P. T.; Kitaev, V. *Langmuir* 2008, *24*, 1714-1720.
[53] Ma, D.; Kell, A. J.; Tan, S.; Jakubek, Z. J. Simard B. *J. Phys. Chem. C* 2009, *113*, 15974-15981.
[54] Tan, W.; Wang, K.; He, X.; Zhao,X.; Drake, T.; Wang, Li.; Bagwe R. P. *Med. Res. Rev.* 2004, *24*, 621-638.
[55] Santra, S.; Wang, K.; Tapec, R.; Tan, W. *J. Biomed. Opt.* 2001, *6*, 160-166.
[56] Zhang, L. H.; Liu, B. F.; Dong, S. J. *J. Phys. Chem. B* 2007, *111*, 10448-10452.
[57] Zhang, L. H.; Dong, S. J. *Anal. Chem.* 2006, *78*, 5119-5123.
[58] Zhang, L. H.; Dong, S. J. *Chem. Commun.* 2006, *8*, 1687-1691.
[59] Qian, L.; Yang, X. *Adv. Funct. Mater.* 2007, *17*, 1353-1358.
[60] Rossi, L.; Shi, L.; Quina, F.; Rosenzweig, Z. *Langmuir* 2005, *21*, 4277-4280.
[61] Zhao, X. J.; Bagwe, R. P.; Tan, W. H. *Adv. Mater.* 2004, *16*, 173-176.
[62] Ow, H.; Larson, D. R.; Srivastava, M.; Baird, B. A.; Webb, W. W.; Wiesner. U. *Nano Lett.* 2005, *5*, 113-117.
[63] Zhang, Y.; Lu, M. *Nanotechnol*ogy 2007, *18*, 275603.
[64] Nakamura, M.; Shono, M.; Ishimura, K. *Anal. Chem.* 2007*, 79*, 6507-6514.
[65] Liu, F.; Carlos, L. D.; Ferreira, R. A.; Rocha, S. J.; Ferro, M. C.; Tourrette, A.; Quignard, F.; Robitzer, M. *J. Phys. Chem. B* 2010, *114*, 77-83.

[66] Hashino, K.; Ikawa, K.; Ito, M.; Hosoya, C.; Nishioka, T.; Makiuchi, M.; Matsumoto, K. *Anal. Biochem.* 2007*, 364*, 89-91.
[67] Iwu, K. O.; Soares-Santos, P. C. R.; Nogueira, H. I. S.; Carlos, L. D.; Trindade T. *J. Phys. Chem. C* 2009, *113*, 7567-7573.
[68] Paula, C. R.; Trindade T. *Chem. Mater*. 2003, *15*, 100-108.
[69] Zhang, D.; Wang, X.; Qiao, Z.; Tang, D.; Liu, Y.; Huo Q. *J. Phys. Chem. C* 2010, *114*, 12505-12510.
[70] Li Z.; Zhang, Y. *Angew. Chem. Int. Ed.* 2006, *45*, 7732-7735.
[71] Fedorenko, S. V.; Bochkova, O. D.; Mustafina, A. R.; Burilov, V. A.; Kadirov, M. K.; Holin, C. V.; Nizameev, I.R.; Skripacheva, V. V.; Menshikova, Y. A.; Antipin, I. S.; Konovalov, A. I. *J. Phys. Chem. C* 2010, *114*, 6350-6355.
[72] Gerhards, C.; Schulz-Drost, C.; Sgobba, V.; Guldi, D. M. *J. Phys. Chem. B* 2008, *112*, 14482-14491.
[73] Michalet, X.; Pinaud, F.; Bentolila, L.; Tsay, J.; Doose, S.; Li, J.; Sundaresan, G.; Wu, A.; Gambhir, S.; Weiss, S. *Science* 2005, *307*, 538-544.
[74] Klostranec, J.; Chan, W. *Adv. Mater.* 2006, *18*, 1953-1964.
[75] Gerion, D.; Pinaud, F.; Williams, S. C.; Parak, W. J.; Zanchet, D.; Weiss, S.; Alivisatos, A. P. *J. Phys. Chem. B* 2001, *105*, 8861-8871.
[76] Rogach, A. L.; Nagesha, D.; Ostrander, J. W.; Giersig, M.; Kotov, N. A. *Chem.Mater.* 2000, *12*, 2676-2685.
[77] Nann, T.; Mulvaney, P. *Angew. Chem. Int. Ed.* 2004, *43*, 5393-5396.
[78] Kobayashi, Y.; Nozawa, T.; Nakagawa, T.; Gonda, K.; Takeda, M.; Ohuchi, N.; Kasuya, A. *J Sol-Gel Sci Technol*. 2010, *55*, 79-85.
[79] Panigrahi, S.; Bera, A.; Basak, D. *J. Colloid Interf. Sci.* 2011, *353*, 30-38.
[80] Panigrahi, S.; Bera, A.; Basak, D. *ACS Appl. Mater. Interfaces* 2009, *1*, 2408-2411.
[81] Panigrahi, S.; Bera, A.; Basak D. *J. Colloid Interf. Sci.* 2011, *353*, 30-38.
[82] Koole, R.; Schooneveld, M. M.; Hilhorst, J.; Donegá, C. M.; Hart, D. C.; Blaaderen, A.; Vanmaekelbergh, D.; Meijerink A. *Chem. Mater*. 2008, *20*, 2503-2512.
[83] Ziegler, Jan.; Xu, S.; Kucur, E.; Meister, F.; Batentschuk, M.; Gindele, F.; Nann T. *Adv. Mater.* 2008, *20*, 4068-4073.
[84] Darbandi, M.; Thomann, R.; Nann, T. *Chem. Mater*. 2005, *17*, 5720-5275.
[85] Farmer, S. C.; Patten T. E. *Chem. Mater*. 2001, *13*, 3920-3926.
[86] Lai, C. W.; Wang, Y. H.; Chen, Y. C.; Hsieh, C. C.; Uttam, B. P.; Hsiao, J. K.; Hsu, C. C.; Chou, P. T. *J. Mater. Chem.* 2009, *19*, 8314-8319.
[87] Gerion, D.; Pinaud, F.; Williams, S. C.; Parak, W. J.; Zanchet, D.; Weiss, S.; Alivisatos, A. P. *J. Phys. Chem. B* 2001, *105*, 8861-8871
[88] Dong, B. H.; Gao, L. X.; Su, G.; Liu, W.; Qu, H.; Jiang, D.X.; *J. Colloid Interf. Sci.* 2009, *339*, 78-82.
[89] Tan, T. T.; Selvan, S. T.; Zhao, L.; Gao, S.; Ying, J. Y. *Chem. Mater*. 2007, *19*, 3112-3117.
[90] Abdullah, M.; Shibamoto, S.; Okuyama, K. *Opt. Mater.* 2004, *26*, 95-100.
[91] Peng, Y. Y.; Hsieh, T. E.; Hsu, C.H. *Nanotechnol*ogy 2006, *17*, 174-180.
[92] Mayer, G.; Fonin, M.; Rudiger, U.; Schneider, R.; Gerthsen, D.; JanBen, N.; Bratschitsch, R. *Nanotechnol*ogy 2009, *20*, 075601.
[93] Torimoto, T.; Reyes, J. P.; Iwasaki, K.; Pal, B.; Shibayama, T.; Sugawara, K.; Takahashi, H.; Ohtani, B. *J. Am. Chem. Soc.*, 2003, *125*, 316-317.

[94] Pal, B.; Torimoto, T.; Iwasaki, K.; Shibayama, T.; Takahashi, H.; Ohtani, B. *J. Phys. Chem. B*, 2004, *108*, 18670-18674.
[95] Iwasaki, K.; Torimoto, T.; Shibayama, T.; Nishikawa, T.; Ohtani, B. *Small* 2006, *2*, 854-858.
[96] Selvan, S. T.; Tan, T. T.; Ying, J. Y. *Adv. Mater.* 2005, *17*, 1620-1625.
[97] Yang, Y. H.; Gao, M. Y. *Adv. Mater.* 2005, *17*, 2354-2357.
[98] Yang, Y. H.; Jing, L. H.; Yu, X. L.; Yan, D. D. *Chem. Mater*. 2007, *19*, 4123-4128.
[99] Jing, L.; Yang, C.; Qiao, R.; Niu, M.; Du, M.; Wang, D.; Gao, M. *Chem. Mater*. 2010, *22*, 420-427.
[100] Darbandi, M.; Urban, G.; Krüger. M. *J. Colloid Interf. Sci.* 2010,*351*, 30-34.
[101] Sun, Y.; Masia, F.; Langbein, W.; Borri P. *Phys. Status Solidi A* 2009, *206*, 2822-2825 .
[102] Hu X.; Gao, X. *ACS nano* 2010, *4*, 6080-6086.
[103] Hu, X.; Zrazhevxkiy, P.; Gao, X. *Ann. Biomed. Eng.* 2009, *37*, 1960-1966.
[104] Yu, S.; Chow, G. M. *J. Mater. Chem.* 2004, *14*, 2781-2786.
[105] Vogt, C.; Toprak, M. S.; Muhammed, M.; Laurent, S.; Bridot, J.; Mülle r, R. N. *J. Nanopart. Res*. 2010, *12*, 1137-1147.
[106] Ennas, G.; Marongiu, G.; Marras, S.; Piccaluga, G. *J. Nanopart. Res.* 2004, *6*, 99-105.
[107] Albuquerque, A. S.; Ardisson, J. D.; Macedo, W. A. A. *J. Magn. Magn. Mater.* 1999, *192*, 277-280.
[108] Yu, J. H.; Lee, C. W.; I, S. S.; Lee, J. S. *Rev. Adv. Mater. Sci.* 2003, *4*, 55-59.
[109] Klug, K. L.; Dravid, V. P.; Johnson, D. L. *J. Mater. Res.* 2003, *18*, 988-993.
[110] Banerjee, S.; Roy, S.; Chen, J. W.; Chakravorty, D. *J. Magn. Magn. Mater.* 2000, *219*, 45-52.
[111] Liu, X.; Ma, Z.; Xing, J.; Liu, H. *J. Magn. Magn. Mater.* 2004, *270*, 1-6.
[112] Philipse, A. P.; van Bruggen, M. P. B.; Pathmamanoharan, C. *Langmuir* 1994, *10*, 92-99.
[113] Barnakov, Y. A.; Yu, M. H.; Rosenzweig, Z. *Langmuir* 2005, *21*, 7524-7527.
[114] Im, S. H.; Herricks, T.; Lee, Y. T.; Xia, Y. *Chem. Phys. Lett.* 2005, *40*,1-3.
[115] Lu, Y.; Yin, Y.; Mayers, B. T.; Xia, Y. *Nano. Lett.* 2002, *2*, 183-186.
[116] Deng, Y. H.; Wang, C. C.; Hu, J. H.; Yang, W. L.; Fu, S. K. *Colloid. Surface. A: Physicochem. Eng. Aspects* 2005, *262*, 87-93.
[117] Almeida, M. P. S.; Caiado, K. L.; Sartoratto, P. P. C.; Cintra e Silva, D. O.; Pereira, A. R.; Morais, P. C. *J. Alloys Compd.* 2010, *500*,149-152.
[118] Ohmori, M.; Matijevic, E. *J. Colloid Interf. Sci.* 1992, *150*, 594-598.
[119] Ammar, M.; Mazaleyrat1, F.; Bonnet, J. P.; Audebert, P. Brosseau, A. ; Wang, G. ; Champion, Y. *Nanotechnol*ogy 2007, *18*, 285606-285614.
[120] Kobayashi, Y.; Horie, M.; Konno, M.; Rodrí guez-González, B.; Liz-Marzán L. M. *J. Phys. Chem. B* 2003, *107*, 7420-7425.
[121] Ni , X.; Zheng, Z.; Hu, X.; Xiao, X. *J. Colloid Interf. Sci.* 2010, *341*, 18-22.
[122] Tartaj, P.; Serna, C. J. *J. Am. Chem. Soc.* 2003, *125*, 15754-15755.
[123] Tartaj, P.; Serna, C. J. *Chem. Mater*. 2002, *14*, 4396-4402.
[124] Gao, X.; Yu, K. M. K.; Tamb, K. Y.; Tsang, S. C. *Chem. Comm*. 2003, 2298-2999.
[125] Cannas, C.; Ardu, A.; Musinu, A.; Peddis, D.; Piccaluga, G. *Chem. Mater*. 2008, *20*, 6364-6371.

[126] Landfester, K.; Ramírez, L. P. *J. Phys.: Condens. Matter* 2003, *15*, 1345-1361.
[127] Vestal, C. R.; Zhang, Z. J. *Nano Lett.* 2003, *3*, 1739-1743.
[128] Santra, S.; Tapec, R.; Theodoropoulou, N.; Dobson, J.; Hebard, A.; Tan, W. *Langmuir*. 2001, *17*, 2900-2906.
[129] Yu, C. H.; Lo, C. C. H.; Tam, K.; Tsang, S. C. *J. Phys. Chem. C* 2007, *111*, 7879-7882.
[130] Lee, D. C.; Mikulec, F. V.; Pelaez, J. M.; Koo, B.; Korgel, B. A. *J. Phys. Chem. B* 2006, *110*, 11160-11166.
[131] Zhang, M.; Cushing , B. L.; O'Connor, C. J. *Nanotechnol*ogy 2008, *19*, 085601.
[132] Tago, T.; Hatsuta, T.; Miyajima, K.; Kishida, M.; Tashiro, S.; Wakabayashi, K. *J. Am. Ceram. Soc.* 2002, *85*, 2188-2194.
[133] Zhao, W.; Gu, J. L.; Zhang, L. X.; Chen, H. R.; Shi, J. L. *J. Am. Chem. Soc.* 2005, *127*, 8916-8917.
[134] Tie, S. L.; Lee, H. C.; Bae,Y. S.; Kim, M. B.; Lee, K.; Lee. C. H. *Colloid. Surface. A, Physicochem. Eng. Aspects* 2007, *293*, 278-285.
[135] Kim, J.; Lee, J. E.; Lee, J.; Yu, J. H.; Kim, B. C.; An, K.; Hwang, Y.; Shin, C. H.; Park, J. G.; Hyeon, T. *J. Am. Chem. Soc.* 2006, *128*, 688-689.
[136] Kim, J.; Kim, H. S.; Lee, N.; Kim, T.; Kim, H.; Yu, T.; Song, I. C.; Moon, W. K.; Hyeon, T. *Angew. Chem. Int. Edit.* 2008,*47*, 8438-8441.
[137] Deng, Y. H.; Qi, D. W.; Deng, C. H.; Zhang, Xi. M.; Zhao D. Y. *J. Am. Chem. Soc.* 2008, *130*, 28-29.
[138] Cao, Y.; Jin, R.; Nam, J.; Thaxton, C.; Mirkin, C. *J. Am. Chem. Soc.* 2003, *125*, 14676-14677.
[139] Cao, Y.; Jin, R.; Mirkin, C. *Science* 2002, *297*, 1536-1540.
[140] Doering, W.; Nie, S. *Anal. Chem.* 2003, *75*, 6171-6176.
[141] Liz-Marzán,L. M.; Giersig, M.; Mulvaney, Paul. *Langmuir* 1996, *12*, 4329-4335.
[142] Mine, E.; Yamada, A.; Kobayashi, Y.; Konno, M.; Liz-Marzan, L.M. *J. Colliod Interface Sci.* 2003, *264*, 385-390.
[143] Jung, S. H.; Kyo-IlKim.; Jung-HoRyu.; Seong-HoChoi.; Jong-BumKim.; Jin-HoMoon.; Jin, J. H. *Appl. Radiat. Isotopes* 2010, *68*, 1025-1029.
[144] Wu, C. L.; Xu, Q. H. *Langmuir* 2009, *25*, 9441-9446.
[145] Lu, Y.; Yin, Y. D.; Li, Z. Y.; Xia, Y. N. *Nano Lett.* 2002, *2*, 785-788.
[146] Zhang, K.; Wang, W.; Cheng, W. D.; Xing, X. Q.; Mo, G.; Cai, Q.; Chen, Z. G.; Wu, Z. G. *J. Phys. Chem. C* 2010, *114*, 41-49.
[147] García-Santamaría, F.; o-Maceira,V. S.; López, C.; Liz-Marzán,L. M. *Langmuir* 2002, *18*, 4519-4522
[148] Graf, C.; Vossen, D. L. J.; Imhof, A.; Blaaderen, A. *Langmuir* 2003, *19*, 6693-6700.
[149] Han, Y.; Jiang, J.; Lee, S. S.; Ying, J. Y. *Langmuir* 2008, *24*, 5842-5848.
[150] Xu , J.; Perry, C. C. *J. Non-Cryst. Solids* 2007, *353*, 1212-1215.
[151] Li, D.; Li, D. W.; Li, Y.; Fossey, J. S.; Long, Y. T. J. *Mater. Chem.* 2010, *20*, 3688-3693.
[152] Djoumessi, D.; Lekeufack; Brioude, A.; Mouti, A.; Alauzun, J. G.; Stadelmann, P.; Coleman, A. W.; Miele, P. *Chem. Commun.* 2010, *46*, 4544-4546.
[153] Wang, W.; Asher, S. A. *J. Am. Chem. Soc.* 2001, *123*, 12528-12535.
[154] Lea, Y.; Houa, P. T.; Wanga, J. X.; Chena, J. F. *Mater. Chem. Phys.* 2010, *120*, 351-355.

[155] Zhang, F.; Braun, G. B.; Shi, Y. F.; Zhang, Y. C.; Sun, X. H.; Reich, N. O.; Zhao, D. Y.; Stucky, G. *J. Am. Chem. Soc.* 2010, *132*, 2850-2851.
[156] Aslan, K.; Wu, M.; Lakowicz, J. R.; Geddes, C. D. *J. Am. Chem. Soc.* 2007, *129*, 1524-1525.
[157] Aslan, K.; Wu, M.; Lakowicz, J. R.; Geddes, C. D. *J Fluoresc* 2007*,17*, 127-131.
[158] Guo, L. Q.; Guan, A.; Lin, X. L.; Zhang, C. L.; Chen, G. N. *Talanta* 2010, *82*, 1696-1700.
[159] Mori, K.; Kawashima, M.; Che, M.; Yamashita, H. *Angew. Chem. Int. Ed.* 2010, *49*, 8598 -8601.
[160] Wang, W.; Li, Z. P.; Gu, B. H.; Zhang, Z. Y.; Xu, H. X. *ACS nano* 2009, *3*, 3493-3496.
[161] Xu, K.; Wang, J. X.; Kang, X. L.; Chen, J. F. *Mater. Lett.* 2009, *63*, 31-33.
[162] Mulvaney, S. P.; Musick, M. D.; Keating, C. D.; Natan, M. J. *Langmuir* 2003, *19*, 4784-4790.
[163] Gong, J. L.; Jiang, J. H.; Yang, H. F.; Shen, G. L.; Yu, R. Q.; Ozaki, Y. *Anal. Chim. Acta* 2006, *564*, 151-157.
[164] Gong, J. L.; Jiang, J. H.; Liang, Y.; Shen, G. L.; Yu, R. Q. *J. Colloid Interf. Sci.* 2006, *298*, 752-756.
[165] Xu, S. P.; Hartvickson, S.; Zhao, J. X. *Langmuir* 2008, *24*, 7492-7499.
[166] Qi, Y. L.; Chen, M.; Liang, S.; Zhao, J.; Yang, W. *Colloid. Surface. A: Physicochem. Eng. Aspects* 2007, *302*, 383-387.
[167] Correa-Duarte, M. A., Sobal, N.; Liz-Marzán, L. M.; Giersig, M. *Adv. Mater.* 2004, *16*, 23-24.
[168] Cong, H. P.; Toftegaard, R.; Arnbjerg, J.; Ogilby, P. R. *Langmuir* 2010, *266*, 4188-4195.
[169] Wang, D.; He, J.; Rosenzweig, N.; Rosenzweig, Z. *Nano Lett.* 2004, *4*, 409-413.
[170] Kwon, K. W.; Shim, M. *J. Am. Chem. Soc.* 2005, *127*, 10269-10275.
[171] Yoon, T.; Kim, J. S.; Kim, B. G.; Yu, K. N.; Cho, M.; Lee, J. *Angew. Chem. Int. Ed.* 2005, *44*, 1068-1071.
[172] Hong, X.; Li, J.; Wang, M.; Xu, J.; Guo, W.; Li, J.; Bai, Y.; Li, T. *Chem. Mater*. 2004, *16*, 4022-4027.
[173] Kim, J.; Lee, J. E.; Lee, J.; Jang, Y.; Kim, S.; An, K.; Yu, J. H.; Hyeon, T. *Angew. Chem.*, *Int. Ed.* 2006, *45*, 4789-4793.
[174] Lu, H.; Yi, G.; Zhao, S.; Chen, D.; Guo, L. H.; Cheng, J. *J. Mater.Chem.* 2004, *14*, 1336-1341.
[175] Ma, D.; Guan, J.; Normandin, F.; Dénommée, S.; Enright, G.; Veres, T.; Simard, B. *Chem. Mater*. 2006, *18*, 1920-1927.
[176] Li, M. J.; Chen, Z. F.; Yam, V. W.; Zu, Y. B. *ACS nano* 2008, *25* , 905-912.
[177] Choi, J.; Kim, J. C.; Lee, Y. B.; Kim, I. S.; Parka, Y. K.; Hur, N. H. *Chem. Commun.* 2007, *16*, 1644-1646.
[178] Feng, J.; Song, S. Y.; Deng, R. P.; Fan, W. Q.; Zhang, H. J. *Langmuir* 2010, *265*, 3596-3600.
[179] Yu, S. Y.; Zhang, H. J.; Yu, J. B.; Wang, C.; Sun, L. N.; Shi, W. D.; *Langmuir* 2007, *23*, 7836-7840.
[180] Yi, D. K.; Selvan, S. T.; Lee, S. S.; Georgia, C. *J. Am. Chem. Soc.* 2005, *127*, 4990-4991.

[181] Selvan, S. T.; Patra, P. K.; Ang, C. Y.; Ying, J. Y. *Angew. Chem. Int. Ed.* 2007, *46*, 2448-2452.
[182] Zhang, Y. X.; Pan, S. S.; Teng, X. M.; Luo, Y. Y.; Li, G. H. *J. Phys. Chem. C* 2008, *112*, 9623-9626.
[183] Knopp, D.; Tang, D. P.; Niessner, R. *Anal.Chim. Acta* 2009, *647*, 14-30.
[184] Zhu, S.; Xiang, J.; Li, X.; Shen, S.; Lu, S.; Zhou, J.; Xiong, W.; Zhang, B.; Nie, X.; Zhou, M.; Tang, K.; Li, G. *Biotechnol. Appl. Biochem.* 2004, *39*, 179-187.
[185] Wei, H.; Wang, E. *Chem. Lett.* 2007, *36*, 210-211.
[186] Ren, X. L.; Meng, X. W.; Tang, F. Q.; Zhang, L. *Mater. Sci. Eng.* 2009, *29*, 2234-2238.
[187] Wang, F. C.; Yuan, R.; Chai, Y. Q. *Appl. Microbiol. Biotechnol.* 2006, *72*, 671-675.
[188] Liang, H. F.; Wang, Z. C. *Mater. Chem. Phys.* 2010, *124*, 964-969.
[189] Luckarift, H.; Balasubramanian, S.; Paliwal, S.; Johnson, G.; Simonian, A. *Colloid. Surface. B* 2007, *58*, 28-33.
[190] Luckarift, H.; Dickerson, M.; Sandhage, K.; Spain, J. *Small* 2006, *2*, 640-643.
[191] Luckarift, H.; Johnson, G.; Spain, J. *J. Chromatogr. B* 2006, *843*, 310-316.
[192] Jain, T.; Roy, I.; De, T.; Maitra, A. *J. Am. Chem. Soc.* 1998, *120*, 11092-11095.
[193] Tsagkogeorgas, F.; Ochsenkühn-Petropoulou, M.; Niessner, R. ; Knopp, D. *Anal. Chim. Acta* 2006, *573*, 133-137.
[194] Das, S.; Jain, T.; Maitra, A. *J. Colloid Interf. Sci.* 2002, *252*, 82-88.
[195] Yang, H.; Zhang, S.; Chen, X.; Zhuang, Z.; Xu, J.; Wang, X. *Anal. Chem.* 2004, *76*, 1316-1321.
[196] Prokopowicz, M. ; Lukasiak, J. ; Przyjazny, A. *J. Biomater. Sci.* 2004, *15*, 343-356.
[197] Gelman, F.; Blum, J.; Avnir, D. *J. Am. Chem. Soc.* 2002, *124*, 14460-14463.
[198] Voss, R.; Brook, M.; Thompson, J.; Chen, Y.; Pelton, R.; Brennan, J. *J. Mater. Chem.* 2007, *17*, 4854-4863.
[199] Tang, D. P.; Su, B. L.; Tang, J.; Ren, J. J.; Chen, G. N. *Anal. Chem.* 2010, *82*, 1527-1534.
[200] Sivakumar, S.; Diamente, P.; van Veggel, F. C. *Chem. Eur. J.* 2006, *12*, 5878-5884.
[201] Wang, L.; Tan, W. H. *Nano Lett.*, 2006, *6*, 84-88.
[202] Ashtari, P.; He, X.; Wang, K.; Gong, P. *Talanta* 2005, *67*, 548-554
[203] Tapec, R.; Zhao, X.; Tan, W.; *J. Nanosci. Nanotechnol.* 2002, *2*, 405-409.
[204] Jana, N.; Earhart, C.; Ying, J. *Chem. Mater*. 2007, *19*, 5074-5082.
[205] Wang, L.; Wang, K.; Santra, S.; Zhao, X. J.; Hilliard, L. R.; Smith, J. E.; Wu, Y. R.; Tan, W. H. *Anal. Chem.* 2006, *78*, 646-654.
[206] Wang, H.; Li, J.; Ding, Y.; Lei, C.; Shen, G.; Yu, R. *Anal. Chim. Acta* 2004, *501*, 37-43.
[207] Gerion, D.; Pinaud, F.; Williams, S. C.; Parak, W. J; Zanchet, D.; Weiss, S.; Alivisatos, A. P. *J. Phys. Chem. B* 2001, *105*, 8861-8871.
[208] Sun, Y. Y.; Yan, F.; Yang, W. W.; Zhao, S.; Yang, W.; Sun C. Q. *Anal. Bioanal. Chem.* 2007*, 387*, 1565-1572.
[209] Hilliard, L. R.; Zhao, X.; Tan, W. *Anal. Chim. Acta* 2002, *470*, 51-56.
[210] Santra, S.; Zhang, P.; Wang, K.; Tapec, R.; Tan, W. *Anal. Chem.* 2001, *73*, 4988-4993.
[211] Herr, J. K.; Smith, J. E.; Medley, C. D.; Shangguan, D.; Tan, W. *Anal. Chem.* 2006, *78*, 2918-2919.
[212] Smith, J. E.; Medley, C. D.; Tang, Z.; Shangguan, D.; Lofton, C.; Tan, W. *Anal.Chem.* 2007, *79*, 3075-3082.

[213] Zhang, T. T.; Stilwell, J. L.; Gerion, D.; Ding, L. H.; Elboudwarej, O.; Cooke, P. A.; Gray, J. W.; Alivisatos, A. P.; Chen. F. F. *Nano Lett.* 2006, *6*, 800-808.
[214] Bardi, G.; Malvindi, M. A.; Gherardini, L.; Costa, M.; Pompa, P. P.; Cingolani, R.; Pizzorusso, T. *Biomaterials* 2010, *31*, 6555-6566.
[215] Tang, X. S.; Choo, E. S. G.; Li, L.; Ding, J.; Xue J. *Chem. Mater*. 2010, *22*, 3383-3388.
[216] Kumar, R.; Ding, H.; Hu, R.; Yong, K. T.; Roy, I.; Bergey, E. J. Prasad, P. N. *Chem. Mater*. 2010, *22*, 2261-2267.
[217] Han, R. C.; Yu, M.; Zheng, Q.; Wang, L. J.; Hong, Y. K.; Sha Y. L. *Langmuir* 2009, *25*, 12250-12255.
[218] Villanueva, A.; Presa, P. D. L.; Alonso, J. M.; Rueda, T.; Martínez, A.; Crespo, P.; Morales, M. P.; Gonzalez-Fernandez, M. A.; Valdés, J.; Rivero G. *J. Phys. Chem. C* 2010, *114*, 1976-1981.
[219] Yang, H.; Zhuang, Y.; Hu, H.; Du, X. X.; Zhang, C. X.; Shi, X. Y.; Wu, H. X.; Yang, S. *Adv. Funct. Mater.* 2010, *20*, 1733-1741.
[220] Tang, F.; He, F.; Cheng, H. c.; Li, L. D. *Langmuir* 2010, *26*, 11774-11778
[221] Gole, A.; Agarwal, N.; Nagaria,P.; Wyattc, M. D.; Murphy, C. J. *Chem. Commun.*, 2008, *46*, 6140-6142.
[222] Lua, P.; Zhang, J. L.; Liu, Y. L.; Sun, D. H.; Liu, G. X.; Hong, G. Y.; Ni, J. Z. *Talanta* 2010, *82*, 450-457.
[223] He, Q. J.; Zhang, J. M.; Chen, F.; Guo, L. M.; Zhu, Z. Y.; Shi, J. L. *Biomaterials* 2010, *31*, 7785-7796.
[224] Wu, C. L.; Chen, C.; Lai, J. P.; Chen, J. B.; Mu, X.; Zheng, J. S.; Zhao Y. B. *Chem. Commun.*, 2008, *23*, 2662-2664.
[225] Kim, J. H.; Kim, J. S.; Choi, H.; Lee, S. M. Jun, B. H.; Yu, K. N.; Kuk, E.; Kim, Y. K.; Jeong, D. H.; Cho, M. H.; Lee, Y. S. *Anal. Chem.* 2006, *78*, 6967-6973.
[226] Sharma, P.; Brown, S.; Walter, G.; Santra, S.; Moudgil, B. *Adv. Colloid Interface. Sci.* 2006, *123*, 471-485.
[227] Zhao, X.; Rovelyn, T.; Tan, W. *J. Am. Chem. Soc.* 2003, *125*, 11474-11475.
[228] Zhu, N.; Cai, H.; He, P.; Fang, Y. *Anal. Chim. Acta* 2003, *481*, 181-189.
[229] Liang, Y.; Gong, J.L.; Huang, Y.; Zheng, Y.; Jiang, J. H.; Shen, G. L.; Yu, R. Q. *Talanta* 2007, *72*, 443-449.
[230] He, X. X.; Huo, H.L.; Wang, K.; Tan, W.; Gong, P.; Ge. J. *Talanta* 2007, *73*, 764-769.
[231] Park, M. E.; Chang, J. H. *Mater. Sci. Eng. C* 2007, *27*, 1232-1235.
[232] Kang, K.; Choi, J.; Nam, J. H.; Lee, S. C.; Kim, K. J.; Lee, S. W.; Chang, J. H. *J. Phys. Chem. B* 2009, *113*, 536-543.
[233] Ruiz-Hernández, E.; Baeza, A.; Vallet-Regí. *ACS Nano* 2011, *5*, 1259-1266.
[234] Santra, S.; Wang, K.; Tapec, R.; Tan, W. *J. Biomed. Opt.* 2001, *6*, 160-166.
[235] Sendroiu, I. E.; Warner, M. E.; Corn, R. M. *Langmuir* 2009, *25*, 11282-11284.
[236] Cerruti, M.G.; Sauthier, M.; Leonard, D.; Liu, D.; Duscher, G.; Feldheim, D. L.; Franzen, S. *Anal. Chem.* 2006, *78*, 3282-3288.
[237] Liu, S. H.; Zhang, Z. H.; Han, M. *Anal. Chem.* 2005, *77*, 2595-2600.
[238] Liu, S.; Zhang, Z. H.; Wang, Y.; Wang, F.; Han, M. Y. *Talanta* 2005, *67*, 456-461.
[239] Liu, S. H.; Han, M. Y. *Adv. Funt. Mater.* 2005, *15*, 961-967.
[240] Qin, P. Z.; Niu, C. G.; Zeng, G. M.; Ruan, M.; Tang, L.; Gong, J. L. *Talanta* 2009, *80*, 991-995.
[241] Zhou, X.; Zhou, J. *Anal. Chem.* 2004, *76*, 5302-5312.

[242] Hong, C. L.; Yuan, R.; Chai, Y. Q.; Zhuo, Y. *Anal. Chim. Acta* 2009, 633, 244-249.
[243] Laurent, S.; Forge, D.; Port, M.; Roch, A.; Robic, C.; Elst, L. V.; Muller, R. N. *Chem. Rev.* 2008, *108*, 2064-2110.
[244] Wang, G. H.; Zhang, L. M. *J. Phys. Chem. B* 2006, *110*, 24864-24868.
[245] Tang, D.; Yuan, R.; Chai, Y.; Fu, Y. *Electrochem. Commun*. 2005, *7*, 177-182.
[246] Dattelbaum, A. M.; Baker, G. A.; Fox, J. M.; Iyer, S.; Dattelbaum, J. D. *Bioconjugate Chem*. 2009, *20*, 2381-2384.
[247] Wang, B.; Zhang, J.; Pan, Z.; Tao, X.; Wang, H. *Biosens. Bioelectron*. 2009, *24*, 1141-1145.
[248] Šulek, F.; Knez, Ž.; Habulin, M. *Appl. Surf. Sci.* 2010, *256*, 4596-4600.
[249] Qiu, J. D.; Guo, J.; Liang, R. P.; Xiong, M. *Electroanalysis* 2007, *19*, 2335- 2341.
[250] Di, J. W.; Shen, C. P.; Peng, S. H.; Tu,Y. F.; Li, S. J. *Anal. Chim. Acta* 2005, *553*, 196-200.
[251] Zhang, F. F.; Wan, Q.; Wang, X. L.; Sun, Z. D.; Zhu, Z. Q.; Xian, Y. Z.; Jin, L. T. *J. Electroanal. Chem*. 2004, *571*,133-138.
[252] Yang, H. P.; Zhu, Y.F. *Talanta* 2006, *68*, 569-574.
[253] Ye, J. S.; Ottova, A.; Tien, H. T.; Sheu, F.S. *Bioelectrochemistry* 2003, *59*, 65-72.
[254] Ren, X. L.; Meng, X .W.; Tang, F. Q.; Zhang, L. *Mater. Sci. Eng. C* 2009, *29*, 2234-2238.
[255] Jia, T. T.; Cai, Z. M.; Chen, X. M.; Lin, Z. J.; Huang, X. L.; Chen, X.; Chen, G. N. *Biosens. Bioelectron.* 2009, *25*, 263-267.
[256] Kang, X. H.; Mai, Z. B.; Zou, X. Y.; Cai, P. X.; Mo, J. Y. *Talanta* 2008, *74*, 879-886.
[257] Sun,Y. Y.; Yan, F.; Yang, W. S.; Sun, C. Q. *Biomaterials* 2006, *27*, 4042-4049.
[258] Di, J. W.; Peng, S. H.; Shen, C. P.; Gao, Y. S.; Tu, Y. F. *Biosens. Bioelectron*. 2007, *23*, 88-94.
[259] Ye, C.; Kong, Q. C.; Wu, R.; Hu, J. Q.; Chen, Z. W.; Li, A. Q. *Mater. Lett*. 2010, *64*, 1720-1723.
[260] Liu, M. C.; Shi, G. Y.; Zhang, L.; Zhao, G. H.; Jin, L. T. *Anal. Bioanal. Chem*. 2008, *391*, 1951-1959.
[261] Zhang, F. F.; Wan, Q.; Li, C. X.; Wang, X. L.; Zhu, Z. Q.; Xian,Y. Z.; Jin, L. T.; Yamamoto, K. *Anal. Bioanal. Chem*. 2004, *380*, 637-642.
[262] Šulek, F.; Drofenik, M.; Habulin, M.; Knez, Ě. *J. Magn. Magn. Mater.* 2010, *322*, 179-185.
[263] Qian, J.; Zhou, Z. X.; Cao, Xi. D.; Liu, S. Q. *Anal. Chim. Acta* 2010, *665*, 32-38.
[264] Hun, X.; Zhang, Z. J. *Biosens. Bioelectron*. 2007, *22*, 2743-2748.
[265] Yang, X.; Yuan, R.; Chai, Y. Q.; Zhuo, Y.; Mao, L.; Yuan, S. R. *Biosens. Bioelectron*. 2010, *25*, 1851-1855.
[266] Yuan, S. R.; Yuan, R.; Chai, Y. Q.; Mao, L.; Yang, X.; Yuan, Y. L.; Niu, H. *Talanta* 2010, *82*, 1468-1471.
[267] Gong, J. L.; Liang, Y.; Huang, Y.; Chen, J. W.; Jiang, J. H.; Shen, G. L.; Yu R. Q. *Biosens. Bioelectron*. 2007, *22*, 1501-1507.
[268] Wang, C. G.; Ma, Z. F.; Wang, T. T.; Su, Z. M. *Adv. Funct. Mater*. 2006, *16*, 1673-678.
[269] Qu, B.; Chu, X.; Shen, G. L.; Yu, R. Q. *Talanta* 2008, *76*, 785-790.
[270] Jin, X. Y.; Jin, X. F.; Ding, Y. J.; Jiang, J. H.; Shen, G. Li.; Yu, R. Q. *Chin. J. Chem*. 2008, *26*, 2191-2196.

[271] Wang, J.; Liu, G. D.; Lin, Y. H. *small* 2006, *2*, 1134-1138.
[272] Liu, Y.; Jiang, H. *Electroanalysis* 2006, *18*, 1007-1013.
[273] Wei, Q.; Xin, X. D.; Du, B.; Wu, D.; Han, Y. Y.; Zhao, Y. F.; Cai, Y. Y.; Li, R.; Yang, M. H.; Li, H. *Biosens. Bioelectron*. 2010, *26*,723-729.
[274] Yang, M.; Li, H.; Javadi, A.; Gong, S. *Biomaterials* 2010, *31*, 3281-3286.
[275] Sardesai, N.; Pan, S. M.; Rusling J. *Chem. Commun*. 2009, 4968-4970
[276] Wolcott, A.; Gerion, D.; Visconte, M.; Sun, J.; Schwartzberg, A.; Chen, S. W.; Zhang, J. Z. *J. Phys. Chem. B* 2006, *110*, 5779-5789.
[277] Pan, J.; Yang, Q. W. *Anal. Bioanal. Chem*. 2007, *388*, 279-286.
[278] Ye, Z.; Tan, M.; Wang, G.; Yuan, J. *J. Mater. Chem*. 2004, *14*, 851-856.
[279] Ye, Z.; Tan, M.; Wang, G. Yuan, J. Anal. Chem. 2004, 76, 513-518.
[280] Zhang, H.; Xu, Y.; Yang, W.; Li, Q. G. *Chem. Mater*. 2007, *19*, 5875-5881.
[281] Lee, K. G.; Wi, R.; Park, T. J.; Yoon, S. H.; Lee, J.; Lee, S. J.; Kim, D. H. *Chem. Commun*., 2010, *46*, 6374-6376.
[282] Wu, J.; Ye, Z.Q.; Wang, G. L.; Yuan, J. L. *Talanta* 2007, *72*, 1693-1697.
[283] Yuan, J. I.; Wang, G. L.; *Trends Anal. Chem*. 2006, *25*, 490-500.
[284] Wang, G.; Yuan, J.; Hai, X.; Matsumoto, K. *Talanta* 2006, *70*, 133-138.
[285] Ye, Z.; Tan, M.; Wang, G.; Yuan, J. *Talanta* 2005, *65*, 206-210.
[286] Wu, Y.F.; Chen, C.L.; Liu, S.Q. *Anal. Chem*. 2009, *81*, 1600-1607.
[287] Chen, L.Y.; Chen, C. L.; Li, R.N.; Li, Y.; Liu, S.Q. *Chem. Commun*. 2009, 2670–2672.
[288] Qian, J.; Zhang, C.Y.; Cao, X.D.; Liu, S.Q. *Anal. Chem.* 2010, 82, 6422-6429.
[289] Chen, L.Y.; Qi, Z.J.; Chen, R.J.; Li, Y.; Liu, S.Q. *Clin. Chim. Acta* 2010, 411, 1969-1975.

In: Silica Nanoparticles
Editor: Juan Vivero-Escoto
ISBN 978-1-61324-452-4
© 2012 Nova Science Publishers, Inc.

Chapter 2

REACTIVITY OF INORGANIC RADICALS AND EXCITED TRIPLET STATES IN COLLOIDAL SILICA SUSPENSIONS

Valeria B. Arce, Paula Caregnato, Mónica C. Gonzalez and Daniel O. Mártire*
Instituto de Investigaciones Fisicoquímicas Teóricas y Aplicadas (INIFTA),
Universidad Nacional de La Plata, Casilla de Correo, Sucursal, La Plata, Argentina

ABSTRACT

Aquatic photochemistry studies the degradation of contaminants induced by light (either terrestrial sunlight or artificial light used in engineered water treatment systems). In addition to the "direct photolysis" or "direct phototransformation" route there exist a variety of photochemical reactions involving chromophores already present in natural waters and producing reactive species that initiate the degradation of the target contaminant ("indirect phototransformation"). Since the main absorber of light in natural waters is colored dissolved natural organic matter (CDOM), the excited triplet states of CDOM are involved in the indirect phototransformation of contaminants. However, irradiation of CDOM leads to the formation of other species, such as singlet molecular oxygen, solvated electrons, hydrogen peroxide, and hydroxyl radicals among others. Most of these species are able to initiate chemical reactions in which undesirable organic components are attacked and ultimately destroyed, thus providing a mechanism for self-cleansing of the water sources.

Silica is a ubiquitous material in the environment, which is present in great amounts in natural waters. This material is an excellent sorbent of contaminants, as well as reactive species involved in their degradation. Thus, it is relevant to know the mechanisms of the reactions that take place at the silica/water interfaces.

*Corresponding Author: Daniel O. Mártire (CIC Researcher),
Casilla de correo 16, sucursal 4 (1900), La Plata, Argentina,
Phone: +54 221 4257430/7291. Fax: -54 221 4254642,
E-mail: dmartire@inifta.unlp.edu.ar.

Because colloidal silica has a very high specific surface area and is optically transparent in the near-infrared, visible and ultraviolet regions, it is very appropriate for investigating interfacial reaction kinetics involving photochemically generated species.

This chapter reviews recent research concerned with the kinetic behavior of two kinds of reactive species in colloidal silica suspensions. On one hand, excited triplet states, mainly those of benzophenone, and on the other hand inorganic radicals, such as $SO_4^{\bullet-}$, $Cl^{\bullet}$, $Cl_2^{\bullet-}$, $HPO_4^{\bullet-}$, $(SCN)_2^{\bullet-}$.

1. INTRODUCTION

Aquatic photochemistry studies the degradation of contaminants induced by light (either terrestrial sunlight or artificial light used in engineered water treatment systems). In addition to the "direct photolysis" or "direct phototransformation" route there exist a variety of photochemical reactions involving chromophores already present in natural waters and producing reactive species that initiate the degradation of the target contaminant ("indirect phototransformation").

In natural waters, humic substances (HS) represent the main fraction of colored dissolved organic carbon (CDOM) that absorb solar radiation and, therefore, they play an important role in aquatic photochemistry (*1*). In particular, HS act as singlet oxygen, $O_2(a^1\Delta_g)$, sensitizers *(2-5)*. Photolysis of HS also leads to the formation of other reactive species including free radicals and hydrated electrons, $e^-_{aq.}$ (*6*), reactive triplet states (*7,8*), hydroxyl radicals, $HO^{\bullet}$ (*9,10*), superoxide, $O_2^{\bullet-}$ (*11*), and hydrogen peroxide (*12,13*). Most of these species are able to initiate chemical reactions in which undesirable organic components are attacked and ultimately destroyed, thus providing a mechanism for self-cleansing of the water sources.

Excited triplet states of colored dissolved natural organic matter appear to play a crucial role in the oxidation of organic contaminants in surface waters and UV-irradiated natural waters. Phenols, phenylureas and 4-amino-benzenesulfonamides have been identified so far as important classes of compounds particularly subject to such an oxidation (*7,14*).

Halladja et al. (*15*) using photo-oxygenation of furfuryl alcohol as a probe for singlet molecular oxygen (*16*). showed that the electron-rich compound 2,4,6-trimethylphenol is directly oxidized by triplet excited states deriving from HS substances.

Aryl ketones, benzophenone and quinones, model compounds for the chrompophores present in HS are major light absorbers in the 350 nm region. They undergo photochemical reactions, which involve n,π*, π,π*, as well as charge transfer transitions. Photoexcitation of aromatic ketones, quinoids and phenolics that may occur in fulvic acid (*17,18*), mainly involve π,π* character transitions if excited with $\lambda^{exc} < 310$ nm and n,π* character for $\lambda^{exc} > 320$ nm.

Free radicals are important intermediates in chemical changes occurring in aqueous reactions systems of our hydrosphere. Photolysis of organic chromophors and the photochemical redox reaction of Fe^{3+} with organic ligands are other important sources of oxidants such as H_2O_2, $O_2(a^1\Delta_g)$, $HO^{\bullet}$ and $HO_2^{\bullet}/O_2^{\bullet-}$. Moreover, scavenging of hydroxyl and sulfate radicals by chloride, phosphate, and carbonate ions also present in natural waters (*19*) leads to the formation of $Cl^{\bullet}/Cl_2^{\bullet-}$(*20,21*), $H_2PO_4^{\bullet-}$/ $HPO_4^{\bullet-}/PO_4^{\bullet 2-}$ (*22-29*), and $CO_3^{\bullet-}$ radicals, respectively. These radicals behave as oxidizing agents and are thus able to initiate the degradation of organic compounds present in the water reservoirs.

In this aspect, the application of Advanced Oxidation Processes (AOP) for the elimination of refractive organic contaminants is based on the generation of reactive species such as sulfate, $SO_4^{\bullet-}$, and $HO^{\bullet}$ radicals (*30-34*). Sulfate radicals, $SO_4^{\bullet-}$ with a redox potential $E(SO_4^{\bullet-}/SO_4^{2-})$ = 2.4 V (*35*), may significantly accelerate the kinetics of contaminant oxidation in a wide range of matrix conditions.

Silica, SiO_2, is a ubiquitous material in the environment present in all natural waters. In surface and well water it is found in concentrations of 1 to 100 mgL^{-1}. Most of the silica found in well waters is a result of dissolving silica-containing rock. The silica content in surface water streams depends on climatic conditions such as quantity of atmospheric precipitation, and intensity and character of weathering. The highest silica content is observed in regions of recent tectonic movements and of modern volcanism (*36*).

There is strong evidence in the literature that silica may affect water photochemistry in many ways, related to the diverse properties of its reactive surface.

Silica in water is colloidal. This material is an excellent sorbent of contaminants (*37*) and of reactive species. Silica immersed in an aqueous environment orients its surface silicon atoms in a tetrahedral configuration with each Si atom holding approximately one OH group *(38)*. A number of 4.6-4.9 OH groups per nm^2 are found for all types of fully hydroxylated silica, independent of its origin *(38)*. There are at least two types of silanol groups at the water/silica interface characterized by pKa's of 4.5-6.5 for about 20% of the silanol sites, and a pKa value of 8.5-9.0 for the remaining 80% *(39-46)*. The pKa, values were associated with the geminal and single silanols, respectively (*47,48*).

Adsorbed substrates on silica gel show spectral changes dependent on the nature of the physical adsorption process and on the polarity of the excited and ground states *(49)*. In general, red shifts occur on adsorption of a compound onto the polar adsorbent silica gel if the excited state of the molecule has an increased permanent dipole or if it is more polarizable than the ground state; the blue shifts occur if the reverse is true. These effects of physical adsorption on electronic absorption spectra suggest a novel means of influencing the course of a photochemical reaction. Moreover, the H- bonding ability of surface silanol groups *(50)* determines the chemistry on the particle/water interface. It is well reported that the H-bonding ability of silica with constituents of the cell membranes and tissues contributes to the silica particle cytotoxic effects *(51)*. In addition, the surface chemistry of crystalline silica can result in the production of reactive oxygen species *(52)*. Reactive species such as superoxide radical anion are reported to enhance desorption of hydrophobic sorbents such as dodecane from silica surfaces (*53*).

This chapter reviews recent research concerned with the kinetic and reaction mechanisms of two kinds of reactive species at the silica/water interfaces. On one hand, excited triplet states, mainly those of benzophenone, were considered. Since alcohols are widely used in industrial processes, chemical adsorption of alcohols on the silica surface of sediments and on silica-based nanomaterials in contaminated waters is a process of no little significance in the environment (*54*). The results related to the reactivity of the excited triplet states of benzophenone with alcohols chemisorbed on silica nanoparticles are reported. On the other hand the reaction mechanisms of inorganic radicals, such as $SO_4^{\bullet-}$, $Cl^{\bullet}$, $Cl_2^{\bullet-}$, $HPO_4^{\bullet-}$, and $(SCN)_2^{\bullet-}$ with bare silica nanoparticles are summarized. Because colloidal silica has a very high specific surface area and is optically transparent in the near-infrared, visible and ultraviolet regions, it is very appropriate for investigating the reaction kinetics at the silica/water interface by conventional time-resolved and steady state photochemical methods.

2. QUENCHING OF BENZOPHENONE TRIPLET STATES BY MODIFIED SILICA NANOPARTICLES

Functionalized silica nanoparticles (NP) were obtained by esterification of silanol groups of silica nanoparticles with *n*-butanol (NP1) and benzyl alcohol (NP2).

The particles were characterized by Fourier transform infrared spectroscopy (FTIR), ^{13}C and ^{29}Si nuclear magnetic resonance spectroscopy using cross-polarization combined with magic-angle sample spinning (CPMAS NMR), and thermogravimetric analysis (TGA) (*55-57*).

Specific surface areas (SSA) were evaluated using the Brunauer–Emmett–Teller (BET) equation (*58*) (Table 1).

A decrease in SSA upon silica functionalization with the organic groups was observed for different systems (*59-62*). The nitrogen molecules adsorption, which preferentially takes place on the silanol groups, is partially precluded as the silica is chemically modified. Thus, surface modification of the silica nanoparticles results in a decrease in SSA (*63*). From the SSA data it is possible to calculate with eq. 1 the fraction of derivatized silanol groups, f(SiOR), by neglecting the nitrogen adsorption on the functionalized silanols (seeTable 1).

$$\%OG = \frac{f(SiOR)\times m\times 708\times 1.66\times 10^{-24} g}{(f(SiOR)\times m\times 708\times 1.66\times 10^{-24} g + 3.95\times 10^{-19} g)}\times 100 \qquad (1)$$

where m is the relative mass of one organic group (m = 57 for C_4H_9 and m = 91 for C_7H_7), 1.66 x 10^{-24} is the reciprocal of the Avogadro constant, 708 is the average number of silanol groups in one NP of bare SiO_2 estimated assuming spherical nanoparticles of radius r = 3.5 nm and 4.9 OH groups/ nm^2 (*38*), and 3.95 x 10^{-19} g is the mass of one bare SiO_2 NP, calculated from the average volume of the NP and the density of silica (2200 kg/m^3) (*64*).

Table 1. Specific surface area (SSA), decrease of SSA with respect to the bare SiO_2 NP (ΔSSA), fraction of functionalized silanol groups, *f*(SiOR), and percentage of organic compounds in mass (%OG) (*55-57*)

Sample	SSA/ m^2g^{-1}	ΔSSA/ m^2g^{-1} [b]	*f*(SiOR) [b,c]	% OG [d]	% OG [e]	% OG [b,f]
NP1	250 ± 3	140 ± 40	0.36 ± 0.14	11	7	6 ± 3
NP2	230 ± 2	160 ± 40	0.41 ± 0.14	12	11	10 ± 3
Bare SiO_2 NP	390 ± 40 [a]	0	0	0	0	0

[a] Provided by the supplier.

[b] Error bars calculated from the propagation of the error bars in SSA. [c] Calculated as ΔSSA/ 390 m^2g^{-1}. [d] % OG calculated from TOC measurements. [e] % OG calculated from the thermogravimetry experiments. [f] % OG calculated with eq. 1.

The percentage of organic groups in mass (%OG) was obtained from the *f*(SiOR) values calculated with eq. 1, from total organic carbon (TOC) measurements (*55-57*) and from TGA measurements (*56,57*). There is good agreement between the data of %OG calculated from TGA and SSA experiments. The slightly higher value of %OG obtained from total organic carbon (TOC) measurements for NP1 (Table 2) can also account for the CO_2(g) adsorption generated during the acidification of the samples performed previous to the TOC measurement (*65,66*).

These particles were suspended in acetonitrile / water mixtures in the presence of benzophenone (BP) to study the photogeneration of surface-grafted radicals and their reactivity. For that purpose, the decay kinetics of triplet BP in time-resolved phosphorescence experiments was investigated (*55,57*). The formation of organic radicals attached to the nanoparticles surface was studied by laser flash-photolysis (LFP) (*56,57*).

2.1. Time- Resolved Phosphorescence Experiments

Irradiation of Ar-saturated acetonitrile or water-acetonitrile solutions of benzophenone (BP) yields the corresponding triplet states (*67,68*). Figure 1 shows time-resolved BP emission traces obtained in 1:1 water acetonitrile suspensions of the modified silica nanoparticles.

Experiments in the presence of different amounts of the nanoparticles (NP) showed that the phosphorescence decay rates (followed at λ = 500 nm), increased with the concentration of NP. The quenched phosphorescence traces were well fitted to the sum of two exponential decays (eq. 2).

$$I(t) = a_F \exp(-k_F t) + a_S \exp(-k_S t) \tag{2}$$

k_F and k_S correspond to the faster and slower decay components, respectively, and the coefficients a_F and a_S represent the amplitude of the respective processes at t = 0.

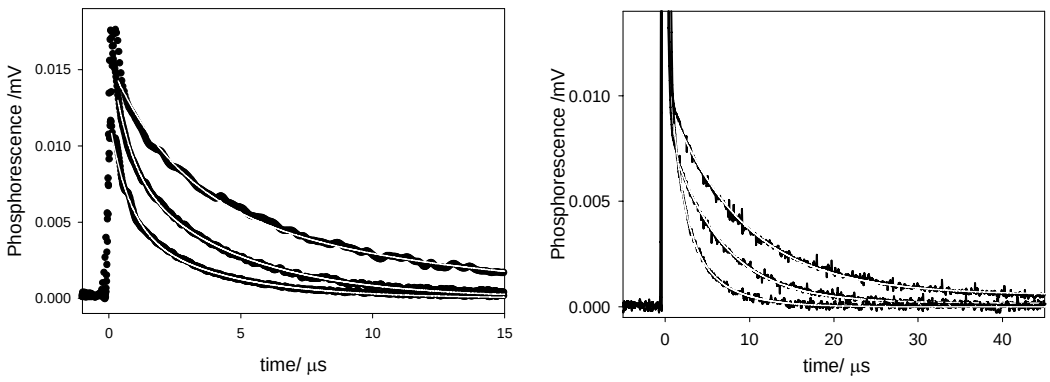


Figure 1. Time-resolved emission traces obtained from nanoparticles suspended in BP solutions (from top to bottom): Left: 0, 0.4, and 0.6 g L^{-1} NP1. Right: 0, 0.2, and 1.0 g L^{-1} NP2. The white lines show fitting to eq. 2.

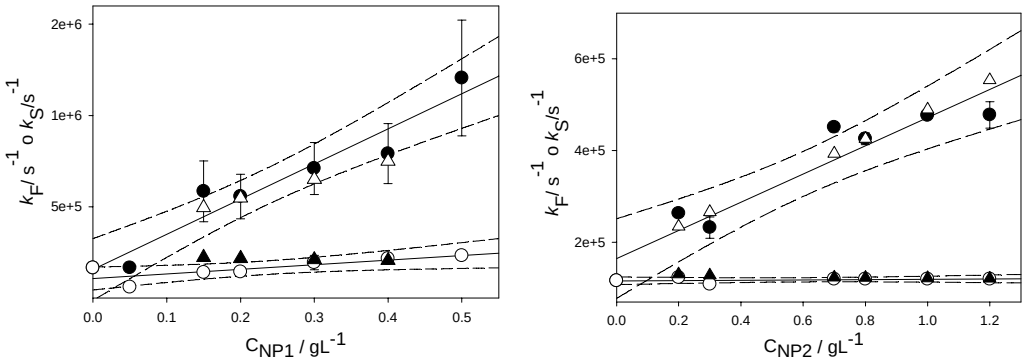


Figure 2. Rate constants k_F (●) and k_S (○) vs. C_{NP} obtained from experiments with 1.0×10^{-4} M BP suspensions in 1:1 acetonitrile: phosphate buffer. The triangles represent the values of k_F and k_S obtained from the simulations (see below). The solid and dashed lines represent the linear regression and the 95% confidence interval, respectively. Left: NP1 Right: NP2.

To determine the rate constants of the triplet quenching by NP1 and NP2 of the faster and slower components of the biexponential decay, k_F and k_S obtained from dispersions with different nanoparticle concentrations, were plotted versus the concentration of NP (C_{NP1} or C_{NP2}) (Figure 2). The Stern-Volmer plots converge on the same intercept, as expected from the single exponential decay of ^{3}BP observed in the absence of the nanoparticles.

The bimolecular rate constants for quenching of the faster (k^{QF}) and slower (k^{QS}) components of the biexponential decay (slope of the straight line in Figure 2) are shown in Table 2 shows k^{QF} and k^{QS}.

The results were interpreted by the reaction mechanism shown in Table 3, which considers the reversible adsorption of ground- state BP on to the nanoparticles to yield BP(NP) (process 1). Reactions 2 and 3 show the light absorption followed by the intersystem crossing process to yield free and adsorbed BP triplet states, ^{3}BP and ^{3}BP(NP), respectively. Reaction 4 represents the reversible adsorption process of the triplet state; processes 5 and 6 stand for the first order radiative (r) and non-radiative (nr) decay of ^{3}BP and ^{3}BP(NP), respectively. The quenching reaction 7 takes place when ^{3}BP collides with a nanoparticle (NP) moiety in a geometric configuration favorable for the chemical reaction. P, P´, and P" are the products of reactions 5nr, 6nr, and 7, respectively.

Table 2. Bimolecular rate constants for quenching of the faster (k^{QF}) and slower (k^{QS}) components of the biexponential decay

Sample	k^{QF} ($s^{-1}g^{-1}L$)	k^{QS} ($s^{-1}g^{-1}L$)
NP1	$(1.9 \pm 0.2) \times 10^6$	$(2.5 \pm 1) \times 10^5$
NP2	$(3.1 \pm 0.5) \times 10^5$	(*)

(*) A constant value $k_S = 1.2 \times 10^5$ s^{-1} independent of the concentration of NP was obtained.

Shield and Harris (*69*) investigated the quenching of ^{3}BP by commercial silica nanoparticles with methyl groups covalently bound to the silicon atoms in acetonitrile: water suspensions and observed biexponential phosphorescence decays. From chromatographic retention of BP on the methylated silica and the rate of adsorption of BP to the silica, they proposed that the adsorption contribution to heterogeneity would be averaged during the excited state lifetime. However, this could not be a valid argument because there are many other kinetic systems including a reversible reaction whose solution yields a biexponential behavior for the species involved in the reversible step (*55*,*57*). Systems that fall into this category include two nearly isonergetic excited states (*70*), excimers and exciplexes, and excited state acid-base reactions (*71*).

The resolution of the mechanism shown in Table 3 yields biexponential decays for ^{3}BP and ^{3}BP (NP) (eqs. 3 and 4),

$$[^3\mathrm{BP}] = c_F \times \exp(-k_F \times t) + c_S \times \exp(-k_S \times t) \quad (3)$$

$$[^3\mathrm{BP(NP)}] = d_F \times \exp(-k_F \times t) + d_S \times \exp(-k_S \times t) \quad (4)$$

with the apparent rate constants k_F' and k_S' given by eq. 5. (*71*).

$$k'_{F,S} = \frac{1}{2}\left\{(X+Y) \pm \left[(X-Y)^2 + 4k_4k_{-4}[NP]\right]^{1/2}\right\} \quad (5)$$

With X = k_5 + (k_6 + k_7) [NP] and Y = k_{-4} + k_6. The overall emission I_{Ph} is given by eq. 6, and also shows biexponential decay with apparent rate constants k_F' and k_S'.

$$I_{Ph} = \kappa \times (k_{5r} \times [^3\mathrm{BP}]) + k_{6r} \times [^3\mathrm{BP(NP)}] \quad (6)$$

κ is a proportionality constant.

To prove the proposed mechanism, computer simulations were performed (*55*,*57*). The rate constants of the reactions involved in the mechanism were systematically varied until the best coincidence between values of k_F and k_S obtained from the simulated and the experimental traces was observed. Reaction 1 was assumed in equilibrium, with an equilibrium constant $K_1 = 10^4 - 10^5$, in line with reported values for the adsorption equilibrium of neutral molecules on silica (*69*).

In agreement with the experimental observations, the simulated concentrations of both ^{3}BP and ^{3}BP(NP) could be well fitted to biexponential decays with apparent rate constants k_F and k_S shown in Figure 3. The good agreement observed between the apparent rate constants obtained from experimental traces and those obtained from the simulated concentrations of ^{3}BP and ^{3}BP(NP) taking the set of reaction constants shown in Table 4 (see Figure 2), supports the proposed mechanism.

Table 3. Proposed reaction mechanism

Reaction	
BP + NP → BP(NP)	1
BP(NP) → BP + NP	-1
BP + hν→ ^{3}BP	2
BP(NP) + hν→ ^{3}BP(NP)	3
^{3}BP + NP → ^{3}BP(NP)	4
^{3}BP(NP) → ^{3}BP + NP	-4
^{3}BP → P	5nr
^{3}BP → BP + hν	5r
^{3}BP (NP) → P'	6nr
^{3}BP(NP) → BP(NP) + hν'	6r
^{3}BP + NP → P"	7

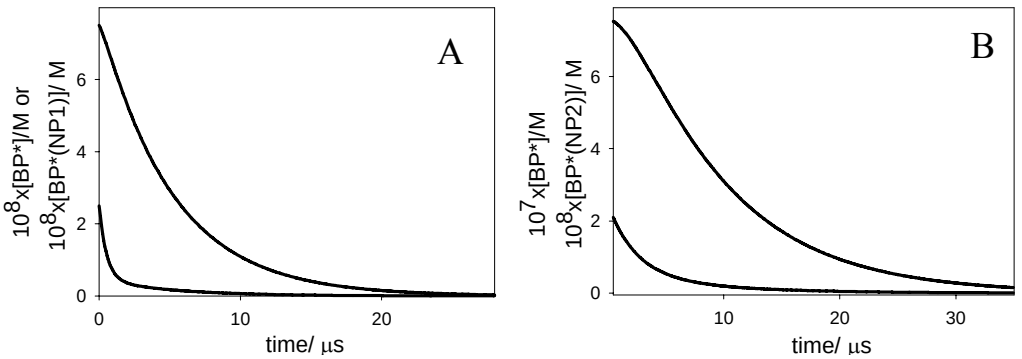


Figure 3. Biexponential decays of ^{3}BP (lower trace) and ^{3}BP (NP) as obtained from the computer simulations for A: 3×10^{-5} M NP1; B: 3×10^{-6} M NP2.

Table 4. Rate constants employed for simulations of the experimental data

Rate Constant	NP1	NP2
k_4	9×10^{10} $M^{-1}s^{-1}$	1×10^{10} $M^{-1}s^{-1}$
k_{-4}[(a)]	1×10^5 s^{-1}	1×10^5 s^{-1}
k_5[(b)]	2×10^5 s^{-1}	1×10^5 s^{-1}
k_6[(c)]	1.8×10^5 s^{-1}	1×10^5 s^{-1}
k_7	9×10^{10} $M^{-1}s^{-1}$	5×10^{10} $M^{-1}s^{-1}$

[(a)] Good simulations of the experimental results with k_{-4} in the range from 1×10^5 - 2×10^5 s^{-1} were obtained. [(b)] Coincident with the measured apparent first-order decay of ^{3}BP in the absence of NP. [(c)] The use of the same values for k_5 and k_6 is supported by the similarity of kinetics of ^{3}BP in fluid solution, in solid matrixes, and on a silica surface (*72*).

According to the proposed mechanism, the initial concentration of ^{3}BP is expected to decrease and that of ^{3}BP(NP) to increase with increasing [NP]. Thus, since the overall observed emission, given by eq. 6, increases with increasing [NP], k_{6r} should be higher than k_{5r}, which is in line with the enhanced amplitude of the emission spectra observed at 77 K obtained in the presence of NP (see below). From equations 3, 4 and 6, the emission at t = 0, I_{Ph}^0, is given by eq. 7 (*55*).

$$I_0^{Ph} = \kappa \times (k_{5r} \times c_F + k_{6r} \times d_F) + \kappa \times (k_{5r} \times c_S + k_{6r} \times d_S) \qquad (7)$$

The first and second parentheses in eq. 7 yield a_F, and a_S, respectively. The simulations show that d_S strongly increases and c_S slightly decreases with increasing [NP1], in line with the observed increase of a_S with [NP1], but the program also predicts a decrease of both c_F and d_F with increasing [NP1], and thus a decrease of a_F with [NP1], opposite to the observed behavior (*55*).

It should be taken into account that although the environment sensed by the adsorbed BP is not expected to be very much sensitive to [NP1], at higher concentrations of the NP1, where formation of bigger hydrophobic aggregates is favored (*55*), the content of water in the bulk solvent should increase and thus k_{6r} would depend on [NP1]. Indeed, time-resolved phosphorescence experiments performed at λ^{exc} = 266 nm with water: acetonitrile solutions at constant concentration of BP in the absence of NP1, show an increase of I_0^{Ph} with increasing amounts of water in the samples, in line with a k_{6r} value increasing with the water content of the samples.

To analyze the spectra of the emitting species the signals obtained by laser excitation (λ^{exc} = 266 nm) of Ar- saturated 0.1 gL^{-1} NP1 suspensions in 1:1 acetonitrile: aqueous phosphate buffer were taken at different wavelengths in the range from 340 to 600 nm. All the signals could be well fitted to eq. 1 and since ^{3}BP and ^{3}BP(NP1) are expected to emit in the same region, a bilinear regression analysis (*73*) was applied to the experimental emission matrix to obtain information on the individual spectra of the emitting species. The analysis shows that the emission at all the wavelengths can be expressed as a linear combination of two spectra.

One of them was coincident with that obtained in the absence of NP1 and otherwise identical conditions and, thus, assigned to phosphorescence of ^{3}BP. The other with a different shape should be due to ^{3}BP(NP1) phosphorescence (see Figure 4). This broadening effect in the emission spectrum of ^{3}BP compared to that of ^{3}BP(NP1) suggests an increased flexibility in the former, due to the lower mobility of ^{3}BP(NP1), as observed in emission and absorption spectra of other systems (*74*). The changes in the shape of the spectra are in line with the BP emission spectra recorded at 77 K, temperature at which the adsorption process should be favored, both in the presence and absence of NP1 (Figure 5).

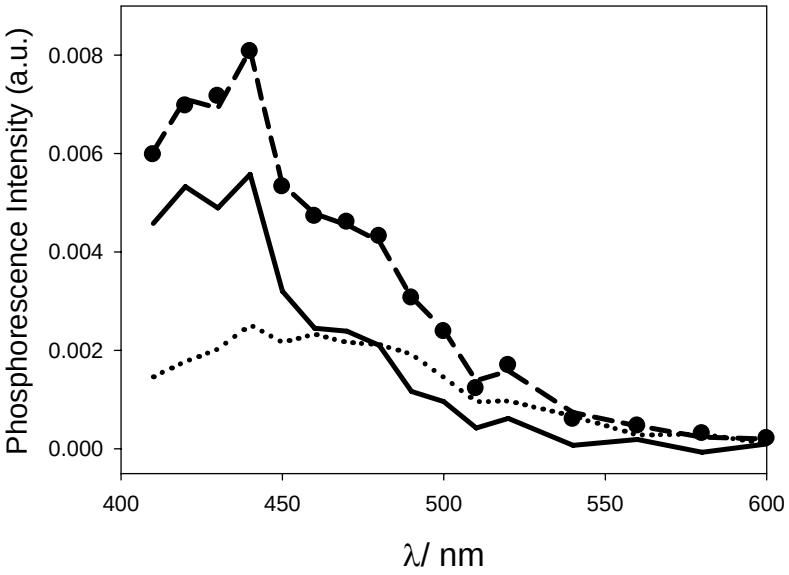


Figure 4. Phosphorescence emission spectrum obtained at 1.3 μs after the 266 nm laser shot (circles and dashed line), and contributions of ^{3}BP(NP1) (solid line) and ^{3}BP (dotted line) to the phosphorescence spectrum.

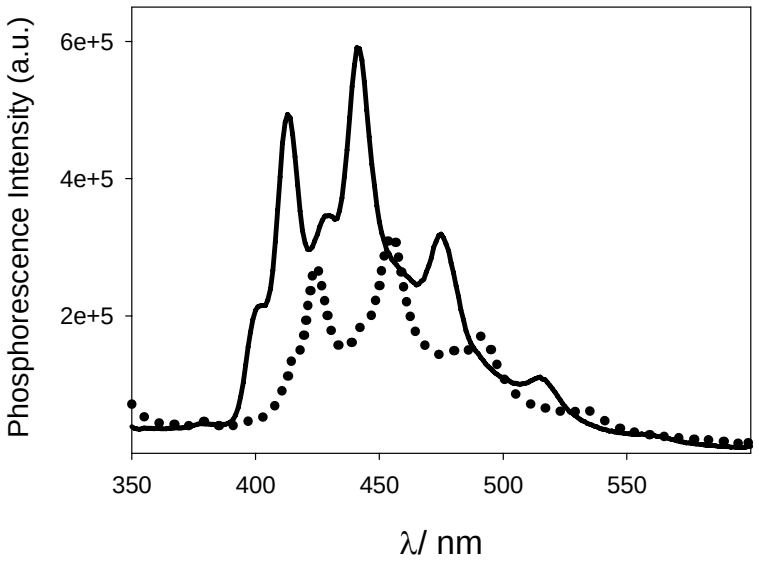


Figure 5. Phosphorescence spectra obtained at 77 K of BP in the presence (solid line) and absence (dotted line) of 0.9 g L^{-1} NP1.

The phosphorescence emission spectra of BP (λ^{exc} = 337 nm) adsorbed on NP1 at 77 K exhibits a fingered pattern of vibrational structure with a maximum at 441 nm (Figure 5). The spacing between vibronic bands in the phosphorescence spectrum is around 1600 cm^{-1}. The triplet energy of ^{3}BP(NP1), E_T[BP(NP1)], evaluated from the 0-0 band of the emission spectrum (413 nm) is 290 $kJmol^{-1}$, very similar to the value determined here for the free benzophenone, E_T[BP] = (281 ± 1) kJ mol^{-1}, and reported for benzophenone and its derivatives (*75*). On the basis of the spacing between bands, the lowest triplet energy of BP(NP1) is assigned to an nπ* triplet state (*75*), as for the free BP. The vibrational fine structure due to the stretching of the C=O bond of BP is absent at room temperature (Figure 4).

The excitation spectra obtained at 77 K at the emission wavelength of 440 nm (λ^{max} = 291 and 339 nm) is shown in Figure 6. From this spectrum, the energy of the lowest nπ* singlet excited state, 324 kJ mol^{-1}, was calculated from the 0-0 band at 369 nm. The singlet-triplet splitting was found to be equal to 2800 cm^{-1}.

The emission and excitation peaks are similar to those obtained when BP is adsorbed on the surface OH groups of oxides without any strong acidic sites such as SiO_2 and Vycor glass (PVG, major composition: SiO_2 97% and B_2O_3 3%) through hydrogen-bonding. In such systems, the phosphorescence peak of BP is observed at around 430 nm with its excitation peak at around 330 nm (*76*).

Benzophenone triplet state is able to abstract an H atom from acetonitrile and from the organic groups of NP1 to yield the diphenylketyl radical (*77*). Detection of diphenylketyl radical emission within one single nanosecond laser pulse from argon purged solid powdered samples of benzophenone adsorbed onto different reversed-phase silicas was reported in the literature (*67*). However, the absence of room-temperature emission contribution centered at around 575 nm shows that the luminescence from this radical is negligible.

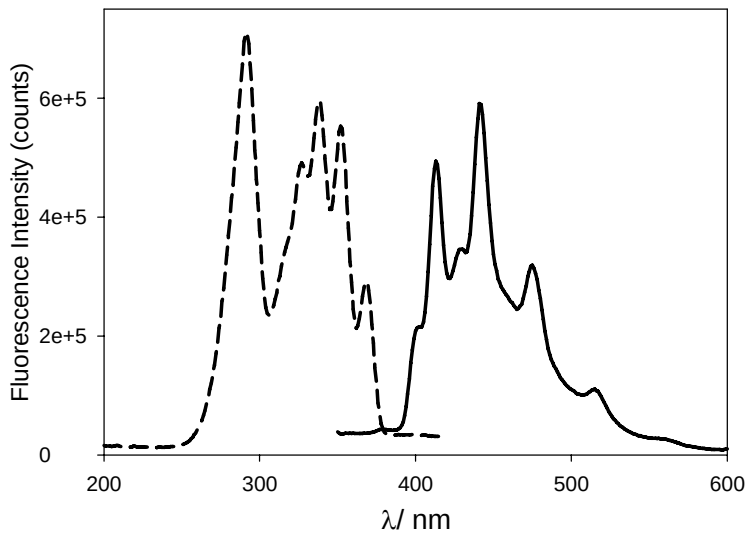


Figure 6. Excitation spectrum obtained at $\lambda^{emission}$ = 440 nm with air- saturated 0.90 gL^{-1} NP1 suspension containing 3.2 mM BP ($A^{337} \approx 0.05$) in the 1:1 acetonitrile: aqueous phosphate buffer mixture (dashed line) and corresponding emission spectrum (λ^{exc} = 337 nm).

Some of the bimolecular rate constants shown in Table 4 are in the range 1×10^{10} -1×10^{11} $M^{-1}s^{-1}$. The rate constant of the elementary reaction between reactant A in solution and reactant B immobilized at the surface of a spherical particle S as derived from the Smoluchowski equation, is given by eq. 8 (*55,57,71,76*).

$$k_{A,B} = \frac{4\pi N_{AV} R_{A+S} D_{A+S} f}{1000} \exp(-\frac{E_a}{kT}) \quad (8)$$

where N_{AV} is Avogadro´s constant, R_{A+S} is the sum of the radii of species A and particle S, D_{A+S} is the mutual diffusion coefficient given by the sum D_A+D_S. The Arrhenius factor, $\exp(-E_a/kT)$, corrects for the fraction of collisions that do not result in reaction. Factor $\boldsymbol{f} = \exp(-w/kT)$, accounts for the coulombic work, w, needed for bringing a charged radical anion from the electrolyte solution to the charged NP surface (*78*). Because the benzophenone excited state has no charge, $\boldsymbol{f} = 1$ for these reactions.

For the reactions of ^{3}BP with the NP, the average radius of the individual particles (3.5 nm) is much larger than the size of the benzophenone molecule (0.37 nm), (*79*) so that R_{A+S} is dominated by the radius of the NP. TEM experiments show NP aggregation, and thus in average $R_{A+S} \geq R_S = 3.5 \times 10^{-7}$ cm and NP diffusion is much slower than that of the ^{3}BP. The mutual diffusion coefficient, D_{A+S}, is mainly due to the motion of the excited states, i.e,, $D_{A+S} \approx D_A = 1.0 \times 10^{-5}$ cm^2 s^{-1}, the value reported for ground-state BP in ethanol (*79*). Thus, the calculated pre-exponential factor, i.e., the rate constant of the diffusion-controlled reaction results $k^{diff} \geq 3 \times 10^{10}$ $M^{-1}s^{-1}$. From the aggregation observed by TEM (*55*), the assumption of $R_S > 3.5 \times 10^{-7}$ cm seems reasonable and thus, the values of k_4 and k_7 shown in Table 4 should be below the diffusion-controlled rate constant.

2.2. Laser Flash-Photolysis (LFP) Experiments

2.2.1. LFP with BP Solutions

LFP experiments were performed with Ar-saturated solutions of BP. The absorption traces obtained from photolysis experiments of BP, in the absence of NP, showed a spectrum immediately after the laser shot with maxima at around 530 nm and at 330 nm (spectrum at t = 0 in Figure 7), corresponding to the T1 → T2 and T1 → T3 absorption bands of this ketone, respectively (*80*). The absorbance changes could be well fitted to eq. 9.

$$\Delta A = \Delta A_0 \exp(-k_{app}(\lambda) \times t) + C(\lambda) \quad (9)$$

The dependence of the decay rate $k_{app}(\lambda)$ on the observation wavelength is responsible for the faster decay of the 520 nm band compared to that centered at 320 nm. This behavior is indicative of the contribution of more than one species to the time evolution of the absorbance changes. Since ^{3}BP is able to abstract an H-atom from acetonitrile to yield the diphenylketyl radical, DPK (*77*), at least ^{3}BP and DPK should contribute to the traces. Other species could also contribute to our LFP signals, such as the hydroxyl radical adduct of benzophenone

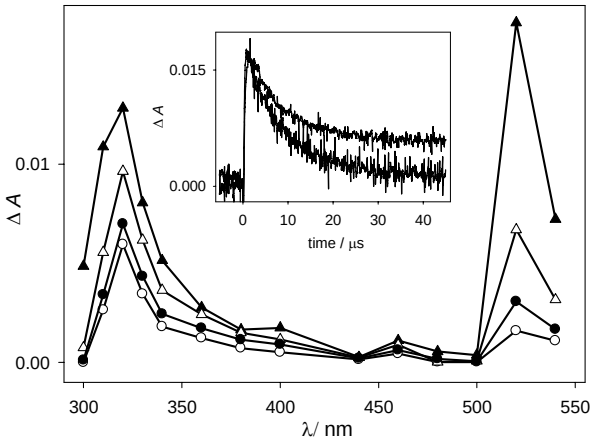


Figure 7. Experimental absorption spectra obtained with Ar- saturated 4×10^{-5} M solutions of BP taken at: 0 μs (▲); 10 μs (Δ); 20 μs (●); and 40 μs (○) after the laser shot. Inset: Traces obtained at 320 nm (upper trace) and 520 nm (lower trace).

(λ^{max} = 390 nm), which is formed by the reaction with water of the BP radical cation, the latter obtained by UV photoionization (*81*).

To obtain information on the kinetics and spectra of the absorbing species a bilinear regression analysis (*73*) was applied to the experimental absorption matrix. The analysis shows that the absorption at all the wavelengths can be expressed as a linear combination of two spectra (Figure 8). One of them was coincident with that reported for the T-T absorption spectrum of BP and the other is due to DPK (*67,77*). The bilinear analysis shows that this radical is formed from the decay of ^{3}BP (inset of Figure 8). The DPK radical under these experimental conditions decays in a longer time scale. The program shows that DPK is generated by ^{3}BP H-abstraction from acetonitrile, and that the contribution of other species is negligible.

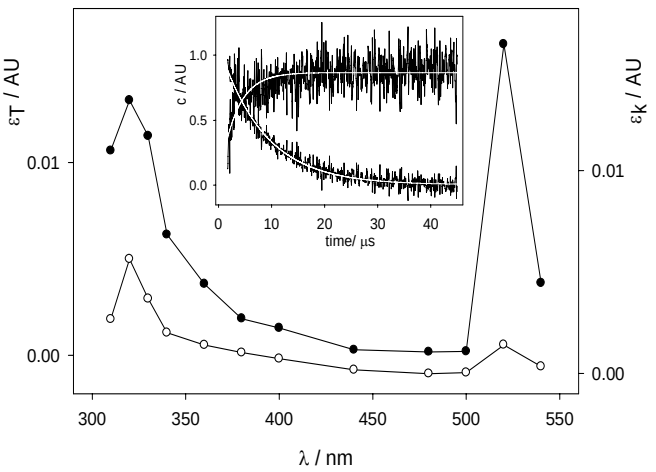


Figure 8. Absorption coefficients obtained from the analysis with the bilinear program of the experiments shown in Figure 7 for the triplet state of BP (●) and DPK (○). Inset: Kinetic profiles of the triplet state of BP (decaying curve) and DPK, as obtained from the bilinear program.

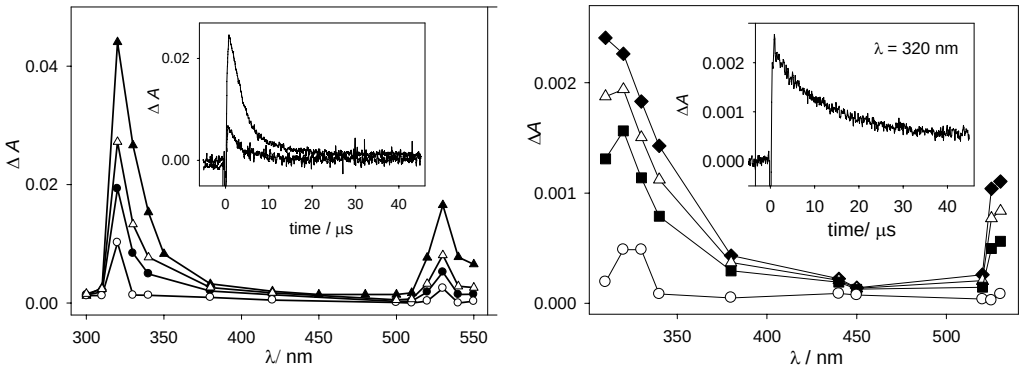


Figure 9. Left: Experimental absorption spectra obtained with Ar-saturated suspensions of NP1 (0.4 gL^{-1}) in 4×10^{-5} M BP solutions taken at: 0 μs (▲); 3 μs (Δ); 5 μs (●); and 40 μs (○) after the laser shot. Inset: Traces obtained at 320 nm (upper trace) and 520 nm (lower trace). Right: Absorption spectra obtained with Ar-saturated 0.2 gL^{-1} NP2 suspensions in the presence of 4×10^{-5} M BP taken at different times after the laser shot (from top to bottom): 0 μs; 2 μs; 5 μs y 45 μs. Inset: Traces obtained at 320 nm.

2.2.2. LFP with NP1 and NP2 Suspensions in BP Solutions

The absorption traces obtained in LFP experiments performed with Ar-saturated suspensions of NP1 or NP2 in BP solutions (insets of Figure 9) could also be fitted to eq. 9. The absorption spectra taken at different times after the laser shot are shown in Figure 9.

Detection of the DPK emission within one single ns laser pulse from Ar-purged solid powdered samples of benzophenone adsorbed onto different reversed-phase silicas was also reported in the literature (*67*). However, the absence of room temperature emission contribution centered at around 575 nm shows that this radical is not formed within our laser pulse by excitation of BP in NP suspensions (*55*), although it is expected to be formed by H-abstraction from acetonitrile and from the organic groups of NP. Furthermore, BP excitation with 266 nm radiation, may also lead to formation of the benzoyl radical (*82*). This transient species peaks at about 360 nm and has a lower intensity absorption band near 500 nm (*82*).

To investigate if other species different from the triplet state of BP, ^{3}BP, and DPK contribute to the absorbance traces, the bilinear program was used.

For NP1 the analysis of the absorption matrix with two species shows that one of them is formed immediately after the laser shot and its decay is well fitted to a biexponential function. The second species is formed with a risetime identical to the decay of the former species (see Figure 10).

All the previous results are in agreement with the reported biexponential BP phosphorescence decay in acetonitrile: aqueous phosphate buffer suspensions of NP1 and NP2 (*55,57*) (see above). Thus, the first species obtained from the bilinear analysis of the LFP traces should contain the contribution of these triplet states. From its absorption spectrum, and since it is formed by the decay of the former species, it is clear that both the free and adsorbed DPK radicals contribute to the second species (*67,71*).

It can be concluded that (if any) the contribution of other species, such as the hydroxyl radical adducts or the benzoyl radicals (see above) to the LFP signals is negligible.

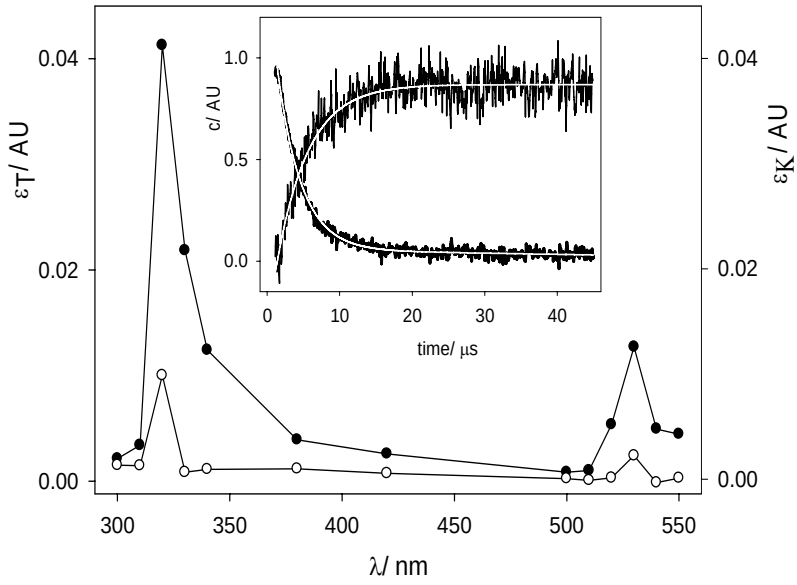


Figure 10. Absorption coefficients obtained from the analysis with the bilinear program of the experiments shown in Figure 9 (left) for ^{3}BP (●) and DPK (○). Inset: Kinetic profiles of the two species obtained from the bilinear program (see text).

The use of the bilinear program showed that only the triplet states of benzophenone and the ketyl radicals contribute to the laser flash-photolysis traces obtained with NP1 suspended in Ar-saturated benzophenone solutions.

The good agreement between the experimental and calculated traces, the corresponding residuals and parity plots (ΔA_{calc} vs. ΔA_{exp}) are shown in Figure 11 for two different wavelengths.

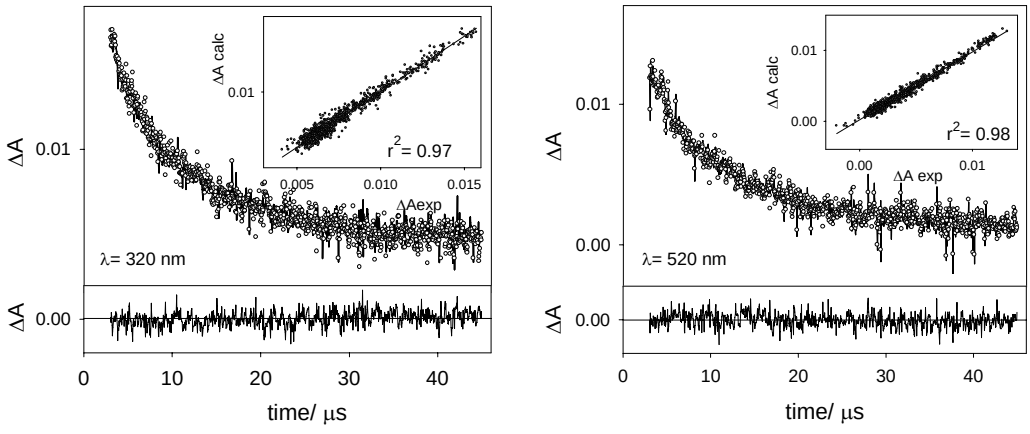
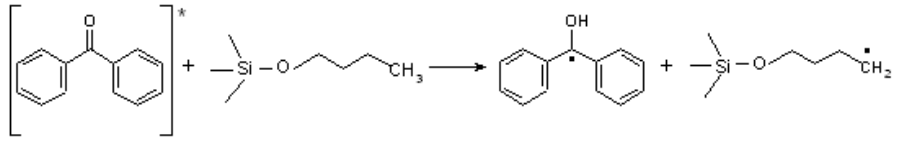


Figure 11. Experimental (lines) and calculated (dots) absorption traces obtained with Ar-saturated suspensions of NP1 (0.4 gL^{-1}) in 4 × 10^{-5} M BP at different wavelengths, as indicated. Inset: Parity plots. Below: The corresponding residuals.

These results indicate that the reaction between ^{3}BP with NP1 can be written as follows:



^{3}BP DPK (10)

Since the UV absorption of alkyl radicals takes place below 270 nm (*83*) high absorbance of our colloidal suspensions below 300 nm detection prevents the absorption of alkyl radical covalently linked to the NP1, one of which isomers is shown as a product in reaction 10.

For NP2 the analysis of the absorption matrix with two species does not reproduce the observed traces. However, a good agreement between experimental and calculated data is obtained when three species are considered. The kinetic profiles of the three species are shown in Figure 12.

The absorption spectrum of the species present at t = 0 (upper spectrum in Figure 13) is coincident with the T-T absorption spectrum of BP (*67,71*), and thus it is assigned to a combination of ^{3}BP and ^{3}BP(NP). The decay of this species (see Figure 12) is coincident with that of the phosphorescence measurements in suspensions of the same concentration of NP2. A second species is formed from the decay of ^{3}BP and partially decays within the time window of the experiment (Figure 12). The absorption spectrum of this species (middle spectrum in Figure 13) is coincident with that of DPK (*56, 67*), and is assigned to this radical. The third species is also formed from the decay of ^{3}BP and its absorption (λ^{max} = 320 nm) remains constant even at 45 μs after the laser shot (Figure 13). Therefore, it may be assigned to an organic radical attached to the nanoparticles obtained from the ^{3}BP H-abstraction from the organic groups of the nanoparticles. The lower C-H bond dissociation energies for the

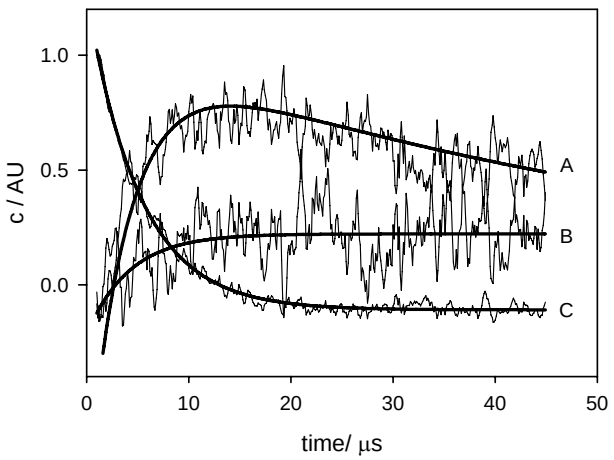


Figure 12. Kinetic profiles obtained for the three species (A: DPK, B: attached benzyl radical, C: BP triplet states) with the bilinear program for the analysis of the experiments shown in Figure 9 (right).

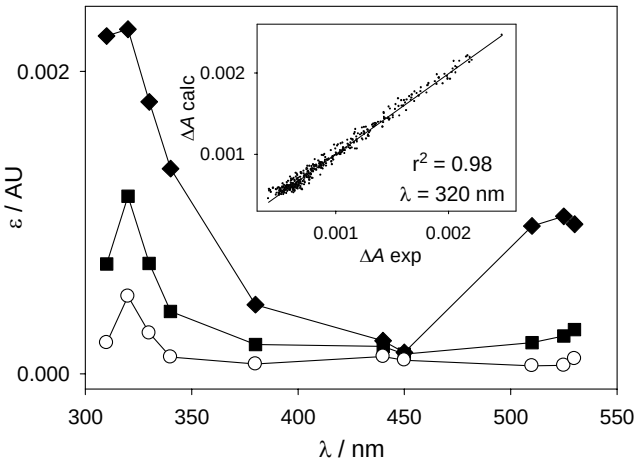
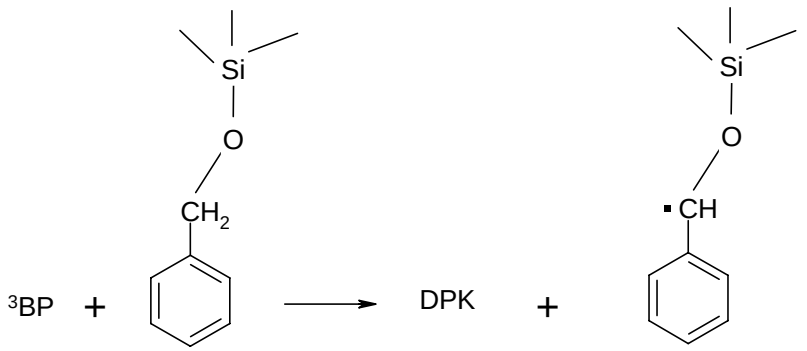


Figure 13. Absorption spectra obtained from the bilinear analysis of the experimental data for (from top to bottom): BP triplet states, DPK radical, and benzyl radical. Inset: Parity plot of the traces obtained at 320 nm in Figure 9 (right).

methylene groups of benzyl alcohol (79 kcal mol^{-1}) (*84*) compared to those for the aromatic C-H (113 kcal mol^{-1}) (*85*), indicates that the H-abstraction should take place from the methylene group. This is confirmed by the coincidence between the spectrum of the organic radical obtained from the bilinear program and that published for the benzyl radical (*86*).

Thus, the reaction between ^{3}BP and NP2 can be written as follows:



(11)

The fraction of BP triplet states which leads to benzyl radical in the experiments performed with 0.2 gL^{-1} NP2, f_{BR} = 0.26, can be calculated from the rate constants used to simulate the time-resolved phosphorescence data. From the value f_{BR} = 0.26, and the absorbance profiles shown in Figure 12, if one assumes that the molar decadic absorption coefficients of free and adsorbed BP triplet states are the same at 320 nm (ε^{320} = 11800 M^{-1} cm^{-1}) (*86*), the estimated absorption coefficient of the chemisorbed benzyl radical at 320 nm is 2200 M^{-1} cm^{-1}, in good agreement with the value reported by Meiggs et al. for the free radical in methanol (*87*).

Poutsma et al. investigated the thermolysis of surface immobilized 1,2-diphenylethane and concluded that immobilization of benzyl radicals covalently attached to silica surfaces leads to enhancement of unimolecular radical decay pathways relative to bimolecular ones (*88*). Long lifetime benzyl radicals adsorbed on zeolites were also reported to be related to the absence of radical-radical combination, which is the main decay route in nonviscous solvents (*89*). Surface immobilization of thiyl radicals was also reported to hinder the formation of disulfide radicals, a major recombination channel for free thiyl radicals in solution (*90*).

These results show that H-abstraction from methylene groups of benzyl alcohol chemically sorbed on silica nanoparticles leads to the formation of long lifetime benzyl radicals covalently attached to the silica surface.

Benzyl alcohol chemically bonded on silica nanoparticles is a clean source of benzyl radicals, which would be useful to simulate non-diffusional reactions involved in radicals attached on macromolecules, and as a precursor in the organic synthesis of products involving these radicals as intermediates. The generation method reported by Arce et al. (*57*) may be useful when the interest is focused in the study of the reactivity of benzyl radicals under conditions where the recombination route to yield bibenzyl is unfavored.

The mechanism proposed from phosphorescence experiments (Table 3) and validated by LFP measurements shows that the competition between the reversible adsorption of ^{3}BP on NP and the chemical reaction of ^{3}BP with the organic groups of the functionalized silica is responsible for the observed biexponential phosphorescence signals.

From Table 4 the value of the triplet energy of adsorbed BP on NP1, E_T[BP(NP1)], can be calculated as $-\Delta G^o_4 + E_T[BP] + \Delta G^o_1$ taking $\Delta G^o_1 = -RT \ln K_1$, with $K_1 = 10^4$. From the value of the triplet energy of free BP, $E_T[BP] = (281 \pm 1)$ kJ mol^{-1}, $\Delta G^o_1 = -RT \ln k_1/k_{-1} = -22{,}8$ kJmol^{-1} and $\Delta G^o_4 = -RT \ln k_4/k_{-4} = -28$ kJmol^{-1} with an error bar of $\pm$ 2 kJ estimated from the range of values of k_{-4} that results in good agreement with the simulations of the experimental results. This calculation yields E_T[BP(NP1)] = (286 $\pm$ 3) kJ mol^{-1}, in excellent agreement with the value determined from the phosphorescence spectrum (290 $\pm$ 1) kJmol^{-1}, further supporting the proposed mechanism.

3. Reaction Mechanisms of Inorganic Radicals at the Silica/Water Interface

3.1. Generation of Grafted Radicals

In the presence of silica nanoparticles, the kinetics and spectra of sulfate radicals ($SO_4^{\bullet-}$), chlorine $Cl^\bullet$ / $Cl_2^{\bullet-}$ radicals, $SCN^\bullet$ and $(SCN)_2^{\bullet-}$ radicals, and phosphate radicals ($HPO_4^{\bullet-}$) are modified due to their interaction with the nanoparticles surface groups (*91-93*). The reaction rates at interfaces differs from analogous reactions occurring in homogeneous phase because of energetic and geometric differences, such as accessibility and orientation of reactants and the space dimensionality of their motions (*94,95*). In some cases, surface defects are formed as a consequence of the radical surface reactions (*91*).

3.2. $SO_4^{\bullet-}$

In aqueous solutions, $SO_4^{\bullet-}$ are generated using conventional (excitation wavelength λ_{exc} > 200 nm) and laser (λ_{exc} = 266 nm) flash photolysis of aqueous $S_2O_8^{2-}$ solutions (reaction 12) (*91,92,96*) and detected at its absorption maximum λ_{max} = 450nm (ε= 1650 M^{-1} cm^{-1}) (*97*)

$$S_2O_8^{2-} \xrightarrow{h\nu} 2SO_4^{\bullet-} \qquad (12)$$

Laser photolysis experiments with excitation light of 266nm, shows a transient formation with an absorption spectrum in agreement with that published for $SO_4^{\bullet-}$ radicals (see Figure 14 inset). In the presence of SiO_2 nanoparticles, the transient profiles show formation of other species, whose contribution to the absorbance profiles increases with increasing particle concentration.

A bilinear regression analysis (*73*). was used to retrieve kinetic and spectroscopic information on the individual species formed. The analysis indicates the presence of two transients, one with absorption spectrum similar to that reported for $SO_4^{\bullet-}$ radicals and a second transient with absorbance maximum at 320 nm, see Figure 14 inset. As will be discussed later on, the transient absorbing at 320 nm may be assigned to an adsorbed $SO_4^{\bullet-}$ radical, and is then named $NPS^{\bullet}$.

Since the contribution of $NPS^{\bullet}$ absorbance at 450 nm is of no significance, absorbance profiles at this wavelength allows the detection of the absorbance profile of $SO_4^{\bullet-}$ (produced in reaction 12). The apparent first order decay rate constant, k_{app}, of the 450 nm absorbance linearly increases with increasing [NP], see Figure 14. The observed decay is due to $SO_4^{\bullet-}$ radical reaction in solution with $S_2O_8^{2-}$, reaction 13 with a second–order rate constant k_{13} = (6.3 ± 1.5)×10^5 $M^{-1}s^{-1}$, and to the reaction of $SO_4^{\bullet-}$ radicals with silica NP to yield $NPS^{\bullet}$, reaction 14. The slope of the straight line shown in Figure 14, yields the rate constant value for reaction 14, k_{14}= (7.8 ± 0.2)×10^3 $g^{-1}Ls^{-1}$ at 291.7 K. To convert the values of k_{14} given in units of $g^{-1}L$ s^{-1} to M^{-1} s^{-1}, an average NP mass of 3.95 × 10^{-19} g was used. This value was calculated from the density value 2.2 g cm^{-3} for spherical amorphous silica particles (*98-100*) and a NP volume of 1.8×10^{-19} cm^3.

$$SO_4^{\bullet-} + S_2O_8^{-2} \rightarrow S_2O_8^{\bullet-} + SO_4^{-2} \qquad k_9 = (6.3 \pm 1.5)\times10^5\ M^{-1}s^{-1} \qquad (13)$$

$$SO_4^{\bullet-} + NP \rightarrow NPS^{\bullet} \qquad k_{10} = (2.5 \pm 0.6)\times10^9\ M^{-1}s^{-1} \qquad (14)$$

The error bars for these rate constants and for all other data reported here are the standard deviations, σ.

Experiments performed at different temperatures in the range from 291.2 K to 313.2 K yield an Arrhenius plot for k_{14} from which an activation energy E_{14} = (9 ± 2) kJ mol^{-1} is retrieved.

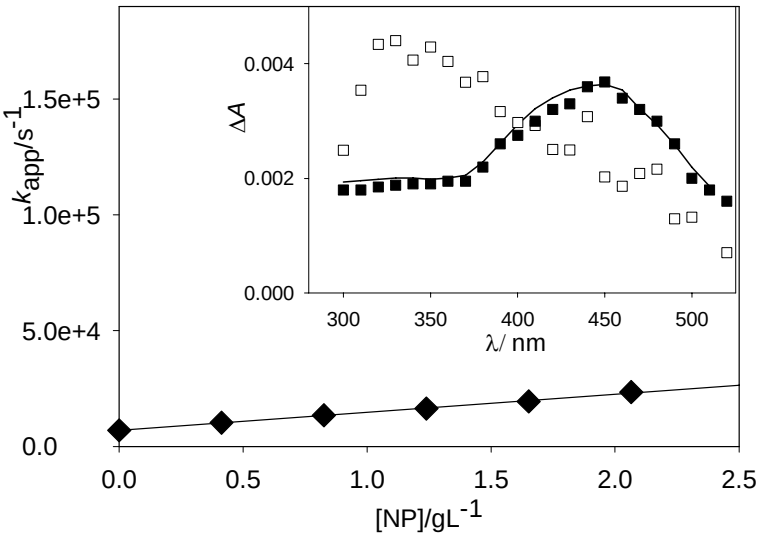


Figure 14. Plot of k_{app} vs. [NP] obtained at 291.7 K. *Inset*: Absorption spectra at 298.2 K obtained from 1.6 gL^{-1} NP suspensions containing 2.4×10^{-2} M $S_2O_8^{2-}$ at different times after the 266nm laser shot: 1 μs (■), 10 μs (□). The solid line shows the absorption spectrum reported for $SO_4^{\bullet-}$.

3.2.1. NPS$^\bullet$ Formation and Reactivity

NPS$^\bullet$ shows absorption in the wavelength range from 300 to 400 nm. Due to the absorption of $SO_4^{\bullet-}$ at these wavelengths (Figure 14, inset), the bilinear regression analysis (*73*) was used to retrieve kinetic and spectroscopic information on NPS$^\bullet$. The analysis shows that the contribution of the NPS$^\bullet$ transients to the absorbance profiles at 320 nm grows reaching its maximum value at about 30 μs and decays to a very small value within 450 μs. The transient decay was observed to be sensitive to peroxodisulfate concentration and pH. Therefore, NPS$^\bullet$ was considered to react with peroxodisulfate (reaction 15) and with water and single and geminal SiO^- sites (surface reactions all included in reaction 16).

$$NPS^\bullet + S_2O_8^{2-} \rightarrow \qquad k_{15} = (1.3 \pm 0.2)\times10^5\ M^{-1}\ s^{-1} \qquad (15)$$

$$NPS^\bullet \rightarrow \qquad k_{16} = (1.01 \pm 0.03)\times10^4\ s^{-1} \qquad (16)$$

Considering reactions 10 to 16, the absorption profile of NPS$^\bullet$ is given by eq. 17, with ε^{320} the absorption coefficient of NPS$^\bullet$ at 320 nm. The term k_G stands for the decay rates of reactions 15 and 16.

$$\Delta A^{320}\left(NPS^\bullet\right) = \frac{\varepsilon^{320}\times k_{14}\times[NP]\times[SO_4^{\bullet-}]_o}{(k_G - k_{13} - [NP]\times k_{14})}\left(e^{-\left(k_{13}+[NP]\times k_{14}\right)\times t} - e^{-k_G\times t}\right) \qquad (17)$$

Under the used experimental conditions, the initial radical concentration $[SO_4^{\bullet-}]_0$ may be determined from $SO_4^{\bullet-}$ absorption traces at 450 nm obtained in the absence of NP and considering ε^{450}= 1650 $M^{-1}cm^{-1}$. Taking $[SO_4^{\bullet-}]_0$, [NP] and $[S_2O_8^{2-}]$ for the different experiments, the fitting of the NPS$^{\bullet}$ transient profiles to eq.17 yields the values ε^{320}= (2.0 ± 0.4)×10^4 $M^{-1}cm^{-1}$ and k_G= (4.4 ± 0.2)×10^4 s^{-1}.

To gain information on the nature of the NPS$^{\bullet}$ radicals, conventional flash photolysis experiments were performed under different experimental conditions: 1×10^{-3} M ≤ $[S_2O_8^{2-}]$ ≤ 5×10^{-2} M, 0.00025 gL^{-1} ≤ [NP] ≤ 0.25 gL^{-1}, and pH in the range from 3 to 9. Higher concentrations of NP were avoided because they act as a filter to the absorption of light by $S_2O_8^{2-}$ ions. The pH value of 8 was used in most experiments because silica sols were reported to remain stable even in the presence of salt concentrations of the order of 0.15 M (*101*).

Experiments with conventional flash photolysis allowed the observation of transients in a time window of hundreds of μs to ms. Under these conditions, photolysis of aqueous $S_2O_8^{2-}$ in the presence of silica NPs show the presence of two transients with absorption maxima around 320 and 600 nm.

The spectrum of the species absorbing at 320 nm agrees with that of NPS$^{\bullet}$ radicals obtained in laser flash photolysis experiments. The absorption spectrum of the observed transient is independent of pH in the range studied (see Figure 15), which indicates that NPS$^{\bullet}$ formation is not due to a chemical reaction between $SO_4^{\bullet-}$ radicals and hydroxyl surface groups.

Experiments with samples containing 0.025 gL^{-1} NP and various $S_2O_8^{2-}$ concentrations showed traces whose decay follows a first-order law. The pseudo first order rate constant, k_{app}, linearly increases with $[S_2O_8^{2-}]$. From the slope of the graph k_{app} vs. $[S_2O_8^{2-}]$, k_{15} = (1.3 ± 0.2) × 10^5 $M^{-1}s^{-1}$ is obtained.

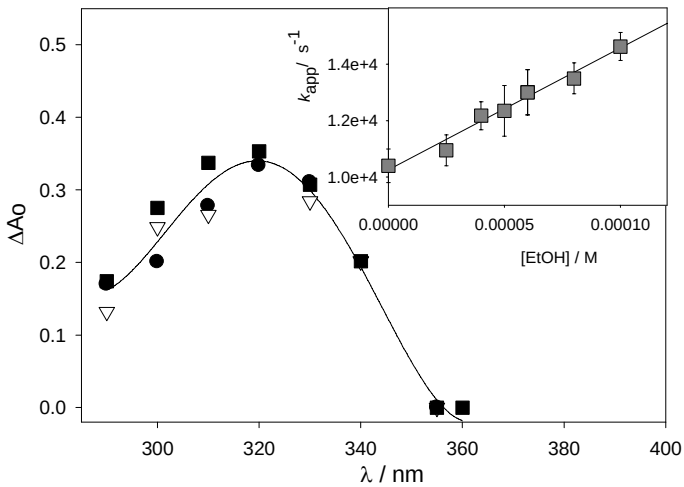


Figure 15. Absorption spectrum of the transient with λ_{max} around 320 nm for experiments at 298.2 K with 0.025 gL^{-1} NP (Ludox) suspensions containing 5×10^{-3} M $S_2O_8^{2-}$ at pH (●) 3.0, (■) 7.0, and (▽) 9.0. *Inset.* Plot of k_{app} *vs*. ethanol concentration for experiments at 298.7 K with [NP]= 0.025 gL^{-1}, $[S_2O_8^{2-}]$ = 5×10^{-3} M and pH 8. The error bars represent standard deviations.

Irradiation of samples of variable ionic strength in the range from 3×10^{-3} to 0.15 M, pH = 8, 0.025 gL^{-1} NP, and $[S_2O_8^{2-}] = 10^{-3}$ M at 293.2 K yields traces with, within the experimental error, identical decay rate constants. Therefore, $NPS^{\bullet}$ decay involves either a chemical reaction between uncharged substrates or a surface process between adsorbed molecules.

To obtain information on the reactivity of the $NPS^{\bullet}$ radical, experiments in the presence of various amounts of ethanol were performed. The decay rate of the $NPS^{\bullet}$ traces followed a first-order kinetics with k_{app} linearly increasing with the molar concentration of ethanol, [EtOH] (see Figure 15, inset). The slope of the straight line in Figure 15 yields the absolute rate constant for reaction 18, $k_{18} = (3.1 \pm 0.2) \times 10^7$ M^{-1} s^{-1}.

$$NPS^{\bullet} + C_2H_5OH \rightarrow \qquad k_{18}= (3.1 \pm 0.2)\times10^7\ M^{-1}\ s^{-1} \qquad (18)$$

The evidence herein presented indicates that $NPS^{\bullet}$ may be assigned to a NP-sulfate adduct. This is supported by the low activation energy for the reaction of $SO_4^{\bullet-}$ with NP, reaction 14, and by the rate constants of the reactions of $NPS^{\bullet}$ with $S_2O_8^{2-}$ and with ethanol, which are similar to those reported for $SO_4^{\bullet-}$ (*19*).

The rate constant of the elementary reaction between a reactant A in solution and a reactant B immobilized at the surface of a spherical particle S, as derived from the Smoluchowski equation (*69,94,102*), is given by eq. 8. Here, factor ***f*** accounts for the coulombic work, w, needed for bringing the radical anion from the electrolyte solution to the negatively charged NP surface (*78*). Taking a surface charge density ≤ 5 *e*/nm^2 for the dissociation of fully hydroxylated silica (*38*) and an equilibrium distance of 3.5 nm for the formation of an activated complex, ***f*** is approximately 1.

For the reactions of $SO_4^{\bullet-}$ with the silica NP, the average radius of the particles is 3.5 nm and the size of the sulfate radical is 0.24 nm (*103*). Therefore, R_{A+S} is dominated by the radius of the spherical particles. Similarly, diffusion of the NP is much slower than that of $SO_4^{\bullet-}$ and $D_{A+S} \approx 2\times10^{-5}$ cm^2 s^{-1} is of the order of the diffusion coefficients of sulfate anions.

Introducing the previous considerations in eq. 8, a pre-exponential factor for the reaction between $SO_4^{\bullet-}$ and the NP, results $k_{14} = 5.3 \times 10^{10}$ M^{-1} s^{-1}. Assuming E_a = 9 kJ mol^{-1}, the experimental activation energy of reaction 14, the value $k_{14} = 1.2\times10^9$ M^{-1} s^{-1} is predicted, in coincidence with the experimental value at 298 K (*vide supra*). Therefore, the reaction of $SO_4^{\bullet-}$ with the NP surface is not a diffusion-controlled reaction.

Reaction of $SO_4^{\bullet-}$ with surface silanol groups is already neglected since k_{14} is pH independent (*vide supra*). Other reactive sites homogenously distributed on the silica surface are siloxane bridges. Dividing k_{14} (given per mole of silica NP), by the number of siloxane bridges on each particle, yields a rate constant of $5.6\times10^7\times \exp(-9\times10^3/8.31\times T)$ M^{-1} s^{-1} per mol of siloxane bridges.

The surface reaction of $NPS^{\bullet}$ with adsorbed H_2O (reaction 19a) yields H^+, a similar reaction takes place in aqueous solutions with $SO_4^{\bullet-}$ (*19*).

Reaction of $NPS^{\bullet}$ with surface silanols, SiOH, or with their conjugate base, SiO^-, should also be considered. Both, an H- abstraction of $NPS^{\bullet}$ radicals from Si-OH or an electron-transfer process between $NPS^{\bullet}$ and SiO^-, reaction 19b y 19c, yield surface $SiO^{\bullet}$ radicals.

$$[NPS^{\bullet} + H_2O(ads)] \rightarrow NP + HO^{\bullet} + H^{+} \qquad k=1.5\times10^{14}\exp[-(58\pm12)/RT]\ s^{-1} \qquad (19a)$$

$$[NPS^{\bullet} + {>}Si(OH)O^{-}] \rightarrow {>}Si(OH)O^{\bullet}\ (+ SO_4^{2-}) \qquad k<1\times10^{11}\exp[-(46\pm13)/RT]\ s^{-1} \qquad (19b)$$

$$[NPS^{\bullet} + {\equiv}Si{-}O^{-}] \rightarrow {\equiv}Si{-}O^{\bullet}\ (+ SO_4^{2-}) \qquad k<1\times10^{3}\exp[-(2\pm17)/RT]\ s^{-1} \qquad (19c)$$

3.2.2. $SiO^{\bullet}$ Formation and Reactivity

The absorption spectrum of the transient in the wavelength range 480-680nm is shown in Figure 16. The transient absorption decreases with pH in the range from 9 to 6 and no signal is observed below pH 5.4 where all surface silanols are in their undissociated form (the pK_a of single and germinal silanols are 4.5-6.5 and 8.5-9.0, respectively (*38*), as expected for the transient formed by the surface reactions 19b and 19c. The observed transient spectrum closely resembles those reported for nonbridging oxygen hole centers (*104,105*) and for $SiO_3^{\bullet-}$ radicals in aqueous solutions (*106*).

The decay of the experimental traces in the wavelength range 480-680nm may be well fitted to a biexponential function, eq 20, which indicates the presence of two transient components, *g* and *s*.

$$\Delta A = C_g e^{-k_g t} + C_s e^{-k_s t} \qquad (20)$$

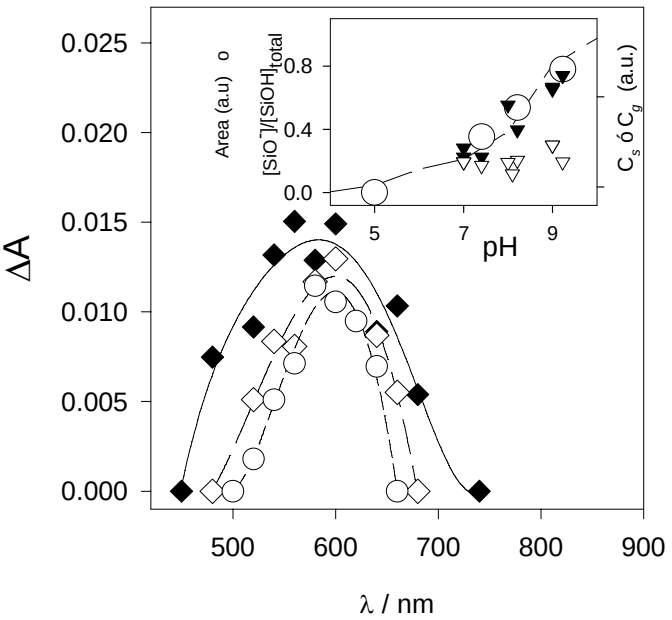


Figure 16. Absorption spectrum of the transient with maximum around 600 nm for experiments with $[S_2O_8^{2-}] = 2.7\times10^{-4}$ M and [NP] = 0.00025 gL^{-1} at different pH: (◆) 9.2, (◇) 8.2, and (O) 7.4. Inset: pH dependence: (O) the area below the curves in the main figure, (▽) Cg, and (▼) Cs, all in arbitrary units. The solid lines stand for the fraction of dissociated silanols, $[SiO^-]/[SiOH]_{total}$ vs. pH.

The k_g and k_s values at 298.2 K and pH = 8 linearly increase with increasing concentrations of NP, ethanol and $Na_2S_2O_8$. These concentrations were varied in the range: 0.25 gL^{-1} > [NP] > 0.0025 gL^{-1}, 10^{-3} M ≤ $[S_2O_8^{2-}]$ ≤ 2×10^{-2} M and 0 ≤ [EtOH] ≤1×10^{-4} M. Therefore, the transient components *g* and *s* react with these reactants, as shown in reactions 21 to 23.

$$SiO^{\bullet} + NP \rightarrow \begin{matrix} k_g = (1.9\pm0.2)\times10^7\ M^{-1}s^{-1} \\ k_s = (1.5\pm0.8)\times10^6\ M^{-1}s^{-1} \end{matrix} \quad (21)$$

$$SiO^{\bullet} + S_2O_8^{2-} \rightarrow \begin{matrix} k_g = (2500 \pm 300)\ M^{-1}s^{-1} \\ k_s = (630 \pm 50)\ M^{-1}s^{-1} \end{matrix} \quad (22)$$

$$SiO^{\bullet} + C_2H_5OH \rightarrow \begin{matrix} k_g = (3.5 \pm 1)\times10^6\ M^{-1}s^{-1} \\ k_s = (8 \pm 5)\times10^4\ M^{-1}s^{-1} \end{matrix} \quad (23)$$

The previous observations suggest that the transient formed from the $NPS^{\bullet}$ radical with absorption maxima at 600nm, may be assigned to surface $SiO^{\bullet}$ radicals. This assignment is also supported by the similar reactivity toward ethanol observed for the 600 nm transient (reaction 23) and that reported for $SiO_3^{\bullet-}$ radicals (*vide supra*).

The increase in the concentration of $SiO^{\bullet}$ surface radicals with the fraction of total deprotonated silanols indicate that the two types of silanol sites (single and germinal) participate in reaction 19b y 19c. The two components of the decay rates of the 600 nm transient may be assigned to $SiO^{\bullet}$ radicals formed from geminal and single SiO^- as indicated by the pH dependence of the weight factors Cg and Cs shown in Figure 16 (inset).

The $SiO^{\bullet}$ surface defects in both sites show identical absorption spectrum. The geminal silanols have been regarded as the reactive sites for adsorption and chemical reaction (*107*). It can be concluded that the $SiO^{\bullet}$ radicals arising from geminal SiO^- are more reactive than those radicals arising from single SiO^- and their reactivity toward ethanol resembles that of $SiO_3^{\bullet-}$ radicals in aqueous solutions (*106*).

3.2. $Cl^{\bullet}$ / $Cl_2^{\bullet-}$

In aqueous solutions, $Cl^{\bullet}$ and $Cl_2^{\bullet-}$ radical ions may be formed upon the reaction of Cl^- ions with strong oxidant sulfate radical ions, $SO_4^{\bullet-}$ (*93,108*), as shown in reaction 24. Reaction of $Cl^{\bullet}$ and Cl^- ions reversibly yields $Cl_2^{\bullet-}$ radical ions, reactions 25 and 26 (*19*). In the absence of $Cl^{\bullet}$ and $Cl_2^{\bullet-}$ scavengers, the bimolecular recombination of $Cl_2^{\bullet-}$, reaction 26, and their reaction with water and hydroxyl ions are the main decay reactions. The latter reactions involve a complex sequential set of reversible reactions (*20*). Both $Cl^{\bullet}$ and $Cl_2^{\bullet-}$ radicals show absorption with molar absorption coefficients at 340 nm of ε^{340} = 3800 M^{-1} cm^{-1} and 9600 M^{-1} cm^{-1}, respectively (*109*).

$$SO_4^{\bullet-} + Cl^- \rightarrow Cl^{\bullet} + SO_4^{2-} \quad \log k = 8.43 + 1.0\ I^{1/2} \quad (24)$$

$$Cl^- + Cl^{\bullet} \rightarrow Cl_2^{\bullet-} \quad 8.5\times10^9\ M^{-1}s^{-1} \quad (25)$$

$$Cl_2^{\bullet-} \rightarrow Cl^- + Cl^{\bullet} \quad 6.0\times10^4\ s^{-1} \quad (26)$$

$$Cl_2^{\bullet-} + Cl_2^{\bullet-} \rightarrow Cl_2 + Cl^- \quad \log k = 8.8 + 1.6\ I^{1/2}/(I^{1/2}+1) \quad (27)$$

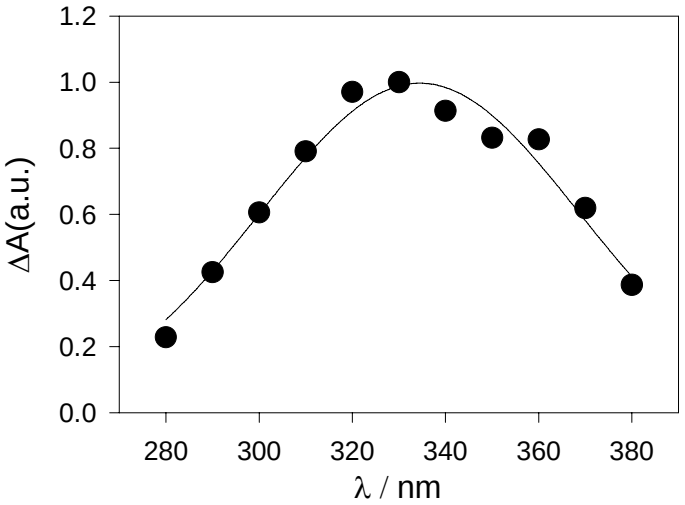


Figure 17. Absorption spectrum of the transient with maximum around 340 nm obtained in experiments with suspensions of pH = 8.2, $[S_2O_8^{2-}] = 5\times10^{-3}$ M, and $[Cl^-] = 1.0\times10^{-3}$ M.

Time-resolved experiments at 293 K with 0.025–0.6 gL^{-1} silica suspensions containing 0.1 M > $[Cl^-]$ > 10^{-3} M and $[S_2O_8^{2-}] = 5\times10^{-3}$ M show fast formation of a transient with absorption maximum at 340 nm whose spectrum is in agreement with that reported for the $Cl_2^{\bullet-}$ radical shown Figure 17.

Experiments performed with suspensions of pH in the range from 6 to 9 and at a given $[S_2O_8^{2-}]$ and $[Cl^-]$, show faster decay rates for suspensions with increasing NP concentrations. Figure 18 shows the linear dependence of the pseudo-first order decay constants (k_F) with the particle concentration. At pH ≤ 5, where silica NP have almost all of its surface silanols undissociated, no dependence of the transient decay rate with the NP concentration is observed. These observations suggest that $Cl^\bullet$ and $Cl_2^{\bullet-}$ radicals interact with the deprotonated silanols of the NP surface.

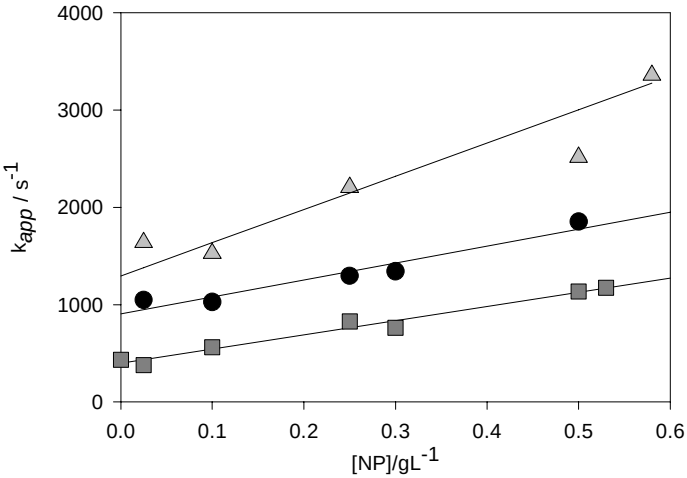


Figure 18. Plots of k_F vs. [NP] for experiments with suspensions of pH 8.2 containing 5×10^{-3} M $S_2O_8^{2-}$ and $[Cl^-] = 4.0\times10^{-3}$ M (□), 1.7×10^{-3} M (●) and 1.2×10^{-3} M (▲).

$$\begin{array}{lllll} Cl^{\bullet} + \equiv Si{-}O^{-} & \rightarrow & Cl^{-} + \equiv Si{-}O^{\bullet} & k_{28} = (9\pm6)\times107\ M{-}1 & (28) \\ Cl^{\bullet} + >Si{-}(OH){-}O^{-} & & >Si{-}(OH){-}O^{\bullet} & s{-}1 & \end{array}$$

$$\begin{array}{lll} Cl_2^{\bullet-} + \equiv Si{-}O^{-} & & k_{29} = (7\pm4)\times105\ M{-}1 \\ Cl_2^{\bullet-} + >Si{-}(OH){-}O^{-} & \rightarrow & s{-}1 \end{array} \quad (29)$$

Under our experimental conditions, reactions 25 and 26 may be assumed in fast equilibrium ($K_{25,26}\times[Cl^-] > 1$) and the decay reactions of $Cl^{\bullet}$ and $Cl_2^{\bullet-}$ with water and hydroxyl ions is assumed irreversible (*20*). Under such conditions, the first order decay constant k_{app} is given by eq. 30 taking $[SiO^-] = \boldsymbol{e}\ [NP]$. **a**, ***b***, ***c*** and ***d***, stand for the rate constants of $Cl^{\bullet}$ / $Cl_2^{\bullet-}$ with water and hydroxyl ions in solution (*93*); and ***e*** depends on the properties of silica nanoparticles as surface area, the number of single and germinal silanols per nanoparticles, and the fraction of deprotonated silanols.

$$k_{app} = a + \frac{b}{[Cl^-]} + \left(c + \frac{d}{[Cl^-]}\right)[OH^-] + \left(k_{29} + \frac{k_{28}}{K_{25,26}[Cl^-]}\right)[SiO^-]_T \quad (30)$$

At constant pH, eq. 30 indicates a linear dependence of k_{app} with [NP], with a slope *s* given by eq. 31.

$$s = c\left(k_{29} + \frac{k_{28}}{K_{25,26}[Cl^-]}\right) \quad (31)$$

Plots of *s* vs. $1/[Cl^-]$ for experiments at 293 K and pH 8.3, yield a straight line (see Figure 19) whose slope and intercept yield $k_{28} = (9 \pm 6)\times10^7\ M^{-1}\ s^{-1}$ and $k_{29} = (7 \pm 4)\times10^5\ M^{-1}\ s^{-1}$, respectively.

Experiments with bare silica NP suspensions of pH > 6.5 and $[Cl^-] < 10^{-2}$ M show the formation of a transient absorbing in the 550– 670 nm range subsequent to the decay of $Cl^{\bullet}$ / $Cl_2^{\bullet-}$ radicals, as depicted in Figure 20. Formation of the transient at 600 nm is only observed for suspensions of pH > 6.5. The observed absorption spectrum is assigned to the $SiO^{\bullet}$ surface radicals.

Dichloride radical anions are the main species present in experiments with $[Cl^-] > 10^{-2}$ M. The inability to detect at 600 nm any transient formation in this chloride ion concentration range clearly indicates that the reaction of $Cl_2^{\bullet-}$ with surface deprotonated silanols, reaction 29, does not lead to the formation of $SiO^{\bullet}$ surface radicals. Thus the products of reaction 29 are unknown. Therefore, only $Cl^{\bullet}$ atoms are capable of generating $SiO^{\bullet}$ surface defects.

Reactions 28 and 29 involve a solution reactant and a second species immobilized on the surface of a spherical particle. Application of the Smoluchowski equation (eq. 8) to such reaction predicts a diffusion-controlled reaction rate constant of $5.3 \times 10^{10}\ M^{-1}\ s^{-1}$ (*91,92*).

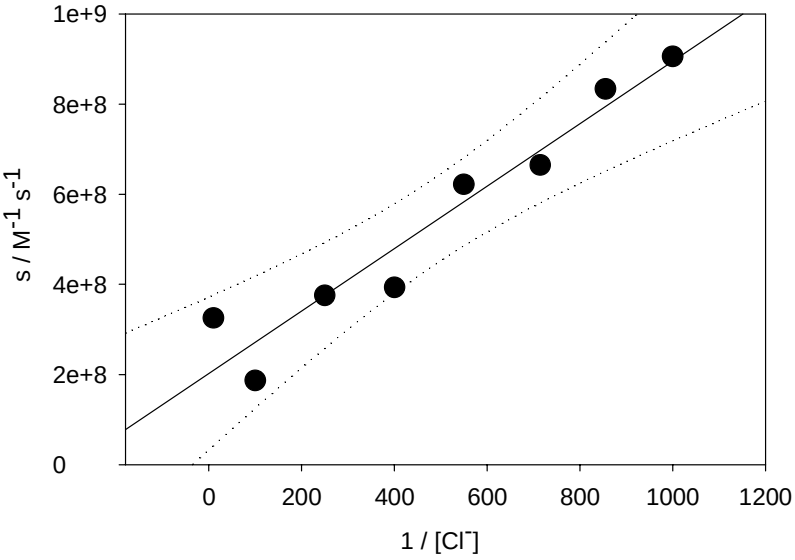


Figure 19. Plot of ***s*** vs. 1/[Cl^-] for experiments at 293 K with NP suspensions of pH 8.3 and 5×10^{-3} M $S_2O_8^{2-}$. The dashed lines correspond to the 99% confidence interval.

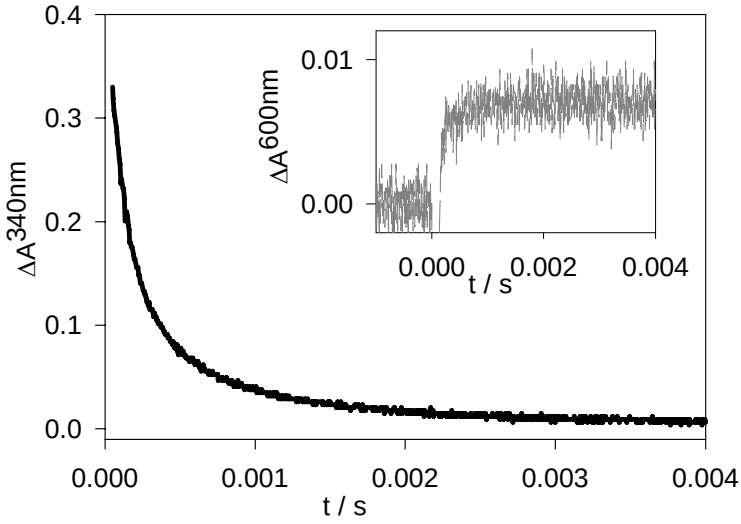


Figure 20. Absorbance profile obtained at 340 nm (main figure) and 600 nm (inset) from flash photolysis experiments at 293 K with 0.25 gL^{-1} silica NP suspensions of pH 8.3 containing 5×10^{-3} M $S_2O_8^{2-}$, and 2.5×10^{-3} M NaCl.

Taking a total number of 676 silanol groups on the surface of a fully hydroxylated silica particle (*91,92*), a reaction rate constant of the order of 8×10^7 M^{-1} s^{-1} is predicted for each deprotonated silanol, coincident within the experimental error, with the reaction rate constant determined experimentally for reaction 28. Therefore, reaction 28 may be assumed to be diffusion controlled.

Reaction 29 is two orders of magnitude slower than reaction 28, in agreement with the reactivity tendency observed for the reactions of $Cl^{\bullet}$ and $Cl_2^{\bullet-}$ with organic and inorganic substrates (*110*). The higher reduction potential of $Cl^{\bullet}$ atoms compared with that of $Cl_2^{\bullet-}$ radicals, *vide supra*, is in line with the observation that SiO• radicals are only formed from the one electron oxidation of deprotonated silanols by chlorine atoms, reaction 28.

The effect of humic substances on the reaction of chlorine radicals with the surface of silica nanoparticles was also investigated. Flash photolysis experiments of solutions at pH 8 containing 5×10^{-3} M $S_2O_8^{2-}$, 1×10^{-3} M NaCl, 0.25 gL^{-1} NP and 1 mgL^{-1} of Aldrich humic Acid (HA) were performed as a rough approximation to aquatic natural systems. Experimental limitations restrict SiO_2:HA w / w ratios to values > 50 as NP suspensions of 0.25 gL^{-1} are required for an efficient surface scavenging of $Cl^{\bullet}$ / $Cl_2^{\bullet-}$ radicals and HA solutions < 5 mgL^{-1} should be used to avoid HA photolysis.

Computer simulations of the obtained $Cl_2^{\bullet-}$ absorption profiles were performed considering the reaction scheme used for the experiments with silica NP (*vide supra*) and taking into account the reactions of $Cl^{\bullet}$ / $Cl_2^{\bullet-}$ with HA ($(3 \pm 2)\times10^{10}$ M^{-1} s^{-1} and $(1.2 \pm 0.3) \times 10^9$ M^{-1} s^{-1}, respectively (*93*)). The simulation of the traces obtained at 340 nm in experiments with SiO_2:HA = 250 showed a very good agreement with experimental data, as shown in Figure 21. Therefore, the reaction behavior of the system towards $Cl^{\bullet}$ / $Cl_2^{\bullet-}$ radicals may be predicted by summing up the individual scavenging efficiency of the NP surface and that of the HA. These results indicate that, under the experimental conditions used, any specific interaction such as adsorption and / or H-bond formation between HA and SiO_2-NP does not significantly disturb the silica surface.

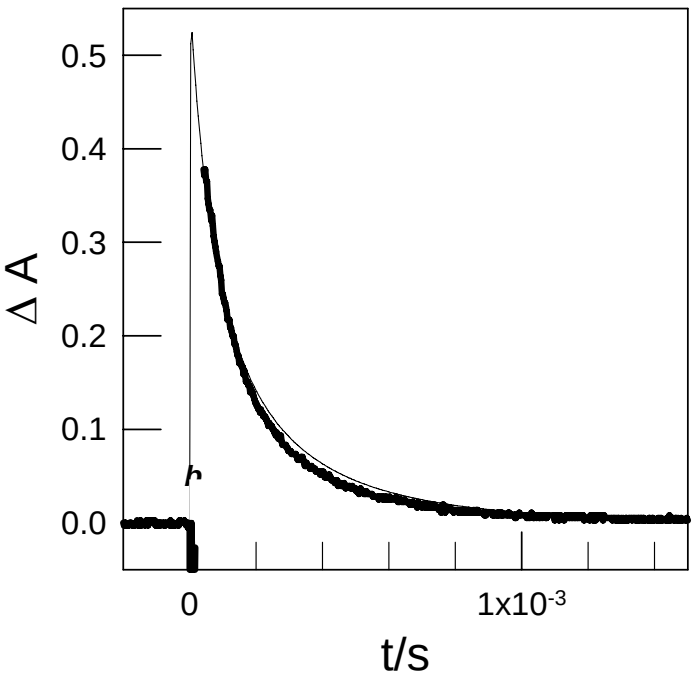


Figure 21. Absorbance profiles obtained at 340 nm from flash photolysis experiments at 293 K with solutions of pH 8 containing 5×10^{-3} M $Na_2S_2O_8$, 1.0×10^{-3} M NaCl, 0.25 g L^{-1} NP and 1 mg L^{-1} HA. The solid lines stand for computer simulations.

3.3. $HPO_4^{\bullet-}$

Phosphate radicals were generated by photolysis of peroxodiphosphate aqueous solutions $P_2O_8^{4-}$ (λ_{exc} > 200 nm), reaction 32. These radicals present three acid base forms depending on the solution pH, as observed in the acid-base equilibria 33 (*19,93,111*). To study the reactions of $HPO_4^{\bullet-}$ the most abundant acid form present in neutral natural waters, the pH of the samples was adjusted to 7.1 ± 0.1 with mixtures of KH_2PO_4/K_2HPO_4.

$$H_2P_2O_8^{2-} \xrightarrow{h\nu} 2\ H_2PO_4^{\bullet} / HPO_4^{\bullet-} / PO4^{\bullet 2-} \quad (32)$$

$$H_2PO_4^{\bullet} \underset{pK_a = 5.7}{\overset{-H^+}{\rightleftarrows}} HPO_4^{\bullet-} \underset{pK_a = 8.9}{\overset{-H^+}{\rightleftarrows}} PO_4^{\bullet 2-} \quad (33)$$

Phosphate radicals show maximum absorption at 510nm. Figure 22 shows the absorption spectrum of $HPO_4^{\bullet-}$ in aqueous solutions of pH 7.

The reactions of $HPO_4^{\bullet-}$ radicals with the NP surface, reaction 34, are conveniently studied following the $HPO_4^{\bullet-}$ radical decay rate as a function of the concentration of the NP aqueous suspension in the range $0 \le [NP] \le 0.5\ gL^{-1}$.

$$2\ HPO_4^{\bullet-} + NP \rightarrow NPP^{\bullet} \quad (34)$$

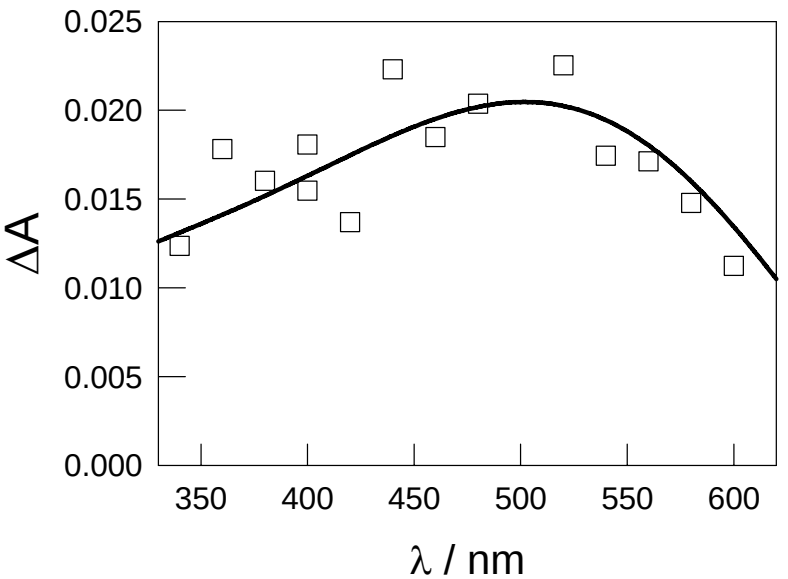


Figure 22. Absorption spectrum of $HPO_4^{\bullet-}$ obtained at 298.2 K from 2.4×10^{-2} M $P_2O_8^{4}$ aqueous solutions of pH 7.

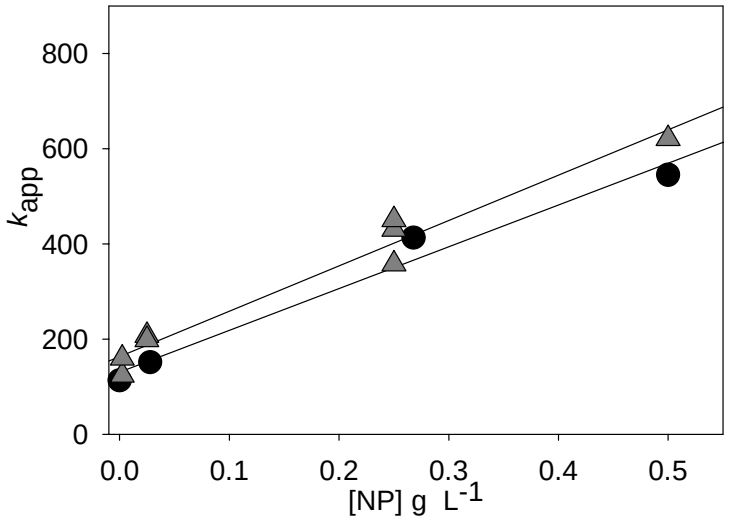


Figure 23. Plot of k_{app} vs. [NP] for different batches of silica nanoparticles.

Conventional flash photolysis experiments with 0.25 gL^{-1} Ludox suspensions of pH 7.1 containing 2.4×10^{-2} M $P_2O_8^{4-}$ showed absorption traces at $\lambda > 300$ nm, whose spectrum at 280 μs after the flash of light agreed with that of the $HPO_4^{\bullet-}$ radicals. However, a new transient species denominated as NPP$^{\bullet}$ absorbing more to the UV-region is also observed. Due to the overlapping of the absorption spectra of $HPO_4^{\bullet-}$ and NPP$^{\bullet}$, a bilinear regression analysis was applied to the absorbance matrix in order to retrieve individual kinetic and spectroscopic information of the reaction intermediates.

The absorbance profiles of the phosphate radical with various amounts of NP, may be fitted to a mixed first- and second-order kinetics with the first-order apparent decay rate constant, k_{app}, linearly increasing with increasing [NP], as shown in Figure 23. The slopes of these plots yield $k_{34} = (2.2 \pm 0.3)\times10^8$ in units of mole of NP.

The intermediate specie, NPP$^{\bullet}$, is formed at the same rate $HPO_4^{\bullet-}$ are depleted by NP, reaction 34, and therefore, they are assumed to be formed after this reaction. The absorption spectrum of NPP$^{\bullet}$ shows a maximum at around 350 nm, see Figure 24. A lower limit absorption coefficient $\varepsilon^{350} > 500$ M^{-1} cm^{-1} is estimated for this transient, assuming all phosphate radicals formed react with NP to yield NPP$^{\bullet}$ radicals.

The decay of the NPP$^{\bullet}$, radicals follows a first order kinetics with a rate constant of 50 s^{-1}. Formation of surface SiO$^{\bullet}$ is not observed.

The transient can be identified with a surface-trapped phosphate radical in line with the results obtained for $SO_4^{\bullet-}$ radicals. Phosphate radicals are known to react with several compounds by reaction channels similar to those of sulfate radicals. The value of k_{34} measured here for the reaction of $HPO_4^{\bullet-}$ with NP is in line with the fact that the relative oxidation capability of this radical is smaller than sulfate radical (*19*).

Therefore, a similar reaction channel of $SO_4^{\bullet-}$ and $HPO_4^{\bullet-}$ radicals toward the NP surface may be expected, and the participation of the siloxane bridges in the adsorption of $HPO_4^{\bullet-}$ radicals on the silica surface is further supported by the electrophilic nature of the hydrogen phosphate radicals.

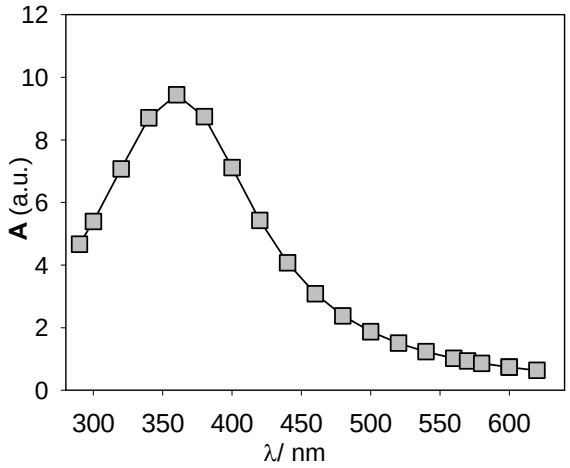


Figure 24. Absorption spectrum of the NPP• transient at 298.2 K obtained from a bilinear regression analysis of the transients obtained for 0.0025–0.5 gL^{-1} NP suspensions containing 2.4×10^{-2} M $P_2O_8^{4-}$.

3.4. $(SCN)_2^{\bullet-}$

In aqueous solutions, SCN^- ions react with $SO_4^{\bullet-}$ radicals (reaction 35) to yield $SCN^\bullet$ radicals, which reversibly react with SCN^- to yield $(SCN)_2^{\bullet-}$ radical ions (reaction 36) (*92,19*). The absorption spectra of $SCN^\bullet$ and $(SCN)_2^{\bullet-}$ radicals present maxima at around 330 (ε^{330}=900 M^{-1} cm^{-1}) and 475 nm (ε^{475}= 7600 M^{-1} cm^{-1}), respectively (*112*). In conventional flash photolysis experiments with solutions containing 5×10^{-3} M $S_2O_8^{2-}$ and [SCN^-] in the range from 1 $\times10^{-2}$ to 0.25 M, the condition [$(SCN)_2^{\bullet-}$]/[$SCN^\bullet$] > 21 applies, and any contribution of $SCN^\bullet$ to the observed absorption traces can be neglected. The absorption maximum at λ=475 nm observed in these experiments corresponds to $(SCN)_2^{\bullet-}$ radical ions, as shown in Figure 25.

$$SO_4^{\bullet-} + SCN^- \rightarrow SCN^\bullet + SO_4^{-2} \qquad (35)$$

$$SCN^\bullet + SCN^- \rightleftharpoons (SCN)_2^{\bullet-} \qquad K = 2.1\times10^5\ M^{-1} \qquad (36)$$

The $(SCN)_2^{\bullet-}$ radical decay in the presence of NP is well fitted to a mixed first- and second-order kinetics. The second-order term, which corresponds to the radical self recombination (*113*), remains independent on [NP], although the contribution of the bimolecular recombination to the overall decay decreases with increasing [NP].

The first-order decay component, k_{app}, increases with increasing [NP] at constant pH and with increasing pH at constant [NP]. Plots of k_{app} vs. pH yield a sigmoidal curve (see Figure 26), suggesting the involvement of an acid–base equilibrium with a pKa in the range of 6.0–9. In fact, surface silanols (pKa values in the range 4.5–6.5 and 8.5–9.0, *vide supra*) are suspected to participate in the reaction. These observations clearly indicate that the first-order component is due to the reaction of $(SCN)_2^{\bullet-}$ radicals with silanol surface groups.

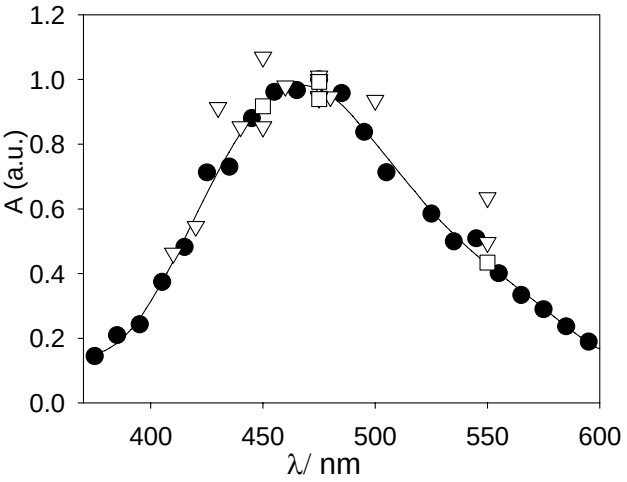


Figure 25. Normalized absorption spectrum of the $(SCN)_2^{\bullet-}$ radical at 298.2 K as obtained from flash photolysis experiments of 5×10^{-3} M $S_2O_8^{2-}$ solutions containing 0.1 M SCN^- in the absence (●) and presence of either 0.75 gL^{-1} NP at pH 7 (Δ) or 0.27 gL^{-1} NP at pH 5 (□).

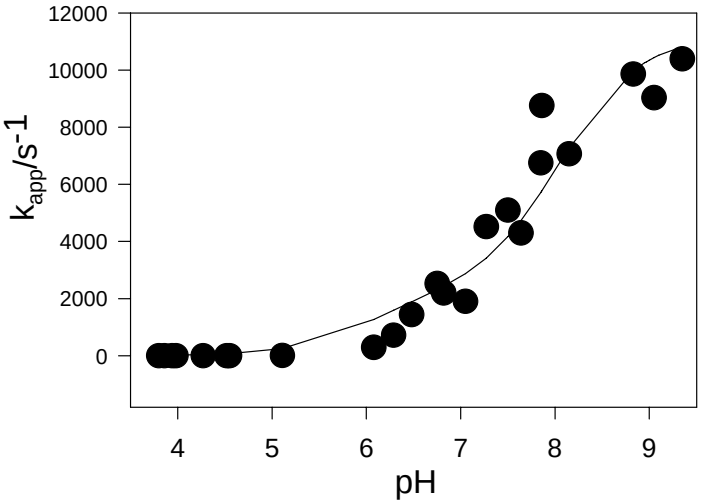


Figure 26. Plot of k_{app} vs. pH obtained for 0.045 gL^{-1} NP suspensions in the presence of 5×10^{-3} M $S_2O_8^{2-}$ and 1.5×10^{-2} M SCN^- at 303.2 K.

Because higher decay rates are observed with increasing pH, the dissociated silanols are the groups directly involved in $(SCN)_2^{\bullet-}$ reaction with the NP surface, reaction 37. The intercepts of the linear plots of k_{app} vs. the total concentration of deprotonated silanols, $[SiO^-]_T$, (Figure 27) are, within the experimental error, equal to zero, indicating that any reaction of $(SCN)_2^{\bullet-}$ radicals with other moieties of the silica NP are insignificant. No product absorption was detected in the wavelength range from 320 to 600 nm.

$$(SCN)_2^{\bullet-} + \geqslant Si{-}O^-/ > Si{-}(OH){-}O^- \rightarrow \text{Products} \qquad (37)$$

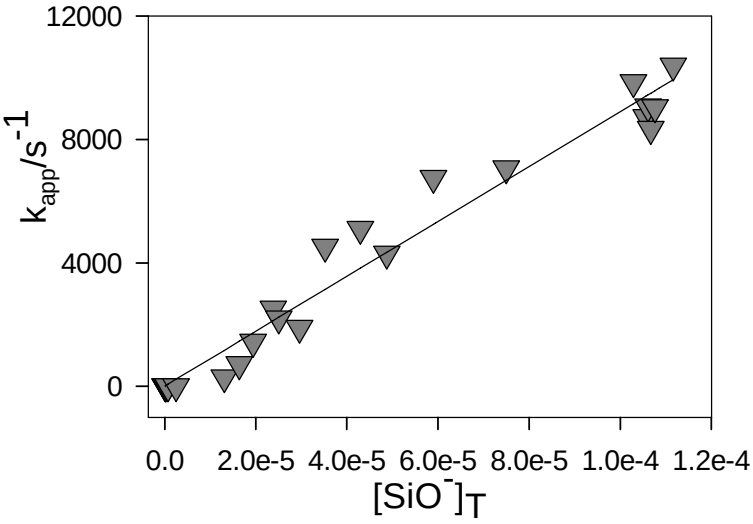


Figure 27. Plot of k_{app} vs. $[SiO^-]_T$ obtained for (0.01–0.1 g L^{-1}) NP suspensions containing 5×10^{-3} M $S_2O_8^{2-}$ and 1.5×10^{-2} M SCN^- at 303.2 K and various pH values from 3.5 to 9.5.

From the slopes of the plots of k_{app} vs. $[SiO^-]_T$, the values k_{37}= (7.9 ± 0.5)×10^7, (8.3 ± 0.6)×10^7 and (9.0 ± 0.3)×10^7 $M^{-1}s^{-1}$ at 293.2, 298.2 and 303.2, respectively, were obtained. The corresponding Arrhenius plot yields E = (8.5 ± 1.5) kJ mol^{-1} for this reaction.

Application of eq. 8 with f = 1 to reaction 28 also predicts a value of 5.3× 10^{10} M^{-1} s^{-1} for its pre-exponential factor, which divided by the number of silanol groups contained per particle (*vide supra*), yields a diffusion-controlled rate constant of 7.8×10^7 M^{-1} s^{-1} at 298.2 K for the reaction of the $(SCN)_2^{\bullet-}$ radicals with the unprotonated silanols, in agreement with the experimental rate constant at this temperature. Thus, according to this simple model, the reaction of $(SCN)_2^{\bullet-}$ radicals with the surface silanols is diffusion-controlled, and the coulombic interactions between the charged nanoparticle and the $(SCN)_2^{\bullet-}$ radical ion seem to be of lesser importance. The 8.5 kJ/mol activation energy measured for reaction 37 is of the order expected for the activation energy of a diffusion controlled rate (*114*).

CONCLUSION

The excited triplet states of benzophenone are able to react with the organic groups chemisorbed on the silica nanoparticles by H-atom abstraction leading to the formation of radicals, as shown by time-resolved phosphorescence and laser flash-photolysis experiments. In particular, the reaction of benzophenone triplet state with benzyl alcohol chemically bonded on silica nanoparticles yield benzyl radicals which are not able to recombine to bibenzyl. Benzyl radicals are therefore stabilized on the particle surface and reaction with O_2 to yield oxidized products (*115*) may be their most significant reaction in the environment.

Surface-stabilized radicals might undergo reactions which are not favored in solution. In this context, grafted radicals might behave as in biological matrices and in soil organic matter (116).

The behavior of sulfate, hydrogen phosphate, chlorine and dithiocyanate radicals at the silica interface depends on the redox potential of the radical.

On one hand, sulfate and hydrogen phosphate radicals adsorb on the silica NP. The absorption maxima of the adsorbed radicals shift more than 100 nm to the UV. However, it is noteworthy that the absorption spectra of the adsorbed radicals are narrower and overlap those of the free radicals. The reaction of adsorbed sulfate radicals with unprotonated silanol groups leads to $SiO^{\bullet}$ surface defects absorbing at 600 nm. Whether the hydrogen phosphate radicals react similarly with the unprotonated silanol groups could not be evaluated because of the necessity of controlling the pH of the suspensions at 7.1, where only about 18% of the silanol groups are dissociated.

On the other hand, there is no evidence for the adsorption of the chlorine and dithiocyanate radicals. These radicals do not react with the silanol groups themselves, but with their unprotonated forms. The latter observation is in agreement with the electrophylic character of these radicals. The formation of the $SiO^{\bullet}$ surface defects as products of reaction is not observed, even at high pH, except for chlorine atoms.

As $SiO^{\bullet}$ surface defects are formed from the reaction with $SO_4^{\bullet-}$ ($E(SO_4^{\bullet-}/SO_4^{-2}) = 2.4$ V) and $Cl^{\bullet}$ ($E(Cl^{\bullet} / Cl^{-}) = 2.4$ V), but not with $Cl_2^{\bullet-}$ ($E(Cl_2^{\bullet-} / 2Cl\text{-}) = 2.0$ V) (*35,117*) and $(SCN)_2^{\bullet-}$ ($E((SCN)_2^{\bullet-} / 2\ SCN^{-}) = 1.31$ V (*92*)), the $SiO^{\bullet}$ reduction potential is expected to be $2.0 < E(SiO^{\bullet} / SiO^{-}) < 2.4$ V vs. NHE.

The results herein reviewed indicate that the presence of silica particles might affect the oxidizing capacity of natural waters, as highly oxidizing radicals in solution are efficiently scavenged by the silica surface. Moreover, formation of surface defects with a reduction potential in the range $2.0 < E(SiO^{\bullet} / SiO^{-}) < 2.4$ V vs. NHE imply that mainly those contaminants adsorbed on, or in the neighborhood of the silica surface will be depleted, selectively oxidizing contaminants contained in the water reservoir.

REFERENCES

[1] Cooper, WJ. Sunlight induced photochemistry of humic substances in natural waters: major reactive species. *Adv. Chem. Ser.,* 1989 219, 332–362.

[2] Paul, A; Hackbarth, S; Vogt, RD; Röder, B; Burnison, BK; Steinberg, CE. Photogeneration of singlet oxygen by humic substances: Comparison of humic substances of aquatic and terrestrial origin. *Photochem. Photobiol. Sci.,* 2004 *3*, 273-280.

[3] David Gara, PM; Bosio, GN; Arce, VB; Poulsen, L; Ogilby, PR; Giudici, R; Gonzalez, MC; Martire, DO. Photoinduced degradation of the herbicide clomazone model reactions for natural and technical systems. *Photochem Photobiol,* 2009 *85*, 686-692.

[4] Haag, WR; Hoigné, J; Gassman, E; Braun, AM. Singlet oxygen in surface waters - Part II: Quantum yields of its production by some natural humic materials as a function of wavelength. *Chemosphere,* 1984 13, 641-650.

[5] Frimmel, FH; Bauer, H; Putzien, J.; Murasecco, P.; Braun, A. M. Laser flash photolysis of dissolved aquatic humic material and the sensitized production of singlet oxygen. *Environ. Sci. Technol.,* 1987 21, 541-545.

[6] Zepp, RG; Braun, AM; Hoigne, J; Leenheer, JA. Photoproduction of hydrated electrons from natural organic solutes in aquatic environments. *Environ. Sci. Technol.,* 1987 21, 485-490.

[7] Canonica, S. Oxidation of aquatic organic contaminants induced by excited triplet states. *Chimia,* 2007 61, 641-644.

[8] Richard, C; Vialaton, D; Aguer, JP; Andreux, F. Transformation of monuron photosensitized by soil extracted humic substances: Energy or hydrogen transfer mechanism? *J. Photochem. Photobiol. A,* 1997 111, 265-271.

[9] Vaughan, PP; Blough, NV. Photochemical formation of hydroxyl radical by constituents of natural waters. *Environ. Sci. Technol,.* 1998 32, 2947-2953.

[10] Haag, WR; Hoigne, J. Photo-sensitized oxidation in natural water via ·OH radicals. *Chemosphere,* 1985 14, 1659-1671.

[11] Goldstone, JV; Voelker, BM. Chemistry of superoxide radical in seawater: CDOM associated sink of superoxide in coastal waters. *Environ. Sci. Technol.,* 2000 34, 1043-1048.

[12] Scully, NM; McQueen, DJ; Lean, DRS. Hydrogen peroxide formation: The interaction of ultraviolet radiation and dissolved organic carbon in lake waters along a 43-75°N gradient. *Limnol. Oceanog.,* 1996 41, 540-548.

[13] Herut, B; Shoham-Frider, E; Kress, N; Fiedler, U; Angel, DL. Hydrogen peroxide production rates in clean and polluted coastal marine waters of the mediterranean red and Baltic seas. *Mar. Pollut. Bull*., 1998 36, 994-1003.

[14] Canonica, S; Hellrung, B; Müller, P; Wirz, J. Aqueous oxidation of phenylurea herbicides by triplet aromatic ketones. *Environ. Sci. Technol*., 2006 40, 6636–6641.

[15] Halladja, S; ter Halle, A; Aguer, JP; Boulkamh, A; Richard, C. Inhibition of humic substances mediated photooxygenation of furfuryl alcohol by 2,4,6-trimethylphenol. Evidence for reactivity of the phenol withhumictriplet excited states. *Environ. Sci. Technol*., 2007 41, 6066–6073.

[16] Barbieri, Y; Massad, WA; Díaz, DJ; Sanz, J; Amat-Guerri, F; García, NA. Photodegradation of Bisphenol A and related compounds under natural-like conditions in the presence of riboflavin. *Chemosphere,* 2008 73, 564–571.

[17] Scott, DT; Mc Knight, DM; Blunt-Harris, EL; Kolesar, SE; Loveley, DR. Quinone moieties act as electron acceptors in the reduction of humic substances by humics-reducing microorganisms, *Environ. Sci. Technol*., 1998 32, 2984-2989.

[18] Hayes, M. Humic Substances II (In search of structure). Chapters 13 and 14, John Wiley & Sons, Toronto, 1989.

[19] Ross, AB ; Mallard, WG; Helman, WP; Buxton, GV; Huie, RE; Neta, P. NDRL-NIST Solution Kinetics Database, Ver. 3.0x, Notre Dame Radiation Laboratory, Notre Dame, IN, US and National Institute of Standards and Technology, Gaithersburg,MD, US, 1998. Available on the web at: http://kinetics.nist.gov/solution/ (January 2011).

[20] Alegre, ML; Geronés, M; Rosso, JA; Bertolotti, SG; Braun, AM, Mártire, DO; Gonzalez, MC. Kinetic study of the reaction of chlorine atoms and $Cl_2^{\bullet-}$ radicals anions in aqueous solutions. I. Reaction with benzene *J. Phys. Chem. A*, 2000 104, 3117-3125.

[21] Mártire, DO; Rosso, JA; Bertolotti, SG; Carrillo LeRoux, G; Braun, AM; Gonzalez, MC. Kinetic Study of the Reactions of Chlorine Atoms and $Cl_2^{\cdot-}$ Radical Anions in

Aqueous Solutions. II. Toluene, Benzoic Acid and Chlorobenzene. *J. Phys. Chem. A,* 2001, 105, 5385-5392.

[22] Rosso, JA; Rodríguez Nieto, FJ; Gonzalez, MC; Mártire, DO. Reactions of phosphate radicals with substituted benzenes. *J.Photochem. A: Chemistry*, 1998 116, 21- 25.

[23] Cencione, SS; Gonzalez, MC; Mártire, DO. Reactions of phosphate radicals with substituted benzenes. A Reactivity- Structure Correlation Study. *J. Chem. Soc., Faraday Transactions,* 1998 94, 2933- 2937.

[24] Rosso, JA; Allegretti, PE; Mártire, DO; Gonzalez, MC. Reactions of sulphate and phosphate radicals with α, α, α- trifluorotoluene. *J. Chem. Soc., Perkin Transactions*, 1999 2, 205- 210.

[25] Criado, S; Marioli, JM; Allegretti, PE; Furlong, J; Rodríguez Nieto, FJ; Mártire, DO; García, NA. Oxidation of di- and tripeptides of Tyrosine and Valine mediated by singlet molecular oxygen, phosphate radicals and sulfate radicals. *J. Photochem. Photobiol. B: Biol*., 2001 65, 74-84.

[26] Rosso, JA; Caregnato, P; Mora, VC; Gonzalez, MC; Mártire, DO. Reactions of phosphate radicals with monosusbtituted benzenes. A mechanistic investigation. *Helvetica Chimica Acta,* 2003 86, 2509-2524.

[27] Rosso, JA; Criado, S; Bertolotti, SG; Allegretti, P; Furlong, J; García, NA; Gonzalez, MC; Mártire, DO. Kinetic Study of the Reactions of Singlet Molecular Oxygen [$O_2(^1\Delta_g)$] and Hydrogen Phosphate Radicals with Phenolic Derivatives of α, α, α-Trifluorotoluene. *Photochemical & Photobiological Sciences,* 2003 2, 882-887.

[28] Bosio, G; Criado, S; Massad, W; Gonzalez, MC; García, NA; Mártire, DO. Kinetics of the Interaction of Sulfate and Hydrogen Phosphate Radicals with Small Peptides of Glycine, Alanine, Tyrosine, and Tryptophan.*Photochemical & Photobiological Sciences*, 2005 4, 840 – 846.

[29] Villata, LS; Gonzalez, MC; Mártire, DO. A kinetic study of the reactions of sulfate and dihydrogen phosphate radicals with Epicatechin, Epicatechingallate and Epigalocatechingallate. *Int. J. Chem. Kinet.,* 2010 42, 391-396.

[30] Liang, C; Wang ZS; Bruell CJ. Influence of pH on peroxydisulfate oxidation of TCE at ambient temperatures. *Chemosphere,* 2007 66, 106–113.

[31] Mora, VC; Rosso, JA; Carrillo Le Roux, G, Mártire, DO; Gonzalez, MC. Thermally activated peroxydisulfate in the presence of additives: a clean method for the degradation of pollutants. *Chemosphere*, 2009 75, 1405-1409.

[32] Waldemer R; Tratnyek PG; Johnson R; Nurmi MT. Oxidation of Chlorinated Ethenes by Heat-Activated Persulfate: Kinetics and Products. *Environ. Sci. Technol.,* 2007 41, 1010-1015.

[33] Glaze, WH; Kang, JW; Chapin, DH. The chemistry of water treatment processes involving ozone, hydrogen peroxide and UV radiation. *Ozone: Sci. Eng.*, 1987 9, 335–352.

[34] Li, K; Critenden, J. Computerized Pathway Elucidation for Hydroxyl Radical-Induced Chain Reaction Mechanisms in Aqueous Phase Advanced Oxidation Processes. *Environ. Sci. Technol*., 2009 43, 2831–2837.

[35] Schwarz, HA; Bielski, HJ. Reactions of hydroperoxo and superoxide with iodine and bromine and the iodide (I_2^-) and iodine atom reduction potentials. *J. Phys. Chem.*, 1986 90, 1445–1448.

[36] Bogomolov, GV; Plotnikova, GN; Titova, EA. Silica in the subterranean waters of certain regions of the USSR and other countries. *Hydrological Sciences Journal*, 1966 1, 24 – 33.

[37] Rodriguez-Mozaza, S; Lopez de Alda, MJ; Barceló a, D. Advantages and limitations of on-line solid phase extraction coupled to liquid chromatography–mass spectrometry technologies versus biosensors for monitoring of emerging contaminants in water. *Journal of Chromatography A*, 2007 97-115.

[38] Zhuralev, LT. The surface chemistry of amorphous silica. Zhuravlev model. *Colloids Surfaces A: Physicochem. Eng. Aspects*, 2000 173, 1-38.

[39] Maciel, GE; Sindorf, DW. Silicon-29 NMR study of the surface of silica gel by cross polarization and magic-angle spinning. *J. Am. Chem. Soc.*, 1980 102, 7606-7607.

[40] Morrow, BA; Gay, ID. Silicon-29 cross-polarization/ magic angle spinning NMR evidence for geminal silanols on vacuumactivated aerosil silica. *J. Phys. Chem.*, 1998 92, 5569-5571.

[41] Tuel, A; Hommel, H; Legrand, AP; Kovats, ES. A silicon-29 Nh4R study of the silanol population at the surface of derivatized silica. *Langmuir,* 1990 6, 770-775.

[42] (42) Van Roosmalen, AJ; Mol, JC. An infrared study of the silica gel surface. 1. Dry silica gel. *J. Phys. Chem.,* 1978, 2748-2751.

[43] Allen, LH; Matijevic, E. Stability of colloidal silica, I. Effect of simple electrolyte. *J. Colloid Interface Sci*., 1969 31, 287-296.

[44] Allen, LH; Matijevic, E. Stability of colloidal silica. *J. Colloid Interface Sci*., 1970 33, 420-429.

[45] Allen, LH; Matijevic, E; Meites, L. Exchange of Na+ for the silanolic protons of silica. *J. Inorg. Nucl. Chem.,* 1971 33, 1293-1299.

[46] Ong, S; Zhao, X; Eisenthal, KB. Polarization of water molecules at a charged interface: second harmonic studies of the silica/ water interface. *Chem. Phys. Lett.*, 1992 191, 327-335.

[47] Vance, FW; Lemon, BI; Ekoff, JA; Hupp, JT. Interrogation of nanoscale silicon dioxide/water interfaces via hyper-Rayleigh scattering. *J. Phys. Chem. B,* 1998 102, 1845-1848.

[48] Kropp, PJ; Daus, KA; Tubergen, MW; Kepler, KD; Wilson, VP; Craig, SL; Baillargeon, MM; Breton, GW. Surfacemediated reactions. 3. Hydrohalogenation of alkenes. *J. Am. Chem.Soc*., 1993 115, 3071-3079.

[49] Leermakers, PA; Thomas, HT; Weis, LD; James, FC. Spectra and Photochemistry of Molecules Adsorbed on Silica Gel. *J. Am. Chem. Society* 1, 1966 88:22, 5075 – 5083.

[50] Jenkins, S; Kirk, SR; Persson, M; Carlen, J; Abbas, Z. The role of hydrogen bonding in nanocolloidal amorphous silica particles in electrolyte solutions. *J Colloid Interface Sci*., 2009 339, 351-61.

[51] Brant, JA; Childress, AE. Colloidal adhesion to hydrophilic membrane surfaces. J. Membrane Sci., 2004 241, 235–248.

[52] Fubini, B; Hubbard; A. Reactive oxygen species (ROS) and reactive nitrogen species (RNS) generation by silica in *Free Radic Biol Med,* 2003 34, 1507-16.

[53] Corbin, JF; Teel, A; Allen-King, RM; Watts, RJ. Reactive Oxygen Species Responsible for the Enhanced Desorption of Dodecane in Modified Fenton's Systems. *Water Environm. Res.*, 2007 79, 37-42.

[54] Wiesner, MR; Lowry, GV; Jones, KL; Hochella, MF; Di Giulio, RT; Casman, E; Bernhardt, ES. Decreasing uncertainties in assessing environmental exposure, risk, and ecological implications of nanomaterials. *Environ. Sci. Technol*., 2009 43, 6458- 6462.

[55] Ruiz, AE; Caregnato, P; Arce, VB; Schiavoni, MM; Mora, VC; Gonzalez, MC; Allegretti, PE; Mártire, DO. Synthesis and Characterization of Butoxylated Silica Nanoparticles. Reaction with Benzophenone Triplet States *J. Phys. Chem. C*., 2007 111, 7623–7628.

[56] Arce, VB; Bertolotti, SG; Oliveira, FJVE; Airoldi, C; Gonzalez, MC; Allegretti, PE; Mártire, DO. The use of molecular probes for the characterization of dispersions of functionalized silica nanoparticles. *Spectrochim. Acta A,* 2009 73, 54–60.

[57] Arce, VB; Rosso, JA; Oliveira, FJVE; Airoldi, C; Soria, DB; Gonzalez, MC; Allegretti, PE; Mártire, DO. Generation of Chemisorbed Benzyl Radicals on Silica Nanoparticles. *Photochemistry & Photobiology*, 2010 86, 1208-1214.

[58] Brunauer, S; Emmett, PH; Teller, E. Adsorption of gases in ultimolecular layers. J. Am. Chem. Soc., 1938 60, 309-319.

[59] Jitianu, A; Crisan, A; Meghea, A; Raub, I; Zaharescua, MJ. Influence of the silica based matrix on the formation of iron oxide nanoparticles in the Fe_2O_3-SiO_2 system obtained by sol-gel method. *Mater. Chem.,*2002 12, 1401-1407.

[60] Fryxell, GE; Lin, Y; Fiskum, S; Birnbaum, JC; Wu, H; Kemner, K; Kelly, S. Actinide Sequestration Using Self-Assembled Monolayers On Mesoporous Supports. *Environ. Sci. Technol.*, 2005 39, 1324-1331.

[61] Makkuni, A; Varma, RS; Sikdar, SK; Bhattacharyya, D. Aqueous And Vapor Phase Mercury Sorption By Inorganic Oxide Materials Functionalized With Thiols And Poly-Thiols. Clean Tech. *Environ. Policy*, 2005 7, 87-96.

[62] Silva, ALP; Sousa, KS; Germano, AFS; Oliveira, VV; Espínola, JGP; Fonseca, MG; Airoldi, C; Arakaki, T; Arakaki, LNH. A New Organofunctionalized Silica Containing Thioglycolic Acid Incorporated For Divalent Cations Removal - A Thermodynamic Cation/ Basic Center Interaction. *Colloids Surf. A,* 2009 332, 144-149.

[63] Jal, PK; Patel, S; Mishra, BK. Chemical Modification Of Silica Surface By Immobilization Of Functional Groups For Extractive Concentration Of Metal Ions. *Talanta,* 2004 62, 1005-1028.

[64] Kammler, HK; Beaucage, G; Mueller, R; Pratsinis, SE. Structure Of Flame-Made Silica Nanoparticles By Ultra-Small-Angle X-Ray Scattering. *Langmuir*, 2004 20, 1915-1921.

[65] Yang, J; Duan, J; Fornasiero, D; Ralston, J. Very Small Bubble Formation at the Solid−Water Interface. *J. Phys. Chem. B,* 2003 107, 6139-6147.

[66] Yang, J; Duan, J; Fornasiero, D; Ralston, J. Kinetics Of CO2 Nanobubble Formation At The Solid/Water Interface. *Phys. Chem. Chem. Phys.,* 2007 9, 6327-6332.

[67] Vieira Ferreira, LF; Ferreira Machado, I; Da Silva, JP; Branco, TJF. Surface photochemistry: Benzophenone as a probe for the study of silica and reversed-phase silica surfaces. *Photochem. Photobiol. Sci.* 2006 5, 665-673.

[68] Major, JS; Blanchard, GJ. Strategies for Covalent Multilayer Growth. 1. Polymer Design and Characterization. *Chem. Mater*, 2002 14, 2567-2573.

[69] Shield, SR; Harris, J M. Reaction kinetics at dispersed-colloid / solution interfaces: Benzophenone triplet-state quenching by methylated silica particles. *J. Phys. Chem. B*, 2000 104, 8527- 8535.

[70] Mártire, DO; Jux, N; Aramendía, PF; Negri, RM; Lex, J; Braslavsky, SE; Schaffner, K; Vogel, E. Photophysics and photochemistry of 22.pi. and 26.pi. acetylene-cumulene porphyrinoids *J. Am. Chem. Soc*., 1992 114, 9969-9978.

[71] Demas, JN. Excited State Lifetime Measurements; Academic Press: New York, 1983; pp 59-63.

[72] Thomas, JK. Effect of SiO2 and zeolite surfaces on the excited triplet state of benzophenone, BT; a spectroscopic and kinetic study. *Photochem. Photobiol. Sci*., 2004 3, 483-488.

[73] San Román, EA; Gonzalez, MC. Analysis of spectrally resolved kinetic data and time-resolved spectra by bilinear regression. *J. Phys. Chem.*, 1989 93, 3532- 3536.

[74] Vieira Ferreira, LF; Vieira Ferreira, MR; Da Silva, JP; Ferreira Machado, I; Oliveira, AS; Prata, JV. Novel laser-induced luminescence resulting from benzophenone/O-propylated p-tert-butylcalix[4]arene complexes. A diffuse reflectance study Photochem. Photobiol. Sci., 2003 2, 1002-1010.

[75] Lhiaubet, V; Gutierrez, F; Penaud-Berruyer, F; Amouyal, E; Daudey, J; Poteau, R; Chouini Lalanne, N; Paillous, N. Spectroscopic and theoretical studies of the states of fenofibric acid and ketorofen in relation with their photosensitizing properties. *New J. Chem.*, 2000 24, 403-410.

[76] Nishiguchi, H; Zhang, JL; Anpo, M; Masuhara, HJ. Characteristics of the phosphorescence spectra of benzophenone adsorbed on Ti–Al binary oxides. Phys. Chem. B, 2001 105, 3218-3222.

[77] Yousry, R; Naguib, MA; Steel, C; Cohen, SG; Young, MA. Photoreduction of benzophenone by acetonitrile: correlation of rates of hydrogen abstraction from RH with the ionization potentials of the radicals R.cntdot. *J. Phys. Chem.*, 1987 91, 3033-3036.

[78] Bellino, M. G.; Calvo, E. J.; Gordillo, G. Adsorption kinetics of charged thiols on gold nanoparticles. *Phys. Chem. Chem. Phys.* 2004 6, 424–428.

[79] Ren, FY; Waite, SW; Harris, JM. Temperaturejump investigation of adsorption ⁄ desorption kinetics at methylated silica ⁄ solution interfaces. *Anal. Chem.*, 1995 67, 3441- 3447.

[80] Wilkinson, F; Willsher, CJ. Detection of triplet-triplet absorption in microcrystalline benzophenone by diffuse-reflectance laser flash photolysis. *Chem. Phys. Lett*., 1984 104, 272–276.

[81] Baral-Tosh, S; Chattopadhyay, SK; Das, PK. A laser flash photolysis study of paraquat reduction by photogenerated aromatic ketyl radicals and carbonyl triplets. *J. Phys. Chem.*, 1984 88, 1404–1408.

[82] Ferreira Machado, I; Vieira Ferreira, LF; Branco, TJF. Surface photochemistry: Ketones included within a channel type solid support, the aluminophosphate AlPO4-5. *J. Mol. Structure*, 2007 831, 1–9.

[83] Brandi, P; Galli, C, Gentili, P. Kinetic study of the hydrogen abstraction reaction of the benzotriazole-N-oxyl radical (BTNO) with H-donor substrates. *J. Org. Chem.*, 2005 70, 9521–9528.

[84] Davico, GE; Bierbaum,VM; DePuy, CH; Barney Ellison, JG; Squires, RR. The C–H bond energy of benzene. *J. Am. Chem. Soc.*,1995 117, 2590–2599.

[85] Sehested, K; Corfltzen,H; Christensen, HC, Hart, EJ. Rates of reaction of oxygen (1-) ions, hydroxyl radicals, and atomic hydrogen with methylated benzenes in aqueous solution. Optical spectra of radicals. *J. Phys. Chem.*, 1975 79, 310–315.

[86] Carmichael, I; Hug, GL. Triplet–triplet absorption spectra of organic molecules in condensed phases. *J. Phys. Chem. Ref. Data*, 1986 15, 54.

[87] Meiggs, TO; Grossweiner, LI; Miller, SI. Extinction coefficient and recombination rate of benzyl radicals. I. Photolysis of sodium phenylacetate. *J. Am. Chem. Soc.*, 1972 94, 7981–7986.

[88] Poutsma, ML; Douglas, EC; Leacht, JE. Modification of the free-radical thermolysis of bibenzyl by surface immobilization. *J. Am. Chem. Soc.,* 1984 106, 1136–1137.

[89] Turro, NJ. From boiling stones to smart crystals: Supramolecular and magnetic isotope control of radical–radical reactions in zeolites. *Acc. Chem. Res*., 2000 33, 637–646.

[90] Caregnato, P; Forbes, MDE; Soria, DB; Mártire, DO; Gonzalez, MC. Chemisorbed thiols on silica particles: Characterization of reactive sulfur species. *J. Phys. Chem. C*, 2010 114, 5080–5087.

[91] Caregnato, P.; Mora, V.C.; Carrillo Le Roux, G.; Martire, D.O.; Gonzalez, M.C. A kinetic study of the reactions of sulfate radicals at the silica nanoparticle-water interface. *J. Phys. Chem. B,* 2003 107, 6131–6138.

[92] Caregnato, P; Bertolotti, SG; Gonzalez, MG; Martire, DO. Water ⁄ silica nanoparticles interfacial kinetics of sulfate, hydrogen phosphate and dithiocyanate radicals. *Photochem. Photobiol*., 2005 81, 1526–1533.

[93] Caregnato, P; David Gara, P; Bosio, GN; Martire, DO; Gonzalez, MC Reactions of $Cl^{\bullet}$ / $Cl_2^{\bullet-}$ Radicals with the Nanoparticle Silica Surface and with Humic Acids: Model Reactions for the Aqueous Phase Chemistry of the Atmosphere. *Photochem. Photobiol.* 2007 *83*, 944–951.

[94] Astumian, RD; Schelly, ZA. Geometric effects of reduction of dimensionality in interfacial reactions. *J. Am. Chem. Soc*., 1984 106, 304–308.

[95] Astumian, RD; Chock, PB. Interfacial reaction dynamics. *J. Phys. Chem*., 1985 89, 3477–3482.

[96] Choure, SC; Bamatraf, MMM; Rao, BSM; Das, R; Mohan, H; Mittal, JP. Hydroxylation of chlorotoluenes and cresols: a pulse radiolysis, laser flash photolysis, and product analysis study. *J. Phys. Chem. A*, 1997 101, 9837–9845.

[97] Jiang, PY; Katsumura, Y; Nagaishi, R; Domae, M; Ishikawa, K; Ishigure, K; Yoshida, Y. Pulse radiolysis study of concentrated sulfuric acid solutions. Formation mechanism, yield and reactivity of sulfate radicals**.** *J. Chem. Soc., Faraday Trans.*, 1992 88, 1653-1658.

[98] Iler, RK. The Chemisry of Silica; Wiley, New York, 1979.

[99] Leite, CAP; de Souza, EF; Galembeck, F. Core-andshell nature of Sto¨ber silica particles. *J. Braz. Chem. Soc.*, 2001 12, 519–525.

[100] Beaucage, G; Kammler, HK; Mueller, R; Strobel, R; Agashe, N; Pratsinis, SE; Narayanan, T. Probing the dynamics of nanoparticle growth in a flame using synchrotron radiation. *Nat. Mater*., 2004 3, 370–373.

[101] Bergna, HE. The colloid Chemistry of Silica-An Overview *Advances in Chemistry* Series *234*, Ed., American Chemical Society: Washington, DC, 1994; p 147.

[102] Smoluchowski, MV. Versuch einer mathematischen Theorie der Koagulationskinetik kolloider Lo¨sungen. Z. *Phys. Chem.*, 1917 92, 129–168.

[103] Churio, MS; Brusa, MA; Grela, MA. Application of photoacoustic calorimetry to the determination of volume changes in reactions involving radical anions in aqueous solutions. *Photochem. Photobiol. Sci.*, 2003 2, 754–758.

[104] Skuja, L. The origin of the intrinsic 1.9eV luminescence band in glassy SiO_2. *J. Non-Cryst. Solids,* 1994 *179*, 51-69.

[105] Glinka, YD; Lin, SH; Chen, YT. Two-photon-excited luminescence and defect formation in SiO_2 nanoparticles induced by 6.4-eV ArF laser light. *Phys. Rev. B,* 2000 62, 4733-4743.

[106] Kuzmin, VA; Chibisov, AK. The OH radical in condensed systems, studied by using pulsed illumination. *High Energy Chem.,* 1970 4, 146-147.

[107] Kropp, PJ; Daus, KA; Tubergen, MW; Kepler, KD; Wilson, VP.; Craig, SL; Baillargeon, MM; Breton, GW. Surface–Mediated Reactions. 3. Hydrohalogenation of Alkenes. *J. Am. Chem. Soc.,* 1993 115, 3071-3079.

[108] George, C; Chovelon, JM. A laser flash photolysis study of the decay of $SO_4^{\bullet-}$ and $Cl_2^{\bullet-}$ radical anions in the presenceof Cl) in aqueous solutions. *Chemosphere*, 2002 47, 385–393.

[109] Yu, XY; Bao, ZC; Barker, JR. Free radical reactions involving $Cl^{\bullet}$, $Cl_2^{\bullet-}$, and $SO_4^{\bullet-}$ in the 248 nm photolysis of aqueous solutions containing S2O82_ and Cl^- *J. Phys. Chem. A*, 2004 108, 295–308.

[110] Zhu, L; Nicovich, JM; Wine, PH. Kinetics studies of aqueous phase reactions of $Cl^{\bullet}$ atoms and $Cl_2^{\bullet-}$ radicals with organic sulfur compounds of atmospheric interest. *J. Phys. Chem. A*, 2005 109, 3903–3911.

[111] Maruthamuthu, P; Neta, P. Phosphate radicals. Spectra, acid-base equilibriums, and reactions with inorganic compounds. *J. Phys. Chem.* 1978 82, 710–713.

[112] Hug, GL. Optical Spectra of Nonmetallic Inorganic Transient Species in Aqueous Solution, 1981, p. 69. U.S. Department of Commerce, National Bureau of Standards, Washington, D.C.

[113] Czapski, G; Holcman, J; Bielski, BHJ. Reactivity of nitric oxide with simple short-lived radicals in aqueous solutions. *J. Am. Chem. Soc.*, 1994 116, 11465–11469.

[114] Okamoto, K; Terazima, M; Hirota, N. Temperature dependence of diffusion processes of radical intermediates probed by the transient grating method. *J. Chem. Phys.,* 1995 103, 10445–10452.

[115] da Silva, G; Hamdan, MR; Bozzelli, JW. Oxidation of the Benzyl Radical: Mechanism, Thermochemistry, and Kinetics for the Reactions of Benzyl Hydroperoxide. *J. Chem. Theory Comput.,* 2009 5, 3185–3194.

[116] Panagiota, S; Louloudi, M; Deligiannakis, Y. EPR study of phenolic radical stabilization by grafting on SiO_2. *Chem. Phys. Lett*. 2009 472, 85-89.

[117] Huie, RE. Free radical chemistry of the atmospheric aqueous phase. Advanced Series in Physical Chemistry, Vol. 3 (Edited by J. R. Barker), pp. 374–419. World Scientific, Hackensack, NJ. 1995.

In: Silica Nanoparticles
Editor: Juan Vivero-Escoto
ISBN 978-1-61324-452-4
© 2012 Nova Science Publishers, Inc.

Chapter 3

MULTIFUNCTIONAL MESOPOROUS SILICA NANOPARTICLES FOR CONTROLLED DRUG DELIVERY, MULTIMODAL IMAGING AND SIMULTANEOUS IMAGING AND DRUG DELIVERY

Juan L. Vivero-Escoto*
Department of Chemistry, University of North Carolina at Chapel Hill, NC, US

DEDICATION

In memory of my mentor and esteemed colleague, Victor S.Y. Lin. Deceased on May 4th, 2010.

ABSTRACT

The application of nanotechnology in the field of biomedicine has received enormous attention in the latest decades. Recent breakthroughs on the morphology control and surface functionalization of inorganic-based imaging/delivery vehicles, such as mesoporous silica nanoparticles (MSNs), have brought new possibilities to this burgeoning area of research. The ability to functionalize the surface of mesoporous-silica-based nanocarriers with stimuli responsive groups, nanoparticles, polymers, optical and MR imaging agents that work as caps and gatekeepers for controlled release of various cargos and multimodal imaging probes is just one of the exciting results reported in the literature that highlights MSNs as a promising platform for various biotechnological and biomedical applications. This chapter focuses on the most recent progresses in the application of MSNs in the areas of controlled drug delivery and biomedical imaging. The versatility of MSNs as controlled drug delivery system is shown, with special emphasis given to stimuli-responsive nanodevices containing nanoparticles as gatekeepers. The latest research on the development of mesoporous

*Corresponding Author: E-mail: jlvivero@email.unc.edu.

multimodal nanoparticles is described. In addition, the current research progress on the biocompatibility of this material *in vivo* is discussed. Finally, the latest breakthroughs in the simultaneous application of MSNs as therapeutic and diagnostic (theranostic) agents *in vivo* are presented.

1. INTRODUCTION

Remarkable progresses in our understanding of the fundamental biological processes underlying many diseases have been reached in the past decades. Despite these achievements, we have not observed similar advances in the detection, diagnosis, and treatment of these diseases. Current clinical imaging or therapeutic agents are limited by their nonspecific biodistribution, rapid clearance, poor pharmacokinetics, and high side effects.[1] Conventional imaging and therapeutic agents, such as antitumor drugs, require high doses resulting in significant side effects and limited effectiveness that restrict their clinical application. Nanomaterials are novel systems with the potential to alleviate many of these issues and have received an increasing amount of attention for imaging and therapeutic applications over the past decades.[2-4] Some of the key properties of nanoparticle-based imaging and therapeutic platforms are tunable size, high agent loading, tailorable surface properties, controllable or stimuli-responsive drug release kinetics, improved pharmacokinetics, and biocompatibility.[5, 6] Additionally, nanoparticles can be specifically targeted to certain regions of the body (e.g. tumors) by conjugation with targeting ligands. They can also be engineered to contain multiple agents (e.g. imaging and therapeutic agents) for real-time monitoring of the drug uptake and/or therapeutic responses. Both of these features are difficult to achieve with conventional small molecule drugs.

The first generation of nanoparticle platforms that have been extensively explored for biomedical applications are predominantly purely organic materials. For instance; liposomes, which are spherical vesicles with a lipid bilayer membrane structure, can encapsulate both therapeutic and imaging agents, protecting the cargo during circulation in the body.[7] They can also be functionalized with ligand to cell surface receptors to promote targeting to specific cells and tissues. In addition, they can be coated with polymers to prolong the circulation half-life. Liposomes have the most successful nanoparticle platform for biomedical applications, with several formulations clinically available; liposome-encapsulated doxorubicin (Doxil; OrthoBiotech), liposomal amphotericin B (AmBisome; Gilead) and liposomal morphine (DeporDur; Pacira Pharmaceuticals).[7, 8] Polymer-therapeutic/contrast conjugates have also been extensively investigated, and several have received regulatory approval.[9-11] Despite these outstanding progresses in organic-based nanoparticulate platforms still some drawbacks need to be overcome in the near future, such as increasing the loading of imaging and therapeutic agents and the common premature release of toxic drugs. In recent years different nanotechnologies are being explored to alleviate these issues. Inorganic-based materialsare a novel approach to developed effective therapeutic and contrast agents. For instance, the archetypical inorganic nanoparticle, quantum dots (QDs), are nanomaterials generally composed of elements from either groups I-VII, II-VI or III-V. QDs are nearly spherical semiconductor particles with diameters in the order of 2-10 nm, containing roughly 200-10000 atoms.[12] They display unique optical properties, including sharp and symmetrical emission spectra, high quantum yields, broad

absorption spectra, good chemical and photostability, and tunable size-dependent emission wavelengths. As a result, they have been very attractive for their use in optoelectronic devices and biological detection both *in vitro* and *in vivo*. Another class of inorganic nanoparticles that have been evaluated for a wide variety of biomedical applications is iron oxide nanoparticles (IONPs). IONPs have been used in cellular therapy, tissue repair, drug delivery, hyperthermia, magnetic resonance imaging (MRI), as spoilers for magnetic resonance spectroscopy, for magnetic separation, and more recently as sensors for metabolites and other biomolecules.[13, 14] Gold nanoparticles (AuNPs) have also been exploited for therapeutic and imaging applications due to their unique physical and chemical properties.[15] For example, the gold core is essentially inert and non-toxic. A second advantage is that the size and morphology of AuNPs can be easily manipulated based on well-established protocols. In addition, the nanoparticles can be further functionalized with a wide variety of biogenic molecules generally through thiol linkage. Moreover, they can be engineered to exhibit strong absorption in the NIR region. Actually, AuNPs have also been explored for photothermal therapy, where absorbed light by small gold nanoparticles (10-30 nm) is rapidly converted into thermal energy to lead to hyperthermia.[16-18]

Among these nanoparticulate platforms explored, mesoporous silica nanoparticles (MSNs) have attracted much research attention for their potential application in the fields of

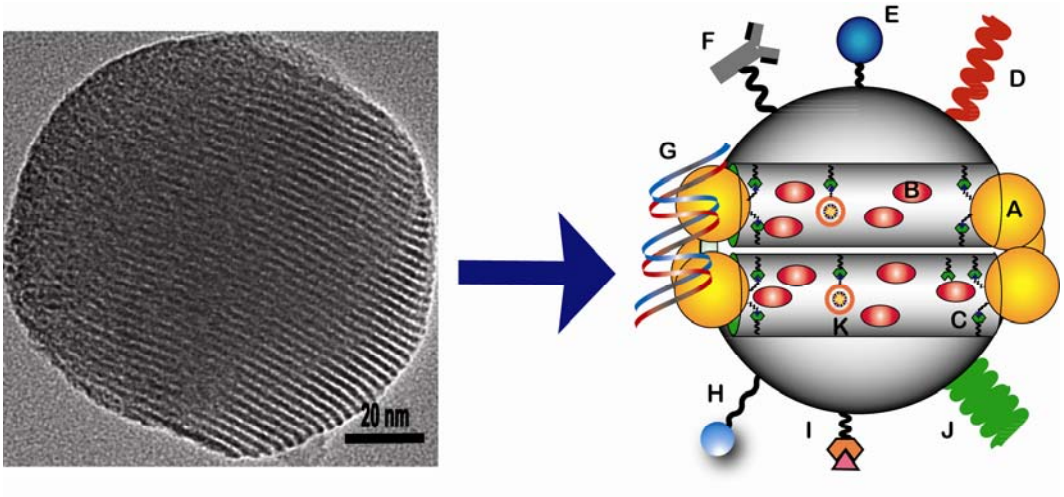


Figure 1.Transmission electron microscopy of mesoporous silica nanoparticles (left) and schematic representation of MSNs as imaging and therapeutic platform (right). A) Nanoparticles attached to MSNs as functional gatekeepers. B) Hydrophobic/hydrophilic guest molecule entrapped in the channels. C) Stimuli-responsive linkers. D) Grafting with a protecting polymer. E) Imaging contrast agents, such magnetic nanoparticles, Gd-chelates, quantum dots or fluorophores. F) Antibodies as targeting ligands. G) Double-stranded DNA as biomolecular gatekeeper. H) Additional ligands such as cell-penetrating peptides. I) Incorporation of a diagnostic label. J) Stimuli-responsive polymers. K) Attachment of functional groups that may modify the cell metabolism.

catalysis, biotechnology and nanomedicine.[19-25] MSNs are solid materials, which contain hundreds of empty channels (mesopores) arranged in a 2D network of honeycomb-like porous structure (Figure 1). As has been recently described,[19, 26] these silica-based nanoparticles also offer several unique and advantageous structural properties, such as high surface area (> 1000 m^2g^{-1}), pore volume (> 1.0 cm^3g^{-1}), stable mesostructure, tunable pore diameter (2–10 nm), two functional surfaces (exterior particle and interior pore faces), and modifiable morphology (controllable particle shape and size). For instance, their large surface area and pore volume allow for high loading of imaging and therapeutic agents. The tunable diffusional release of drug molecules from the highly ordered mesoporous structure gives rise to a biogenic local concentration at the targeted area, which reduces the overall dosage and prevents any acute or chronic complications. In addition, MSNs offer the ability to further functionalize the surface of MSNs with a wide variety of stimuli-responsive groups, target agents, polymers, biomolecules, molecular gatekeepers, etc (Figure 1). Finally, MSNs can effectively protect the pharmaceutical cargoes, such as drugs, imaging agents, enzymes, and oligonucleotides, from premature release and the undesired degradation in harsh environments before reaching the designated target. In summary, MSNs offer ideal characteristics to fulfill most of the requisites to be the platform to develop imaging and drug delivery nanovehicles. In fact, recent studies have already established MSNs as drug delivery system that effectively transports imaging/therapeutic agents through the cell membrane, and efficiently releases its cargo in the cytoplasm.[27] Despite these encouraging results, several steps have to be accomplished before translating this platform into clinic. In this chapter, we will focus on both the versatility of MSNs as drug delivery system and their recent *in vivo* applications. For that, we will explore the most current progresses in the application of MSNs in the areas of controlled drug delivery and biomedical imaging. The versatility of MSNs as controlled drug delivery system is shown, with special emphasis given to stimuli-responsive nanodevices containing nanoparticles as gatekeepers. The latest research on the development of mesostructured multimodal nanoparticles is described. In addition, the current research progress on the biocompatibility of this material *in vivo* is discussed. Finally, the latest breakthroughs in the simultaneous application of MSN as therapeutic and diagnostic (theranostic) agents *in vivo* are presented.

2. MSN-BASED CONTROLLED DRUG DELIVERY SYSTEMS

Vallet-Regi and co-workers were the first group to explore the use of mesoporous silica materials for drug loading and release;[28]since then, many mesoporous silica-based drug delivery systems have been studied.Lately,the research efforts have been directed to attaining controlled release.For example, drug delivery systems (DDS) based on MSNs capped with solid nanoparticles such as cadmium sulfide (CdS-),[29] gold (Au-),[30-32] and iron oxide (IO-NPs),[33, 34] and soft nanoparticles such as dendrimers,[35] proteins,[36] and polymers have been developed.[37-39] This gatekeeper approach has been applied to afford site- and time-control on the release of biogenic agents based on stimuli responsive linkers. Different biocompatible stimuli responsive triggers such as pH, enzymatic activity, redox potential and irradiation have been used. Moreover, it has been demonstrated that these DDS with nanoparticulate caps show “zero premature release” performance before reaching the targeted

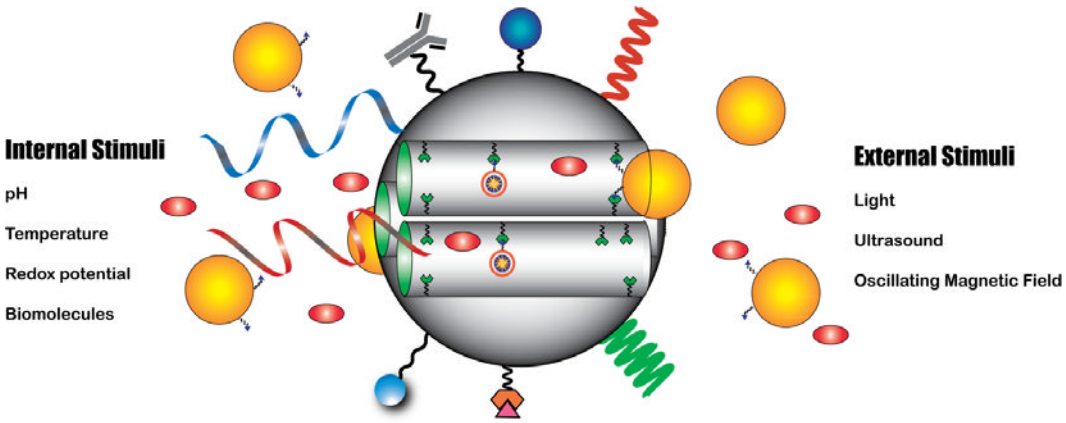


Figure 2. Schematic representation of drug release from MSNs trigger by different stimuli-responsive strategies (pH, redox potential, temperature, light, ultrasound and magnetic field).

site. All these advantages have resulted in promising applications of MSNs as drug delivery vehicles *in vitro*. It is envisioned that soon these strategies will be applied to *in vivo* models. Non-capped MSNs have also shown their efficacy in the release of different cargoes. For instance, the release of a membrane-impermeable protein (cytochrome c) was recently reported.[40] To achieve this goal, a large pore MSNs (5.4 nm) was synthesized. It was demonstrated that the enzymatic activity of the cytochrome c after being loaded and released in solution is preserved. In addition, the efficient transport of cytochrome c through the cell membrane and release into the cytoplasm by MSNs was corroborated by confocal fluorescence microscopy. Other biogenic molecules have been released using non-capped MSNs, such as camptothecin,[41]propidium iodide,[42] paclitaxel,[43] doxorubicin,[44] and different fluorophores.[45] To improve the release efficiency of these drug delivery vehicles Zink, Stoddart, and co-workers have developed nanoimpeller platform.[42] The working principle for this system is based on the photoisomerization of azobenzene derivatives. The back and forth wagging act regulates the release of cargoes from the channels of MSNs, as a molecular impeller. The authors have demonstrated the successful application of this strategy *in vitro* using rhodamine B, propidium iodide, and camptothecin as cargoes.

2.1. MSN-Based Stimuli-Responsive Drug Delivery Systems

For many biomedical applications, an ideal delivery system should have the ability to deliver a large amount of guest molecules to a targeted site and release the cargo in a controllable fashion. In addition, it is well established that an efficient delivery system should have the capability to transport the desired therapeutic agents without any loss before reaching the targeted location.[46] Any premature release of toxic drugs poses a challenging problem. To achieve precise spatial and temporal delivery of therapeutic agents to target sites, a variety of stimuli-responsive groups have been introduced to MSN, including groups that respond to stimuli found internally in biological systems (pH, temperature, redox potential and biomolecules) and stimuli that can be applied externally from biological systems (light, ultrasound and oscillating magnetic field) (Figure 2). Various responses to stimuli are feasible, including bond cleavage, competitive binding and conformational changes. MSN

Table 1. Stimuli and triggers applied in MSNs

Stimuli		Trigger	Cap	Responsive moiety of linker or stalk	Ref
Internal Stimuli	pH	Acid	Poly-(dimethydiallylammonium chloride) (PDDA)	Carboxylic acid	[49]
		Acid	Cyclodextrin (CD)	Polyethyleneimine (PEI)	[50]
		Acid	Cucurbit[6]uril (CB[6])	Trisammonium	[51]
		Acid	CB[6]	Dialkyl-4,4'-bipyridinium (viologen)	[52]
		Acid	Borate	Saccharide	[53]
		Acid		Metal ions	[54]
		Acid		Hydrazone	[55]
	Redox	Dithiothreitol (DTT), Mercaptoethanol (ME)	CdS NP	Disulfide	[29, 56]
		DTT, Dihydrolipoic acid (DHLA)	Fe_3O_4 NP	Disulfide	[33]
		DTT	Au NP	Disulfide	[30]
		DTT, tris(2-carboxyethyl)phosphine (TCEP)	Polyamidoamine (PAMAM) dentrimer	Disulfide	[35, 56]
		DTT	cross-linked Poly(N-acryloxysuccinimide) (PNAS)	Disulfide	[38]

		DTT	Polyelectrolyte multilayers PEM-aptamer	Disulfide	[57]
		DTT	Collagen	Disulfide	[58]
	Biomolecule	Porcine liver esterase (PLE)	α-CD	Ester-linked adamantyl stopper	[59]
		β-D-Galactosidase	Lactose	Glycosidic bond	[60]
		Protease (trypsin)	Biotin–Avidin	Avidin	[61]
		Glucose	G-Insulin	Phenylboronic acid	[36]
		Sulfathiazole (STZ)	Antibody	Hapten	[62]
		DNase I/Heating	DNA	d-s oligonucleotides	[63]
		Complementary binding	DNA	d-s oligonucleotides	[64]
		Hybridization	DNA-Biotin	d-s oligonucleotides	[65]
External stimuli	Light	UV light	Au NP	o-Nitrobenzyl ester	[31]
		UV light	β-CD	o-Nitrobenzyl ester	[66]
		UV light	Py-β-CD	Azobenzene stalks	[67]
		NIR		7-amino-coumarin	[68]
	Magnetic field	Oscillating Mag Field	Cucurbituril	(aminohexyl)aminomethyl TES	[69]
	ultrasound	ultrasound	ferrocene	amide	[70]

systems are designed to take advantage of these responses and to trigger the release of encapsulated molecules. An overview of stimuli and triggers that have been applied to mesoporous silica materials for controlled release is given in Table 1, some of these platforms have already been described somewhere else.[47, 48] In this section, the most recent stimuli responsive approaches found in the literature are analyzed, with a particular focus on pH, redox potential, biomolecules, and irradiation controlled release systems.

2.2. MSN-Based Internal Stimuli-Responsive Drug Delivery Systems

Stimuli-responsive controlled release systems are especially advantageous when the triggering stimuli are unique to the targeted pathology. This allows the drug carriers to respond specifically to the desired target and release drugs in a self-regulated fashion. Examples of internal stimuli that have been exploited for intracellular drug include pH, temperature, redox potential and some specific biomolecules such as enzymes, DNA, carbohydrates and antigens.

2.2.1. pH

Of the stimuli responsive systems, the pH-sensitive system is of special interest. The extracellular pH of tumors is more acidic (pH 5.7-6.8) than that of blood and normal tissue, and the pH values in endosomes and lysosomes reach values as low as 5.5 and 5.0, respectively.[71] Therefore, a finely pH-responsive system, sensitive to small pH variations, that would release encapsulated drugs when passing through a region of low pH (5-7) while staying stable under physiological conditions to reduce side effects, has been pursue for some time. A series of MSN-based pH-responsive systems have been developed using different strategies for controlling the release of drug molecules such as pH-sensitive linkers or caps including polyelectrolytes, pseudorotaxanes and organic molecules, some of these platforms are summarized in Table 1.Recently, L.-W. Lo and coworkers reported on the development of a pH-sensitive dye-doped MSN-based drug delivery system.[55] Firstly, the authors incorporated a near-infrared (NIR) fluorophore (Atto-647) within the MSN silica framework to provide a means of non-invasively tracking its biodistribution in vivo. The pH-sensitive strategy was based on hydrazine bonds between the MSN framework and the chemotherapeutic agent (doxorubicin-DOX) (MSN-hydrazone-DOX). The authors tested the release of DOX at different pHs (pH 7.4, 5.5, 4.5, and 1.0), the data obtained showed that DOX was selectively released at pH 5.5 or below. The endocytosis and endosomes/lysosomes accumulation of MSN-hydrazone-DOX was corroborated by using confocal laser scanning microscopy (CLSM) and transmission electron microscopy (TEM) in liver carcinoma cell line (Hep-G2). Cytotoxicity, terminal deoxynucleotidyltransferasedUTP nick-end labeling (TUNEL), and DNA fragmentation assays were used to study the toxic effect of MSN-hydrazone-DOX on Hep-G2 cells. The results showed that indeed the DOX was intracellularly released and the cell proliferation was reduced by 70%. Taking advantage of the NIR Atto-647 dye attached to MSN, the authors were able to investigate the biodistribution of this material in mice. Visceral group fluorescence imaging of the organs revealed that the overwhelming majority of Atto-647-MSN-hydrazone-DOX resided within the liver. Unfortunately, the authors did not demonstrate the in vivo release and anticancer effect of DOX. Interestingly, not only chemical bonds have been used for developing pH-

responsive strategies, also the coordination bonding between metal ions and functional groups has been recently reported as potential approach for that purpose.[54] Despite the current development of pH-responsive drug delivery platforms, there are still major drawbacks that need to be overcome in the future for the *in vivo* application of this approach. Just to mention some of them, the cleavage of widely used acid-labile linkages, such as esters or hydrazones, is a rate dependent phenomenon as the hydrolysis is proportional to the pH. In these linkages, for a decrease of one pH unit a 10-fold difference in the hydrolysis rate can be expected.[72] Therefore, premature (extracellular) release of the cargo in an acidic environment found in the vicinity of tumors or inflamed tissue is possible. This is a significant concern in cancer therapy, as they are often associated with inflammation. Hence, acid-labile linkages must compromise between a fast hydrolysis rate in the intracellular compartment and a slower hydrolysis in the extracellular space.[72, 73].

2.2.2. Redox Potential

The existence of a redox gradient between intra- and extracellular space was shown some time ago. While the extracellular space is oxidizing, most cellular compartments are reducing. Nature has exploited this fact for the ‘‘delivery’’ of toxins (like diphtheriaor cholera toxin) and viruses that have served as templates for artificial therapeutic disulfide conjugates such as Gemtuzumabozogamicin (Mylotarg).[74] Cellular disulfide reduction and isomerization is mediated by small redox molecules, either alone or in conjunction with redox proteins. It is known that the intracellular glutathione (GSH) levels in most tumor cells are 100 - 1000-fold higher than the extracellular levels, therefore the naturally occurring redox potentials between the mildly oxidizing extracellular space and the reducing intracellular space can be utilized as stimulus to trigger the release of encapsulated molecules form drug carriers.[75] The fact that disulfide containing carriers can take advantage of the large intra-/extracellular redox gradient renders them very attractive for the design of drug delivery systems. A few examples will be described in this section that shows the use of redox-responsive uncapped and capped nanovehicles. Lin and coworkers demonstrated the versatility of MSNs by covalently linking a biogenic molecule onto its surface and trigger its release by redox potential.[76] The idea was developed by synthesizing a cysteine-loaded MSN system. Cysteine is an amino acid required for the biological synthesis of glutathione (GSH), which is of vital importance for controlling the homeostasis of live cells. Cysteine molecules were chemically anchored on the surface of MSNs through a labile disulfide linker and its release was measured after been triggered by different reducing agents in solution. It was demonstrated that the cysteine molecules have been chemically incorporated in MSNs with high efficiency through this approach. Moreover, the efficient endocytosis and cargo release of this material in HeLa cells by flow cytometry and CLSM was proven. By means of a viability assay in HeLa cells, it was found that this system is roughly 400 times more effective than conventional cysteine prodrugs (i.e. N-acetyl cysteine) for inhibiting cell growth. On the other hand, redox potential was the first stimuli-responsive strategy to develop MSN-based capped/gatekeepers platforms for biological applications. Indeed, the first system was developed using quantum dots.[29] The continuous progress in this area has resulted in a wide variety of nanovehicles, Table 1 summarized some of them, and still new strategies are being developed. For instance, H. J. Park, C. Kim and coworkers reported on the synthesis of redox-responsive MSNs with cyclodextrins (CD) gatekeepers covalently connected via a disulfide unit.[77] To test the redox release principle both calcein and DOX were loaded to the nanoparticles. Not leaking

of guest molecules were observed after 4 days in absence of reducing agents, as an indication of both the effective entrapment in the pores of MSNs and that the CD cap with disulfide stalk was very effective to block the calcein/DOX in the channel. The authors tested the successful release of agents by reduction of the disulfide stalk moieties after the addition of GSH and DTT. The intracellular release of DOX was investigated in the A549 cells containing high concentration of GSH. The CLSM images and the cytotoxicity assay showed the successful release and therapeutic effect of DOX in vitro. As was mentioned above, MSN material is a versatile platform that not only allows to load and release therapeutic agents in a stimuli-responsive fashion, but also can be further functionalized to develop target-specific nanovehicles. These multifunctional features of MSNs were recently tested by K. Cai and coworkers using MSNs capped with collagen, which is one of the extracellular matrix components.[58] Collagen was immobilized on the exterior surface of the MSNs by disulfide bonds; moreover, lactobionic acid(LA), which bears a galactose group, was introduced as the targeting moiety. The stimuli-responsive release of a fluorescence agent (fluorescein) was tested using DTT as reducing agent. After addition of DTT around 80% of fluorescein was released; on the contrary, without any reducing agent presented in solution less than 6.5% of fluorescent dye was observed. The intracellular release of fluorescein was confirmed by CLSM using HepaG2 cells. The target ability of this material was evaluated using HepaG2 and endothelial cells. Flow cytometry showed that the endocytosis of nanoparticles by HepaG2 was twice higher than that of endothelial cells. This result strongly demonstrated the target property of LA functionalized collagen-MSNs toward HepaG2 cells.

2.2.3. Biomolecules

Recently, the use of biomolecules as stimuli-responsive gatekeepers has emerged as a new strategy to develop biocompatible nanomaterials with interesting biological activities. Despite of recent reports on capped MSNs that can be triggered by certain enzymes or carbohydrates (see Table 1), the utility of MSN-based devices involving biomolecules for real delivery systems is still in its infancy. Therefore, the search for effective strategies that, in particular, respond to internal biological stimuli still remains a big challenge in this field. So far, the types of biomolecule that have been introduced to cap mesoporous silica materials include enzymes, blood sugars, and antigens.[36, 59, 60] However, recently the development of MSN systems capped by double-stranded oligonucleotides has attracted a big deal of attention. Recently, T. Bein and coworkers developed a thermo-responsive biomolecule-based valve MSN system.[65] The nanovehicle consists of DNA oligomers with complementary strands carrying biotin functionality, which coordinate with the avidin protein and thus close the pores of the colloidal particles. The opening of the valve is achieved by DNA strand melting at the specific melting temperature of the oligonucleotide. To prove the working principle, fluorescein was used as guest molecule. The release of fluorescein was investigated using oligonucleotides with two different lengths (15 and 25 mers) at different temperatures (25, 45, 65 ºC). As was expected not considerable release of fluorescein was observed at 25 ºC for both systems; however, when the temperature was raised up to 45 ºC, the system containing the 15 mers oligonucleotides opens the pores, the longer 25 mers DNA oligomer was still in a tightly sealed state. The sample with 25 mer released fluorescein until further heating to 65 ºC. These results showed that avidin-DNA-capped MSNs allow the release of guest molecules by a temperature-responsive trigger, which can be adjusted precisely for a desired application. J. Ren and coworkers were also able to show the thermo-responsive

release of guest molecules using DNA-capped MSNs.[63] In addition, the enzymatic release by endonucleases was tested. By using Rhodamine B and camptothecin (CPT) as guest molecules, the authors observed their successful release after the addition of deoxyribonuclease I (DNase I). Moreover, the performance of this system was also evaluated *in vitro* using human liver cancer cells (HepG2). CLSM and cytotoxic assay revealed that the CPT-loaded DNA-MSNs are endocytosed by HepG2 cells and indeed the therapeutic agent is released intracellularly inhibiting the cell proliferation. The advantage of using DNA as capping approach is that the unique structural motif and self-recognition properties of double-stranded oligonucleotides allows the design of a wide variety of stimuli-responsive strategies. The highly specific binding between complementary strands was used as pore opening strategy by R. Martinez-Mañez and coworkers.[64] MSNs were grafted with aminopropyltriethoxysilane and loaded with fluorescein as guest molecule. Taking advantage of the positively surface charge of the nanoparticle under biological conditions, the authors attached a 21 mers in length oligonucleotide to MSNs by electrostatic interaction. The release of fluorescein was tested with and without the addition of the complementary strand. In absence of the complementary oligonucleotide strand not considerable release of fluorescein was observed; on the contrary, after adding the complementary strand and immediate release of fluorescein was detected by fluorescence spectroscopy. Interestingly, even with the addition of a same length oligonucleotide strand, but a two-base mismatch sequence, not release of dye was detected.

2.3. External Stimuli-Responsive Drug Release

The traditional pre-requisites for a DDS are biocompatibility, high loading and protection of the guest molecule, “zero” premature release, and cell and tissue targeting. In addition to these requirements to have the ability of time- and spatial-controlled release in a remote control fashion would be the last paradigm to reach in this area. Different strategies have been investigated with partial success to achieve this goal such as radiation and oscillating magnetic field.

2.3.1 Radiation

Radiation is very attractive as a remote control for the site-specific delivery of drugs. The proposed strategy is that the release of the entrapped molecules can be rapidly induced on exposure to radiation with determined wavelength at a specific time and location without any change in the chemical environment. Suitable chromophores, such as azobenzene,[39, 67]spiropyran[53] and photocleavable linker *o*-nitrobenzyl ester[66, 78] have been used on MSNs to render them susceptible to radiation for photoresponsive controlled release.

Recently, Lin and coworkers synthesized a MSN system using photo-responsive gold nanoparticles (PR-AuNPs) as caps.[31] The working principle of this system is based on the electrostatic interaction between MSNs and PR-AuNPs. Upon irradiation with UV light, the umpolung of surface charge leads to repulsion of AuNPs resulted in cargo release (Figure 3). The concept was demonstrated through photo-induced release of encapsulated fluorescein dyes. In addition, human cells were inoculated with paclitaxel-loaded PR-AuNPs-MSNs and the viability of the cells was measured. The cell proliferation was inhibited with the drug-loaded PR-AuNPs-MSN material after irradiation under mild conditions. These results

showed that the PR-AuNPs-MSN system can be efficiently loaded with drugs or fluorescein and release its cargo in a control fashion using an external trigger. For *in vivo* applications photoresponsive systems based on near-infrared (NIR) light excitation have to be developed. The use of near-infrared (NIR) irradiation is thus critical to avoid the cytotoxic effects of UV light whose intensity attenuates quickly in living tissue.[79] To reach this target L. Zhu and coworkers reported on a novel MSN-based nanophotocaged DDS whose drug can be effectively uncaged by external precise manipulations under two-photon NIR excitation at 800 nm.[68] To achieve NIR sensitivity, 7-amino-coumarin chromophore was grafted in the MSN framework. In addition, 7-amino-coumarin was modified with anticancer drug chloroambucil. Precise control of the photolytic release was demonstrated by monitoring the progress of chloroambucil release after period of exposure to light and dark conditions. These results indicated that the NIR stimuli-responsive MSN drug delivery system could precisely control drug release by manipulating external light intensity, irradiation wavelength and time. Moreover, the cytotoxic properties of this system were measured by MTT assay using both HeLa and MCF-7 cells. The cell proliferation was inhibited by the release of chloroambucil after irradiation; moreover the toxic effect can be regulated by the duration of the applied light.

2.3.2. Oscillating Magnetic Field

For clinical applications, an external and noninvasive method of actuation is preferable for control of therapeutic effects. As was explained above, the controlled release by irradiation *in vitro* has been already proved, but its practical applicability is still limited

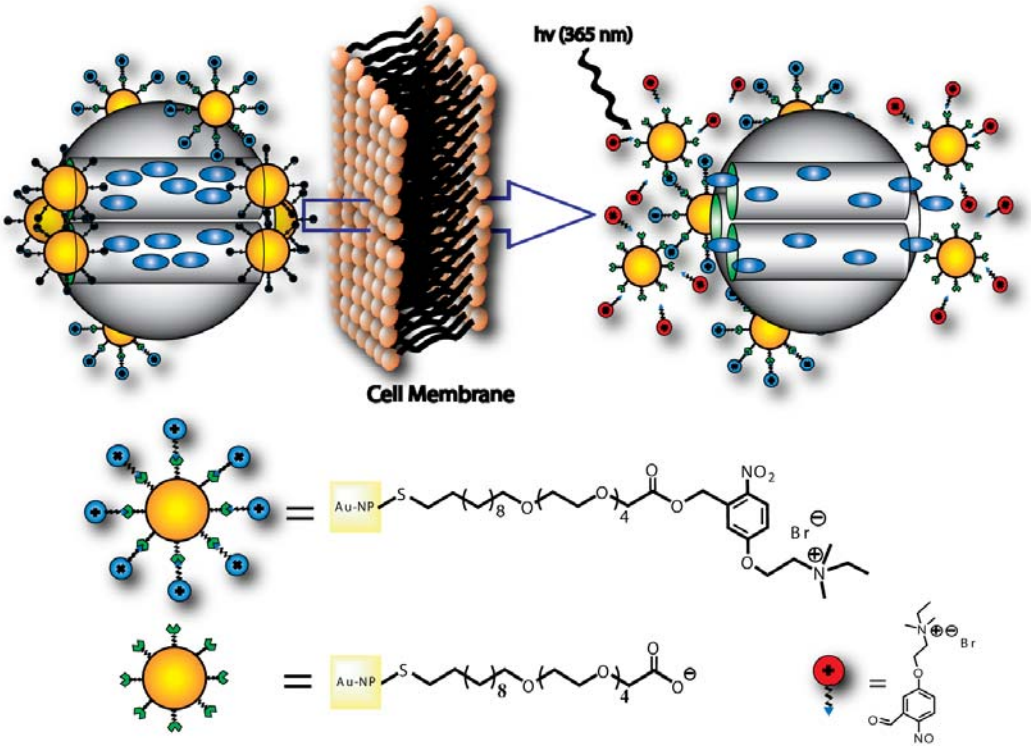


Figure 3.Schematic representation of a photoresponsive gold nanoparticle-capped MSN.

because of shallow tissue penetration for photodynamic therapies. On the other hand, pH- and redox-responsive systems cannot be controlled by an external stimulus. This lack of an effective, external control for *in vivo* applications can be overcome by a new class of materials driven by a magnetic core. Magnetic nanocrystals are of importance in biomedical applications, as they can be used for both therapeutics and imaging. In addition, magnetic materials can induce hypothermic effects when placed in an oscillating magnetic field.[80] Recently, Zink and coworkers have combined the advantages of nanovalve-capped MSNs with those of zinc-doped iron oxides to create a new generation of DDS responsive to heat activation.[69] The system consists of zinc-doped iron oxides nanoparticles embedded on MSNs and thermally-responsive nanovalves. The working principle was successfully tested using rhodamine B and DOX. In addition, *in vitro* experiments using the breast cancer cell line MDA-MB-231 showed that the cell proliferation can be inhibited by both the local heating caused by the magnetic core and the release of DOX from the silica pores after the nanovalves are opened by the same heating effect.

3. MSN-BASED IMAGING PROBES

During the past few years, research in biomedical imaging has been one of the most successful interdisciplinary fields. Multimodal techniques are quickly becoming important tools for developing breakthroughs in the areas of biomedical research, clinical diagnosis, and therapeutics.[81] For instance, tracking the distribution of soft tissues *in vivo* for distinguishing anatomical images and assess disease pathogenesis by biomarkers is crucial for therapeutical treatments.[82] The development of methods to determine the fate and distribution of transplanted stem cells is vital for finding future advances in this area.[83, 84] The recent contribution of nanotechnology to these research areas has boosted their advance, in special the use of inorganic nanoparticles in the biomedical fields has resulted in the development of several techniques for cellular and *in vivo* imaging. For example, Au nanoparticles, semiconducting quantum dots, and magnetic nanoparticles have found a wide application in detection of biomolecules such as DNA and cancer markers, optical imaging of small organelles and tumors, cellular magnetotransduction signaling and magnetic resonance imaging (MRI) agents.[85-90] However, despite such outstanding progresses these techniques still suffer from some drawbacks such as low target sensitivity, poor spatial resolution, low tissue penetration, and each technique is limited to a single imaging modality.[81] To overcome these issues the combination of different imaging methods into a single system has been proposed. Due to their unique properties, such as biocompatibility, optical transparency, easy incorporation of nanoparticles (i.e. Au, and Fe_3O_4), and functionalization with optical groups (fluorescein, Rhodamine B), MSNs have attracted a great deal of attention as suitable platform for multimodal imaging and multifunctional probes.

3.1. MSN-Based Optical Imaging Agents

Optical imaging has been a versatile and easy-of-use approach, in terms of availability of a variety of contrast agents for molecular targeting, avoidance of radiopharmaceuticals, and

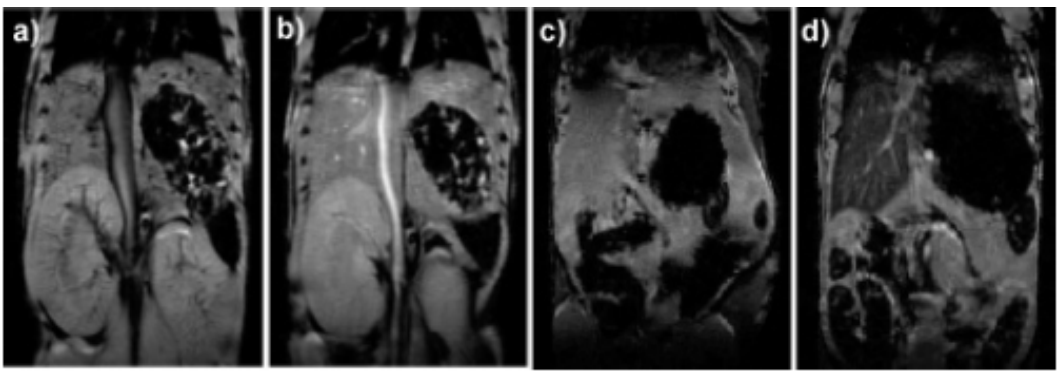
relatively low cost of instrumentation. These features make it complementary to other modalities such as MRI. The use of optical imaging agents has being prevailing for investigating cellular and intracellular imaging of MSNs since the beginning of this field.[29, 35] Different fluorescent molecules for cell imaging such as fluorescein isothiocyanate, Rhodamine B, Texas red and others have been incorporated in the silica framework by conjugating the reactive dye molecules with organo-alkoxysilanes.[19] However, for *in vivo* applications, optical imaging usually suffers from the attenuation of photon propagation in living tissue and poor signal to noise ratio due to tissue autofluorescence. The use of NIR contrast agents is thus critical for *in vivo* optical imaging since the blood and tissues are relatively transparent in the range of 700-1000 nm wavelength so minimizing complications resulting from intrinsic background interference. Recently, L.-W. Lo and coworkers focused on the development of NIR MSN-base probes.[91]Indocyanine green (ICG) was entrapped in MSNs by electrostatic interaction. ICG is a FDA approved optical agent for clinical use; moreover, its characteristic fluorescent excitation and emission wavelengths (ex: 800 nm; em: 820 nm) in NIR window, make this agent ideal for *in vivo* imaging. Several advantages by using MSNs as nanovehicles of ICG were demonstrated in this paper; for instance, the dispersion of ICG molecules in the large surface area of MSNs efficiently prevents them from aggregation and self-quenching. Moreover, the nanochannels protect ICG molecules from degradation and also diminish the immune response. Using this ICG-MSN optical imaging platform, the authors were able to noninvasively image its*in vivo* biodistribution in both rat and mouse models. The optical images show that the nanoparticles after intravenous injection are immediately accumulated in liver followed by kidney, lung, spleen and heart. Recently, the same group reported on a systematic investigation of the effect of the surface charge of ICG-MSNs on their *in vivo* biodistribution.[92] The results showed that by judiciously tailoring the surface charge of MSNs it would be possible to control both MSN rates of excretion and biodistribution.

3.2. MSN-Based MR Imaging Agents

Among various imaging technologies, MRI is currently one of the most powerful *in vivo* imaging technologies. MRI has the advantages of being a noninvasive diagnostic tool that provides high three-dimensional resolution of anatomical images of soft tissue. MRI exploits the remarkable range of physical and chemical properties of water protons (i.e. hydrogen nuclei).[93, 94] The signal detected in MRI is created through the interaction of total water signal (proton density) and the magnetic properties of the tissues being imaged. The magnetic properties in question are the longitudinal relaxation time, T_1; and transverse relaxation time, T_2. The reciprocal of these values represent the longitudinal and transverse relaxation rates, r_1 and r_2, respectively. Proton longitudinal and transverse relaxation times are dependent upon the physicochemical environment of a given tissue and are modified in the presence of a pathological state. Contrast agents are used in imaging to increase the signal difference between the area of interest and the background. In MRI the sensitivity and exceptional soft tissue contrast are further improved by the use of MR contrast agents that change the local MR signal intensity. There are two main classes of contrast agents for MRI: paramagnetic complexes and superparamagnetic iron oxide particles. The former class includes mainly chelates of Mn(II), Mn(III) and Gd(III) ions, with gadolinium-based agents being the most

commonly used.[95] The gadolinium contrast agents currently on the market lack sensitivity and often do not provide satisfactory image contrast enhancement; because of that, high concentrations of contrast agent are required. A possible solution to overcome these drawbacks is to use nanoparticulate MR contrast agents. Some of the advantages that can be envisioned using nanoparticulate MRI agents are; a high payload of a molecular contrast agent can be incorporated in a single nanoparticle, thus increasing the effective relaxivity per nanoparticle; consequently, the signal detected during imaging increases. In addition, molecular MRI contrast agents can be protected from the harsh environment under physiological conditions. Based on these advantages, MSNs have been used as a potential alternative for MRI contrast agents. Lin and co-workers demonstrated the use of MSNs as nanoparticulate T_1-weighted MR contrast agent in*in vitro* and *in vivo* conditions.[96] The synthesis of the nanoprobe was carried out through the traditional grafting method of a silane derivative, Gd-Si-DTTA complex, by refluxing the material in organic solvent. The MR properties were characterized by a 3T and 9.4T MR scanner. The nanoparticles exhibited very large longitudinal (r_1) and transverse relaxivities (r_2). The material was labeled with a fluorescent agent (rhodamine B) to study the *in vitro* properties with immortalized murine monocyte cell line. Both CLSM and *in vitro* phantom images showed that the nanoparticles were successfully internalized by the monocytes. Finally, the material was intravenously injected to a mouse via tail vein to study the *in vivo* MR contrast enhancement properties. A T_1-weighted contrast enhancement was clearly observed in the aorta of the mouse 15 min post-injection, this shows the potential of the Gd-MSN platform as intravascular MR contrast agent (Figure 4). Moreover, it was also demonstrated that this nanoprobe can be used as T_2-weighted contrast agent, the authors reported the signal loss in the liver after several days of the administration of the MSN contrast agent.

D.-M. Huang, C.-Y.Mou and co-workers have actively pursued the application of silica nanoparticles as multimodal contrast agents for tracking stem cells.[97, 98] The ability to monitor cell trafficking *in vivo* and its biodistribution is a prerequisite for developing successful stem cell therapies. MR is an ideal noninvasive imaging technique for tracking stem cells; however, cells must be labeled magnetically by endocytic internalization. Hence,



Source: Reproduced with permission from ref. 96.

Figure 4.a) Precontrast and b) postcontrast (2.1 μmol/Kg dose) T_1-weighted mouse MR image showing aorta signal enhancement. C) Precontrast and d) postcontrast (31 μmol/Kg dose) mouse MR images showing liver signal loss due to T_2-weighted enhancement.

more efficient noninvasive cellular-internalizing platforms are highly desirable. This research group has developed a dual-modal contrast agent platform based on MSNs. This system combines a green fluorescent agent (FITC) and a MR contrast agent. The group has reported the use of both T_2- and T_1-weighted MR contrast agents; small particles of iron oxide act as negative contrast agents to afford Mag-Dye@MSNs,[98] and Gd-base chelates were grafted to MSNs to afford Gd-Dye@MSNs.[97] Both systems were efficiently internalized into human mesenchymal stem cells (hMSCs) without affecting cell viability growth or differentiation. The efficient hMSCs tracking was visualized *in vitro* and *in vivo* by a clinical 1.5T MRI system. *In vivo*, the labeled cells remained detectable by MRI after long-term growth or differentiation, as further evidence of the biocompatibility and durability of both Mag-Dye and Gd-Dye@MSNs nanoprobes. In addition, C.-Y.Mou and coworkers used the dual-modality Mag-Dye@MSNs system to follow the biodistribution of MSNs *in vivo* (mice) after eye vein injection.[98] The Mag-Dye@MSNs darken liver/spleen/kidneys T_2-weighted MR images showed that the MSNs start to accumulate in these organs predominantly through a vascular mechanism in the early stages, and that the signal darkening, mainly in liver and spleen, was due to nanoparticle accumulation within the RES in the late stages. To further confirm these results, histology slides taken from the above mentioned organs of mice sacrificed 30 min after administration of Mag-Dye@MSNs were visualized by a fluorescence microscope. Green spots were observed in the liver and spleen, but not in the kidneys. Long-term MRI tracking study in the liver showed that Mag-Dye@MSNs are highly resistant to decomposition and not easily excreted from the body. Some other approaches using DOTA as Gd chelate have been published.[99] In addition, the use of micro-size mesoporous silica as an alternative to nanoparticulate MRI contrast agent in vivo has been recently reported.[100]

4. BIOCOMPATIBILITY, PHARMACOKINETICS AND BIODISTRIBUTION OF MESOPOROUS SILICANANOPARTICLES

A full understanding of the toxicological and pharmacokinetic (PK) parameters describing MSNs safety and disposition would greatly facilitate further development and clinical translation of MSNs as multifunctional platform. The biocompatibility of MSN with cellular systems has already been demonstrated by different methods and in a wide variety of cells lines, a thoroughly description of this research has been reported elsewhere.[27] In this section we will focused on the latest findings related with the toxicology, PK and biodistribution of MSN*in vivo* models. The *in vivo* biocompatibility, PK and biodistribution of nanoparticles and its following mechanisms of biodegradation and/or excretion determine the feasibility and applicability of such delivery platform in the practical clinic.[5] Recent reports on the PK and biodistribution of silica nanoparticles (SiNPs) are also relevant to this topic because they are giving insights on the *in vivo* performance of silica-based materials, some of their more significant results will be included in this section. Due to the growing interest of using silica nanoparticles for biomedical applications most of the research in this area has been generated in the last decade, some of the main findings are summarized in Table 2. The study of the biodistribution in real time of SiNPs was first reported by K. Wang and coworkers using $Ru(byp)^{3+}$-doped silica nanoparticles with different surface coatings (OH, COOH, and monomethyl ether PEG (MW ~ 428)) on nude mice by optical imaging (ex:

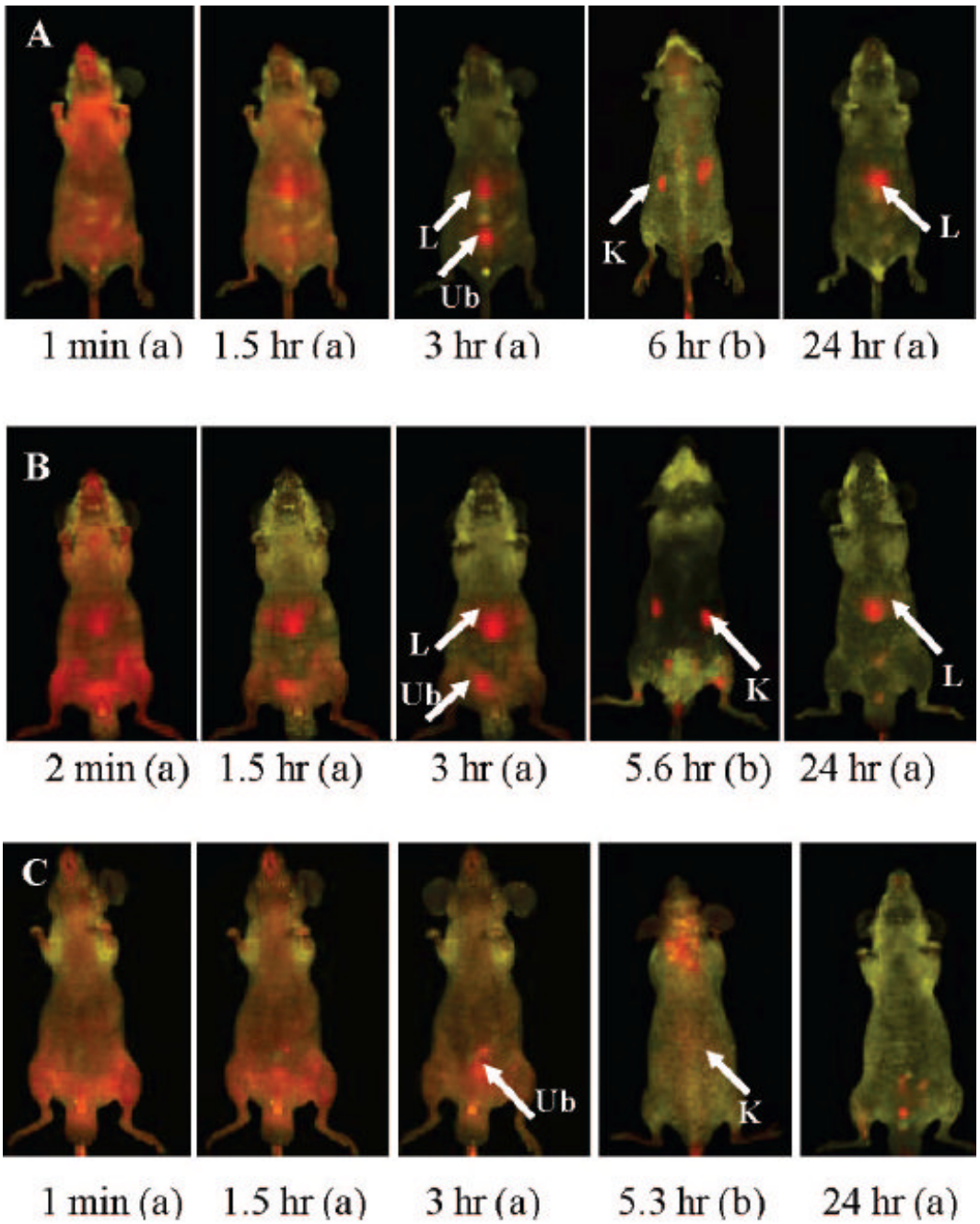
465-495 nm; em: 515 nm long-pass).[101] Some interesting outcomes were obtained from this study; the blood circulation time and clearance half-life are surface coated dependent, PEG-, OH-, and COOH-SiNPs exhibited blood circulation life time ($t_{1/2}$) of 180±40 min, 80±30 min and 35±10min, respectively. The nanoparticles were located mainly in the liver, urinary bladder, and kidney in a time dependent manner. Interestingly, the optical imaging results also demonstrated that all three types of SiNPs were presented in some organs involved in the formation and excretion of urine, as an indication that part of the SiNPs are cleared through the renal route (Figure 5). These results were confirmed by TEM, EDS and using rats as animal model. Other SiNPs surface coating strategies have been explored; for example, the use of phospholipids for coating inorganic nanoparticles is well-established and has been one of the most successful strategies of nanotechnology for biomedical applications. QD containing SiNPs of ~35 nm in diameter were coated with both a monolayer of PEGylated phospholipids (PEG(2K)-DSPE) and a paramagnetic lipid coating (Gd-DTPA-DSA).[102] The short-term cytotoxicity and PK of this platform was investigated by fluorescence imaging, MRI, ICP-MS, CSLM and TEM. This wide variety of complementary techniques allowed investigating the performance of the lipid-coated QD-SiNPs material at different levels; from organ, tissue, cellular and at subcellular level. The PEG-lipid coating increased the blood circulation time by a factor of 10; from 14±2 min for the bare SiNPs to 162±34 min. The bare SiNPs accumulate in the liver, spleen, and lungs; however, SiNPs were not observed in kidneys. Moreover, the accumulation peak in liver and spleen is reach in the first hour after i.v. injection, later the amount of SiNPs started to decrease as a possible indication that the material is being cleared from the animal body. In the case of lipid-coated SiNPs the main accumulation is in the liver and spleen; nevertheless, the accumulation rate is much slower than bare SiNPs (Figure 6). The short-term cytotoxicity showed that bare SiNPs were accumulated in the lungs, to cause breathing problems and liver necrosis, indeed 3/11 mice died after base SiNPs was administrated. However, lipid-coated SiNPs did not show considerable cytotoxic effects. The influence of particle size in the biodistribution and PK of SiNPs*in vivo* has also being studied. Nanoparticles containing a fluorescence group (Rhodamine B isothiocyanate – RITC) with 50, 100 and 200 nm in size were synthesized and characterized (50-, 100-, and 200-SiNPs, respectively).[103] The data show that 50-SiNPs are excreted faster by both renal and hepatobiliary route than 100- and 200-SiNPs. However, all materials are eliminated in a slower rate via feces than urine. The fluorescence intensity of all three sized SiNPs was detected in the kidney, the liver and spleen; nevertheless, the 200-SiNPs are taken up faster and in a higher amount than the smaller-size particles by macrophages of the spleen and liver. A transient inflammatory response in the case of 100- and 200-SiNPs was detected after 12 h post-injection; but, there was no significant difference observed in pathological level after 24h for all the sized particles used in the study and it remained the same till 4 weeks. This study demonstrated that tissue distribution and excretion are different depending on particle size. As particle sizes increased, more particles were trapped by macrophages in the liver and spleen.

On the contrary, small nanoparticles are cleared by urine and bile at higher concentrations than larger particles.

Table 2. Compatibility, biodistribution and pharmacokinetics of solid and mesoporous silica nanoparticles

Material	Size (nm)	Functionalization	Biodistribution/PK	Excretion route	Toxicity	Ref.
$Ru(bpy)^{3+}$-doped SiNPs	45	OH-SiNPs COOH-SiNPs PEG(0.4K)-SiNPs	Blood circulation time: (OH: 80 ± 30 min; COOH: 35 ± 10 min; PEG: 180 ± 40 min) Biodistribution: Surface coated dependent (liver, urinary bladder and kidney)	Renal	Nontoxic after 24 h	[101]
Hydrophobic SiNPs	40	Hydrophobic-SiNPs Lipid-SiNPs	Blood circulation time: (Hydrophobic: 14 ± 2 min; Lipid: 162 ± 34 min) Biodistribution: Surface coated dependent (liver, spleen and lungs)	Not investigated	3/11 mice were death after i.v. administration	[102]
Si-NPs	50, 100 and 200	OH-SiNPs	Biodistribution: 50 nm: kidney/liver/spleen 100 nm: Liver/spleen 200 nm: Liver/Spleen immediately after injection	Both Renal and Hepatobiliary	100/200 nm inflammatory response after 12 h. However, they remained nontoxic after 4 weeks	[103]
ORMOSIL	20	PEG-SiNPs	Biodistribution: Liver and spleen (almost 75%) Lung, kidney, and heart (less than 5%)	Hepatobiliary	Nontoxic after 15 days	[104]
SiNPs	20 and 80 nm	OH-SiNPs	Biodistribution: 20 nm (%ID/g @ 24h): Liver (43.3), spleen (48.7), and lung (14.9) 80 nm (%ID/g @ 24h): Liver (13.6), spleen (5.9) and lung (26.9)	Hepatobiliary	Inflamatory response and liver injury after injection	[105]

MSNs	50-100	MSN-TA-ICG (Negatively charged) MSN-NH2-Cy5.5 (Positively charged)	Biodistribution: MSN-TA-ICG (%ID): Liver (35.3), Kidney (9.0), and Lung (8.3) MSN-NH2-Cy5.5: Liver and gastrointestinal tract	Hepatobiliary	Nontoxic	[91, 92]
MSNs	80, 120, 200, and 360	OH-MSN PEG(10K)-MSN	Blood circulation time:* 80-MSN/80-PEG-MSN (2/2.3 h) 120-MSN/120-PEG-MSN (1.8/1.9 h) 200-MSN/200-PEG-MSN (1.3/1.9 h) 360-MSN/360-PEG-MSN (1.2/1.4 h)	Both Renal (major) and Hepatobiliary	Nontoxic after 1 month	[106]



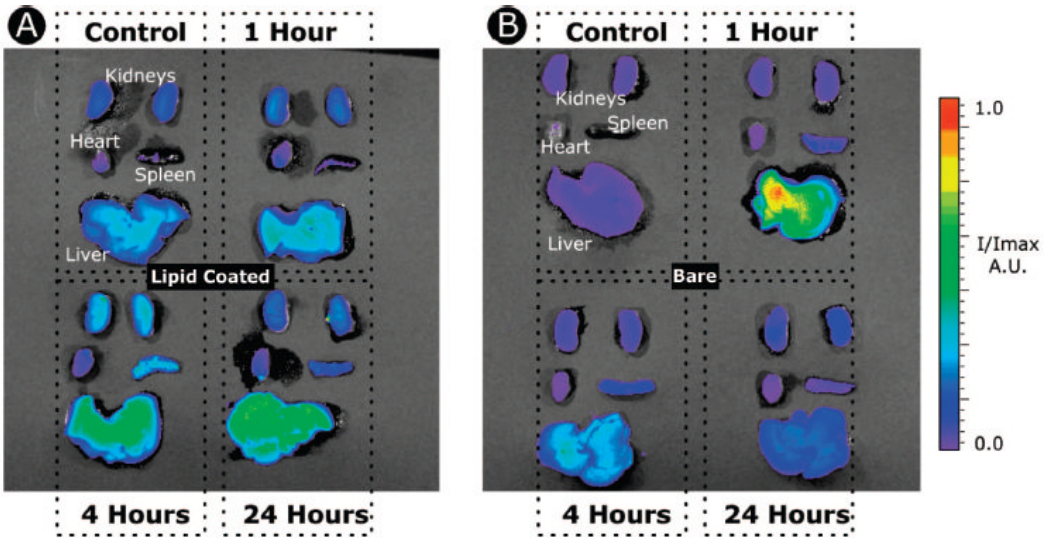
Source: Reproduced with permission from ref. 101.

Figure 5. *In vivo* imaging biodistribution of different i.v. injected surface-modified SiNPs at different time points, postinjection (A-C; (a), abdomen imaging; (b), back imaging). (A) OH-SiNPs; (B) COOH-SiNPs; (C) PEG-SiNPs. Arrows mark the location of the kidney (K), liver (L), and urinary bladder (Ub).

From the previously described outcomes we learnt that SiNPs have a short blood circulation time; however, it can be improved by functionalizing the surface with different groups. Moreover, SiNPs tend to accumulate in liver, spleen, and kidney in a relatively short period of time. Nevertheless, these studies were qualitative and do not provide quantitative information about SiNPs. In addition, although the tissues in which most SiNPs are located in vivo have a clear tendency, time-dependent and quantitative information about the biodistribution of SiNPs in these tissues is lacking. It is necessary to understand how long and how much of SiNPs are retained, as well as why SiNPs accumulate in these tissues. Therefore, monitoring the quantitative biodistribution and analyzing the localization mechanism, will improve our understanding their efficacy and side effects for the biomedical use. Recently, Prasad and coworkers studied quantitatively the biodistribution and PK of organically modified SiNPs (ORMOSIL).[104] They synthesized a 20 nm NIR dye DY776 containing SiNPs, this particle was further functionalized with PEG chains and ^{124}I Bolton-Hunter reagent to afford a bimodal contrast agent with optical and positron emission tomography properties. The authors took advantage of the bimodal features of this system to quantify its biodistribution and PK by both methods NIR fluorescence intensity and radioactivity measurements.

The NIR images showed that DY776-SiNPs accumulate mainly in the liver and spleen (almost 75%) 2h post intravenous injection; on the contrary, less than 5% of material was localized in the lung, kidney, and heart. This data was further corroborated by radioactivity measurements where 58 and 37% ID/g were found in the spleen and liver, respectively. These amounts increased to 61 and 46 %ID/g for spleen and liver after 24h. Similar to the optical measurements, the quantities found in the lung (4.7%) and kidneys (1.22%) were less than 5% ID/g after 24h. In addition, an increase in the fluorescence intensity on stomach and intestine were detected after 120h. This is a clear indication that these particles are taken up by macrophages in the liver and excreted with the fecal matter via the hepatobiliary transport mechanism through the stomach. No particle toxicity was observed in these studies after 15 days of injection. J. Sun and coworkers investigated the long-term (30 days) quantitative tissue distribution, subcellular distribution and potential toxicity of two sizes (20 and 80 nm) of SiNPs administrated by i.v. in mice using radiolabeling.[105]

The results showed that the tissues in which SiNPs mainly accumulated were liver, spleen and lungs. For instance, for the 20-SiNPs 43.3, 48.7, 14.96, 2.38, and 0.62% ID/g were found in the liver, spleen, lungs, bone and kidney, respectively after 1 day post injection. Nevertheless, after 30 days the same tissues showed 16.8, 15.01, 1.95, 0.83 and 0.11% ID/g, respectively. In the case of the 80-SiNPs the distribution pattern was similar to the small particle; however, the amount of SiNPs in these tissues was smaller than the 20-SiNPs. For example, 13.64, 5.89, 26.9, 0.29 and 0.3% ID/g was determined after 1 day post injection. The increased accumulation of 80-SiNPs in the lungscould be related to the aggregation of SiNPs. The retention of SiNPs observed in the liver and spleen after long-term measurements are due to the endocytosis of the particles by the macrophages as was demonstrated by TEM images and histological studies. Finally, the results of toxicology assay indicated an inflammatory response in liver injury occurred after injection of SiNPs, suggesting potential side effects involving the liver.



Source: Reproduced with permission from ref. 102.

Figure 6. Fluorescence imaging of liver, spleen, kidneys, and heart of control mice and mice sacrificed 1, 4, and 24 h postinjection with (A) Lipid-coated SiNPs and (B) Bare-SiNPs. While an immediate uptake of bare silica particles in the liver was observed, the lipid-coated silica particles accumulated gradually over time in the liver which is in agreement with their prolonged circulation half-life value.

As far as we know, the first systematic investigation on the biocompatibility of MSNs *in vivo* was published by R. Langer and co-workers.[107] For this study, the authors selected three different routes of administration; subcutaneous, intraperitoneal, and intravenous. The subcutaneous administration did not show a significant toxicity after long-term investigation on rats (3 months), even though high doses of MSNs were introduced (75 mg/kg). In the case of peritoneal administration, the authors found that the material is lethal to SV129 mice during the first 24h post injection when injecting 1.2 g/kg of material, but reducing the dose to 40 mg/kg or less resulted in significant reduction of the toxicity. The same lethal effect as in the peritoneal injection was observed on the intravenous administration with the high concentration of MSNs (1.2 g/kg). The authors hypothesized that this toxicity may be due to pulmonary embolism and/or thrombosis, however the death mechanism is still under investigation. There was not report of the biodistribution of MSNs in this study. Recently, L.-W. Lo and coworkers studied the biodistribution of MSNs using a near-IR MSN-base probe.[91, 92]Indocyanine green (ICG) was entrapped in MSNs by electrostatic interaction. The optical imaging properties of this system allowed the observation of the biodistribution of ICG-MSN in both anesthetized rat and nude mice models. After i.v. injection the material evidently started to accumulate in the liver and also some mild fluorescent intensity was observed in the spleen, kidney and lungs. To corroborate these observations, inductively coupled plasma-atomic emission spectroscopy (ICP-AES) was practiced to quantitatively analyze the silicon content in major organs such as the liver, spleen, kidney, lungs and heart. The data obtained from the ICP-AES analysis were liver (35.3%), followed by kidney (9.0%), lung (8.3%), spleen (8.0%), and heart (4.5%).

These results were well consistent with the fluorescent visceral group imaging of organs. Following the same line of research, the authors demonstrated that the rate of hepatobiliary excretion of MSNs can be regulated by the surface charge of the nanoparticles. The authors found that a more highly charged nanoparticles (+34.4 mV at pH 7.4) is more quickly excreted from the liver into the intestinal tract, while less charged nanoparticles (-17.6 mV, pH 7.4) remained sequestered into the liver after 3 days of i.v. injection. It is noteworthy to mention that not silica was detected in the urine; a finding consistent with the last reports on the biodistribution of large size SiNPs. Recently, Y. Li, J. Shi and coworkers studied the effect of particle size and PEGylation on the *in vivo* biodistribution and urinary excretion of MSNs.[106] The authors synthesized MSNs with four different sizes (80, 120, 200 and 360 nm) and their respective PEGylated version.

The fluorescence data obtained after different time periods (30 min, 1 day, 5 days and 1 month) showed clearly that MSNs of different particle sizes were mainly located in liver and spleen, a minority of them in lung, and a few in kidney and heart. However, the amount of the corresponding PEG-MSN sample in the same organ was visibly lower as an indication that PEGylation prevented the MSNs from being captured by these tissues. In addition, it was found that the rate of PEG-MSNs clearance from the blood stream is slower than the rate of MSNs of the same particle size. For instance, for the *in vivo* test the blood circulation half-life time in rats for 80-MSNs is around 2.0h and for the PEGylated version is 2.3h; in the case of 120-MSNs is 1.8h and the respective PEG-MSNs is 1.9h; similarly, 200-MSNs has a $t_{1/2}$ in blood of 1.3h and the PEG version is around 1.9h; finally, for 360-MSNs $t_{1/2}$ is 1.2h and the corresponding PEG-MSNs is 1.4h. The toxicity assay indicated that neither MSNs nor PEG-MSNs caused significant tissue toxicity and inflammation during 1 month. Finally, the authors reported on the urinary excretion of degraded MSNs and PEG-MSNs at different time periods; from 30 min, 1 day, 5 days, and 1 month. Interestingly, they found that the excretion of MSNs is time-, size- and surface functionalization-dependent. The maximum amount of silica degradation products were excreted from urine at 30 min for both MSNs and PEG-MSNs; and according to the authors are related to the *in vivo* mean degradation rate of material captured mainly by liver and spleen. It is noteworthy to mention that the excreted quantities remarkable increased with the increase in particle size of MSNs or PEG-MSNs. In addition, the excreted quantities of degradation products of PEG-MSNs were distinctly less than those of the corresponding MSNs.

5. IN VIVO SIMULTANEOUS IMAGING AND DRUG DELIVERY

Despite that MSNs have attracted a great deal of attention, since the beginning of this century, for their potential use in nanomedicine; MSNs' *in vivo* application is still in its infancy, with only few examples in the literature. As far as we know, one of the first applications of MSNs was as human stem cell tracking agent. As was mentioned above, D.-M. Huang and co-workers developed a dual-modal MSNs platform Mag- or Gd-Dye@MSNs with the ability of tracking stem cells by both fluorescence and MR imaging.[97, 98] The authors demonstrated the efficient labeling of hMSCs without any toxicity or effect on cell

viability, growth, or differentiation. In addition, the visualization *in vivo* of the labeled stem cells was successfully carried out in a clinical 1.5T MRI system. It is noteworthy to mention that the labeled cells remained MRI detectable after long-term growth or differentiation, as further evidence of the biocompatibility and durability of this platform. Gd-based MSNs have also been shown to be a highly efficient contrast agent *in vitro* and for intravascular MR imaging.[96] In addition, as it was described in the previous section of this chapter, MSN-based NIR fluorescence agents have been developed to determine the biodistribution, PK and clearance of this platform.[91, 92] However, the first MSN-based "theranostic" system was reported by K. Moon, T. Hyeon and coworkers.[108] They showed the potential of MSN platform for simultaneous MR and fluorescence imaging, and for drug delivery *in vivo*. The authors synthesized a discrete and monodisperse core-shell MSNs consisting of a single iron oxide nanocrystal core and a mesoporous silica shell (IO@MSNs). The size of this material can be easily controlled below 100 nm. Furthermore, for *in vivo* applications the IO@MSNs were functionalize with PEG chains to render them biocompatible by preventing the nonspecific adsorption of proteins.

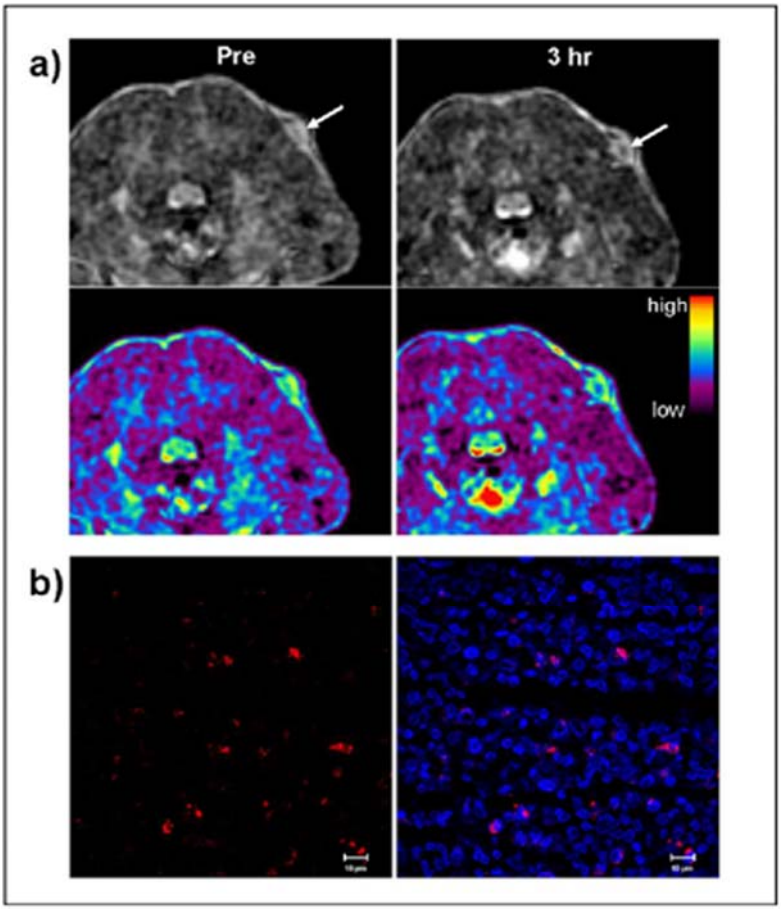
The multimodal imaging capabilities of this platform were applied in MCF-7 breast cancer cells by using fluorescein and rhodamine B as imaging agents to determine the intracellular internalization of this material by CLSM. Moreover, the T_2-weighted properties of IO@MSNs-PEG as MR contrast agent were measured; the r_1 and r_2 relaxivity values of the core-shell system were 3.40 and 245 $mM^{-1}s^{-1}$, respectively. The fluorescent and T_2-weighted MR images of phantoms showed that as the concentration of the nanoparticles was increased; a brighter fluorescence of rhodamine B and a darker T_2 signal were observed. To test the drug delivery properties of IO@MSNs-PEG, doxorubicin (DOX) a well-known anti-cancer agent was loaded and evaluated on SK-BR-3 cell line. The cytotoxicity assay demonstrated the efficacy of this nanovehicle to successfully transport and deliver DOX inside SK-BR-3 cells. The authors investigated the potential for *in vivo* imaging of IO@MSNs-PEG by tracking the nanoparticles' passive accumulation in a breast cancer xenograft model. At 2h after intravenous injection, the accumulation of nanoparticles in tumor was detected by T_2-weighted MR images. The accumulation of IO@MSNs-PEG was further confirmed by fluorescence imaging of tumor and several organs of sacrificed mice 24 h after injection. This paper reported for the first time on the accumulation of intravenously injected MSNs in a tumor site. Inspired by this success the authors published a following paper on the synthesis of dye-doped iron oxide capped MSNs for multimodal imaging and drug delivery applications.[34] In this case, the fluorophore (fluorescein or rhodamine B) was doped in the interior channels and the IO nanoparticles were chemically attached on the exterior surface of MSNs. Similar to the previous study, the nanoparticles were further functionalized with PEG(5K). The T_2-weighted properties of this material were characterized; interestingly, the assembly of multiple IO nanoparticles on MSN resulted in a remarkable enhanced MR contrast (r_2 for free IO nanoparticles 26.8 $mM^{-1}s^{-1}$ and IO-MSN 76.2 $mM^{-1}s^{-1}$). To corroborate the *in vitro* multimodal imaging, fluorescence and T_2 weighted MR images of IO-MSN labeled cell phantom were acquired.

As the concentration of IO-MSN was increased during the incubation, the rhodamine B fluorescence signal was clearly enhanced and the T_2 weighted MR image was darkened. This demonstrated that IO-MSN can be used as probe for simultaneous T_2 MR and optical

fluorescence imaging. To examine drug delivery, the chemotherapeutic agent DOX was loaded into IO-MSNs. The antitumor efficacy of DOX loaded IO-MSN was successfully tested using the B16-F10 melanoma cell line. The platform was evaluated *in vivo* by injecting it intravenously into a nude mouse bearing a tumor on its shoulder. At 3h after injection, a drop in the MR signal was detected at the tumor site, demonstrating passive targeting of IO-MSNs caused by the EPR effect. The accumulation of the material on the tumor site was confirmed by fluorescence imaging on sections of the tumor tissue (Figure 7). Delivery of drug to tumor tissue was demonstrated by direct visualization with CLSM of red fluorescence emitted by DOX accumulation at the tumor site of mice treated with DOX loaded IO-MSNs. The antitumor activity was corroborated using TUNEL assay (Figure 8). These results showed that DOX was delivered to the tumor site successfully and its antitumor activity was retained.

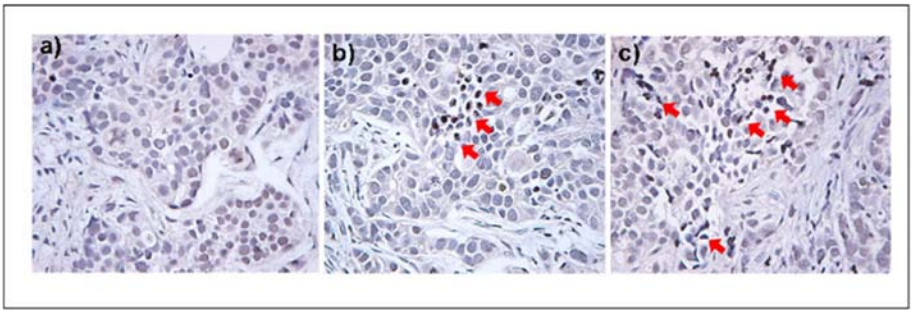
This report proved for the first time that MSNs can indeed deliver and release a chemotherapeutic agent to solid tumors in animals through EPR effect. Recently, F. Tamanoi and coworkers published a thorough investigation on the toxicity, biodistribution, PK and therapeutic properties of MSNs.[109] The authors studied the short-term toxicity using different concentrations of MSNs (3, 6, 12.5, 25, 50 mg/Kg) for 14 days (five doses) and the long-term toxicity using a fixed concentration of 50 mg/Kg for two months (18 doses). In both experiments, no infection, impaired mobility, or reduced food taking was observed. No obvious histological lesion with any of the tissues, neither gross nor pathological abnormality, was observed in major organs, such as the liver, spleen, kidney, heart, intestine, stomach, muscle, or lungs. The authors studied the biodistribution and excretion of MSNs by fluorescence imaging (fluorescein) and ICP-OES, respectively. The fluorescence intensity of the MSNs in tumors was much stronger than that from the other tissues at 4 and 24h. The next strongest fluorescence intensities were found in the kidney and liver. Interestingly, after quantitatively analyzing the amount of Si excreted from the animal body the authors found out that the material is cleared through both renal and hepatobiliary pathways. Within the first 24h after injection, 26.3% of the injected Si was detected in urine.

The renal excretions were decreasing with the following days (23.2% for the 2nd day, 13.2% for the 3rd day, and 10.6% for the 4th day). On the contrary, in the feces, the excretion increases with the highest amount of Si being detected on the 4th day (1.98, 5.18, 5.86, and 7.96% for the 1st, 2nd, 3rd, and 4th days, respectively). The authors tested the therapeutic effects of MSNs loaded with camptothecin (CPT) as chemotherapeutic on human breast cancer cells, SK-BR-3 and MCF-7, and a breast fibroblast, MCF10F. In addition, to enhance MSNs' tumor accumulation, the material was further functionalized with folic acid (F-MSNs), which specifically binds to folate receptors that is up-regulated in various types of human cancers. The cytotoxicity assays demonstrated that both MSNs and F-MSNs are capable of delivering CPT into cells and exert cell-killing effects. Moreover, F-MSNs showed a target-specific performance toward SK-BR-3 in comparison to MCF10F, which is a further indication of the targeting to folate-receptors. Finally, the CPT-loaded MSNs and CPT-loaded F-MSNs were tested in nude mice with established xenografts of human breast cancer cell MCF-7. The tumors in the mice treated with these materials were virtually eliminated at the end of the experiments. These results proved that the high drug-loading ability, low toxicity, and tumor accumulating effect of MSNs provide a promising drug-delivery vehicle for anticancer drugs. In this paper, the authors demonstrated for the first time, that MSNs are effective vehicles for antitumor drug delivery.



Source: Reproduced with permission from ref. 34.

Figure 7.In vivo accumulation of iron oxide MSN at tumor site. (a) In vivo T2-weighted MR images (upper) and color mapped (lower) images of tumor site before and 3 h after i.v. injection of iron oxide IO-MSN (arrows indicate tumor site). (b) CLSM of sectioned tumor tissue harvested 24h after injection. Left; red fluorescence showing IO-MSN internalized cells. Right; Merged image with DAPI stained nuclei (blue).



Source: Reproduced with permission from ref. 34.

Figure 8.TUNEL assay for apoptotic cell death. Tumor section from mouse that was given i.v.inhection of (a) free IO-MSN, (b) DOX loaded IO-MSN (DOX 2mg/Kg), and (c) DOX loaded IO-MSN (DOX 4 mg/Kg). Arrows indicate examples of TUNEL-positive (brown color) cells with apoptotic morphology. The mice were sacrificed 48 h after injection.

CONCLUSION

In summary, we have highlightedthe latest research breakthroughs on the design of stimuli-responsive mesoporous silica nanoparticles. Recent developments on biomolecular caps such as DNA and control remote systems have provide even higher degrees of specificity and control in drug delivery by capped MSN. Although there is now a large number of release strategies available, the field remains open for the development of even more effective stimuli to expand the diversity of triggers for controlled release by MSN nanocarriers. However, significant challenges remain, as the controlled release properties and efficiency of many of the existing stimuli-responsive MSN systems are yet to be tested *in vivo*. The capability of MSN platform as single- and multimodal contrast agent has been successfully shown *in vitro* and *in vivo*. Two modalities, optical and magnetic resonance imaging have been the focus of the pioneering research in this area; however, it is envisioned that more modalities could be incorporated to MSN material in the near future. Moreover, these multimodal mesoporous agents have been an excellent tool for the current investigation on the biodistribution and pharmacokinetics of MSNs. Despite the high potential of silica-based nanoparticles for biomedical applications, little had been reported in the literature related to the biocompatibility, pharmacokinetics, and biodistribution *in vivo* of these nanomaterials. Nevertheless, in the past three years some reports have been published where it is described some of their PK and biodistribution features. For example, it was shown that both SiNPs and MSNs after intravenous injection have an ephemeral blood circulation time; however, this parameter can be increased by coating the nanoparticles with different functional groups (PEG and phospholipids). In addition, according to recent investigations these materials follow the two main routes of excretion, renal and hepatobiliary. There are still some discrepancies regarding to which of these excretion mechanism is more important to eliminate silica-based particles from the organism. Certainly, the degradation of SiNPs and MSNs has to be taken in account and more systematic studies need to be done to fully understand the pharmacokinetics of these materials. On the other hand, it is very exciting to witness the first report on the theranostic application of MSNs in mice.[109] This recent report indeed confirms the potential of MSNs as imaging and drug delivery platform for diagnosis and therapeutic applications *in vivo*. Additional work is required to fully prove the therapeutic efficacy, target ability and diagnostic capabilities of MSNs in biological systems. As more PK, biodistribution and drug delivery data become available, it is foreseen that these multifunctional MSN platforms will play a significant role in clinical and other biomedical and biotechnological applications.

ACKNOWLEDGMENTS

Dr. Juan L. Vivero-Escoto acknowledges the Carolina Postdoctoral Program for Faculty Diversity for financial support.

REVIEWED BY

Prof. Kevin C.-W.Wu, Department of Chemical Engineering, National Taiwan University, Taiwan.

REFERENCES

[1] Ferrari M: Cancer nanotechnology: opportunities and challenges. *Nature Reviews Cancer* 2005, 5(3):161-171.

[2] Petros RA, De Simone JM: Strategies in the design of nanoparticles for therapeutic applications.*Nature Reviews Drug Discovery* 2010, 9(8):615-627.

[3] Davis ME, Chen Z, Shin DM: Nanoparticle therapeutics: an emerging treatment modality for cancer. *Nature Reviews Drug Discovery* 2008, 7(9):771-782.

[4] Kim J, Piao Y, Hyeon T: Multifunctional nanostructured materials for multimodal imaging, and simultaneous imaging and therapy. *Chemical Society Reviews* 2009, 38(2):372-390.

[5] Li S-D, Huang L: Pharmacokinetics and Biodistribution of Nanoparticles. *Molecular Pharmaceutics* 2008, 5(4):496-504.

[6] Alexis F, Pridgen E, Molnar LK, Farokhzad OC: Factors Affecting the Clearance and Biodistribution of Polymeric Nanoparticles. *Molecular Pharmaceutics* 2008, 5(4):505-515.

[7] Torchilin VP: Recent advances with liposomes as pharmaceutical carriers. *Nature Reviews Drug Discovery* 2005, 4(2):145-160.

[8] Mulder WJM, Strijkers GJ, van Tilborg GAF, Cormode DP, Fayad ZA, Nicolay K: Nanoparticulate Assemblies of Amphiphiles and Diagnostically Active Materials for Multimodality Imaging. *Accounts of Chemical Research* 2009, 42(7):904-914.

[9] Haag R, Kratz F: Polymer therapeutics: concepts and applications. *Angewandte Chemie, International Edition* 2006, 45(8):1198-1215.

[10] Nayak S, Lyon LA: Soft nanotechnology with soft nanoparticles. *Angewandte Chemie, International Edition* 2005, 44(47):7686-7708.

[11] Gao D, Xu H, Philbert MA, Kopelman R: Ultrafine hydrogel nanoparticles: synthetic approach and therapeutic application in living cells. *Angewandte Chemie, International Edition* 2007, 46(13):2224-2227.

[12] Smith AM, Duan H, Mohs AM, Nie S: Bioconjugated quantum dots for in vivo molecular and cellular imaging. *Adv Drug Delivery Rev* 2008, 60(11):1226-1240.

[13] Sun C, Lee Jerry SH, Zhang M: Magnetic nanoparticles in MR imaging and drug delivery. *Adv Drug Deliv Rev* 2008, 60(11):1252-1265.

[14] Lin W, Hyeon T, Lanza GM, Zhang M, Meade TJ: Magnetic nanoparticles for early detection of cancer by magnetic resonance imaging. *MRS Bulletin* 2009, 34(6):441-448.

[15] Ghosh P, Han G, De M, Kim CK, Rotello VM: Gold nanoparticles in delivery applications. *Adv Drug Delivery Rev* 2008, 60(11):1307-1315.

[16] Cobley CM, Au L, Chen J-Y, Xia Y-N: Targeting gold nanocages to cancer cells for photothermal destruction and drug delivery. *Expert Opinion on Drug Delivery* 2010, 7(5):577-587.

[17] Jain PK, Huang X, El-Sayed IH, El-Sayed MA: Noble Metals on the Nanoscale: Optical and Photothermal Properties and Some Applications in Imaging, Sensing, Biology, and Medicine. *Accounts of Chemical Research* 2008, 41(12):1578-1586.

[18] Lal S, Clare SE, Halas NJ: Nanoshell-Enabled Photothermal Cancer Therapy: Impending Clinical Impact. *Accounts of Chemical Research* 2008, 41(12):1842-1851.

[19] Vivero-Escoto JL, Trewyn BG, Lin VSY: Mesoporous silica nanoparticles: synthesis and applications. *Annual Review of Nano Research* 2010, 3:191-231.
[20] Slowing II, Vivero-Escoto JL, Trewyn BG, Lin VSY: Mesoporous silica nanoparticles: Structural design and applications. *Journal of Materials Chemistry* 2010, 20(37):7924-7937.
[21] Coti KK, Belowich ME, Liong M, Ambrogio MW, Lau YA, Khatib HA, Zink JI, Khashab NM, Stoddart JF: Mechanised nanoparticles for drug delivery. *Nanoscale* 2009, 1(1):16-39.
[22] Hom C, Lu J, Tamanoi F: Silica nanoparticles as a delivery system for nucleic acid-based reagents. *Journal of Materials Chemistry* 2009, 19(35):6308-6316.
[23] Rosenholm J, Sahlgren C, Linden M: Cancer-cell targeting and cell-specific delivery by mesoporous silica nanoparticles. *Journal of Materials Chemistry* 2010, 20(14):2707-2713.
[24] Slowing II, Vivero-Escoto JL, Wu C-W, Lin VSY: Mesoporous silica nanoparticles as controlled release drug delivery and gene transfection carriers. *Adv Drug Delivery Rev* 2008, 60(11):1278-1288.
[25] Trewyn BG, Slowing II, Giri S, Chen H-T, Lin VSY: Synthesis and Functionalization of a Mesoporous Silica Nanoparticle Based on the Sol-Gel Process and Applications in Controlled Release. *Accounts of Chemical Research* 2007, 40(9):846-853.
[26] Vivero-Escoto JL, Slowing II, Lin VSY: Tuning the cellular uptake and cytotoxicity properties of oligonucleotide intercalator-functionalized mesoporous silica nanoparticles with human cervical cancer cells HeLa. *Biomaterials* 2010, 31(6):1325-1333.
[27] Vivero-Escoto JL, Slowing II, Trewyn BG, Lin VSY: Mesoporous Silica Nanoparticles for Intracellular Controlled Drug Delivery. *Small* 2010, 6(18):1952-1967.
[28] Vallet-Regi M, Ramila A, del Real RP, Perez-Pariente J: A New Property of MCM-41: Drug Delivery System. *Chemistry of Materials* 2001, 13(2):308-311.
[29] Lai C-Y, Trewyn BG, Jeftinija DM, Jeftinija K, Xu S, Jeftinija S, Lin VSY: A mesoporous silica nanosphere-based carrier system with chemically removable CdS nanoparticle caps for stimuli-responsive controlled release of neurotransmitters and drug molecules. *Journal of the American Chemical Society* 2003, 125(15):4451-4459.
[30] Torney F, Trewyn BG, Lin VSY, Wang K: Mesoporous silica nanoparticles deliver DNA and chemicals into plants. *Nat Nanotechnol* 2007, 2(5):295-300.
[31] Vivero-Escoto JL, Slowing II, Wu C-W, Lin VSY: Photoinduced Intracellular Controlled Release Drug Delivery in Human Cells by Gold-Capped Mesoporous Silica Nanosphere. *Journal of the American Chemical Society* 2009, 131(10):3462-3463.
[32] Liu R, Zhang Y, Zhao X, Agarwal A, Mueller LJ, Feng P: pH-Responsive Nanogated Ensemble Based on Gold-Capped Mesoporous Silica through an Acid-Labile Acetal Linker. *Journal of the American Chemical Society* 2010, 132(5):1500-1501.
[33] Giri S, Trewyn BG, Stellmaker MP, Lin VSY: Stimuli-responsive controlled-release delivery system based on mesoporous silica nanorods capped with magnetic nanoparticles. *Angewandte Chemie, International Edition* 2005, 44(32):5038-5044.
[34] Lee JE, Lee N, Kim H, Kim J, Choi SH, Kim JH, Kim T, Song IC, Park SP, Moon WK *et al*: Uniform Mesoporous Dye-Doped Silica Nanoparticles Decorated with Multiple Magnetite Nanocrystals for Simultaneous Enhanced Magnetic Resonance Imaging,

Fluorescence Imaging, and Drug Delivery. *Journal of the American Chemical Society* 2010, 132(2):552-557.

[35] Radu DR, Lai C-Y, Jeftinija K, Rowe EW, Jeftinija S, Lin VSY: A Polyamidoamine Dendrimer-Capped Mesoporous Silica Nanosphere-Based Gene Transfection Reagent. *Journal of the American Chemical Society* 2004, 126(41):13216-13217.

[36] Zhao Y, Trewyn BG, Slowing II, Lin VSY: Mesoporous Silica Nanoparticle-Based Double Drug Delivery System for Glucose-Responsive Controlled Release of Insulin and Cyclic AMP. *Journal of the American Chemical Society* 2009, 131(24):8398-8400.

[37] Radu DR, Lai C-Y, Wiench JW, Pruski M, Lin VSY: Gatekeeping Layer Effect: A Poly(lactic acid)-coated Mesoporous Silica Nanosphere-Based Fluorescence Probe for Detection of Amino-Containing Neurotransmitters. *Journal of the American Chemical Society* 2004, 126(6):1640-1641.

[38] Liu R, Zhao X, Wu T, Feng P: Tunable Redox-Responsive Hybrid Nanogated Ensembles. *Journal of the American Chemical Society* 2008, 130(44):14418-14419.

[39] Liu R, Zhang Y, Feng P: Multiresponsive Supramolecular Nanogated Ensembles. *Journal of the American Chemical Society* 2009, 131(42):15128-15129.

[40] Slowing II, Trewyn BG, Lin VSY: Mesoporous Silica Nanoparticles for Intracellular Delivery of Membrane-Impermeable Proteins. *Journal of the American Chemical Society* 2007, 129(28):8845-8849.

[41] Lu J, Liong M, Zink JI, Tammanoi F: Mesoporous silica nanoparticles as a delivery system for hydrophobic anticancer drugs. *Small* 2007, 3(8):1341-1346.

[42] Lu J, Choi E, Tamanoi F, Zink JI: Light-activated nanoimpeller-controlled drug release in cancer cells. *Small* 2008, 4(4):421-426.

[43] Lu J, Liong M, Sherman S, Xia T, Kovochich M, Nel AE, Zink JI, Tamanoi F: Mesoporous silica nanoparticles for cancer therapy: energy-dependent cellular uptake and delivery of paclitaxel to cancer cells. *NanoBiotechnology* 2007, 3(2):89-95.

[44] Lebold T, Jung C, Michaelis J, Braeuchle C: Nanostructured Silica Materials As Drug-Delivery Systems for Doxorubicin: Single Molecule and Cellular Studies. *Nano Letters* 2009, 9(8):2877-2883.

[45] Rosenholm JM, Peuhu E, Eriksson JE, Sahlgren C, Linden M: Targeted Intracellular Delivery of Hydrophobic Agents using Mesoporous Hybrid Silica Nanoparticles as Carrier Systems. *Nano Letters* 2009, 9(9):3308-3311.

[46] Slowing II, Trewyn BG, Giri S, Lin VSY: Mesoporous silica nanoparticles for drug delivery and biosensing applications. *Adv Funct Mater* 2007, 17(8):1225-1236.

[47] Ambrogio MW, Pecorelli TA, Patel K, Khashab NM, Trabolsi A, Khatib HA, Botros YY, Zink JI, Stoddart JF: Snap-Top Nanocarriers. *Organic Letters* 2010, 12(15):3304-3307.

[48] Zhao Y, Vivero-Escoto JL, Slowing II, Trewyn BG, Lin VSY: Capped mesoporous silica nanoparticles as stimuli-responsive controlled release systems for intracellular drug/gene delivery. *Expert Opinion on Drug Delivery* 2010, 7(9):1013-1029.

[49] Yang Q, Wang S, Fan P, Wang L, Di Y, Lin K, Xiao F-S: pH-Responsive Carrier System Based on Carboxylic Acid Modified Mesoporous Silica and Polyelectrolyte for Drug Delivery. *Chemistry of Materials* 2005, 17(24):5999-6003.

[50] Park C, Oh K, Lee SC, Kim C: Controlled release of guest molecules from mesoporous silica particles based on a pH-responsive polypseudorotaxane motif. *Angewandte Chemie, International Edition* 2007, 46(9):1455-1457.

[51] Angelos S, Khashab NM, Yang Y-W, Trabolsi A, Khatib HA, Stoddart JF, Zink JI: pH Clock-Operated Mechanized Nanoparticles. *Journal of the American Chemical Society* 2009, 131(36):12912-12914.

[52] Khashab NM, Belowich ME, Trabolsi A, Friedman DC, Valente C, Lau Y, Khatib HA, Zink JI, Stoddart JF: pH-Responsive mechanised nanoparticles gated by semirotaxanes. *Chemical Communications* 2009(36):5371-5373.

[53] Aznar E, Marcos MD, Martinez-Manez R, Sancenon F, Soto J, Amoros P, Guillem C: pH- and Photo-Switched Release of Guest Molecules from Mesoporous Silica Supports. *Journal of the American Chemical Society* 2009, 131(19):6833-6843.

[54] Gao C, Zheng H, Xing L, Shu M, Che S: Designable Coordination Bonding in Mesopores as a pH-Responsive Release System. *Chemistry of Materials* 2010, 22(19):5437-5444.

[55] Lee C-H, Cheng S-H, Huang IP, Souris JS, Yang C-S, Mou C-Y, Lo L-W: Intracellular pH-Responsive Mesoporous Silica Nanoparticles for the Controlled Release of Anticancer Chemotherapeutics. *Angewandte Chemie, International Edition* 2010, 49(44):8214-8219.

[56] Gruenhagen JA, Lai C-Y, Radu DR, Lin VSY, Yeung ES: Real-time imaging of tunable adenosine 5-triphosphate release from an MCM-41-type mesoporous silica nanosphere-based delivery system. *Appl Spectrosc* 2005, 59(4):424-431.

[57] Zhu C-L, Song X-Y, Zhou W-H, Yang H-H, Wen Y-H, Wang X-R: An efficient cell-targeting and intracellular controlled-release drug delivery system based on mesoporous silica nanoparticle-polyelectrolyte multilayer-aptamer conjugates. *Journal of Materials Chemistry* 2009, 19(41):7765-7770.

[58] Luo Z, Cai K, Hu Y, Zhao L, Liu P, Duan L, Yang W: Mesoporous Silica Nanoparticles End-Capped with Collagen: Redox-Responsive Nanoreservoirs for Targeted Drug Delivery. *Angew Chem Int Ed* 2011, 50(3):640-643.

[59] Patel K, Angelos S, Dichtel WR, Coskun A, Yang Y-W, Zink JI, Stoddart JF: Enzyme-Responsive Snap-Top Covered Silica Nanocontainers. *Journal of the American Chemical Society* 2008, 130(8):2382-2383.

[60] Bernardos A, Aznar E, Marcos MD, Martinez-Manez R, Sancenon F, Soto J, Barat JM, Amoros P: Enzyme-Responsive Controlled Release Using Mesoporous Silica Supports Capped with Lactose. *Angewandte Chemie, International Edition* 2009, 48(32):5884-5887.

[61] Schlossbauer A, Kecht J, Bein T: Biotin-Avidin as a Protease-Responsive Cap System for Controlled Guest Release from Colloidal Mesoporous Silica. *Angewandte Chemie, International Edition* 2009, 48(17):3092-3095.

[62] Climent E, Bernardos A, Martinez-Manez R, Maquieira A, Marcos MD, Pastor-Navarro N, Puchades R, Sancenon F, Soto J, Amoros P: Controlled Delivery Systems Using Antibody-Capped Mesoporous Nanocontainers. *Journal of the American Chemical Society* 2009, 131(39):14075-14080.

[63] Chen C, Geng J, Pu F, Yang X, Ren J, Qu X: Polyvalent Nucleic Acid/Mesoporous Silica Nanoparticle Conjugates: Dual Stimuli-Responsive Vehicles for Intracellular Drug Delivery. *Angew Chem Int Ed* 2011, anie.201005471.

[64] Climent E, Martinez-Manez R, Sancenon F, Marcos MD, Soto J, Maquieira A, Amoros P: Controlled delivery using oligonucleotide-capped mesoporous silica nanoparticles. *Angewandte Chemie, International Edition* 2010, 49(40):7281-7283.

[65] Schlossbauer A, Warncke S, Gramlich PME, Kecht J, Manetto A, Carell T, Bein T: A Programmable DNA-Based Molecular Valve for Colloidal Mesoporous Silica. *Angewandte Chemie, International Edition* 2010, 49(28):4734-4737.

[66] Park C, Lee K, Kim C: Photoresponsive cyclodextrin-covered nanocontainers and their sol-gel transition induced by molecular recognition. *Angewandte Chemie, International Edition* 2009, 48(7):1275-1278.

[67] Ferris Daniel P, Zhao Y-L, Khashab Niveen M, Khatib Hussam A, Stoddart JF, Zink Jeffrey I: Light-operated mechanized nanoparticles. *J Am Chem Soc* 2009, 131(5):1686-1688.

[68] Lin Q, Huang Q, Li C, Bao C, Liu Z, Li F, Zhu L: Anticancer Drug Release from a Mesoporous Silica Based Nanophotocage Regulated by Either a One- or Two-Photon Process. *Journal of the American Chemical Society* 2010, 132(31):10645-10647.

[69] Thomas CR, Ferris DP, Lee J-H, Choi E, Cho MH, Kim ES, Stoddart JF, Shin J-S, Cheon J, Zink JI: Noninvasive Remote-Controlled Release of Drug Molecules in Vitro Using Magnetic Actuation of Mechanized Nanoparticles. *Journal of the American Chemical Society* 2010, 132(31):10623-10625.

[70] Kwon EJ, Lee TG: Surface-modified mesoporous silica with ferrocene derivatives and its ultrasound-triggered functionality. *Applied Surface Science* 2008, 254(15):4732-4737.

[71] Gerweck LE, Seetharaman K: Cellular pH gradient in tumor versus normal tissue: potential exploitation for the treatment of cancer. *Cancer Research* 1996, 56(6):1194-1198.

[72] Garnett MC: Targeted drug conjugates: principles and progress. *Adv Drug Delivery Rev* 2001, 53(2):171-216.

[73] Ou M, Wang X-L, Xu R, Chang C-W, Bull DA, Kim SW: Novel Biodegradable Poly(disulfide amine)s for Gene Delivery with High Efficiency and Low Cytotoxicity. *Bioconjugate Chemistry* 2008, 19(3):626-633.

[74] Bauhuber S, Hozsa C, Breunig M, Goepferich A: Delivery of Nucleic Acids via Disulfide-Based Carrier Systems. *Advanced Materials* 2009, 21(32-33):3286-3306.

[75] Saito G, Swanson JA, Lee K-D: Drug delivery strategy utilizing conjugation via reversible disulfide linkages: role and site of cellular reducing activities. *Adv Drug Delivery Rev* 2003, 55(2):199-215.

[76] Mortera R, Vivero-Escoto J, Slowing II, Garrone E, Onida B, Lin VSY: Cell-induced intracellular controlled release of membrane impermeable cysteine from a mesoporous silica nanoparticle-based drug delivery system. *Chem Commun* 2009(22):3219-3221.

[77] Kim H, Kim S, Park C, Lee H, Park HJ, Kim C: Glutathione-Induced Intracellular Release of Guests from Mesoporous Silica Nanocontainers with Cyclodextrin Gatekeepers. *Advanced Materials*2010, 22(38):4280-4283.

[78] Park C, Kim H, Kim S, Kim C: Enzyme Responsive Nanocontainers with Cyclodextrin Gatekeepers and Synergistic Effects in Release of Guests. *Journal of the American Chemical Society* 2009, 131(46):16614-16615.

[79] Li Z-B, Cai W, Chen X: Semiconductor quantum dots for in vivo imaging. *Journal of Nanoscience and Nanotechnology* 2007, 7(8):2567-2581.

[80] Banerjee R, Katsenovich Y, Lagos L, McIintosh M, Zhang X, Li CZ: Nanomedicine: magnetic nanoparticles and their biomedical applications. *Current Medicinal Chemistry* 2010, 17(27):3120-3141.

[81] Cheon J, Lee J-H: Synergistically Integrated Nanoparticles as Multimodal Probes for Nanobiotechnology. *Accounts of Chemical Research* 2008, 41(12):1630-1640.
[82] Weissleder R: Molecular Imaging in Cancer. *Science* 2006, 312(5777):1168-1171.
[83] Weissleder R, Cheng HC, Bogdanova A, Bogdanov A, Jr.: Magnetically labeled cells can be detected by MR imaging. *J Magn Reson Imaging* 1997, 7(1):258-263.
[84] Bulte JWM, Douglas T, Witwer B, Zhang S-C, Strable E, Lewis BK, Zywicke H, Miller B, van Gelderen P, Moskowitz BM *et al*: Magnetodendrimers allow endosomal magnetic labeling and in vivo tracking of stem cells. *Nat Biotechnol* 2001, 19(12):1141-1147.
[85] Cao YC, Jin R, Mirkin CA: Nanoparticles with Raman spectroscopic fingerprints for DNA and RNA detection. *Science* 2002, 297(5586):1536-1540.
[86] Elghanian R, Storhoff JJ, Mucic RC, Letsinger RL, Mirkin CA: Selective colorimetric detection of polynucleotides based on the distance-dependent optical properties of gold nanoparticles. *Science* 1997, 277(5329):1078-1080.
[87] Michalet X, Pinaud FF, Bentolila LA, Tsay JM, Doose S, Li JJ, Sundaresan G, Wu AM, Gambhir SS, Weiss S: Quantum Dots for Live Cells, in Vivo Imaging, and Diagnostics. *Science* 2005, 307(5709):538-544.
[88] Laurent S, Forge D, Port M, Roch A, Robic C, Vander Elst L, Muller RN: Magnetic Iron Oxide Nanoparticles: Synthesis, Stabilization, Vectorization, Physicochemical Characterizations, and Biological Applications. *Chem Rev* 2008, 108(6):2064-2110.
[89] Medintz IL, Uyeda HT, Goldman ER, Mattoussi H: Quantum dot bioconjugates for imaging, labelling and sensing. *Nat Mater* 2005, 4(6):435-446.
[90] Jun Y-w, Seo J-w, Cheon J: Nanoscaling Laws of Magnetic Nanoparticles and Their Applicabilities in Biomedical Sciences. *Accounts of Chemical Research* 2008, 41(2):179-189.
[91] Lee C-H, Cheng S-H, Wang Y-J, Chen Y-C, Chen N-T, Souris J, Chen C-T, Mou C-Y, Yang C-S, Lo L-W: Near-infrared mesoporous silica nanoparticles for optical imaging: characterization and in vivo biodistribution. *Adv Funct Mater* 2009, 19(2):215-222.
[92] Souris JS, Lee C-H, Cheng S-H, Chen C-T, Yang C-S, Ho J-aA, Mou C-Y, Lo L-W: Surface charge-mediated rapid hepatobiliary excretion of mesoporous silica nanoparticles. *Biomaterials* 2010, 31(21):5564-5574.
[93] Na HB, Song IC, Hyeon T: Inorganic Nanoparticles for MRI Contrast Agents. *Advanced Materials*2009, 21(21):2133-2148.
[94] Villaraza AJL, Bumb A, Brechbiel MW: Macromolecules, Dendrimers, and Nanomaterials in Magnetic Resonance Imaging: The Interplay between Size, Function, and Pharmacokinetics. *Chemical Reviews* 2010, 110(5):2921-2959.
[95] Na HB, Hyeon T: Nanostructured T1 MRI contrast agents. *Journal of Materials Chemistry* 2009, 19(35):6267-6273.
[96] Taylor KML, Kim JS, Rieter WJ, An H, Lin W, Lin W: Mesoporous Silica Nanospheres as Highly Efficient MRI Contrast Agents. *Journal of the American Chemical Society* 2008, 130(7):2154-2155.
[97] Hsiao J-K, Tsai C-P, Chung T-H, Hung Y, Yao M, Liu H-M, Mou C-Y, Yang C-S, Chen Y-C, Huang D-M: Mesoporous silica nanoparticles as a delivery system of gadolinium for effective human stem cell tracking. *Small* 2008, 4(9):1445-1452.

[98] Liu H-M, Wu S-H, Lu C-W, Yao M, Hsiao J-K, Hung Y, Lin Y-S, Mou C-Y, Yang C-S, Huang D-M *et al*: Mesoporous silica nanoparticles improve magnetic labeling efficiency in human stem cells. *Small* 2008, 4(5):619-626.

[99] Carniato F, Tei L, Cossi M, Marchese L, Botta M: A Chemical Strategy for the Relaxivity Enhancement of GdIII Chelates Anchored on Mesoporous Silica Nanoparticles. *Chemistry--A European Journal* 2010, 16(35):10727-10734.

[100] Steinbacher JL, Lathrop SA, Cheng K, Hillegass JM, Butnor KJ, Kauppinen RA, Mossman BT, Landry CC: Gd-Labeled Microparticles in MRI: in vivo Imaging of Microparticles After Intraperitoneal Injection. *Small* 2010, 6(23):2678-2682.

[101] He X, Nie H, Wang K, Tan W, Wu X, Zhang P: In Vivo Study of Biodistribution and Urinary Excretion of Surface-Modified Silica Nanoparticles. *Anal Chem* 2008, 80(24):9597-9603.

[102] van Schooneveld MM, Vucic E, Koole R, Zhou Y, Stocks J, Cormode DP, Tang CY, Gordon RE, Nicolay K, Meijerink A *et al*: Improved Biocompatibility and Pharmacokinetics of Silica Nanoparticles by Means of a Lipid Coating: A Multimodality Investigation. *Nano Letters* 2008, 8(8):2517-2525.

[103] Cho M, Cho W-S, Choi M, Kim SJ, Han BS, Kim SH, Kim HO, Sheen YY, Jeong J: The impact of size on tissue distribution and elimination by single intravenous injection of silica nanoparticles. *Toxicology Letters* 2009, 189(3):177-183.

[104] Kumar R, Roy I, Ohulchanskky TY, Vathy LA, Bergey EJ, Sajjad M, Prasad PN: In Vivo Biodistribution and Clearance Studies Using Multimodal Organically Modified Silica Nanoparticles. *ACS Nano* 2010, 4(2):699-708.

[105] Xie G, Sun J, Zhong G, Shi L, Zhang D: Biodistribution and toxicity of intravenously administered silica nanoparticles in mice. *Archives of Toxicology* 2010, 84(3):183-190.

[106] He Q, Zhang Z, Gao F, Li Y, Shi J: In vivo Biodistribution and Urinary Excretion of Mesoporous Silica Nanoparticles: Effects of Particle Size and PEGylation. *Small* 2011, 7(2):271-280.

[107] Hudson SP, Padera RF, Langer R, Kohane DS: The biocompatibility of mesoporous silicates. *Biomaterials* 2008, 29(30):4045-4055.

[108] Kim J, Kim HS, Lee N, Kim T, Kim H, Yu T, Song IC, Moon WK, Hyeon T: Multifunctional uniform nanoparticles composed of a magnetite nanocrystal core and a mesoporous silica shell for magnetic resonance and fluorescence imaging and for drug delivery. *Angewandte Chemie, International Edition* 2008, 47(44):8438-8441.

[109] Lu J, Liong M, Li Z, Zink JI, Tamanoi F: Biocompatibility, Biodistribution, and Drug-Delivery Efficiency of Mesoporous Silica Nanoparticles for Cancer Therapy in Animals. *Small* 2010, 6(16):1794-1805.

In: Silica Nanoparticles
Editor: Juan Vivero-Escoto
ISBN 978-1-61324-452-4
© 2012 Nova Science Publishers, Inc.

Chapter 4

MESOPOROUS SILICA NANOPARTICLES AS A DRUG DELIVERY SYSTEM

Dennis Douroumis[1,*], Ichioma Onyesom[1], Mohammed Maniruzzaman[1] and Mark Edwards[1]
[1]University of Greenwich, School of Science, Medway Campus,
Chatham Maritime, ME4 4TB, Kent, UK

ABSTRACT

During the last decade a substantial progress in utilizing mesoporous silica nanoparticles (MSNs) has taken place. These nanosized inorganic materials can be synthesized to act as imaging, targeting and drug delivery systems. The surface area and the pore size can be tailored to selectively encapsulate the desired molecules, the shape and the size can be tuned to enhance cellular uptake, while the surface can be functionalized for active targeting. In the current chapter we discuss the MSNs preparation methods, uses and biological applications both *in vit*ro and *in vivo*.

1. INTRODUCTION

The history of mesoporous silica nanoparticles (MSNs) dates back to nineties when MSNs were firstly synthesized by Mobil researchers and were called Mobil crystalline materials (MCM) (Beck et al. 1992, Kresge et el. 1992) with the two most studied MSNs being MCM-41 and MCM-48 which belong to the M41S family. Ever since, MSNs have drawn a lot of attention due to their pore properties (Vallet-Regi et al. 2007; Che et al. 2003) and medical applications in various fields such as controlled drug release, imaging, cancer treatment, biosensors and gate-keeping (Slowing et al. 2008). IUPAC rules classify porous

[*]Corresponding Author: Dennis Douroumis,
School of Science, Department of Pharmaceutical,
Chemical and Environmental Sciences, University of Greenwich,
Chatham Maritime, ME4 4TB, Kent, UK, email: D.Douroumis@gre.ac.uk.

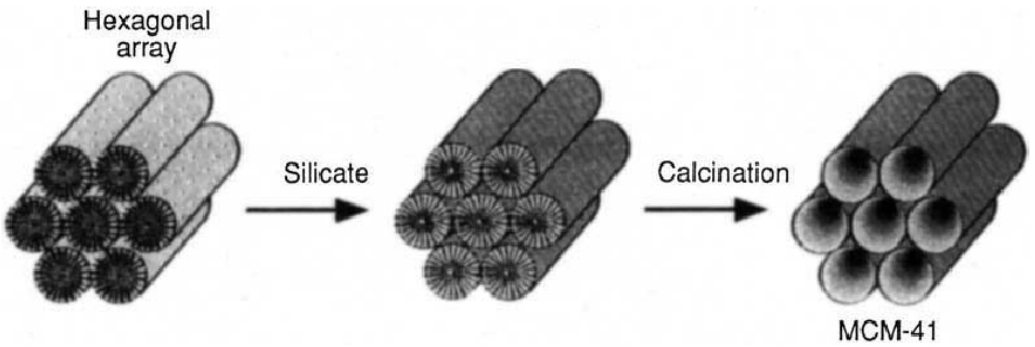
materials into several categories depending on their sizes pore or dimensions. Micro porous and macro porous materials are materials with pore diameters less than 2nm and greater than 50 nm respectively. Mesoporous materials fall into the category with pore size diameters in the range between 2 and 50 nm (Katiyar et al. 2006). Mesoporous silica nanoparticles are synthesized *via* different mechanism routes (Kresge et al. 1992) which involve the use of surfactants in alkaline or acidic media as in sol-gel or spray-drying methods. MSNs can be modified with functional organic groups for applications in controlled drug delivery systems and can be labelled with fluorescent dyes when used in imaging or photodynamic therapy (Yang et al. 2008).

2. SILICA PREPARATION METHODS

Generally, the methods used for the synthesis of nanoparticles with porous matrices involve the impregnation of a matrix with the help of a solution of precursors which is then followed by precursor reduction based on chemical, thermal, radiolytic or photochemical processes. In many cases the produced yields are typically ~95% by using nonionic surfactants or low molecular weight cationic surfactants.

2.1. Conventional Preparation Method

Kresge *et al.* (1992) first reported the synthesis of mesoporous silicas (Figure 1) from the calcination of aluminosilicate gels in the presence of quaternary ammonium surfactants where they proposed the liquid-crystal 'templating' mechanism to form the mesoporous silicas along with the formations of the inorganic walls by silicate materials between ordered surfactant micelles. The silica materials showed regular arrays of uniform channels and the dimensions were tailored from 16-100Å or more by using different surfactants and auxiliary chemicals or by changing the reaction conditions.



Source: With permission from Kresge et al.1992.

Figure 1. Preparation of MCM-41.

In another process Bagshaw *et al*. (1995,1996) have used alkyl poly(oxyethylene) surfactants and poly(oxyalkylene) block copolymers in aqueous solutions to synthesize wormlike disordered mesoporous silica and alumina in neutral media assembled by hydrogen-bonding interactions. Attard *et al* .(1995) have synthesized hexagonal mesoporous silica phases using concentrated (50 wt %) $C_{12}EO_8$ solutions and suggested that the formation of mesoporous silica under these conditions occurs by a "real" liquid crystal template route. An important aspect during the hydrolysis and condensation of varying tetramethyl orthosilicate (TMOS) concentrations under acid synthesis is the production of methanol wich destroys the liquid – crystalline meshophase. Thus the removal of methanol is important to reform the mesophase (Attard et al. 1995).

In a later study, Zhao *et al*. (1998) reported various new mesoporous silica structures such as cubic, three-dimensional hexagonal, two-dimensional hexagonal, possibly continuous sponge and lamellar mesostructures. All these mesoporous silicas were synthesized by using low molecular weight non-ionic ethylene oxide (EO) surfactants and poly(alkylene oxide) block copolymers in acid media *via* a $(S_0H^+)(X^-I^+)$ structure directing route to create highly ordered mesoporous structures where S_0 is the nonionic surfactant, X^- is the halide anion, and I^+ is a protonated Si-OH moiety in an H^+ excess. The experimental findings showed that the selected surfactant species control predominantly the structure of the ordered mesoporous silica formed. Therefore the formations of specific mesostructured silica phases are favoured by each type of surfactants used.

In the same study Zhao and co workers synthesized cubic mesoporous silica phase (SBA-11) with a diffraction-related space group structure in the presence of $C_{16}EO_{10}$ surfactant species with a BET surface area of 1070 m^2/g and pore size of 25 Å. They also synthesized three-dimensional hexagonal *P*63/*mmc* mesoporous silica (SBA-12) phase by using $C_{18}EO_{10}$ surfactant species under otherwise similar conditions. They also used non-ionic alkyl-EO/furan surfactants, such as Tween 60, to form cubic mesoporous silica. Surfactants with shorter EO moieties form a less ordered material, which may be an L3 sponge mesophase or lamellar mesostructured silica. Zhao and co workers also prepared SBA-15 mesoporous structures with BET surface areas of 690-1040 m^2/g and a novel cubic (*Im*3h*m*) cage-structured, mesoporous silica structure called SBA-16. Silica wall thickness was measured between 31-64 Å, and pore volumes were as large as 2.5 cm^3/g. The large cell parameters were synthesized using tri-block copolymers with large polyethyleneoxide PEO segments.

In two similar studies Huo and co workers (1994) supported by Stucky *et al*.(1994) assembled charge-associated EO units together with cationic silica species by a combination of electrostatic, hydrogen-bonding, and van der Waals interactions. Coordination sphere expansion around the silica atom by anions may play an important role during the hydrolysis and condensation of the silica species. Hexagonal, cubic, or lamellar mesostructures were sometimes observed at some point during the silica preparation.

From the need to improve the currently available post-synthesis grafting and organosiloxane/siloxane co-condensation methods in order to control the amount and location of the incorporated functional groups, Huh *et al.* (2003) reported and analyzed a new synthetic method that could combine efficient organic functionalization of mesoporous silicas with the control of particle morphology. The authors' strategy involved a co-condensation method based on sodium hydroxide catalyzed reactions of tetraethoxysilane (TEOS) with various organoalkoxysilanes such as 3-aminopropyltrimethoxysilane (APTMS), *N*-(2-aminoethyl)-3-aminopropyltrimethoxysilane (AAPTMS), 3-(2-(2-aminoethylamino) ethylamino)propyltrimethoxysilane (AEPTMS), ureidopropyltrimethoxysilane (UDPTMS),

3-isocyanatopropyltriethoxysilane (ICPTES), 3-cyanopropyltriethoxysilane (CPTES), and allyltrimethoxysilane (ALTMS) in the presence of a low concentration of cetyltrimethylammonium bromide (CTAB) surfactant. Sadasivan *et al.* (2003) reported a controlled quenching method that involved organic co-solvents or instantaneous neutralization of alkaline solutions during the co-condensation reaction. By systematically varying the type and the amount of organoalkoxysilanes Sadasivan and co-workers obtained a series of nanoparticles in the form of spheres, rods, and hexagonal tubes.

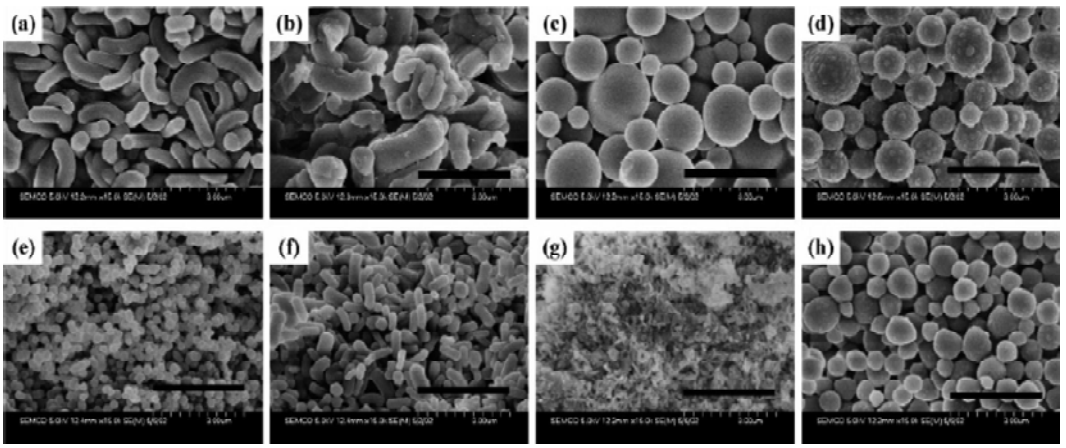
Having large surface areas and very narrow pore size distributions, with pore diameters tunable from 15 to 100 Å, M41S has been designated as a new type of mesoporous structures. Qye *et al.*(2001) described the synthesis, modification, characterization and potential applications of M41S family's nano materials consisting of MCM-48, MCM-41 and MCM-50. All prepared MCM-48 nanoparticles have cubic ordered pore structure and MCM-41 and MCM-50 nanoparticles show a hexagonally ordered pore structure and an unstable lamellar structure respectably.

Zhao *et al*. (2003) reported the synthesis of nanosize MCM-48 (with a uniform particle size of 125 nm) through the addition of an aqueous solution of water glass (Na2O:SiO2 7.4:25.4%) to a mixed solution of poly(ethylene glycol) mono-octylphenyl ether (OP-10) and cetyltrimethylammonium bromide (CTAB). The structural characterization and thermal stability of this material studied showed nanosize MCM-48 with excellent thermal stability that can retain its cubic structure even after calcination at 1000°C in air for 2 h

Another MSNs preparation method relating to a direct synthesis in which the organoalkoxysilane is introduced to the basic, aqueous CTAB and TEOS solution during the condensation has been applied to prepare MSNs by Trewyn and co workers. In addition to the systhesis methods this method controls the morphology of the particles by the addition of functional cocondensing reagents (Figure 2). Trewyn *et al.*(2007) showed the degree of functionalization and particle morphology in reference with the concentration as well as molecular size and hydrophobicity/hydrophilicity of the co-condensing reagents. The use of 12.8 mol % co-condensing reagents led to MSNs with homogeneously distributed functional groups with surface coverages varied between 13 and 33% in solid-state nuclear magnetic resonance (NMR).

Organically modified silica (ORMOSIL) nanoparticles are prepared from oil-in-water micro-emulsions. The preparation methods avoid the use of corrosive solvents such as cyclohexane through a complex purification process. The organic groups can be possibly biodegraded through the biochemical decomposition of the silicon–carbon bond (Das et al. 2002; Jain et al. 1998). Bharali *et al.* (2005) prepared amino-functionalized ORMOSIL nanoparticles by precipitation with 3-aminopropyltriethoxysilane, resulting in the incorporation of cationic amino groups on the surface of the ORMOSIL nanoparticles followed by the removal of the surfactants by dialysis. In the study the authors found that the addition of cationic groups to the surface of the ORMOSIL enhanced the binding with negatively charged plasmids thereby promoting successful carriage.

Han *et al.*(2006) successfully synthesized carboxylic group functionalized mesoporous silicas (CFMSs) using cationic surfactants as templates and carboxyethylsilanetriol sodium salt (CES) as a co-structure directing agent (CSDA). Cagnol and co workers reported a synthesis route of functionalised CTAB-templated silica thin films of nanoparticles, using different organotrialkoxysilanes with different physico-chemical properties such as hydrophobic, aromatic, polymerisable *etc* (Cagnol et al. 2004).



Source: With permission from Trewyn et al. 2006.

Figure 2. Field emission scanning electron microscopy (FESEM) images of (a) 3-aminopropyl-MSN, (b) *N*-(2-aminoethyl)-3-aminopropyl- MSN, (c) 3-(2-(2-aminoethylamino)ethylaminopropyl-MSN, (d) 3-ureidopropyl-MSN, (e) 3-isocyanatopropyl MSN, (f) 3-cyanopropyl-MSN, (g) allyl-MSN, and (h) nonfunctionalized MSN. All images are presented using the same scale, with the scale bar) 3 μm.

Ha and co workers (2009) developed a new synthetic route where derivatized dye molecules were successfully incorporated into silica nanoparticles by co-condensation with TEOS in a basic, ethanol solution. In this study aqueous NH_3 was employed to facilitate thiourea linkage formation. As a result fluorescent silica nanoparticles were produced without employing isothiocyanate functionalized dye molecules and (3-aminopropyl)triethoxysilane(APS) . All synthesized fluorescent silica nanoparticles showed excellent photochemical, thermal and pH stabilities and possessed good biocompatibility.

2.2. Fluorescent Silica Nanoparticles

The incorporation of both organic and inorganic dyes into silica nanoparticles have been utilized widely in different applications. The silica nanoparticle matrix, due to its physicochemical properties, provides a chemically and mechanically stable environment for entrapped fluorescent dyes by effectively providing a barrier that protects the dyes from the surrounding environment (Yan et al. 2007); hence minimizing photobleaching and photodegradation phenomena that are often associated with conventional dyes (Kim et al. 1999).

Fluorescent silica nanoparticles can be synthesized *via* two main methods either the St*ö*ber process or the reverse micro-emulsion process. The St*ö*ber process was first developed in the 1960s by St*ö*ber and co-workers who brought forward a synthetic process to grow monodisperse, spherical silica nanoparticles based on the sol-gel method of silicon alkoxide hydrolysis (Burns et al. 2006).

The St*ö*ber process involves the hydrolysis and condensation of tetraethoxysilane (TEOS) in a mixture of ethanol and aqueous ammonium hydroxide which acts as a catalyst to create uniformly disperse, spherical and electrostatically stable particles (Burns et al. 2006). During the hydrolysis process, silicic acid is formed that nucleates homogeneously and produces

silica particles of submicron size just as its concentration increases above its solubility limit in ethanol. The synthesis of fluorescent silica nanoparticles is made possible by covalently attaching isocyanate-modified dye molecules to an amine-containing silane reagent such as 3-aminopropyltriethoxysilane (APTS) (Knopp et al. 2009).

In an another study Jeon *et al*.(2006) investigated the feasibility of a fluorescent imaging system for sentinel lymph node detection by using fuctionalized silica nanoparticles synthesized *via* rhodamine B isothiocyanate (RITC)-doped silica nanoparticles using the St*ö*ber method. In this process APTS was added to RITC and stirred to covalently conjugate the RITC to the nanoparticles. The dye conjugated nanoparticle was further modified by the addition of PEG-silane resulting in amine-modified RITC-doped silica nanoparticles. A uniform size of 75±7nm was obtained for the RITC-doped silica nanoparticles with increased photo-stability where only 8% decrease in fluorescence intensity was observed compared to pure RITC, which showed 62% decrease in fluorescent intensity (Jeon et al. 2010).

Mascharak et al. (2010) synthesized fluorescent silica nanoparticles using the St*ö*ber method via controlled hydrolysis of TEOS in a water/oil micro-emulsion in the presence of APTS, fluorescein-5-isothiocyanate (FITC) and 3-(Trihydroxylsilyl) propylmethylphosphonate (THPMP). As a result, consistent, uniform, spherical shaped particles with a size of 70nm were obtained.

A reverse micro-emulsion process was explored in the 1990's by Arriagada and Osseo-Asare. The process relies on the controlled aqueous environment surrounded by the surfactant-confined micelles in a non-polar solvent to generate thermodynamically stable aggregates of amphiphilic surfactant. In this process the monodisperse particles obtained are a result of the presence of nanodroplets of water in the bulk oil phase, which act as nanoreactors (Burns et al. 2006). The size diameter of the nanoparticles obtained from this process is dependent on the size of the water droplet cores and the water-to-surfactant molar ratio (W_0). However, unlike the St*ö*ber process the reaction time is much longer i.e. about 1-2 days when compared to a -few hours processing time in the St*ö*ber process (Knopp et al. 2009).

The reverse micro-emulsion technique was demonstrated by Bagwe *et al.* 2004 in the studies of the formation of tris(2,2'-bipyridyl)dichlororuthenium(II) (Ru(bpy)) dye-doped silica nanoparticles by ammonia-catalyzed hydrolysis of tetraethyl orthosilicate (TEOS) in a water-in-oil micro-emulsion. In this study the fluorescence spectra, particle size, and size distribution of Ru(bpy) dye-doped silica nanoparticles was examined as a function of (i) reactant concentrations (TEOS and ammonium hydroxide), (ii) nature of surfactant molecules (iii) molar ratios of water to surfactant and co-surfactant to surfactant. This study concluded with the findings that particle size and fluorescence spectra of the MSN synthesised is dependent upon the type of micro-emulsion system chosen. In addition, the particle size of the MSN was found to decrease with an increase in concentration of ammonium hydroxide and increase in water to surfactant and co-surfactant to surfactant molar ratios (Bagwe et al. 2004).

2.3. Functionalised Silica Nanoparticles

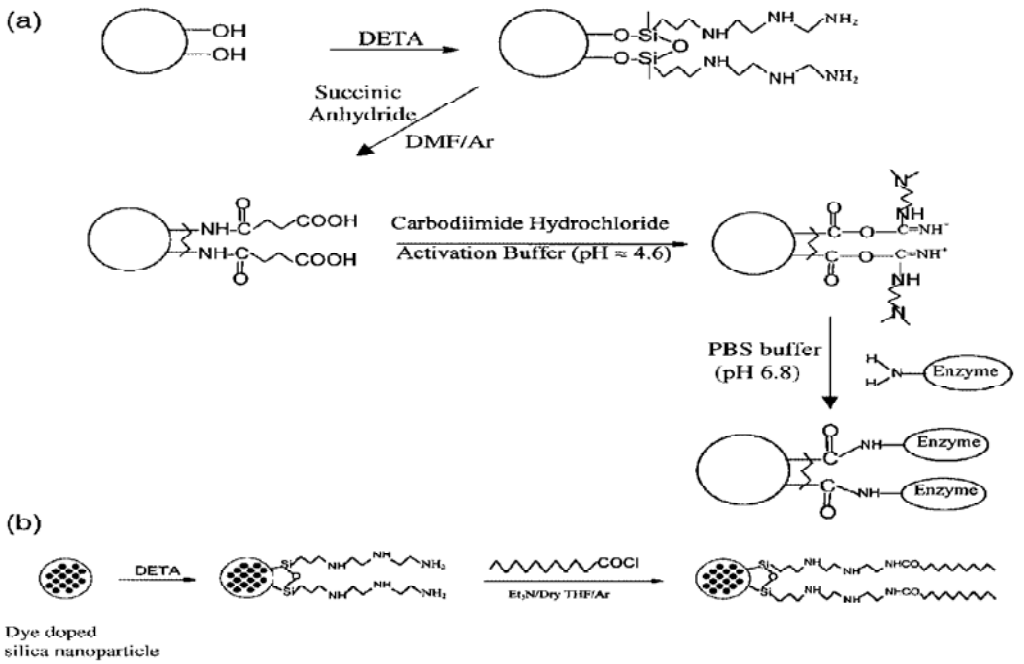
A major advantage of using silica nanoparticles in biomedical and pharmaceutical applications is the ability to functionalize or conjugate the nanoparticle pores and surface. Mesoporous silica contains high amount of silanol (Si-OH) groups on their surface which

allows the attachment of a large variety of polar molecules. These molecules are covalently bound to the silanol group including carboxylate, amine, amine/phosphonate, polyethylene glycol), octadecyl, and carboxylate/octadecyl groups (Bagwe et al. 2006). The higher the concentration of the silanol groups found on the nanoparticle the higher is its affinity for polar molecules. The surface of mesoporous silica particles is usually modified through a variety of techniques such as imprint coating, grafting(post-synthesis modification) and one-pot synthesis (Slowing et al. 2008). Tetraalkoxysilane and other organoalkoxysilanes have been used for the formulation of inorganic and organic hybrid networks via the co-condensation technique. This technique enables control of the particles' morphology by the addition of a co-condensing reagent. However, the degree of functionalization and particle morphology relies on the molecular size, concentration, hydrophobicity or hydrophilicity of the co-condensing reagents (Trewyn et al. 2007).

Several investigations on strategies to introduce organic functional groups on the surfaces of silica particles has been of great interest since the surface properties of silica particles are mainly influenced by the nature of the surface functional groups. Surface functionalized silica particles have been found useful in applications such as protein immobilization, catalysis and sensors. One of the most commonly used methods for functionalizing the surface of silica particles is the co-hydrolysis technique, which involves the co-hydrolysis of organosilanes with a tetra alkoxysilicate (Vallet-Regi et al. 2007).

Surface modification of silica nanoparticles for biochemical functionality was studied using two approaches (Qhobosheane et al. 2001) which include aqueous solution reactions and water-in-oil micro-emulsions as illustrated in Figure 3. These two approaches were utilised in the preparation of uniform silica nanoparticles comprising pure silica nanoparticles and dye-doped silica nanoparticles. Synthesis of pure silica nanoparticles was achieved following the St*ö*ber synthesis and the pure silica nanoparticles were modified with two diverse enzymes (glutamate dehydrogenase and lactate dehydrogenase). The dye-doped silica nanoparticles incorporated with highly luminescent water-soluble dye, Rubpy was prepared by the water-in-oil microemulsion method. Uniform size distributed nanoparticles with a particle size of 62nm, under TEM, was obtained for both silica nanoparticles. The findings of this study present silica nanoparticles as a good biocompatible solid support for enzyme immobilization and indicate that the immobilized enzyme molecules on the nanoparticle surface show tremendous enzymatic activity in their respective enzymatic reactions. The surface biochemical functionalization of the nanoparticle obtained in this study clearly demonstrates the feasibility of utilizing nanoparticles for bio-marking applications and as a potential biosensor *via* surface modification of the silica nanoparticles (Qhobosheane et al. 2001).

A functionalized MSNs (FMSNs) based-drug delivery system was developed by Cho *et al.* (2008) whereby MSNs were encapsulated with hydralazine and covalently linked with polyethylene glycol. FMSNs with mean diameter of approximately 100nm were obtained. An increase in the average particle size and decreases in the pore volume of the MSNs were also observed under TEM for the functionalized MSNs, which have polyethylene glycol coated on the surface. In terms of the encapsulation efficiency of the MSNs loaded with hydralazine (MSN-Hy) and the functionalized MSN (MSN-Hy-PEG), the adsorption/desorption isotherms showed a lower drug loading for the functionalised MSNs (MSN-Hy-PEG) 23.1% compared to the non-functionalised MSN (MSN-Hy) 30.1%.



Source: With permission from Qhobosheane et al. 2001.

Figure 3. Surface modification of the pure silica nanoparticles for enzyme immobilization (a), and surface modification of the dye doped silica nanoparticles for membrane probing (b).

Deng *et al*. (2000) in their studies also demonstrated the effect of specific terminal functional groups of the added organosilane on the density and pore volume of MSNs using TEM and surface area studies. They demonstrated the effect of varied time of organosilane addition to micro-emulsion of the MSN. Their findings revealed that increase or decrease of the surface area, pore volume and particle size are dependent on the organosilane used in the functionalization of the MSN. Their findings also demonstrated that the addition of organosilane at a different time interval also plays a role in the particle size obtained for the MSN.

3. Influence of Structural Characteristics

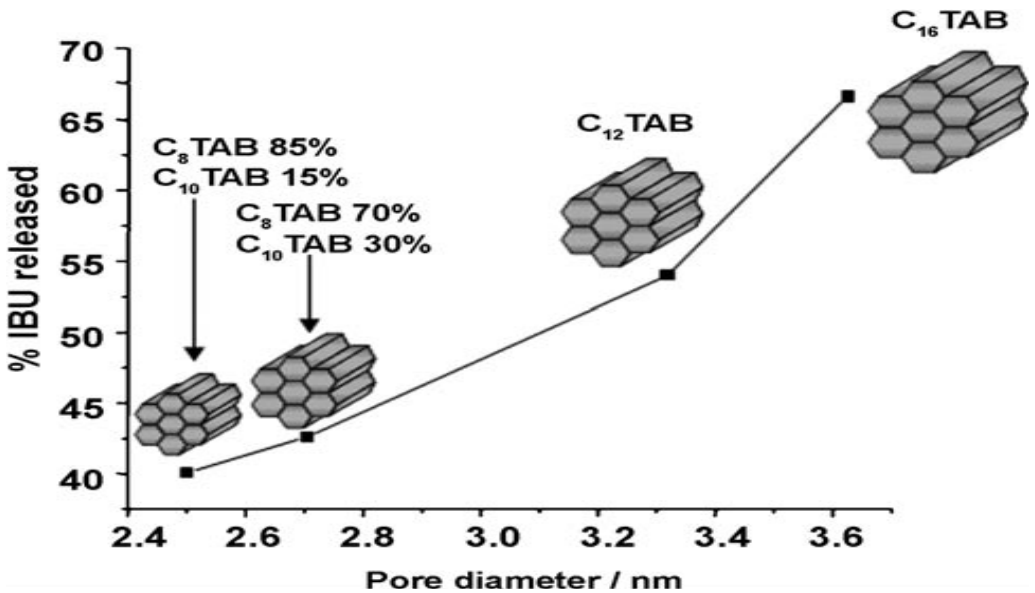
3.1. Pore Size

The tunable, highly uniform pore size of mesoporous silica nanoparticles is one of their unique features. The size of the molecule that can be absorbed into the mesopores is determined by the pore size of mesoporous materials. The pore size can vary from 1.5-10 nm and can be easily adjusted by varying the process parameters such as by changing the chain length of the surfactant, employing structure-directing agents or solubilising auxiliary substances. Consequently, size selectivity governs the adsorption of molecules in the mesoporous matrix by adjusting the loading of different drug molecules and helping the study of drug release kinetics with high precision (Beck et al. 1992; Yu et al. 2003). Molecular-sieve properties for relatively large molecules are exhibited by mesoporous materials and

therefore Hata and co workers (1999) reported that FSM-type mesoporous silica with pores size larger than 1.8 nm absorbed an anticancer substance known as taxol (Hata et al. 1999). For controlled drug delivery systems, the pore size exerts control on the drug-release rate. Vallet-Regi *et al.* obtained MCM-41 with a larger pore size using C_{16}TAB, released 68% of the loaded ibuprofen in 24hrs in stimulated body fluid while C_{12}TAB released only 55% (Figure 4). In the same study the authors found the role of pore size as drug-delivery controller since MCM-41 mesoporous materials with pore diameters between 2.5 and 3.6 nm exhibited a high increase of ibuprofen release rate (Vellet-Regi et al. 2007). The principle of pore size as a kinetic-release controller is applicable both in MCM-41 and MCM-48 mesoporous materials with 2D hexagonal and 3D cubic symmetries respectively. Furthermore pore size of 5.7nm in MCM-48 LP-Ia3d showed faster release of ibuprofen compared to Ia3d symmetry and a pore size of 3.6 nm demonstrating the influence of the pore – size effect.

Andesson *et al.* (2004) reported the consequences of pore geometry, pore connectivity and matrix degradation, in addition to pore size, which may have affected the porosity and kinetic release. In the same article the authors also noted that the cage-like or corrugated pores structures seem to be excellent matrices for long-term drug delivery as larger pores are connected through the smaller windows on the drug delivery route.

Qu and co workers reported that the release kinetics, as well as the final amount of drug loading kinetics of captopril from different MSNs structures, was influenced by pore size when the morphology was similar at the microstructure level. Similarly Vallet-Regi and co workers reported that the pore size of powder and disk-shaped mesoporous samples at different macroscopic levels increased the kinetic release of amoxicilin (Qu et al. 2006; Vallet-Regi et al. 2004).



Source: With permission from Vellet-Regi et al. 2004.

Figure 4. IBU fraction released from MCM-41 after 24 h in SBF. The plot is represented as a function of pore diameter and the surfactants used are indicated for each case.

3.2. Surface Area

Pore properties mainly determine the drug-loading process by exhibiting the adsorptive characteristics of mesoporous nanoparticles. This significantly means that pore properties have the choice of incorporating high or low doses of a drug into the matrix. Thus, the surface area of MSNs becomes the most important factor to determine the amount of drug adsorbed. Consequently increasing or reducing the surface area and modifying the surface–drug affinity are two important challenges to overcome in order to incorporate high or low dosages into the MSNs matrix. The amount of the surface available for drug molecules is very important as the larger the surface area the higher the drug amount loaded would be adsorbed into the matrix. Vallet-Regi *et al.* synthesized MCM-41 and SBA-15 in similar structures with S_{BET} values of 1157 and 719 m^2g^{-1} respectively loaded with alendronate. After a careful observation, the maximum loads of alendronate obtained were $139mgg^{-1}$ for MCM-41 which was higher than that of SBA-15 ($83mmg^{-1}$). Thus, the larger the value of S_{BET} the higher the maximum load of drug in the matrix surface (Vellet-Regi et al 2007).

The same researchers found three to five times larger areas compared to the MCM-41 inorganic mesoporous materials alone in some metal–organic frameworks (MOFs) that exhibit large S_{BET} values as well as high drug loading with controlled release. These materials are denoted as Materials Institute Lavoisier-100 (MIL-100) and Materials Institute Lavoisier-101 (MIL-101). MIL-100 showed a larger surface area of $3340m^2g^{-1}$ while MIL-101 had an area of $5510m^2g^{-1}$. Under same conditions MIL-100 and MIL-101 adsorbed about $350mgg^{-1}$ and $1400mgg^{-1}$ of ibuprofen respectively. In comparison with that of silica-based MCM-41 with $S_{BET}=1157m^2g^{-1}$, these differences were attributed particularly to the accessible dimensions of the windows of the cages in the solids, which are larger in MIL-101 which takes into account that the adsorption of drug is a influence of the high surface area of the external micropores. There is a big dfference in the surface between MCM-41 and MIL-100 (Vellet Regi et al. 2007).

3.3. Pore Volume

The pore volume of mesoporous silica nanoparticles varies from $0.9cm^3/g$ to $2.0cm^3/g$. The pore volume of these silica nanoparticles is very large helping in drug loading, as large quantities of the drug molecules can be loaded and delivered according to experimental requirements (Serre et al. 2002).

The drug–mesopore interaction is a surface phenomenon; however, weak drug–drug interactions can result under loading conditions and could lead to pore filling. In this case, the pore volume is a key factor in determining the amount of drug adsorbed (Horcajada et al. 2006). Azais *et al.* (2006) recently reported that several consecutive loadings of drug in ordered mesoporous materials leads to larger attribution to the increased drug intermolecular interactions within the pore voids, whereby larger pore volumes result in greater drug loading.

4. SILICA NANOPARTICLES AS A DRUG DELIVERY SYSTEM

MSNs are considered to be novel, multifunctional drug delivery systems. Owing to their unique features, they are used for effective delivery of drug and other functional materials

with the ease of monitoring the structural properties and chemical functionalization for biotechnological and biomedical applications. MSNs can be used for the storage of strongly hydrophobic drugs. The internal porous surface helps to enhance the release of drugs, which are poorly soluble, facilitated by breaking up the intermolecular interactions normally present within the drug crystals. Recent advances revealed that the mesoporous silica nanoparticles can be easily incorporated with therapeutic drugs for chemical therapy, as photo-sensitizers for photo-dynamic therapy (PDT) and as magnetic nanoparticles for hyperthermia treatment and magnetic resonance imaging (MRI).

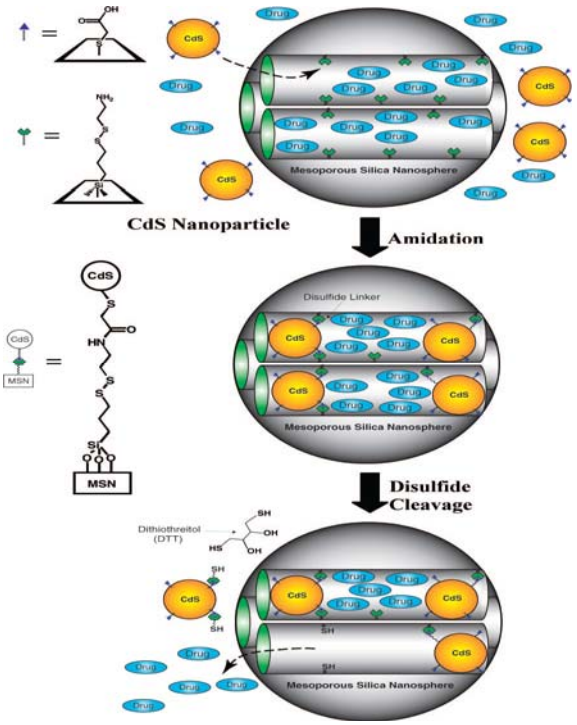
4.1. Controlled Drug Delivery

Since the mesoporous material MCM-41 was proposed as a drug delivery system (DDS) by Vallet-regi and co workers in 2001, MSNs have been used for controlled drug delivery of various types of guest molecules. The desired drug is incorporated into the MSNs either by dissolving, entrapment, adsorption, attachment or through encapsulation into the matrix of the silica nanoparticles. The key step in the development of silica mesoporous materials as DDSs is the modification or functionalization of the matrix surface with organic groups. The drug release can be effectively controlled by different methods such as increasing the drug–surface interaction.

Controlled DDS can be described as a formulation that controls the rate and period of drug delivery and targets specific areas of the body in order to maintain therapeutic drug levels during the treatment period. Therefore, Vallet-regi *et al.* (2007) studied the controlled adsorption of ibuprofen (IBU) on functionalized matrices of MSNs where the drug was incorporated in MSN systems on the assumption that its carboxyl group links to the silanol groups at the surface. The drug release of IBU was effectively controlled by the surface functionalization with chemical groups that are able to link to the drug molecules through ionic bonds or through ester groups. However, this situation is not exclusive in non-functionalized matrices.

Balas *et al.*(2006) recently reported on the controlled release of the bisphosphonate family member, alendronate, contained by amino-functionalized MCM-41 and SBA-15 mesoporous silica-based materials. The purpose of the release was for bone repair or regeneration inhibiting bone resorption by osteoclasts. The authors' work demonstrated that the drug delivery rate of adsorbed bisphosphonated drug was modulated through modification of the surface of the pore walls through organic molecules. Another milestone for effective control of drug release is functionalization of the surface with hydrophobic species. Thereby the drug, whilst being transported out of the matrix, is seriously impeded by the presence of multi-hydrophobic-drug interactions. In this process the aqueous medium does not easily enter through the pores (Giri et al. 2005, Vivero-Escoto et al. 2010).

Doadrio and co-workers described functionalized SBA-15, which showed a controlled release of an antibiotic that belongs to the macrolide family known as erythromycin. In this study the authors modified the surface nanoparticles with octyl and octadecyl moieties by treating the mesoporous matrix with trimethoxyoctylsilane and trimethoxyoctadecylsilane, correspondingly. A decrease of the effective pore size as well as a decrease of the wettability of the surface by aqueous solutions was the resultant impact on the mesoporous SBA-15 (Doadrio et al. 2006). Qu *et al.*(2006) also obtained similar results with mesoporous materials



Source: With permission from Trewyn et al. 2006.

Figure 5. Schematic representation of the CdS nanoparticle-capped MSN-based drug/neurotransmitter delivery system.

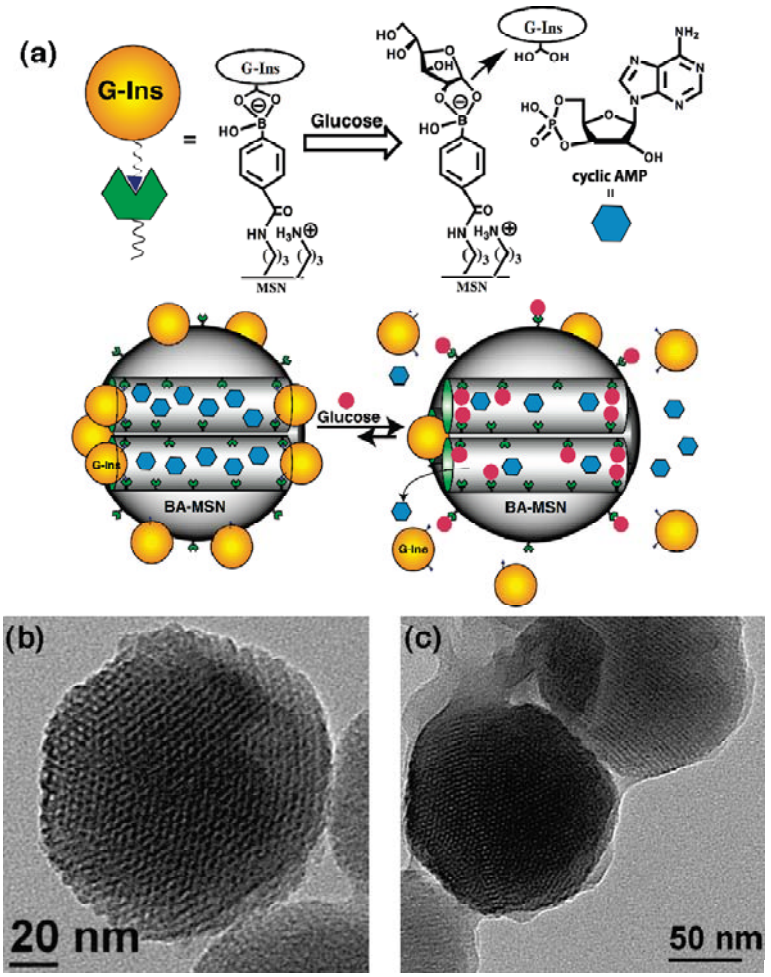
modified by silylation where Captopril and ibuprofen were incorporated into MSNs. In both cases the drugs showed a lower drug loading while carrying out the silylation therefore well-defined controlled drug release can be achieved by tailoring the surface properties of mesoporous silica materials if the silylation is regulated by varying degrees.

In another study Tanaka and co-workers demonstrated the ability of coumarin-modified mesoporous silica to be used as a photo-controlled reversible guest molecule release vehicle in an organic solvent. Tanaka and co workers showed that the uptake, storage, and release of organic molecules using coumarin-modified MCM-41 can be regulated through the photo-controlled and reversible intermolecular dimerization.

The report produced by the authors was the first to demonstrate a photo-controlled release of guest molecules from MCM-41 material by reversible photo-responsive dimerization techniques (Tanaka et al. 2003; Slowing et al. 2007).

Trewyn *et al.* (2007) also developed a series of stimuliresponsive, MCM-41-type MSN-based controlled release delivery systems (Figure 5) where the mesopores loaded with guest molecules were capped by CdS nanoparticles *via* a chemically cleavable disulfide linkage to the MSN surface. Being physically blocked, guest molecules were unable to leach out from the MSN host, thus preventing any premature release. The release was triggered by exposing the capped MSNs to chemical stimulation that could cleave the disulfide linker, thereby removing the nanoparticle caps and releasing the pore entrapped guest molecules.

Zhao *et al.* (2009) reported on the synthesis of a glucose-responsive MSN based double delivery system for both insulin and cAMP with precise control over the sequence of release.



Source: With permission from Zhao et al. 2009.

Figure 6. (a) Schematic representation of the glucose-responsive MSNbased delivery system for controlled release of bioactive G-Ins and cAMP. Transmission electron micrographs of (b) boronic acid-functionalized MSN and (c) FITC-G-Ins-capped MSN.

They also demonstrated that the uncapped MSN can be efficiently endocytosed by live mammalian cells, leading to effective intracellular release of the cell-membrane-impermeable cAMP.

The authors also described (Figure 6) that gluconic acid-modified insulin (G-Ins) proteins to be immobilized on the exterior surface of MSN to be served as caps to ancapsulate cAMP molecules inside the mesopores of MSN. The release of both G-Ins and cAMP from MSN can be triggered by the introduction of glucose. The average particle size was small enough to evade rapid sequestration by phagocytotic cells of the spleen and to allow long blood circulation.

Vivero-Escoto *et al.*(2010) demonstrated the application of MSNs as stimuli-responsive drug delivery system (DDS) based on the controlled release of neurotransmitters using CdS-NPs as caps where the CdS-NPs-MSNs system was synthesized using MSNs as the guest reservoir. They used a chemically labile disulfide as bond linker which was chemically

attached to the CdS-NPs to afford the stimuliresponsive gatekeeper approach. The MSNs and their release were triggered AND controlled by reducing agents such as dithiothreitol (DTT) and mercaptoethanol (ME).

4.2. MSNs in Cancer Treatment

Recent studies involving the use of MSNs have shown their effectiveness in cancer therepy. Lu *et al.* (2007) investigated the use of MSNs in the delivery of the hydrophobic cancer drug paclitaxel to pancreatic cancer cells (PANC-1). Their studies illustrated MSNs as a valuable vehicle in the delivery of hydrophobic anticancer drugs to human cancer cells. FITC conjugated MSNs (FMSN) was loaded with paclitaxel at different concentration and tested on PANC-1 cell. The cytotoxicity and confocal microscopy studies of the formulated FMSN loaded paclitaxel showed cell induced inhibition of cancer proliferation when compared to the unformulated paclitaxel. Development of multidrug resistance in cancer cells and adverse side effects are the main problems that prevent effective cancer chemotherapy. Therapeutic strategies to surmount drug resistance and specific tumor targeting with negligible premature drug release have a great impact on cancer treatment therapy. MSN as reported by (Chen et al. 2009) was utilized as a system to simultaneously deliver Doxorubicin and Bcl-2 targeted siRNA into multidrug resistant A2780/AD human ovarian cancer for enhanced efficacy of cancer treatment. Their results demonstrated that the Bcl-2 siRNA can effectively silence the Bcl-2 mRNA and significantly suppress the non-pump resistance and substantially enhance the anti-cancer action of Doxorubicin; In addition the result shows MSNs Doxorubicin minimal premature release in the extracellular environment and primary localisation in the peri-nuclear region after internalization thus enhancing cytotoxicity (Chen et al. 2009). Other reports (Lu et al. 2010; Rosenholm et al. 2010) have also shown MSN as a promising material for drug delivery. Bio-distribution studies using human cancer xenografts carried out with *in vivo* imaging and fluorescent microscopy imaging, as well as with inductively coupled plasma mass spectroscopy showed that MSNs preferentially accumulate in tumors as demonstrated by the drug-delivery capability of MSNs loaded with camptothecin (Lu et al. 2010). Targeted delivery of the chemotherapeutic agent methotrexate to cancer cells using poly(ethyleneimine)-functionalized mesoporous silica particles as drug-delivery vectors was also reported to enhance cancer cell apoptosis (Rosenholm et al. 2010).

Modified MSNs are promising platforms for loading both hydrophilic and hydrophobic anticancer drugs for tumour therapy. Surface functionalization of magnetic mesoporous silica nanoparticles for controlled drug release in cancer treatment was demonstrated by Chang e*t al.* well-structured magnetic mesoporous silica nanoparticles (M-MSNs) which consist of magnetic nanoparticles resided within the mesoporous nanoparticles were synthesised using a modified sol-gel approach and the surface was functionalised with diverse functional groups (the carboxyl (—COOH), methyl phosphonate (—PO_3^-), amino (—NH_2) and phenyl (—Ph)). The hydrophilic modified M-MSNs with —COOH and —PO_3^- were reported to be beneficial for loading the water-soluble doxorubicin hydrochloride (DOX) through electrostatic attraction. The findings illustrated that M-MSNs-PO_3^- achieved a higher loading content and M-MSNs-COOH presented a distinct pH-responsive release behavior. The drug-loaded MSNs apparently were reported to demonstrate cell proliferation inhibition on human epithelial cervical cancer cells as a result of the sustained release of drugs (Chang et al. 2010)

Most anticancer drugs such as irinotecan hydrochloride trihydrate (CPT-11), cisplatin, taxol, navcelbine doxorubicin, and fluorouracil are very expensive, while most commonly used surfactants are very cheap and easy to use as structure-directing agents in the synthesis of MSNs. Therefore the development of new, low-cost anticancer drug delivery systems of porous nanoparticles like MSNs with various cheap surfactants like CTAB is of great significance. The use of various charged surfactants in MSNs and their effect on cancer proliferation was recently investigated. Three types of surfactant-templated mesoporous silica nanoparticles with diameter 150-660nm were developed as anticancer drug delivery systems to inhibit the proliferation of MCF-7 cells by He *et al.* The surfactant-templated MSNs were reported to exhibit high dug loading, sustained drug realease and long term anticancer efficacy of the anticancer agent, irinotecan hydrochloride trihydrate (CPT-11). The effect of the type of surfactant on cancer cell proliferation was reported in the study. Cell proliferation inhibition of the surfactant-templated MSNs was reported to be in the order of CTAB@MSNs>SDBS@MSNs>Triton@MSNs with CTAB@MSNs having remarkably higher anticancer efficacy than CPT@MSNs even at very low particle concentrations (He et al. 2010).

4.3. MSNs as Biosensors

Immobilization of enzymes in well-defined mesoporous silica materials has been established to show potential usefulness for enhancing the thermal stability and maintaining the catalytic activity of enzymes (Pandya et al. 2005). Enzymes encapsulated on the inside of silica mesopores are less prone to pH and temperature changes as well as organic solvent interactions. The sensor systems based on mesoporous silica nanoparticles enable the easy detection of analytes in the microscopic space within the individual cells for both *in vivo* and *in vitro* detection due to the unique features of mesoporous nanoparticles such as their surface properties and their small particle size (Guzman et al. 2006). Of all the different nanoparticle biosensors, enzyme immobilized nanoparticles have been reported the most in several publications. Although enzyme-based sensors demonstrate great specificity and low concentration detection limits, they suffer from denaturation and inactivation. In addition, nanoparticles sensors lack two vital features held by mesoporous silicas i.e. high porosity, which results in large surface areas available for the immobilization of the sensing molecules and optical transparency which enables optical detection through the layers of the material matrix (Trewyn et al. 2007). A novel bienzyme biosensor based on the assembly of the glucose oxidase (GOD) and horseradish peroxidase (HRP) onto the gold nanoparticles encapsulated mesoporous silica SBA-15 composite (AuNPs-SBA-15) was reported by Zhang *et al.* for the detection of glucose. The results illustrated that the presence of mesoporous AuNPs-SBA-15 significantly enhanced the protein loadings, accelerated interfacial electron transfer of HRP and the electro-conducting surface, resulting in the realization of direct and specific electrochemistry of HRP. Due to the electrocatalytic effect of AuNPs-SBA-15 composite, the biosensor exhibits a sensitive response to H_2O_2 generated from enzymatic reactions (Zhang et al. 2009). Another study exploited the application of mesoporous SBA-15 in entrapping HRP and constructed an amperometric GA/SBA-15(HRP)/PANI/Pt biosensor by immobilizing the SBA-15(HRP) on the electrochemically synthesized PANI film onto a Pt electrode. The composite biosensor was characterized and evaluated for the detection of H_2O_2

by cyclic voltammetry. Furthermore, its linear correlation, sensitivity and stability were also investigated. The results demonstrated that the constructed biosensor displayed a fine linear correlation between cathodic response and H_2O_2 concentration with enhanced sensitivity (William III et al. 2007).

4.4. Gatekeeping

A system intended for the delivery of a drug or gene needs to fulfil certain criteria in order to attain the release of the drug or gene in a suitable concentration at the chosen target in a given amount of time to achieve the desired therapeutic properties.

The main advantage of these drug delivery systems is the use of chemical entities like nanoparticles as gate keepers for the regulation of the encapsulation and release of the drug molecules. These types of drug delivery systems show zero premature release in their performance, which is very significant when the substances to be delivered are toxic (Slowing et al. 2008; Radu et al. 2004).

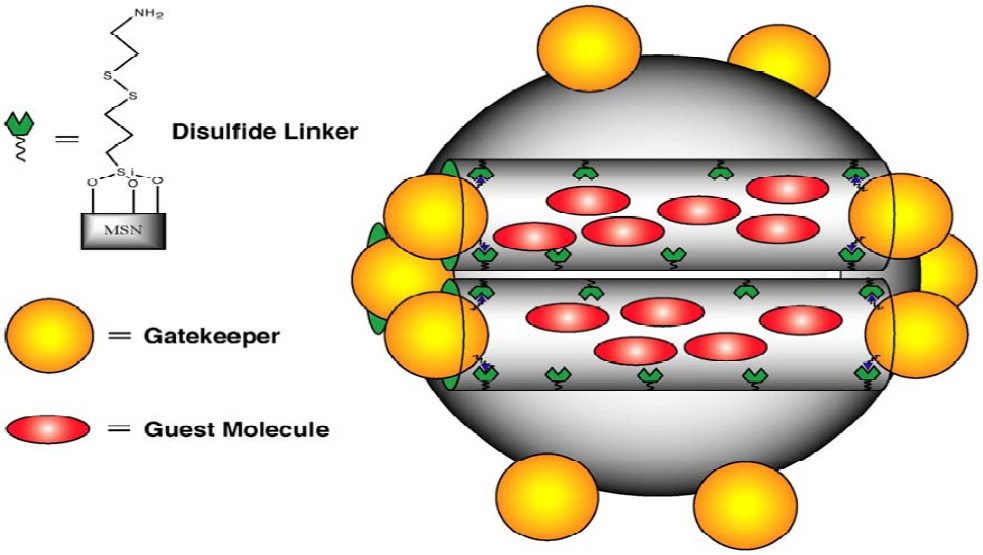
In addition, the ability to closely monitor the release of drugs or genes the precise control on the location of target and the timing of the release of the drug would be very advantageous for many site – specific delivery applications. These MSN based stimuli-responsive controlled drug release systems have real potential to fulfil the above requirements. Many MSN-based nano-devices are achieved by the development of photochemical, pH-responsive, and redox-active gatekeepers (Figure 7).

Radu *et al.* (2004) developed a synthetic strategy for the multifunctionalization of mesoporous silica nanoparticle (MSN) materials as gatekeepers in a Redox-controlled drug delivery system, which involves MSN capped-off with cadmium sulfide nanoparticles (CdS). Here the CdS is chemically attached to the MSN through a disulfide linker, which is chemically labile and iseasy to cleave with many disulfide reducing agents, such as dithiothrietol (DDT) and mercaptoethanol (ME).

Vancomycin and ATP are used as guest molecules; the capping ability of CdS was tested by suspending that MSN in phosphate-saline buffer and it has been observed that no leaching of guest molecule occurred. The release properties of the CdS-MSN system are evaluated *in vitro* by using different concentrations of reducing agents.

The biocompatibility and utility of the CdS-MSN system is demonstrated by site-selective stimulation of astrocytes. Thus it is observed that the CdS-MSN system is very useful as a stimuli-responsive redox controlled drug delivery system (Torney et al. 2007). Kim *et al.* (2009) described the cyclodextrin covered porous silica nanoparticles (Si-MPs) exhibited enzyme responsive characteristics when cyclodextrin gatekeepers on the surface of Si-MPs were hydrolyzed by α-amylase to release guest molecules from the porous reservoir.

Not only solid nanoparticles like CdS NP,Fe_3O_4 NP, Au NP but also flexible organic molecules are used as gatekeepers for MSNs. Organic molecules like coumarin are used in reversible, photo–triggered, controlled release mesoporous silica (MCM-41), diaminoethylenepropylsilane derivative used in the development of an ionically-controlled mesoporous silica sensor. The combination of supramolecular assemblies with mesoporous silica materials resulted in organic or inorganic hybrid materials with highly improved functionalities . Lai *et al.* (2003) synthesized a poly(lactic acid) coated MCM-41-type



Source: With permission from Slowing et al. 2008.

Figure 7. Representation of an MSN loaded with guest molecules and end-capped with a general gatekeeper.

Table 1. Some of the Gate keeping systems applied in the release of various molecules for MSN

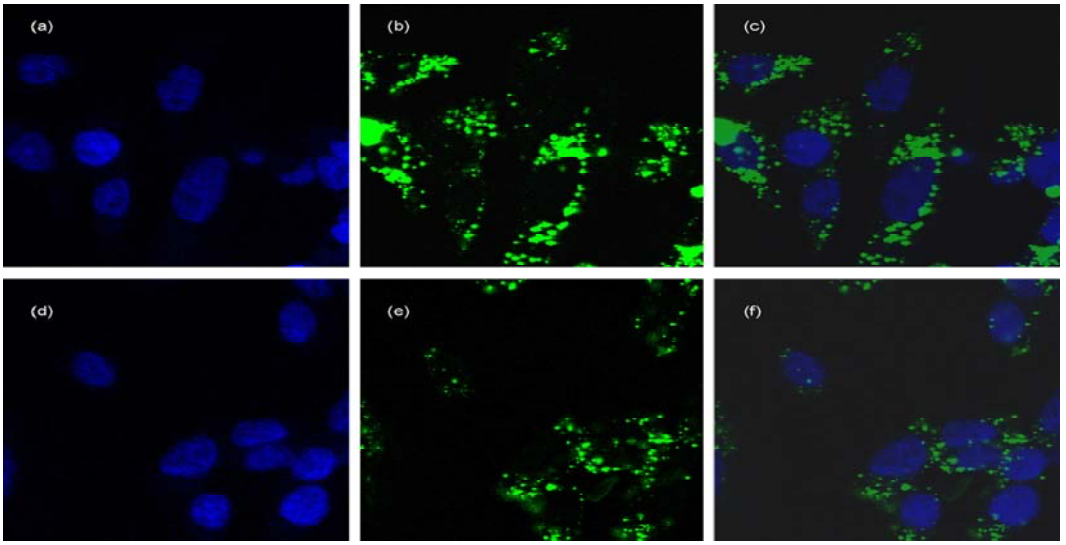
Gate keeper	Stimulus	Trigger	Guest molecule
CdS-Nanoparticles	Redox	Reducing agent(DTT,ME)	ATP, Vancomycin
Fe_3O_4-NanoParticles	Redox	Reducing agent (DTT,DHLA)	Fluorescein
Au-Nanoparticles	Redox	Reducing agent (DTT)	β-oestradiol, DNA

Source: With permission from Slowing et al. 2008.

mesoporous silica nanoparticles (PLA-MSN) material by utilizing the PLA layer as a gatekeeper which can serve as a fluorescence sensor system for the detection of amino-containing neurotransmitters in neutral aqueous buffer. Lai *et al.* also investigated the molecular recognition events between several structurally simple neurotransmitters, i.e., dopamine, tyrosine, and glutamic acid.

5. BIOCOMPATIBILITY OF SILICA NANOPARTICLES

The property of a medical device being biologically compatible in terms of not producing toxicity or generating an immune response remains an issue with all drug delivery systems. The ability to control the particle morphology and surface properties of mesoporous silica-based functional materials for both biotechnology and biomedical applications is of



Source: With permission from Trewyn et al. 2008.

Figure 8. Fluorescence confocal micrographs of CHO cells incubated with 50µgmL^{-1} T-FITC-MSN (a–c) and S-FITC-MSN (d–f). (a and d) Fluorescence image excited at 340 nm to visualize the cell nuclei stained with DAPI. (b and e) Fluorescence image excited at 488 nm to visualize the FITC doped MSN that have been.

fundamental importance. Many reports (Radu et al. 2004; Slowing et al. 2006; Torney et al. 2007) have demonstrated the importance of morphological control and surface functionalisation on improved *in-vitro* biocompatibility of MSNs.

The biocompatibility of two MCM-41 fluorescein labeled mesoporous silica nanoparticles with different shapes and size was determined in Chinese hamster ovarian (CHO) cells. Spherical fluorescein isothiocyanate-doped MSNs (S-FITC-MSN) and tube shaped fluorescein isothiocynate-doped MSNs (T-FITC-MSN) were prepared following surfactant-template synthesis. The shape and particle size of the MSNs was determined under SEM which showed S-FITC-MSN with all certainty to be monodispersed material consisting of spherical particles with a narrow size distribution ranging from 80 to 150nm in particle diameter.

The SEM micrograph of the T-FITC-MSN on the other, also confirmed the shape of the MSN to have tube-like particle morphology with an average particle size of 600nm in length and 100nm in width. Furthermore, the two different shape MSNs (T-FITC-MSN and S-FITC-MSN) of concentration 50µg/ml were incubated overnight (12h) in CHO cells. The biocompatibility of the MSNs on the CHO cells was investigated using a fluorescence confocal microscope to show the presence of healthy round nuclei that were stained blue using 4,6-diamidino-2-phenylindole (DAPI) as seen in Figure 8.

The existence of oval and healthy-looking nuclei observed under the microscope indicates that the two different shaped MSNs are in fact biocompatible and do not affect the cell cycle in a detrimental way during the process of endocytosis (Trewyn *et al*. 2008).

Mesoporous silica nanoparticles apart from being multifunctional have also demonstrated high biocompatibility as indicated in previous studies which show that MSN are biocompatible and accumulate in tumor cells (Lu et al. 2010; Brian et al. 2008). In a relative study Lin *et al.* (2009) reported size-controlled multifunctional mesoporous silica

nanoparticles (Fe_3O_4@FITC-MSNs) having large surface areas, embedded luminescence, high magnetization, and excellent aqueous dispersity were prepared by using a simple one-pot synthesis. MTT and hemolysis assays were employed to evaluate the biocompatibility of the smallest synthesized multifunctional mesoporous silica nanoparticles (33nm) on HeLa, PC-12, and HCT-116 cell lines. The MTT results indicated that HeLa, PC-12, and HCT-116 cell viability were not affected even with 12 h exposures of up to 200μg/mL of the functionalised mesoporous nanoparticles. The hemolytic activity of the same sized functionalised mesoporous silica nanoparticles also showed no hemolysis of red blood cells at a concentration less than 100ug/ml of the 33nm functionalised MSN. The biocompatibility and cellular uptake of FITC-MSNs on human mesenchymal stem cells (hMSCs) was also investigated by Huang *et al.* (2008). The objective of the study was to investigate the effect of MSNs on osteogenesis induction and to examine their biocompatibility in hMSCs. Their findings indicated that the uptake of MSNs into hMSCs did not affect the cell viability, proliferation and regular osteogenic differentiation of the cells. Furthermore, the internalization of MSNs induced actin polymerization and activated the small GTP-bound protein RhoA.

Rhodamine B (RhB) (He *et al.* 2007) covalently grafted SBA-15 structured mesoporous silica nanoparticles (MSNs-RhB) with high surface area, large pore volume, uniform particle size and positively charged surface were developed and their blood compatibility was determined by evaluating the hemolysis and coagulation behaviours with various concentrations on LX-2 cells. Their findings shows that the positive surface potential of SBA-15 type MSNs-RhB co-condensed with quaternary ammonium groups (that could curb the damage to RBC membranes) linked with the trimethyl-ammonium head groups. Good blood compatibility of the MSNs-RhB was reported. The following findings were also reported (i) hemolysis percentages of both SBA-15 type MSNs and MSNs-RhB increased with increase in nanoparticle concentration (ii) the hemolysis percentages of SBA-15-type MSNs-RhB was remarkably lower than SBA-15-type MSNs at the same concentrations (iii) difference in the haemolytic activities between SBA-15-type and MCM-41-type MSNs could be attributed to their mesopore structures (He *et al.* 2007).

Surface functionalized MSNs with various amounts of positively charged quaternary ammonium group was also reported by Chung *et al.* (2007) to be quite biocompatible and also capable of enhancing the uptake of MCM-41 type MSNs for more efficient cellular labelling. The differentiation potential of human mesenchymal stem cells into adipocytes and osteocytes was reported not to be affected by the different surface charge of the red emitting rhodamine B dye (RITC) attached MSNs (RITC–MSNs) as there were no significant difference observed in the oil-red O stain assay between particle-treated and non-treated cells. Similar results of biocompatibility were also reported for 3T3-L1 cells illustrated using cytotoxity assay, cell proliferation examination and adipogenic differentiation (Chung *et al.* 2007).

5.2. Cellular Uptake

Cellular uptake of molecules depends on specific binding of the molecule and the membrane-bound receptors and materials for which cells lack receptors can easily be taken up

by adsorptive endo-cytosis or by fluid phase pinocytosis. The mechanism of the cellular uptake of the biological system governs various cellular behaviours such as cell growth, apoptosis, adhesion, migration, cell differentiation, survival and tissue organisation[116]. Therefore understanding the mechanism of cellular uptake of silica nanoparticles and systemic level trafficking is essential for future development of new strategies for the development of efficient drug delivery system of the nanoparticles. Many physicochemical properties of the nanoparticles such as particle size, shape, chemical composition and surface chemistry has been said to affect the cellular uptake ability of the nanoparticles (Vallhov *et al*. 2007; Chung et al. 2007; Tao et al 2009).

Functionalised MSN by aminofluorescein (AMF) with diethylenetriaminepentaacetic acid spacer molecules, which provide free carboxylic groups for binding cell-specific ligands such as folate, was reported by Fisichella *et al.* (2010). AMF was used to explore cellular uptake by HeLa cells using confocal microscopy and flow cytometry. The functionalized nanoparticles (MSN-AMF) penetrated efficiently into HeLa cell cytoplasm through a clathrin dependent endocytosis mechanism as observed under the microscope. The number of endocytosed MSN-AMF was also reported to be enhanced when folate is used as a targeting molecule. Uptake kinetics also revealed that most of MSN-AMF was internalized within 4 h of incubation.

In order to make surface functionalized MSN a more efficient drug delivery system Xia *et al.* (2009) modified the surface of the MSN particles by a functional group that enhances cellular uptake and allows nucleic acid delivery in addition to traditional drug delivery. In their study, Polyethyleneimine (PEI) polymers was non-covalently attached to the surface of the MSN in order to increase the cellular uptake of the MSN and also to generate a cationic surface to which DNA and siRNA constructs could easily be attached. Thus, by increasing the cellular uptake of the MSN *via* means of functionalisation, they were able to demonstrate that MSN when functionalised enhances cellular uptake for the delivery of the hydrophobic anticancer drug, paclitaxel, to pancreatic cancer cells (HEPA-1).

The effect of shape of mesoporous silica nanoparticles on cellular uptake and cell function was also investigated (Huaug *et al*. 2010). Different shaped MSNs were synthesized by condensation. To confirm the cellular uptake of the three different shaped MSN synthesised, TEM images of the three different shaped MSN incubated in a human melanoma (A375) cells were evaluated alongside fluorescent images obtained using a confocal microscope. The TEM images were reported to show encapsulation of the three different shaped MSN in the vesicular or cytosolic compartments of the A375 cells. The MSNs was demonstrated to be taken up by nonspecific cellular uptake and merge with endosomes which subsequently escapes into the cytoplasm. Presence of the MSN particles conjugated with FITC and RITC in the cytoplasm was also confirmed in their study with the images obtained from the fluorescence confocal microscope study. They further concluded that the Shape of the MSN plays a role in the internalization of the nanoparticles.

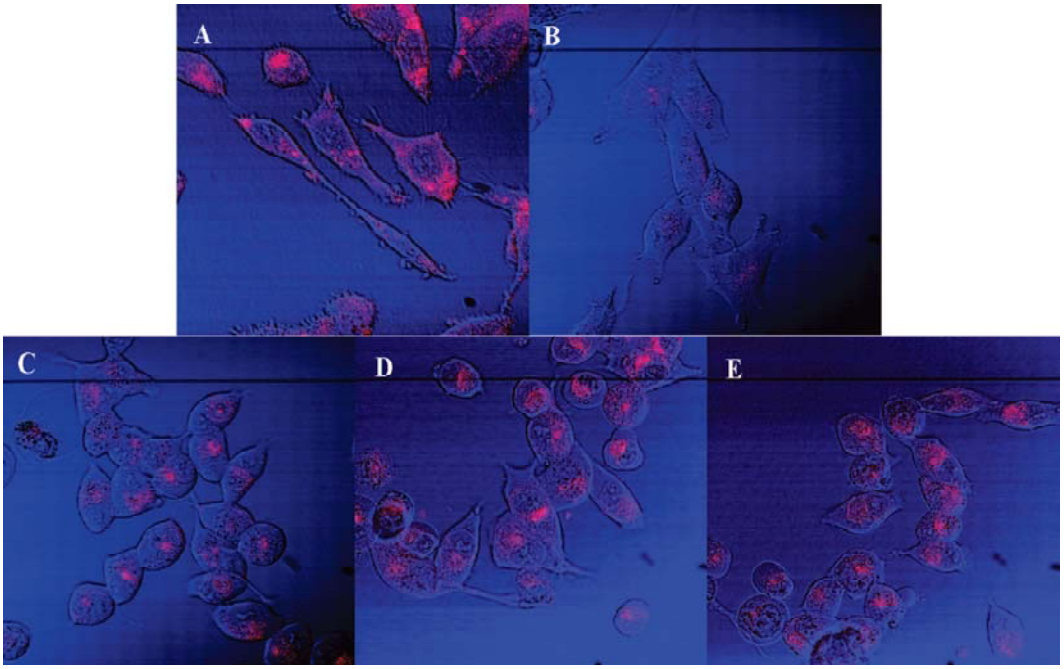
The cellular uptake of series of organically functionalised MCM-41 type MSN with different pore sizes 5.7 nm and 2.5 nm respectively was determined in human cervical cancer cells (Hela). The exterior particle surface of **"**ethoxycarbonyl-protected" phenanthridium aminopropyl LP-MSN (PAP-LP-MSN) and the interior surface phenanthridium aminopropyl MSN (AP-PAP-MSN) functionalised with oligonucleotide intercalating phenanthridinium show that PAP-LP-MSN nanoparticles with the phenanthridium groups located on the exterior surface were able to bind to cytoplasmic oligonucleotides, such as messenger RNAs,

of HeLa cells causing severe cell growth inhibition (Vivero-Escoto *et al*. 2010). Although phenanthridinium itself is a cell membrane impermeable molecule, their studies demonstrated that both phenanthridinium-immobilized PAP-LP-MSN and AP-PAP-MSN materials could indeed be internalized by live human cervical cancer cells (HeLa). Fluorescent images observed within the cell bodies of the human cervical cancer cells giving strong indications that the particles surface functionalised MSN were indeed endocytosed by the Hela cells was also reported.

Yu *et al.* (2009) in their studies on the effect of surface functionality of magnetic silica nanoparticles on cellular uptake by glioma cells *in vitro* also reported that different surface functionalities regulate the ability of the nanoparticles to cross the cell membranes. In their studies amine- and ester-terminated polyamidoamine (PAMAM) dendrimers were used to functionalize fluorescein-doped magnetic mesoporous silica nanoparticles (FMNPs) to evaluate the effect of surface functionality on cellular uptake by glioma cells. The uptake of the nanoparticles was confirmed in their studies as green fluorescence of FITC and was clearly seen around the nucleus which indicates nanoparticle internalization within the cells. TEM images were reported to reveal the plasma membrane invagination caused by the binding of the nanoparticles to the cell surface. The effect of surface charge on cellular uptake efficiency of functional FMNPs was further investigated. Functionalised FMNPs with G2 PAMAM dendrimers and methyl acrylate (MA) were incubated at different concentration and time in 9L glioma cells. Higher cellular uptake was reported for FMNPs functionalised with (cationic) G2 PAMAM compared to the neutral FMNPs functionalised with methyl acrylate. The cellular uptake efficiency was attributes to the electrostatic interaction between cationic amino-functionalised nanoparticles and the anionic cellular membrane. This difference confirmed in this study gives shows the use of surface charge in MSN for the regulation of cellular uptake.

In addition to the effect of surface charge of MSN on cellular uptake Chung *et al.* (2007) investigated the cellular uptake of positively charged MSN in 3T3-L1 cells and human mesenchymal stem cells (hMSCs). A clear correlation of positive surface charge and number of fluorescence labelled cells mainly observed with 3T3-L1 cells compared to hMSCs cells was reported. The uptake mechanism of unmodified MSNs was suggested to be a clathrin- and an actin-dependent endocytosis. The findings illustrated that, MSNs uptake by hMSCs could be regulated by a threshold of positive surface charge and also imply that surface charge modulation on MSNs uptake is specific to cell type.

Kumar et al. (2008) reported the significantly difference in the cellular uptake of bioconjugated nanoparticles. Organically modified silica (ORMOSIL) nanoparticles with fluorophore rhodamine-B, and surface-functionalized with a variety of active groups such as hydroxyl, thiol, amine, and carboxyl for targeted delivery to pancreatic cancer cell lines was reported in the study. The confocal microscope images as seen in Figure 9 demonstrate the cellular uptake of amino-terminated nanoparticles to be much higher than that of the carboxyl-terminated. Thus their study speculates that favorable electrostatic interaction between the cationic amino-functionalized nanoparticles and anionic cellular membrane influences cellular uptake.



Source: With permission from Kumar et al. 2008.

Figure 9. Confocal images of MiaPaca cells treated with RORM-NH2 (panel A), RORM-COOH nanoparticles (panel B), transferrinconjugated RORM-COOH (panel C), anti-claudin 4-conjugated RORM-COOH (panel D), and anti-mesothelin conjugated RORM-COO (panel E) nanoparticles.

5.3. Cytotoxicity

Although mesoporous silica nanoparticles are currently used in many modern biomedical applications, there is a lack of information on the health impact of synthesised silica nanoparticles. The toxicology of inhalation of the crystalline form of silica has been a well established route and historical association with the development of severe respiratory disease (Wang et al 2007; Fenoglio et al 2000; Gazzano et al 2007). However, the toxicities of the amorphous synthesised silica macro and nano-sized particles have not yet been widely investigated (Heikkila et al 2009).

The cytotoxicity of mesoporous silica nanoparticles in relation to different cell lines has been widely investigated. It has been observed that factors such as particle size, shape and funtional groups of the silica plays an important role in determining the cytotoxicity. In order to elucidate silica nanoparticles induced cyto-toxicity and its mechanism Wang *et al (*2009) studied the effect of two different particle sized silica nanoparticles (20nm and 50nm) on cultured human embryonic kidney (HEK293) cells. A dose range of 20 to 100ug of two different sized silica nanoparticles were incubated in the culture HEK293 cells. The MTT assay and morphology study revealed silica nanoparticles induced cytotoxicity, which is size, time and dose dependent. The greater toxicity observed for the 20nm silica nanoparticles compare to the 50nm silica nanoparticle is said to be as a result of larger surface area which is generally associated with smaller particle size and hence easier penetration into the cell (Wang *et al*. 2009). It is however believed that the ability of silica to generate reactive oxygen

species (ROS) contributes to their ability to cause cell apoptosis. Increase in intracellular ROS level and reduction in GSH content were also observed in the above studies after 24 hours of cells exposure to silica nanoparticles which suggests that free radical species were generated by the silica nanoparticles hence reduced intracellular antioxidant levels and cell viability (Allison *et al*. 1980)

The cytotoxicity of monodispersed amorphous spherical silica particles of different sizes on endothelial cells was also investigated. Monodispersed amorphous spherical nanoparticles with different sizes and surface area introduced into EAHY926 endothelial cell line demonstrated size and surface dependence cytotoxicity of the monodispered silica nanoparticles. Release of lactate dehydrogenase (LDH) and decrease in cell viability as determined by the tetrazolium reduction (MTT assay) indicated cytotoxic effects of the particles. Particles with smaller size diameter (14,15 and 16nm) were reported to have lesser cytotoxic effect compare to the bigger particle size diameter of 19 and 60nm. In addition, faster cell death was also reported for the smaller particle sized silica nanoparticles (Napierska *et al.* 2009).

Oxidative stress and pro-inflammatory response induced by nanoparticles seems to be one of the toxic mechanisms recently focused on. Silica nanoparticles were evaluated by Park *et al.* (2009) in ICR mice and RAW264.7 cell line. In order to verify the pro-inflammatory mechanism of silica nanoparticles *in vivo*, an *in-vitro* study using the RAW264.7 cell line derived from mouse peritoneal macrophage was carried out. Treatment of silica nanoparticles on the cultured cell line was reported to have generated reactive oxygen species (ROS) with decreased intracellular GSH and also increased the level of nitric oxide released from the cultured macrophage cell line thus suggesting that silica nanoparticles generate ROS triggering the pro-inflammatory responses both *in-vivo* and *in-vitro*.

Tao *et al.* (2008) reported the cytotoxicity of two MSNs types (MCM-41 and SBA-15) with pore diameters of 31 and 55 Å on cellular bioenergetics in terms of cellular respiration and ATP content in myeloid and lymphoid cells as well as in isolated mitochondria. MSNs with larger size and larger pores showed concentration and time-dependent inhibition of cellular respiration upon exposure to cells, and both mesoporous silica nanoparticles were reported toxic on the isolated mitochondria.

Evaluation on the influence of size and concentration of mesoporous silica nanoparticles with particle size of 190, 420 and 1220nm on cytotoxicity in human breast cancer cells and monkey kidney cells was also reported by He *et al.* (2009). The cytotoxicity of the particles was associated with particle size. Mesoporous silica of 190 and 420nm in diameter showed significant cytotoxicity at concentrations more than 25μg/ml and MSN particles of 1220nm in diameter showed low cytotoxicity at concentration of 480μg/ml. The smaller the particles the larger the surface area therefore smaller sized particles were suggested to be more easily endocytosed and subsequently located within lysosomes.

Surfactants are widely utilised and in some occasions ar concidered to be cytotoxic i.e. they are able to cause damage to biological membranes and release of intracellular enzymes (Dickson *et al.* 1993; Lewis *et al*. 1993). The cytotoxity of the different types of surfactants is evaluated to be in the order of cationic (CTAB)>anionic (SDBS)>non-ionic (Triton) (Grant *et al*. 1992). However, the cytotoxicity report of the surfactants were mainly based on use of free surfactants, the role of various surfactant in mesoporous silica nanoparticles is now being extensively evaluated. The cytotoxicity of three types of surfactant-templated

mesoporous silica nanoparticles (150-660nm in diameter) were evaluated on MCF-7 cells proliferation by (He *et al*. 2010). Surfactant-templated mesoporous silica nanoparticles was reported to induce cytotoxic effect in the following order CTAB@MSNs > SDBS@MSNs > Triton@MSNs. Higher particle concentrations and longer time incubation also played a role in inducing cytotoxicity. Cationic surfactant-templated mesoporous silica nanoparticles with particle concentration range of 80-320μg/ml were also reported to have a remarkably high toxicity on the MCF-7 cells with less than 5 percent cell viability.

A measure of the cytotoxicity of materials that are used *in vivo* as drug delivery vehicles is very important and must be clearly defined. Mesoporous silica nanoparticles as drug delivery vehicles are usually conjugated with various functional groups. Apart from verifying the toxicity of a drug, the measure of the toxic effect of other materials used as the drug delivery vehicles must also be clarified. The cytotoxicity of non-and functionalised types of MCM-41 mesoporous silica nanoparticles was determined on human neuroblastoma (SK-N-SH) cells: a cancer of the sympathetic nervous system. The toxic effect of MSNs was reported in terms of Q_{50} i.e the number of particles required to reduce normal cell growth by 50 %. MCM-41 and two of its functionalised analogs, AP-T, which has grafted aminopropyl groups and MP-T, which has grafted mercaptopropyl groups was reported to kill human neuroblastoma. The Q50 of the nanoparticles was reported to increase in the order of MCM-41 < MP-T < AP-T ≈ silica nanospheres. The data suggested that the most toxic mesoporous silica nanoparticles are those with the largest BET surface area. However the nature of the attached functional group also plays a role on cytotoxicity and thus cannot be ruled out (Di Pasqua *et al*. 2008) as seen with the spherical silica nanoparticles, which have relatively low surface area and exhibit cytotoxicity comparable to AP-T with a much higher surface area.

Vivero-Escoto *et al.* (2010) reported the cytotoxicity of HeLa cells exposure to synthesised interior grafted phenanthridium aminopropyl MSN (AP-PAP-MSN) to be significantly lowered upon endocytosis by human cervical cancer cells where the same oligonucleotide intercalation molecules were anchored inside the pores. It was envisioned in their report that the approach of combining selective functionalization of the two different surfaces (exterior particle and interior pore surfaces) with morphology control of mesoporous silica nanoparticles would lead to a new generation of nano-devices with tunable biocompatibility and cell membrane trafficking properties for many biomedical applications.

REFERENCES

[1] Allison DC, Riddolpho P (1980) Cytotoxicity of Mesoporous Silica nanomaterials. *Journal of Histochemistry and Cytochemistry*, 28:8520-8530.

[2] Andersson J, Rosenholm J, Areva S, Linden M (2004) Influences of Material Characteristics on Ibuprofen Drug Loading and Release Profiles from Ordered Micro- and Mesoporous Silica Matrices. *Chem. Mater*. 16:4160 – 4167.

[3] Attard GS, Glyde JC, Go¨ltner CG (1995) Liquid-crystalline phases as templates for the synthesis of mesoporous silica .*Nature*, 378: 366-368.

[4] Azais T, TournQ-PQteilh C, Aussenac F, Baccile N,Coelho C, Devoisselle JM, Babonneau F (2006) Solid-State NMR Study of Ibuprofen Confined in MCM-41 Material. *Chem. Mater*. 18: 6382 – 6390.

[5] Bagshaw SA, Pinnavaia TJ (1996) Mesoporous alumina molecular sieves. *Angew. Chem.Int. Ed. Engl*. 35: 1102.

[6] Bagshaw SA, Prouzet E, Pinnavaia (1995) Templating of mesoporous molecular-sieves by nonionic polyethelyne surfactants. *T. J. Science*, 269: 1242.

[7] Bagwe RP, Hilliard LR, Tan W (2006) Surface Modification of Silica Nanoparticles to Reduce Aggregation and Nonspecific Binding. *Langmuir,* 2006(*22)* 4357-4362.

[8] Bagwe RP, Yang C, Hilliard LR, Tan W (2004) Optimization of dye-doped silica nanoparticles prepared using a reverse microemulsion method. *Langmuir*, *20* (19):8336–8342.

[9] Balas F, Manzano M, Colilla M et al.(2008) *L*-Trp adsorption into silica mesoporous materials to promote bone formation. *Acta Biomater.***4**:514–22.

[10] Balas F, Manzano M, Horcajada P, et al. (2006) Confinement and controlled release of bisphosphonates on ordered mesoporous silica-based materials. *J Am Chem Soc*.128:8116–7.

[11] Beck JS, Vartuli JC, Roth WJ, Leonowicz ME. Kresge CT, Schmitt KD,.Chu CTW, Olson D, Sheppard EW, Mccullen SB, Higgins JB, Schlenkert JL (1992) A New family of mesoporous molecular sieves prepared with liquid crystals templates. *American Chemical society*, 114:10834-10843.

[12] Bharali DJ, Klejbor I, Stachowiak EK, Dutta P, Roy I et al (2005) Organically modified silicananoparticles: A nonviral vector for in vivo gene delivery and expression in the brain. *The National Academy of Sciences*, 102: 11539–11544.

[13] Trewyn .BG, Jennifer A. Nieweg, Yannan Zhao and Victor S.-Y. Lin (2008) Biocompatible mesoporous silica nanoparticles with different morphologies for animal cell membrane penetraton *Chemical Engineering Journal*, 137(1): 23-29.

[14] Burns A, Ow H, Wiesner U (2006) Fluorescent core–shell silica nanoparticles: towards ‘‘Lab on a Particle’’ architectures for nanobiotechnology. *Chem. Soc. Rev*. 35:1028–1042.

[15] Cagnol F, Grosso D and Sanchez C (2004) A general one-pot process leading to highly functionalised ordered mesoporous silica films. *Chem . Commun*. 1 7 4 2 – 1 7 4 3.

[16] Casasus R, Marcos MD, Martinez-Manez R, Ros-Lis JV, Soto J, Villaescusa LA, Amoros P, Beltran D, Guillem C, Latorre, J (2004) Toward the development of ionically controlled nanoscopic molecular gates, *Journal of American Chemical Society*. 126: 8612-8613.

[17] Chang B, Guo J, Liu C, Qian J, Yang W, (2010) Surface functionalisation of magnetic mesoporous silica nanoparticles for controlled drug release. *J. Mater. Chem.* 20:9941-9947.

[18] Che S, Garcia-Bennett A E, Liu X (2003) Synthesis of Large-Pore Ia3d Mesoporous Silica. *Angew. Chem. Int*. 42(1):3930 –3934.

[19] Chen AM, Zhang M, Wei D, Stueber D, Taratula O, Minko T, He H. (2009) Co-delivery of doxorubicin and Bcl-2 siRNA by mesoporous silica nanoparticles enhances the efficacy of chemotherapy in multidrug-resistant cancer cells. *Small*, 5(23):2673-7.

[20] Cho Y, Shi R, Borgens RB, Ivanisevic A, 2008. Functionalized mesoporous silica nanoparticle-based drug delivery system to rescue acrolein-mediated cell death. Nanomedicine (Lond) 3:507-19.

[21] Chung T, Wub S, Yao M, Lua C, Linb Y, Hung Y, Mou C, Chena Y, Huang D (2007) The effect of surface charge on the uptake and biological function of mesoporous silica

nanoparticles in 3T3-L1 cells and human mesenchymal stem cells. *Biomaterials*, 28:2959–2966.

[22] Das S, Jain TK, Maitra A (2002) Inorganic-organic hybrid nanoparticles from n-octyl triethoxy silane. *J. Colloid Interface Sci*. 252: 82–88.

[23] Deng G, Markowitz M, Kust P, Gaber GP (2000) Control of surface expression of functional groups on silica particles. *Materials Science and Engineering*, 11:65–172.

[24] Di Pasqua AJ, Sharma KK, Shi Y, Toms BB, Ouellette W, Dabrowiak JC, Asefa T (2008) Cytotoxicity of mesoporous silica nanomaterials. *Journal of Inorganic Biochemistry*, 102(7):1416-1423.

[25] Dickson FM, Lawrence JN, Benford DJ (1993) Surfactant-induced cytotoxicity in cultures of human keratinocytes and a commercially available cell line (3T3). *Toxicol In Vitro*, 7:381–384.

[26] Doadrio JC, Sousa EMB, Izquierdo-Barba I et al. (2006) Functionalization of mesoporous materials with long alkyl chains as a strategy for controlling drug delivery pattern. *J Mater Chem*. 16:462–7.

[27] Fenoglio I, Croce A, Di Renzo F, Tiozzo R, Fubini B (2000) Pure silica zeolites(porosils)as model solids for the evaluation of the physicochemical features determining silica toxicity to machroaphages. *Chemical Research in Toxicology*, 13: 489-500.

[28] Ferey G, Mellot-Draznieks M, Serre C, Millange F, Dutour J, Surble S, Margiolaki I (2005). *Science*, 309: 2040 – 2042.

[29] Fisichella M, Dabboue H, Bhattacharyya S, Lelong G, Saboungi ML, Warmont F, Midoux P, Pichon C, Guérin M, Hevor T, Salvetat JP (2010) Uptake of functionalized mesoporous silica nanoparticles by human cancer cells. *J Nanosci Nanotechnol*. 10(4):2314-2324.

[30] Fubini B, Hubbard A (2003) Reactive oxygen species and reactive nitrogen species generation by silica in inflammation and fibrosis. *Free Radical Biolody and Medicine*, 34: 1507-1516.

[31] Gazzano E, Turci F, Foresti E, Putzu MG, Aldieri E, Silvagno F, Lesci IG, Tomatis M, Riganti C, Romano C, Fubini B, Roveri N, Ghigo D (2007) Iron loaded synthetic chrysotile: A new model solid for studying the role of iron in asbestos toxicity. *Chemical Research in Toxicology*, 20:380-387.

[32] Giri S, Trewyn BG, Stellmaker MP and Lin VSY (2005) Stimuli-Responsive Controlled-Release Delivery System Based on Mesporous Silica Nanorods Capped with Magnetic Nanoparticles. Angewandte Chemie International Edition 44:5038.

[33] Go¨ltner CG, Antonietti M. (1997) Preparation of amino-functionalized mesostructured cellular foams and application as hosts for large biomolecules. *Adv. Mater*. 9: 431.

[34] Grant RL, Yao C, Gabaldon D, Acosta D (1992) Evaluation of surfactant cytotoxicity potential by primary cultures of ocular tissues: I. characterization of rabbit corneal epithelial cells and initial injury and delayed toxicity studies. *Toxicol*. 76:153–176.

[35] Guzman et al. (2006) Environmental risks of nanotechnology: national nanotechnology initiative funding. *Environmental science technology*, 40:1401-1407.

[36] Ha SH, Camalier CE, Beck GR, and Lee JK (2009) New method to prepare very stable and biocompatible fluorescent silica nanoparticlesw. *Chem. Commun*., 2881–2883.

[37] Han L, Sakamoto Y, Terasaki O, Li Y, Che S (2006) Synthesis of carboxylic group functionalized mesoporous silicas (CFMSs) with various structures. *Journal of Materials Chemistry*, 17: 1216–1221.

[38] Hata H, Saeki S, Kimura T, Sugahara Y, Kuroda K (1999) Adsorption of Taxol into Ordered Mesoporous Silicas with Variou Pore DiametersChem. Mater. 11, 1110 – 1119.

[39] He Q, Shi J, Chen F, Zhu M, Zhang L (2010) An anticancer drug delivery system based on surfactant-templated mesoporous silica nanoparticles. *Biomaterials*, 31(12):3335-3346.

[40] He Q, Zhang J, Chen F, Guo L, Zhu Z, Shi J (2007) An anti-ROS/hepatic fibrosis drug delivery system based on salvianolic acid B loaded mesoporous silica nanoparticles. *Biomaterials*, 28:2959–2966.

[41] He Q, Zhang Z, Gao Y, Shi J, Li Y (2009) Intracellular localization and cytotoxicity ofspherical mesoporous silica nano- and microparticles. *Small*, 5:2722-2729.

[42] Heikkilä T, et al. (2009) Cytotoxicity study of ordered mesoporous silica MCM-41 and SBA-15 microparticles on Caco-2 cells. European *Journal of Pharmaceutics and Biopharmaceutics*, 74: 483-494.

[43] Horcajada A, Pamila R, Perez-Pariente J, Vallet-Regi M (2004) Influence of pore size of MCM-41 matrices on drug delivery rate. *Micropor. Mesopor. Mater*. 68: 105 – 109.

[44] Horcajada P, Serre C, Vallet-Regi M, Sebban M, Taulelle F, FQrey G (2006) Angew. Chem. 118: 6120 – 6124; Angew. Chem. Int. Ed. 45: 5974 – 5978

[45] Huang D, Tsai-Hua Chung, Yann Hung, Fang Lu, Si-Han Wu, Chung-Yuan Mou, Ming Yao and Yao-Chang Chen (2008) Internalization of mesoporous silica nanoparticles induces transient but not sufficient osteogenic signals in human mesenchymal stem cells. *Toxicology and Applied Pharmacology*, 23(2):208-215.

[46] Huang X, Teng X, Chen Dong, Tang F, He J (2010) The effect of the shape of mesoporous silica nanoparticles on cellular uptake and cell function. *Biomaterials*, 31:438–448.

[47] Hudson SP, Padera RF, Langer R, Kohane DS (2008) The biocompatibility of mesoporous silicates. *Biomaterials*, 29:4045-55.

[48] Huh S, Jerzy W, Wiench W, Yoo J, Pruski M, Lin, VSY (2003) Organic Functionalization and Morphology Control of Mesoporous Silicas via a Co-Condensation Synthesis Method. *Chem. Mater*. 15 (22): 4247–4256.

[49] Huo Q, Margolese DI, Ciesla U, Demuth DG, Feng P, Gier TE, Sieger P et al (1994) Rapid synthesis of mesoporous silica with micrometer sized hexagonal prism structure. *Chem. Mater*. 6: 1176.

[50] Izquierdo-Barba I, Martinez A, Doadrio A L, Perez- Pariente J, Vallet-Regi M (2005) Release evaluation of drugs from ordered three-dimensional silica structures. *Eur. J. Pharm. Sci*. 26: 365 – 373.

[51] Jain TK, Roy I, De TK, Maitra A (1998) Nanometer silica particles encapsulating active compounds: A novel ceramic drug carrier. *J. Am. Chem. Soc*. 120: 11092–11095.

[52] Jeon YH et al. (2010) In Vivo Imaging of Sentinel Nodes Using Fluorescent Silica Nanoparticles in Living Mice. *Mol Imaging Biol*. 12(2):155-62.

[53] Katiyar A, Yadav S, Smirniotis PG, Pinto NG (2006) Synthesis of ordered large pore SBA-15 spherical particle for adsorption of biomolecules. *Journal of Chromatography*, 1122:13-20.

[54] Kim HK et al. (1999) Highly Efficient Organic/Inorganic Hybrid Nonlinear Optic Materials via Sol−Gel Process: Synthesis, Optical Properties, and Photobleaching for Channel Waveguides. *Chem. Mater*. 11(3):779-788.

[55] Knopp D, Tang D, Niessner R (2009) Review: Bioanalytical applications of biomolecule-functionalized nanometer-sized doped silica particles. *Analytica Chimica Acta*, 647:14–30.

[56] Kresge CT, Leonowicz ME, Roth WJ, Vartuli J C, Beck J S (1992) Ordered mesoporous molecular sieves synthesized by a liquid-crystal template mechanism. *Nature*, (London) 359: 710-712.

[57]Kumar R, Roy I, Ohulchanskyy TY, Goswami LN, Bonoiu AC, Bergey EJ, Tramposch KM, Maitra A, Prasad PN (2008) Covalently Dye-Linked, Surface-Controlled, and Bioconjugated Organically Modified Silica Nanoparticles as Targeted Probes for Optical Imaging. ACSnano, 2:449-456.

[58] Lai CY, Trewyn BG, Jeftinija DM, Jeftinija K, Xu S, Jeftinija S,Lin VSY (2003) A Mesoparticle silica nanosphere based carrier system with chemically removable CdS-nanoparticle caps for stimuli-responsive controlled release of neurotransmitters and drug molecules. *Journal of the American Chemical Society*, 125: 4451-4459.

[59] Lewis RW, McCall JC. Botham PA (1993) A comparison of two cytotoxicity tests for predicting the ocular irritancy of surfactants. *Toxicol In Vitro*, 7:155–158.

[60] Lin YS, Haynes CL, (2009) Synthesis and Characterization of Biocompatible and Size-Tunable Multifunctional Porous Silica Nanoparticles. *Chem. Mater*., 21, 3979–3986.

[61] Lu et al. (2007) Mesoporous Silica Nanoparticles for Cancer Therapy: Energy-Dependent Cellular Uptake and Delivery of Paclitaxel to Cancer Cells. *Nanobiotechnology*, 3(2): 89–95.

[62] Lu J, Liong M, Li Z, Zink JI, Tamanoi F (2010) Biocompatibility, Biodistribution, and Drug-Delivery Efficiency of Mesoporous Silica Nanoparticles for Cancer Therapy in Animals. *Small*, 6(16): 1794–1805.

[63] Mal K, Fujiwara M, Tanaka Y, Taguchi T, Matsukata M (2003) Photo-Switched Storage and Release of Guest Molecules in the Pore Void of Coumarin-Modified MCM-41. *Chem. Mater*. 15: 3385 – 339.

[64] Mascharak S (2010) Synthesis of fluorescent silica nanoparticles conjugated with rgd peptide for detection of invasive human breast cancer cells. *Young scientist Journal*, 8:37-41.

[65] Monnier A, Schu¨th F, Huo Q, Kumar D, Margolese D, Maxwell RS, Stucky GD, Krishnamurty M, Petroff P, Firouzi A, Janicke M, Chmelka BF (1993), *Science*, 261:1299.

[66] Napierska D, Thomassen LC, Rabolli V, Lison D, Gonzalez L, Kirsch-Volders M, Martens JA, Hoet PH (2009) Size-dependent cytotoxicity of monodisperse silica nanoparticles in human endothelial cells. *Small,* 5(7):846-53.

[67] Oye G, Sjöblom J, Stöcker M (2001) Synthesis, characterization and potential applications of new materials in the mesoporous range. *Adv Colloid Interface Sci*. 89-90:439-66.

[68] Pandya PH, Jasra RV, Newalkar BL, Bhatt PN (2005) Studies on the activity and stability of immobilized alpha-amylase in ordered mesoporous silicas. *Microporous Mesoporous Mat*. 17: 4577-4593.

[69] Park EJ and Park K **(**2009) Oxidative stress and pro-inflammatory responses induced by silica nanoparticles in vivo and in vitro. Toxicology Letters, 184:118-25

[70] Qhobosheane M, Santra S, Zhang P, Tan W (2001) Biochemically functionalized silica nanoparticles. *Analyst* 126:1274–1278.

[71] Qu F, Zhu G, Huang S, Li S, Sun J, Zhang D, Qiu S (2006) Controlled release of Captopril by regulating the pore size and morphology of ordered mesoporous silica. *Microporous Mesoporous Mater*. 92: 1–9

[72] Radu DR, Lai CY,Jeftinija K, Rowe EW, Jeftinija S,Lin, VSY (2004) A Polyamidoamine Dendrimer-Capped Mesoporous Silca Nanosphere Based Gene Transfection Reagent. Journal of the American Chemical Society 126: 13216.

[73] Rosenholm JM, Peuhu E, Bate-Eya LT, Eriksson JE, Sahlgren C, Lindén M (2010) Cancer-Cell-Specific Induction of Apoptosis Using Mesoporous Silica Nanoparticles as Drug-Delivery Vectors. *Small*, 6(11) 1234–1241.

[74] Sadasivan S, Khushalani D, Mann S (2003) Synthesis and shape modification of organo-functionalized silica nanoparticles with ordered mesostructured interiors. *J. Mater. Chem*.13 (5): 1023–1029.

[75] Serre C, Millang F, Thouvenot C, Nogues M, Marsolier G, Louer D, Ferey G (2002). *J. Am. Chem. Soc*. 124: 13519 – 13526.

[76] Slowing I., Trewyn BG, Lin VSY (2006) Effect of Surface Functionalization of MCM-41-Type Mesoporous Silica Nanoparticles on the Endocytosis by Human Cancer Cells. *J. Am. Chem. Soc*. 128:14792–14793.

[77] Slowing I.I. et al (2008) Mesoporous silica nanoparticles as controlled release drug delivery and gene transfection carriers. *Advanced Drug Delivery Reviews*, 60:1278–1288.

[78] Slowing II, Trewyn BG, Lin VS-Y (2007) Meoporous silica nanoparticles for intracellular delivery of membrane-impermeable proteins. *J Am Chem Soc*. 129:8845–9.

[79] Slowing II, Vivero-Escoto JL, Wu CW, Lin VS (2008) Mesoporous silica nanoparticles as controlled release drug delivery and gene transfection carriers. *Adv Drug Deliv Rev*. 60(11):1278-88.

[80] Stucky GD, Monnier A, Schu¨th F, Huo Q, Margolese D, Kumar D, Krishnamurty M et al (1994) Formation of Novel Oriented Transparent Films of Layered Silica-Surfactant Nanocomposite. *Mol. Cryst. Liq*. Cryst.240: 187.

[81] Tanaka Y, Mal NK, Fujiwara M (2003) Photocontrolled reversible release of guest molecules from coumarin-modified mesoporous silica. *Nature (London)*, *421* (6921), 350–353.

[82] Tao Z, Toms BB, Goodisman J, and Asefa T (2009) Mesoporosity and functional group dependent endocytosis and cytotoxicity of silica nanomaterials. *Chem. Res. Toxicol***. 22:**1869–1880

[83] Tao Z, Morrow MP, Asefa T, Sharma KK, Duncan C, Anan A, Penefsky HS, Goodisman J, Souid AK (2008) Mesoporous silica nanoparticles inhibit cellular respiration. *Nano Lett*. 8:1517-1526

[84] Torney F, Trewyn BG, Lin VSY and Wang K (2007) Mesoporous Silica Nanoparticles delivery DNA and chemicals into plants. *Nature Nanotechnology*, 2: 295-300

[85] Trewyn BG, Nieweg JA, Zhao Y, Lin VSY (2008) Biocompatible mesoporous silica nanoparticles with different morphologies for animal cell membrane penetration. Chemical Engineering Journal 137:23–29.

[86] Trewyn BG, Giri S, Slowing II, Lin VSY (2007) Mesoporous silica nanoparticle based controlled release, drug delivery, and biosensor systems. *Chem. Commun*. 31:3236–3245.

[87] Trewyn BG, Slowing II, Giri S, Chen H, Lin VSY (2007) Synthesis and Functionalization of a Mesoporous Silica Nanoparticle Based on the Sol–Gel Process and Applications in Controlled Release. *Acc. Chem. Res* 40(9):846-853.

[88] Vallet-Regi M, Balas F, Arcos D (2007) Mesoporous Materials for Drug Delivery. *Angewandte Chemie*. 46 (2):7548-7558.

[89] Vallet-Regí M (2001) Ceramics for medical applications. Perspective Article. *J Chem Soc Dalton Trans*. 2:97–108.

[90] Vallet-Regi M (2006) Synthesis and in vitro bioactivity of novel mesoporous hollow bioactive glass microspheres. *European Journal of Chemistry*, 12:5934.

[91] Vallet-Regí M, Arcos D (2006) Nanostructured Hybrid materials for bone tissue regeneration. *Current Nanosci*. 2:179–89.

[92] Vallet-Regi M, Doadrio JC, Doadrio AL, Izquierdo- Barba I,Qrez-Pariente JP (2004) *Solid State Ionics*. 172: 435 – 439.

[93] Vallet-Regí M, Rámila A, Del Real RP et al. (2001) A new property of MCM-41: Drug delivery system. *Chem Mater*. 13:308–11

[94] Vallhov H, Gabrielsson S, Stromme M, Scheynius A, Garcia-Bennett AE (2007) Mesoporous silica particles induce size dependent effects on human dendritic cells. *Nano Lett*. **7**:3576–3582.

[95] Vivero-Escoto JL, Slowing I, Lin VSY (2010) Tuning the cellular uptake and cytotoxicity properties of oligonucleotide intercalator-functionalized mesoporous silica nanoparticles with human cervical cancer cells HeLa. *Biomaterials*, 31:1325-33.

[96] Vivero-Escoto JL, Slowing II, Trewyn BG, and Lin VSY (2009) Mesoporous Silica Nanoparticle-Based Double Drug Delivery System for Glucose-Responsive Controlled Release of Insulin and Cyclic AMP. *J. Am. Chem. Soc*. 131 (24): 8398–8400.

[97] Vivero-Escoto JL, Slowing II, Trewyn BG, and Lin VSY (2010) Mesoporous Silica Nanoparticles for Intracellular Controlled Drug Delivery. *J. Am. Chem. Soc*. 18: 1952–1967.

[98] Voegtlin AC, Ruch F, Guth JL, Huve PJ (1997) F- mediated synthesis of mesoporous silica with ionic and non ionic surfactants. A new templating pathway L. *Microporous Mater*. 9: 95.

[99] Wang JJ, Sanderson BJS, Wang H (2007) Cytotoxicty and genotoxicty of ultrafine crystalline SiO_2 particulate in cultered human lymphoblastiod cells. *Environmental and Molecular Mutagenesis*, 48:151-157.

[100] Wang F et al (2009) Oxidative stress contributes to silica nanoparticle-induced cytotoxicity in human embryonic kidney cells. *Toxicology in Vitro,* 23(5): 808-815

[101] William III RO, Vaughn JM (2007) Nanoparticle Engineering. *Enclopedia of pharmaceutical technology*, 4:1170.

[102] Xia T, Kovochich M, Liong M, Meng H, Kabehie S, George S, Zink JI, Nel AE (2009) Polyethyleneimine Coating Enhances the Cellular Uptake of Mesoporous Silica Nanoparticles and Allows Safe Delivery of siRNA and DNA Constructs. *ACS Nano*, *3*(10):3273–3286.

[103] Yan J, Estévez MC, Smith JE, Wang K, He X, Wang L, Tan W (2007) Dye dopped nanoparticles for bioanalysis. *Nanotoday*, 2(3):44-50.

[104] Yang Y, Yan X, Cui Y, He Q, Li D, Wang A, Fei J, Li J (2008) Preparation of polymer-coated mesoporous silica nanoparticles used for cellular imaging by a "graft-from" method. *J. Mater. Chem*. 18:5731-5737.

[105] Yu J, Zhao H, Ye L, Yang H, Ku S, Yang N, Xiao N (2003) Effect of surface functionality of magnetic silica nanoparticles on the cellular uptake by glioma cells in vitro. *J. Mater. Chem*. 19:1265–1270.

[106] Zhang JJ, Zhu JJ (2009) A novel amperometric biosensor based on gold nanoparticles-mesoporous silica composite for biosensing glucose. *Science in China Series B: Chemistry*, 52(6):815-820.

[107] Zhao DY, Feng J, Huo Q, Melosh N, Fredrickson GH, Chmelka BF, Stucky GD (1998) Triblock Copolymer Syntheses of Mesoporous Silica with Periodic 50 to 300 Angstrom Pores. *Science*, 279: 548-552.

[108] Zhao W, Li Q (2003) Synthesis of Nanosize MCM-48 with High Thermal Stability. *Chem. Mater*. 15 (22): 4160–4162.

[109] Zhao Y, Trewyn BG, Slowing II, Lin VSY (2009) Mesoporous Silica Nanoparticle-Based Double Drug Delivery System for Glucose-Responsive Controlled Release of Insulin and Cyclic AMP, *J.Am.Chem.Soc*. 131, 8398–8400.

In: Silica Nanoparticles
Editor: Juan Vivero-Escoto
ISBN 978-1-61324-452-4
© 2012 Nova Science Publishers, Inc.

Chapter 5

SILICA-BASED HYBRID NANOMATERIALS WITH WELL-DEFINED ARCHITECTURES

Haiqing Li and Il Kim*

The WCU Center for Synthetic Polymer Bioconjugate Hybrid Materials,
Department of Polymer Science and Engineering,
Pusan National University, Pusan, Korea

ABSTRACT

Silica nanomaterials with well-defined architectures exhibit low cytotoxicity, uniform size, and excellent chemical stability, which in addition to their low-cost, versatile functionalization chemistry and relative ease of large-scale preparation make them very suited to the role of host material for the development of novel silica-based nanoarchitectures targeted to biomedical, catalytic and photoelectronic applications. This chapter surveys the recent research progresses on the fabrication strategies and the corresponding applications of silica and silica-based hybrid nanostructures: 1) silica nanostructures with varied morphologies such as silica solid spheres, capsules, wires, tubes and novel multilevel interior structures; 2) silica-based hybrid nanostructures with various compositions such as silica/polymer hybrids obtained by "grafting from" approach or templating methods, silica/metal nanoparticles achieved by "surface deposition", "matrix entrapping" and templating strategies, silica/carbon nanotubes hybrids achieved on the basis of covalent and non-covalent surface-modified carbon nanotubes, as well as other hierarchical complex structures; 3) silica-based Janus spheres. In the last section of this chapter, the perspectives and outlook of the current research challenges and future research directions in the related fields are presented.

1. INTRODUCTION

Nanostructured silica materials with well-defined architectures occupy an important position in scientific and engineering research fields owing to their non-toxic bio-

*Corresponding Author: E-mail: ilkim@pusan.ac.kr,
Tel.: +82-51-510-2466; Fax: +82-51-513-7720.

compatibility, versatile surface functionalities, low-cost production, in addition to their extensive applications in biomedical, catalytic and photoelectronic areas [1-3]. Targeted to some specific applications, those silica nanomaterials generally need to be further functionalized with certain functionalities by suitably integrating diverse components into silica nanoparticles or lab-on-a-particle architectures, yielding fascinating silica-based hybrid nanomaterials. Since such hybrid nanostructures tend to demonstrate effectively tailored properties with synergistic advantages compared with individual component, tremendous interest have been devoted to the creation of novel silica-based hybrid nanomaterials aimed to specific applications in the recent decades. To date, a wide range of silica-based hybrid nanomaterials, such as silica/polymer, silica/metal nanoparticles, silica/carbon and so on, have been successfully fabricated by means of versatile protocols.

According to the different ways to incorporation of silica component into the silica-based hybrid nanostructures, the fabrication of silica-based nanomaterials with well-defined architectures can be mainly classified into two categories: 1) “growing from” method in which the functional components (small molecules, polymer, metal nanoparticles etc.) are grafted or immobilized onto the surface-modified pre-formed silica nanoparticles to create hybrid nanomaterials; 2) “deposited to” approach where the silica is in-situ produced and deposited onto the various substrates including carbon nanostructures (carbon nanotubes (CNTs), grapheme sheets, nanodiamonds, etc.), metal nanostructures, quantum dots, polymer architectures and supramolecular self-assemblies, to produce versatile hybrid nanostructures.

In the “growing from” method to fabricate silica-based nanomaterials, zero, one, two and three dimensional (termed as 0D, 1D, 2D and 3D, respectively) silica nanostructures with well-defined architectures including solid spheres, capsules, nanowires, nanotubes and colloidal crystals are generally fabricated firstly. Those obtained silica nanostructures generally contain numerous hydroxyl moieties bearing on their surfaces, which provide flexible alternatives to covalently bond diverse functional motifs onto their surfaces using versatile silane coupling agents based on the well-established chemical methods. In addition, the surface of silica tends to be negatively charged, which provides numerous electrostatic binding sites to physically dope a wide variety of positively charged molecules and thus leads to their surface modifications. Based on such surface modified silica nanostructures, various functional matters such as polymers, metal nanostructures or oxides can be allowed to attached, yielding various silica-based nanostructures.

In the “deposited to” approach, the utilized substrates generally serve as templates to allow the in-situ formed silica to be deposited onto their surfaces, yielding silica-coated core/shell nanostructures. The silica coatings of the resultant hybrids not only stabilize the core components but also endow the hybrid materials with versatile functionality based on the well-established silica chemistry. In “deposited to” fabrications processes, the intrinsic properties of the templates surfaces tend to play critical roles. If the surfaces of templates such as CNTs and monodispersed PS colloids are hydrophobic and chemically inert, the suitable surface modifications of such templates are quite necessary for the promotion of silica nucleation and growth on their surfaces. So far, although considerable efforts have been devoted to the achievement of silica-based core/shell nanostructures, it still remains great challenges in the development of facile and green protocols to manipulate their uniformities, sizes, morphologies, and thus discovery of their unique properties targeted to specific applications.

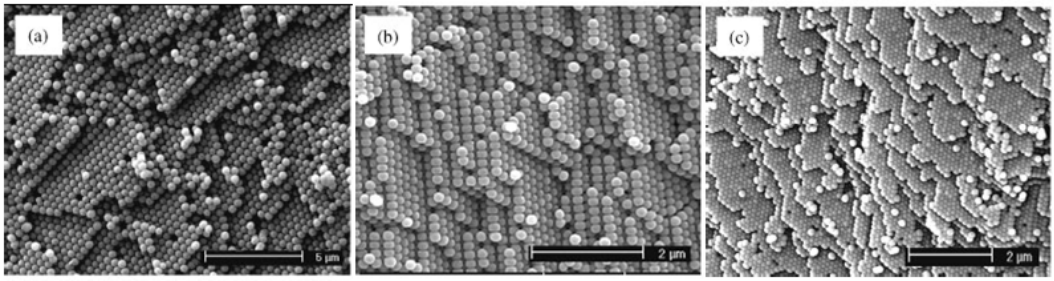
To date, most of silica-based hybrids have been fabricated on the basis of these two methodologies. In view of a large number of publications in the related topics, we will mainly focus on the recent advances in the fabrication and applications of novel silica-based hybrid nanomaterials with well-defined architectures in this chapter. Based on the chemical composition and structure features of the hybrids, the corresponding contents including silica-polymer, silica-metal nanoparticles, silica-carbon and silica-based Janus hybrid nanostructures targeted to some specific applications have been systematically overviewed.

2. FABRICATION OF SILICA NANOSTRUCTURES

2.1. Solid Silica Nanostructures

Relevant recent research on silica materials includes production of 0D silica spheres, capsules, and mesoporous textured architectures, 1D silica nanowires and nanotubes, 2D silica films and 3D silica colloidal crystals. Of all these materials, solid and hollow nanoparticles have been investigated most intensively. For the synthesis of nanosized solid silica spheres, Stöber et al. [4] firstly described a pioneering method for the synthesis of monodisperse silica nanoparticles via hydrolysis and condensation of silicon alkoxides in alcoholic solutions in the presence of water and with ammonia as catalyst. The particle size can be easily tuned from 200-800 nm by simply varying the proportions of the components. After that, a large number of works were reported to prepare silica nanospheres. For instance, Branda et al. [5] have modified Stöber method and synthesized monodisperse silica nanoparticles through the ethanol solutions of tetraethylorthosilicate (TEOS) and 3-aminopropyl-triethoxysilane. Alternatively, Arriagada and coworkers [6] developed a method for the growth of more uniform and smaller-sized silica nanospheres by means of water-in-oil reverse microemulsion techniques. These monodisperse silica nanospheres can be further assembled into 2D membranes via spin-coating [7], dip-coating [8], soft lithography [9], and evaporation-induced self-assembly techniques [10]. In addition, the gravitational sedimentation process was also used to induce the self-assembly of uniform silica nanospheres into 3D colloidal crystals (Figure 1).[11,12] These 2D and 3D silica self-assemblies possess interior cavities among the packed silica spheres, which provide the accessible surfaces and spaces to accommodate functional substances to form novel hybrid nanostructures.

1D silica nanowires have been a subject of intense research in view of their potential for several unique applications such as localization of light, low dimensional waveguides for functional microphotonics, optical interconnectors on a futuristic integrated optical microchip, reinforcement candidates in high performance nanocomposite materials, sacrificial templates, biosensors, and optical transmission antennae [13]. For the synthesis of silica nanowires, protocols based on vapor-liquid-solid (VLS) mechanism have been proven to be very reliable. In this method, the cluster acting as a seed for subsequent nanowire growth is either commonly synthesized by heating thin films or preformed. Recently, Sood et al. [14] developed a new method for selective growth of silica nanowires on silicon (100) wafers by using Pd ions implantation trough a mask. Pd ions are implanted into Si (100) to form nanoclusters of Pd. The clusters get activated and act as catalyst silicide seeds for silica



Source: Reprinted with permission from Ref. 11. Copyright 2005 Wiley-VCH.

Figure 1. SEM images of silica crystal colloidal made of monodisperse silica spheres with (a) 361 nm, (b) 214 nm, and (c) 114 nm in average diameters.

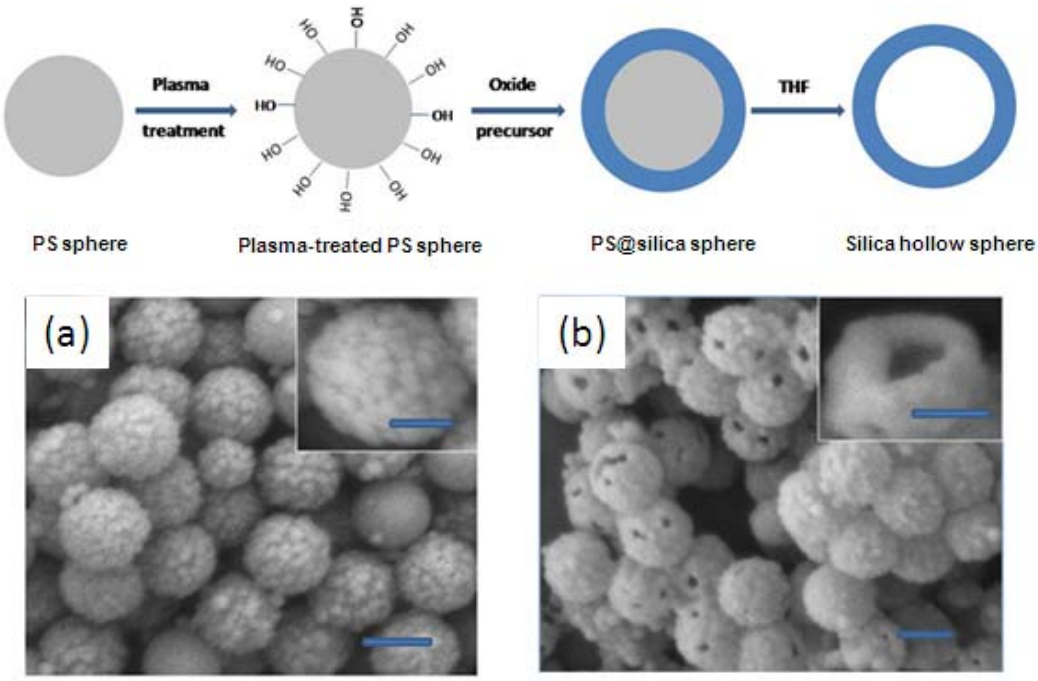
nanowire selective growth on the implanted region. VLS method for preparation of silica nanowires generally conducted at high temperature. To conquer this shortcoming, Christian explored to synthesize ultrafine silica nanowires with diameters less than 5 nm by using iron-based surfactant micelles as templates.[15] These ultrafine silica nanowires provide very promising candidates for reinforcement in high performance nanocomposites.

2.2. Hollow Silica Nanostructures

Hollow silica spheres (capsules) have attracted broad interests because of their potential applications in drug delivery, adsorption, and microreactors. The conventional techniques for fabrication of silica capsules include hard-template,[16] layer-by-layer (LBL),[17] and emulsion methods [18]. LBL technique possesses several main advantages including: 1) The thickness of polymer coatings can be fine tuned by altering the number of layers deposited and the solution conditions from which the polymer are absorbed; 2) The multicomposite polymer films can be assembled through choice of a large variety of polymers; 3) Colloids of different size, shapes and composition can be employed as templates since polyelectrolyte self-assemble onto numerous surface. However, the biggest limitation of the LBL method is the time-consuming sequential polyelectrolyte deposition cycles and purification steps. In contrast, emulsion method is a simple and more direct route for preparing silica hollow spheres. But the resulting spheres tend to possess rather broad size distribution and form aggregates. To fabricate well-defined silica hollow spheres with uniform size, the hard-template method seems to be the optimal alternative so far. For instance, Tissot and coworkers synthesized PS beads bearing silanol groups on the surface *via* emulsion polymerization using 3-(trimethoxysily)propyl methacrylate as a comonomer [19]. Using this functionalized PS beads as template, the hollow silica spheres were synthesized by co-condensation between the silanol groups bearing on the surface of PS latex and TEOS, followed by thermal degradation of PS core. Recently, we have firstly demonstrated a novel post modification approach, plasma-treatment technique, to modify the PS surface (Figure 2) [20]. The plasma treatment process can easily introduce hydroxyl groups onto the surface of PS spheres. Moreover, in comparison to the previous modification approaches mentioned above, no more solvent and chemicals are involved in this process, which can simplify the modification process, reduce the preparation cost and decrease the hazard to environment. By using these plasma-treated PS spheres as sacrificial template, silica-coated PS composites

have been successfully fabricated by the co-condensation between hydroxyl groups with TEOS in a sol-gel process. Followed by the removal of PS cores with tetrahydrofuran (THF), the hollow silica spheres were generated. Moreover, the shell thickness of the resulting hollow silica spheres is well controllable by simply changing the employed concentration of precursors. Following the similar procedures, mesoporous titania and germania hollow spheres have also been successfully prepared.[20,21] In addition, it has found that microfluidic technology is an ideal method for obtaining uniform-sized microspheres and has the advantages of continuous, reproducible, and scalable production. For example, Li et al. [22] have produced monodisperse, size-tunable silica hollow spheres via hydrolysis and polymerization of TEOS at the interface of water-in-oil droplets by means of microfluidic method. More interestingly, the achieved morphologies of silica materials were well-controllable from hollow, to partially hollow, to solid by altering the concentration of TEOS in oil phase and CTAB in aqueous phase.

Besides of these templating methods to fabricate silica hollow spheres, free-temple approaches also have been developed in recent years. Yin and coworkers have reported a spontaneous transformation of silica colloids from solid spheres to hollow structures with high morphological fidelity in aqueous solutions of $NaBH_4$ [23]. The corresponding formation mechanism was revealed that the high pH value and gradual decomposition of $NaBH_4$ facilitate the formation of hollow structures first by partial dissolution of the silica cores and then by re-deposition of the silicate species back onto the core surfaces to form



Source: Reprinted with permission from Ref. 20. Copyright 2010 American Chemical Society.

Figure 2. Schematic illustration for fabrication of silica hollow spheres by using plasma-treated PS spheres as sacrificial templates; SEM images of (a) PS/SiO_2 composite and (b) hollow SiO_2 spheres obtained by removal of PS core from the corresponding PS/silica hybrids using THF. The scale bars are 200 nm.

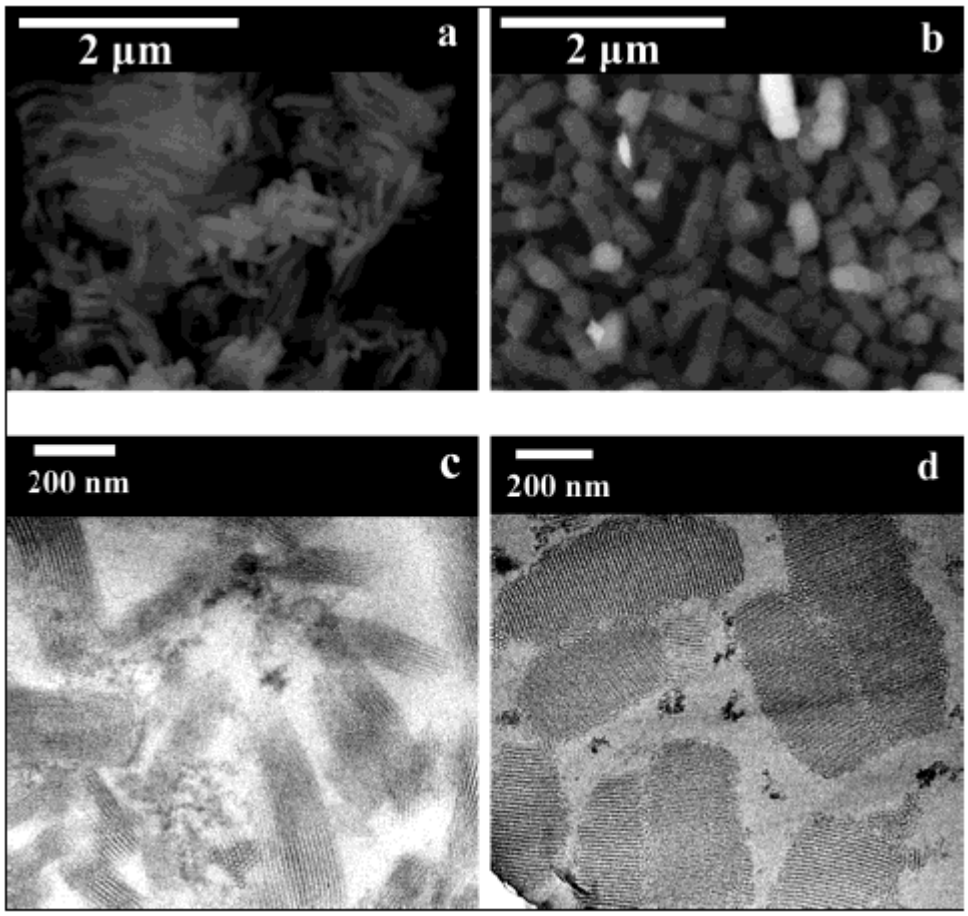
shells. Surprisingly, this hollowing process has been found to be general to silica colloids with various size and shapes. Note that this work provides an extremely simple, mild, and effective recipe to transform silica or silica-coated composite materials into hollow structures with various functions.

As another type of silica hollow nanostructures, silica nanotubes have received a great deal of attention because of their potential for newly emerging applications in drug-delivery systems, organic molecular separation, sing-DNA sensing, decomposition of pollutes and inorganic ion sensing [24-28]. These applications take advantage of the inherent characteristics of silica nanotubes that involve their hollow core structure, ultrahigh specific surface area, very narrow inner pores and catalytic surface properties. Silica nanotubes are generally fabricated by a wide range of template-guided protocols. For instance, Martin's group has explored to use a typical alumina (AAO) template membrane with an electrochemical process to synthesize silica nanotubes [29,30]. As a matter of fact, most of the developed methods for fabrication of silica nanotubes are on the basis of self-assembled organic templates, which are also well summarized in Section 3.2.

2.3. Nanoporous Silica Nanostructures

Interest in nanoporous including microporous, mesoporous and macroporous silica materials has been attracted dramatically over the past few years because of their extremely large specific surface area, excellent mechanical stability, versatile surface chemistry, good biocompatibility, and facile fabrication [31]. On the basis of these unique intrinsic properties, nanoporous silica materials have been extensively explored to be utilized in catalytic and biomedical areas. Particularly, ordered mesoporous silica materials with well-defined architectures such as MCM41 spheres and SBA15 rods have received the most intensive explorations. For example, Grün et al. developed a modified Stöber method to produce the first mesoporous silica spheres with micrometer and submicrometer sizes by adding a freshly distilled silica precursor in an alcoholic solution of diluted surfactant under basic conditions. Since then, by carefully adjusting reaction parameters such as silica sources, surfactant templates, solvents and catalysts, a variety of mesoporous silica with well-defined morphologies have been achieved [32-34]. For instance, Lelong et al. used a simple route to prepare uniform MCM41-type silica spheres in all-water medium by tuning the employed ratio of silicate and surfactant [35].

Since the first SBA15 materials had been successfully achieved by Zhao et al. [36] using P123 self-assemblies as templating agents, enormous efforts have been devoted to the fabrication of SBA15 nanostructures. Although both of MCM41 and SBA15 exhibit two-dimensional hexagonal structures, they have notable differences [37]: 1) SBA15 generally possess larger pores and thicker pore walls than MCM41; 2) MCM41 is purely mesoporous in nature, whereas typical SBA15 silica contains a significant amount of micropores within the pore walls; and 3) while the channels of MCM41 are not connected to each other, those of SBA15 are interconnected via micropores or secondary mesopores. Therefore, generally speaking, SBA15 silica materials are more suitable for the applications where the substance diffusion and transportation are essential. Typical SBA15 materials exhibit most common morphologies consisting of bundles of fibers with a relatively uniform length of around 1 μm and the channels running parallel to the long axis of the rods [38]. More exotic particles



Source: Reprinted with permission from Ref. 40. Copyright 2004 American Chemical Society.

Figure 3. SEM images (a-b) and TEM images (c-d) of mesoporous silica SBA-15 synthesized at different weight ratios of decane to P123 in the presence of NH4F: (a) and (c) 0.4:1; (b) and (d) 5.8:1.

having doughnut-, rope-, egg-sausage-, gyroid-, and discoidlike shapers have been obtained by Zhao et al. [39] But all those materials have curving and even orbicular channel structures, which are less favorable for the mass transfer in separation and catalysis. Inspired by that, Zhang et al. [40] explored to synthesize an unusual SBA15 silica rods with parallel channels running along the short axis in the presence of catalysts NH_4F by using P123 and excel amounts of decane as templating agents and co-solvent, respectively (Figure 3). Such obtained SBA15 materials are highly expected to be favorable for mass transportations duo to their short-pore channels.

Distinct from the conventional synthetic strategies, co-structure-directing routes have been developed to fabricate functional mesoporous silica materials more recently. In those fabrication systems, organosilane serves as the co-structure-directing agent, which provides critical interactions between the template and organic part of the organosilane to form mesostructures, thus retaining the organic groups on the pore surface after removal of the template by extraction. The corresponding pioneering works have been well documented in the recent publication [41].

2.4. Other Silica Nanostructures

More recently, some novel type of silica nanostructures, such as high-surface-area silica nanospheres with fibrous morphology [42], ball-in-ball silica nanoparticles [43], mesoporous rattle-like silica nanostructures [44], nanotubes and nanodisks [45] have also been successfully fabricated. All those nanostructured silica materials with well-defined architectures provide effective platforms for the generation of various silica-based hybrid nanomaterials by incorporation of suitable functional guest matters.

3. SILICA/POLYMER HYBRID NANOSTRUCTURES

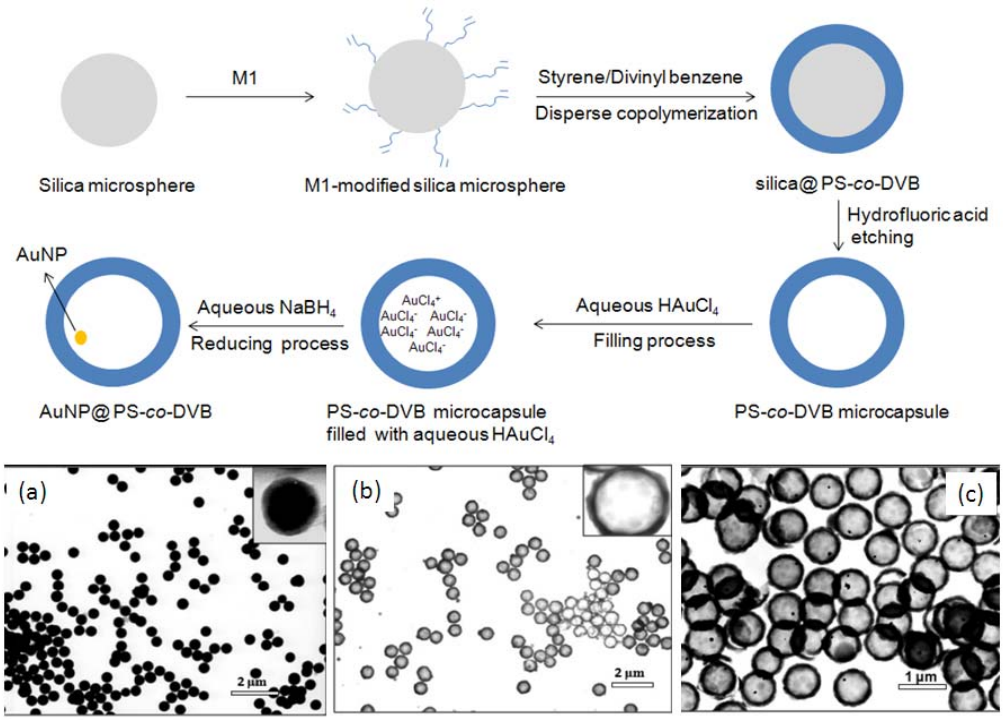
Silica/polymer hybrids tend to possess synergistic properties derived from not only the chemical resistance, mechanical stability, variable particle size, and specific surface area of silica component, but also the versatile physic-chemical properties of surface-tethered polymer chains. To fabricate silica/polymer hybrid, both "grafting to" and "grafting from" approaches have been extensively utilized [46, 47]. The "grafting to" approach can be straightforwardly used to graft well-defined pre-synthesized homopolymers or block copolymers to a silica surfaces. However, the obtained hybrid materials tend to possess rather low grafting density owing to the steric repulsion between the polymer chains and thus greatly decreased the reaction efficiency. In contrast, "grafting from" approach generally allows to graft polymer chains through a monomer covalently linked to the particle surface or from a surface modified with polymerization initiators, leading to the formation of hybrid materials with much higher polymer grafting density but with less control over the molecular weight, polydispersity and chain defects of the resultant polymers. Even so, as an efficient method to graft polymers onto the silica surfaces, "grafting from" approach still attracts more and more interest.

3.1. Polymer Grafting from Silica Surfaces

So far, various grafting polymerization approaches, such as surface-initiated controlled radical polymerization (SI-CRP), click reaction and their combination, as well as dispersion polymerization have been used to create silica/polymer hybrid materials. SI-CRP techniques have been proved a powerful technique to achieve silica/polymer hybrid nanomaterials with well-controllable polymer structures. For instance, Wang et al. [48] modified the surface of ultrafine silica spheres with peroxide groups. Thereafter, well-defined poly(methyl methacrylate) (PMMA) and polystyrene (PS) chains were sequentially grown from the surfaces-modified nanoparticle by reverse surface-initiated atom transfer radical polymerization (SI-ATRP) and conventional SI-ATRP technique, yielding individual particles composed a silica core and a well-defined densely grafted outer polymer layer. More specifically, successful polymerization from nanoparticles typically requires the covalent attachment of initiators, which form monolayers that foster particle dispersion and mitigate polymer bridging. Therefore, the molecular structures of initiator, type of catalysts and reaction solvents tend to play key roles in the achievement of hybrid nanomaterials with well-

defined architectures by means of SI-CPR techniques. In the case of aqueous ATRP of methycrylate, it has found that the use of CuBr catalyst will yield faster polymerizations but with less control over the grafting polymers such as polydispersity, compared with the use of CuCl catalyst [49]. Also the faster polymerization rates can lead to less dense polymer grafting layers [50]. More recently, Huang et al. [51] quantified the impact of the carbon spacer length of immobilized alkoxysilanes initiators on grafting PMMA from the surface of silica nanospheres via SI-ATRP in methanol-water solutions at room temperature. They have found that the PMMA grafting densities increased with the initiator carbon spacer length. But the longer carbon spacer length makes silica nanoparticle surfaces hydrophobic, causing nanoparticle aggregation in reaction solutions. Another typical example includes the synthesis of high grafting density mixed poly(*tert*-butyl acrylate) (P*t*BA)/PS brushes with a fixed P*t*BA M_n and various PS molecular weight by sequential ATRP and nitroxide-mediated radical polymerization from Y-initiator-functionalized silica particles [52]. Interestingly, the high density mixed polymer brushes exhibited two distinct glass transitions, suggesting that the two grafted polymers were microphase separated in the brush layer.

In our group, we have explored to graft crosslinked poly[styrene-*co*-(divinyl benzene)] (PS-*co*-DVB) layers on $H_2C{=}CH(CH_2)_2OC(O)NH(CH_2)_3Si(CH_2CH_3)_4$ modified monodisperse silica spheres by means of a dispersion polymerization, yielding uniform silica/polymer core/shell structures (Figure 4) [53]. After etching silica cores, stable polymer



Source: Reprinted with permission from Ref. 53. Copyright 2009 Wiley-VCH.

Figure 4. Schematic illustration of the preparation of poly[styrene-*co*-(divinyl benzene)] (PS-*co*-DVB) microcapsules that contain single Au nanopartilce. M1 is the surface-modifier of silica spheres, $H_2C{=}CH(CH_2)_2OC(O)NH(CH_2)_3Si(CH_2CH_3)_4$; TEM images of (a) silica/polymer hybrid spheres, (b) polymer capsules and (c) polymer/Au rattle-like hybrid particles.

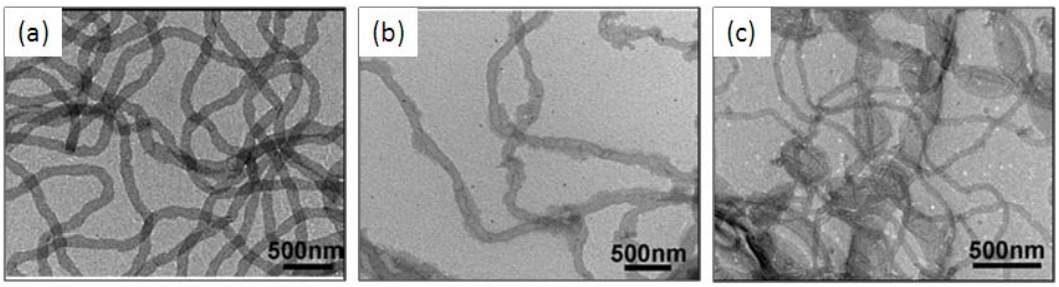
capsules with uniform size were achieved. More interestingly, the obtained polymer capsules can be used as microreactors to in-situ generate and encapsulate a single metal nanoparticle with tunable size into each capsule, yielding fascinating polymer/metal nanoparticle rattle-like hybrid nanostructures.

Taking advantage of the well-known nontoxic, biocompatible and biodegradable properties of silica, mesoporous silica provides very promising drug delivery platforms. With suitable surface modification, these silica nanostructures can be further endowed with diagnosis, MRI and specific targeting functions. Aimed to that, Rosenholm et al. [54] reported to graft poly(ethylene imine) (PEI) onto the mesoporous silica nanospheres by surface hyperbranching polymerization. Thereafter, the PEI layers were further modified by introducing both fluorescent (FITC) and targeting moieties (folic acid). The resulting hybrid nanoparticles exhibited excellent HeLa cell targeting capacity. It has also found that the total number of particles internalized by the folate-receptor high cancer cells was about an order of magnitude higher than the that of low normal cells, making the particles highly promising candidates for targeted drug delivery for cancer treatment or imaging agents for early tumor diagnosis.

Concerning 2D silica/polymer hybrid materials, a representative example is demonstrated by Schepelina et al. [55] They fabricated free-standing silica colloidal membranes with varied thickness and nanopore size, and then modified them with pH-responsive poly(2-(dimethylamino)ethyl methacrylate) brushes by SI-ATRP. The resulting hybrid membranes demonstrated excellent acid-controlled gating behavior for molecular diffusion. For 3D silica/polymer hybrid materials, we have explored to introduce syndiotactic homogeneous polymers (PS and poly(*p*-methyl styrene)) or styrene/*p*-methyl styrene copolymers via in-situ coordination polymerizations within the confined cavities of 3D silica colloidal crystals [11, 56-58]. After selective etching the silica templates, 3D ordered macroporous polymers have been generated. More importantly, such reaction systems build effective platforms for the study on the confinement polymerization behavior in the nanopore-sized space. It has found that such confinement polymerization can not only effectively lower the molecular weight, crystallinity, melting temperature, but also narrower the polydispersity of resulting syndiotactic PS [11]. Our further study also demonstrated that the confinement polymerization also rendered significant effects on the macromolecular conformations and molecular stacking manners of syndiotactic polystyrene and poly(*p*-methyl styrene) [59] .

3.2. Silica Deposited onto Polymer Self-Assembled Architectures

Amphiphilic block copolymers display diverse lyotropic phase behavior such that a variety of supramolecular structures in the form of spherical or cylindrical mecelles, hexagonal, cubic or bicontinuous liquid crystals, and unilamellar or mutilamellar spherical vesicles can be assembled spontaneously depending on polymer molecular weight and concentration, block length and composition, solvent composition and temperature. Such fascinating structures provide important functional platforms for the design of silica-based hybrid nanostructures by depositing silica components onto their surfaces. One of the most representative examples is the use of P123 self-assembles as templates to allow the in-situ obtained silica deposited onto their surfaces to synthesize periodic mesoporous SBA15 silica materials (See section 2.3). Another typical example was demonstrated by Yuan et al. [60]



Source: Reprinted with permission from Ref. 61. Copyright 2008 Wiley-VCH.

Figure 5. TEM images of silica–polymer myelins prepared at TEOS:E16B22 molar ratios of 3.6:1 (a) and 7.4:1 (b) showing highly uniform or roughened nanotubes, respectively; (c) TEM image of silica–myelin sample after heating the TEM grid to 400 ^{o}C to produce intact replicas in the form of well-defined silica nanofilaments.

They used diblock copolymer micelles comprising cationic poly(2-(dimethylamino)ethyl methacrylate) (PDMA) coronas and hydrophobic poly(2-(diisopropylamino)ethyl methacrylate) (PDPA) cores as nanosized templates for the deposition of silica from aqueous solution at pH 7.2 at 20 oC. It was found that both noncrossliked and shell crosslinked micelles can be coated with silica without loss of colloidal stability. Interestingly, the silica deposition is confined to the partially quaternized cationic PDMA chains, leading to the hybrid copolymer/silica nanoparticles with well-defined core/shell morphologies. Similar to this reported work, Li et al. [61] recently synthesized silica/polymer myelin nanofilaments with uniform width and capped ends via a one-pot reaction, where poly(ethylene oxide)-*b*-poly(1,2-butylene oxide) ($E_{16}B_{22}$) self-assembles formed in basic conditions and simultaneously used as templates to incorporate in-situ formed silica component. After removal of polymer components by calcinations treatment, intact silica replicas with nanotubules architectures were generated (Figure 5). This protocol offers a promising alternative to fabricate well-defined silica nanotubules with higher aspect ratio.

4. SILICA/METAL NANOPARTICLES HYBRID NANOSTRUCTURES

Metal nanoparticles play important roles in many different areas. For example, they can serve as model system to experimentally probe the effects of quantum confinement on electronic, magnetic, and other related properties. Also they have been widely exploited to use in photography, catalysis, biological labeling, photonics, optoelectronics, information storage, surface enhanced Raman scattering and formulation of magnetic ferrofluids. Generally, the intrinsic properties of a metal nanoparticle can be mainly determined by its size, shape, composition, crystallinity, and structure (solid versus hollow). In principle, one could control any one of these parameters to fine-tune the properties of this nanoparticle. The relative studies on the synthesis, properties and applications of metal nanoparticles have been well documented in several review publications [62-64].

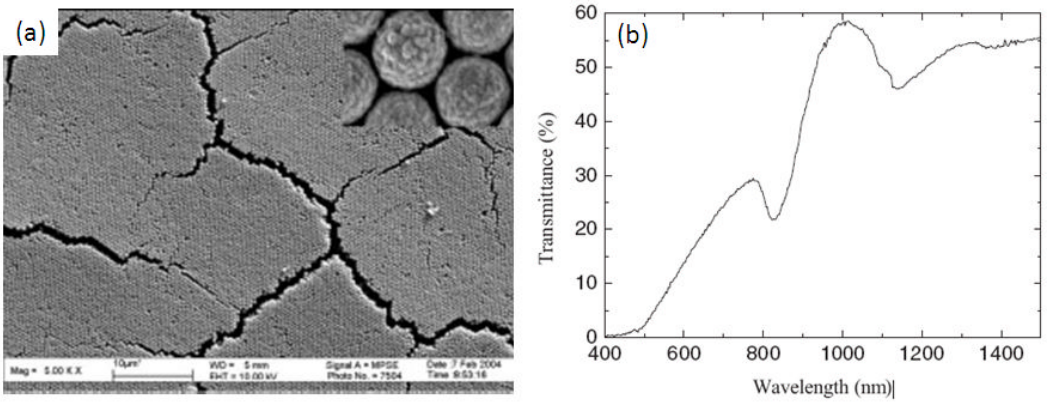
Silica nanostructures are frequently used as supporting or entrapping matrices to incorporate various metal nanoparticles to engineer a variety of functional nanomaterials. So far, several wet-chemistry methods have been developed to fabricate metal nanoparticles immobilized silica hybrids, including covalent attachment of particles onto surface-modified

silica materials [65], deposition-precipitation method [66], electroless plating [67], sonochemical approach [68], and sol-gel methods [69]. According to the differences in the incorporating manners of metal nanoparticles in silica matrices, the silica/metal hybrid nanostructures can be classified into three types: 1) surfaces immobilized metal nanoparticles, in which metal nanoparticles are randomly distributed onto the silica surfaces; 2) matrix entrapped metal nanoparticles, where metal nanoparticles are randomly distributed within the silica matrices; 3) core/shell or rattle-like hybrids, in which metal nanoparticles serves as core and encapsulated by a silica shell.

4.1. Surfaces Immobilized Metal Nanoparticles

To deposit metal nanoparticles onto the surfaces of silica colloids, one effective pathway includes the assembly of preformed nanoparticles on support colloids, which includes electrostatic deposition of metal nanoparticles by means of adhesives such as polyelectrolytes covering the silica surface and ligand-mediated immobilization of metal colloids on the functionalized silica surface. For instance, silica colloids immobilized gold nanoparticles with 30% coverage has been fabricated by covalently binding between amine group ligands on the surface of silica colloids and the gold nanoparticles [70]. In our group, we have explored to fabricate thiol-groups modified SWCNT/silica hybrid obtained by silica coating onto the plasma-treated SWCNT surfaces [71]. Based on such thiol groups bearing on the silica coatings, Ag ions were in-situ reduced and coalescence into Ag nanoparticles which are tightly attached onto the silica coatings via covalent bonds. Moreover, in this fabrication processes, no additional reducing agents were involved. In an alternative protocol, Wang et al. [72] recently explored to firstly grafting a thin layer of coordination polymer containing chelate ligand of β-diketone by dispersion polymerization. Thereafter, the metal precursors were trapped into such polymer layer and in-situ reduced, forming silica/metal nanostructured materials. The obtained silica/Pd exhibited excellent catalytic activities towards the hydrogenation of cinnalmul alcohol in water.

The other strategy to incorporate metal nanoparticle onto the silica surface consists in precipitation and surface reactions. According to this way, finely grained polymeric and also inorganic supports dispersed in aqueous solutions can be coated with varied metals either by precipitation deposition of an appropriated metal precursor onto the support surface or by direct surface reaction using specific functional groups to induce coating, which always is followed by controlled chemical reduction, photochemical or radiation-chemical, photocatalytic and sonochemical reduction to create fine metal nanoparticles. All these processes generally followed three different plating mechanisms [73]. autocatalytic, substrate catalyzed and galvanic displacement processes. Autocatalytic plating baths are commonly employed in electronic fabrication and typically contain metal salt, the reducing agent and other additives. Similarly substrate catalyzed deposition baths also consist in metal salt and the reducing agent, but the metal reduction is facilitated on the substrate surface. In both processes, the reducing agents, $NaBH_4$ or some solvent such as alcohol, are necessary for the reducing reaction. As a typical example [74], since silica surfaces are negative charged derived from numerous Si-OH groups, $[Ag(NH_3)_2]^+$ ions can be absorbed onto the silica surfaces via electrostatic interactions. Following a reducing process in the presence of KBH_4, the Ag nanoparticles were in-situ generated and uniformly covered on the silica surfaces.



Source: Reprinted with permission from Ref. 75. Copyright 2004 Wiley-VCH.

Figure 6. (a) SEM image of the opals made of silica/Ag composite colloids and (b) transmission spectrum at normal incidence of the opal.

After a further seed growth process, uniform core/shell structured Ag coated silica hybrid nanostructures can be achieved. Similarly, Zhang et al. [75] used polyvinylpyrrolidone (PVP)-stabilized silica colloids to absorb the complex $[Ag(NH_3)_2]^+$ ions rather than silver ions owing to the reduction of former is more controllable and uniform. After the rapid reduction reaction with KBH_4, very small sized Ag nanoparticles formed on the silica surfaces. Subsequent seed growth process allowed those obtained nanoparticles to further grow into a rough shell, leading to the formation of uniform silica/Ag core/shell microspheres. Interestingly, these monodisperse hybrid particles can self-assemble into long-range-ordered colloidal crystals via gravitational sedimentation and utilized them as fascinating photonic crystal materials to detect photonic bandgap, and as SERS stubstrates for the detection of organic molecular species (Figure 6).

Galvanic displacement proceeds in an entirely different manner, in that deposition is carried out in the absence of an external reducing agent, and the reducing electrons are derived from the bonding electrons of the substrate lattice. With exception of the in-situ formation of metal nanoparticles on the surface of substrates mentioned above, some other methods for anchoring metal nanoparticles on oxide colloids also have been explored, such as transition metal by direct reduction of organometallic complexes of the type $[Li(THF)_2]_2{\cdot}[MR_4]$, with THF being tetrahydrofurane, M being Ni, Pt, Pd, and R being methyl or phenyl ligands, on oxide surfaces [76]. Alternatively, Lalonde et al. [77] used plasma-enhanced chemical vapor deposition technique to directly synthesize Au nanoparticles onto the surfaces of silica nanowires. Moreover, the nanoparticle size can be easily controlled by deposition conditions such as temperature and pressure. In addition, ultrasonic irradiation of a slurry of silica spheres, $HAuCl_4$ and ammonia water in an aqueous medium also can deposit in-situ generated Au nanoparticles onto silica surfaces [78].

4.2. Matrix Entrapped Metal Nanoparticles

To introduce metal nanoparticles into the matrices of silica nanostructures, two methodologies including Route I and Route II have been extensively used. In Route I, the

metal nanoparticles are in-situ generated and accommodated within the matrices of preformed silica nanomaterials. While in Route II, the preformed metal nanoparticles were directly incorporated into the in-situ formed silica nanostructures via sol-gel processes.

4.2.1. Route I to Silica/Metal Nanostructures

In the case of Route I, to facilitate the in-situ generation of metal nanoparticles, the intra-environments of silica tend to be tailored with certain functions which not only allow the metal precursors are absorbed and reduced but also permit the in-situ nucleation and growth of the resultant metal nanoparticles. As a typical example, Jiang et al. [79] have explored to graft polyamidoamine (PAMAM) dendrimers onto the pore-walls of mesoporous SBA15 nanostructures. Those grafted dendrimers served as soft adsorbents for the Pd(II) ions. Followed by a reducing process in the presence of BH_4-, Pd nanoparticles were in-situ generated and accommodated into the SBA15 matrices. By means of intrinsically structural properties of dendrimers, those obtained hybrid nanostructures were explored to be used as heterogeneous catalysts with excellent catalytic activity towards the hydrogenation of allyl alcohol. Following similar procedures, highly dispersed, stable Cu, Pd, Rh, Pt, and Pd/Pt nanoparticles with both size and site control were incorporated into the PAMAM modified SBA15 nanostructures [80, 81]. More simply, metallic Ru nanoparticles were in-situ produced and incorporated into the pores of SBA15 by means of a simple ultrasound-assisted polyol method in the medium of ethylene glycol [82]. These hybrid nanostructures showed very high activity and CO selectivity to the partial oxidation of methane.

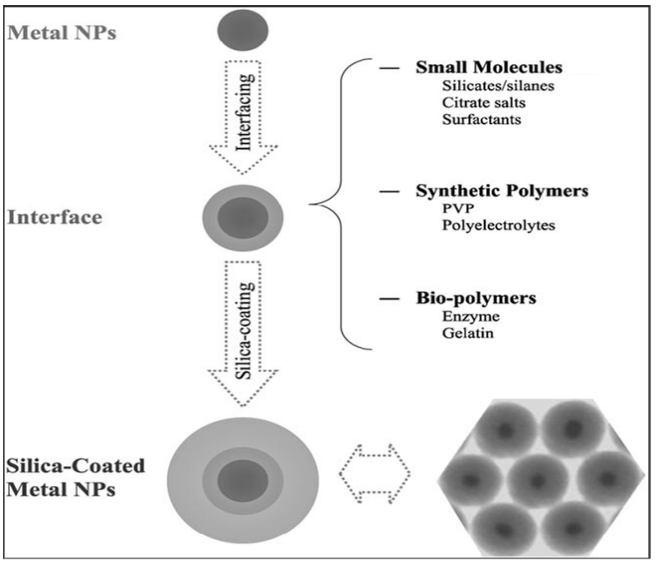
Besides the ordered mesoporous silica materials, other porous silica materials also have been utilized as hosts to incorporate metal nanoparticles. A typical example includes the fabrication of highly monodispersed thiol-functionalized porous silica spheres via a surfactant-directed co-condensation of tetramethylorthosilicate and 3-mercaptopropyltrimethoxysilane in a dilute alkaline methanol-water mixture [83]. By using the thiol groups as adsorption sites of a gold precursor, the thiol-functionalized porous silica spheres were converted into monodisperse gold-nanoparticle-embedded nanoporous spheres. Also these resultant spheres were readily self-assembled into a close-packed colloidal crystalline array, which exhibited an optical stop band corresponding to Bragg diffraction as well as a surface-plasmon-derived adsorption peak.

4.2.2. Route II to Silica/Metal Nanostructures

Concerning the fabrication of silica/metal hybrid nanostructures by means of Route II, the employed preformed metal nanoparticles generally possess functional moieties onto their surfaces which provide suitable surface environments for the deposition of silica components via sol-gel processes. Such surface functionalities tend to be derived from the stabilizer of metal nanopartilces. For instance, very recently, we have synthesized a series of hyperbranched polyglycidol (HBP)-stabilized metal nanoparticles using HBP as both reducing and stabilizing agents in water.[84] Because that HBP contains numerous hydroxyl groups, the multiple HBP-stabilized metal nanoparticles can be directly incorporated within the silica nanoparticles via co-condensation reactions of the hydroxyl groups bearing on the surfaces of metal nanoparticles and TEOS in a Stöber protocol. Note that this facile protocol is very suitable for the production of silica/metal hybrid nanostructures in a large scale.

Unfortunately, most of synthesized metal nanoparticles are lack of surface functionalities.[84] To successfully incorporate these metal nanoparticles into the matrices of

silica materials, the surface of metal nanoparticles need to be suitably modified with surfactants through strong surface-coordination or electrostatic interactions (Figure 7).[85] For example, sodium citrate-stabilized Au nanoparticles can be easily tailored by surface-ligand-exchange reaction with vitreophilic 3-aminopropyltrimethoxysilane (APTMS).[86] On the basis of such surface-modified Au nanoparticals, a thin layer of amorphous silica can be attached onto the surfaces of Au nanoparticles in basic conditions. Furthermore, these thin silica layer can grow into a thicker shell in a Stöber conditions, yielding well-defined Silica/Au core/shell nanostructures. Using the obtained core/shell nanospheres as silica source, spherical mesoprous-silica/Au nanostructures were further synthesized via a pseudomorphic transformation process in an alkaline solution of CTAB [87]. Alternatively, Kang et al. [88] immobilized the thiol-group-containing ATRP initiator onto the surface of Au nanoparticles. Thereafter, poly(2-(dimethylamino)ethyl methacrylate) chains were grafted from Au nanoparticles via surface-initiated ATRP. Followed by a biomimetic polycondensation of silicic acid by using polymer as a synthetic counterpart for silaffins, silica/Au nanostructures with controllable thickness of silica shell were successfully achieved. More recently, we have directly deposit a uniform silica shell onto the PVP-passivated Ag nanoparticles obtained by traditional polyol process following a Stöber method (Figure 8) [89]. Interestingly, after a confined galvanic replacement reaction between the silica/Ag nanospheres and aqueous HAuCl4 solution, silica nanocapsules containing Ag/Au alloy nanostructures (SNCAs) were fabricated following alloying and de-alloying processes. Moreover, the structures and morphologies of the resulting SNCAs are diversified by simply controlling the relative amount of Ag/Au, exhibiting tunable optical absorptions in visible region. Similarly, Liong et al. [90] explored to absorb CTAB layers onto the oleylamine-capped Ag nanocrystals. Such surface modified Ag nanoparticles were further covered uniform silica shells. The resulting silica/Ag hybrids showed antimicrobial effects in both liquid media and LB-agar plates.



Source: Reprinted with permission from Ref. 85. Copyright 2010 Wiley-VCH.

Figure 7. Schematic illustration of strategies for fabrication of silica/metal nanoparticles core/shell nanostrcutrures.

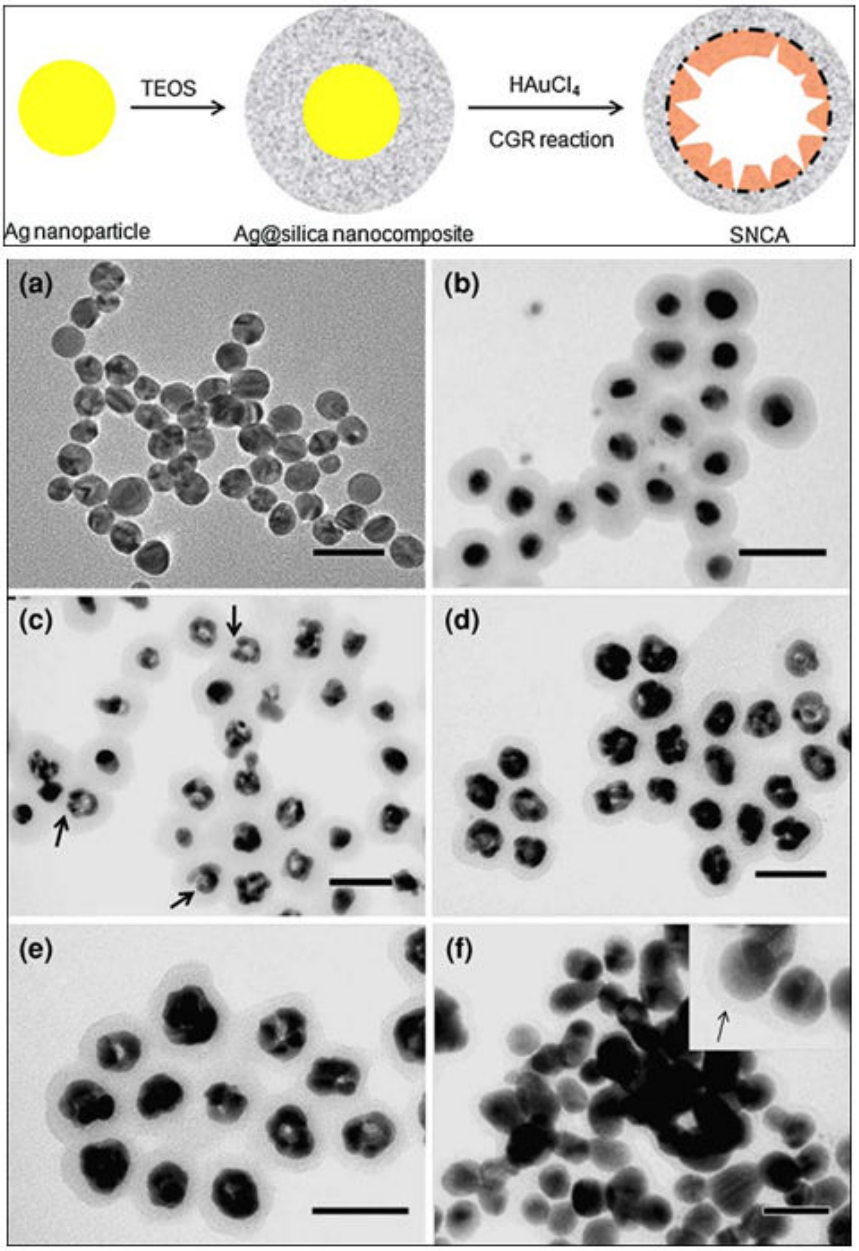
4.3. Rattle-Like Silica/Metal Nanoparticle Hybrids

Rattle-like nanostructures representing a new type of hollow structures have attracted numerous attentions because of their considerable advantages in many applications, such as drug delivery systems, confined nanoreactores, and catalysts [91, 92]. So far, various chemical and physicochemical strategies have been developed to produce silica/metal rattle-like nanostructures. Among them, template-assisted methods have proven to be the most general and effective. In conventional template-assisted processes, hard templates (colloids or polymer particles) or soft templates (liquid or gaseous) were used to double-coat different materials by sol-gel processes, LBL approach, or chemical deposition. By removing the middle layer by chemical dissolution or thermal calcinations, a rattle-like structure can be formed. For example, Yeo et al. [93] recently encapsulated Fe_3O_4/Au hybrid nanostructures into silica nanospheres. After selective removal of Fe_3O_4 grains by reductive dissolution in the presence of $NaBH_4$, silica/Au nanorattles were generated. These obtained nanostructures can be utilized as nanoreactors to template the growth of nanocrystals inside of the cavities.

Although traditional templating method provides an effective approach to fabricate nanorattles, the synthetic processes are often tedious and they are also difficult to scale up. Therefore, the intense efforts on the development of more facile strategies to prepare rattle-like nanostructures have drawn considerable attentions. As a typical example [43], sodium citrate-stabilized Au nanoparticle were sequentially coated with an organic silica layer and a pure silica layer in one-pot sol-gel process, forming "sandwich" structured silica-based hybrids. After selective etching the less-dense organic silica layer with HF, silica/Au nanorattles were synthesized. Following the similar idea, Roca et al. [94] have fabricate silica/Au nanorattles and utilized them as viable SERS substrates for the reproducible detection of 2-naphthalenethiol. And Lee et al. also prepared porous silica/Au nanorattles and utilized them as novel nanoreactors for catalytic reduction of *p*-nitrophenol [95].

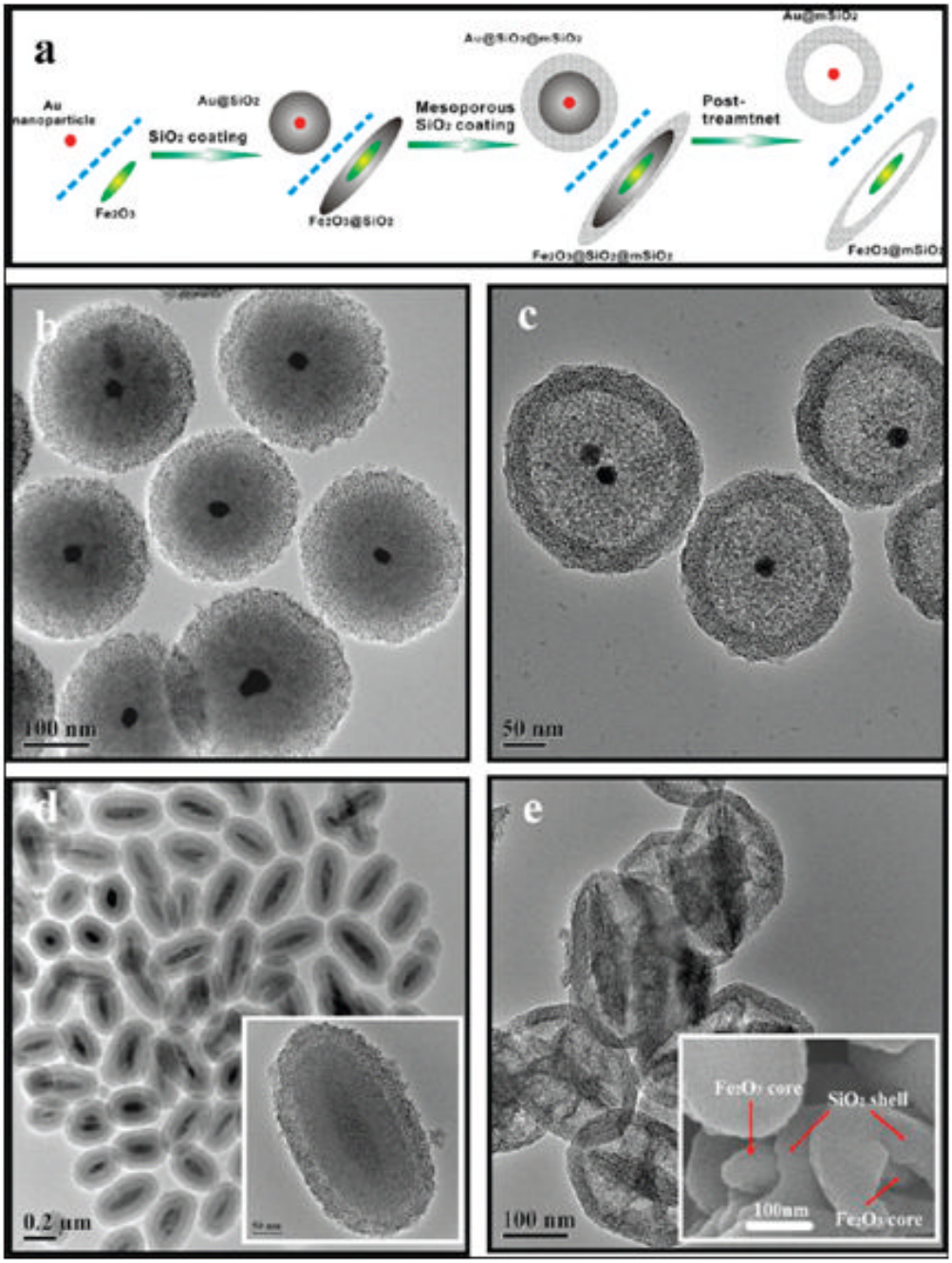
In those synthetic strategies mentioned above, the dissolution processes for removing the middle cores strongly depend on the compositional variations. More recently, Chen et al. [96] proposed a novel homogeneous templating route, namely. "structural difference-based selective etching" and applied it to fabricate silica-based heterogeneous nanorattles (Figure 9). Specifically, Au nanospheres and Fe_2O_3 ellipsoid were sequentially coated with a dense silica shell and a mesoporous silica ($mSiO_2$) shell, yielding $Au@SiO_2@mSiO_2$ or $Fe_2O_3@SiO_2@mSiO_2$ core/shell nanostructures, which can be converted into rattle-type structures by etching processes in $NaCO_3$ solutions and under hydrothermal conditions in ammonia solution, respectively.

As another interesting example, Han and coworkers found that denatured collagen-derived positively charged gelatin polypeptides can be adsorbed on the negatively charged citrate-capped Au nanoparticle through the electrostatic interactions [97]. Fascinatingly, after a simple sol-gel process, silica/Au nanorattles with a quite high yield were directly generated. Besides these typical examples, many other silica-based rattle-type nanostructures also have been extensively fabricated by means of various strategies.[98] Although the significant advances in the related fields have been achieved, the explorations of more facile and general synthetic strategies to produce silica-based nanorattles in a good yield still remain a great challenges.



Source: Reprinted with permission from Ref. 89. Copyright 2010 Springer.

Figure 8. Schematic illustration for fabrication of silica nanocapsules containing Ag/Au alloy nanostructures (SNCA) by means of confined galvanic replacement (CGR) reactions between the Ag@silica nanocomposites and aqueous $HAuCl_4$; TEM images of (a) Ag nanoparticles, (b) Ag@silica nanocomposites, and the SNCAs resulting from the CGR reactions between Ag@silica and various amounts of aqueous HAuCl4 (1.0 mM), (c) 0.2 mL, (d) 0.4 mL, (e) 0.6 mL, and (f) 0.8 mL. The scale bars are 50 nm.



Source: Reprinted with permission from Ref. 96. Copyright 2010 American Chemical Society.

Figure 9. (a) Schematics of the synthetic procedures of heterogeneous rattle-type mesoporous nanostructures with inorganic nanocrystals (*e.g.*, spherical Au and ellipsoidal Fe_2O_3 nanoparticles) as the core and mesoporous silica as the shell; TEM images of $Au@SiO_2@mSiO_2$ (b), rattle-type $Au@mSiO_2$ (c), ellipsoidal $Fe_2O_3@SiO_2@mSiO_2$ (d and inset), rattle-type $Fe_2O_3@mSiO_2$ (e, inset: SEM image of deliberately selected broken ellipsoids).

5. SILICA/CARBON NANOSTRUCTURES

Graphene is the name given to a two-dimensional sheet of sp2-hybridized carbon. Its extended honeycomb network is the basic building block of other important allotropes; it can be stacked to form 3D graphite, rolled to form 1D nanotubes, and wrapped to form 0D fullerenes. Long-range π-conjugation in graphene yields extraordinary thermal, mechanical, and electrical properties, which have long been the interest of many theoretical studies and more recently became an exciting area for experimentalists. However, the applications of these carbon nanomaterials tend to suffering from their intrinsically hydrophobic and chemically inert surface properties, which greatly hinder their extensive applications in various areas. To conquer these disadvantages, surface-modification of these carbon materials by depositing suitable functional components onto their surfaces seems to provide a promising alternative. Such obtained carbon-based hybrid nanostructures generally exhibit synergistic properties and reserve the intrinsic properties of original carbon components. Therefore, the applications of those carbon materials can be greatly extended. In view of excellent properties of silica, great efforts have been devoted to depositing silica components onto the surfaces of such carbon materials, yielding versatile silica/carbon hybrid nanomaterials. Herein, we would give an overview in the related topics based on the recent publications.

5.1. Silica/CNT Hybrid Nanostructures

CNTs are allotropes of carbon with a cylindrical nanostructure. These cylindrical carbon molecules have many novel properties including high aspect ratio and tubular geometry, which provides ready gas access to a large specific surface area and percolation at very low volume fractions. They also exhibit extraordinary mechanical, thermal, electrical and optical properties, which support CNTs as ideal building blocks in hybrid materials with potentially useful in many applications in nanotechnology, electronics and optics. By templating against CNTs, silica components can be used to decorate CNTs sidewalls or fill CNTs matrix, forming varied silica/CNT hybrid nanomaterials. However, CNTs generally exist in the form of solid bundles, which are entangled together giving rise to a highly complex network. Together with the chemically inert surfaces, pristine CNTs tend to lack of solubility and be difficult manipulated in any solvents, which have imposed great limitations to the use of CNTs as templates to assemble silica components. To efficiently synthesize silica/CNT nanohybrids, it is necessary to activate the graphitic surface of CNT. In this direction, two main approaches including covalent and non-covalent methodologies have been extensively explored in recent years. In this section, the silica/CNT nanohybrids fabricated by templating against surface modified CNTs in sol-gel processes are mainly considered.

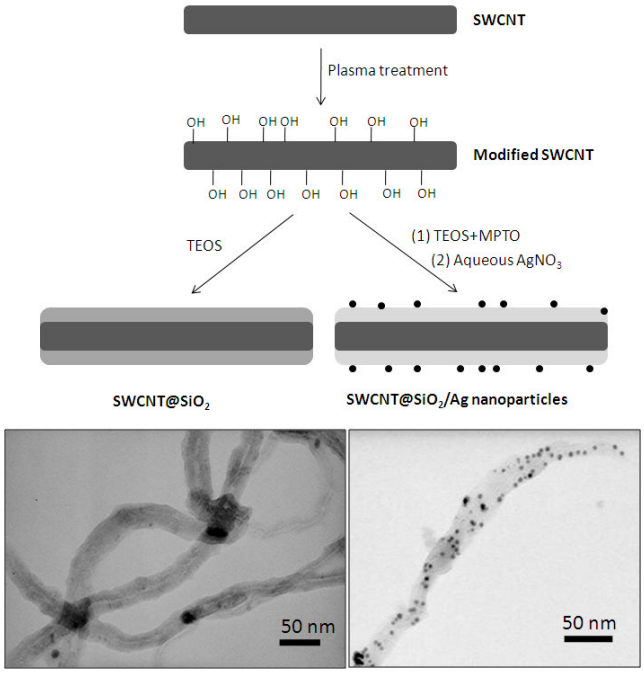
5.1.1. Covalent Processes

The end caps of CNTs (when not closed by the catalyst particles) tend to be composed of highly curved fullerene-like hemispheres, which are therefore highly reactive, as compared with the sidewalls.[99] The sidewalls themselves contain defective sites such as pentagon-heptagon pairs called Stone-Wales defects, sp3-hybridized defects and vacancies in the

nanotube lattice.[100] Frequently, these intrinsic defects are supplemented by oxidative damage to the nanotube framework by strong acids which leave holes functionalized with oxygenate functional groups such as carboxylic acid, ketone, alcohol, and ester groups.[101] In particular, the treatment of CNTs with strong acids such as nitric acid or with other strong oxidizing agents including KMnO4/H2SO4, oxygen gas, K2Cr2O7/ H2SO4 and OsO4,[102] tends to open these tubes and to subsequently generate oxygenated functional moieties that serve to tether many different types of chemical functionalities, such as oxides, polymers and metal nanoparticles, onto the ends and defect sites of CNTs, yielding a wide range of CNT-based nanohybrids with promising applications.

For example, Bottini et al. [103] grafted tetraethyl or tetramethyl- orthosilicate (TEOS or TMOS) onto carboxylic acid groups containing CNTs obtained under concentrated HNO3 oxidizing conditions, forming coupling aninopropyltriethyoxysiane functionalized CNTs through a carboxamide bond. On the basis of these surface-modified CNTs, silica beads were generated and decorated along the CNTs by a sol-gel process in the presence of ammonia water. Based on the strong acid treated CNTs, the silica nanobeads also can be directly fabricated onto the sidewalls of CNTs in the presence of small molecular surfactants. For example, mediated by anionic sodium dodecyl sulfate, Fan et al. [104] grew the silica nanobeads onto the concentrated acid treated CNTs by means of vapor-phase method. Another typical example was reported by Liu et al. [105] who used cationic surfactant cetyltrimethyl ammonium bromide to suspend oxidized CNTs in aqueous solution. Followed by a sol-gel process catalyzed by ammonia water, silica decorated CNTs nanohybrids were successfully synthesized.

The above described pioneering works are very interesting but unfortunately, during all those processes for modifying CNT surfaces, more chemicals such as modifier agents, surfactants, organic solvents, amphiphilic polymers or other additives are indispensable. These would inevitably increase the hazard to environment; enhance the preparation cost and complex the functionalization processes. Therefore, it is still a challenging work to develop a facile, low-cost and green CNT surface-modification method for fabricating CNT-based nanocomposites. Recently, we have demonstrated an effective route to introduce hydroxyl groups onto the side walls of pristine SWCNTs by means of plasma treatment technique [106]. Followed by a co-condensation process between these hydroxyl groups bearing on the SWCNTs and TEOS (or together with MPTO), a uniform SiO_2 and thiol groups-functionalized SiO_2 coating on the CNTs can be fabricated effectively. Utilizing SWCNT@SiO_2-SH, a stable SWCNT@SiO_2/Ag heterogeneous hybrid has been generated via in-situ growth process in the absence of any additional reducing agents (Figure 10). Particularly, in this synthetic strategy, no more solvent and chemicals are involved, which simplifies the modification process, reduces the preparation cost and decreases the hazard to environment. Moreover, this facile procedure could offer a promising alternative to create varied SWCNT/inorganic oxide (TiO_2, GeO_2 etc.) composites and the corresponding SWCNT/inorganic oxide/metal nanoparticles hybrids.



Source: Reprinted with permission from Ref. 106. Copyright 2009 Springer.

Figure 10. Schematic illustration of fabrication of SiO_2 coated single wall carbon nanotubes (SWCNT@SiO_2) and Ag nanoparticles immobilized SWCNT@SiO_2 (SWCNT@SiO_2/Ag nanoparticles) based on the plasma treated SWCNTs. TEOS and MPTO in scheme are tetraethoxysilane and 3-mercaptopropyl-triethoxysilane, respectively.

5.1.2. Non-Covalent Processes

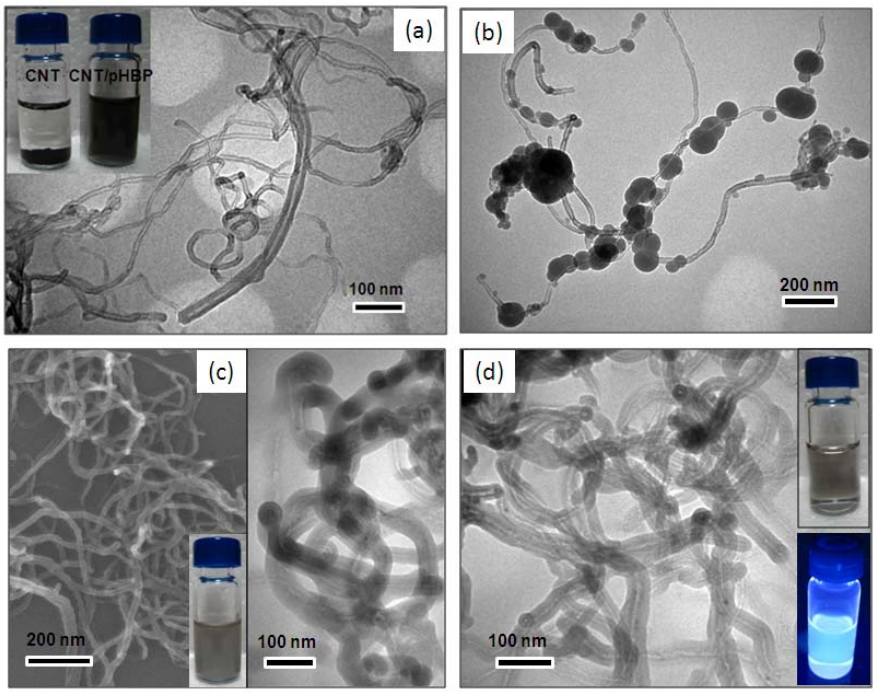
Although the strong oxidizing acids treatments can introduce a variety of organic groups on the CNTs surfaces, these functional groups tend to be with limited control over their number, type and location. Moreover, such treatment processes generally cause the surface etching and shortening of CNTs, resulting in the compromise of the electronic and mechanical properties thus suppress their extensive applications. In addition, the deposition of functional components on such acid-treated CNTs often leads to the non-uniform coatings. Therefore, to achieve uniform coatings on CNTs sidewalls, recently developed non-covalent (non-destructive) protocols provide facile and efficient ways.

By means of non-covalent attractions, π-π stacking and/or wrapping interactions in the presence of surfactants and/or polymers, aqueous-based CNT sols can be achieved. These surface modified CNTs can be further assembled with a variety of functional components including silica materials by means of in-situ synthesis techniques. The resulting CNT-based hybrids exhibit tailored properties while still reserving nearly all the intrinsic properties of CNTs. For example, More recently, Li et al. [107] have developed a simple and efficient non-destructive approach to decorate pristine CNTs with silica nanoparticles mediated by 1-aminopyrene surfactant. The inherently hydrophobic surfaces of pristine CNTs are first irreversibly modified with bifunctional 1-aminopyrene molecules using the non-covalent interactions between the pyrenyl groups of 1-aminopyrene and the six-membered carbon rings of the nanotubes. The resulting amino-modified CNTs specially adsorb in-situ formed

silica nanoparticles *via* preferential affinity in a sol-gel process in the presence of amino water. As another typical example, Bourlinos et al.[108] wetted pristine CNTs with vinyl silane molecules *via* non-covalent interactions between the vinyl groups and CNT surface. After condensation to an oligomeric siloxane network and subsequent calcinations, the authors obtained silica nanoparticles (5-12 nm), which were well-dispersed on the CNT surface. Similarly, by using different metal halides as precursors, silica coatings on the CNT surface have also been successfully addressed in the presence of SDS surfactant.[109]

Need to note that the use of small molecules as surface modifiers of CNTs generally lead to the formation of hybrid nanostructures with less stability owing the limit interaction sites between the small molecules and CNTs. Instead of small molecular surfactants, amphiphilic linear polymers provide another promising candidate and are often used for the modification of CNTs, since the polymers not only reduce the entropic penalty of micelle formation, but also have significantly higher energy of interaction than small molecules with CNTs.[110] Polymer-wrapping techniques, including the coating of mono- or multilayer polyelectrolytes onto CNT surfaces via electrostatic interactions, represent one of the common approaches used to non-covalently modify CNTs. Seeger et al. have functionalized the CNTs with the polyelectrolyte PEI which provided positive charges on the CNT surface.[111] Using TEOS as precursor, the negatively charged SiOx colloids can be easily attached onto CNT surface to form an amorphous silica coating *via* electrostatic interactions. However, it took rather long time (exceeded 100 h) to complete reaction since the reaction was carried out at room temperature. However, these functionalized CNTs tend to sensitive to surrounding environments such as pH value and ionic strength, which greatly limits the fabrication of versatile CNT-based nanohybrids in varied reaction conditions. To avoid the potentially complicated and tedious surface modification of CNTs, amphiphilic linear block copolymers have been developed to functionalize CNTs using hydrophobic or π-π stacking interactions in the selective solvents.[112] Nevertheless, this method always failed to separate the modified products from the selective solvent due to the adsorption mature, limiting the applications of the modified CNTs.

To conquer the disadvantages brought by the use of small molecules and linear polymers CNT surface-modifiers, recently, our group has developed a new type of noncovalent surface modifier of CNTs, pyrenyl moieties decorated hyperbranched polyglycidol (pHBP) [113]. The use of pHBP possesses several advantages over the other publications: 1) multiple pyrene moieties bearing on the periphery of pHBP can be tightly attached onto the CNT surfaces through π-π stacking interactions; 2) the uniform molecular composition of pHBP effectively avoid the formation of free polymer micelles and allows free pHBP to be easily removed from the CNT/pHBP sols using pure solvent; 3) the dendritic polyether structure of pHBP provides void-containing electron-negative environment, which is well-suitable to attract metal ions to be in-situ reduced to form and accommodate metal NPs; 4) the hydroxyl groups bearing on the periphery of pHBP facilitate the in-situ nucleation and growth of inorganic oxides via a sol-gel process, resulting in the formation of CNT/pHBP/inorganic oxides nanohybrids. Using pHBP modified CNTs, silica beads decorated CNT/pHBP and uniform silica coated CNT/pHBP hybrid have been successfully obtained by the NH_4OH catalytic and HCl catalytic sol-gel processes, respectively (Figure 11). In addition, by incorporation of Rhodamine 6G into the silica coating, the uniform fluorescent CNT/pHBP/silica nanofibers were also fabricated.



Source: Reprinted with permission from Ref. 113. Copyright 2010 Wiley-VCH.

Figure 11. TEM images of (a) CNT/pHBP and (b) CNT/pHBP/silica obtained in the presence of NH4OH; (c) SEM and TEM images of CNT/pHBP/silica prepared in the presence of HCl; (d) TEM image of fluorescent CNT/pHBP/silica-Rhodamine 6G nanofibers. Insets of (a) and (c) show the typical photographs of the corresponding hybrid sols in DMF solvent; inset of (d) shows typical photographs of fluorescent CNT/pHBP/silica-Rhodamine 6G nanofibers sols in DMF without (upper) and with UV irradiation (bottom).

5.2. Silica/Graphene Sheets Nanostructures

Graphene sheets consisting of 2D "aromatic" monolayer of carbon atoms have demonstrated exceptional properties, including ultrahigh electron mobility and ballistic charge carrier transport [114]. Comprehensive chemical methods such as Brodie, Staudenmaier or Hummers methodologies have been used to oxidize graphene sheet with polar oxygen functional groups including hydroxyl, epoxide, carbonyl and carboxyl moieties to yield graphene oxide (GO) [115]. The presence of these oxygen-functionalized groups renders GO sheets negatively charged. On the basis of that, Yang et al. [116] explored to electrostatically adsorb positive charged cetyltrimethyl ammonium bromide (CTAB) and self-assembled them onto the surfaces of GO sheets in alkaline solution. After a sol-gel process, mesoporous silica layer was deposited onto the GO surfaces, forming a sandwich GO/silica hybrid nanostructures with quite high specific surface area. Promisingly, when these yielded 2D hybrid nanomaterials exhibited excellent lithium ion storage properties, such as very high first reversal capacity and excellent rate performance, as well as continuous and progressive capacity decay along with cycling processes. Except this pioneering work, unfortunately, few examples concerning the generation of GO/silica and graphene/silica hybrid nanostructures have been involved in recent years.

5.3. Other Silica/Carbon Nanomaterials

Fullerenes including C_{60}, C_{70} C_{74}, C_{76}, and C_{78}, are probably the most studied individual type of nanomaterials. So far, a number of attempts to incorporate fullerene into inorganic matrices appeared with the hope that 3D inorganic networks prepared via sol-gel routes, leading to the development of highly stable, resistant and long-lasting fullerene-based materials [117]. Unfortunately, unsatisfactory outcomes were obtained mainly owing to the low solubility of fullerene and its tendency to aggregate, which resulted in inhomogeneous mixtures or nano-transparent glasses [118]. Hence, fullerene has been functionalized with the aim to covalently link it onto inorganic oxides and several sol-gel processes have subsequently been developed. For example, Jeong et al. [119] have described the synthesis of highly photoluminescent fullerene/silica nanospheres with very uniform size (61 nm in average diameter). This material was obtained by a reverse microemulsion method in which fullerene reacted with TEOS in the presence of TX-100 in n-hexanol as surfactant and co-surfactant, respectively, employing NH_4OH as catalyst. Interestingly, this material showed an excellent PL intensity and it was successfully employed as bioimaging materials. Alternatively, Ozin and co-workers reported on the synthesis of “periodic mesoporous buckysilica” prepared by self-assembly of a multi-substituted fullero-tri(ethoxy)silane derivative hydrolyzed in the presence of tetraethyl orthosilicate (TEOS) under basic and acid conditions [120]. The latter resulted in the best homogeneous mesoporous silica /C60 hybrids obtained so far.

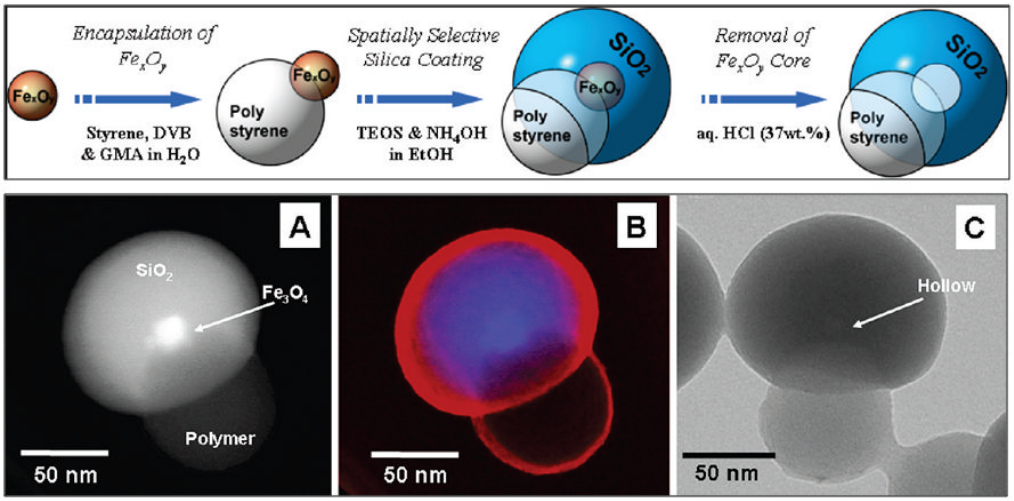
Another typical carbon nanomaterials is detonation nanodiamond (DND). When an explosive mixture of TNT/RDX is detonated, diamond particles with a diameter of ca. 5 nm are formed. DND grains mostly have diamond cubic lattice with multiple twins-defects. The grains are unstable with respect to aggregation and spontaneously form micrometre-sized clusters. DND has extremely large relative surface area. As a result, its surface spontaneously attaches water and hydrocarbon molecules from the ambient atmosphere. DND-based materials can be used as additives to engine oils and galvanic electrolytes, dry lubricants for metal industry, reinforcing fillers for plastics and rubbers. Especially, DNDs can shuttle chemotherapy drugs to cells without producing the negative effects of today's delivery agents. Therefore, DNDs provide very promising platform for biomedical applications. To date, many publications concerning the synthesis of surface-modified DND nanostructures and their applications in life area have been well-documented.[121-123] Although the possibility of deposition of DND layers onto the various substrates including tungsten wires, silicone carbide, copper and titanium, have been explored to fabricate DND-based hybrid nanostructures,[124-127] quite few reports for the fabrication of silica/DND nanostructures with well-defined architectures involved. As a representative example, Singh et al.[128] demonstrated an effective method to fabricate α-silica/DND nanohybrids by coating of as-grown α-silica fibers with DND via microwave plasma chemical vapor deposition. Even so, how to fabricate silica/DND nanostructures via facile even green protocols still remain great challenges. Therefore, the corresponding researches will open a new direction in the near future.

6. SILICA-BASED JANUS NANOSTRUCTURES

A traditional goal in colloid and particle science is to obtain particles whose chemical composition is homogeneous. In contrast, of emerging interest is the idea of achieving "Janus" particles whose surface composition differs on two sides of the particles. During the past decades, considerable efforts have been devoted to fabrication of Janus spheres. For the silica-based Janus spheres, one of the most typical method is topselective functionalization. Initially, bulk solid substrates were used to support a monolayer of silica spheres. Thus the functionalization could occur only on the top face area of the anchored silica particles. Owing to the limited surface area of a bulk substrate often led to low yield of Janus particles, a modified method was later adapted by using colloidal particles as the supporting substrates. As a typical example, Granic and coworkers have developed a protocol to produce silica-based Janus particles in a large quantity.[129] That idea is that at the liquid-liquid interface of emulsified molten wax and water, untreated silica particles adsorb and are frozen in place when the wax solidifies. The exposed surface of the immobilized silica particles are modified chemically. Finally, wax is dissolved to release the silica spheres with Janus surfaces. Using those partial-surface-modified silica spheres as templates, various functional components can be selectively deposited onto modified silica hemispheres, producing hierarchically Janus nanostructures. In a typical example [130], the aminopropyltrimethyoxysilane modified silica colloids are partially embedded at the solidified wax/water Pickering emulsion interface. After the exposed corona pointing towards the outer aqueous phase is selectively etched with NH_4F, Janus spheres with tunable morphologies ranging from spherical colloids to mushroom-like architectures can be achieved by simply controlling the etching period. If the exposed silica corona were further modified with vinyl groups, following a one-step emulsion polymerization, PS chains were grafted from the modified side of silica spheres and grow into a cap or nanospheres, leading to the formation of well-defined silica/PS Janus spheres.

Another typical example for synthesis of silica-based Janus spheres were demonstrated by Feyen et al. [131]. They designed a facile and controllable synthetic route to fabricate Fe_3O_4@Poly(divinyl benzene)-silica mushroom nanostructures (Figure 12). The synthesis consists of partial coating of Fe_3O_4 with crosslinked Poly(divinyl benzene) spheres, followed by attaching silica hemispheres. It was found that the surface-accessible Fe_3O_4 nanopartciles are the key for the directing the growth of silica hemispheres onto the Janus-type Fe_3O_4@Poly(divinyl benzene) particles. Moreover, the size and porosity of silica component are tunable by adjusting the amount of TEOS used and by addition of proper surfactants in Stöber process.

Since it is difficult to fine-tune the surface tension and lattice mismatch between the silica and metal materials owing to the intrinsically amorphous nature of silica, the fabrication of silica/metal nanoparticle Janus spheres becomes more difficult. As a valuable exploration, more recently, Chen et al. developed a new approach to control silica deposition on partial surface of Au nanospheres, forming silica/Au Janus particles [132]. The selective deposition was driven by the partitioned surface functionalities on Au nanospheres through competitive ligand coordination. More specifically, 4-mercaptophenylacetic acid and poly(acrylic acid) were used as competitive ligands to tailor citrate-stabilized Au nanospheres. After a ammonia-catalyzed sol-gel process, the surface of Au nanoparticles was partially encapsulated with silica with a good yield (>99%), generating silica/Au Janus particles.



Source: Reprinted with permission from Ref. 131. Copyright 2010 American Chemical Society.

Figure 12. Illustration of the synthesis procedures for mushroom nanostructures (upper); dark filed STEM image (A), SEM and dark field STEM overlapping image (B) of Fe_3O_4@DVB-silica nanoparticles and TEM image (C) of Fe_3O_4@DVB-silica nanoparticles after HCl etching.

Many other methods assisted with microfluidic techniques [133], interfacial ligand-exchanges [134] and phase-seperation processes[135] have been extensively developed for the fabrication of Janus particles. However, most of those methods were used to prepare polymer- or metal-based Janus spheres rather than silica-based Janus particles.

7. Challenges and Outlook

The fabrication of silica-based hybrid nanomaterials with well-defined architectures including silica/polymer, silica/metal nanoparticles and silica/carbon, is enjoying ever-increasing research interests for their important properties and diverse applications in catalytic, biomedical, SERS, and photoelectronic fields. Although considerable efforts have been devoted to the related researches, currently, several great challenges still remain and need to be appropriately addressed: 1) Producing silica-based nanostructures in a large-scale for practical commercialization, while keeping the regular morphologies unchanged. This highly requires developing reaction systems with good stability and easy operation; 2) Considering the safety, energy and environment issues aroused in the recent years, facile and green synthetic strategies are high desired. In this direction, three main steps need to be considered: the choice of the environmentally benign solvent media and nontoxic reactants used for the synthesis, the choice of low temperature reaction with good yield and less side reactions, and the choice of facile and low-cost synthetic strategies; 3) The incorporation of functional components, and the novel morphologies of silica-based hybrid nanostructures could arouse side effects on the human health, thus hinders their safe use in various areas especially in in-vivo applications. Therefore, it is highly desired to build reliable evaluation systems to fully evaluate the possible side effects rendered by the use of hybrid materials; 4) Because that the properties of hybrid nanomaterials heavily depend on their morphologies,

the exploration in the synthesis of hybrid nanostructures with novel morphologies and well-controllable morphologies will continue to attract increasingly attentions; 5) To further expand the applications of silica-based hybrid nanostructure, the fabrication of multifunctional hybrid materials by surface-modification or incorporation of more functional components provide the most direct and promising alternatives.

ACKNOWLEDGMENTS

This work was supported by grants-in-aid for the *World Class University Program* (No. R32-2008-000-10174-0) and the *National Core Research Center Program* from MEST (No. R15-2006-022-01001-0), and the *Brain Korea 21 program* (BK-21).

REFERENCES

[1] J. H. Jung, M. Park, S. Shinkai, *Chem. Soc. Rev.* 2010, *39*, 4286.
[2] Y. Klichko, M. Liong, E. Choi, S. Angelos, A. E. Nel, J. F. Stoddart, F. Tananoi, J. I. Zink, *J. Am. Ceram. Soc.* 2009, *92*, S2.
[3] S. M. Hussain, L. K. Braydich-Stolle, A. M. Schrand, R. C. Murdock, K. O. Yu, D. M. Mattie, J. J. Schlager, M. Terrones, *Adv. Mater.* 2009, *21*, 1549.
[4] W. Stöber, A, Fink, E. Hohn, *J. Colloid Inter. Sci.* 1968, *26*, 62.
[5] F. Branda, B. Silvestri, G. Luciani, A. Costantini, *Colloids Surf. A* 2007, *299*, 252.
[6] F. J. Arriagada, K. Osseo-Asare, *J. Colloid Interface Sci.* 1995, *170*, 8.
[7] Q. Y. Zhang, J. Wang, G. Wu, J. Shen, S. Buddhudu, *Mater. Chem. Phys.* 2001, *72*, 56.
[8] P. Nostell, A. Roose, B. Karlson, *Thin Solid Films* 1999, *351*, 170.
[9] H. Y. Koo, D. K. Yi, S. J. Yoo, D. Y. Kim, *Adv. Mater.* 2004, *16*, 274.
[10] A. S. Dimitrov, t. Miwa, K. Nagayama, *Langmuir* 1999, *15*, 5257.
[11] W. Yan, H. Li, X. Shen, *Macromol. Rapid Commun.* 2005, *26*, 564.
[12] C. López, *Adv. Mater.* 2003, *15*, 1679.
[13] L. Tong, J. Lou, R. R. Gattas, S. He, X. Chen, L. Liu, E. Mazur, *Nono Lett.* 2005, *5*, 259.
[14] D. K. Sood, P. K. Sekhar, S. Bhansali, *Appl. Phys. Lett.* 2006, *88*, 143110.
[15] P. Christian, *Langmuir* 2010, *26*, 1405.
[16] M. Chen, L. Wu, S. Zhou, B. You, *Adv. Mater.* 2006, *18*, 801.
[17] F. Caruso, *Adv. Mater.* 2001, *13*, 11.
[18] M. Zhao, L. Zheng, X. Bai, N. Li, L. Yu, *Colloid Surf. A Physicochem. Eng. Aspects* 2009, *346*, 229.
[19] Tissot, J. P. Reymond, F. Lefebvre, E. Bourgeat-Lami, *Chem. Mater.* 2002, *14*, 1325.
[20] H. Li, C-S. Ha, I. Kim, *Langmuir* 2008, *24*, 10552.
[21] H. Li, C-S. Ha, I. Kim, *J. Sol-gel Sci. Technol.* 2010, *53*, 232.
[22] D. Li, Z. Guan, W. Zhang, X. Zhou, W. Y. Zhang, Z. Zhuang, X. Wang, C. J. Yang, *Appl. Mater. Interf.* 2010, *2*, 2711.
[23] T, Zhang, J. Ge, Y. Hu, Q. Zhang, S. Aloni, Y. Yin, *Angew. Chem. Int. Ed.* 2008, *47*, 5806.

[24] C. R. Martin, P. Kohli, Nat. Rev. *Drug Discovery* 2003, *2*, 29.
[25] S. B. Lee, D. T. Mitchell, L. Trofin, T. K. Nevanen, H. Soederlund, C. R. Martin, *Science* 2002, *296*, 2198.
[26] R. Fan, R. Karnik, M. Yue, D. Li, A. Majumdar, P. Yang, *Nano Lett.* 2005, *5*, 1633.
[27] X. Quan, S. Yang, X. Ruan, H. Zhao, *Environ. Sci. Technol.* 2005, *39*, 3770.
[28] S. J. Lee, S. S. Lee, J. Y. Lee, J. H. Jung, *Chem. Mater.* 2006, *18*, 4713.
[29] C. R. Martin, Z. Silwy, *Nat. Mater.* 2004, *3*, 284.
[30] S. J. Son, J. Reichel, B. He, M. Schuchman, S. B. Lee, *J. Am. Chem. Soc.* 2005, *127*, 7316.
[31] S. Polarz, B. Smarsly, *J. Nanosci. Nanotechn.* 2002, *2*, 581.
[32] Q. Cai, Z. Luo, W. Pang, Y, Fan, X. Chen, F. Cui, *Chem. Mater.* 2001, *13*, 258.
[33] R. I. Nooney, D. Thirunavukkarasu, Y. Chen, R. Josephs, A. E. Ostafin, *Chem. Mater.* 2002, *14*, 4721.
[34] Suzuki, K. Ikari, H. Imai, *J. Am. Chem. Soc.* 2004, *126*, 462.
[35] G. Lelong, S. Bhattacharyya, S. Kline, T. Cacciaguerra, M. A. Gonzalez, M.-L. Saboungi, *J. Phys. Chem. C* 2008, *112*, 10674.
[36] D. Zhao, J. Feng, Q. Huo, N. Melosh, G. H. Fredrickson, B. F. Chmelka, G. D. Stucky, *Science* 1998, *279*, 548.
[37] A. Sayari, B.-H. Han, Y. Yang, *J. Am. Chem. Soc.* 2004, *126*, 14348.
[38] C. Yu, J. Fan, B. Tian, D. Zhao, G. D. Stucky, *Adv. Mater.* 2002, *14*, 1742.
[39] D. Zhao, J. Sun, Q. Li, G. D. Stucky, *Chem. Mater.* 2000, *12*, 275.
[40] H. Zhang, J, Sun, D. Ma, X. Bao, A. Klein-Hoffmann, G. Weinberg, D. Su, R. Schlögl, *J. Am. Chem. Soc.* 2004, *126*, 7440.
[41] C. Gao, S. Che, *Adv. Funct. Mater.* 2010, *20*, 2750.
[42] V. Polshettiwar, D. Cha, X. Zhang, J. M. Basset, *Angew. Chem. Int. Ed.* 2010, *49*, 9652.
[43] D. Chen, L. Li, F. Tang, S. Qi, *Adv. Mater.* 2009, *21*, 3804.
[44] Y. Chen, H. Chen, L. Guo, Q. He, F. Chen, J. Zhou, J. Feng, J. Shi, *ACSNANO* 2010, *4*, 529.
[45] S. Banerjee, A. Datta, *Langmuir* 2010, *26*, 1172.
[46] R. Barbey, L. Lavanant, D. Paripovic, N. Schüwer, C. Sugnaux, S. Tugulu, H.-A. Klok, *Chem. Rev.* 2009, *109*, 5437.
[47] Y. Huang, T. Hou, X. Cao, S. Perrier, Y. Zhao, *Polym. Chem. 2010*, *1*, 1615.
[48] Y.-P. Wang, X.-W. Pei, X.-Y. He, K. Yuan, *Eur. Polym. J.* 2005, *41*, 1326.
[49] S. Edmundson, W. T. S. Huck, *J. Mater. Chem.* 2004, *14*, 730.
[50] N. Cheng, O. Azzaroni, S. Moya, W. T. S. Huck, *Macromol. Rapid Commun.* 2006, *27*, 1632.
[51] C. Huang, T. Tassone, K. Woodberry, D. Sunday, D. L. Green, *Langmuir* 2009, *25*, 13351.
[52] X. Jiang, B. Zhao, G. Zhong, N. Jin, J. M. Horton, L. Zhu, R. S. Hafner, T. P. Lodge, *Macromolecules* 2010, *43*, 8209.
[53] H. Li, C.-S. Ha, I. Kim, *Macromol. Rapid Commun.* 2009, *30*, 188.
[54] M. Rosenholm, A. Meinander, E. Peuhu, R. Niemi, J. E. Erisson, C. Sahlgren, M. Lindén, *ACSNANO* 2009, *3*, 197.
[55] O. Schepelina, N. Poth, I. Zharov, *Adv. Funct. Mater.* 2010, *20*, 1962.
[56] W. Yan, H. Li, X. Shen, *Macromol. Rapid Commun.* 2005, *26*, 564.
[57] X. Zhang, W. Yan, H. Li, X. Shen, *Polymer* 2005, *46*, 11958.

[58] W. Yan, H. Li, X. Shen, *Eur. Polym. J.* 2005, *41*, 992.
[59] H. Li, S. Abraham, W. Yan, C.-S. Ha, I. Kim, *Macromol Rapid Commun.* 2007, *28*, 1534.
[60] J. J. Yuan, O. O. Mykhaylyk, A. J. Ryan, S. P. Armes, *J. Am. Chem. Soc.* 2007, *129*, 1717.
[61] Li, S. Mann, *Angew. Chem. Int. Ed.* 2008, *47*, 9476.
[62] R. M. Crooks, M. Zhao, L. Sun, V. Chechik, L. K. Yeung, *Acc. Chem. Res.* 2001, *34*, 181.
[63] P. K. Jain, I. H. Ei-Sayed. M. A. Ei-Sayed, *Nano Today* 2007, *2*, 18.
[64] X. Peng, Q. Pan, G. L. Rempel, *Chem. Soc. Rev.* 2008, *37*, 1619.
[65] J. D. S. Newman, J. M. Roberts, G. J. Blanchard, *Anal. Chem.* 2007, *79*, 3448.
[66] H. Zhu, C. Liang, W. Yan, S. H. Overbury, S. Dai, *J. Phys. Chem. B* 2006, *110*, 10842.
[67] K. Kim, H. S. Kim, H. K. Park, *Langmuir* 2006, *22*, 8083.
[68] V. G. Pol, A. Gedanken, J. Calderon-Moreno, *Chem. Mater.* 2003, *15*, 1111.
[69] G. Budroni, A. Corma, *Angew. Chem. Int. Ed.* 2006, *45*. 3328.
[70] S. L. Westcott, S. J. Oldenburg, T. R. Lee, N. J. Halas, *Chem. Phys. Lett.* 1999, *300*, 651.
[71] H. Li, C-S. Ha, I. Kim, *Nanoscale Res. Lett.* 2009, *4*, 1384.
[72] S. Wang, M. Zhang, L. Zhong, W. Zhang, J. Mol. *Catal. A Chem.* 2010, *327*, 92.
[73] J. L. Ou, C. P. Chang, Y. Sung, K. L. Ou, C. C.Tseng, H. W. Ling, M. D. Ger, *Colloids Surf. A: Physcochem. Eng. Aspects* 2007, *305*, 36.
[74] J. H. Zhang, P. Zhan, Z. L. Wang, W. Y. Zhang, N. B. Ming, *J. Mater. Lett.* 2003, *18*, 649.
[75] J. Zhang, J. Liu, S. Wang, P, Zhan, Z. Wang, N. Ming, *Adv. Funct. Mater.* 2004, *14*, 1089.
[76] H. Hofmeister, P.-T. Miclea, M. Steen, W. Mörke, H. Drevs, *Top. Catal.* 2007, *46*, 11.
[77] A. D. LaLonde, M. G. Norton, *J. Mater. Sci.* 2005, *20*, 3021.
[78] V. G. Pol, A. Gedanken, J. Calderon-Moreno, *Chem. Mater.* 2003, *15*, 1111.
[79] Y. Jiang, Q. Gao, *J. Am. Chem. Soc.* 2006, *128*, 716.
[80] C. Wang, G. Zhu, J. Li, X. Cai, Y. Wei, D. Zhang, S. Qiu, *Chem. Eur. J.* 2005, *11*, 4975.
[81] W. Huang, J. N. Kuhn, C.-K. Tsung, Y. Zhang, S. E. Habas, P. Yang, G. A. Somorijai, *Nano Lett.* 2008, *8*, 2027.
[82] H. Li, R. Wang, Q. Hong, L. Chen, Z. Zhong, Y. Koltypin, J. Calderon-Moreno, A. Gedanken, *Langmuir* 2004, *20*, 8352.
[83] T. Nakamura, Y. Yamada, K. Yano, *J. Mater. Chem.* 2007, *17*, 3726.
[84] H. Li, J. K. Jo, L. Zhang, C.-S. Ha, H. Suh, I. Kim, *Langmuir* 2010, *26*, 18442.
[85] S. Liu, M.-Y. Han, *Chem. Asian J.* 2010, *5*, 36
[86] M. Liz-Marzan, M. Giersig, P. Mulvaney, *Langmuir* 1996, *12*. 4329.
[87] P. Botella, A. Corma, M. T. Navarro, *Chem. Mater.* 2007, *19*, 1979.
[88] S. M. Kang, K.-B. Lee, D. J. Kim, I. S. Choi, *Nanotechnology* 2006, *17*, 4719.
[89] H. Li, C.-S. Ha, I. Kim, *J. Nanopart. Res.* 2010, *12*, 985.
[90] Liong, B. France, K. A. Bradley, J. I. Zink, *Adv. Mater.* 2009, *21*, 1.
[91] W. M. Zhang, J. S. Hu, Y. G. Guo, S. F. Zheng, L. S. Zhong, W. G. Song, L. J. Wan, *Adv. Mater.* 2008, *20*, 1160.

[92] H. X. Li, Z. F. Bian, J. Zhu, D. Q. Zhang, G. S. Li, Y. N. Huo, H. Li, Y. F. Lu, *J. Am. Chem. Soc.* 2007, *129*, 8406.
[93] K. M. Yeo, J. Shin, I. S. Lee, *Chem. Commun.* 2010, *46*, 64.
[94] M. Roca, A. J. Haes, *J. Am. Chem. Soc.* 2008, *130*, 14273.
[95] J. Lee, J. C. Park, J. U. Bang, H. Song, *Chem. Mater.* 2008, *20*, 5839.
[96] Y. Chen, H. Chen, L. Guo, Q. He, F. Chen, J. Zhou, J. Feng, J. Shi, *ACSNANO* 2010, *4*, 529.
[97] S. Liu, Z. Zhang, M.-Y. Han, *Adv. Mater.* 2005, *17*, 1862.
[98] Y. Ren, M. Chen, Y. Zhang, L. Wu, *Langmuir* 2010, *26*, 11391.
[99] S. Niyogi, M. A. Hamon, H. Hu, B. Zhao, P. Bhowmik, R. Sen, M. E. Itkis, R. C. Haddon, *Acc. Chem. Res.* 2002, *35*, 1105.
[100] A. Hirsch, *Angew. Chem. Int. Ed.* 2002, *14*, 1853.
[101] J. Chen, M. A. Hamon, H. Hu, Y. Chen, A. M. Rao, P. C. Eklund, R. C. Huddon, *Science* 1998, *282*, 95.
[102] S. Banerjee, T. Hemraj-Benny, S. S. Wong, *Adv. Mater.* 2005, *17*, 18.
[103] M. Bottini, L. Tautz, H. Huynh, E. Monosov, N. Bottini, M. I. Dawson, S. Bellucci, T. Mustelin, *Chem. Commun.* 2005, 785.
[104] W. Fan, L. Gao, *Chem. Lett.* 2005, *34*, 954.
[105] Y. Liu, J. Tang, X. Chen, R. Wang, G. K. H. Pang, Y. Zhangm J. H. Xin, *Carbon* 2006, *44*, 158.
[106] H. Li, C-S. Ha, I. Kim, *Nanoscale Res. Lett.* 2009, *4*, 1384.
[107] X. Li, Y. Liu, L. Fu, L. Cao, D. Wei, Y. Wang, *Adv. Funct. Mater.* 2006, *16*, 2431.
[108] A. B. Bourlinos, V. Georgakilas, R. Zboril, P. Dallas, *Carbon* 2007, *45*, 2136.
[109] K. Hernadi, E. Ljubovic, J. W. Seo, L. Forro, *Acta Mater.* 2003, *51*, 1447.
[110] D. Tasis, N. Tagmatarchis, A. Bianco, M. Prato, *Chem. Rev.* 2006, *106*, 1105.
[111] T. Seeger, T. Kohler, T. Frauenheim, N. Grobert, M. Ruhle, M. Terrones, G. Seifert, *Chem. Commun.* 2002, 34.
[112] G. Mountrichas, S. Pispas, N. Tagmatarchis, *Small* 2007, *3*, 404.
[113] H. Li, J. K. Jo, L. Zhang, C.-S. Ha, H. Suh, I. Kim, *Adv. Funct. Mater.* 2010, *20*, 3864.
[114] A. K. Geim, K. S. Novoselov, *Nat. Mater.* 2007, *6*, 183.
[115] Y. Zhu, S. Murali, W. Cai, X. Li, J. W. Suk, J. R. Potts, R. S. Ruoff, *Adv. Mater.* 2010, *22*, 3906.
[116] S. Yang, X. Feng, L. Wang, K. Tang, J. Maier, K. Müllen, *Angew. Chem. Int. Ed.* 2010, *49*, 4795.
[117] F. Wudl, *J. Mater. Chem.* 2002, *12*, 1959.
[118] F. Giacalone, N. Martin, *Adv. Mater.* 2010, *22*, 4220.
[119] J. Jeong, M. Cho, Y. T. Lim, N. W. Song, B. H. Chuang, *Angew. Chem. Int. Ed.* 2009, *48*, 5296.
[120] W. Whitnall, L. Cademartiri, G. A. Ozin, *J. Am. Chem. Soc.* 2007, *129*, 15644.
[121] V. Vaijayanthimala, H.-C. Chang, *Nanomedicine* 2009, *4*, 47.
[122] B. I. Kharisov, O. V. Kharissova, L. Chávez-Guerrero, *Syn. React. Inorg. Met.-Org. Nano-Met. Chem.* 2010, *40*, 84.
[123] A. M. Schrand, S. A. C. Hens, O. A. Shenderova, *Crit. Rev. Solid State Mater. Sci.* 2009, *34*, 18.
[124] W. May, *Endeavour* 1995, *19*, 101.

[125] V. Baranauskas, H. J. Ceragioli, A. C. Peterlevitz, S. F. Durrant, *Thin Solid Films* 2001, *398-399*, 250.
[126] G. Chollon, R. Naslain, C. Prentice, R. Shatwell, P. May, *J. Eur. Ceram. Soc.* 2005, *25*, 1929.
[127] S. Xie, G. Shafer, C. G. Walson, H. B. Martin, *Diamond Relat. Mater.* 2006. *15*, 225.
[128] M .K. Singh, E. Titus, J. C. Madaleno, L. Pereira, G. Cabral, V. F. Neto, J. Gracio, *Diamond Reatl. Mater.* 2008, *17*, 1106.
[129] S. Jiang, S. Granick, *Langmuir* 2008, *24*, 2438.
[130] B. Liu, C. Zhang, J. Liu, X. Qu, Z. Yang, *Chem. Commu.* 2009, 3871.
[131] M. Feyen, C. Weidenthaler, F. Schüth, A.-H. Lu, *J. Am. Chem. Soc.* 2010, *132*, 6791.
[132] T. Chen, G. Chen, S. Xing, T. Wu, H. Chen, *Chem. Mater.* 2010, *22*, 3826.
[133] T. Nisisako, T. Torii, T. Takahashi, Y. Takizawa, *Adv. Mater.* 2006, *18*, 1152.
[134] S. Pradhan, L. P. Xu, S. W. Chen, *Adv. Funct. Mater.* 2007, *17*, 2385.
[135] H. W. Gu, P. K. Zheng, X. X. Zhang, B. Xu, *J. Am. Chem. Soc.* 2004, *126*, 5664.

In: Silica Nanoparticles
Editor: Juan Vivero-Escoto
ISBN 978-1-61324-452-4
© 2012 Nova Science Publishers, Inc.

Chapter 6

FUNCTIONAL SILICA NANOPARTICLES SYNTHESIZED BY WATER-IN-OIL MICROEMULSION

Tangi Aubert, Stéphane Cordier and Fabien Grasset
Université de Rennes, UMR, Sciences Chimiques de Rennes, UR1-CNRS
Campus de Beaulieu, CS, F-Rennes Cedex, France

ABSTRACT

The elaboration of monodisperse and size-controlled silica nanoparticles has already been perfectly mastered for years. However, creating functional nanoparticles with sophisticated structural designs is still an open challenge and offers the scientific community a wide range of possibilities and opportunities. Among the different techniques available for the elaboration of such materials, the water-in-oil (w/o) microemulsion appears as a particularly dedicated tool. Indeed, the aqueous inverted micelles that constitute the w/o microemulsion is a well-suitable confined reacting medium for the synthesis of structured functional nanoparticles with controlled size and shape. This process allows the encapsulation in silica nanoparticles of different type of core elements (nanocrystals, molecules, etc.) with a high control on the structure of the obtained nanoparticles and on the concentration of the encapsulated elements. In this chapter will be presented the synthesis via microemulsion processes of different functional silica nanoparticles. The obtained materials exhibit interesting properties such as optical properties (photoluminescence, UV absorption, etc.) and/or magnetic properties. They should therefore find numerous applications in a broad range of technologies, such as biotechnologies, photonics, cosmetics, etc.

1. INTRODUCTION

1.1. Interest of Functional Nanoparticles and Interest of Silica as Matrix

The need of new materials offering new properties for an increasing amount of applications is an endless motivation for the scientific community. The design of more and more complex functional materials is therefore one of the main task of the material scientists.

Among the arising nanotechnologies, multifunctional nanoparticles with complex architectures constitute one of the most promising and studied research fields. However, the new properties resulting from the reduction of the size of colloidal materials also bring new physical limitations in their handling. Indeed due to their high specific surface area, nanoparticles often show a low stability and a high chemical reactivity, which result in non-desired aggregation effects. Thus, the encapsulation of these novel nanomaterials in nano-sized silica matrix allow to overcome these limitations while preserving the desired properties of the original material. Indeed, silica coatings provide to nanomaterials a good colloidal and chemical stability. In addition, it is relatively easy to control the size and shape of colloidal silica. Finally, it offers many possibilities of surface functionalization, a necessary step for numerous applications and rendering the material bio-compatible [1]. Functional silica nanoparticles have therefore tremendous potential applications in the fields of biotechnologies [1-5], photonics [6-9], catalysis [10-11], etc.

1.2. Possibilities for the Synthesis of Silica Nanoparticles

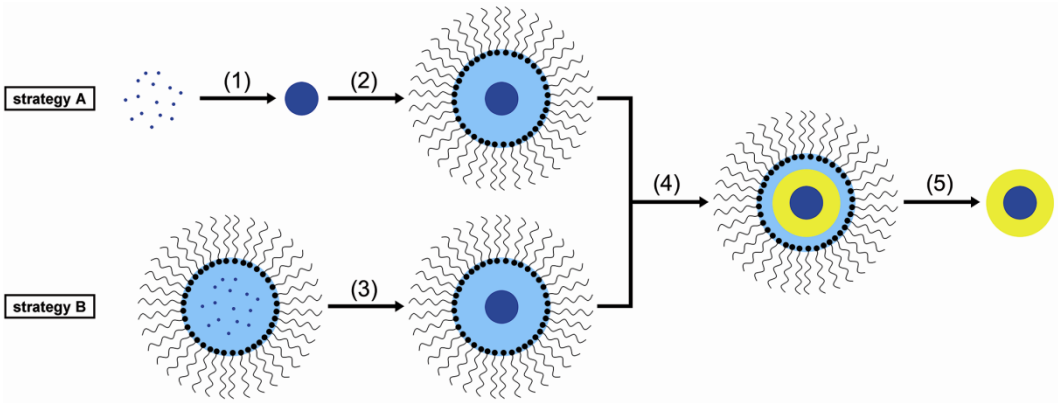
There are several possibilities for the preparation of colloidal silica nanoparticles or silica coatings on other colloidal materials. The historical and classical route for the preparation of perfectly spherical and monodisperse silica nanoparticles is the well known Stöber process [12], which is a base catalyzed sol-gel process consisting in the hydrolysis and condensation of an alkoxysilane precursor, generally the tetraethyl orthosilicate (TEOS). This technique is also suitable for coating core particles with a silica shell. However, for coatings on hydrophobic or vitreophobic materials it requires to pass by a pre-silanization step using silane coupling agents and/or through the water-glass method using a sodium silicate precursor [13-15]. More recently Yokoi et al. developed another technique for producing silica nanoparticles using biphasic systems and amino acids as catalyst for the hydrolysis and condensation of TEOS [16-18].

1.3. Synthesis of Silica Nanoparticles by Water-in-Oil Microemulsion

Since the 90s, it is also known that monodisperse and sized-controlled silica nanoparticles can be prepared by a water-in-oil (w/o) microemulsion process [19-21]. Basically, w/o microemulsions are homogeneous dispersions of nanodroplets of water in an oil phase, stabilized at their interface by surfactant molecules. These nanodroplets, also called inverted micelles, can be used as nanoreactors for the synthesis of highly monodisperse silica nanoparticles with a good control on their size and morphology. The confined character of these inverted micelles makes the microemulsions particularly suitable for the preparation of functional silica nanoparticles.

1.4. Different Synthesis Strategies

Functional silica nanoparticles are usually achieved through the encapsulation in a silica matrix of core elements (molecules, nanocrystals, etc.) exhibiting specific properties



Source: Adapted from Guerrero-Martínez et al. [23].

Figure 1. Schematic representation of the different strategies for encapsulating a core element in a silica nanoparticle by water-in-oil microemulsion. The core element can be synthesized ex-situ (1) and introduced in the micelle via a colloidal solution (2), or it can be synthesized in-situ directly in the micelle (3). Then in both case the silica shell is formed by addition of TEOS and a base in the microemulsion (4). Finally, after destabilizing the microemulsion the particles can be washed and collected by centrifugation (5).

(luminescent, magnetic, catalytic, etc.) [22]. Besides the intended synthesis of the silica matrix in the w/o microemulsion, there is mainly two strategies for introducing these core elements in the system [23]. In the mostly spread approach, the elements to encapsulate in the silica nanoparticles are pre-synthesized in a separate process and are introduced in the microemulsion via a colloidal solution [24-26]. If the microemulsion remains stable, they would then migrate in the aqueous micelles for the silica coating step. The other approach consists in the in-situ synthesis of the core elements directly inside the inverted micelles where they are then coated with silica [27-35]. These two different strategies are depicted in Figure 1.

1.5. Different Nanoparticle Microstructures

Depending on the nature of these core elements and their affinity with the silica matrix and/or aqueous phase, several type of microstructures are accessible through microemulsion processes as depicted in Figure 2. When the encapsulated elements are small enough (~ few nanometers), with good stability in the aqueous phase, homogeneous structures are generally obtained with the encapsulated elements being homogeneously distributed in the silica matrix. This is usually the case in the encapsulation of organic molecules, complexes or metal atom clusters [36-38]. When core elements are bigger (from few nanometers up to few tens of nanometers), core-shell structures are obtained with the encapsulated elements being located in the middle of the nanoparticles [24, 39-43]. Then bi-functional nanoparticles can be obtained by co-encapsulation of small and big elements [44-46]. Although these are the most common structures, some research groups have developed other multifunctional nanoparticles with more complex structures such as layer-by-layer structures [39, 47], each layer being possibly synthesized by successive steps directly in the microemulsion. Thanks to the porosity of the silica shell, yolk-shell (also referred to as rattle-type) or hollow silica nanoparticles can be obtained by selective etching of a sacrificial material in layer-by-layer or

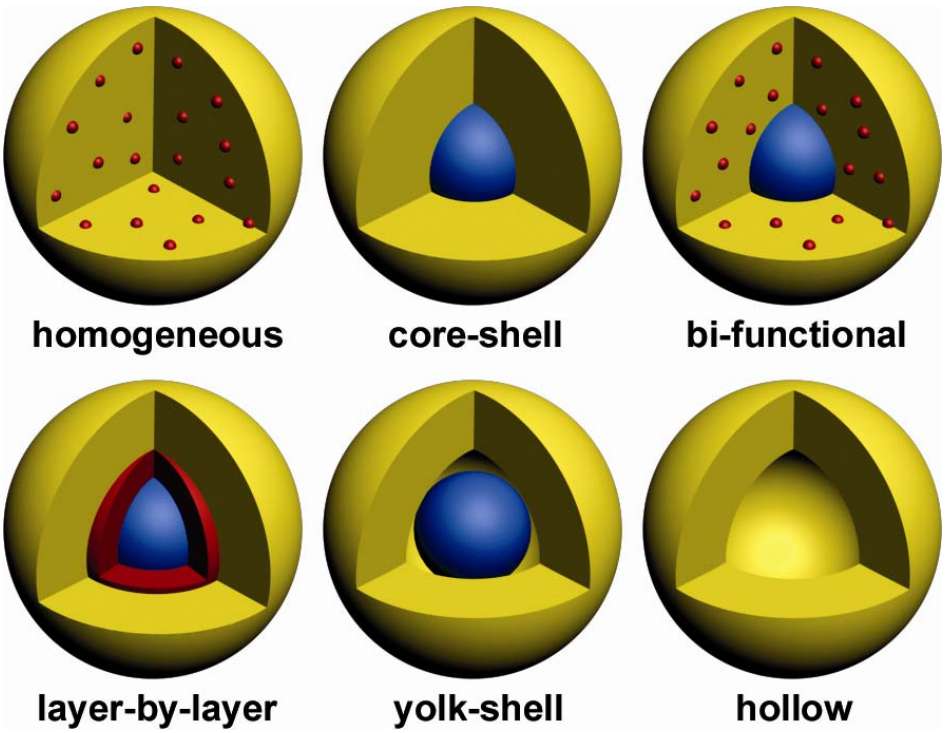


Figure 2. Schematic representation of the different type of nanoparticle structures which can be obtained by microemulsion processes.

core-shell structures [25, 47-51]. In these hollow nanoparticles, a new core material, such as gold nanoparticles, can then be grown [52]. Finally, the overall complexity of these nanoparticles can still be increased by structuring the silica matrix in itself, as it is the case with a layer of mesoporous silica for instance [48].

1.6. A Wide Range of Already-Published Materials

Through this microemulsion process, a wide range of @SiO_2 based materials have already been prepared by research groups from all over the world. Various kinds of luminescent silica nanoparticles have been already reported, by encapsulation of all sort of luminophores, such as the well known quantum dots (QDs) [28, 39, 43, 53], organic dyes [54-58], complexes [38, 58-59], or lanthanide based nanocrystals [42, 60-61]. The preparation of magnetic silica nanoparticles is also widely documented, by encapsulation of maghemite, magnetite or other spinel type structures [30, 62-65]. Moreover, by combining these two approaches, bi-functional nanoparticles with luminescent and magnetic properties have been reported [45-46, 66-68]. Although luminescence and magnetism are probably the most investigated functionalities, other types of functional materials have also been encapsulated in silica nanoparticles by w/o microemulsion processes, such as gold, silver, platinum, palladium or rhodium [29, 31, 33, 40, 47]. These metal@SiO_2 nanoparticles can find numerous applications as catalysts, in the CO hydrogenation or butane combustion reactions for instance [34-35].

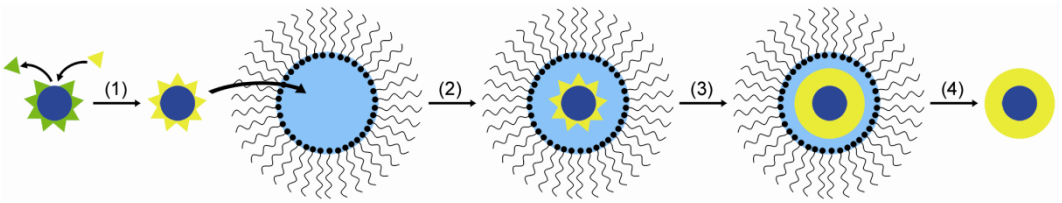


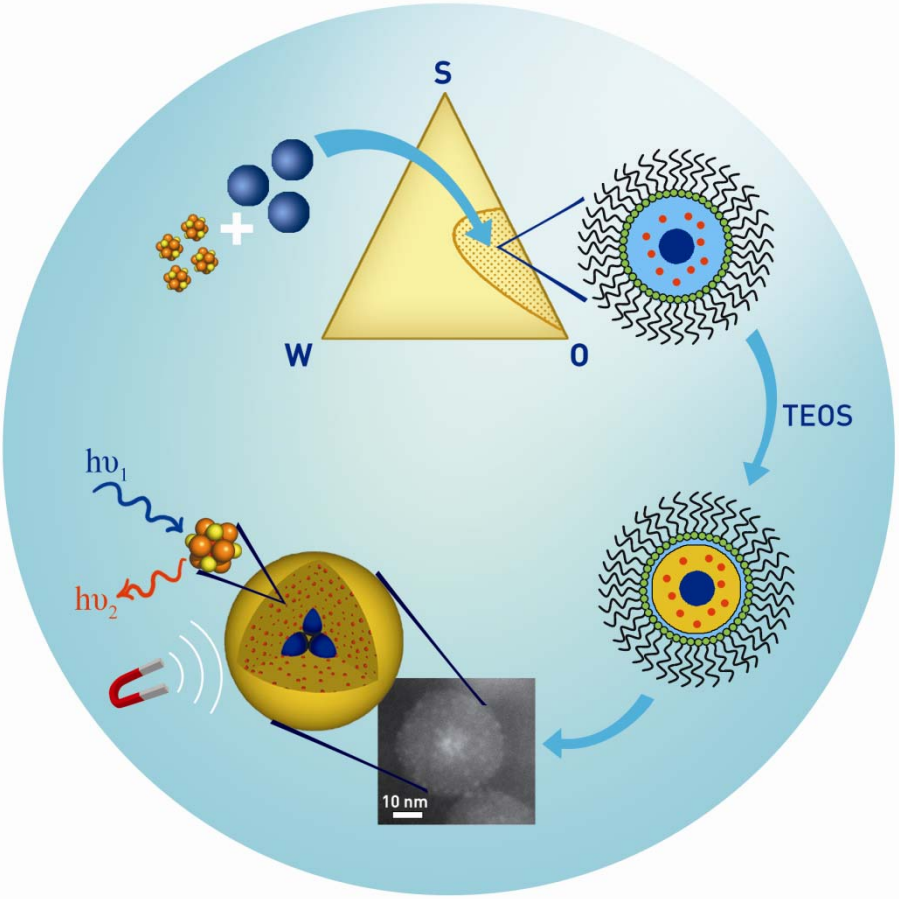
Figure 3. Schematic representation of the encapsulation of hydrophobic particles in silica via a w/o microemulsion process. The hydrophobic ligands capping the core particle which is initially located in the oil phase are replaced by hydrolyzed silica monomers (1). The silanized core particle can then migrate in the aqueous inverted micelle (2) for further growth of the silica shell (3). Finally, after destabilizing the microemulsion the particles can be washed and collected by centrifugation (4).

1.7. Complementary of Microemulsions to Other Techniques

The important amount of reported synthesis through microemulsions shows the good complementary of this technique to the Stöber process. Indeed, microemulsions are particularly suitable for the one-pot synthesis of small silica nanoparticles with complex architectures. It is especially dedicated for the preparation of particles in the range 20 to 100 nm, whereas the Stöber process is more efficient for particles from 100 nm up to few micrometers. Actually, in microemulsions the size of the obtained spherical nanoparticles is mainly controlled by the size of the inverted micelles and this process is therefore highly reproducible. In addition, the confined character of these micelles allows a fine control on the concentration of the encapsulated elements, and highly concentrated particles with very thin silica shells (down to a few nanometers) are easily obtained. This property of microemulsions also allows using weaker base than ammonia, the traditional base in a Stöber process, such as tetramethylammonium hydroxide (TMAOH) for encapsulation of elements too sensitive to high pH. However, in microemulsions using weaker bases will still result in spherical and monodispersed nanoparticles thanks to confined character of the inverted micelles. Last but not least, microemulsions allow the one-pot encapsulation of hydrophobic particles, such as QDs, gold or iron oxide nanocrystals [39-40, 53, 65], without any pre-silanization step. In this case the core elements to encapsulate are firstly dispersed in an organic colloidal solution with capping agents, such as trioctylphosphineoxide (TOPO), octadecylamine (ODA) or oleic acid, being adsorbed on their surface, and are therefore initially located in the oil phase. Then, during the microemulsion process the hydrophobic ligands are replaced by hydrolyzed TEOS molecules and the particles can migrate in the aqueous phase for further growth of the silica shell. This mechanism is depicted in Figure 3.

1.8. Surface Functionalization in Microemulsions

In addition to these advantages, the microemulsion technique allows to easily functionalize the surface of the silica nanoparticles. The addition of all kind of organosilane coupling agents directly in the microemulsion process have already been reported to produce silica nanoparticles presenting amine, phosphonate, aldehyde, carboxylate, octadecyl, epoxide, vinyl, or thiol functional groups at their surface [20, 40, 69-73]. This



Source: Reprinted from the front cover of the Journal of Colloid and Interface Sciences, volume 341, issue 2, January 2010. Copyright 2010, with permission from Elsevier.

Figure 4. Preparation of functional silica nanoparticles by water-in-oil microemulsion.

functionalization step can be of particular interest for coupling the silica nanoparticles with more complex molecules such as fluoresceins, proteins, DNA, etc. Other approaches such as chlorination of the surface of the silica nanoparticles followed by the functionalization with polymers have also been reported [74]. Thus, surface modified silica nanoparticles find numerous applications such as DNA/RNA detection and manipulation, gene delivering, cell targeting, vectorization, biosensor or nanoparticles self assembling [1, 75-77].

1.9. Our Materials and Chapter Topic

After providing few generalities on the w/o microemulsion process, this chapter will focus on the materials we successfully prepared with this technique [22, 24-25, 36-37, 44, 78-80]. Indeed, the confined environment offered by w/o microemulsions was involved during the last decade in our research activities to synthesize silica nanoparticles with several types of structures and properties. This contribution summarizes our own results on the synthesis through water-in-oil microemulsion of anti-UV CeO_2@SiO_2 nanoparticles [78], luminescent

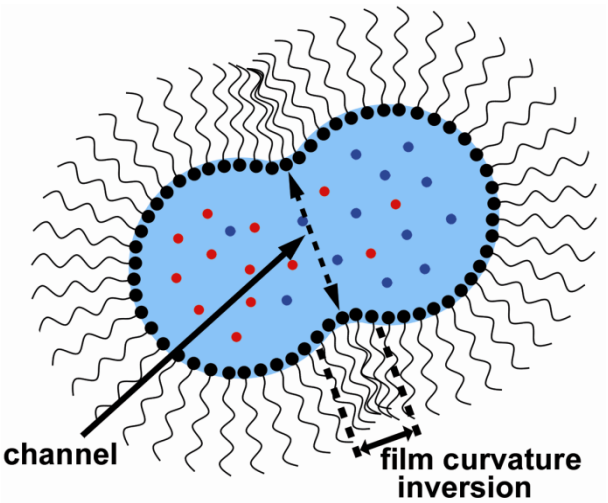
cluster@SiO_2 nanoparticles [36-37], magnetic M@SiO_2 nanoparticles (M = γ-Fe_2O_3 or $ZnFe_2O_4$) [24-25] and even bi-functional luminescent and magnetic γ-Fe_2O_3-$Cs_2Mo_6Br_{14}$@SiO_2 nanoparticles [44]. The morphologies of the different materials were observed by scanning electron microscopy (SEM) and transmission electron microscopy (TEM). The specific properties of these functional nanoparticles were evidenced by UV-Vis spectroscopy, photoluminescence spectroscopy, Raman spectroscopy, and SQUID magnetometer analysis. Figure 4 illustrates the overall process of synthesis and characterization of our materials.

2. SYNTHESIS OF THE FUNCTIONAL SILICA NANOPARTICLES

2.1. Water-in-Oil Microemulsions

Microemulsions consist of water nanodroplets, also called inverted micelles, dispersed in an oil phase and stabilized at their interface by surfactant molecules. The molar ratio of each component is a critical parameter as it will ensure the stability of the microemulsion. It will also determine the size and shape of the inverted micelles and therefore enable to tailor the size and shape of the nanoparticles that will be synthesized within these inverted micelles. Indeed, these inverted micelles can be used as confined nanoreactors for the synthesis of a wide range of monodisperse and size controlled nanoparticles [27, 81-85]. However, this chapter will only deal with the synthesis in w/o microemulsions of silica nanoparticles or silica shells on pre-synthesized nanoparticles. An important characteristic of microemulsions is their transparency (optical isotropy). Indeed, due to the size of the inverted micelles (inferior to one tenth of the visible wavelengths) dispersed in the oil phase, they do not scatter the visible light as indicated by the Rayleigh theory. Microemulsions are thermodynamically stable, but should still be considered as dynamic systems due to the Brownian motion of the inverted micelles. When two droplets collide, they can fuse and interchange both their content and their surfactant molecules [27, 82]. This phenomenon, depicted in Figure 5, is called intermicellar exchange and is strongly dependent on the elasticity of the surfactant film [86]. Classically, the microemulsion exchange characteristic time τ_{ex} is in the range 10 μs < τ_{ex} < 1 ms depending on the film flexibility, i.e. the surfactant used [82]. However, the exchange of particles (core nanoparticles and/or condensed nanoparticles) is generally inhibited, depending on the size of the particles, by the inversion of the film curvature [27, 82].

As previously mentioned, the ratio between the oil phase, the aqueous phase and the surfactant is important, but the nature of these three phases is also important. The choice of the surfactant in particular is a crucial point. Many publications report the influence of the surfactant depending on its alkyl chain length, head group size or ionic character. Thus, it is well assumed that the choice of the surfactant will have an influence on the final shape and size of the product synthesized in the microemulsion [82, 86]. Numerous surfactants are commercially available, either ionic or non-ionic ones, offering different hydrophilic-lipophilic balance indices (hlb) resulting in different elasticity of the surfactant film [87-88]. Some of the most commonly used surfactants are dioctyl sulfosuccinate (AOT), Triton X series, Brij® series, Igepal CO-520, cetyltrimethylammonium bromide (CTAB), sodium dodecyl sulfate (SDS), etc. In addition, they often require the use of a co-surfactant which can



Source: Adapted from López-Quintela et al. [27].

Figure 5. Schematic representation of the intermicellar exchange mechanism.

be any of the previously mentioned surfactants but alcohols, such as hexanol, are also quite often used. Using a co-surfactant can lead to a higher fluidity of the interface film between the droplets and the oil phase, resulting in a higher rate of intermicellar exchange, but also in a higher curvature of the droplets, resulting in smaller final particles [81]. The choice of the oil phase is less critical and will mainly depend on its affinity with the chosen surfactant and its relative toxicity. However, it can still have an influence on the synthesized particles [59]. It is generally cyclohexane, n-heptane, or less commonly toluene, chloroform, octane, etc. On its side, the nature of the aqueous phase can vary. It might contain the precursors for an in-situ synthesis of nanoparticles or can be a colloid solution of the elements to encapsulate in a silica matrix. The aqueous phase can also be a mixture of water and ethanol, but in this case it remains unclear where is located the alcohol, as it can actually be in the inverted micelles, play the role of co-surfactant, or even being partially solubilized in the oil phase as shown by Arriagada et al. [21].

2.2. Silica Synthesis in Water-in-Oil Microemulsions

The synthesis of the silica matrix within the aqueous nanodroplets is a classical 2 steps sol-gel process, based on the hydrolysis of a silica precursor followed by the condensation of hydrolyzed silica monomers. The mechanisms and kinetic of the synthesis of silica nanoparticles in water-in-oil microemulsions have been widely studied by Arriagada and Osseo-Asare [21, 89-92]. The silica precursor, usually an alkoxysilane such as tetraethyl orthosilicate (TEOS) or tetramethyl orthosilicate (TMOS), is initially miscible in the oil phase but it hydrolyzes by diffusion at the contact of the inverted micelles. The hydrolyzed silica monomers migrate then in the aqueous phase where it will condense and form the silica nanoparticle. The hydrolysis of the silica precursor can be either base catalyzed or acid catalyzed, but Finnie et al. showed that hydrolysis is faster in the case of an acid catalyzed process with silica precursor being fully hydrolyzed in about 30 minutes [93]. The

condensation of the hydrolyzed silica monomers can only be base catalyzed and required the addition of a base which is usually an aqueous ammonia solution, but other bases such as TMAOH or NaOH can be use with similar results. After a time of reaction which can vary between few hours to few days, depending on the targeted nanoparticle size, the microemulsion is usually destabilized by addition of ethanol. The silica nanoparticles can then be collected and washed by centrifugation cycles.

Many studies showed that the size of the obtained silica nanoparticles can be controlled by changing the molar ratio between the water phase and the surfactant [89]. Alternatively the size of the silica nanoparticles/shells can be controlled by varying the reaction time [41, 65], the nature of the oil phase [59], or the amount of silica precursor [64-65] which can alternatively be added stepwise [40, 94]. Finally, the size of the obtained particles will be also determined by the size of the core particles [78].

2.3. Washing and Collection of the Silica Nanoparticles

It is well known that a major drawback of the microemulsion process is the difficulties to properly wash and redisperse the particles. Indeed, when the microemulsion is destabilized, an important amount of the surfactant molecules get strongly adsorbed on the surface of the particles, resulting in the aggregation and precipitation of the particles. In addition, when the surfactant is sufficiently removed from the particles, their colloidal stability makes them hardly gatherable by centrifuging. A good way for washing and collecting the particles is to repeat several washing in water by high speed centrifuging with relative centrifugal forces (RCF) up to 40000 g. However, if such acceleration is not available, the particles can still be washed and successfully collected in ethanol/heptane mixtures. Some research groups have developed other alternative techniques such as shock cooling processes for destabilizing the microemulsion [65], or strong alkaline treatments on aggregated nanoparticles [51]. When properly washed, the particles can finally be redispersed in water or ethanol solutions with high dispersion stability.

2.4. Experimental Part

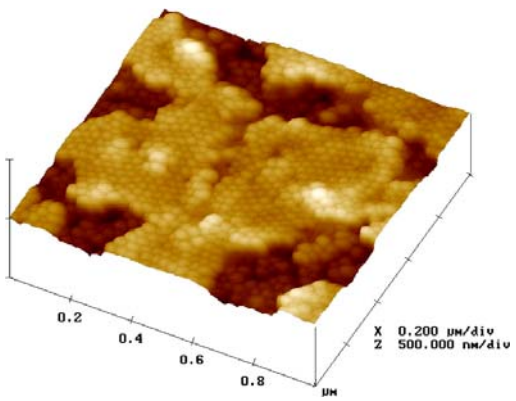
All the materials presented in the following section were obtained by w/o microemulsions using n-heptane as the oil phase, Brij®30 as surfactant, TEOS as the silica precursor and aqueous ammonia solutions as the base for catalyzing the hydrolysis and/or condensation of TEOS. N-heptane was always chosen as the oil phase for its low toxicity compared to other similar reactants such as cyclohexane. Brij®30 (Polyoxyethylene (4) lauryl ether), a nonionic surfactant, was chosen since it showed the best results in preliminary trials. This surfactant does not require the use of any co-surfactant but then temperature should be kept below 25°C in order to avoid any possible thermally induced phase inversion. The silica precursor was chosen to be tetraethyl orthosilicate (TEOS) since it can be easily handled in the ambient air contrary to other precursors, such as the air-sensitive tetramethyl orthosilicate (TMOS). Ammonia has been chosen since it preferentially dissolves in the water phase and easily decomposes without any possible contaminant. Finally, the aqueous phases were always colloidal solutions of the pre-synthesized nanoparticles intended for encapsulation in the silica nanoparticles. Here, the core elements were never synthesized in-situ. Using these pre-

synthesized colloidal suspensions allows increasing the concentration of core elements without destabilizing the microemulsion, and also allows avoiding a subsequent calcination stage. Moreover, by choosing appropriate concentrations for these aqueous colloidal solutions or by playing on its aggregation state [78], it is then possible to control the number of nanocrystals or core elements embedded in the silica nanoparticles.

3. Characterizations and Potential Applications of the Functional Silica Nanoparticles

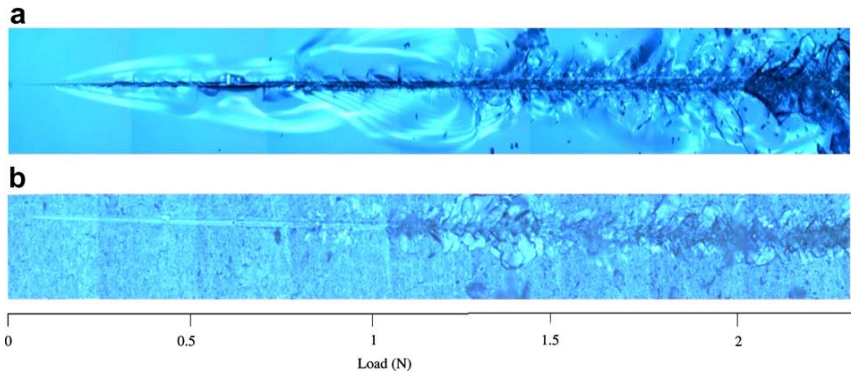
3.1. SiO_2 Nanoparticles for Scratch Resistant Glass

Pure silica nanoparticles prepared through a w/o microemulsion process (without core elements) already showed to have interesting potential applications in itself. Tartivel *et al.* prepared thin films of pure silica particles on glass slides in order to get superscratch-resistant transparent glass [79]. Thin films were obtained by dip-coating of a soda-lime silica (SLS) glass slide directly in the microemulsion. Then, the samples were heated for 15 min at 400°C in air, both to drive silica condensation and particle formation and to remove the remaining solvents. The resulting material appeared as arrangements of monodisperse silica spheres of roughly 35 nm in size as observed by AFM analysis (Figure 6). Indentation (Vickers) scratching experiments were conducted to estimate the resistance toward mechanical damage, with a load increasing from 0 to 2.5 N and a loading rate of 0.01 $N.s^{-1}$. The loading cycle typically leads to three different regimes as the load increases: the micro-ductile regime, the micro-cracking regime and the micro-abrasive regime. Figure 7 shows pictures of the resulting glass slides after application of this loading cycle for both coated and uncoated samples. It appeared that coated samples show a longer micro-ductile regime, with the micro-cracking and micro-abrasive regimes occurring at higher load compared to uncoated SLS slides. As a consequence, the coated samples did not show any sub-surface lateral crack and remain optically transparent, while the uncoated samples exhibit large cracks that scatter light.



Source: Reprinted from Tartivel et al. [79]. Copyright 2007, with permission from Elsevier.

Figure 6. AFM pattern of silica nanoparticles synthesized by w/o microemulsion and deposited by dip-coating on a soda-lime silica glass substrate.



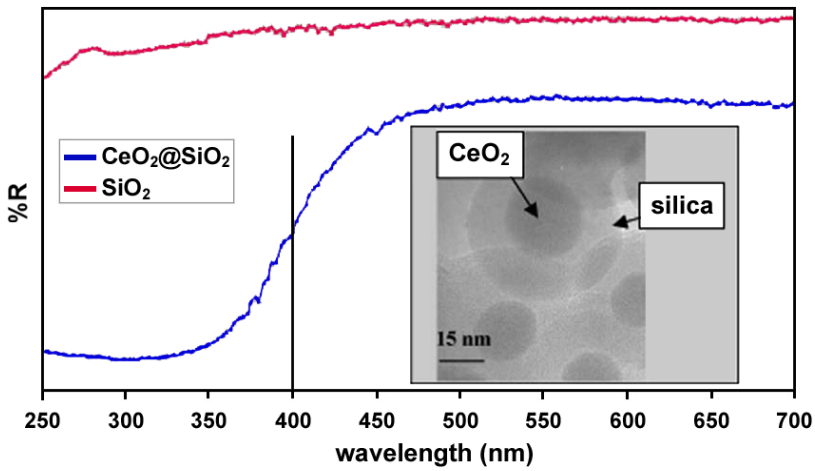
Source: Reprinted from Tartivel et al. [79]. Copyright 2007, with permission from Elsevier.

Figure 7. Scratch test patterns for a 0-2.5 N loading frame on a) SLS glass (substrate annealed 15 min at 350°C), and b) silica nanoparticles-based coating on the same substrate.

3.2. CeO_2@SiO_2 Anti-UV Nanoparticles

CeO_2 nanocrystals display very promising UV-absorption properties. However, three important issues must be previously solved: a refractive index equal to 2.50 at λ = 550 nm, a strong yellow color [95] and catalytic oxidation properties [96]. One way to reduce the refractive index of such nanoparticles is to coat them by a thin layer of a material displaying a much lower refractive index such as silica (n = 1.45) [97]. Another way is to replace in CeO_2 a part of the anionic network of O^{2-} ion by anions with low-polarizability such as F^- [95].

In this frame, CeO_2@SiO_2 nanoparticles have been successfully prepared by w/o microemulsion processes [78]. The use of concentrated aqueous CeO_2 colloidal solutions allowed preparing CeO_2@SiO_2 systems containing more than 25% (weight mass) of CeO_2. The obtained nanoparticles were spherical and monodisperse, and the core-shell structure of the system has been evidenced by HRTEM as shown in Figure 8.



Source: Reprinted from Aubert et al. [22]. Copyright 2010, with permission from Elsevier.

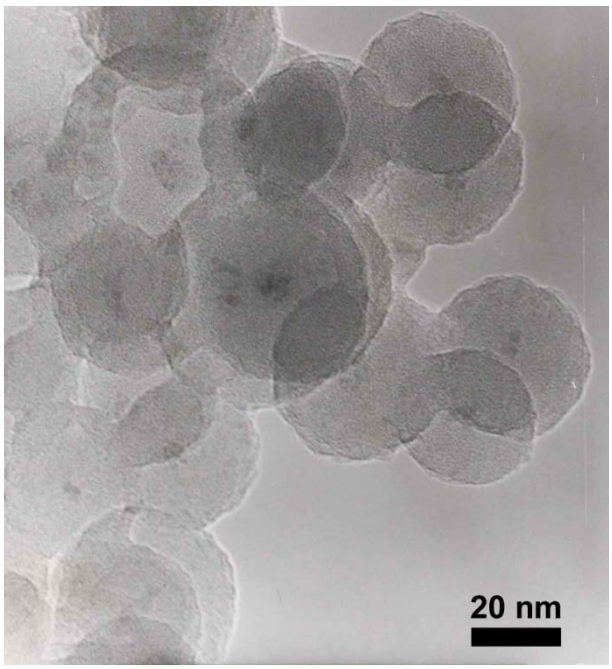
Figure 8. UV-Vis absorption spectra of pure SiO_2 and CeO_2@SiO_2 nanoparticles. Inset: HRTEM image of CeO_2@SiO_2 core-shell nanoparticles.

The size of the nanoparticles was depending on the size of the CeO_2 core nanocrystals, but it was also shown that the thickness of the silica shell could be controlled from 5 to 20 nm. Figure 8 shows the UV-Vis absorption spectrum of these prepared $CeO_2@SiO_2$ nanoparticles, which confirms the absorption in the UV domain. From these functional silica nanoparticles, it was then possible to prepare anti-UV thin films using a similar procedure as that described in section 3.1.

3.3. $ZnFe_2O_4@SiO_2$ and γ-$Fe_2O_3@SiO_2$ Magnetic Nanoparticles

Magnetic nanoparticles have been prepared through w/o microemulsion processes by the encapsulation in silica nanoparticles of either $ZnFe_2O_4$ [24] or γ-Fe_2O_3 nanocrystals [25]. In both cases, the obtained nanoparticles showed a core-shell structure as evidenced by TEM (Figure 9 and 10).

The evolution of magnetization versus temperature was studied in both DC (ZFCM (Zero Field Cooled Magnetization) and FCM (Field Cooled Magnetization)) and AC modes with a SQUID magnetometer. Through this study, we demonstrated clearly that the surface of SiO_2 induced systems with a minimum degree of aggregation and modified strongly the interactions between magnetic nanocrystals and most likely surface effects. After the coating of each magnetic nanocrystal, significant changes in the magnetic behavior could be highlighted, particularly with regard to the blocking temperature [24, 98].



Source: Reprinted with permission from Grasset et al. [24]. Copyright 2002 American Chemical Society.

Figure 9. TEM image of $ZnFe_2O_4@SiO_2$ nanoparticles.

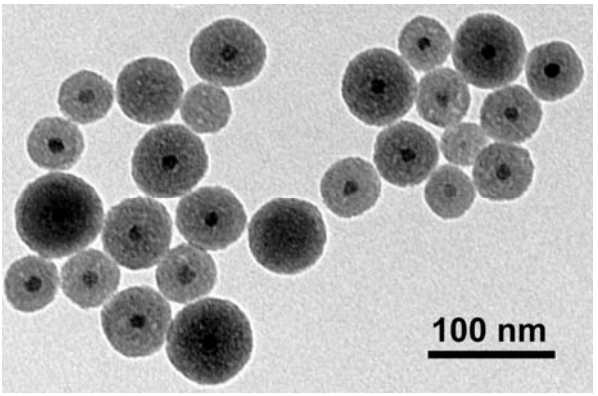
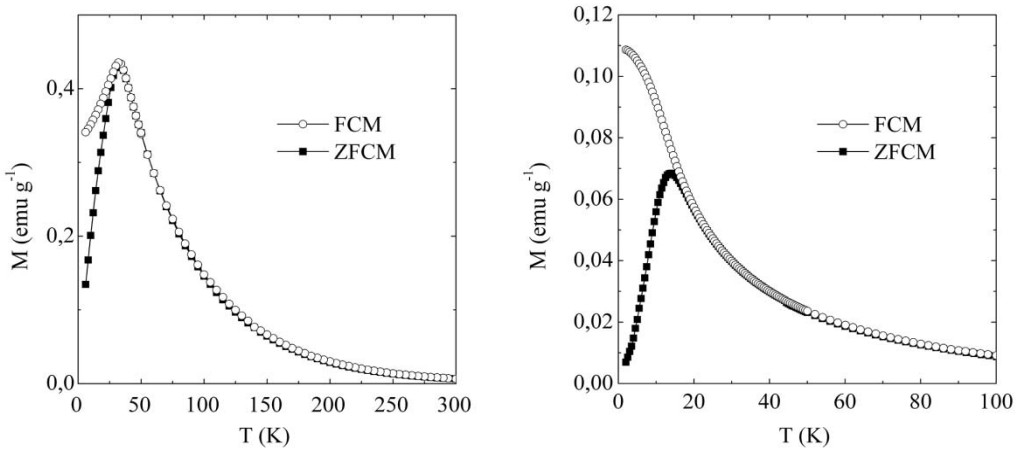


Figure 10. TEM image of γ-Fe_2O_3@SiO_2 nanoparticles.

As first example, a system consisting of aggregated or silica coated zinc ferrite nanocrystals was studied using DC and AC magnetization measurements [24, 98]. The temperature dependence of the ZFCM and FCM curves of an aggregated sample and a silica coated sample recorded under 10 Oe are presented in Figure 11. The ZFCM increases when the temperature increases, passing through a broad maximum at *T*max = 32.5 K. On cooling, the FCM coincides with the ZFCM down to 30 K and then both curves significantly differ on cooling. As a result, the FCM also passes through a maximum at *T*max, but much less pronounced than in the ZFCM mode. One of the striking features of the silica coated nanocrystals is that the broad maximum on the FCM curve has disappeared compared to the uncoated ones. The FCM increases as the temperature is lowered and tends to saturate in the low-temperature limit as usual for superparamagnetic entities (Figure 11). For the aggregated nanocrystals, a superparamagnetic–super-spin-glass phase transition at Tg was identified and explained clearly these behaviors. The relaxation time diverges at Tg and the nonlinear susceptibility shows an abrupt increase. This critical behavior vanishes when the nanocrystals are not in close contact in case of silica coated particles or dispersed sols [24, 98]. As second example, it was demonstrated that the silica coating of single γ-Fe_2O_3 nanocrystals induced a shift of the transition temperature of maghemite (γ-Fe_2O_3) into hematite (α-Fe_2O_3). Indeed, classically maghemite turns into hematite at 450°C [43] while after coating with silica it remains stable until 1000°C [25]. The magnetic studies realized on non-coated and coated nanocrystals have shown (i) a shift to lower value of the blocking temperature as observed in the magnetic curve recorded as a function of temperature by cooling the sample in zero-field (ZFCM) revealing a significant decline of magnetic interactions between the nanocrystals after coating; ii) the preservation of inverse spinel structure with ferromagnetic behavior up to 1000°C (Figure 12). Moreover, we should notice that in addition to these magnetic characterizations, studies by X-ray diffraction showed that the silica shell also acts as a diffusion barrier for temperatures up to 1000°C (data not shown). Thus, in this section it has been clearly shown through several examples that the average magnetic behavior of magnetic nanocrystals depends on their environment and that the magnetic properties of these nanocrystals at low temperature are essentially governed by the interface particle-habitat.



Source: Reprinted with permission from Grasset et al. [24]. Copyright 2002 American Chemical Society.

Figure 11. Temperature dependence of the ZFCM and FCM curves of an aggregated (left) or silica coated (right) samples recorded under 10 Oe.

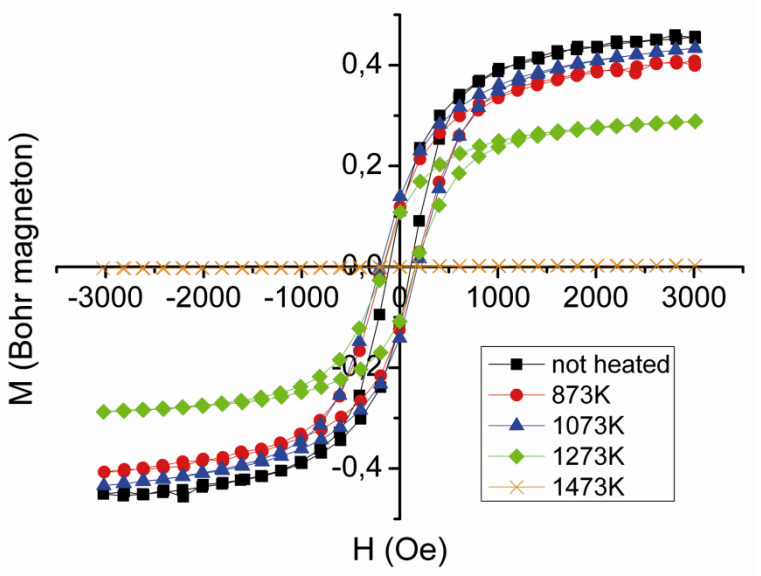


Figure 12. Field versus temperature curves of γ-Fe_2O_3@SiO_2 nanoparticles.

3.4. Cluster@SiO_2 Luminescent Nanoparticles

Luminescent silica nanoparticles with homogeneous structures were obtained by encapsulation in silica nanoparticles of nanosized metal atom clusters. Octahedral clusters are nanosized inorganic entities offering a strong and robust emission in the red and near-infrared

regions under UV or visible excitation [80, 99-101]. They consist in octahedral clusters of 6 metal atoms (M_6, M = Mo or Re) bonded to 8 face capping inner ligands (Q^i, Q = halogens or chalcogens), and 6 terminal apical ligands (L^a, L = halogens, OH, CN, etc.). The resulting $[M_6Q^i_8L^a_6]^{n-}$ cluster units are negatively charged and therefore need to be charge balanced by cations (A^+, A = Cs, K, *n*-C_4H_9N, etc.). A generic $[M_6Q^i_8L^a_6]$ cluster unit is depicted in Figure 13. In solid state, they form a crystalline cluster compound de noted $A_n[M_6Q^i_8L^a_6]$. These cluster compounds offer a strong and stable luminescence in the red and near-infrared fields under UV excitation, but this luminescence is usually quenched in solution because of the presence of solubilized oxygen [102].

In addition, especially in the case of molybdenum clusters, they can easily react in solution and exchange their apical ligands for OH groups, resulting in their precipitation [103]. Thanks to their luminescence properties, metal atom clusters could be good candidates as luminophores for numerous biotechnological applications but they should then be encapsulated in a silica matrix to avoid quenching and precipitation effects. Thus, several types of cluster@SiO_2 nanoparticles have been prepared by w/o microemulsion processes, by encapsulation of a family of Mo_6 cluster compounds ($Cs_2[Mo_6Br_{14}]$, $Cs_2[Mo_6Cl_{14}]$ and $Cs_2[Mo_6I_{14}]$) [37] and encapsulation of a family of Re_6 cluster compounds ($K_4[Re_6Se_8(OH)_6]$, $K_4[Re_6S_8(OH)_6]$, $K_4[Re_6S_8Br_6]$ and $Cs_{1.68}K_{2.32}[Re_6S_8(CN)_4(OH)_2]$) [36]. The solubilization of the cluster precursors and the stability of the cluster sols are strongly depending on the nature of the metal core. Thus, Mo_6 clusters are stable in water/ethanol mixtures with pH adjusted at 2 with HBr. They were then introduced in the microemulsion as an acidic pseudo-aqueous phase. As a result, the hydrolysis of TEOS was in this case acid catalyzed, and had to be followed, after complete hydrolysis, by the addition of ammonia in the system for the base catalyzed condensation of the silica matrix. In contrast, Re_6 clusters are soluble in pure water and are preferentially stable at high pH, because they can form aquahydroxo and hexaaqua cluster complexes at low pH [104].

Then, in order to avoid precipitation of the clusters, microemulsions with Re_6 clusters were obtained by adding the ammonia prior to the aqueous cluster sol. Hence, in this case both the hydrolysis and the condensation of the silica were base catalyzed. All the obtained particles were perfectly spherical and monodisperse as observed from the SEM picture of Figure 14, showing an example of $K_4[Re_6S_8(OH)_6]@SiO_2$ nanoparticles. However, while keeping the same ratios between the oil, aqueous and surfactant phases, the size of the $Mo_6@SiO_2$ and $Re_6@SiO_2$ nanoparticles were slightly different (50 and 30 nm respectively) due to a probable influence of the ethanol in the synthesis of $Mo_6@SiO_2$ nanoparticles, which might actually played the role of a co-surfactant as previously mentioned. The homogeneous structure of these functional particles was evidenced by scanning transmission electronic microscopy in annular dark field mode (ADF-STEM) [37]. This technique, by detecting the electron scattered at high angles, provides what is known as Z-contrast images, since atoms with high atomic numbers will be more scattered at higher angle than atoms with lower atomic numbers. It is therefore the only suitable tool for imaging the cluster units in the silica matrix. Figure 14 shows an example of an ADF-STEM image of $K_4Re_6S_8(OH)_6]@SiO_2$ nanoparticles were cluster units are visible as bright spots of 1 nm in size and appear as homogeneously dispersed in the silica matrix.

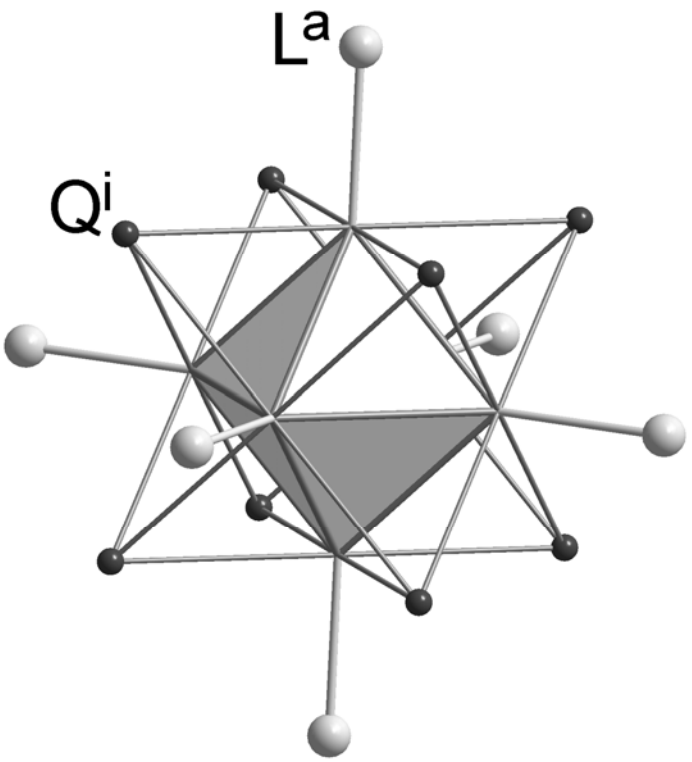
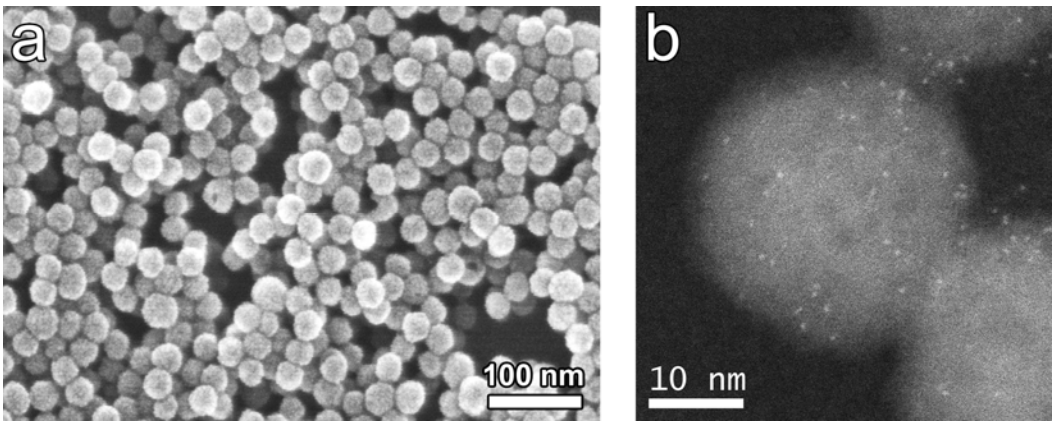
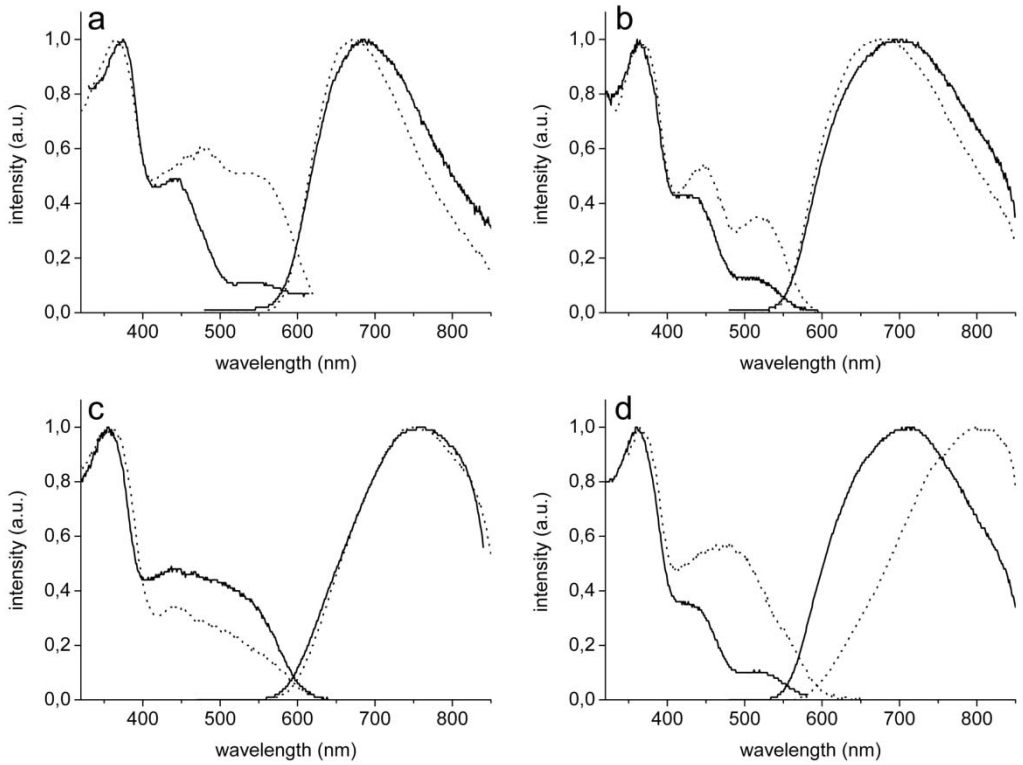


Figure 13. Schematic representation of a generic $[M_6Q^i_8L^a_6]$ cluster unit (M = Mo or Re; Q = halogens or chalcogens; L = halogens, OH, CN, etc.).



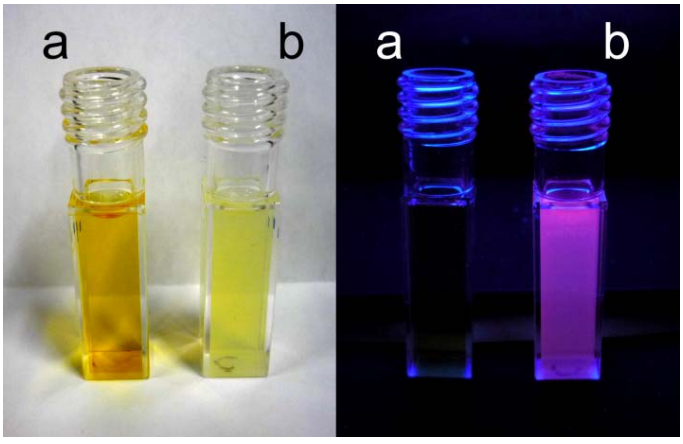
Source: Reprinted with permission from Aubert et al. [36]. Copyright 2010 American Chemical Society.

Figure 14. $K_4[Re_6S_8(OH)_6]@SiO_2$ nanoparticles viewed by a) FE-SEM and b) ADF-STEM.



Source: Reprinted with permission from Aubert et al. [36]. Copyright 2010 American Chemical Society.

Figure 15. Normalized excitation and emission spectra (corrected signals) for both $A_4[Re_6Q_6L_6]$ cluster precursors (---) and the corresponding $A_4[Re_6Q_6L_6]@SiO_2$ nanoparticles (—) for $A_4[Re_6Q_6L_6]$ = (a) $K_4[Re_6Se_8(OH)_6]$, (b) $K_4[Re_6S_8(OH)_6]$, (c) $Cs_{1.68}K_{2.32}[Re_6S_8(CN)_4(OH)_2]$, and (d) $Cs_4[Re_6S_8Br_{14}]$.



Source: Reprinted with permission from Aubert et al. [36]. Copyright 2010 American Chemical Society.

Figure 16. Aqueous solutions of $[Re_6S_8(OH)_6]^{4-}$ clusters (a) before and (b) after embedding in silica nanoparticles, under daylight (left picture) and under UV irradiation at 365 nm (right picture).

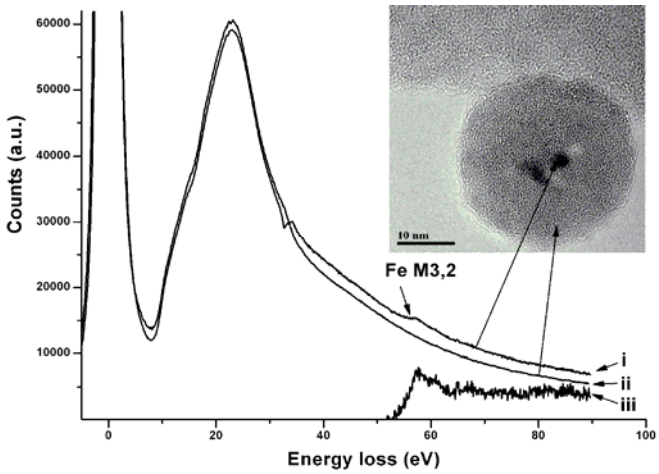
The luminescence properties of the obtained cluster@SiO_2 nanoparticles were investigated by photoluminescence spectrometry in the solid state form. Figure 15 gathers the excitation and emission spectra of the $A_4[Re_6Q_6L_6]$ cluster precursors and those of the corresponding $A_4[Re_6Q_6L_6]@SiO_2$ nanoparticles (A = Cs or K, Q = S or Se, L = Br, CN or OH). It appeared that the luminescence properties of the clusters are generally preserved without any drastic change after they are encapsulated in the silica matrix. The only noticeable change was observed when starting with the $Cs_4[Re_6S_8Br_{14}]$ precursor, in this case the corresponding "$Cs_4[Re_6S_8Br_{14}]@SiO_2$" nanoparticles showed a shift of the emission, resulting in the same luminescence properties as $K_4[Re_6S_8(OH)_6]@SiO_2$ nanoparticles. This shift was suspected to be due to an exchange of the apical Br ligands of the clusters for OH groups during the microemulsion process. However, this phenomenon did not affect the stability of the microemulsion. In addition, an important feature of all these cluster@SiO_2 nanoparticles is that their luminescence property is preserved in water solutions. Indeed, once they are encapsulated in the silica matrix, the clusters are protected from the oxygen and their luminescence is not quenched anymore, as visible on Figure 16 showing the luminescence of $K_4[Re_6S_8(OH)_6]@SiO_2$ nanoparticles in water solution, and under UV excitation.

3.5. γ-Fe_2O_3-$Cs_2[Mo_6Br_{14}]@SiO_2$ Bi-Functional Nanoparticles

By combining the two synthesis strategies described in sections 3.3. and 3.4. for the preparation of core-shell magnetic nanoparticles and homogeneous luminescent nanoparticles respectively, we prepared bi-functional γ-Fe_2O_3-$Cs_2[Mo_6Br_{14}]@SiO_2$ nanoparticles [44]. The co-encapsulation of γ-Fe_2O_3 nanocrystals and $Cs_2[Mo_6Br_{14}]$ clusters resulted in silica nanoparticles with both magnetic and luminescence properties. Such bi-functional nanoparticles should find interesting applications in the field of nano-biotechnologies [47-71]. Indeed, magnetic properties would make the particles suitable for bio-imaging techniques such as Magnetic Resonance Imaging (MRI) or hyperthermia therapy [105]. On its side, the luminescence properties would allow an optical tracking of the particles [106], and the NIR emission window of the metal atom clusters makes them particularly suitable for in-vivo tracking as it corresponds to the minimum of absorption of the tissues and fluids constituting the human body [77, 107]. In addition, silica coated particles are good candidates for biological applications since silica is a particularly inert material, it can prevent the diffusion of toxic metal cations from the cores and its surface can be easily functionalized by further treatment in order to get a bio-compatible, targetable and dispersed material at neutral pH. Indeed, for imaging applications, the current probes (organic dyes or quantum dots) encounter several challenges, such as a limited tissue penetration and a potential toxicity. To address these needs, it is important to develop new low toxicity near-infrared emitters coupled with silica coatings in order to improve tissue penetration depth and colloidal stability.

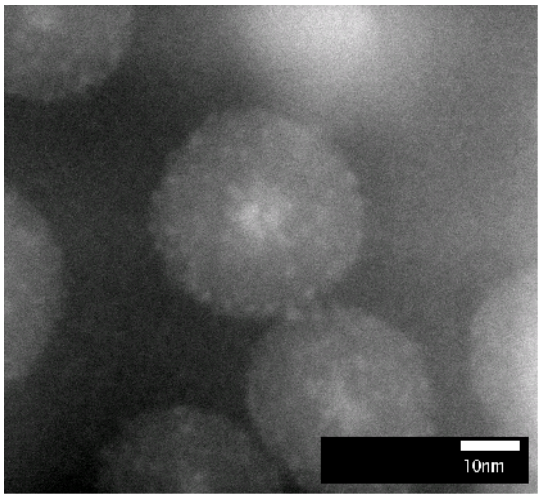
The bi-functional microstructure of these γ-Fe_2O_3-$Cs_2[Mo_6Br_{14}]@SiO_2$ nanoparticles was evidenced by coupling transmission electronic microscopy techniques and electron energy loss spectroscopy (EELS). Figure 17 shows with a bright field TEM image (BF-TEM) of a nanoparticle, the γ-Fe_2O_3 nanocrystals at the core of the nanoparticles. The EELS technique (Figure 17) confirmed the chemical nature of this core and that iron was only present in this core and not in the shell. Then, ADF-STEM images (Figure 18) confirmed the presence of homogeneously dispersed cluster units in the silica shell.

As previously mentioned, the encapsulation of the clusters did not affect their luminescence properties. Figure 19 shows the excitation and emission spectra of the obtained particles. The magnetization of those particles was also checked in both ZFC and FC modes, and the magnetic behavior was found to be typical of moderately monodisperse superparamagnetic ferrite nanocrystals dispersed in silica matrix [44]. Finally the bi-functional character of these nanoparticles was highlighted by dispersing the nanoparticles in an aqueous ethanolic solution (pH = 8) and applying an UV excitation and a magnetic field on this dispersion (Figure 20). Optical microscope observations as function of time showed that the nanoparticles are accumulating on the wall of the cell, close to the magnet, as the time increases.



Source: Reproduced by permission of The Royal Society of Chemistry.

Figure 17. EELS spectra of a γ-Fe_2O_3-$Cs_2[Mo_6Br_{14}]$@SiO_2 nanoparticle core (i), shell (ii), and nanoparticle core after background removal (iii). Inset: BF-TEM image of a γ-Fe_2O_3-$Cs_2[Mo_6Br_{14}]$@SiO_2 nanoparticle. From Grasset et al. [44].



Source: Reproduced by permission of The Royal Society of Chemistry.

Figure 18. ADF-STEM image of γ-Fe_2O_3-$Cs_2[Mo_6Br_{14}]$@SiO_2 nanoparticles. From Grasset et al. [44].

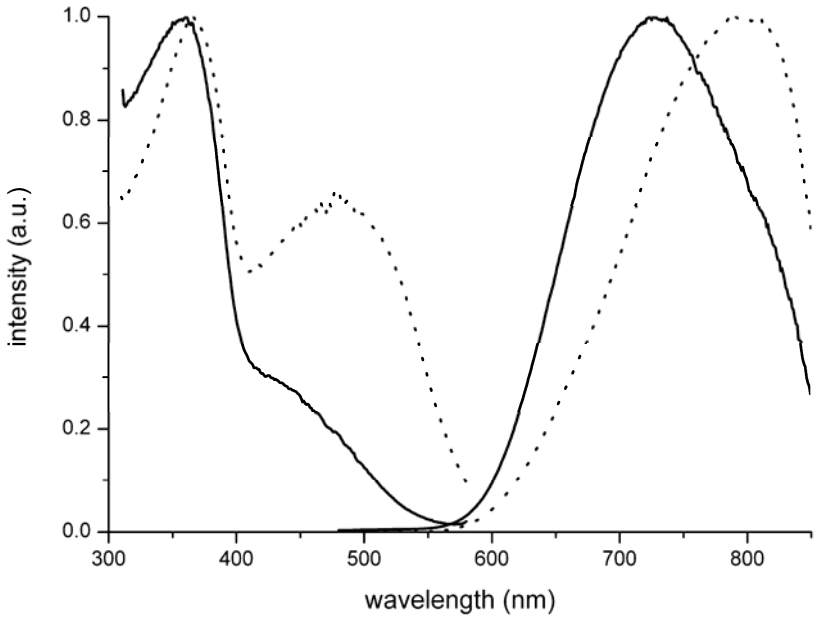


Figure 19. Normalized excitation and emission spectra (corrected signals) of $Cs_2Mo_6Br_{14}$ cluster precursor (---) and $Cs_2Mo_6Br_{14}@SiO_2$ nanoparticles (—).

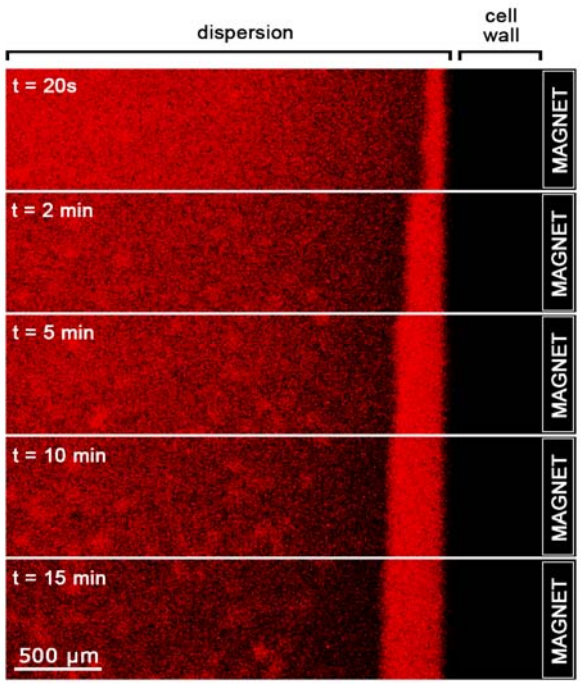


Figure 20. Optical microscope images of γ-Fe_2O_3-$Cs_2[Mo_6Br_{14}]@SiO_2$ nanoparticles under light excitation (λ_{ex} = 405 nm) and magnetic field (1.5 T). The nanoparticles, which are dispersed in solution, accumulate on the wall of the cell as a function of time. From Grasset et al. [44] – Reproduced by permission of The Royal Society of Chemistry.

CONCLUSION

In this chapter, we showed that the water-in-oil microemulsion method is an efficient and highly reproducible technique for the preparation of monodisperse functional silica particles in the nanometric range (< 100 nm). Moreover, this technique is particularly suitable for the elaboration of nanoparticles with complex structural designs. Besides the widely documented materials prepared through this process, we presented in this chapter the functional silica nanoparticles showing anti-UV, luminescent, or magnetic properties, that we prepared by encapsulation of CeO_2 nanocrystals, metal atom clusters, or ferrite nanocrystals respectively. The complementary of this w/o microemulsion process to the more classical Stöber method is well demonstrated in the preparation of monodisperse bi-functional nanoparticles with complex architecture such as the luminescent and magnetic γ-Fe_2O_3-$Cs_2Mo_6Br_{14}$@SiO_2 nanoparticles which were presented in this chapter.

These materials present real interests for a wide range of applications such as bio-nanotechnology, catalysis, mechanical reinforcement of substrates, etc. However, increasing the complexity of such materials is still an ongoing research field. In the future, the design of these functional nanoparticles will probably be enhanced by the addition of mesoporous silica layers, or the growth of an anisotropic silica shell, as depicted in Figure 21 showing for instance a shamrock-like structure (data not shown). These complex nanoparticles, in terms of properties as well as in terms of geometries, will constitute the nanobuilding blocks for the development of the materials of future, such as colloidal molecules or hybrid materials [108-109].

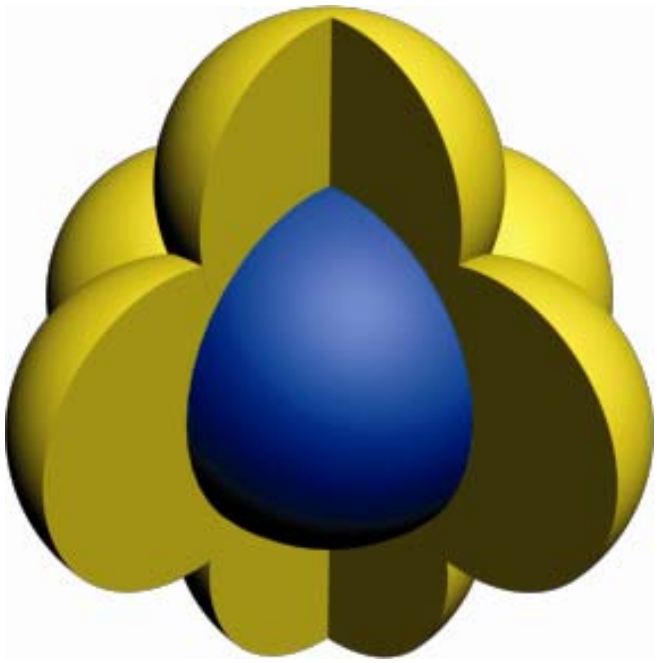


Figure 21. Schematic representation of a nanoparticle with a shamrock-like structure.

ACKNOWLEDGMENTS

The authors thank Y. Molard, V. Demange, O. Cador, F. Dorson, C. Perrin, V. Marchi-Artzner, A. Y. Ledneva, N. G. Naumov, K. Kimoto, N. Saito, H. Haneda, T. Sasaki, Y. Bando, M. Mortier, E. Duguet, S. Mornet, A.-M. Marie, R. Marchand, D. Fauchadour, F. Fajardie, N. Labhsetwar, D. Li, D. C. Park, T. Roisnel, J. Portier, J. Etourneau, R. Tartivel, E. Reynaud, J.-C. Sangleboeuf, and T. Rouxel for their participation in these works.

REFERENCES

[1] Knopp, D.; Tang, D.; Niessner, R. *Anal. Chim. Acta* 2009, 647, (1), 14-30.
[2] Burns, A.; Ow, H.; Wiesner, U. *Chem. Soc. Rev.* 2006, 35, 1028-1042.
[3] Bulte, J. W. M.; Modo, M. M. J., *Nanoparticles in biomedical imaging*. Springer Science+Business Media: New York, 2008; Vol. 102, p 524.
[4] Zhao, Y.-L.; Li, Z.; Kabehie, S.; Botros, Y. Y.; Stoddart, J. F.; Zink, J. I. *J. Am. Chem. Soc.* 2010, 132, (37), 13016-13025.
[5] Slowing, I. I.; Vivero-Escoto, J. L.; Trewyn, B. G.; Lin, V. S. Y. *J. Mater. Chem.* 2010, 20, (37), 7924-7937.
[6] Reculusa, S.; Ravaine, S. *Chem. Mater.* 2003, 15, (2), 598-605.
[7] Dechézelles, J.-F.; Aubert, T.; Grasset, F.; Cordier, S.; Barthou, C.; Schwob, C.; Maitre, A.; Vallée, R. A. L.; Cramail, H.; Ravaine, S. *PCCP* 2010, 12, (38), 11993-11999.
[8] Ma, X.; Tan, H.; Kipp, T.; Mews, A. *Nano Lett.* 2010, 10, (10), 4166-4174.
[9] Noginov, M. A.; Zhu, G.; Belgrave, A. M.; Bakker, R.; Shalaev, V. M.; Narimanov, E. E.; Stout, S.; Herz, E.; Suteewong, T.; Wiesner, U. *Nature* 2009, 460, 1110-1112.
[10] Eriksson, S.; Nylén, U.; Rojas, S.; Boutonnet, M. *Appl. Catal., A* 2004, 265, (2), 207-219.
[11] Sreedhar, B.; Radhika, P.; Neelima, B.; Hebalkar, N.; Mishra, A. K. *Catal. Commun.* 2008, 10, (1), 39-44.
[12] Stöber, W.; Fink, A.; Bohn, E. *J. Colloid Interface Sci.* 1968, 26, (1), 62-69.
[13] Philipse, A. P.; van Bruggen, M. P. B.; Pathmamanoharan, C. *Langmuir* 1994, 10, (1), 92-99.
[14] Liz-Marzán, L. M.; Giersig, M.; Mulvaney, P. *Langmuir* 1996, 12, (18), 4329-4335.
[15] Liz-Marzán, L. M.; Giersig, M.; Mulvaney, P. *Chem. Commun.* 1996, (6), 731-732.
[16] Yokoi, T.; Sakamoto, Y.; Terasaki, O.; Kubota, Y.; Okubo, T.; Tatsumi, T. *J. Am. Chem. Soc.* 2006, 128, (42), 13664-13665.
[17] Yokoi, T.; Wakabayashi, J.; Otsuka, Y.; Fan, W.; Iwama, M.; Watanabe, R.; Aramaki, K.; Shimojima, A.; Tatsumi, T.; Okubo, T. *Chem. Mater.* 2009, 21, (15), 3719-3729.
[18] Hartlen, K. D.; Athanasopoulos, A. P. T.; Kitaev, V. *Langmuir* 2008, 24, (5), 1714-1720.
[19] Yamauchi, H.; Ishikawa, T.; Kondo, S. *Colloids Surf.* 1989, 37, 71-80.
[20] Espiard, P.; Mark, J.; Guyot, A. *Polym. Bull.* 1990, 24, (2), 173-179.
[21] Arriagada, F. J.; Osseo-Asare, K. *Colloids Surf.* 1992, 69, (2-3), 105-115.
[22] Aubert, T.; Grasset, F.; Mornet, S.; Duguet, E.; Cador, O.; Cordier, S.; Molard, Y.; Demange, V.; Mortier, M.; Haneda, H. *J. Colloid Interface Sci.* 2010, 341, (2), 201-208.

[23] Guerrero-Martínez, A.; Pérez-Juste, J.; Liz-Marzán, L. M. *Adv. Mater.* 2010, 22, (11), 1182-1195.
[24] Grasset, F.; Labhsetwar, N.; Li, D.; Park, D. C.; Saito, N.; Haneda, H.; Cador, O.; Roisnel, T.; Mornet, S.; Duguet, E.; Portier, J.; Etourneau, J. *Langmuir* 2002, 18, (21), 8209-8216.
[25] Mornet, S.; Grasset, F.; Portier, J.; Duguet, E. *Eur. Cell. Mater.* 2002, 3, (2), 110-113.
[26] Mornet, S.; Grasset, F.; Duguet, E.; J, P. In *Silica nanoparticles with a γ-Fe_2O_3 magnetic core. Synthesis, thermal behaviour and magnetic properties*, Proceedings of the Eighth International Conference on Ferrites, Kyoto and Tokyo, Japan, Japan Society of Powder and Powder Metallurgy, 2000; p 766.
[27] López-Quintela, M. A. *Curr. Opin. Colloid Interface Sci.* 2003, 8, (2), 137-144.
[28] Chang, S.-Y.; Liu, L.; Asher, S. A. *J. Am. Chem. Soc.* 1994, 116, (15), 6739-6744.
[29] Li, T.; Moon, J.; Morrone, A. A.; Mecholsky, J. J.; Talham, D. R.; Adair, J. H. *Langmuir* 1999, 15, (13), 4328-4334.
[30] Tago, T.; Hatsuta, T.; Miyajima, K.; Kishida, M.; Tashiro, S.; Wakabayashi, K. *J. Am. Ceram. Soc.* 2002, 85, (9), 2188-2194.
[31] Bae, D.-S.; Han, K.-S.; Adair, J. H. *J. Mater. Chem.* 2002, 12, (10), 3117-3120.
[32] Son, J. H.; Kim, S. W.; Bae, D. S.; Han, K. S.; Lee, J. K.; Kim, C. Y.; Kim, B. I.; Adair, J. H. *Mater. Sci. Eng., A* 2008, 498, (1-2), 2-4.
[33] Son, J. H.; Park, H. Y.; Kang, D. P.; Bae, D. S. *Colloids Surf., A* 2008, 313-314, 105-107.
[34] Tago, T.; Hanaoka, T.; Dhupatemiya, P.; Hayashi, H.; Kishida, M.; Wakabayashi, K. *Catal. Lett.* 2000, 64, 27-31.
[35] Yu, K. M. K.; Yeung, C. M. Y.; Thompsett, D.; Tsang, S. C. *J. Phys. Chem. B* 2003, 107, (19), 4515-4526.
[36] Aubert, T.; Ledneva, A. Y.; Grasset, F.; Kimoto, K.; Naumov, N. G.; Molard, Y.; Saito, N.; Haneda, H.; Cordier, S. *Langmuir* 2010, 26, (23), 18512-18518.
[37] Grasset, F.; Dorson, F.; Cordier, S.; Molard, Y.; Perrin, C.; Marie, A. M.; Sasaki, T.; Haneda, H.; Bando, Y.; Mortier, M. *Adv. Mater.* 2008, 20, (1), 143-148.
[38] Bagwe, R. P.; Yang, C.; Hilliard, L. R.; Tan, W. *Langmuir* 2004, 20, (19), 8336-8342.
[39] Darbandi, M.; Thomann, R.; Nann, T. *Chem. Mater.* 2005, 17, (23), 5720-5725.
[40] Han, Y.; Jiang, J.; Lee, S. S.; Ying, J. Y. *Langmuir* 2008, 24, (11), 5842-5848.
[41] Wang, J.; Tsuzuki, T.; Sun, L.; Wang, X. *ACS Appl. Mater. Interfaces* 2010, 2, (4), 957-960.
[42] Jalil, R. A.; Zhang, Y. *Biomaterials* 2008, 29, (30), 4122-4128.
[43] Jing, L.; Yang, C.; Qiao, R.; Niu, M.; Du, M.; Wang, D.; Gao, M. *Chem. Mater.* 2010, 22, (2), 420-427.
[44] Grasset, F.; Dorson, F.; Molard, Y.; Cordier, S.; Demange, V.; Perrin, C.; Marchi-Artzner, V.; Haneda, H. *Chem. Commun.* 2008, (39), 4729-4731. http://dx.doi.org/10.1039/B806919K.
[45] Lai, C.-W.; Wang, Y.-H.; Lai, C.-H.; Yang, M.-J.; Chen, C.-Y.; Chou, P.-T.; Chan, C.-S.; Chi, Y.; Chen, Y.-C.; Hsiao, J.-K. *Small* 2008, 4, (2), 218-224.
[46] Lin, Y.-S.; Wu, S.-H.; Hung, Y.; Chou, Y.-H.; Chang, C.; Lin, M.-L.; Tsai, C.-P.; Mou, C.-Y. *Chem. Mater.* 2006, 18, (22), 5170-5172.
[47] Park, J. C.; Kim, J. Y.; Heo, E.; Park, K. H.; Song, H. *Langmuir* 2010, 26, (21), 16469-16473.

[48] Yi, D. K.; Lee, S. S.; Papaefthymiou, G. C.; Ying, J. Y. *Chem. Mater.* 2006, 18, (3), 614-619.
[49] Darbandi, M.; Thomann, R.; Nann, T. *Chem. Mater.* 2007, 19, (7), 1700-1703.
[50] Chang, S.-Y.; Liu, L.; Asher, S. A. *J. Am. Chem. Soc.* 1994, 116, (15), 6745-6747.
[51] Mornet, S. *Synthèse et modification chimique de la surface de nanoparticules de maghémite à des fins d'applications biomédicales*. Université de Bordeaux 1, 2002.
[52] Cavaliere-Jaricot, S.; Darbandi, M.; Nann, T. *Chem. Commun.* 2007, (20), 2031-2033.
[53] Koole, R.; van Schooneveld, M. M.; Hilhorst, J.; de Mello Donegá, C.; Hart, D. C.; van Blaaderen, A.; Vanmaekelbergh, D.; Meijerink, A. *Chem. Mater.* 2008, 20, (7), 2503-2512.
[54] Song, X.; Li, F.; Ma, J.; Jia, N.; Xu, J.; Shen, H. *J. Fluoresc.* 2011, 1-8.
[55] Deng, T.; Li, J. S.; Jiang, J. H.; Shen, G. L.; Yu, R. Q. *Adv. Funct. Mater.* 2006, 16, (16), 2147-2155.
[56] Gao, F.; Wang, L.; Tang, L.; Zhu, C. *Microchim. Acta* 2005, 152, 131-135.
[57] Wu, W.-B.; Liu, C.; Wang, M.-L.; Huang, W.; Zhou, S.-R.; Jiang, W.; Sun, Y.-M.; Cui, Y.-P.; Xu, C.-X. *J. Solid State Chem.* 2009, 182, (4), 862-868.
[58] Santra, S.; Dutta, D.; Moudgil, B. M. *Food Bioprod. Process.* 2005, 83, (2), 136-140.
[59] Jin, Y.; Lohstreter, S.; Pierce, D. T.; Parisien, J.; Wu, M.; Hall, C.; Zhao, J. X. *Chem. Mater.* 2008, 20, (13), 4411-4419.
[60] Ehlert, O.; Thomann, R.; Darbandi, M.; Nann, T. *ACS Nano* 2008, 2, (1), 120-124.
[61] Darbandi, M.; Hoheisel, W.; Nann, T. *Nanotechnology* 2006, 17, (16).
[62] Santra, S.; Tapec, R.; Theodoropoulou, N.; Dobson, J.; Hebard, A.; Tan, W. *Langmuir* 2001, 17, (10), 2900-2906.
[63] Vestal, C. R.; Zhang, Z. J. *Nano Lett.* 2003, 3, (12), 1739-1743.
[64] Stjerndahl, M.; Andersson, M.; Hall, H. E.; Pajerowski, D. M.; Meisel, M. W.; Duran, R. S. *Langmuir* 2008, 24, (7), 3532-3536.
[65] Vogt, C.; Toprak, M. S.; Muhammed, M.; Laurent, S.; Bridot, J. L.; Muller, R. N. *J. Nanopart. Res.* 2010, 12, (4), 1137-1147.
[66] Lu, C.-W.; Hung, Y.; Hsiao, J.-K.; Yao, M.; Chung, T.-H.; Lin, Y.-S.; Wu, S.-H.; Hsu, S.-C.; Liu, H.-M.; Mou, C.-Y.; Yang, C.-S.; Huang, D.-M.; Chen, Y.-C. *Nano Lett.* 2007, 7, (1), 149-154.
[67] Yi, D. K.; Selvan, S. T.; Lee, S. S.; Papaefthymiou, G. C.; Kundaliya, D.; Ying, J. Y. *J. Am. Chem. Soc.* 2005, 127, (14), 4990-4991.
[68] Yu, J.; Zhao, H.; Ye, L.; Yang, H.; Ku, S.; Yang, N.; Xiao, N. *J. Mater. Chem.* 2009, 19, (9), 1265-1270.
[69] Bagwe, R. P.; Hilliard, L. R.; Tan, W. *Langmuir* 2006, 22, (9), 4357-4362.
[70] Zhang, B.; Gong, X.; Hao, L.; Cheng, J.; Han, Y. C. J. *Nanotechnology* 2008, 19, (46), 465604.
[71] Deng, G.; Markowitz, M. A.; Kust, P. R.; Gaber, B. P. *Mater. Sci. Eng., C* 2000, 11, (2), 165-172.
[72] Markowitz, M. A.; Deng, G.; Gaber, B. P. *Langmuir* 2000, 16, (15), 6148-6155.
[73] He, X.-X.; Wang, K.; Tan, W.; Liu, B.; Lin, X.; He, C.; Li, D.; Huang, S.; Li, J. *J. Am. Chem. Soc.* 2003, 125, (24), 7168-7169.
[74] Derouet, D.; Thuc, C. N. H. *J. Appl. Polym. Sci.* 2008, 109, (4), 2113-2127.
[75] Hom, L.; Tamanoi *J. Mater. Chem.* 2009, 19, 6308-6316.
[76] Niemeyer, C. M. *Angew. Chem. Int. Ed.* 2001, 40, (22), 4128-4158.

[77] Sharma, P.; Brown, S.; Walter, G.; Santra, S.; Moudgil, B. *Adv. Colloid Interface Sci.* 2006, 123-126, 471-485.
[78] Grasset, F.; Marchand, R.; Marie, A. M.; Fauchadour, D.; Fajardie, F. *J. Colloid Interface Sci.* 2006, 299, (2), 726-732.
[79] Tartivel, R.; Reynaud, E.; Grasset, F.; Sangleboeuf, J.-C.; Rouxel, T. *J. Non-Cryst. Solids* 2007, 353, (1), 108-110.
[80] Cordier, S.; Dorson, F.; Grasset, F.; Molard, Y.; Fabre, B.; Haneda, H.; Sasaki, T.; Mortier, M.; Ababou-Girard, S.; Perrin, C. *J. Cluster Sci.* 2009, 20, (1), 9-21.
[81] Eastoe, J.; Hollamby, M. J.; Hudson, L. *Adv. Colloid Interface Sci.* 2006, 128-130, 5-15.
[82] López-Quintela, M. A.; Tojo, C.; Blanco, M. C.; García Rio, L.; Leis, J. R. *Curr. Opin. Colloid Interface Sci.* 2004, 9, (3-4), 264-278.
[83] Eastoe, J.; Warne, B. *Curr. Opin. Colloid Interface Sci.* 1996, 1, (6), 800-805.
[84] Pileni, M.-P. *C. R. Chimie* 2003, 6, (8-10), 965-978.
[85] Cushing, B. L.; Kolesnichenko, V. L.; O'Connor, C. J. *Chem. Rev.* 2004, 104, (9), 3893-3946.
[86] Kumar, P.; Mittal, K. L., *Handbook of Microemulsion Science and Technology*. Marcel Dekker, Inc.: New York, 1999.
[87] Hait, S.; Moulik, S. *J. Surfactants Deterg.* 2001, 4, (3), 303-309.
[88] Lawrence, M. J.; Rees, G. D. *Adv. Drug Delivery Rev.* 2000, 45, (1), 89-121.
[89] Arriagada, F. J.; Osseo-Asare, K. *J. Colloid Interface Sci.* 1999, 211, (2), 210-220.
[90] Arriagada, F. J.; Osseo-Asare, K. *Colloids Surf., A* 1999, 154, (3), 311-326.
[91] Osseo-Asare, K.; Arriagada, F. J. *Colloids Surf.* 1990, 50, 321-339.
[92] Osseo-Asare, K.; Arriagada, F. J. *J. Colloid Interface Sci.* 1999, 218, (1), 68-76.
[93] Finnie, K. S.; Bartlett, J. R.; Barbe, C. J. A.; Kong, L. *Langmuir* 2007, 23, (6), 3017-3024.
[94] Darbandi, M.; Urban, G.; Krüger, M. *J. Colloid Interface Sci.* 2010, 351, (1), 30-34.
[95] Sronek, L.; Majimel, J.; Kihn, Y.; Montardi, Y.; Tressaud, A.; Feist, M.; Legein, C.; Buzaré, J. Y.; Body, M.; Demourgues, A. *Chem. Mater.* 2007, 19, (21), 5110-5121.
[96] Yabe, S.; Momose, S. *J. Soc. Cosmet. Chem., Jpn.* 1998, 32, 372.
[97] Marchet, N. *Synthèse et stabilisation de suspensions colloïdales d'oxydes en milieu organique : application à la préparation de matériaux hybrides organiques-inorganiques pour des revêtements à très haute tenue au flux laser*. Université François Rabelais de Tours, 2008.
[98] Cador, O.; Grasset, F.; Haneda, H.; Etourneau, J. *J. Magn. Magn. Mater.* 2004, 268, (1-2), 232-236.
[99] Yarovoi, S. S.; Mironov, Y. V.; Naumov, D. Y.; Gatilov, Y. V.; Kozlova, S. G.; Kim, S.-J.; Fedorov, V. E. *Eur. J. Inorg. Chem.* 2005, 2005, (19), 3945-3949.
[100] Naumov, N. G.; Kim, S. J.; Virovets, A. V.; Mironov, Y. V.; Fedorov, V. E. *Bull. Korean Chem. Soc.* 2006, 27, (5), 635-636.
[101] Naumov, N.; Ledneva, A.; Kim, S.-J.; Fedorov, V. *J. Cluster Sci.* 2009, 20, (1), 225-239.
[102] Jackson, J. A.; Turro, C.; Newsham, M. D.; Nocera, D. G. *J. Phys. Chem.* 1990, 94, (11), 4500-4507.
[103] Sheldon, J. C. *J. Chem. Soc.* 1962, 410-414.

[104] Brylev, K. A.; Mironov, Y. V.; Yarovoi, S. S.; Naumov, N. G.; Fedorov, V. E.; Kim, S.-J.; Kitamura, N.; Kuwahara, Y.; Yamada, K.; Ishizaka, S.; Sasaki, Y. *Inorg. Chem.* 2007, 46, (18), 7414-7422.
[105] Mornet, S.; Vasseur, S.; Grasset, F.; Duguet, E. *J. Mater. Chem.* 2004, (14), 2161-2175.
[106] Dahan, M.; Lévi, S.; Luccardini, C.; Rostaing, P.; Riveau, B.; Triller, A. *Science* 2003, 302, (5644), 442-445.
[107] Contag, C. H.; Ross, B. D. *J. Magn. Reson. Imaging* 2002, 16, (4), 378-387.
[108] Duguet, E.; Désert, A.; Perro, A.; Ravaine, S. *Chem. Soc. Rev.* 2011, 40, (2), 941-960.
[109] Sanchez, C.; Belleville, P.; Popall, M.; Nicole, L. *Chem. Soc. Rev.* 2011, 40, (2), 696-753.

In: Silica Nanoparticles
Editor: Juan Vivero-Escoto
ISBN 978-1-61324-452-4
© 2012 Nova Science Publishers, Inc.

Chapter 7

BIOMEDICAL APPLICATIONS OF NANOSILICA

Seyed Shahabeddin Mirsasaani[1,*], Maedeh Hajipour Manjili[2], Farhad Ghomi[1], Seyed Mohammadreza Mousavi[1], Nasimsadat Mousavi[3] and Masoud Mozafari[1]

[1]Biomaterials Group, Faculty of medical Engineering (Center of Excellence), Amirkabir University of Technology,Tehran, Iran
[2]Faculty of Sciences, Gorgan University of Agricultural Sciences and Natural Resources, Gorgan, Iran
[3]Analytical Chemistry Department, Islamic Azad University (Tehran North Branch), Tehran, Iran

ABSTRACT

Application of nanotechnology to biomedical has increased over the years. There is a great deal of interest in investigating controlling the size and the shape of silica nanoparticles, understanding the overall, and applications of these particles in medicine.

Silica particles have received much attention in biomedical area because of their applications in new drug delivery systems, tissue engineering, dental materials, etc.

In recent decades, significant advances in drug delivery systems have enabled more effective drug administration. For example, nanosilica is used for cancer treatment.

Addition of nanosilica can improve the bioactivity and biocompatibility of scaffolds which are used in bone tissue engineering applications.

Silica is also used in preparation of dental nanomaterials. Most of the fillers which are used to reinforce dental cements and composites are silicate glasses. These materials with nanosilica fillers provide materials with high mechanical properties and low polymerization shrinkage.

In this chapter, three mentioned applications of silica nanoparticles in biomedical are presented.

[*]Corresponding Author: E-mail: shahabmirsasaani@yahoo.com.

INTRODUCTION

Nanotechnology, defined as the application of nanoscience in technological devices/processes/products, is fast emerging as an important enabling technology capable of impacting almost all the sectors of industries and consumer products. Therefore, not surprisingly, all governments and industries the world over are investing heavily in the development of nanotechnology based processes, products and systems. Nanotechnology represents a very broad area and is composed of three main fields, i.e. nanomaterials, nanotools and nanodevices. Of these, both research and commercialization have occurred to a significant level only in the area of nanomaterials.

Nanomaterials represent a class of materials characterized by a feature size of less than 100 nm. In the case of nanoparticles, the feature size is the particle diameter while in nanotubes, it is the nanotube diameter. At the other extreme, in the case of bulk materials, either the grain size in homogeneous materials or the reinforcing particle size and spacing in the case of composites represent the feature size. Thin films having thickness less than 100 nm or multi-layer coatings with the thickness of each layer less than 100 nm also qualify as nanomaterials. Therefore, it is important to note that while nano devices will certainly have to be made from nanomaterials, nanomaterial itself impacts areas beyond nanotechnology. It is also important to understand that merely bringing the feature size to below 100 nm is not enough; more importantly, such a decrease in feature size should result in significant enhancement of strength, toughness or electrical, electronic, optical and magnetic properties [1].

The last decade has witnessed an explosive growth in the area of nanomaterials research and commercialization primarily because of the availability of new methods of synthesis of nanomaterials as well as tools for characterization and manipulation of materials at nanoscale.

Silica is a common material used worldwide. It is found to have many applications in various fields such as cosmetic, abrasive, food, drug, environmental care, dentistry, tissue engineering, etc. [2, 3]. These functions ultimately depend on the surface chemistry, molecular structure, morphology and porosities of silica. There exist a range of methods for the synthesis of silica and include precipitation from sodium silicate; sol-gel route; templated synthesis; synthesis using emulsions; bioinspired methods, etc. It is however unclear how these methods are suited for synthesising silica for a given application [4, 5].

Organic/inorganic composite materials have been extensively studied for a long time. When inorganic phases in organic/inorganic composites become nanosized, they are called nanocomposites. Organic/inorganic nanocomposites are generally organic polymer composites with inorganic nanoscale building blocks. They combine the advantages of the inorganic material (e.g., rigidity, thermal stability) and the organic polymer (e.g., flexibility, dielectric, ductility, and processability). Moreover, they usually also contain special properties of nanofillers leading to materials with improved properties. A defining feature of polymer nanocomposites is that the small size of the fillers leads to a dramatic increase in interfacial area as compared with traditional composites. This interfacial area creates a significant volume fraction of interfacial polymer with properties different from the bulk polymer even at low loadings [6-10]. Inorganic nanoscale building blocks include nanotubes, layered silicates (e.g., montmorillonite, saponite), nanoparticles of metals (e.g., Au, Ag), metal oxides (e.g., TiO_2, Al_2O_3), semiconductors (e.g., PbS, CdS), and so forth, among which

SiO_2 is viewed as being very important. Therefore, polymer/silica nanocomposites have attracted substantial academic and industrial interest. In fact, among the numerous inorganic/organic nanocomposites, polymer/silica composites are the most commonly reported in the literature. They have received much attention in recent years and have been employed in a variety of applications. The organic component can be introduced as (i) a precursor, which can be a monomer or an oligomer, (ii) a preformed linear polymer (in molten, solution, or emulsion states), or (iii) a polymer network, physically (e.g., semicrystalline linear polymer) or chemically (e.g., thermosets, elastomers) cross-linked. The mineral part can be introduced as (i) a precursor (e.g., tetraethyloxysilane) or (ii) preformed nanoparticles [11].

There are three general methods for the preparation of polymer/silica nanocomposites according to the starting materials and processing techniques: blending, sol-gel processes, and in situ polymerization. Blending is generally just mixing of the silica nanoparticles into the polymer; a sol-gel process can be done in situ in the presence of a preformed organic polymer or simultaneously during the polymerization of the monomer(s); the method of in situ polymerization involves the dispersion of nanosilica in the monomer(s) first and then polymerization is carried out. In addition, considerable efforts have been devoted to the design and controlled fabrication of polymer/silica colloidal nanocomposite particles with tailored morphologies in recent years. The colloids represent a relatively new category of nanocomposites.

The preparation, characterization, properties, and applications of polymer/silica nanocomposites have become a quickly expanding field of research [12].

Perhaps it is necessary to make clear the terms “hybrids” and “nanocomposites” before the discussion of the nanocomposites, since it is somewhat ambiguous to identify whether materials fall into “nanocomposites” or not. The most wide-ranging definition of a hybrid is a material that includes two moieties blended on the molecular scale. Commonly the term “hybrids” is more often used if the inorganic units are formed in situ by the sol-gel process. Meanwhile, use of the word “nanocomposites” implies that materials consist of various phases with different compositions, and at least one constituent phase (for polymer/silica nanocomposites, that phase is generally silica) has one dimension less than 100 nm. A gradual transition is implied by the fact that there is no clear borderline between “hybrids” and “nanocomposites” [13-15].

SILICA NANOPARTICLES

Preparation and Properties of Silica Nanoparticles

Two classes of techniques have been developed for silica nanoparticle formation: the sol-gel method and the microemulsion method [16]. In 1968, Stober and Fink [17] reported a simple synthesis of monodisperse spherical silica particles by means of hydrolysis of a dilute solution of tetraethyloxysilane in ethanol at high pH as observed earlier by Kolbe [18]. Uniform amorphous silica spheres whose sizes ranged from 10 nm to 2 μm were obtained simply by changing the concentrations of the reactants. This Stober method was later improved by many others [19-23] and appears to be the simplest and most effective route to

monodispersed silica spheres [24]. In 1990, Osseoasare and Arrigada [25] prepared nanosized and monodisperse silica particles by controlled hydrolysis of tetraethyloxysilane in an inverse microemulsion. This microemulsion method is also widely used to synthesize silica nanoparticles.

Silica nanoparticles are also available from commercial sources now, and they usually exist as powder or colloid. Nanosilica powder is mainly produced by the fuming method and the precipitation method in industry. Fumed silica is a fine, white, odorless, and tasteless amorphous powder. It is manufactured by a high-temperature vapor process in which $SiCl_4$ is hydrolyzed in a flame of oxygen-hydrogen according to the reaction [26]:

$$SiCl_4+2H_2+O_2 \rightarrow SiO_2+4HCl \quad (1)$$

The silica has an extremely large surface area and smooth nonporous surface, which could promote strong physical contact between the filler and the polymer matrix [27]. Precipitated silica is manufactured by a wet procedure by treating silicates with mineral acids to obtain fine hydrated silica particles in the course of precipitation [28]. For the preparation of silica nanocomposites, fumed silica is commonly used and precipitated silica is seldomly used since the precipitated one has more silanol (Si-OH) groups on the surface and consequently it is much easier to agglomerate than fumed one. As for commercial colloidal silica spheres, they are usually in the form of a sol, with water or alcohol as the dispersing medium.

The structure of nanosilica shows a three-dimensional network. Silanol and siloxane groups are created on the silica surface, leading to hydrophilic nature of the particles. The surfaces of the silica are typically terminated with three silanol types: free or isolated silanols, hydrogen-bonded or vicinal silanols and geminal silanols [24]. The silanol groups residing on adjacent particles, in turn, form hydrogen bonds and lead to formation of aggregates, as shown in Figure 1. These bonds hold individual fumed silica particles together and the aggregates remain intact even under the best mixing conditions if stronger filler-polymer interaction is not present [29].

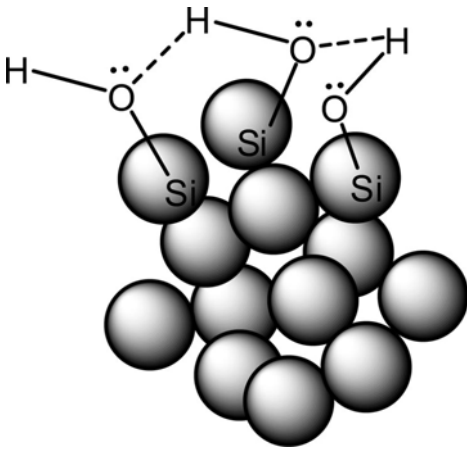


Figure 1. Schematic of aggregate formation between adjacent fumed silica particles through hydrogen bonding among the silanol groups.

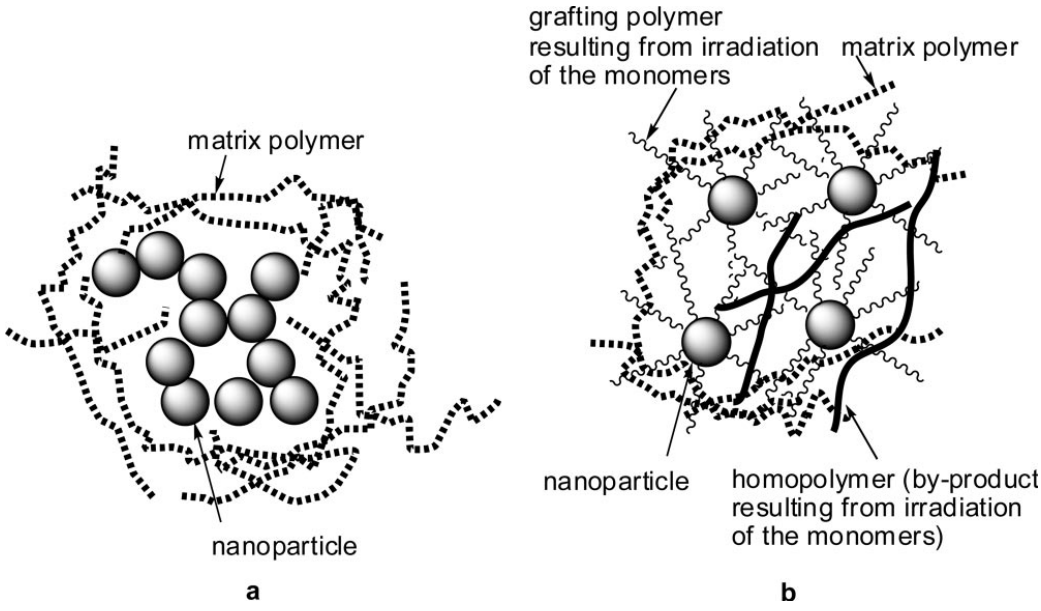


Figure 2. Schematic Drawings of (a) Agglomerated Nanoparticles Dispersed in a Polymer Matrix and (b) the Possible Structure of Grafted Nanoparticles Dispersed in a Polymer Matrix [30].

The dispersion of nanometer-sized particles in the polymer matrix has a significant impact on the properties of nanocomposites. A good dispersion may be achieved by surface chemical modification of the nanoparticles or physical methods such as a high-energy ball-milling process and ultrasonic treatment.

The great differences in the properties of polymer and silica materials can often cause phase separation. Therefore, the interfacial interaction between two phases of nanocomposites is the most decisive factor affecting the properties of the resulting materials (Figure 2).

A variety of methods have been used to enhance the compatibility between the polymer (hydrophobic) and nanosilica. The most frequently used method is to modify the surface of silica nanoparticles (especially for the blending and in situ method), which can also improve the dispersion of nanosilica in the polymer matrix at the same time. In general, surface modification of nanosilica can be carried out by either chemical or physical methods [31].

Much attention has been paid to modification of the surface of the nanosilica by chemical interaction since it can lead to much stronger interaction between modifiers and silica nanoparticles.

Modification by Chemical Interaction

Chemical methods involve modification either with modifier agents or by grafting polymers. Silane coupling agents are the most used type of modifier agents. They generally have hydrolyzable and organofunctional ends. The general structure of the coupling agents can be represented as $RSiX_3$ [32], where the X represents the hydrolyzable groups, which are typically chloro, ethoxy, or methoxy groups. The organo, R, group can have a variety of functionalities chosen to meet the requirements of the polymer. The functional group X reacts

with hydroxyl groups on the SiO2 surface, while the alkyl chain may react with the polymer. Hydrophobic silica can thus be obtained.

Grafting of polymer chains to silica nanoparticles is also an effective method to increase the hydrophobicity of the particles and to bring about tunable interfacial interactions in nanocomposites. Generally, there are two main approaches to chemically attaching polymer chains to a surface: covalent attachment of end-functionalized polymers to the surface ("grafting to" method) and in situ monomer polymerization with monomer growth of polymer chains from immobilized initiators ("grafting from" method). In a sense, the polymergrafted silica nanoparticles can also be viewed as polymer/silica nanocomposites.

Besides above-described chemical methods, grafting of polymers to nanoparticles can also be realized by irradiation. Zhang and co-workers [28, 33] have published a series of studies on irradiation-grafted nanosilica-filled nanocomposites. It was found that modification of nanoparticles through graft polymerization was very effective to construct nanocomposites because of (i) an increase in hydrophobicity of the nanoparticles that is beneficial to the filler/matrix miscibility, (ii) an improved interfacial interaction yielded by the molecular entanglement between the grafting polymer on the nanoparticles and the matrix polymer, and (iii) tailorable structure-properties relationship of the nanocomposites provided by changing the species of the grafting monomers and the grafting conditions since different grafting polymers might bring about different interfacial characteristics.

Modification by Physical Interaction

Surface modification based on physical interaction is usually implemented by using of surfactants or macromolecules adsorbed onto the surface of silica particles. The principle of surfactant treatment is the preferential adsorption of a polar group of a surfactant to the surface of silica by electrostatic interaction. A surfactant can reduce the interaction between the silica particles within agglomerates by reducing the physical attraction and can easily be incorporated into a polymer matrix. For example, silica was treated with cetyl trimethylammonium bromide to improve the chemical interaction between SiO2 and polymer [34] SiO2 nanoparticles were modified with stearic acid to improve their dispersion and the adhesion between the filler and polymer matrix [35, 36] nanosized silica was modified with oleic acid, which was bonded to the silica surface with a single hydrogen bond [37–39].

Adsorption of polymer can also promote the surface hydrophobicity of silica particles. Reculusa et al. [40] modified a silica surface by adsorption of an oxyethylene-based macromonomer. This macromonomer is mainly hydrophilic due to the presence of ethylene oxide groups, which are able to form hydrogen bonds with silanol functions present on the silica surface.

Applications

Since the polymer/silica nanocomposites not only can improve the physical properties such as the mechanical properties and thermal properties of the materials, but can also exhibit some unique properties, they have attracted strong interest in many industries. Many potential and practical applications of this type of nanocomposite have been reported. They have many

potential applications in various areas such as coatings, catalysis, and biotechnologies. Here, only a few biomedical applications of nanosilica will be presented.

DRUG DELIVERY SYSTEMS

One of the topics of the biomedical research is to design and develop new drug delivery systems able to perform time-controlled release of medicals with target specificity. The lack of control of drug release from conventional drug formulations in response to physiological requirements have led to the development of controlled drug delivery systems [41, 42]. In many diseases such as diabetes [43], heart disease [44], and thyroid diseases [45], the administration of a drug is only required at specific time intervals in which constant drug levels could lead to adverse effects. Hence, stimuli-sensitive drug delivery systems were developed to release a drug only in response to metabolic requirements or in the presence of specific stimuli. These environmentally-sensitive delivery systems have been developed to respond to a myriad of stimuli including the presence or absence of specific molecules, magnetic fields, ultrasound, electric fields, temperature, pH, and mechanical forces [46-50].

Polymers Used in Drug Delivery Systems

During the last decades a diversity of polymer based pharmaceutical carrier systems have been developed as new means of controlling temporal or distributional (site-specific) drug delivery. Pharmaceutical controlling delivery systems offer numerous advantages compared to conventionally administrated drugs in dosage forms, such as improved efficiency and reduced toxicity [51]. Conventional dosage forms have the disadvantage not to be able to control either the rate of drug delivery or the target area of drug administration and provide a rapid and an immediate drug release. Thus, frequent administration is necessary in order to maintain a therapeutic level, which in turn causes drug concentration in blood and tissues to fluctuate widely.

Polymeric cross-linked carrier matrices, such as hydrogels and supra-molecular polymer aggregates as well as different types of microencapsulation vehicles, are typical examples of common drug delivery devices [52-54]. Controlled release systems are generally classified based on their physicochemical, pharmaceutical or clinical aspect. They can also be classified according to their release mechanism and preparation methods as follows [55]:

Physical systems, including diffusion controlled systems such as monolithic porous systems and biodegradable/bioerodable systems.
Chemical systems, including immobilization of drugs.
Biological systems, including gene therapy

Depending on the delivery system and the pharmaceutical in use, different release mechanisms are applied. However, there are three primary ways by which active agents can be released from such system: diffusion, degradation, and swelling followed by diffusion. Any or all of these mechanisms may occur in a given release system. Diffusion occurs when a

drug or other active agent passes through the system (a ceramic or polymer based matrix) that forms the controlled-release device. The diffusion can occur on a macroscopic scale—as through pores in the matrix—or on a molecular level, by passing between, for instance, polymer chains. The diffusion controlled release could be activated by several means, including ionic strength, pH and thermal, magnetic or chemical changes. Controlled release based on an eroding matrix (surface or bulk) allow diffusion of drug from the degrading system [55].

Temporal or distributional drug delivery could be beneficial when handling numerous classes of drugs, such as anti-inflammatory agents, antibiotics, chemotherapeutic drugs, steroids, hormones and vaccines, to mention a few [56]. The ability to control over the drug delivery can be an important factor especially at times when traditional oral or injectable drug formulations are difficult to distribute. In some cases there might be a need of a slow release of a water soluble drug or a fast release of low-solubility drugs. It might also be convenient for drug delivery to specific sites, drug delivery using nanoparticulate systems, delivery of two or more agents with the same formulation, and also systems based on carriers that can dissolve or degrade and be readily eliminated.

In recent years there has been an explosion in the use of polymers to solve various biomedical problems. Polymers play a crucial role in controlling drug release rate, enhancing drug solubility and uptake, and limiting drug degradation and toxicity.

Biodegradable polymers have been widely used in biomedical applications because of their known biocompatibility and biodegradability. Biodegradable polymers could be classified into synthetic and natural (biologically derived) polymers. Both synthetic and natural biodegradable polymers have been used for drug delivery, and some of them have been successfully developed for clinical applications. This entry focused on various biodegradable polymers that have been used in development of drug delivery systems. Advances in organic chemistry and nano/micro fabrication/manufacturing methods enable continuous progresses in better utilization of a wide range of novel biodegradable polymers in drug delivery.

Conventional forms of drug delivery generally rely on tablets, eye drops, ointments and intravenous solutions. Recently, a number of novel drug delivery technologies have developed. These newer technological development include drug modification by chemical means, career based drug delivery and drug entrapment in polymeric matrices or within pumps that are placed in desired bodily compartments. These technical development in drug delivery/targeting approaches improve the efficacy of drug therapy thereby improve human health. Still there are many infectious and other deadly diseases are uncured due to the problem encountered by formulation scientists in drug delivery approaches. There is a strong need to develop a proper delivery system to achieve the complete therapeutic effects of the existing drug molecules. Use of polymeric materials in novel drug delivery approaches has attracted the scientists. Polymer chemists and chemical engineers, pharmaceutical scientists are engaged in bringing out design predictable, controlled delivery of bioactive agents. When the drug is delivered to the site of action by using polymer based drug delivery approaches the safety and biocompatibility is questionable. The characterization of biocompatible polymers is more focused in the field of formulation development and drug delivery approaches etc. the biodegradable polymers have properties of degrading in biological fluids with progressive release of dissolved or dispersed drug. There is various novel drug delivery approaches are developed in the pipeline of polymer based drug delivery approaches. The bio-safety and

biocompatibility are the important characteristics needed for the use of polymers in the field of pharmaceutical formulation and in novel drug delivery approaches. The ideal drug delivery system should be inert or biodegradable, biocompatible, mechanically strong, comfortable for the patient, capable of achieving high drug loading, safe from accidental release, simple to administer and remove, and easy to fabricate and sterilize [57].

Application of Nanosilica in Drug Delivery

A very interesting application of silica is to use in the nanotechnology of drug delivery. The application of nanotechnology in the field has attracted much attention in the latest decades. Recent breakthroughs on the morphology control and surface functionalization of inorganic-based delivery vehicles, such as silica nanoparticles, have brought new possibilities to this burgeoning area of research. The ability to functionalize the surface of silica-based nanocarriers with stimuli-responsive groups, nanoparticles, polymers, and proteins that work as caps and gatekeepers for controlled release of various cargos is just one of the exciting results reported in the literature that highlights silica nanoparticle as a promising platform for various biotechnological and biomedical applications.

In cancer therapy, the administered cytostatics show a number of severe side-effects due to their toxicity [58, 59]. Side effects can be reduced by encapsulating the drug in a delivery-system, which protects the body from the toxic drug and prevents the decomposition of the drug prior to reaching the target cells. Furthermore, a specific targeting of this drug carrier onto malign cells combined with a controlled release of drug by diffusion minimizes the amount of drug that has to be administered. Clinically used nanocarriers for drugs consist, for example, of synthetic organic polymers [60-62] or liposomes [63] yet especially cell-targeting and a controlled release still represent a great challenge. Mesoporous silica materials, which contain nanometer-sized channel systems, provide high potential as novel drug-delivery systems due to their high versatility [64-69]. The physical properties that can be controlled include the surface properties, pore topologies, pore sizes, and surface areas. These properties are essential for generating a depot-effect, that is, a retarded controlled release of a drug from the delivery system. They also provide flexibility for the incorporation of a high amount of differently sized guests. Additionally, silica nanostructures have a high potential for cell-targetting approaches as they can be covalently modified. Hence, mesoporous silica materials meet the essential requirements for a novel efficient class of drug-delivery systems. In order to gain control over the release of the drug molecules from the delivery system, understanding the diffusion of the drug inside the porous hosts is of paramount importance. Figure 3 demonstrates the potential of surfactant-templated mesoporous silica materials as delivery system for the anticancer drug. Drug-loaded mesoporous samples are synthesized as thin films. For example, doxorubicin and its analogues are widely used in chemotherapy, for example, for the treatment of sarcoma, ovarian carcinoma, or breast cancer. However, Doxorubicin is also highly toxic especially to the heart and the kidneys, which limits its therapeutic applications. Novel drug-delivery strategies for that drug are thus urgently needed [70].

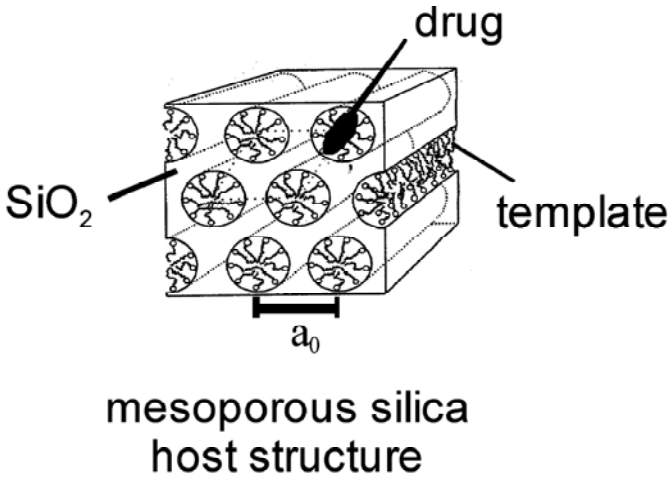


Figure 3. Host-guest-system (a) Schematic of a surfactant-templated mesoporous silica material loaded with the drug. a_0 designates the pore-to-pore distance.

Metal nanoshells are a relatively new class of nanoparticles consisting of a dielectric core nanoparticle surrounded by an ultrathin metal shell. These nanoshells have tunable plasmon resonances that are based on geometric construction. The ratio of shell thickness to core diameter allows nanoshell peak resonance to be tuned while the overall dimensions of the particle allow the relative absorbing and scattering efficiencies to be manipulated [71].

Silica–gold (SiO_2–Au) nanoshells are a new class of nanoparticles that have a silica dielectric core, which is surrounded by a gold shell. In contrast to gold–gold sulfide nanoshells, the peak extinction of SiO_2–Au nanoshells are very easily tunable to absorb or scatter light strongly within the wavelengths of 650–900 nm that is commonly known as the NIR region [71]. This region is of significant biological importance and hence nanoshells are currently being investigated for use in the NIR region for a variety of biomedical applications including their use as diagnostic tools, contrast enhancements for imaging applications and for laser tissue welding [72].

TISSUE ENGINEERING

Biomaterials and Tissue Engineering

Throughout the history of surgery materials have been used in enterprising ways to solve medical problems and improve the quality of life for patients. In previous centuries materials were often chosen more for their familiarity or availability than for their biological compatibility, and so catgut and nylon sutures became predominant in surgery just as the use of stainless steel became universal in bone fixation.

Many modern and almost all historical biomaterials do not necessarily integrate fully with the body, examples including ivory tooth replacements, dental fillings, stainless steel bone prostheses and artificial heart valves. However, advances in the understanding of how

materials function in the body and widespread investment in new technologies has revolutionized the opportunities for employing modern materials in novel functional roles.

Tissue engineering encompasses the implantation of biomaterials to restore function to tissues following disease or injury. Biomaterials can be implanted as porous scaffolds to support tissue in growth from surrounding tissue, or cellularised *in vitro* prior to implantation [73].

Tissue engineering is a multidisciplinary field which involves the 'application of the principles and methods of engineering and life sciences towards the fundamental understanding of structure-function relationships in normal and pathological mammalian tissues and the development of biological substitutes that restore, maintain or improve tissue function' [74]. The goal of tissue engineering is to surpass the limitations of conventional treatments based on organ transplantation and biomaterial implantation. It has the potential to produce a supply of immunologically tolerant 'artificial' organ and tissue substitutes that can grow with the patient. This should lead to a permanent solution to the damaged organ or tissue without the need for supplementary therapies, thus making it a cost-effective treatment in the long term [75].

One of the principle methods behind tissue engineering involves growing the relevant cell(s) in vitro into the required three-dimensional (3D) organ or tissue. But cells lack the ability to grow in favoured 3D orientations and thus define the anatomical shape of the tissue. Instead, they randomly migrate to form a two-dimensional (2D) layer of cells. However, 3D tissues are required and this is achieved by seeding the cells onto porous matrices, known as scaffolds, to which the cells attach and colonise. The scaffold therefore is a very important component for tissue engineering.

Several requirements have been identified as crucial for the production of tissue engineering scaffolds [76]: (1) the scaffold should possess interconnecting pores of appropriate scale to favour tissue integration and vascularisation, (2) be made from material with controlled biodegradability or bioresorbability so that tissue will eventually replace the scaffold, (3) have appropriate surface chemistry to favour cellular attachment, differentiation and proliferation, (4) possess adequate mechanical properties to match the intended site of implantation and handling, (5) should not induce any adverse response and, (6) be easily fabricated into a variety of shapes and sizes. Bearing these requirements in mind, several materials have been adopted or synthesized and fabricated into scaffolds.

Nanotechnology has been increasingly utilized to enhance bone tissue engineering strategies. In particular, nanotechnology has been employed to overcome some of the current limitations associated with bone regeneration methods including insufficient mechanical strength of scaffold materials, ineffective cell growth and osteogenic differentiation at the defect site, as well as unstable and insufficient production of growth factors to stimulate bone cell growth. Among the tremendous technologies of nanoparticles in biological systems, there are three major nanoparticle research areas that have been developed to overcome these limitations and disadvantages: (a) the generation of nanoparticle-composite scaffolds to provide increased mechanical strength for bone graft, (b) the fabrication of nanofibrous scaffolds to support cell growth and differentiation through morphologically-favored architectures, and (c) the development of novel delivery and targeting systems of genetic material, especially those encoding osteogenic growth factors. These nanoparticle-based bone tissue engineering technologies possess a great potential to ensure the efficacy of clinical bone regeneration [75].

Polymers Used in Tissue Engineering Scaffolds

Just a few decades ago, the field of materials science was most closely associated with metallurgy and ceramics which could be used for high strength applications. In recent years, however, the focus has broadened to include plastics, fibers and polymers. The latter in particular has sparked interest because of its potential for use in biomedical applications.

Synthetic and natural polymers are an attractive alternative and versatile in their applications to the growth of most tissues.

Synthetic Polymers

Aliphatic polyesters such as polyglycolic acid (PGA), polylactic acid (PLLA), their copolymers (e.g. PLGA) and polycaprolactone (PCL) are the most commonly used polymers for tissue engineering scaffold applications. The degradation products of these polymers (glycolic acid and lactic acid) are present in the human body and are removed by natural metabolic pathways [77].

Natural Polymers

Naturally derived protein or carbohydrate polymers have been used as scaffolds for the growth of several tissue types. By far the most popular natural polymer used for tissue engineering scaffolds is collagen.

Bioresorbable polymers have been particularly important in modern tissue engineering and surgical procedures, providing resorbable matrices for supporting tissue growth and allowing temporary fixation of medical devices without the requirement for surgical removal. Most resorbable polymers are aliphatic (open chain) polyesters with hydrolysable ester linkages which degrade to generate relatively non-toxic waste products such as carbon dioxide and water [73].

Biodegradable polymers and bioactive ceramics are being combined in a variety of composite materials for tissue engineering scaffolds.

Polymer hydrogels stand out among synthetic materials used as biomaterials because of their good biocompatibility due, mainly, to their ability to absorb large amounts of water. However, they have poor mechanical properties and, as a consequence, they are in need of reinforcement. There are several routes to reinforce a polymer hydrogel, including the copolymerization with a hydrophobic component and the preparation of interpenetrating polymer networks [78, 79]. A different strategy consists in the preparation of hybrid organic/inorganic nanocomposites, which include a silica phase obtained simultaneously with the polymer in a sol–gel process [80].

Apart from reinforcement, there is a great need of providing bioactivity to surfaces in applications where good interaction between the synthetic material and the living tissues is mandatory.

Application of Nanosilica in Tissue Engineering

Various kinds of ceramics such as Na_2O, CaO, SiO_2, P_2O_5 glasses, sintered hydroxyapatite and glass–ceramics containing apatite or wollastonite, are known to bond directly to living bone avoiding the formation of fibrous tissue [81-83]. Some of them or their derivatives are being clinically used in artificial middle-ear bone implants, artificial vertebrae, intervertebral discs, iliac bones, fillers in bone and maxillofacial defects or to fill the gaps around the implants, etc. and have inspired new bioactive materials with varied compositions and structures to fulfill different applications [84–87]. However, the use of bioactive glasses for the stimulated regeneration of tissues is limited by their poor mechanical properties, since their brittleness makes difficult their use in load-bearing applications. One approach to combine bioactivity and enhanced mechanical properties in the same material is the preparation of organic/inorganic hybrids, in which the inorganic phase is incorporated into an organic polymeric matrix. This type of structural organization to a certain extent mimics the composition of mineralized tissues, where the hydroxyapatite (HAp) inorganic phase is dispersed in a collagen matrix with which it interacts at a molecular level yielding a natural composite. Various hybrid systems have been explored employing as inorganic phases bioactive glasses, Hap or pure silica, in the form of particles or fibers. Porous scaffolds of hybrid composites mimicking natural bone structures have been prepared and investigated to serve as a support and guide new tissue in-growth and regeneration [88]. In the recent past many studies have been devoted to organic/inorganic nanocomposites with the aim of combining the properties of both phases at the nanoscale level. Polymer/silica nanocomposites have been prepared by physically mixing silica nanoparticles with polymers or by copolymerization of the organic polymers with surface-functionalized silica nanoparticles [89]. Various surface modification techniques have also been proposed aiming to enhance the bioactivity of polymer surfaces. These methods are based on the introduction of hydrophilic polar groups, such as phosphate, hydroxy groups, Si–OH or Ti–OH, and carboxy and carboxylate groups, which have been found to be effective for apatite nucleation, onto more hydrophobic less bioactive substrates. Nonetheless, the idea of nanohybridizing biocompatible polymers with silica by this simultaneous in situ sol–gel polymerization to improve their bioactivity is a very recent one. Few published works address it [90].

DENTISTRY

Humankind has always been plagued by the problem of restoring parts of the body lost as a result of accident or disease. Practitioners of dentistry have been confronted with this problem since the beginning of dental practice, and the means of replacing missing tooth structure by artificial materials continues to account for a large part of dental science [91].

Dental composites are used to replace missing tooth structure and modify tooth color and contour, thus enhancing facial esthetics. The development of composites about 1960 has resulted in higher mechanical properties, lower thermal coefficient of expansion, lower dimensional change on setting, and higher resistance to wear, thereby improving clinical performance. Later development of bonding agents for bonding composites to tooth structure has also improved the quality of composite restorations [92].

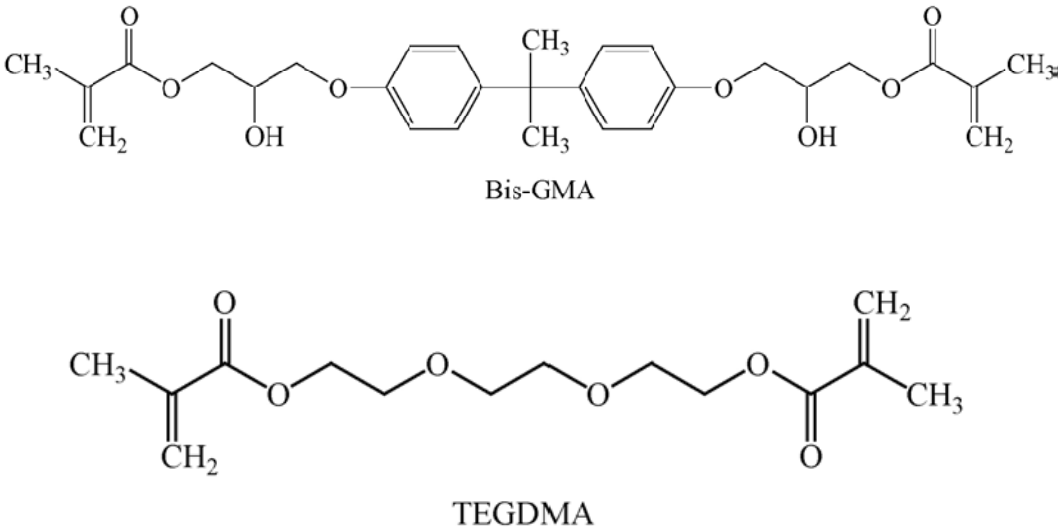


Figure 4. Chemical structures of Bis-GMA and TEGDMA [93].

Dental restorative composites are prepared by the mixing of organic resin matrix with inorganic fillers. Fillers such as silicon dioxide (silica, SiO2), zirconium dioxide (zirconia, ZrO2), and aluminum trioxide (alumina, Al2O3) of micron or submicron particle size are usually used. The organic matrix is often composed of methacrylate resins, such as 2,2-bis[4-(3-methacryloxy-2- hydroxypropoxy)phenyl] propane (Bis-GMA) and triethylene glycol dimethacrylate (TEGDMA) (Figure 4). Bis-GMA is the primary organic ingredient in nearly every commercial restorative resin. Bis-GMA has become a vital monomer for dental restorative composites, due to its superior mechanical strength, less shrinkage, high modulus, and reduced toxicity because of its lower volatility and diffusivity into the tissue. Because of the very high viscosity of Bis-GMA, TEGDMA is added to the resin system to reduce its viscosity in order to enhance filler loading and, as a result, physical and mechanical properties [93].

LIGHT-CURED DENTAL NANOCOMPOSITES

Recently, dental composites cured by visible light have been used, mostly because they are safer and easier to use than resin composite systems activated by ultra-violet (UV) light [94]. The use of argon laser for the photopolymerization of composite resin restoratives was introduced in the early 1980s [95]. This interest has arisen because the 472 nm wavelength of argon laser is optimal for the initiation of polymerization of composite resins, particularly when the camphorquinone, with broad peak activity in the 470 nm range, is used in dental composite as a photo-initiator (Figure 5) [96]. In addition, lasers such as argon laser with its inherent optical characteristics, like generating one wavelength of blue light (i.e., the light is monochromatic), absorption selectivity because of wavelength tunability, coherency, collimation, low beam divergence, and fiber delivery capability, are suitable sources for the

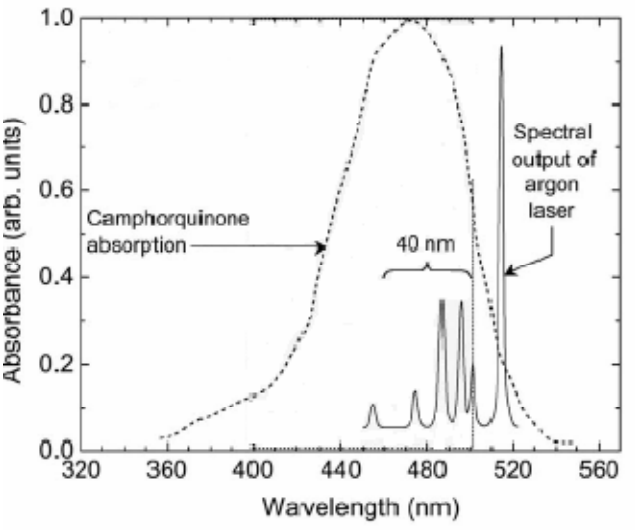


Figure 5. Absorption spectrum of camphorquinone [98].

polymerization of composite resins, which effectively can provide a larger degree of conversion (DC) of monomers, reduce curing time and enhance physical properties of cured composites [97].

APPLICATION OF NANOSILICA IN DENTISTRY

Nanotechnology, also known as molecular nanotechnology or molecular engineering, is the production of functional materials and structures in the range of 0.1 to 100 nanometers—the nanoscale—by various physical or chemical methods. Today, the revolutionary development of nanotechnology has become the most highly energized discipline in science and technology [99].

Polymer/silica nanocomposites have received much attention in dentistry because of their physico-mechanical properties and applications in restorative dental materials. The mechanical properties of dental materials can be modified significantly using fillers like silica.

Currently, an increasing amount of work is being published on polymer/silica nanocomposites. The recent developments on the preparation, characterization, properties, and application of this type of nanocomposite have been reviewed.

Although much work has already been done on various aspects of polymer/ silica nanocomposites, more research is required in order to further understand the complex structure-property relationships. Tailoring the interfacial interaction of filler/matrix is conducive to a better understanding of the relationships [100].

As dental composites cannot withstand heavy occlusal forces, many ways have been introduced to reinforce them, such as using fibers and whiskers as reinforcing agents. Some of dental resins are reinforced with inorganic fillers [101]. A wide variety of fillers have been

employed in composites to improve the properties and developments in filler technology are responsible for many improvements in composites which are used today [102].

New fillers have been prepared for dental restorative composites. Most glass fillers for dental composites, except for colloidal silica, have been manufactured by melting the components at high temperatures and by subsequent grinding [103].

Reinforcement with nanofibers was shown substantial improvements on mechanical properties of dental composites, such as flexural strength, elastic modulus and the work-of-fracture. The small diameter of nanofibers also provides for a large ratio of surface area to volume, which can enhance the intermolecular hydrogen bonding between nanofiber filler and the resin matrix.

Recently, nanosized particles dispersed in the organic matrix to give high strength, hardness and toughness.

CONCLUSION

Recently, a range of nanomaterials have been designed and used in a number of different medical applications such as, drug delivery systems, tissue engineering, and dental composites. The awareness about nanomaterials and nanotechnology and its benefits to biomedical field has continuously increased during the latest decades. The intensity of scientific researches in biomedical applications of nanosilicas has also developed considerably over the recent years.

Silica nanoparticles offer a number of advantages over other materials for developing controlled drug delivery systems, scaffolds in tissue engineering, and dental nanocomposites. For example, silica-based nanocarriers can be used in cancer therapy and design and develop new drug delivery systems that have ability to perform time-controlled release of drugs with target specificity. Also, nanoparticles used in the organic matrix to give excellent physical and mechanical properties due to high strength, hardness and toughness of this component.

REFERENCES

[1] Mitra S.B, Dong W.U, Holmes B.N (2003) An application of nanotechnology in advanced dental materials. *Am Dent Assoc*, 134: 1382-1390 .
[2] Sun L, Gong K (2001) *Ind. Eng. Chem. Res*, 40: 5861.
[3] Tzong-Horng L (2004) *Tiw. Eng. Chem. Res*, A364: 313-323.
[4] Tomozawa M, Kim D.L, Lou V. (2001) *Non-Cryst. Solids*, 296: 102.
[5] Bogush G.H, Tracy M.A, Zukoski C.F (1988) *Non-Cryst. Solids*, 104: 95.
[6] Balazs A.C, Emrick T, Russell T. P (2006) *Science*, 314: 1107.
[7] Winey K.I, Vaia R.A (2007) *MRS Bull*, 32: 314.
[8] Caseri W (2004) In Encyclopedia of Nanoscience and Nanotechnology. American Scientific Publishers: *Stevenson Ranch*, 6: 235-247.
[9] Schadler L.S (2003) Nanocomposite Science and Technology, Wiley-VCH: Weinheim, Germany, Chapter 2.
[10] Schaefer D.W, Justice R.S. (2007) *Macromolecules*, 40: 8501.
[11] Hajji P, David L, Gerard J.F, Pascault J.P, Vigier G. (1999) *Polym. Sci., Part B: Polym. Phys*., 37: 3172.

[12] Althues H, Henle J, Kaskel S (2007) *Chem. Soc. Rev*, 36: 1454.
[13] Kickelbick G (2003) *Prog. Polym. Sci*, 28: 83.
[14] Schmidt G, Malwitz M.M (2003) *Curr. Opin. Colloid Interface Sci*, 8: 103.
[15] Jordan J, Jacob K.I, Tannenbaum R, Sharaf M.A, Jasiuk I (2005) *Mater. Sci. Eng*., 393: 1.
[16] Darbandi M, Thomann R, Nann T (2007) *Chem. Mater*, 19: 1700.
[17] Stober W, Fink A, Bohn E.J (1968) *Colloid Interface Sci*., 26: 62.
[18] Kolbe G (1956) Thesis, Friedrich-Schiller-University Jena, Germany.
[19] Van Helden A.K, Jansen J.W, Vrij A.J (1981) *Colloid Interface Sci*., 81: 354.
[20] Philipse A.P, (1988) *Colloid Polym. Sci*., 266: 1174.
[21] Bogush G.H, Tracy M.A, Zukoski C.F (1988) *Non-Cryst. Solids*, 104: 95.
[22] Van Blaaderen A, van Geest J, Vrij A (1992) *Colloid Interface Sci*., 154: 481.
[23] Iler R.K (1979) The Chemistry of Silica. Wiley, New York.
[24] Kim H.C, Dubois G (2005) Dekker Encyclopedia of Nanoscience and Nanotechnology; Taylor & Francis: New York, 1-10.
[25] Osseo-Asare K, Arriagada F.J, (1990) *Colloids Surf*., 50: 321.
[26] Vassiliou A.A, Papageorgiou G.Z, Achilias D.S, Bikiaris D.N (2007) *Macromol. Chem. Phys*., 208: 364.
[27] Kim S.H, Ahn S.H, Hirai T (2003) Polymer, 44: 5625
[28] Wu C.L, Zhang M.Q, Rong M.Z, Friedrich K (2005) *Compos. Sci. Technol*., 65: 635.
[29] Jana S.C, Jain S (2001) *Polymer*, 42: 6897.
[30] Rong M.Z, Zhang M.Q, Zheng Y.X, Zeng H.M, Walter R, Friedrich K (2001) *Polymer*, 42: 167.
[31] Zhang M.Q, Rong M.Z, Friedrich K (2003) In Handbook of Organic- Inorganic Hybrid Materials and Nanocomposites. Ameican Scientific Publishers: Stevenson Ranch, CA, 2: 113-150.
[32] Blum F.D (2004) In Encyclopedia of Polymer Science and Technology; Kroschwitz, J. I., Ed.; John Wiley & Sons: Hoboken, NJ, 8: 38-50
[33] Rong M.Z, Zhang M.Q, Zheng Y.X, Zeng H.M, Walter R, Friedrich K.J (2000) *Mater. Sci. Lett*., 19: 1159.
[34] Wu T.M, Chu M.S (2005) *Appl. Polym. Sci*., 98: 2058
[35] Ahn S.H, Kim S.H, Lee S.G (2004) *Appl. Polym. Sci*., 94: 812
[36] Lai Y.H, Kuo M.C, Huang J.C, Chen M (2007) *Mater. Sci. Eng*., 458: 158
[37] Ding X.F, Zhao J.Z, Liu Y.H, Zhang H.B, Wang Z.C (2004) *Mater. Lett*., 58: 3126
[38] Mahdavian A.R, Ashjari M, Makoo A.B (2007) *Eur. Polym*. 43: 336
[39] Tang J.C, Lin G.L, Yang H.C, Jiang G.J, Chen-Yang Y.W (2007) *Appl. Polym. Sci*., 104: 4096.
[40] Reculusa S, Poncet-Legrand C, Ravaine S, Mingotaud C, Duguet E, Bourgeat Lami E (2002) *Chem. Mater*., 14: 2354.
[41] Wu Z, Jiang Y, Kim T, Lee K (2007) Effects of surface coating on the controlled release of vitamin B1 from mesoporous silica tablets. *Control. Release*, 119: 215–221.
[42] Arnold M.M, Gorman E.M, Schieber L.J, Munson E.J, Berkland C (2007) NanoCipro encapsulation in monodisperse large porous PLGA microparticles. *Control Release*, 121: 100–109.

[43] Robertson K.J, Schoenle E, Gucev Z, Mordhorst L, Gall M.A, Ludvigsson J (2007) Insulin detemir compared with NPH insulin in children and adolescents with Type 1 diabetes. *Diabet. Med*., 24: 27–34.
[44] Smulyan H (2007) Nitrates, arterial function, wave reflections and coronary heart disease. *Adv. Cardiol*., 44: 302–314.
[45] Malm J, Grover G.J, Farnegardh M (2007) Recent advances in the development of agonists selective for beta1-type thyroid hormone receptor. *Mini Rev. Med. Chem*., 7: 79–86.
[46] Fischel-Ghodsian F, Brown L, Mathiowitz E, Brandenburg D, Langer R, (1988) Enzymatically controlled drug delivery. *Proc. Natl. Acad. Sci. U.S.A*., 85: 2403–2406
[47] Tang M, Zhang R, Bowyer A, Eisenthal R, Hubble J (2003) A reversible hydrogel membrane for controlling the delivery of macromolecules. *Biotechnol. Bioeng*., 82: 47–53.
[48] Matsumoto A, Yoshida R, Kataoka K (2004) Glucose-responsive polymer gel bearing phenylborate derivative as a glucose-sensing moiety operating at the physiological pH. *Biomacromolecules*, 5: 1038–1045.
[49] Hu S.H, Liu T.Y, Liu D.M, Chen S.Y (2007) Nano-ferrosponges for controlled drug release. *Control Release*, 121: 181–189.
[50] Lubbe A.S, Bergemann C, Huhnt W, Fricke T, Riess H, Brock J.W, Huhn D, (1996) Preclinical experiences with magnetic drug targeting: tolerance and efficacy. *Cancer Res*., 56: 4694–4701.
[51] Rosler A, Vandermuelen G.W.M, Klok H.A (2001) *Adv. Drug Delivery Rev*.; 53: 95
[52] Bae Y.H, Huh K.M, Kim Y, Park K.H (2000) *Controlled Release*, 64: 3
[53] Ravi Kumar M.N.V (2000) *Pharmaceut. Sci*., 3: 238.
[54] Ulrich K.E, Cannizzaro S.M, Langer R.S, Shakesheff K.M (1999) Chem. Rev. 99: 3181
[55] Kim C (2000) Controlled release dosage form design. Technomic Publishing Company, Inc.USA.
[56] Uhrich K.E, Cannizzaro S.M, Langer R.S, Shakesheff K.M (1999) Chem Rev., 99: 3181.
[57] Langer R, New methods of drug delivery. Science 1990, DOI: 10.1126/science.2218494
[58] Guchelaar H.J, Ten Napel C.H.H, De Vries E.G.E, Mulder N.H (1994) *Clin. Oncol*., 6: 40–48.
[59] Mann D.L (2006) *Nat. Med*., 12 (8): 881–882.
[60] Langer R. *Science*, 1990, 249 (4976): 1527–1533.
[61] Torchilin V.P (2007) *Pharm. Res*., 24 (1): 1–16.
[62] Uhrich K.E, Cannizzaro S.M, Langer R.S, Shakesheff K.M (1999) *Chem. Rev*., 99: 3181–3198.
[63] Samad A, Sultana Y, Aqil M (2007) *Curr. Drug DeliVery*, 4 (4): 297–305.
[64] Slowing I.I, Trewyn B.G, Giri S, Lin V.S.Y (2007) *AdV. Funct. Mater*., 17 (8): 1225–1236.
[65] Lu J, Liong M, Zink J.I, Tamanoi F. (2007) 3 (8): 1341–1346.
[66] Prokopowicz M, Przyjazny A (2007) *Microencapsulation*, 24 (7): 694–713.
[67] Lai C.Y, Trewyn B.G, Jeftinija D.M, Jeftinija K, Xu S, Jeftinija S, Lin V.S.Y (2003) *Am. Chem. Soc*., 125: 4451–4459.

[68] Roy I, Ohulchanskyy T.Y, Bharali D.J, Pudavar H.E, Mistretta R.A, Kaur N, Prasad P.N (2005) *Proc. Natl. Acad. Sci. U.S.A*., 102 (2): 279–284
[69] Giri S, Trewyn B.G, Stellmaker M.P, Lin V.S.Y (2005) *Angew. Chem*., Int. Ed., 44 (32): 5038–5044
[70] Beck J.S, Vartuli J.C, Roth W.J, Leonowicz M.E, Kresge C.T, Schmitt K.D, Chu C.T.W, Olson D.H, Sheppard E.W, McCullen S.B, Higgins J.B, Schlenker J.L (1992) *Am. Chem. Soc*., 114 (27): 10834–10843.
[71] O'Shaughnessy J (2003) *Oncologist*, 8: 1–2.
[72] Schmidt T, Schuetz G.J, Baumgartner W, Gruber H.J, Schindler H.J (1995) *Phys. Chem*., 99 (49): 17662–17668
[73] James R (2009) Porous Silicon – Polycaprolactone Composites for Orthopaedic Tissue Engineering. Thesis submitted to the University of Nottingham for the Degree of Doctor of Philosophy.
[74] Shalak R, Fox CF (1988) Preface. In: Tissue Engineering. Shalak R, Fox CF, eds. Alan R.Liss, New York, 26-29.
[75] Patrick CW, Mikos AG, McIntire LV (1998) Prospects of tissue engineering. In: Frontiers in Tissue Engineering. Patrick CW, Mikos AG, McIntire LV, eds. Elsevier Science Ltd, Oxford. 3-11.
[76] Lam EXF, Mo XM, Teoh SH, Hutmacher DW (2002) Scaffold development using 3D printing with a starchbased polymer. *Mat Sci Eng*. C20: 49-56.
[77] Freed LE, Vunjak-Novakovic G (1998) Culture of organized cell communities. *Adv Drug Deliver Rev*. 33: 15-30.
[78] Salmern Sanchez M, Gallego Ferrer G, Monlen Pradas M, Gmez Ribelles JL (2003) Influence of the hydrophobic phase on the thermal transitions of water sorbed in a polymer hydrogel based on interpenetration of a hydrophilic and a hydrophobic polymer network. *Macromolecules*, 36: 860.
[79] Salmern Sanchez M, Brigido Diego R, Ianazzo S, Monlen Pradas M, Gmez Ribelles JL (2004) The structure of poly (ethyl acrylate-co-hydroxyethyl methacrylate) copolymer networks by segmental dynamics studies based on structural relaxation experiments. *Polymer*, 45: 2349.
[80] Rodriguez Hernandez JC, Monlen Pradas M, Gmez Ribelles JL (2008) Properties of poly (2-hydroxyethyl acrylate)-silica nanocomposites obtained by the sol–gel technique. *Non Cryst Solids*, 354: 1900.
[81] Ben-Nissan B, Ylanen HO (2006) Bioactive glasses and glass ceramics. In: Akay M, editor. Wiley encyclopedia of biomedical engineering, New Jersey: John Wiley & Sons, 354–66.
[82] Kokubo T (1992) Bioactivity of glasses and glass–ceramics. In: Ducheyne P, Kokubo T, Blitterswijk CA, editors. Bone-bonding biomaterials, Leidendorp: *Reed Healthcare Communications*, 31–46.
[83] Hench LL, Kokubo T. In: Black J, Hastings G, editors (1998) Handbook of biomaterials properties. London: Chapman & Hall, 355.
[84] Kokubo T, Takadama H (2006) How useful is SBF in predicting in vivo bone bioactivity? *Biomaterials*, 27: 2907.
[85] Ohtsuki C, Kokubo T, Yamamuro T (1992) Mechanism of apatite formation on CaO–SiO2–P2O5 glasses in a simulated body fluid. J Non-Cryst Solids,143: 84.
[86] Hench LL (1998) Bioceramics. *Am Ceram Soc*, 81: 1705.

[87] Zhang K, Yan H, Bell DC, Stein A, Francis LF (2003) Effects of materials parameters on mineralization and degradation of sol–gel bioactive glasses with 3D-ordered macroporous structures. *Biomed Mater Res*: A, 66: 860.

[88] Orefice R, Clark A, West J, Brennan A, Hench L (2007) Processing, properties, and in vitro bioactivity of polysulfone–bioactive glass composites. Biomed Mater Res, 80: 565.

[89] Hajji P, David L, Gerard JF, Pascault JP, Vigier G (1999) Synthesis, structure and morphology of polymer-silica hybrid nanocomposites based on hydroxyethyl methacrylate. *Polym Sci: Polym Phys*, 37: 3172.

[90] Kawai T, Ohtsuki C, Kamitakahara M, Hosoya K, Tanihara M, Miyazaki T, et al. (2007) In vitro apatite formation on polyamide containing groups modified with silanol groups. *Mater Sci: Mater Med*, 18: 1037.

[91] Mirsasaani S. Sh, Sarmast Shoushtari M (2010) Dental Nanocomposites: Dental Composites Book. Novapublisher, New York, U. S. A.

[92] Craig RG, Editor (1997) Restorative dental materials. 10th ed. St. Louis, MO: C.V. Mosby Company.

[93] Mirsasaani S.SH, Atai M, Hasani-Sadrabadi M.M. Photopolymerization of a dental nanocomposite as restorative material using the argon laser, *Lasers in Medical Science*, DOI 10.1007/s10103-009-0699-7.

[94] Sun G, Chae K (2000) Properties of 2, 3 butanedione and 1phenyl-1, 2-propanedione as new photosensitizer for visible light cured dental resin composites. *Polymer*, 41:6202–6212.

[95] Blankenau R, Kelsey WP, Kutsch VK (1995) Clinical applications of argon laser in restorative dentistry. In: Miserendino LJ, Pick RM (eds) Lasers in dentistry. Quintessence Publishing, Chicago, 217–230.

[96] Kelsey W, Blankenau R, Powell G, Barkmeier W (1989) Enhancement of physical properties of resin restorative materials by laser polymerization. *Lasers Surg Med*. 9:623–627.

[97] Fleming M, Mailet W (1999) Photopolymerization of composite resin using the argon laser. *Clin Pract*. 65:447–450.

[98] Pradhan. R.D, Melikechi N, Eichmiller F (2002) The effect of irradiaton wavelength bandwidth and spot size on the scraping depth and temperature rise in composite exposed to an argon laser or a conventional quartztungsten-halogen source. 18: 221–26.

[99] Schulz W (2000) Crafting a national nanotechnology effort. *Chem. Eng News*, 78(42):39–42.

[100] Zou H, Wu S, Shen J (2008) Polymer/Silica Nanocomposites: Preparation, Characterization, Properties, and Applications. *Chem. Rev*., 108: 3893–3957.

[101] Antonucci JM, Stansbury JW (1997) Molecular designed dental polymer. In: Arshady R, editor. Desk reference of functional polymers: synthesis and application. *American Chemical Society Publication*, 719–38.

[102] Roberson TM, Heyman H, Swift EJ (2002) Sturtevant's art and science of operative dentistry. 4th ed. St Louis: Mosby.

[103] Bowen R.L, Cleek G.W (1972): A New Series of X-ray opaque Reinforcing Fillers for Composite materials, *Dent. Res*, 51: 177-182.

In: Silica Nanoparticles
Editor: Juan Vivero-Escoto
ISBN 978-1-61324-452-4
© 2012 Nova Science Publishers, Inc.

Chapter 8

MONODISPERSE LUMINESCENT SILICA NANOPARTICLES: SYNTHESIS, CHARACTERIZATION AND APPLICATION TO THE DNA MICROARRAY TECHNOLOGY

F. Enrichi*
CIVEN, Coordinamento Interuniversitario Veneto per le Nanotecnologie, Venezia, Italy

ABSTRACT

The ability to modify the properties of materials by controlling their structure at nanoscale makes them extremely attractive for many applications: from fundamental scientific studies to commercially realizable technologies. In the biological context a variety of nanomaterials promise to offer sensitive, rapid and cost-effective solutions for modern clinical laboratory. In particular, dye-doped silica nanoparticles (NPs) have been demonstrated to be sensitive labeling markers for biosensing and bioimaging. Their flexible conjugation, excellent photostability, and ultrasensitivity make them a powerful tool in bioanalysis. Indeed luminescent dye-doped nanoparticles are excellent candidates for biological applications because (1) they can be analyzed with the standard existing tools (microarray scanners, optical fluorescence microscopes), which are fitted for standard fluorophore excitation and emission curves, (2) a large number of dye molecules can be incorporated in a single particle, increasing the optical signal and (3) the silica matrix provides a protective barrier minimizing photobleaching and photodegradation.

A very efficient synthesis strategy for silica nanoparticles is the Stöber method, which has the advantage that it can be easily scaled up for commercial production and the possibility to effortlessly transfer the nanoparticles into aqueous solutions (typically required for bioanalysis applications). However, modifications on the synthesis process are required to obtain luminescent particles and proper investigation on the particles size control and on the dye-doping process are needed. In this chapter we describe a modifyedStöber synthesis which is based on the use of 3-Aminopropyl-triethoxysilane (APTES) for the efficient incorporation of dye molecules into the silica NPs. The

*Corresponding Author: Francesco Enrichi: E-mail: enrichi@civen.org.

parameters of the modified synthesis have been systematically investigated in order to optimize their morpho-optical properties and to maximize their optical efficiency.

Moreover the application of these luminescent silica nanoparticles to DNA microarray technology is also reported for a specific case study: the detection of carcinogenic risky Human Papilloma Virus, which is one of the primary causes for cervical cancer in women worldwide. In particular, DNA microarray is a powerful tool for the parallel, high-throughput detection and quantification of many nucleic acids and other biologically significant molecules. We show that our luminescent silica nanoparticles in comparison to conventional dye labelling or commercial quantum dots allow achieving a significant tenfold increase in the optical signal, and a related decrease of the limit of detection, thus giving a remarkable improvement in this technique towards early diagnosis of the disease. It is worth noticing the fact that this result can be easily transferred to other pathologies and to other fields like for example trace level detection of dangerous biological contaminants in food or in the environment.

1. INTRODUCTION

Recent advances in research and technologies on materials and in particular the ability to effectively modify their properties by controlling the structure at nanoscale level has opened novel opportunities in many fields, making them extremely attractive candidates for different applications, from fundamental scientific studies to commercial products. In particular, in the biological context a variety of nanomaterials promises to offer sensitive, rapid and cost-effective solutions for modern clinical laboratory. New nanomaterials have been developed with luminescent proprieties for selective optical labeling of a wide range of medically important targets, including DNA sequences, proteins, cancer cells, and bacteria [1-4]. These luminescent nanoparticles (NPs) are acquiring more and more relevance and several significant applications of bioconjugated NPs have been exploited such as DNA microarrays, detection of single molecules, in vivo cellular imaging, extraction of cells and cellular components, and disease targeting [5-7]. The main problem of conventional microarray technology is that organic fluorophores suffer serious problems of photobleaching, low environmental stability and limited sensitivity. To overcome these issues, several types of nanomaterials, such as fluorescent polymeric or inorganic dye-doped NPs, semiconductor nanocrystals (quantum dots, QDs) and metallic NPs have been explored as signaling probes for bioanalysis. Through careful molecular engineering, these probes have been made small (5-100 nm), stable, readily biofunctionalized and easily detectable. Semiconductor nanocrystals have been functionalized to couple biomolecules [8-10]. It has been suggested that these markers are better labeling agent than commonly used organic dyes. However, these luminescent quantum dots have not been extensively used as optical probes because of their poor solubility in water (unless they are modified), agglutination, blinking properties, and moderate quantum yields. Fluorescent latex particles [11-14] (e.g., polystyrene particles) have also been used as labelling materials. However, their large size, tendency to agglomerate, swelling, and dye leaking have prevented their effective application as luminescent biomarkers for ultrasensitive biochemical analysis.

On the contrary, silica dye-doped NPs have all the most important characteristics of an excellent bio-label. Indeed they show high photostability, due to the fact that the silica matrix can protect the fluorescent dye from external environment and stabilize the molecule

preventing photon damaging. Moreover, intense luminescence signal can be obtained, due to the large number of dyes that can be incorporated in each single nanoparticle. Finally, silica is an ideal surface for conjugation with biological molecules because the hydroxyl group on the surface can react with various compounds to form amine, carboxyl, or thiol groups. Moreover, silica surface modification is not limited to chemically-mediated procedures: passive adsorption of molecules such as avidin is also commonly used. In general, the versatility of silica in the synthesis aspects as well as surface modifications offers a great advantage to the use of this material in bioanalysis.

Many successful applications with this kind of NPs have already been experimented [15-18]. The most successful tests have used small NPs (mainly < 100 nm) synthesized through the microemulsion method [19-21]. However, this synthesis route has two main disadvantages: complex synthesis procedures and physical fluorophore linkage which can cause their leach out from the particles. Therefore, the use of a Stöber synthesis route [22] with a modified procedure to incorporate the luminescent molecules can be preferred because it is much simpler, it can be easily scaled up for commercial applications and it has the possibility to effortlessly transfer the NPs into aqueous solutions (typically required by bioanalitical applications). In particular, to realize an efficient covalent bonding of the fluorophores with the silica matrix we used a proper crosslinker: APTES (aminopropyltriethoxysilane). However, modifications to the standard route need detailed investigation to optimize the dopant inclusion in the NPs, to better understand the impact of the different synthesis parameters on the morpho-optical properties of the nanoparticles and to obtain monodisperse NPs of 80 nm size or smaller. That's why we synthesized different series of samples varying the main reagents: ethanol, ammonia, water, silica precursors and dye concentration.

In this work we provide a wide investigation of the synthesis conditions for obtaining highly luminescent monodisperse spherical silica nanoparticles, reporting the possibility to synthesize bright samples from tens to hundreds of nanometers in diameter, which can find applications in bioimaging and biosensors.

Efficient application of the optimized nanoparticles is demonstrated for diagnostic purposes in DNA microarray technology. DNA microarray technology can be efficiently used for the simultaneous detection and identification of many biological contaminants and health risky agents [23-27]. It is a powerful tool for the parallel, high-throughput detection and quantification of many nucleic acids and other biologically significant molecules, therefore it finds application in genetic studies, diagnostic of diseases, detection of biological contaminants in waters and pathogens in foods. Among all these possibilities we focused our attention on a specific case study: the detection of carcinogenic risky Human Papilloma Virus, which is one of the primary causes for cervical cancer in women worldwide. In particular we show that our luminescent silica nanoparticles in comparison to conventional dye labelling or commercial quantum dots allow achieving a significant tenfold increase in the optical signal, and a related decrease of the limit of detection, thus giving a remarkable improvement in this technique towards early diagnosis of the disease.

2. Synthesis, Functionalization and Characterization of Dye Doped Silica Nanoparticles

2.1. Synthesis and Functionalization Procedure

Silica nanoparticles with organic fluorophores were synthesized following a modified Stöber procedure, as reported in figure 1. Different series of nanoparticles were prepared in order to investigate the impact of the various reagents on the final size, morphology, dye amount, luminescence efficiency of the particles. Table 1 briefly summarizes all the series that have been prepared. Firstly, we focused on the optimization of the dye loaded into the silica NPs and therefore on their luminescence intensity. Thus, variations on the fluorophore concentration in the initial solution were investigated through a dimensional and optical characterization of the samples.

Moreover, an optimal fluorophores concentration was defined for the subsequent series maximizing the luminescence intensity and minimizing the fluorophores wasting. Since fluorophores are not the only reagent which influences the luminescence proprieties of the NPs, a study on the variations of 3-Aminopropyl-triethoxysilane (APTES) quantities was then conducted. The importance of this reagent is not limited to the optical proprieties, but it also influences the morphology and the dimensions of the NPs. A study on the lowering ammonia concentration was also performed in order to investigate its effects on the dimension and morphology of the NPs. Indeed, it is well known that a reduction of the particle size is possible with reductions of ammonia. Finally, a last series of samples was synthesized to finally reduce the NPs dimensions under 100 nm by diluting the solution with more EtOH. Slight variations of ammonia and APTES were made considering the previous results to fine-tuning dimensions and luminescence.

According to the description given in previous papers [28, 29], a typical reaction to obtain nanoparticles of 250 nm in diameter is the following. In a 50 mL plastic vessel containing 20 mL of freshly distilled absolute ethanol, 50 µL of a 46 µM DMSO solution of Alexa Fluor 555 NHS ester was added along with 2.5 mL of deionized 18.3 MΩ water, 0.9 mL of TEOS (2.7 mmol) and 0.1 mL of APTES (0.42 mmol). At this step, before any reaction starts, the initial absorbance was measured by a Lambda 25 Perkin-Elmer spectrophotometer.

. After 15 minutes of stirring, 0.8 mL of 30% aqueous ammonia solution (12.6 mmol) was added and the mixture stirred at room temperature overnight (about 16 hours). The resultant suspension was cleaned using threefold centrifugation and sonication in ethanol (20 mL each). The supernatant absorbance was measured in order to evaluate the fluorophore amount incorporated into the silica nanoparticles, while the obtained light pink solid was dried at ambient temperature. Yield in SiO_2 was nearly quantitative (>99%).

Some exceptions have been made for the preparation of the last series of samples. Alexa Fluor 555 this time was dissolved in Ethanol instead of DMSO to avoid the risk of possible undesirable effects caused by this reagent. EtOH dissolved successfully the fluorophore, without any visible difference compared to effectiveness of DMSO. Moreover, in this series of NPs, after over 20 minutes of centrifugation, any visible precipitated settled on the bottom of the Falcon tube due to the lower dimension. Therefore, a different washing method was required and the Ultrafiltration (UF) process has been successfully employed for this scope

Table 1. Summary of the series of samples prepared

Series	Samples names	Varied Parameters	Notes
Dye loading optimization	F0; F7.5; F15; F30; F75; F150	Alexa 555 (from 0 to 150 µg in 24.35ml of initial solution)	Synthesis elaborated from previous results to obtain NPs ~300nm
	F0A0; F7.5A0; F15A0; F30A0; F75A0; F150A0	Alexa 555 (the same variations of the previous series)	Made without APTES
Influence of APTES concentration	A/(A+T)0%; A/(A+T)5%; A/(A+T)25%; A/(A+T)50%; A/(A+T)75%; A/(A+T)100%;	APTES and TEOS (APTES to APTES+TEOS ratio varied from 0 to 100%)	Silica reagents APTES + TEOS constant
	A/T0%; A/T5%; A/T25%; A/T50%; A/T75%; A/T100%;	APTES (APTES to TEOS ratio varied from 0 to 100%)	TEOS constant
Effects of Ammonia	A1.8 NH3 160; A1.8 NH3 80; A1.8 NH3 16; A1.8 NH3 8; A1.8 NH3 4	Ammonia Hydroxide (from 160 to 4 µl in 4.7ml of initial solution)	APTES fixed at 1.8 µl (A/T 1%)
	A18 NH3 160; A18 NH3 80; A18 NH3 16; A18 NH3 8; A18 NH3 4	Ammonia Hydroxide (the same variations of the previous series)	APTES fixed at 18 µl (A/T 10%)
Final Synthesis	D NH3 1; D NH3 .5; D NH3 .25; D NH3 .5 A11x	EtOH	With adjustments varying slightly also NH3 and APTES

using membranes with a nominal molecular weight limit (NMWL) of 100 kDa. Since filtration membranes are sensible to solutions with ethanol concentration higher than 70%, the solution to be filtered was dilute with an equal amount of water. 15 ml of this mixture was filtered with an Amicon Ultra-15 Centrifugal Filter Units in 10 minutes of centrifugation. Then all the mixture solution was filtered by adding each time up to 15 ml of it to the concentrated solution in the filter units. NPs were washed by the further addition of water to the concentrated filtered solution and filtered again. This step was repeated 3 times. At the end of this washing process, NPs result dispersed in water solution.

Surface functionalization with ammine groups for biological applications was obtained using a suitable amount of doped silica nanoparticles suspended in an ethanolic solution of

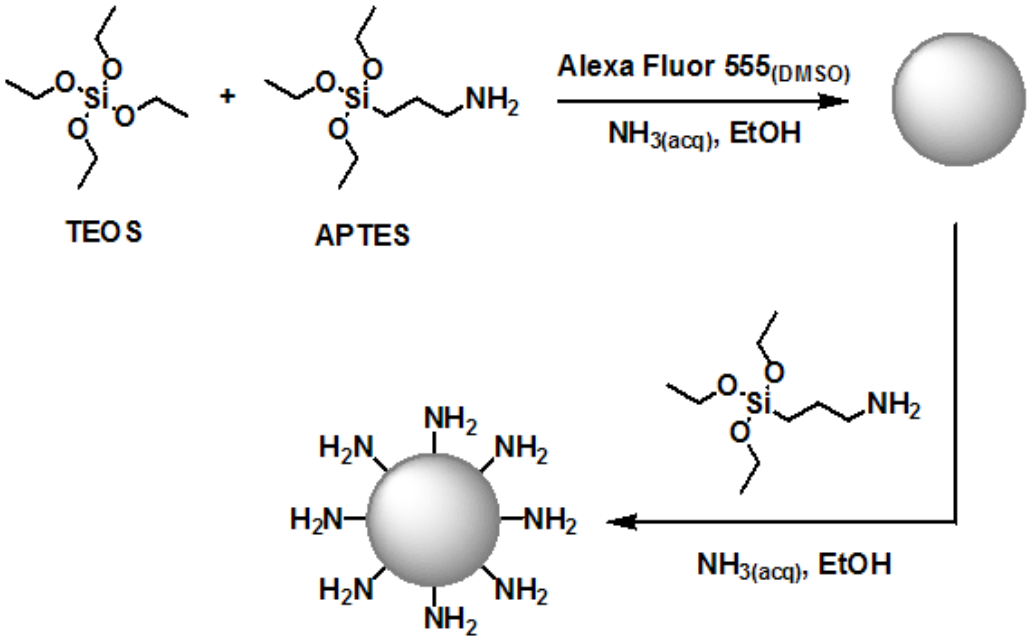


Figure 1. ModifyedStöber synthesis of dye doped silica nanoparticles in alkaline ethanol environment using DMSO solution of Alexa Fluor® 555 (NHS ester) and following surface amine functionalization with APTES.

APTES (10.6 µM, 20 mL) and stirred at room temperature overnight for about 16 hours. The resultant suspension was cleaned and the nanoparticles isolated as previously described. Presence of surface amines was tested using FITC (fluorescein isothiocyanate) and ninhydrine, giving positive results in all cases.

2.2. Optimization of Dye Loading

The first step to optimize the optical efficiency and to obtain bright luminescent nanoparticles is to investigate how much dye can be loaded inside the silica matrix without the occurrence of quenching phenomena. To this respect we need to investigate the luminescence intensity and lifetime over the amount of dye employed, which was varied from 0 to 150 µg in 24.35ml of initial solution.

However, as a general rule, the samples must also be characterized in their morphology and size to be sure that they respect a spherical shape and a monodisperse size in the hundreds of nanometers range. The morphology of the synthesized particles was investigated in terms of dimension, shape and aggregation state by means of Scanning Electron Microscopy (SEM) and Atomic Force Microscopy (AFM). SEM images were performed with a VEGA TS 5130 LM (Tescan) microscope under 30 kV acceleration conditions and AFM analysis was taken using a NTEGRA (NT MDT) microscope with a scanning image processor, SPIP version 4.2, Image Metrology A/S 1998-2005. Measurements were done in semicontact mode. An example of the obtained nanoparticles is reported in figure 2. It was investigated if a variation on dye concentration could influence the particles dimensions. SEM and AFM analysis conveyed to the same results, confirming that the NPs of this first series are all between 250 and 300 nm.

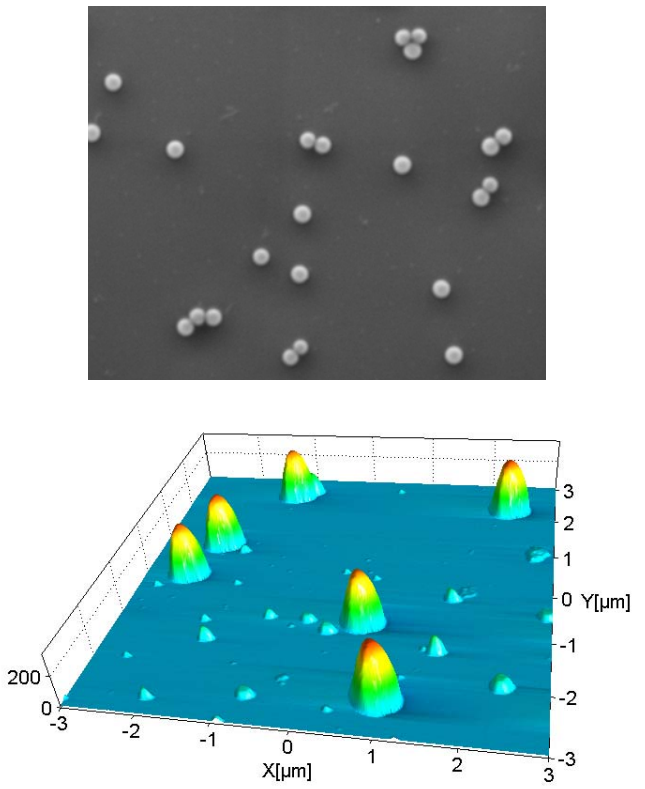


Figure 2. Typical example of SEM micrograph of dye doped silica nanoparticles (left) and the corresponding AFM measurement on the same sample (right).

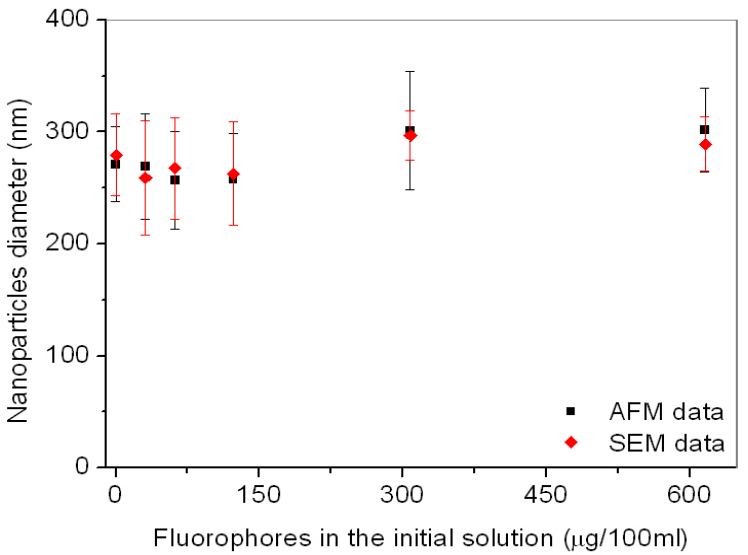


Figure 3.Nanoparticles diameter measurements as a function of the fluorophore concentration.

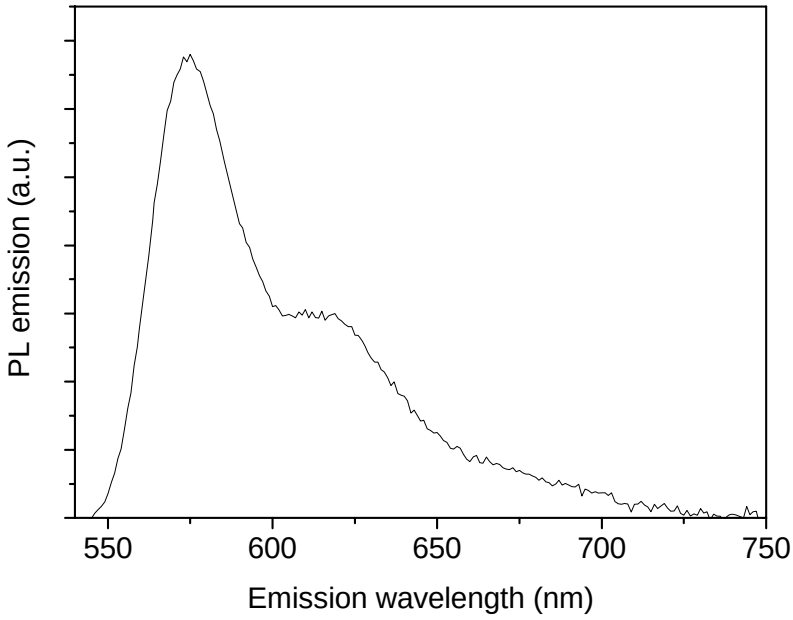


Figure 4.Typical PL emission spectrum of dye doped silica nanoparticles dispersed in ethanol.

Photoluminescence properties in the UV and visible regions (250-750 nm) have been measured with a FluoroLog-3 system (Horiba JobinYvon). This is a modular system equipped with a 450 W Xe lamp for photoluminescence excitation and emission measurements and with a 454 nm NanoLED (1MHz, 2ns pulsed) for time resolved characterization.

The emission spectra of the six NPs samples with variation on fluorophore concentration were measured both as solid powders and dispersed in ethanol. In the first case, dried NPs were finely pulverized, deposited on the sample holder and then covered with a quartz slide. In the second case a fixed amount of 10 μg of powder NPs was dispersed in 10 ml of ethanol and sonicated for five minutes before measurement, showing the typical spectrum reported in figure 4. It is worth noticing the fact that the emission spectrum resembles the one of the original fluorophores, which is a clear indication of the fact that the optical properties of the fluorescent molecule are preserved after inclusion in the silica matrix.

In order to analyze the variation of luminescence intensity with the fluorophore concentration in the initial solution and to get information on the fluorophore amount that can be incorporated into the silica nanoparticles, the integrated PL emission signal has been calculated and graphed as a function of the initial dye concentration. Moreover, PL intensity has been measured also for a series of samples obtained without the addition of APTES. The results for these two series are both reported in figure 5 showing a significant increase of the optical signal, about 10 times, in the samples obtained with APTES in comparison to the ones obtained without APTES. This is a clear demonstration of the role of crosslinker of this molecule to favour incorporation of the dyes into the silica network.

Focusing the attention on the series obtained with APTES we can see a significant increase of the luminescence signal at the beginning followed by a plateau and a final small reduction, reaching a saturation point. This investigation shows that for this synthesis conditions it is not possible to incorporate more fluorophores into the NPs by increasing the initial dye concentration over 100 μg/100ml.

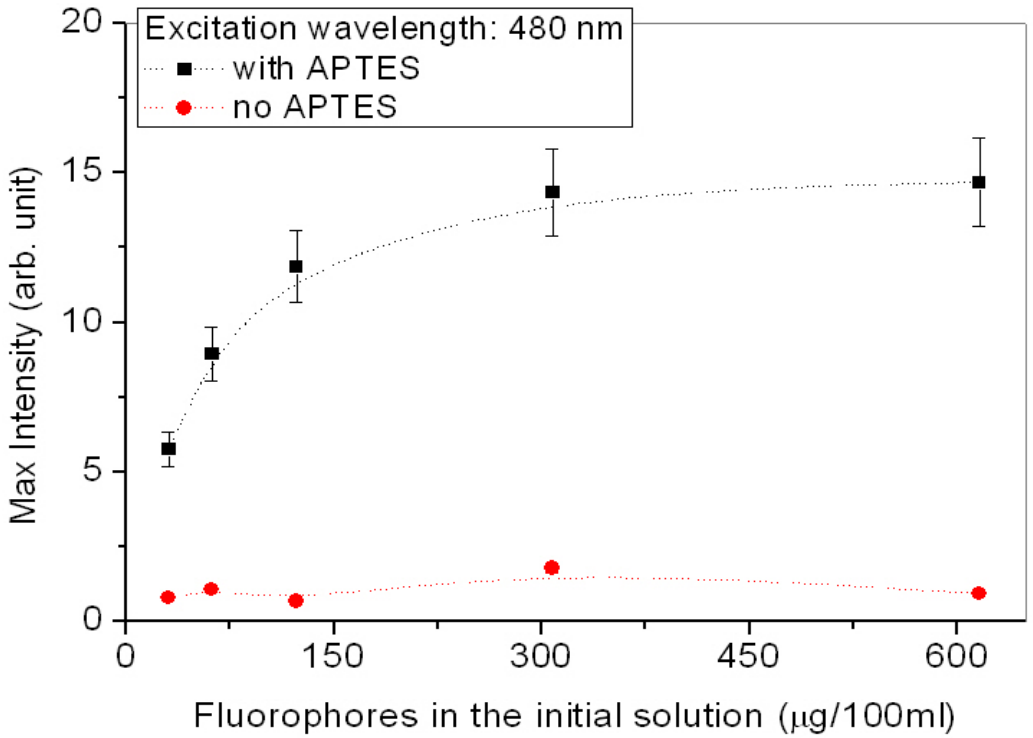


Figure 5. Integrated PL emission of NPs synthesized with increasing concentrations of Alexa Fluor 555 in the synthesis solution. The NPs are in EtOH solution, excitation wavelength 480 nm.

Absorbance analysis confirms these results. Samples were taken directly from the initial synthesis solution and then from the supernatant to evaluate the variations on Alexa concentration. The amount of fluorophores embodied into the nanoparticles was estimated by subtracting the fluorophores concentration in the supernatant from the initial solution. For small concentrations (up to 100 ug / 100 ml of synthesis solution), the amount of fluorophores included into the nanoparticles increases almost linearly. The last two samples (with higher initial Alexa concentrations) seem to incorporate the same quantity of dye of the previous sample (~25 dye μg / g silica NPs), reaching a saturation point. This value roughly corresponds to 5000 dye molecules for each 250 nm silica nanoparticle.

To better investigate this point and to get indication on the optical efficiency of the fluorescent molecules inside the silica network PL lifetimes measurements were also recorded. and compared to the free molecule condition. The samples for this characterization were prepared with the same procedure used for the photoluminescence measurements. In this case, Alexa Fluor 555 was also dispersed in ethanol solution and measured for comparison. Samples were excited by a 454nm NanoLED source (1MHz, 2ns pulsed). The photoluminescence decay curves are reported in figure 6, showing a clear increase of the Alexa lifetime with respect to the free dye. The resulting lifetime values, reported in figure 7, passes from 2 ns for free molecules to more than 3.5 ns for the same dye in silica NPs. This result is related to a better protection of the dye when it is incorporated into the silica network.

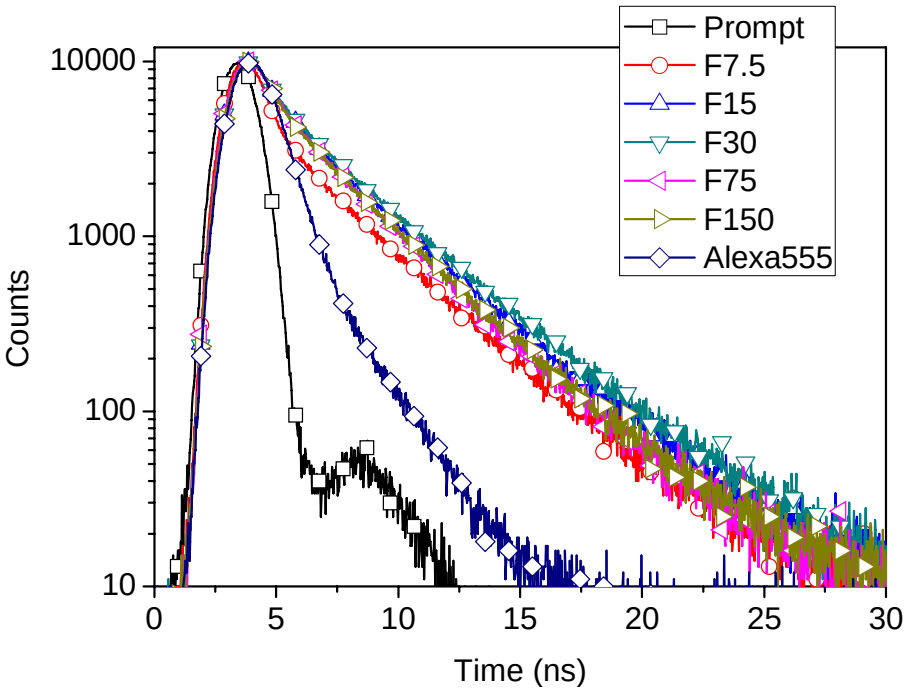


Figure 6. Time resolved photoluminescence emission under pulsed excitation for samples synthesized with increasing concentrations of Alexa Fluor 555 in the synthesis solution. The NPs are in EtOH solution, excitation wavelength 454 nm for 2 ns.

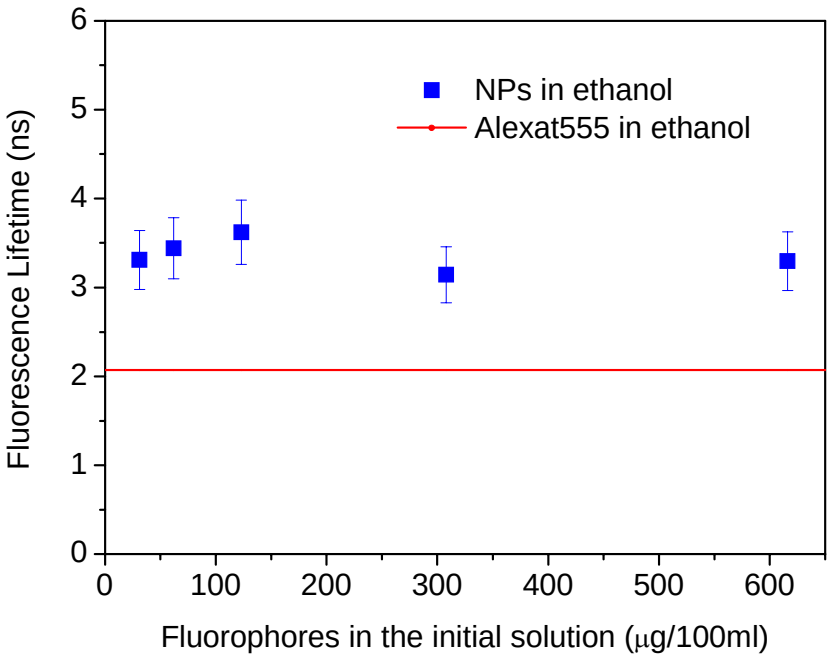


Figure 7. Photoluminescence lifetime values measured on samples synthesized with increasing concentrations of Alexa Fluor 555 in the synthesis solution. The NPs are in EtOH solution, excitation wavelength 454 nm for 2 ns.

2.3. Influence of APTES

APTES is a silica precursor together with TEOS and therefore it influences the total amount of Si that can react to produce the silica network and form nanoparticles. Therefore, the effects of APTES variations have been monitored keeping constant the total amount of silica reagents (TEOS+APTES) from 0 to 100%. Dimensional and morphological characterizations and the optical PL emissions of the obtained dye doped silica NPs have been investigated.

In figure 8 the SEM images of the samples are reported and show that for some increment of APTES with respect to APTES+TEOS (lower than ~25%) the NPs sizes slightly reduce and a minor agglomeration occurs. Higher concentrations of APTES produce agglomerated NPs and amorphous precipitates, which should be avoided if regular and well dispersed nanoparticles are desired.

On the other hand, as already observed in the previous paragraph, APTES is needed for efficient dye incorporation. Indeed, the optical investigation of these samples, reported in figure 9, shows that the photoluminescence intensity strongly increases up to 5% of APTES. However, for higher APTES concentrations the increment in the luminescence intensity grows more slowly.

These observations on the optical intensities together with the morphological limitations suggest that the best compromise in the APTES amount could be around 5 %.

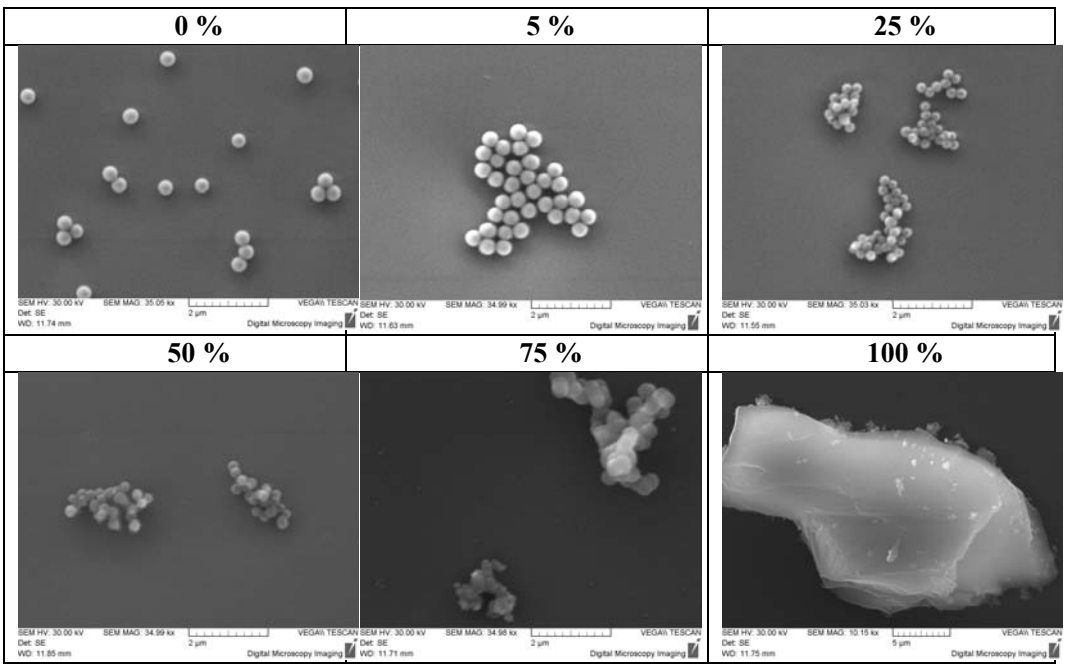


Figure 8. SEM images of silica nanoparticles obtained varying the ratio of APTES to the amount of total silica reagents (APTES+TEOS). Magnification is 35 kx for all the images except for A/(A+T) 100%, which is 10 kx.

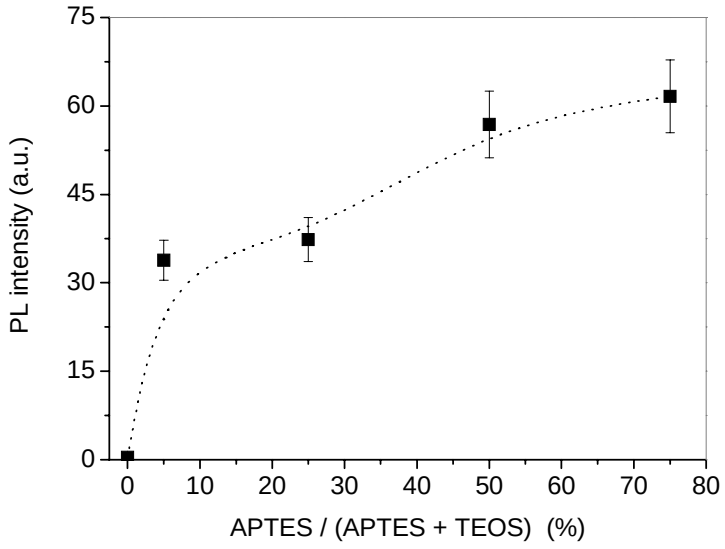


Figure 9. Integrated PL emissions of dye doped NPs in which the ratio of APTES to the total amount of silica reagents in the synthesis solution varies. Dried NPs have been used under 480 nm excitation wavelength.

2.4. Influence of NH3

According to the Stober paper [22], a reduction of the ammonia quantity should lead to a decrease of nanoparticles sizes. Therefore, with the aim of optimizing the synthesis parameters and preparing smaller NPs we decided to investigate the impact of this important reagent. In light of the previous results, two different concentrations of APTES were used: APTES/TEOS 1% and 10%. The results obtained for the two series were very similar, so we will present only the series of data related to the smaller APTES amount. SEM characterization, reported in figure 10, has shown that a slight dimensional reduction was actually possible lowering ammonia. However, for concentrations of NH3(30%)/EtOH lower than 1% the dimensional control was lost. Indeed, broad size distribution and a dual dimensional NPs size were observed.

Investigation of the optical properties of dual sized nanoparticles was performed in order to get a better understanding of the nanoparticle synthesis formation. To do this we used Scanning Near Field Optical Microscopy (SNOM), which can provide at the same time the morphological and optical analysis on single nanoparticles. This technique has an optical resolution beyond the light diffraction limit, since its main feature is the use of <100 nm aperture tip bringing resolution to the 100 nm regime even if 514 nm argon laser excitation is applied. The scheme of the instrument (Witec Alpha SNOM), used in transmission mode, is shown in figure 11.

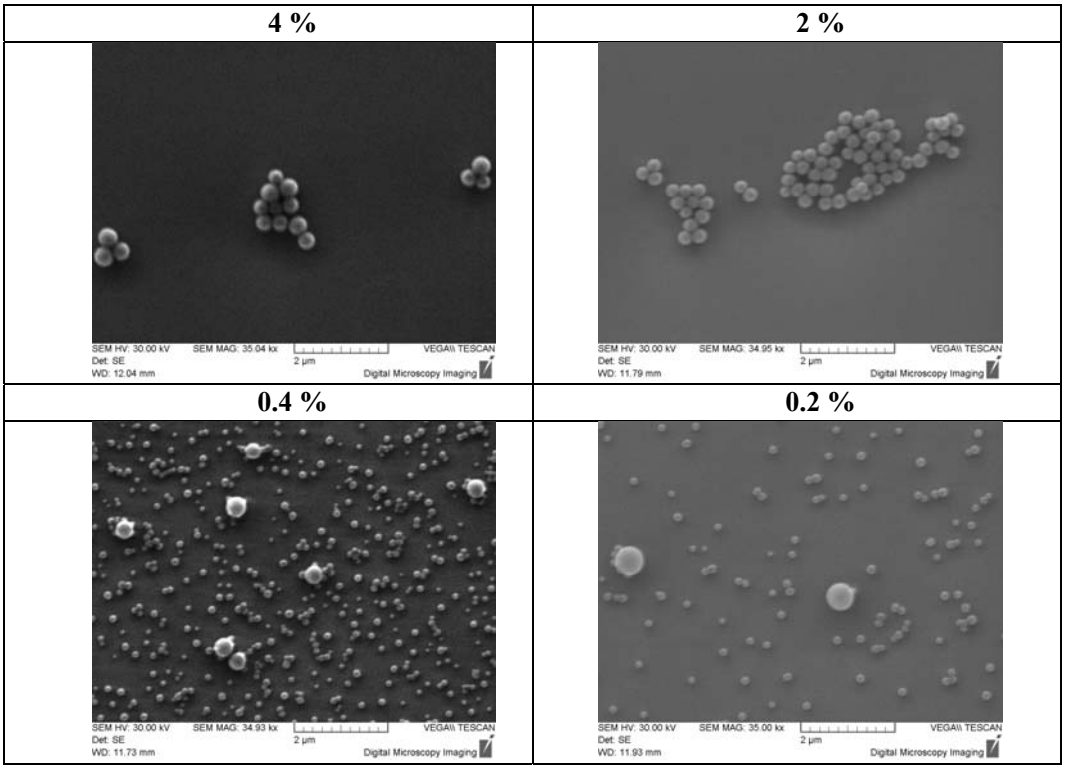


Figure 10. SEM images of silica nanoparticles obtained varying the ratio of ammonia to the amount of ethanol. Magnification is 35 kx for all the images.

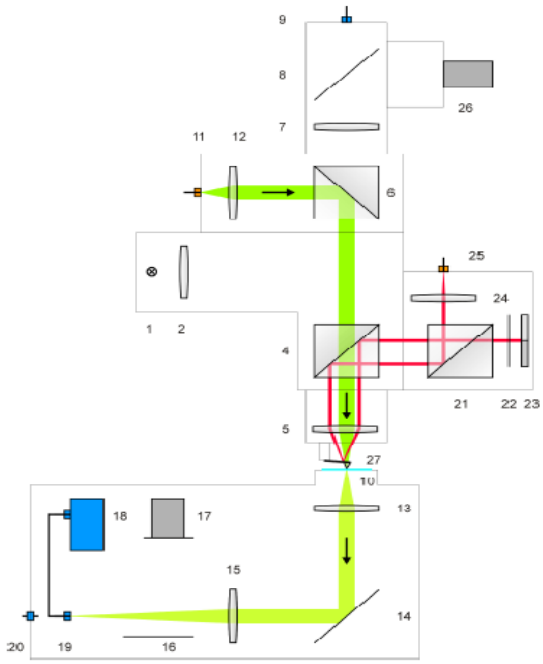


Figure 11.Optical scheme of the SNOM system.

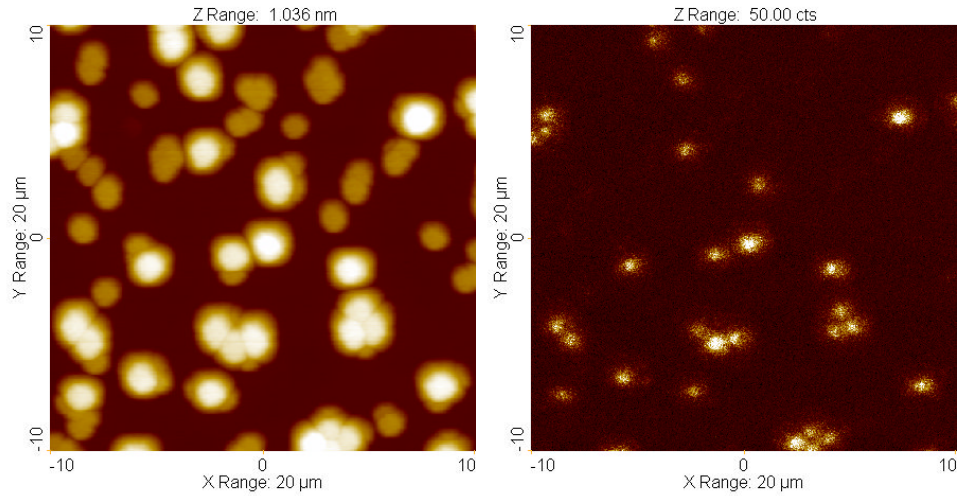


Figure 12.Topography map (left) and optical map (right) of dye doped silica nanoparticles.

Synchronous scan of topography and luminescence emission is reported in figure 12 for a sample containing almost equal number of two sizes of nanoparticles. In the left picture we can clearly detect the two sizes indicated as different color intensities. On the other hand, on the right picture the optical signal is only detected for the big nanoparticles, while the small ones are dark. This could be due to a much smaller signal intensity, but the volume difference of these nanoparticles would account only for a factor of 4 and also the smaller particles should be seen. Therefore we suggest a different explanation related to the role of the ammonia group in the APTES molecule. Indeed, when little amount of ammonia is added to the solution the nucleation and growth of silica is favoured by APTES molecules, which are connected to the luminescent dyes. Therefore dye molecules are better included into bigger nanoparticles related to APTES.

2.5. Diluted Synthesis

Previous analysis pointed out some complexities in the morpho-optical properties of dye-doped nanoparticles and the difficulty in reducing their size by changing APTES or ammonia reagents in the synthesis. Therefore a different approach was followed in order to prepare smaller silica NPs, in the tens nanometers range and it is based on using a much higher dilution of silica reagents in ethanol. In fact this is one of the possible ways to reduce the silica nanoparticles dimensions in the Stöber synthesis. For a general optimization, reductions of ammonia have again been experimented and two different APTES concentrations (0.6% and 6.5%) have been considered. These samples were found to be much smaller than previous ones and their size was evaluated using an Atomic Force Microscope. Resulting data are collected in Table 2.

Table 2. Size and PL emission of silica NPs obtained for different ammonium hydroxide and APTES amount in the synthesis solution, fixing the ratio of TEOS+APTES to EtOH at 2%. Particles diameter determined by AFM

Sample Name	Mean diameter (nm)	σ (nm)	Integrated PL (arb. units)
D NH3 1	64	15	27
D NH3 .5	28	11	68
D NH3 .25	13	6	47
D NH3 .5 A11x	48	10	43

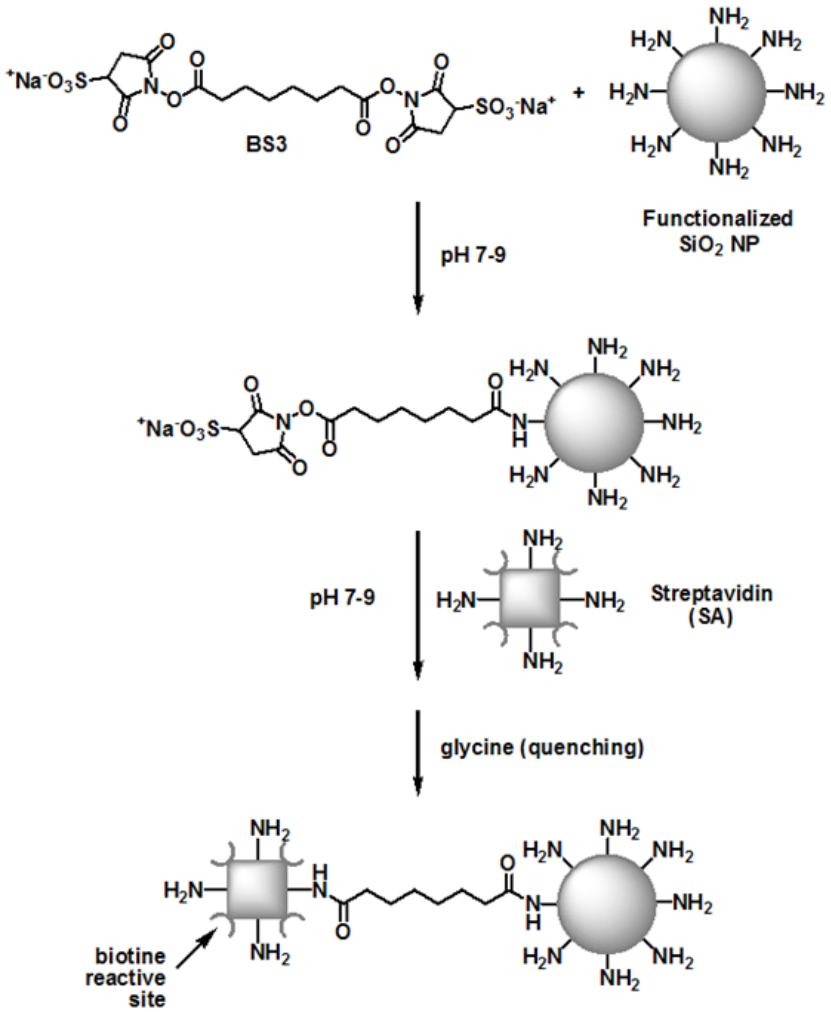


Figure 13.Coupling reactions for silica nanoparticles with streptavidin.

The nanoparticles sizes of these series are very interesting since they have reached diameters as small as 13 nm, the same scale as quantum dots, therefore suitable for biological applications. At the same time the luminescence properties were also investigated dispersing the particles in ethanol solution and showing a well detectable signal.

3. Application of Dye Doped Nanoparticles to DNA Microarray Technology

3.1. Bioconjugation of Nanoparticles with Streptavidin

Luminescent silica NPs were linked to streptavidin molecules for biological applications following the procedure reported in figure 13. In details, a suitable amount of amine modified NPs were mixed with one equivalent of BS3 in carbonate buffer (10mM, pH 8.5) using an orbital rotator for 30 minutes at room temperature, then washed by centrifugation with PBS 1X; subsequently, 0.2 mg streptavidin (3.8 pmol) were added in the same carbonate buffer and reacted for 2 hours at room temperature. At the end, the reaction was quenched with glycine for 15 minutes at room temperature and washed by centrifugation with PSB 1X. The SA-NPs conjugate was stored in PBS 1X at 4°C until use.

3.2. HPV Probe Oligonucleotide Design and Microarray Printing

A choice of viral HPV DNA sequence among "High risk genotypes HPV" was selected from sequences database and submitted to "Array Designer 4" (ScienceSoftware) software (figure 14). The parameters to obtain the probe were: 70 base pairs total length; 80±2°C melting temperature; 45-50% C/G ratio; -6 kcal/mol hairpin max ΔG; -8 kcal/mol self timer max ΔG; 6 base pairs run/repeat max length. The generated pool of probes was checked on BLAST (*Basic Local Alignment Search Tool*) to ensure the ability in univocally identifying the specific virus with 100% of homology and to discard any homology with other microorganisms longer than 20 nucleotides. The selected probe was purchased in lyophilized form from Eurofins MWG Operon with a 5' amine modification, to ensure the binding of the probes on the slide, and suspended in double distilled water (ddH_2O) to obtain a 100 μM stock solution, from which a 15 μM solution in printing buffer 1,5X (300mM sodium phosphate, 0,02% Triton X-100) was prepared and loaded into micro-plates and printed with a Spotter Arrayer instrument (BioRad) using LifeLine slides and Telechem SMP3 microspotting pins. The resulting slides, containing a 4x4 array of identical spots, were incubated overnight in a 75% humidity incubation chamber, blocked at 50°C in 0.1M Tris plus 50mM ethanolamine for 30 minutes, washed at 50°C in 4X SSC buffer (composition: 3M NaCl, 0.3 M Na citrate, pH 7.4) with 0.1% SDS for 30 minutes, and finally washed in ddH_2O, spin-dried and properly stored until use.

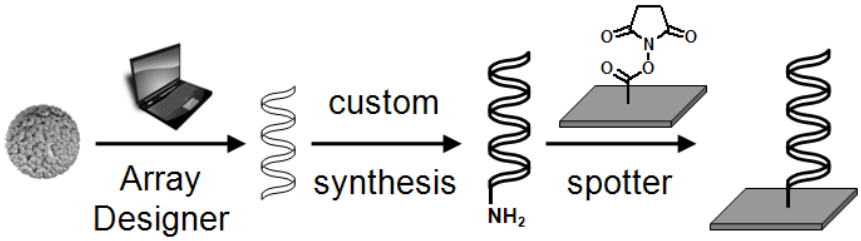


Figure 14.Probe HPV based DNA array selection and immobilization.

3.3. PCR Amplification of the Sample DNA Strands and Hybridization

Polymerase Chain Reaction (PCR) amplification was performed in the selected HPV DNA 400 base sequence to incorporate biotin dCTP for indirect labeling with QDs or SA-NPs, or Alexa Fluor® 555 dCTP for direct dye labeling (figure 15). The reaction was performed using the following set: 4 mM $MgCl_2$, 50 µM MY09 primer, 50 µM MY11 primer, 1U Taq Polymerase, 50 µM each of dATP, dTTP and dGTP, 15 µM dCTP, biotin-11-dCTP 35 µM (for indirect labeling) or ChromaTide® Alexa Fluor® 555-16-OBEA-dCTP 1 mM (for direct dye labeling) in Tris-EDTA buffer. The following PCR cycles were performed: 95°C 5 min; 35 cycles: 95°C 30 sec, 56°C 30 sec, 72°C 1 min; 72°C 7 min, store at 4°C. The amount, integrity and dimension of the amplicons were verified with capillary gel electrophoresis (Agilent 2100 Bioanalyzer). The efficiency of DNA biotinylation was estimated comparing the gel electro mobility of the DNA amplicons with and without biotin in dCTP bases.

The labeled DNA samples were mixed with 3.5X SSC hybridization buffer on the microarray glass slides in different dilution, from 3 to 2840 pM for all the three types, the direct Alexa Fluor® 555 dCTP and the two indirect 565 QDs and NPs (figure 16). After denaturation for 5 minutes at 95°C, cooling in ice and hybridization for 3 hours at 55°C, the slides were removed from the chamber and washed for 10 minutes in 2X SSC with 0.1% SDS at 50°C, 5 minutes in 0.2X SSC, 5 minutes in 0.1X SSC and 2 minutes in double distilled H_2O. Microarray slides were finally spin-dried and ready for laser scanner analysis if directly labeled (Alexa Fluor® 555 dCTP) or for SA-NPs conjugated or Quantum Dots detection if indirectly labeled (biotin dCTP).

For NPs and QDs, preliminary incubation step on the microarray slides were performed with 2 µg of nanoparticles or a 2 nM solution of quantum dots for 1 hour in SSC 1X with BSA 0.2X; subsequently, slides were washed with SSC 0.1X and finally spin-dried. Detection and data analysis were conducted on a GenePix 4000B laser scanner, using both 532 nm and 635 nm wavelengths. The labeled DNA samples were prepared in dilutions from 3 pM to 2.84 nM, after which each mixtures were denatured for 5 minutes at 95°C to obtain single strands, placed on ice and hybridized for 3 hours at 55°C under the same conditions in different wells of the same microarray slide, using one for each labeling technique.

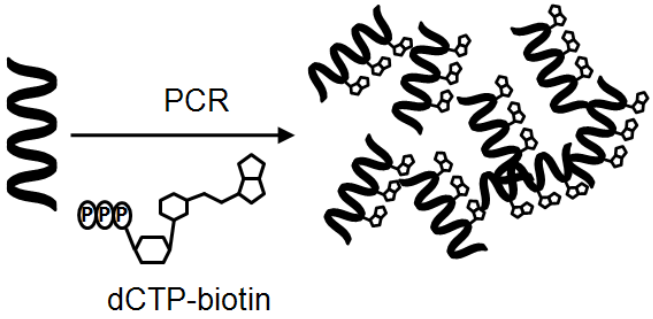


Figure 15.Target viral DNA sequence amplification and biotinylization during PCR.

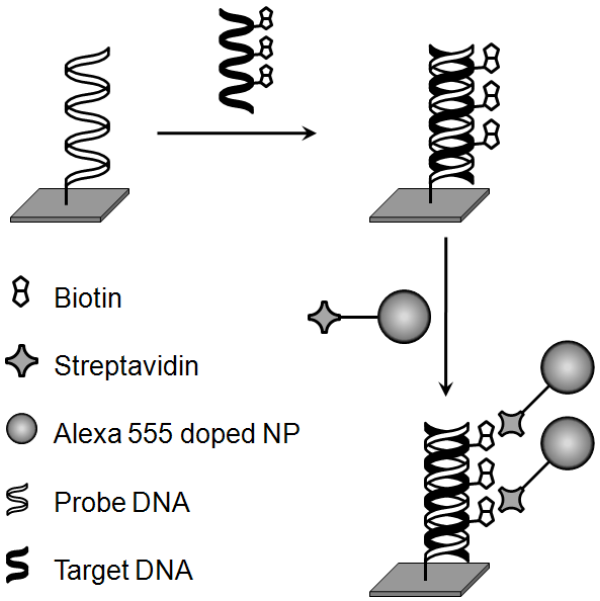


Figure 16.Synthetic scheme of DNA Microarray hybridization with silica nanoparticles.

3.4. Application to the DNA Microarray Technology for HPV Detection

The microarray scanning comparison between direct label *Alexa Fluor® 555 dCTP* (Dye, left), indirect label *Quantum Dots 565 ITK Streptavidin Conjugated* (QD, center) and indirect label *Alexa Fluor® 555 NPs Streptavidin Conjugated* (NP, right) is reported in figure 17, and the corresponding intensity curves are given in figure 18. The limit of detection for each type of biomarker is represented by a horizontal line, defined as the intensity value of twofold background. The microarray image and the corresponding graph clearly show much higher intensity of the NP signal over the other two. Indeed, for the Alexa Fluor® 555 direct labeling method the detection limit can be extrapolated from the graph in 150 pM, for the QDs the detection limit rises to 250 pM, for the Alexa Fluor® 555 NPs the detection limit is 20 pM. These results are summarized in table 3.

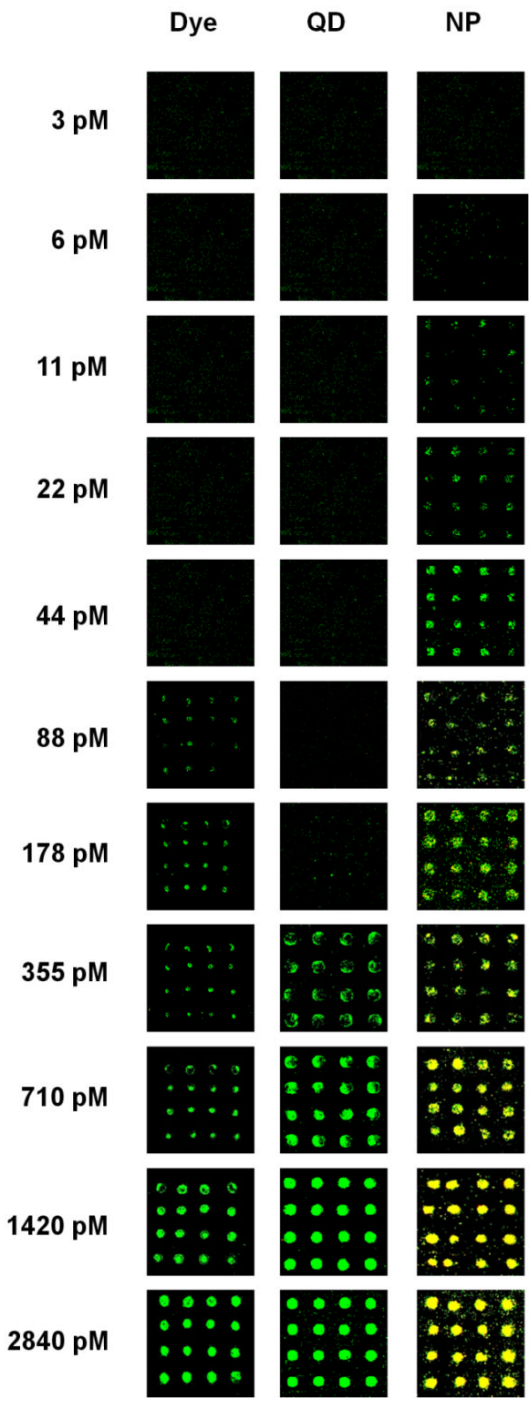


Figure 17. Comparison between DNA microarray experiments obtained using free dyes (left column), quantum dots (center column) or dye doped silica nanoparticles (right column).

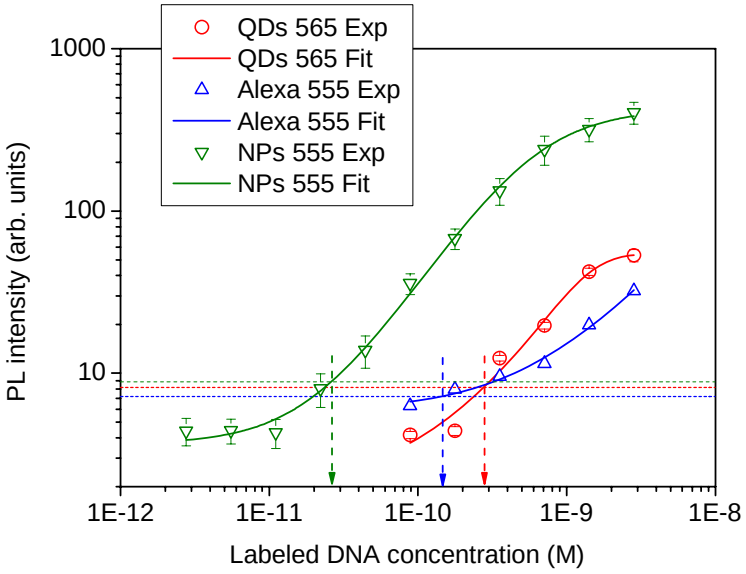


Figure 18. Comparison between detection curves of DNA microarray experiments obtained using free dyes (blue triangles), quantum dots (red squares) and dye doped silica nanoparticles (green circles). Limits of detection for each type are represented by respective horizontal lines.

Table 3. Detection limit (pM) of DNA microarray experiments using different biomarkers

Sample	Marker	Det. limit
Dye	Alexa®555 direct	150
QD	CdSe QDs 565	250
NP	Alexa®555@SiO_2	20

A first remark is the more efficient direct dye labeling than QDs one. This aspect is confirmed also by literature data [30] and is mainly due to the available wavelengths of the microarray slides scanner, 532 nm and 633 nm, while the QDs optimal excitation wavelength is in the UV. A second noteworthy remark is the high photoluminescence intensity given by Alexa Fluor® 555 NPs labeling, that stands about ten times over the direct dye and QDs labels. This allows reaching a much better sensitivity, about seven fold up from direct Alexa Fluor® 555 and twelve fold up from QDs, as extrapolated from the Table 3 data. From another point of view, this enhancement allows a higher signal for the same sample concentration. Indeed, if we compare the photoluminescence intensity of the three systems for a fixed DNA amount (for example 1 nM) we detect a much higher signal of NPs upon Dyes and QDs, the former being roughly between eight and sixteen times more intense than the latters. The reason for this significant improvement resides on the one hand in the high number of dye molecules confined in the very same silica nanoparticle (with respect to single molecule labelling) and on the other hand in the good fitting of the excitation and emission spectra of dyes with the standard features of the commercial scanner system available in most biological laboratories (which does not fit the best excitation of quantum dots).

CONCLUSION

Silica nanoparticles are versatile tools for numerous applications. In particular their low toxicity and easy surface functionalization make them particularly suitable to be used in biological applications. In this work we investigated the synthesis and application of dye doped silica NPs to the field of DNA microarray.

A simple method to prepare bright and photostable luminescent silica nanoparticles of different sizes has been developed, based on the use of a modified Stöber synthesis in the presence of aminopropyltriethoxysilane linked to Alexa Fluor 555 to form highly luminescent silica particles. Although the Stöber method is well-known, its use for the synthesis of silica particles in which fluorescent dyes are physically encapsulated has been systematically investigated and reported, to obtain a better understanding on the impact of the synthesis parameters on the final NPs properties. Through this synthesis method it is possible to avoid microemulsion formulations which are more complex and use undesirable surfactants. Moreover this synthesis allows producing many grams of nanoparticles in few hours, being suitable for industrial production.

We demonstrated that this method is suitable to produce dye doped luminescent silica nanoparticles with higher photostability and longer fluorescence lifetimes compared to the free dyes. Moreover their size can be tuned from hundreds of nanometers down to small sizes which are comparable to quantum dots. Therefore all these samples are extremely promising biological labels, in particular the 10 – 50 nm ones, for applications in biosensors and in biological imaging.

Indeed we tested these dye doped silica NPs as biological labels for the detection of risky HPV in DNA microarray diagnostic tools. We found that the incorporation of dyes into silica spheres instead of free dyes gives very good results in terms of signal intensity (about one order of magnitude signal enhancement). These luminescent nanoparticles were even more suitable than commercial quantum dots with standard scanning equipments, thanks to their better overlap of the excitation and emission spectra to the technical features of commercial instruments. An extensive comparison between different labeling and detection techniques showed an sensitivity enhancement of about seven times when we compared Alexa Fluor® 555 dye-doped NPs with Alexa Fluor® 555 dCTPlabeling. The use of fluorescent NPs as marker for DNA microarrays depicts a higher sensitive labeling technique if compared both to direct labeling with Alexa Fluor® fluorophores and QDs detection.

Results obtained in this work represent a significant improvement towards the enhancement of microarray sensitivity. Some technical problems could nevertheless interfere with the achievement of the optimum result concerning homogeneous NPs distribution in the spots, like non-specific interaction between the microarray glass surface and particles powder and eventual aggregation phenomena. This aspect, along with further optimization of the synthesis parameters, decreasing particles dimension to achieve a better dispersion in solution and maximization of dye molecules loading of the silica spheres are expected to bring much higher improvements in the optical signal and therefore in the detection limit of DNA microarray.

The cheap and easy synthesis of these luminescent silica NPs, the stability in water, the straightforward surface functionalization and bio-compatibility makes them very promising

for present and future bio-labeling and bio-imaging applications. Additional studies will be carried out to evaluate this last possibility.

ACKNOWLEDGMENTS

CIVEN research projects are fully granted by the Veneto Region Government and are developed within the Italian Cluster for Nanotechnologies (Veneto Nanotech).

All the activities and results presented in this chapter are an extension and a more detailed presentation of shorter or limited investigations developed in the last few years. Many people with different expertise contributed to the achievements of all these results. I acknowledgeall my colleagues in particularDr. RaffaeleRiccò, Dr.ssa Anna Meneghello, Dr.ssa Karina Fincati, Dr.ssa Erica Cretaio, Ing. Roberto Pierobon, Dr. Paolo Scopece, Dr. Piero Schiavuta, Dr. Francesco Marinello, Ing. Giulia Canton, Dr.Alvise Parma.Moreover I thank forsupport and cooperation Prof. Alvise Benedetti and Prof. PieroRiellofrom Venice Ca' Foscary University and Prof. Simone Carmignato from Padova University.

REFERENCES

[1] Cao Y C (2008) Nanomaterials for biomedical applications. *Nanomedicine* 3 (4), 467-469.

[2] Rosi N L and Mirkin C A (2005) Nanostructures in Biodiagnostics. *Chem. Rev.* 105 (4), 1547–1562.

[3] Wang F, Tan W B, Zhang Y, Fan X and Wang M (2005) Luminescent nanomaterials for biological labelling. *Nanotechnology* 17 R1.

[4] Fortina P, Kricka L J, Surrey S and Grodzinski P (2005) Nanobiotechnology: the promise and reality of new approaches to molecular recognition. *Trends Biotechnol*. Apr. 23(4):168-73.

[5] Enrichi F, Riccò R, Meneghello A, Pierobon R, Cretaio E, Marinello F, Schiavuta P, Parma A, Riello P, Benedetti A (2010) Investigation of luminescent dye-doped or rare-earth-doped monodisperse silica nanospheres for DNA microarray labelling. *Optical Materials* 32, 1652–1658.

[6] Yan J, Estévez M C, Smith E J, Wang K, He X, Wang L, and Tan W (2007) Dye-doped nanoparticles for bioanalysis. *Nano Today*2 (3), June 2007, 44-50.

[7] Tansil N C and Gao Z (2006) Nanoparticles in biomolecular detection. *Nano Today* 1(1) 28.

[8] Bruchez M Jr, Moronne M, Gin P, Weiss S, Alivisatos A P (1998). *Science*, *281*, 2013.

[9] Chan W C W, Nie S (1998). *Science*, *281*, 2016.

[10] Taylor J R, Fang M M, Nie S M (2000). *Anal. Chem. 72*, 1979.

[11] Harma H, Lehtinen P, Takalo H, Lovgren T (1999). *Anal. Chim. Acta*, *387*, 11.

[12] Giunchedi P, Conte U, Chetoni P, Saettone M F (1999). *Eur. J. Pharm. Sci. 9*, 1.

[13] Adler J, Jayan A, Melia C D (1999). *J. Pharm. Sci.88*, 371.

[14] Bourel D, Rolland, A, Leverge R, Genetet B (1988). *J. Immunol. Methods*, *106*, 161.

[15] Lian W, Litherland SA, Badrane H, Tan W, Wu D, Baker HV, Gulig PA, Lim DV, Jin S (2004) Ultrasensitive detection of biomolecules with fluorescent dye-doped nanoparticles. *Anal Biochem.* Nov 1;334(1):135-44.

[16] Wang L, Wang K, Santra S, Zhao X, Hilliard L R, Smith J E, Wu Y and Tan W (2006) Watching Silica Nanoparticles Glow in the Biological World. *Anal. Chem.* 78 (3), pp 646–654.

[17] Santra S, Wang K, Tapec R, Tan W (2001) Development of novel dye-doped silica nanoparticles for biomarker application. *J Biomed Opt.* Apr;6(2):160-6.

[18] Rossi L M,Shi L, Quina F H, and Rosenzweig Z (2005) Stöber Synthesis of Monodispersed Luminescent Silica Nanoparticles for Bioanalytical Assays. *Langmuir 21,* 4277-4280.

[19] Santra S. et al., Anal. Chem.2001, 73,4988-4993.

[20] Bagwe RP, Yang C, Hilliard LR, Tan W, Langmuir 2004 Sep 14;20(19):8336-42.

[21] Finnie KS, Bartlett JR, Barbé CJA, Kong L, Langmuir, 2007, 23 (6), pp 3017–3024.

[22] Stöber W, Fink A, Bohn E (1968). Controlled Growth of Monodisperse Silica Spheres in the Micron Size Range. *J. Colloid Interface Sci*. 26, 62.

[23] Bilitewski, 2009.

[24] Sobek, J.; Bartscherer, K.; Jacob, A.; Hoheisel, J. D.; Angenendt, P., 2006, Comb. Chem. High Throughput Screen. g, 9(5), 365.

[25] Jayapal M, Melendez A J (2006). *Clin. Exp. Pharmacol. Physiol.* 33, 496.

[26] Joos T, Bachmann J. (2009) Protein microarrays: potentials and limitations. *Front Biosci.* Jan 1, 14, 4376-85.

[27] Wingren C, Borrebaeck C A (2009). *Methods Mol. Biol.* 509, 57.

[28] Enrichi F, Riccò R, Meneghello A, Pierobon R, Marinello F, Schiavuta P (2009) Luminescent dye-doped or rare-earth-doped monodisperse silica nanospheres as efficient labels in DNA microarrays. *Proc. SPIE* 7393, 73930M, DOI:10.1117/12.828217

[29] Enrichi F, Riccò R, Scopece P, Parma A, Mazaheri AR, Riello P, Benedetti A (2009) Comparison of Eu(NO3)3 and Eu(acac)3 precursors for doping luminescent silica nanoparticles. *J Nanopart Res* DOI 10.1007/s11051-009-9756-1.

[30] Son A, Nichkova M, Dosev D, Kennedy I M, Hristova K R (2008). *J. Nanosci. Nanotechnol.* 8(5), 2463-2467.

In: Silica Nanoparticles
Editor: Juan Vivero-Escoto
ISBN 978-1-61324-452-4
© 2012 Nova Science Publishers, Inc.

Chapter 9

DEGREE OF DISPERSION AND COAGULATION OF SILICA NANOPARTICLES DETERMINED BY USING AN ELECTRIC FIELD

Akira Otsuki
University of South Australia, Australia

INTRODUCTION

It is important to manipulate the degree of dispersion and coagulation of fine particles in various media for many industrial processes [1,2]. Therefore, understanding those characteristics of fine particles in the specific media is of great importance. Many techniques have been developed for evaluating them by measuring size [3], turbidity [4], contact angle [5], zeta potential [6], force between particles [7,8] and combination of these techniques [9,10]. However, these techniques usually are not suitable for evaluating those characteristics of particles in highly concentrated suspensions and non transparent suspensions. On the other hand, these kinds of suspensions are commonly used in the many industrial procedures, such as selective separation [11,12] and flocculation of fine particles [13].

In the field of fine particle engineering and biotechnology, many researchers have studied pearl chain formations of dielectric particles and living cells under an electric field. Pearl chain is a linear formation of particles toward an external field. *Electro rheological fluids* (ERFs) are one of the major applications of the pearl chain formation. ERFs show an increase of suspension yield stress with an increase in the applied electric field strength between two electrodes [14]. The *interactive force apparatus* (IFA) is another application of the pearl chain formation to determine the degree of dispersion and coagulation of fine particles. This apparatus will be introduced in the following sections.

This chapter focuses on particle size measurement for evaluating the degree of dispersion and coagulation of nanoparticles. The techniques can be divided in two categories, i.e. measurements in (i) dry condition and (ii) wet condition [2]. In dry condition, microscopic studies based on scanning electron microscope and transmission electron microscope are the common techniques for size measurement of submicron to nanoparticles. In wet conditions,

techniques using laser sources (e.g. the dynamic light scattering and laser diffraction) are the common techniques. Each of the techniques has advantages, and some drawbacks. By definition the techniques for measurement in dry conditions are not applicable for measuring the size of particles in solvents. The techniques for measurements in wet condition are not usually suitable for measuring the size of particles in high particle concentrations and/or solution with no optical transparency.

The interactive force apparatus (IFA) was designed for determining the degree of dispersion and coagulation of fine particles suspended in functional fluid under a magnetic or electric field [19-22]. The apparatus is a direct measurement technique, not depending on both particle concentration and optical transparency of a sample suspension. Moreover, measurements can be conducted in various solvents (e.g. aqueous solution and organic solvent). The current experimental setup allows detection of primary particles and/or aggregates of particles in a sample suspension. In this chapter, the methodology will be introduced followed by describing results of measurements of silica nanoparticles and an attempt to verify the mechanism of the apparatus.

METHODOLOGY

The IFA consists of three parts:

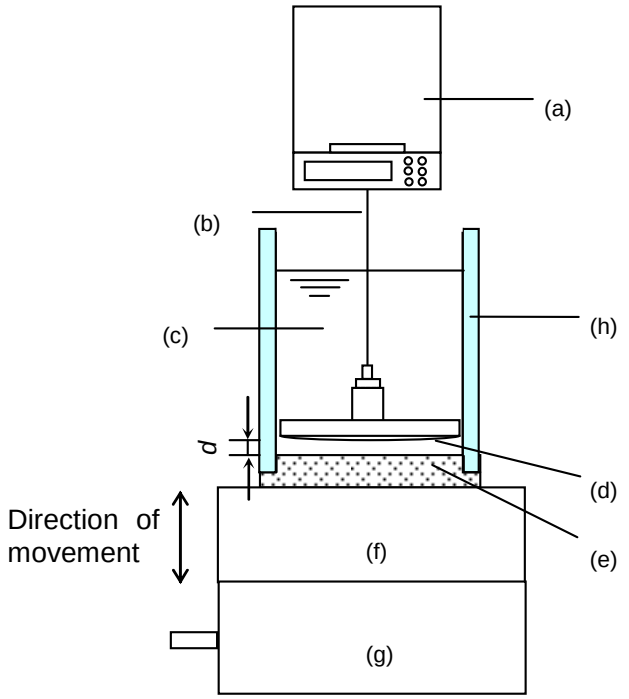
1. A *measurement cell* which consists of an electric balance, hemisphere and flat plate. The IFA measures the interactive force between two surfaces, i.e. a gold-coated glass hemisphere and brass flat plate, (which is fixed at the bottom of the sample cell). In the main part measures the weight of the hemisphere immersed in a sample suspension with decreasing the distance between the two surfaces at a certain speed.
2. In the *control unit* a personal computer, piezo-stage controller and voltage supplier are employed to adjust a supply voltage, regulate the movement of piezo-stage and collect data from the balance and the piezo-stage controller.
3. The contact analysis unit (i.e. a multi-meter and oscilloscope) measures the contact point where the hemisphere and flat plate attach.

Figure 1 shows the measurement cell of the apparatus. The hemisphere is hung from the electric balance into the sample suspension. The weight of the hemisphere is measured by using the electric balance, and recorded by the personal computer. The flat plate moves toward the hemisphere, and the distance d (e.g. from 100 nm) decreases until the hemisphere makes point contact with the flat plate. Applying voltage to the piezo-stage and its subsequent movement is used to regulate the distance between the hemisphere and flat plate. The rate of movement is determined based on an initial separation distance between the hemisphere and flat plate when a measurement starts (e.g. 1 nm/s for 100 nm distance). The piezo stage is located on a z stage. Detecting the contact point of the hemisphere to the flat plate at the bottom of the cell (i.e. $d = 0$) is the important reference point for subsequent distance measurements.

The measured weight is converted to the interactive force by using the Derjaguin equation [25]:

$$\frac{F_{(D)_{sphere}}}{R} = 2\pi W_{(D)_{plane}} \tag{1}$$

where $W_{(D)_{plane}}$ is the interactive free energy, $F_{(D)_{sphere}}$ is the interactive force between the hemisphere and the flat plate, and R is the curvature radius of the glass hemisphere, respectively. The interactive force was plotted as a function of the distance between the hemisphere and flat plate (i.e. force-distance curve). This data is the basis to determine the size of fine particles. Figure 2 shows a typical force curve obtained during a measurement, indicating that both repulsive and attractive forces appear.



(a) Electric balance
(b) Platinum wire
(c) Sample solution
(d) Hemisphere (Gold-coated)
(e) Flat plate (Brass)
(f) Piezo-stage
(g) Z stage
(h) Glass cell

Figure 1. Schematic diagram of main part of experimental setup for interactive force apparatus [23,24].

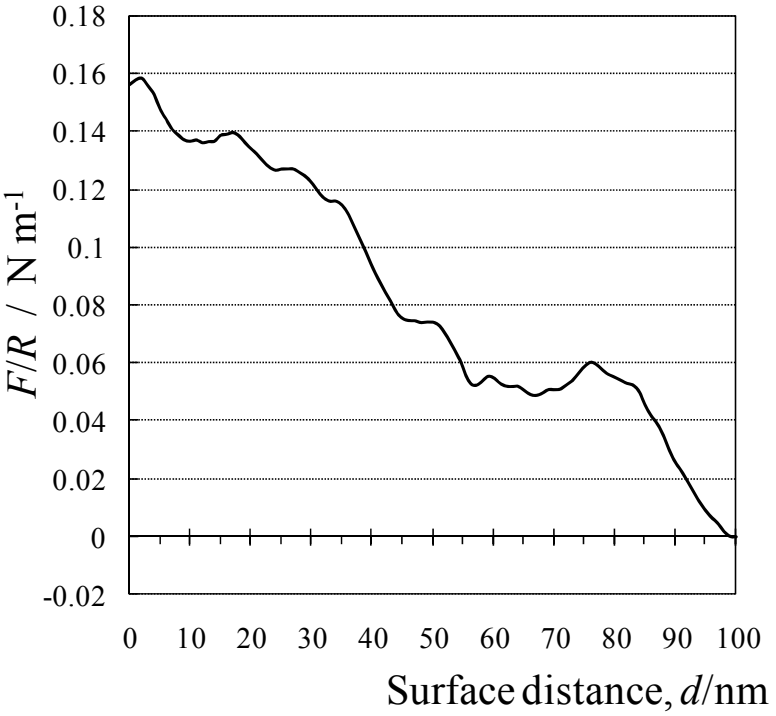


Figure 2. Typical force curve obtained during a measurement (sample: aqueous solution of silica nanoparticles; supply voltage: 0.01 V) [24].

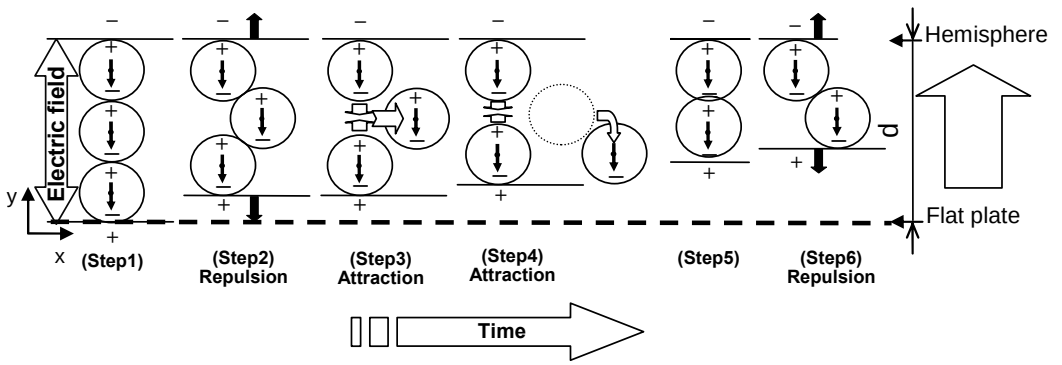


Figure 3. Behavior of dielectric particles during a measurement under an electric field [23,24].

Under an electric field generated between two parallel plates, pearl chains of dielectric particles form towards the direction of electric field [26]. In terms of shape of the chains, linear chains form over triangular chain under the electric field due to the former being more stable in terms of potential energy [27]. During the measurement, an electric field is applied between the hemisphere and flat plate, and dielectric particles are arranged toward the direction of electric field in the area between plate and hemisphere. When the two plates are close to each other, two different forces (i.e. repulsive and attractive forces) are alternately

measured due to changes in the arrangements of the particles (Fig. 3) [23,24]. The repulsive force occurs when the particle chain structure is stretched by compressive force; whereas the attractive force occurs when the particle chain structure is broken. The cycle of repulsive and attractive forces is determined by the primary size of particle or size of aggregate, which depends on the degree of agglomeration.

RESULTS AND DISCUSSION

Effect of Supply Voltages

Otsuki *et al* [23] applied the interactive force apparatus to measure the particle size distribution of silica nanoparticles while increasing the applied voltage in order to evaluate the suitability of IFA for the measurement of size distributions. In addition, an improved data handling process was also proposed. In order to determine the cycle of repulsive and attractive forces precisely, the 1st derivative of the force is plotted. The distance between points at zero value of 1st derivative, where the value turns negative to positive, corresponds to the size of particles or aggregates, which is the same as the cycle of repulsive and attractive forces as shown in Fig. 2 [24]. Figure 4 shows a typical derivative curve as a function of surface distance analyzed from data shown in Fig. 2 when an aqueous solution of silica nanoparticles was measured by IFA under 0.01 V supply voltage. From the Fig. 4, the size of silica nanoparticles was determined in the range from 4 to 23 nm. The wide range of particle size is explained by aggregate formation of particles due to high concentration of solids in sample suspension. Five continuous measurements were conducted and then a particle size distribution was calculated based on the measurements.

The results were compared to those obtained from TEM photographs and dynamic light scattering spectroscopy (ELS-8000, Otsuka Electronics Co., Ltd.) to evaluate the effectiveness and accuracy of the apparatus. An aqueous solution containing silica particles provided by Nissan Chemical (Snowtex XS) was used as a sample for the measurement due to simplicity of controlling dispersion and coagulation state. Averaged particle size was about 5 nm determined by analyzing a series of photographs taken by TEM. The pH of the solution was 9, and concentration of silica nanoparticles in the solution was 30 wt%.

Figure 5 shows that D_{50} measured by IFA was closer to the average particle size determined by TEM. Comparing the results under three different supply voltages, (1) the results at 0.01 and 0.02 V were almost identical while (2) these results were different from the one at 0.04 V. This indicates the results were dependent on supply voltages and the particle size distributions decreased with increasing the supply voltages. The results indicate that breakage of coagulated particles possibly occurs due to electrical breakdown. The distribution measured by IFA (D_{50} = 5 – 7 nm) was larger than the one measured by DLS (D_{50} = 1 nm). The electrical breakdown was explained by curve fitting of three different particle size distribution functions (i.e. Normal distribution, Rosin-Rammler distribution and Gaudin-Schuhmann distribution) with particle size distribution obtained from IFA measurement.

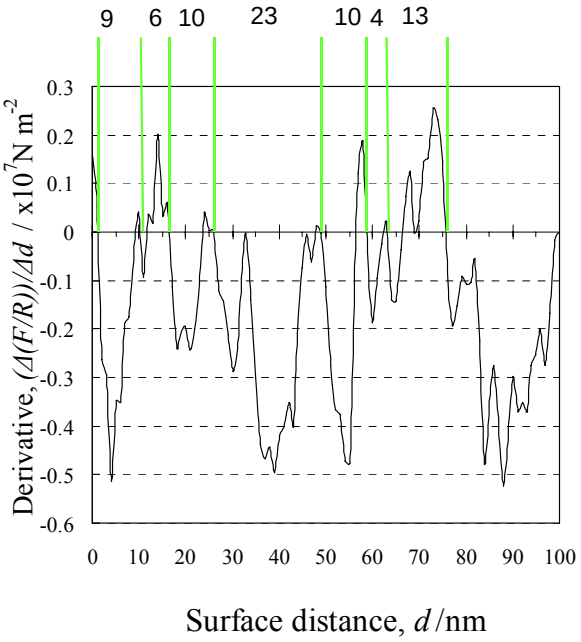


Figure 4. Derivative curve of $F_{(D)sphere}\,R^{-1}$ when an aqueous solution of silica nanoparticles was measured by IFA under 0.01 V supply voltage as a function of surface distance [23,24].

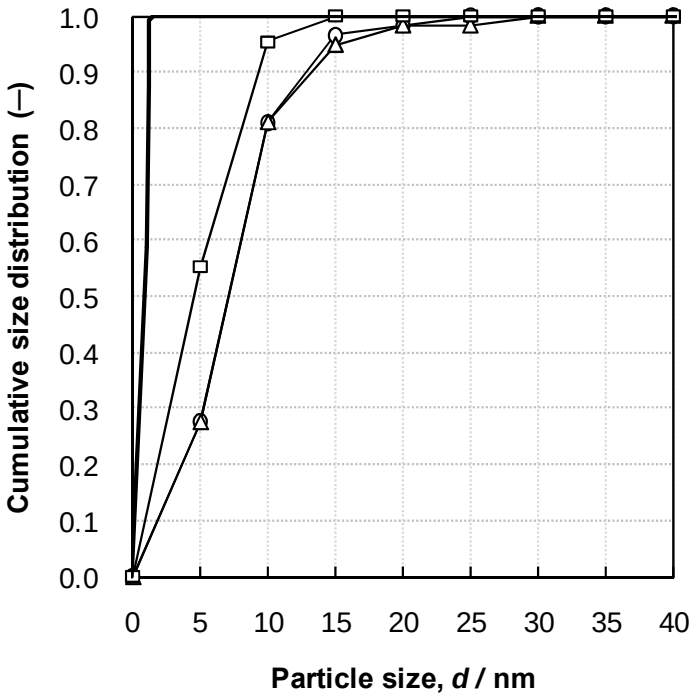


Figure 5. Particle size distribution of silica nanoparticles measured by interactive force apparatus under different supply voltages (a) 0.01 V, (b) 0.02 V and (c) 0.04 V and measured by DLS [23,24].

Mechanism Verification: Configuration of Pearl Chains under an Electric Field

This section describes the configuration of pearl chains under an electric field. The objective was to verify the mechanism of the measurement and determine the appropriate particle size distribution. For the application of IFA to particle size measurement, there is an important assumption to support the mechanism of measurement explained in the Methodology section. It is that the dielectric particles form pearl chains with a linear configuration, which is different from a non-linear configuration (e.g. triangular configuration), under an electric field. In this section, the potential energies of a cluster under an electric field were calculated in order to determine the particle size distribution giving the linear configuration of particle chains. The results verified the mechanism of the measurement by interactive force apparatus in terms of generating linear chain formation under an electric field.

Potential energies of a cluster composed of dielectric fine particles were calculated in order to determine the dominant configuration of particles under an electric field. Otsuki et al. [27] modified a formulation describing the potential energies of the linear and triangular formations composed of magnetic particles under a magnetic field in order to investigate the formation of these structures composed of dielectric particles under the electric field. A case where three particles in contact with each other at their surfaces was considered. The dielectric moments of the three particles is assumed to be aligned with the electric field direction. One of the three particles is denoted by *i* and the others are denoted by *j*. Two particles *j* have the same diameter d_j. The influence of the diameter d_i of particle *i* on potential energies of the linear ($u_{lin}^{(p)}$) and triangular ($u_{tri}^{(p)}$) configurations was evaluated by using Eqs. 2 and 3 derived from the Eqs. developed by Aoshima and Satoh (2005) with the assumption that there are no steric repulsions by layers around the surface of particles [28]:

$$\frac{u_{lin}^{(p)}}{kT\lambda_0} = -2\left(\frac{d_i d_j}{d_0^2}\right)^3 \left(\frac{d_0^3}{\left(\frac{d_i + d_j}{2}\right)^3} + \frac{d_0^3}{\left(\frac{d_i + d_j}{2} + d_j\right)^3} \right) - 2\left(\frac{d_j^2}{d_0^2}\right)^3 \frac{d_0^3}{d_j^3} \tag{2}$$

$$\frac{u_{tri}^{(p)}}{kT\lambda_0} = 2\left(\frac{d_i d_j}{d_0^2}\right)^3 \frac{d_0^3}{\left(\frac{d_i + d_j}{2}\right)^3} \left(1 - 3\frac{4\left(\frac{d_i + d_j}{2}\right)^2 - d_j^2}{4\left(\frac{d_i + d_j}{2}\right)^2} \right) + \left(\frac{d_j^2}{d_0^2}\right)^3 \frac{d_0^3}{d_j^3} \tag{3}$$

where *k* is the Boltzmann's constant, *T* is the absolute temperature, λ_0 is the dimensionless parameters for the particles with the mean diameter d_0.

Potential energies of linear and triangular formation as a function of particle diameter are shown in Fig. 6. The intersections of potential energies of linear and triangular formations were summarized in Table 1. It should be noted that there is no intersection where the ratio of d_j / d_0 are 1.60 and 3.20. At these d_j / d_0, linear configuration has always priority over the triangular configuration. In most of the conditions, the potential energy of linear configuration is less than the one of triangular configuration (Fig. 6). It indicates the probability of forming

linear configuration of particles is generally higher than the one of triangular configuration. In order to use the results of calculation of potential energies of linear and triangular formations for determining the probabilities of their formation, the particle size distribution was calculated by using determined parameters (i.e. d_0 and σ) and normalized by mean diameter d_0 (Fig. 8).

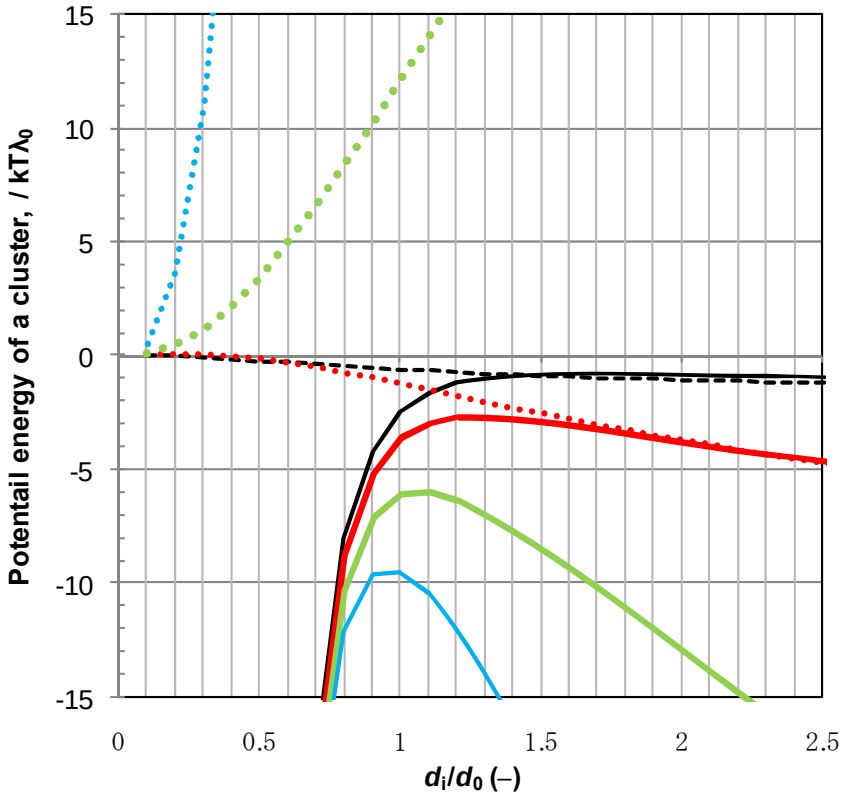


Figure 6. Potential energies of linear and triangular formations as a function of particle diameter d_i / d_0 at different ratio of d_j / d_0 [27].

Table 1. Probabilities of formation of linear configuration of dielectric fine particles under the electric field [27]

d_j/d_0	d_i/d_0 at intersection of $u_{lin.}$ and $u_{tri.}$	Probabilities of formation of linear configuration of particles (%)
0.20	2.10	99.9
0.40	1.50	95.5
0.80	2.50	100
1.60	-	100
3.20	-	100

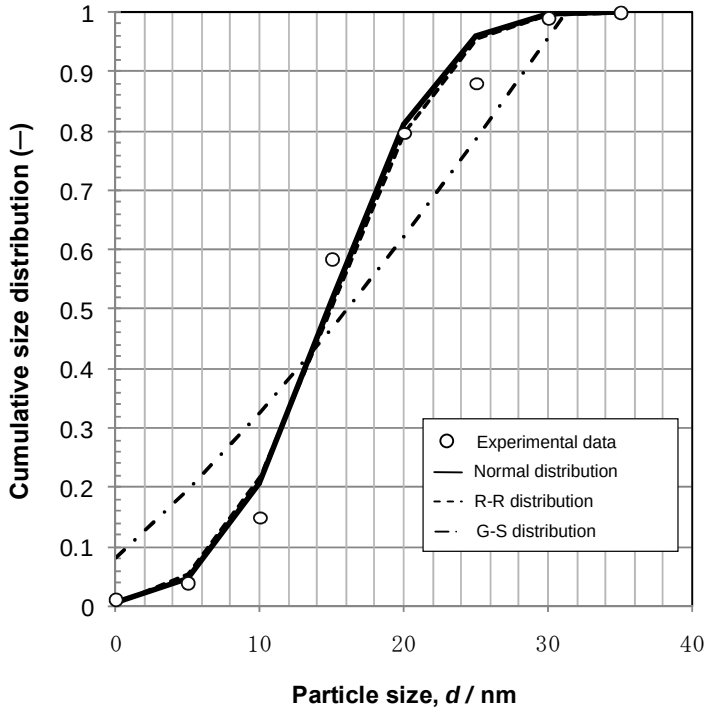


Figure 7. Size distribution of silica nanoparticles measured by DLS fitted with three different particle size distribution functions [27].

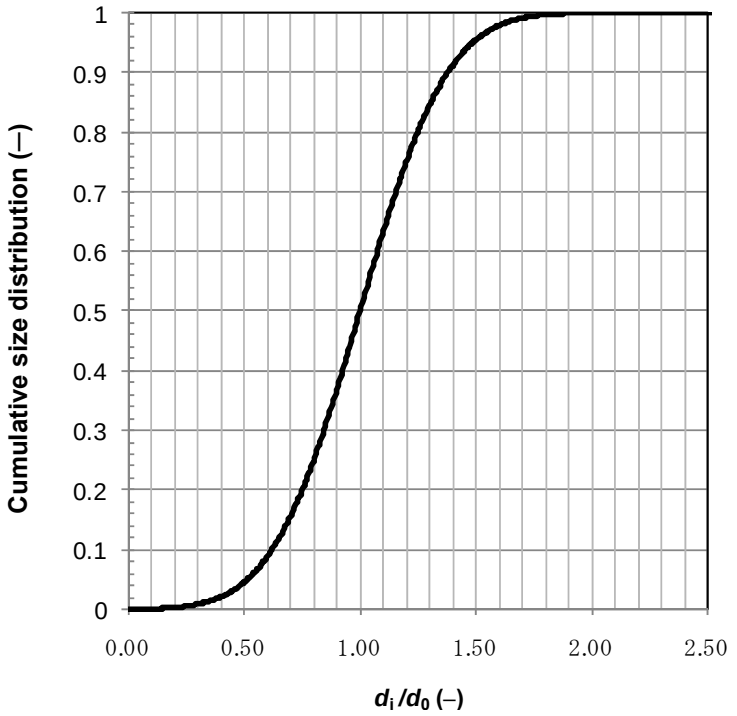


Figure 8. Calculated particle size distribution of silica nanoparticles based on Normal distribution where $d_0 = 1.0$, $\sigma = 5.87$ [27].

In order to determine the probabilities of formation of linear and triangular configuration of particles, type of particle size distribution was determined from three different common distribution functions. They were Normal distribution, Rosin-Rammler distribution and Gaudin-Schuhmann distribution as described in Eqs. (4)-(6), respectively.

$$Q(d) = \frac{1}{\sqrt{2\pi}\sigma} \int_0^d \exp\left(-\frac{(d-d_0)^2}{2\sigma^2}\right) \mathrm{d}d \tag{4}$$

$$Q(d) = 1 - \exp\left\{-\left(\frac{d}{d_e}\right)^n\right\} \tag{5}$$

$$Q(d) = \left(\frac{d}{d_{\max}}\right)^m \tag{6}$$

where d is diameter of particle, d_0 is mean diameter of particle, σ^2 is variance of distribution, d_e is absolute size constant, n is distribution constant, d_{max} is size of the largest particle in the system and m is particle size parameter.

In this study, results of particle size measurement of silica nanoparticles by means of DLS (Fig. 7) were used to fit the particle size distribution functions. The three types of particle size distribution functions were fitted with the experimental data (Fig. 8). Normal distribution, which gave the best fit with the experimental data, was selected at $d_0 = 19.8$ and $\sigma = 5.87$. Assuming that the particle size distribution was normal distribution as calculated in Fig. 8, the probabilities of forming linear configuration over triangular configuration under an electric field were summarized in Table 1. It can be seen that liner configuration is dominant at all conditions over triangular configuration at the calculated conditions. This implies that the assumption of formation of linear particle configuration during the measurement is valid and particle size measurement by interactive force apparatus can be conducted properly where size distribution of feed particles can be described as normal distribution. On the other hand, the triangular configuration may form up to 4.5 % at ratio of particle size $d_j / d_0 = 0.40$. It may cause the slight deviation of the results of particle size distribution by using IFA.

CONCLUSION

In this chapter, a methodology for determining dispersion and coagulation of nanoparticles by using an electric field was introduced. The results of measurement with silica nanoparticles as a function of supply voltage were discussed. The mechanism of the measurement was verified by calculating the potential energies of a pearl chain formation under an electric field.

REFERENCES

[1] M. Elimelech, J. Gregory, X, Jia, R.A. Williams, *Particle deposition and aggregation*, Butterworth-Heinemann, Woburn, 1998, pp. 4-8.

[2] T. Allen*, Particle Size Measurement, in Volume 1*, Powder sampling and particle size measurement Fifth edition, Chapman and Hall, London, 1997, pp.44-111.

[3] A.N. Nguyen, P. George, G.J. Jameson, Determination of a minimum in the recovery of nanoparticles by flotation: Theory and experiment, *Chem. Eng. Sci.* 61 (2006) 2494-2509.

[4] S. Ata, P.D. Yates, Stability and flotation behavior of silica in the presence of a non-polar oil and cationic surfactant, *Colloid. Surf. A* 277 (2006) 1-7.

[5] E. Kusaka, H. Tamai, Y. Nakahiro, T. Wakamatsu, Role of surface free energy in a solid surface during collectorless liquid-liquid extraction, *Minerals Engineering*, 6 (1993) 455-464.

[6] T.K. Mitchell, A.N. Nguyen, G.M. Evans, Heterocoagulation of chalcopyrite and pyrite minerals in flotation separation, *Adv. Colloid Interface Sci*. 114-115 (2005) 227-237.

[7] H.J. Butt, B. Cappella, M. Kappl, Force measurements with the atomic force microscope: Technique, interpretation and applications, *Surface Science Reports* 59 (2005) 1-152.

[8] J. Drelich, J. Long, Z. Xu, J. Masliyah, C.L. White, Probing colloidal forces between a Si_3N_4 AFM tip and single nanoparticles of silica and alumina, *J. Colloid Interface Sci*. 303 (2006) 627-638.

[9] R.H. Yoon, D.H. Flinn, Y.I. Rabinovich, Hydrophobic interactions between dissimilar surfaces, *J. Colloid Interface Sci*. 185 (1997) 363-370.

[10] P.D. Yates, G.V. Franks, S. Biggs, G.J. Jameson, Heteroaggregation with nanoparticles: effect of particle size ratio on optimum particle dose*, Colloid. Surf. A* 255 (2005) 85-90.

[11] J. Laskowski, J. Iskra, Role of capillary effects in bubble-particle collision in flotation, *Trans. Inst. Min. Metall*. 79 (1970) C6-C10.

[12] R. Stratton-Crawly, *Beneficiation of Mineral Fines - Problems and Research Needs, AIM*E, New York, N.Y., 1979, pp. 317-330.

[13] [L. Panda, S.K. Biswal, V. Tathavadkar, Beneficiation of Synthetic Iron Ore Kaolinite Mixture Using Selective Flocculation, *Journal of Minerals & Materials Characterization & Engineering* 9 (2010) 973-983.

[14] D.L. Klass, T.W. Martinek, Electroviscous Fluids. I. Rheological Properties, *J. Appl. Phys.* 38 (1967) 67-74.

[15] A.P. Gast, C.F. Zukoski, Electrorheological fluids as colloidal suspensions, *Adv. Colloid Int. Sci*. 30 (1989) 153-202.

[16] Y. Nakajima, T. Saito, Calculation of electrostatic force between two charged dielectric spheres by the re-expansion method, *Journal of Electrostatics* 45 (1999) 213-226.

[17] Y. Nakajima, T. Matsuyama, Electrostatic field and force calculation for a chain of identical dielectric spheres aligned parallel to uniformly applied electric field, *Journal of Electrostatics* 55 (2002) 203-221.

[18] A. Limsimarat, B. Techaumna, Dynamic simulation using a multipolar model of particles under dielectrophoretic force, *Journal of Electrostatics* 65 (2007) 672-679.

[19] T. Miyazaki, A. Shibayama, T. Sato T. Fujita, Measurement of interaction force between small distances sandwiched with magnetic fluid under magnetic field, *Journal of Magnetism and Magnetic Materials* 252 (2002) 256-258.

[20] A. Shibayama, T. Otomo, K. Shimada, T. Fujita, Measurement of interactive surface force of suspended particles in ER and MR suspensions under electric and magnetic field, *International Journal of Modern Physics B*, 19 (7-9) (2005) 1177-1183.

[21] T. Fujita, T. Miyazaki, T. Tanaka, L.K. Jun, E. Kuzuno, H. Muto, A. Bekkala, Measurements of interaction forces at small distance under electric field in a smectite dispersed silicone oil based ER fluid, *Int. J. Modern Phy. B* 15 (2001) 811-816.

[22] T. Miyazaki, A. Shibayama, T. Fujita, Measurement of surface force of fine particles at a short distance in a magnetic fluid under an electric and magnetic field, *Journal of the Magnetics Society of Japan* 26 (2002) 153-156 (in Japanese).

[23] A. Otsuki, G. Dodbiba, T. Fujita, Measurement of particle size distribution of silica nanoparticles by interactive force apparatus under an electric field*, Adv. Powder Tech.* 21 (2010) 419-423.

[24] A. Otsuki, G. Dodbiba, T. Fujita. Chapter 40. Particle Size Measurements of Dielectric Particles using Pearl Chain Formations of the Particles under an DC Electric Field, in Electrical Phenomena at Interfaces and Biointerfaces: *Fundamentals and Applications in Nano-, Bio-, and Environmental Sciences, Ed*. Hiroyuki Ohshima, John Wiley & Sons, Inc., 2011.

[25] B.V. Derjaguin, *Untersuchungen über die Reibung und Adhäsion, IV, Kolloid Zeits*., 69 (1934) 155-164.

[26] T.C. Jordan, M.T. Shaw, Electrorheology*, IEEE Transactions on Electrical Insulation* 24 (1989) 849-878.

[27] A. Otsuki, G. Dodbiba, T. Fujita, Effect of particle size distribution on formation of linear configuration of dielectric fine particles under the electric field, *J. Phys. Conf. Series* 147 (2009) 012003.

[28] M. Aoshima, A. Sato, Two-demensional Monte Carlo simulations of a colloidal dispersion composed of polydisperse ferromagnetic particles in an applied magnetic field, *J. Colloid Interface Sci*. 288 (2005) 475-488.

In: Silica Nanoparticles
Editor: Juan Vivero-Escoto
ISBN 978-1-61324-452-4
© 2012 Nova Science Publishers, Inc.

Chapter 10

TEMPERATURE-RESPONSIVE DNA-CAPPED MESOPOROUS SILICA NANOPARTICLES BASED DELIVERY SYSTEM

Juan L. Vivero-Escoto[1,2,*] and Victor S.-Y. Lin[1,+]
[1]Department of Chemistry, U.S. Department of Energy Ames Laboratory,
Iowa State University, Ames, IA, US
[2]Current address: Department of Chemistry,
University of North Carolina at Chapel Hill, NC, US

DEDICATION

In memory of my mentor and esteemed colleague, Victor S.-Y. Lin.

ABSTRACT

Recent developments in designing mesoporous silica nanoparticles (MSNs) based delivery systems using "caps and gatekeepers" able to selectively release entrapped guest molecules by specific triggers have attracted a great deal of attention. For example; inorganic nanoparticles, large molecules, biomolecules, and polymers have been used to block the pore openings and prevent guest molecules from leaving the system. The release mechanisms in these platforms include changes in pH, redox potential, UV irradiation or temperature for uncapping the pores. Herein, we report on the synthesis of an organically functionalized MSN material functionalized with an oligonucleotide intercalating phenanthridinium functionality (PAP-MSN). The working principle of this MSN delivery system is based on the strong binding affinity of thephenanthridinium group toward double-stranded oligonucleotides (ds-oligo) to block the pore openings. The release of the guest molecules is achieved once the melting temperature of the ds-

[*]Corresponding Author: E-mail: jlvivero@email.unc.edu.
[+] Deceased on May 4th, 2010.

oligo has been reached breaking the non-covalent interaction between the complementary oligonucleotide strands and the phenanthridium moeity. To prove this hypothesis, PAP-MSNs were loaded with guest molecules, $[Ru(bipy)_3]^{2+}$ complex. The temperature-dependent release profile showed the successful performance of the ds-oligo (36 mers; melting temperature = 67 ºC) as stimuli-responsive cap. In addition, the control sample under similar conditions did not show a considerable release of guest molecule after several hours. In summary, we have shown how the incorporation of ds-oligo into a novel cap system can impart temperature-responsive release behavior. The possibility of expanding the scope of this system based on different supports and tailor-made oligonucleotides makes this approach of interest for a wide variety of biomedical and biotechnological applications.

INTRODUCTION

Recent advancements on the synthesis of mesoporous silica nanoparticles (MSNs) have attracted much attention for their unique structural features, such as high surface area (>800 m^2/g), tunable pore diameter (2–10 nm), and narrow particle size distribution.[1-3] In addition, current breakthroughs in designing MSNs based delivery systems using "caps and gatekeepers" able to selectively release entrapped guest molecules by specific triggers have expanded their scope toward biotechnological and biomedical applications.[4-8] To date, several MSN-based controlled-release platforms have been synthesized by using different kind of capping agents such as inorganic nanoparticles, molecules, macromolecules, and polymers. The release mechanisms rely on changes in pH,[9-14] redox potential,[15-18] enzymatic activity,[19-22] UV irradiation or temperature for uncapping the pores.[9, 23-26] In fact, latest reports have been centered on systems using biomolecules as components for the design of new "bio-gates".[27-29] DNA in particular has shown its ability as cap for the development of temperature-, competitive binding-, and enzyme-responsive MSN-based delivery platforms.[30-32].

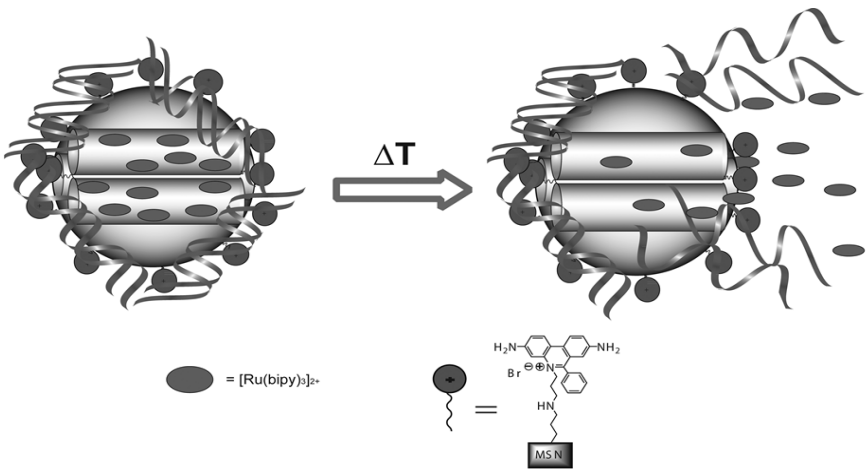


Figure 1. Schematic representation of the temperature-responsive ds-oligo capped $[Ru(bipy)_3]^{2+}$-loaded PAP-MSN platform. The ds-oligo caps are opened after reaching their melting temperature resulting in the release of the guest molecule.

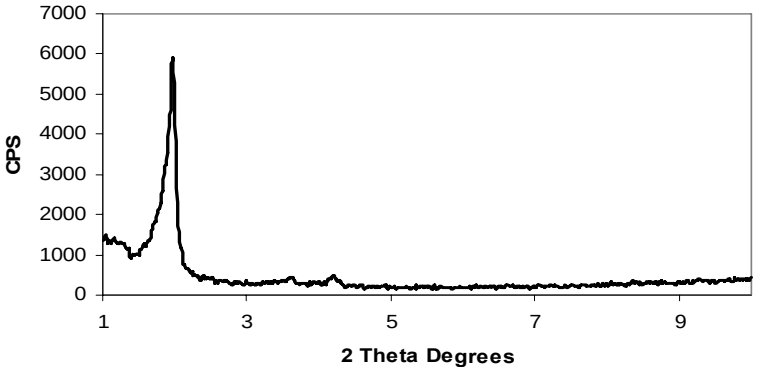


Figure 2. Powder X-ray diffraction patterns of PAP-MSNs. The material exhibited hexagonal type mesoporous structure characteristic of MCM-41.

In this chapter, we report on the synthesis of an organically functionalized MSN material functionalized with an oligonucleotide intercalating phenanthridiniummoiety (PAP-MSN). The working principle of this MSN delivery system is based on the strong binding affinity of phenanthridinium group toward double-stranded oligonucleotides (ds-oligo) to block the pore openings. The release of the guest molecules is achieved once the melting temperature of the ds-oligo has been reached; this will break the non-covalent interaction between the complementary oligonucleotide strands and the phenanthridium functionality (Figure 1). As a proof-of-principle, PAP-MSNs were loaded with a guest molecule, $[Ru(bipy)_3]^{2+}$ complex. The temperature-dependent release profile showed the successful behavior of the ds-oligo(36) as temperature-responsive caps (36 mers; melting temperature = 67 ºC). Moreover, the effect of ds-oligo size on the capping and release efficiency was investigated. For this purpose, three different ds-oligos were synthesized, 18, 36 and 72 mer; and their release performance was evaluated at different temperatures (50, 75, and 90 ºC). Interestingly, a size-dependent capping efficiency was found, where the ds-oligo(36) showed the best performance. Although the temperature required (> 50 ºC) in the present system is not suitable for physiological applications, this proof of concept might provide a principle for the design of temperature-responsive platforms that use the characteristic sequence-specific properties of oligonucleotides to achieve controlled-release properties under physiological conditions. In addition, the possibility of expanding the scope of this system based on different supports and tailor-made oligonucleotides makes this approach of interest for a wide variety of biomedical and biotechnological applications.

RESULTS AND DISCUSSION

The synthesis of PAP-MSNs was previously reported in the literature.[33] The mesoporous structure of PAP-MSN material was characterized by powder X-ray diffraction (XRD) spectroscopy, and nitrogen sorption isotherms (BET method for surface area and BJH method for pore size distribution). The powder XRD measurements of PAP-MSNs exhibited diffraction patterns characteristic of the MCM-41 type hexagonal mesoporous structure with three pronounced (100), (110), and (200) peaks (Figure 2). The N_2sorption isotherms of the PAP- MSN material revealed a type-IV BET isotherm, which is representative of a

cylindrical, channel-like mesoporous structure (Figure 3a). The total surface area was found to be 750 m^2/g. In addition, the BJH analysis of PAP-MSNs indicated a narrow pore size distribution with an average pore diameter of 25 Å (Figure 3b). The amount of phenanthridium functionality on the surfaces of the PAP-MSN was determined to be 0.245 mmol/g by UV/Vis.[33].

Phenanthridium-type molecules are well-known DNA intercalating agents that strongly bind to double stranded oligonucleotides,[34] the binding ability of PAP moiety supported on MSNs toward oligonucleotides was previously corroborated by using yeast tRNA in PBS buffer (pH 7.4).[33] As was mentioned above, this interaction can be disrupted by heating the samples to reach the melting temperature of the ds-oligo. To test this temperature-responsive mechanism, $[Ru(bipy)_3]^{2+}$ complex was loaded on the interior channels of PAP-MSN as it is

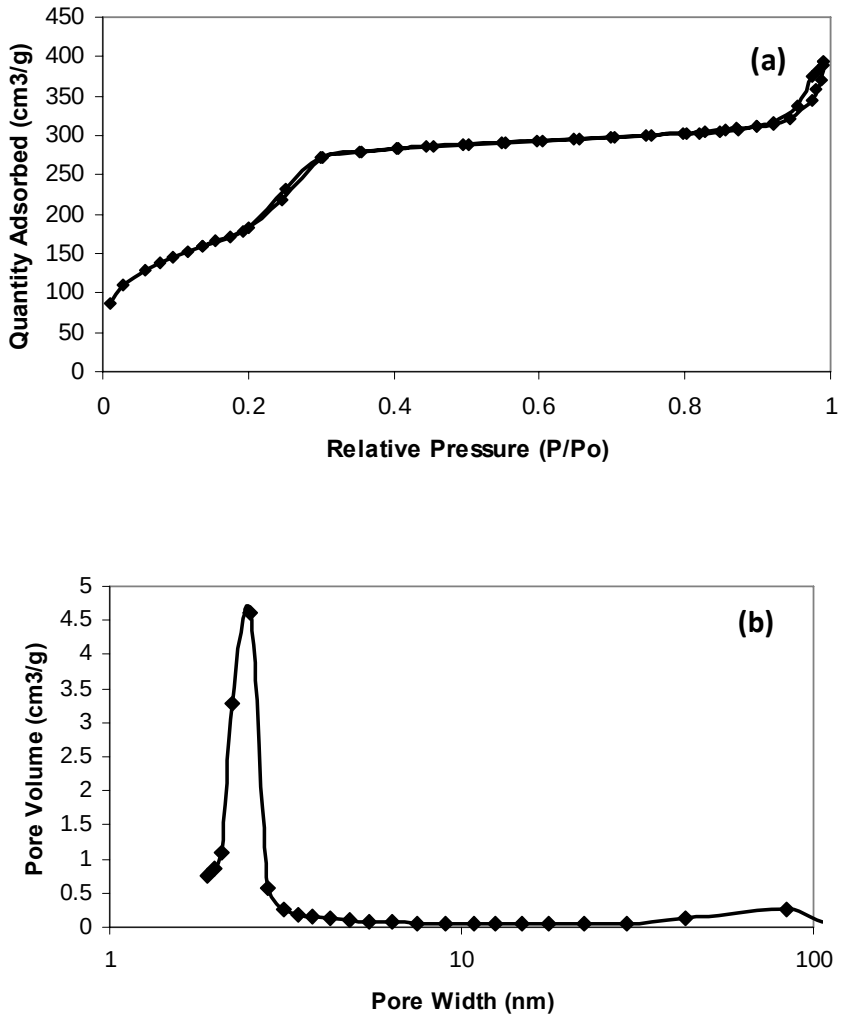


Figure 3. N_2 sorption isotherms of PAP-MSNs. (a) BET nitrogen sorption isotherms, and (b) BJH pore size distribution.

described on the experimental section. To cap the $[Ru(bipy)_3]^{2+}$-loaded PAP-MSN material, the oligonucleotides were pre-hybridized with complementary strands in an annealing solution (100 mMTrisHCl, pH 7.5, 1M NaCl, 10 mM EDTA); the procedure is explained with more detail on the experimental section. To this ds-oligo solution the $[Ru(bipy)_3]^{2+}$-loaded PAP-MSN material was added and stirred for 18h at 4-6 ºC. After washing the material for several times with PBS (150 mM, 100 mMNaCl, pH 7.4) the amount of dye loaded to ds-oligo capped PAP-MSN was 6.59 µmol dye/g PAP-MSN, calculated based on fluorescence spectroscopy measurements. A control sample (dye-physisorbed PAP-MSNs) was prepared following the same experimental conditions without capping with ds-oligo. The amount of $[Ru(bipy)_3]^{2+}$ complex still physisorbed after several washings was 0.87 µmol dye/g PAP-MSN.

To demonstrate the temperature-responsive ability of ds-oligo capped $[Ru(bipy)_3]^{2+}$-loaded PAP-MSN platform; the release kinetics of $[Ru(bipy)_3]^{2+}$ complexusing a 36 mer ds-oligoas cap was determined at 75 ºC. As shown in Figure 4, no considerable leaching of $[Ru(bipy)_3]^{2+}$ complex in solution prior to the increase of temperature was observed;in contrast, the release of $[Ru(bipy)_3]^{2+}$ complex from the physisorbed sample was immediate. As depicted in Figure 4, after the sample was heated up to 75 ºC a burst release of $[Ru(bipy)_3]^{2+}$ complex from the ds-oligo(36) capped PAP-MSN materials was observed, as an indication of its temperature-responsive capabilities. The maximum release (1.73 µmol/g PAP-MSN) was reached after 120 min. The driving force to afford the release of the dye from the mesoporous material is a concentration gradient between the external solution and the interior channels. In our experiment only 26% of the dye-loaded was released, this result showed that the concentration gradient is not strong enough to completely overcome the interaction between $[Ru(bipy)_3]^{2+}$ complex and the silanols in the interior channels of PAP-MSN; however, the mass transfer can be increased by stirring the sample.

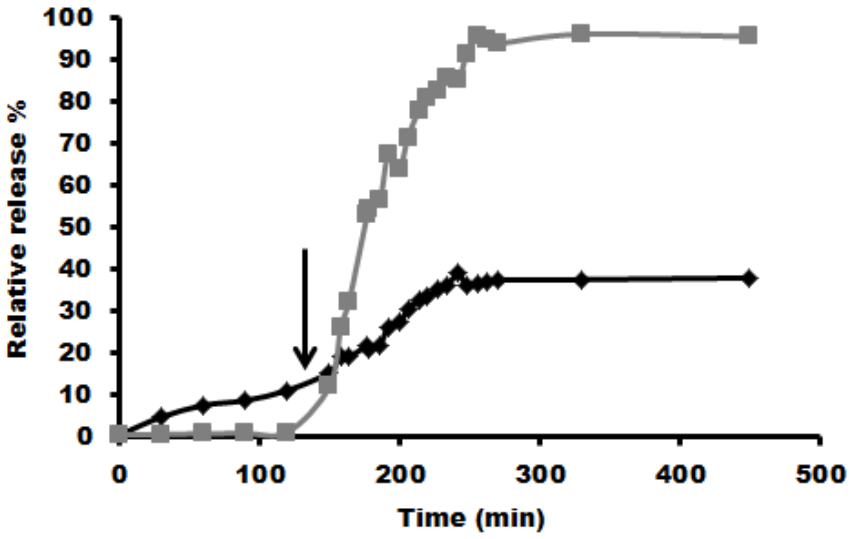


Figure 4. Temperature-responsive release profile of $[Ru(bipy)_3]^{2+}$ complex from ds-oligo(36) capped $[Ru(bipy)_3]^{2+}$ complex-loaded PAP-MSNs. The arrow indicates the point in time where the samples were heated to 75 ºC. ds-oligo(36) capped $[Ru(bipy)_3]^{2+}$ complex-loaded PAP-MSNs (gray squares) and dye-physisorbed PAP-MSNs (black diamonds).

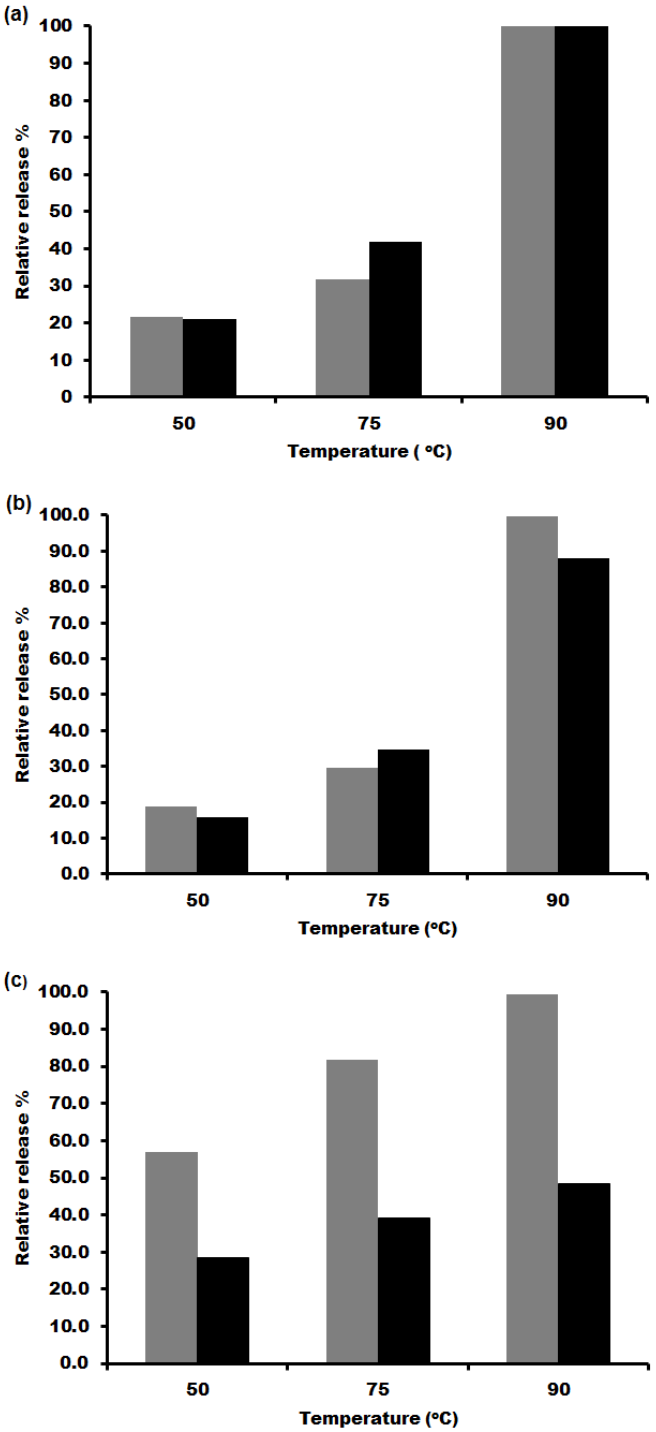


Figure 5. Size- and temperature-dependent release of $[Ru(bipy)_3]^{2+}$ complex from ds-oligo capped $[Ru(bipy)_3]^{2+}$ complex-loaded PAP-MSNs. (a) ds-oligo(18 mer), (b) ds-oligo(72 mer), and (c) ds-oligo(36 mer). ds-oligo capped $[Ru(bipy)_3]^{2+}$ complex-loaded PAP-MSNs (gray bars) and dye-physisorbed PAP-MSNs (black bars).

To optimize the capping efficiency, three different ds-oligo were evaluated;a 18, 36 and 72 mer, the sequences and calculated melting temperature for each oligonucleotide are described in the experimental section. These samples were heated at different temperatures (50, 75, and 90 ºC) for 30 min and the amount of $[Ru(bipy)_3]^{2+}$ complexreleased was quantified by fluorescence spectroscopy. Figures 5a and 5b showed similar performance between the capped samples and the dye-physisorbed PAP-MSN material as an indication that practically there was not capping effect by using 18 and 72 mer ds-oligo. The maximum amount of $[Ru(bipy)_3]^{2+}$ complex released by these samples was 0.557 and 0.742 μmol/g PAP-MSN, respectively. Interestingly, the 36 mer ds-oligo cap showed an increased capping efficiency as it is depicted in Figure 5c. This size-dependent capping efficiency could be due to two factors, the complementary conformation of ds-oligo in the surface of MSNs and the amount of PAP moiety on the exterior surface that is being effectively intercalated into the ds-oligo.

CONCLUSION

In summary, we have shown that by immobilizing a DNA intercalating agent (PAP) on the exterior surface of MSNs a novel temperature-responsive ds-oligo capped delivery system can be developed. The temperature-responsive capability of this platform was successfully tested at 75 ºC. In addition, the ds-oligo size-dependent capping efficiency of PAP-MSNs was evaluated using three different ds-oligo sizes, 18, 36 and 72 mer. Interestingly, only the ds-oligo(36) cap showed effective capping and release properties. This could be due to the conformation acquired by the ds-oligo(36) on the surface of MSNs, which could enhance the intercalation with PAP groups. Although the current temperature-responsive performance in the present system is not suitable for physiological applications, we envision that this proof of concept would lead to the design of new temperature-responsive platforms based on mesoporous silica nanoparticles and DNA intercalating agents.

EXPERIMENTAL SECTION

Reagents and Materials

Tetraethylorthosilicate (TEOS) was purchased from Gelest. Ethyl chloroformate was purchased from Acros. Cetyltrimethylammonium bromide, pyridine (anhydrous), 3-aminopropyltrimethoxysilane (AP-TMS), 3,8-diamino-6-phenyl-phenanthridine, 1,3-dibromopropane, and $[Ru(bipy)_3]^{2+}$ complex were purchased from Aldrich. Yeast tRNA was purchased from Invitrogen, Inc. Oligonucleotides with the following sequence 5'-TGT-AAA-ACG-ACG-GCC-AGT-3'; 5'-TGT-AAA-ACG-ACG-GCC-AGT-TGT-AAA-ACG-ACG-GCC-AGT 3'; 5'-TGT-AAA-ACG-ACG-GCC-AGT-TGT-AAA-ACG-ACG-GCC-AGT-TGT-AAA-ACG-ACG-GCC-AGT-TGT-AAA-ACG-ACG-GCC-AGT-3'; 18 (Tm = 48 ºC), 36 (Tm = 67 ºC), 72 (Tm = 76 ºC) mer and their respective complementary sequence were synthesized at the DNA facility of Iowa State University. All chemicals were used as received.

Characterization of Materials

Surface analysis of PAP-MSNs was performed by nitrogen sorption isotherms in a Micromeritics TriStar surface area and porosity analyzer. The powder X-Ray diffraction patterns of these mesoporous materials were measured by a Scintag XDS-2000 powder diffractometer using Cu Kα irradiation. Fluorescence spectroscopy was measured byFluoroMax-2 fluorimeter.

Synthesis of PAP-MSNs

The detailed synthetic procedures for the preparation and purification of PAP-MSNs were described in the literature.[33]

Loading of the $[Ru(bipy)_3]^{2+}$ Complex to PAP-MSNs

To load the $[Ru(bipy)_3]^{2+}$ complex to PAP-MSN material, 2 mg of PAP-MSNs were added to 1.5 mL of a previously prepared solution of $[Ru(bipy)_3]^{2+}$ complex (1 mM) in PBS (100 mM, 150 mMNaCl, pH 7.4). This dispersion was stirred for 24h at room temperature. The $[Ru(bipy)_3]^{2+}$-loaded PAP-MSN was washed at least twice with PBS (100 mM, 150 mMNaCl, pH 7.4) to remove the $[Ru(bipy)_3]^{2+}$ complex physisorbed on the external surface of MSNs.

Capping of $[Ru(bipy)_3]^{2+}$-Loaded PAP-MSNs with ds-Oligonucleotides

The procedure described below was followed for all the ds-oligos used in this work. First, to produce the ds-oligo, the nextmethod was followed; the ss-oligo and its complementary sequence were dissolved in an annealing solution (100 mMTrisHCl, pH 7.5, 1M NaCl, 10 mM EDTA) using the following amounts of oligonucleotides; 185, 142, and 78 nmol for the 18, 36, and 72 mer, respectively. This solution was heated until 90 ºC for 10 min, the heat source was removed and the solution was slowly cool down to room temperature to afford the corresponding ds-oligo. To cap the $[Ru(bipy)_3]^{2+}$-loaded PAP-MSN material, 2 mL of the previously prepared ds-oligo solution was added to 2 mg of $[Ru(bipy)_3]^{2+}$-loaded PAP-MSNs and stirred for 18h at 4-6 ºC. After that the sample was centrifuged down (4000 rpm, 4 min) and the supernatant was removed. The final material was washed several times with PBS until non fluorescence from the $[Ru(bipy)_3]^{2+}$ complex was detected from the washing solutions. To quantify the amount of $[Ru(bipy)_3]^{2+}$ complex loaded to PAP-MSNs, the supernatant and washing solutions were collected, and the fluorescence intensity was measured by FluoroMax-2 fluorimeter (λ_{ex}= 454 nm; λ_{em}= 610 nm).

Release of $[Ru(bipy)_3]^{2+}$ from Oligo-Capped $[Ru(bipy)_3]^{2+}$-Loaded PAP-MSNs

The oligo-capped $[Ru(bipy)_3]^{2+}$-loaded PAP-MSN samples were re-dispersed in 1.5 mL of PBS (150 mM, 100 mMNaCl, pH 7.4). These dispersions were stirred for at least 12h to keep track of any $[Ru(bipy)_3]^{2+}$ complex leaching from the surface. Then the samples were heated at different temperatures for 30 min. The samples were centrifuged down and the amount of $[Ru(bipy)_3]^{2+}$ complex released was measured by fluorescence spectrometry.

ACKNOWLEDGMENTS

This research was supported by U.S. National Science Foundation (CHE-0809521) and the Biopharmaceuticals &BioindustrialsInitiative of the Plant Science Institute of Iowa State University.Dr. Juan L. Vivero-Escoto would like to acknowledge financial support from the Carolina Postdoctoral Program for Faculty Diversity.

REVIEWED BY

Dr. Renato Mortera,Dipartimento di ScienzadeiMateriali e IngegneriaChimicaPolitecnico di Torino, C.so Ducadegli Abruzzi 24, 10129 Torino, Italy.

REFERENCES

[1] Trewyn BG, Slowing II, Giri S, Chen H-T, Lin VSY: Synthesis and Functionalization of a Mesoporous Silica Nanoparticle Based on the Sol-Gel Process and Applications in Controlled Release. *Acc Chem Res* 2007, 40(9):846-853.

[2] Slowing II, Vivero-Escoto JL, Wu C-W, Lin VSY: Mesoporous silica nanoparticles as controlled release drug delivery and gene transfection carriers. *Adv Drug Delivery Rev* 2008, 60(11):1278-1288.

[3] Vivero-Escoto JL, Trewyn BG, Lin VSY: Mesoporous silica nanoparticles: synthesis and applications. *Annu Rev Nano Res* 2010, 3:191-231.

[4] Vivero-Escoto JL, Slowing II, Trewyn BG, Lin VSY: Mesoporous Silica Nanoparticles for Intracellular Controlled Drug Delivery. *Small* 2010, 6(18):1952-1967.

[5] Zhao Y, Vivero-Escoto JL, Slowing II, Trewyn BG, Lin VSY: Capped mesoporous silica nanoparticles as stimuli-responsive controlled release systems for intracellular drug/gene delivery. *Expert Opinion on Drug Delivery* 2010, 7(9):1013-1029.

[6] Ambrogio MW, Pecorelli TA, Patel K, Khashab NM, Trabolsi A, Khatib HA, Botros YY, Zink JI, Stoddart JF: Snap-Top Nanocarriers. *Organic Letters* 2010, 12(15):3304-3307.

[7] Coti KK, Belowich ME, Liong M, Ambrogio MW, Lau YA, Khatib HA, Zink JI, Khashab NM, Stoddart JF: Mechanised nanoparticles for drug delivery. *Nanoscale* 2009, 1(1):16-39.

[8] Rosenholm JM, Sahlgren C, Linden M: Towards multifunctional, targeted drug delivery systems using mesoporous silica nanoparticles - opportunities & challenges. *Nanoscale* 2010, 2(10):1870-1883.

[9] Aznar E, Marcos MD, Martinez-Manez R, Sancenon F, Soto J, Amoros P, Guillem C: pH- and Photo-Switched Release of Guest Molecules from Mesoporous Silica Supports. *J Am Chem Soc* 2009, 131(19):6833-6843.

[10] Gao C, Zheng H, Xing L, Shu M, Che S: Designable Coordination Bonding in Mesopores as a pH-Responsive Release System. *Chemistry of Materials* 2010, 22(19):5437-5444.

[11] Khashab NM, Belowich ME, Trabolsi A, Friedman DC, Valente C, Lau Y, Khatib HA, Zink JI, Stoddart JF: pH-Responsive mechanised nanoparticles gated by semirotaxanes. *Chem Commun* 2009(36):5371-5373.

[12] Lee C-H, Cheng S-H, Huang IP, Souris JS, Yang C-S, Mou C-Y, Lo L-W: Intracellular pH-Responsive Mesoporous Silica Nanoparticles for the Controlled Release of Anticancer Chemotherapeutics. *Angew Chem, Int Ed* 2010, 49(44):8214-8219.

[13] Liu R, Zhang Y, Zhao X, Agarwal A, Mueller LJ, Feng P: pH-Responsive Nanogated Ensemble Based on Gold-Capped Mesoporous Silica through an Acid-Labile Acetal Linker. *J Am Chem Soc* 2010, 132(5):1500-1501.

[14] Park C, Oh K, Lee SC, Kim C: Controlled release of guest molecules from mesoporous silica particles based on a pH-responsive polypseudorotaxane motif. *Angew Chem, Int Ed* 2007, 46(9):1455-1457.

[15] Liu R, Zhang Y, Feng P: Multiresponsive Supramolecular Nanogated Ensembles. *J Am Chem Soc* 2009, 131(42):15128-15129.

[16] Liu R, Zhao X, Wu T, Feng P: Tunable Redox-Responsive Hybrid Nanogated Ensembles. *J Am Chem Soc* 2008, 130(44):14418-14419.

[17] Mortera R, Vivero-Escoto J, Slowing II, Garrone E, Onida B, Lin VSY: Cell-induced intracellular controlled release of membrane impermeable cysteine from a mesoporous silica nanoparticle-based drug delivery system. *Chem Commun* 2009(22):3219-3221.

[18] Wan X, Wang D, Liu S: Fluorescent pH-Sensing Organic/Inorganic Hybrid Mesoporous Silica Nanoparticles with Tunable Redox-Responsive Release Capability. *Langmuir* 2010, 26(19):15574-15579.

[19] Bernardos A, Aznar E, Marcos MD, Martinez-Manez R, Sancenon F, Soto J, Barat JM, Amoros P: Enzyme-Responsive Controlled Release Using Mesoporous Silica Supports Capped with Lactose. *Angew Chem, Int Ed* 2009, 48(32):5884-5887.

[20] Bernardos A, Mondragon L, Aznar E, Marcos MD, Martinez-Manez R, Sancenon F, Soto J, Barat JM, Perez-Paya E, Guillem C *et al*: Enzyme-Responsive Intracellular Controlled Release Using Nanometric Silica Mesoporous Supports Capped with "Saccharides". *ACS Nano* 2010, 4(11):6353-6368.

[21] Park C, Kim H, Kim S, Kim C: Enzyme Responsive Nanocontainers with Cyclodextrin Gatekeepers and Synergistic Effects in Release of Guests. *J Am Chem Soc* 2009, 131(46):16614-16615.

[22] Patel K, Angelos S, Dichtel WR, Coskun A, Yang Y-W, Zink JI, Stoddart JF: Enzyme-Responsive Snap-Top Covered Silica Nanocontainers. *J Am Chem Soc* 2008, 130(8):2382-2383.

[23] Ferris Daniel P, Zhao Y-L, Khashab Niveen M, Khatib Hussam A, Stoddart JF, Zink Jeffrey I: Light-operated mechanized nanoparticles. *J Am Chem Soc* 2009, 131(5):1686-1688.

[24] Lu J, Choi E, Tamanoi F, Zink JI: Light-activated nanoimpeller-controlled drug release in cancer cells. *Small* 2008, 4(4):421-426.

[25] Park C, Lee K, Kim C: Photoresponsive cyclodextrin-covered nanocontainers and their sol-gel transition induced by molecular recognition. *Angew Chem, Int Ed* 2009, 48(7):1275-1278.

[26] Vivero-Escoto JL, Slowing II, Wu C-W, Lin VSY: Photoinduced Intracellular Controlled Release Drug Delivery in Human Cells by Gold-Capped Mesoporous Silica Nanosphere. *J Am Chem Soc* 2009, 131(10):3462-3463.

[27] Climent E, Bernardos A, Martinez-Manez R, Maquieira A, Marcos MD, Pastor-Navarro N, Puchades R, Sancenon F, Soto J, Amoros P: Controlled Delivery Systems Using Antibody-Capped Mesoporous Nanocontainers. *J Am Chem Soc* 2009, 131(39):14075-14080.

[28] Schlossbauer A, Kecht J, Bein T: Biotin-Avidin as a Protease-Responsive Cap System for Controlled Guest Release from Colloidal Mesoporous Silica. *Angew Chem, Int Ed* 2009, 48(17):3092-3095.

[29] Zhao Y, Trewyn BG, Slowing II, Lin VSY: Mesoporous Silica Nanoparticle-Based Double Drug Delivery System for Glucose-Responsive Controlled Release of Insulin and Cyclic AMP. *J Am Chem Soc* 2009, 131(24):8398-8400.

[30] Schlossbauer A, Warncke S, Gramlich PME, Kecht J, Manetto A, Carell T, Bein T: A Programmable DNA-Based Molecular Valve for Colloidal Mesoporous Silica. *Angew Chem, Int Ed* 2010, 49(28):4734-4737.

[31] Climent E, Martinez-Manez R, Sancenon F, Marcos MD, Soto J, Maquieira A, Amoros P: Controlled delivery using oligonucleotide-capped mesoporous silica nanoparticles. *Angew Chem, Int Ed* 2010, 49(40):7281-7283.

[32] Chen C, Geng J, Pu F, Yang X, Ren J, Qu X: Polyvalent Nucleic Acid/Mesoporous Silica Nanoparticle Conjugates: Dual Stimuli-Responsive Vehicles for Intracellular Drug Delivery. *Angew Chem, Int Ed* 2011, 50(4):882-886.

[33] Vivero-Escoto JL, Slowing II, Lin VSY: Tuning the cellular uptake and cytotoxicity properties of oligonucleotide intercalator-functionalized mesoporous silica nanoparticles with human cervical cancer cells HeLa. *Biomaterials* 2010, 31(6):1325-1333.

[34] Ihmels H, Otto D: Intercalation of organic dye molecules into double-stranded DNA, General principles and recent developments. *Top Curr Chem* 2005, 258(Supramolecular Dye Chemistry):161-204.

INDEX

#

3-aminopropyltriethoxysilane (APTS), 145

A

Abraham, 210
absorption spectra, 50, 57, 61, 62, 63, 82, 83, 86, 93, 99, 228
abstraction, 62, 63, 65, 66, 67, 73, 86, 92, 93
access, 199
accessibility, 28, 68
acetonitrile, 52, 53, 54, 57, 59, 60, 61, 62, 63, 92
acid, 3, 6, 14, 16, 21, 25, 28, 29, 30, 32, 49, 54, 80, 83, 92, 94, 95, 104, 105, 108, 109, 127, 131, 132, 141, 145, 154, 158, 159, 162, 163, 171, 188, 194, 200, 202, 205, 207, 220, 224, 232, 252, 258
acidic, 6, 59, 107, 140, 232
acrylate, 164, 186, 267
acrylic acid, 207
activation energy, 69, 72, 85
active compound, 172
active site, 28
actuation, 112
additives, 89, 191, 200, 205
adenocarcinoma, 21
adenosine, 134
adhesion, 90, 162, 252
adhesives, 190
adolescents, 265
adsorption, 13, 15, 32, 50, 51, 52, 53, 54, 55, 57, 67, 75, 79, 82, 86, 92, 125, 147, 149, 151, 152, 168, 172, 181, 193, 203, 251, 252, 273
advancements, 316
adverse effects, 252
AFM, 226, 277, 278, 287, 311
agar, 194
agglutination, 32, 273
aggregation, 35, 60, 114, 122, 186, 205, 216, 225, 228, 277, 295, 311
albumin, 15
alcohols, 10, 50, 223
alkenes, 90
ambient air, 225
AMF, 20, 162
amine, 18, 23, 135, 145, 146, 163, 164, 190, 220, 273, 277, 289
amino, 15, 17, 24, 25, 26, 27, 30, 31, 33, 48, 105, 106, 109, 111, 143, 152, 156, 159, 164, 170, 202, 206, 216
amino groups, 17, 25, 143
ammonia, 5, 12, 145, 179, 192, 196, 200, 207, 220, 224, 225, 232, 274, 275, 284, 285, 287
ammonium, 3, 140, 145, 146, 161, 162, 200, 204, 287
amorphous precipitate, 283
amplitude, 52, 56
amylase, 158, 173
analgesic, 22
anchoring, 192
annealing, 319, 323
antibiotic, 152
antibody, 15, 30, 31, 32, 33, 34
anti-cancer, 126, 155
anticancer drug, 111, 127, 133, 155, 156, 163, 171, 255
antigen, 2, 15, 16, 30, 31, 32, 33, 34
anti-inflammatory agents, 253
antioxidant, 166
antisense, 15
antisense oligonucleotides, 15
antitumor, 98, 126, 127
aorta, 115, 116
apoptosis, 156, 162, 166
aqueous solutions, xii, 9, 68, 73, 75, 80, 81, 83, 88, 94, 95, 141, 152, 182, 191, 272, 273
aqueous suspension, 81

Argentina, 47
argon, 59, 262, 268, 285
artificial heart valve, 257
asbestos, 170
ascorbic acid, 30, 32
astrocytes, 158
atmosphere, 205
atomic force microscope, 311
atoms, 49, 54, 77, 79, 86, 88, 95, 99, 204, 231, 232
ATP, 158, 159, 166
attachment, 18, 25, 29, 146, 152, 186, 190, 251, 258
attribution, 151
Au nanoparticles, 113, 192, 194, 207
avian influenza, 34
avoidance, 114
awareness, 263
azobenzene, 102, 111

B

bacteria, 25, 272
bandgap, 192
bandwidth, 268
base, xi, 3, 15, 17, 18, 19, 27, 35, 54, 73, 80, 83, 95, 111, 114, 115, 116, 118, 124, 131, 150, 160, 168, 177, 178, 179, 181, 188, 196, 206, 207, 208, 216, 217, 220, 224, 225, 227, 232, 264, 289, 290
base pair, 289
baths, 191
behaviors, 8, 230
benefits, 263
benign, 208
benzene, 88, 93, 186, 187, 207
bile, 118
binary oxides, 92
bioactive agents, 254
bioactive materials, 260
biocatalysts, 29
biocompatibility, x, xii, 2, 9, 20, 33, 98, 101, 111, 113, 116, 117, 123, 125, 129, 137, 144, 158, 160, 161, 162, 168, 171, 178, 183, 245, 254, 259
Biocompatibility, 117, 137, 159, 172
biodegradability, 254, 258
biodegradation, 117
biological activities, 110
biological activity, 25
biological fluids, 254
biological processes, 23, 98
biological systems, 13, 21, 103, 129, 258
biomarkers, 113, 273, 293
biomaterials, 257, 259, 267
biomedical applications, x, 2, 21, 97, 98, 102, 112, 117, 129, 135, 151, 160, 165, 168, 206, 252, 254, 255, 256, 258, 264, 295, 316
biomolecules, ix, xiii, 1, 2, 3, 4, 15, 16, 18, 19, 26, 27, 29, 33, 99, 101, 103, 107, 110, 113, 170, 172, 273, 296, 315, 316
biopolymer, 28, 29
biosensors, ix, 1, 2, 19, 27, 28, 89, 140, 157, 180, 274, 294
bioseparation, 3, 35
biotechnological applications, xiv, 35, 129, 232, 316, 318
biotechnology, 27, 100, 160, 299
biotin, 2, 17, 30, 110, 290
Bis-GMA, 261
blackbody radiation, 26
blood, 19, 30, 107, 110, 114, 117, 122, 124, 129, 155, 161, 253
blood circulation, 117, 122, 124, 129, 155
blood stream, 124
body fluid, 149, 267
bonding, 50, 59, 90, 108, 141, 142, 192, 249, 261, 263, 267, 273
bonds, 24, 107, 109, 152, 190, 249, 252
bone, xii, 122, 152, 168, 174, 245, 257, 258, 259, 267
brain, 28, 169
brass, 300
breakdown, 305
breast cancer, 22, 113, 125, 127, 166, 172, 256
breathing, 118
brittleness, 260
bromine, 89
Brownian motion, 222
building blocks, 13, 199, 247
bulk materials, 246

C

cadmium, 101, 158
calibration, 28, 29, 32
calorimetry, 94
cancer, xii, xiii, 19, 20, 22, 23, 33, 108, 110, 113, 126, 127, 130, 131, 133, 135, 140, 155, 156, 163, 164, 166, 167, 168, 169, 170, 172, 175, 188, 245, 255, 264, 272, 274, 326, 327
cancer cells, 20, 22, 23, 110, 125, 127, 131, 133, 155, 156, 163, 166, 168, 169, 170, 172, 175, 188, 272, 326, 327
candidates, xii, 180, 181, 188, 231, 235, 271, 272
CAP, 94
capillary, 290, 311
capsule, 187

carbohydrate, 16, 259
carbohydrates, 107, 110
carbon, xi, 13, 20, 24, 28, 30, 31, 32, 33, 48, 52, 87, 143, 177, 178, 179, 186, 199, 201, 202, 204, 205, 208, 259
carbon atoms, 204
carbon dioxide, 259
carbon materials, 199
carbon molecule, 199
carbon nanotubes, xi, 13, 20, 28, 177, 178, 201
carboxyl, 152, 156, 164, 204, 273
carboxylic acid, 18, 200
carboxylic acids, 18
carboxylic groups, 26, 162
carcinoembryonic antigen, 32
carcinoma, 21, 108, 256
cargoes, 101, 102
case study, xiii, 272, 274
catalysis, 100, 146, 185, 189, 216, 239, 252
catalyst, 145, 179, 180, 186, 200, 205, 216
catalytic activity, 15, 157, 193
cation, 62
cationic surfactants, 140, 143
cell biology, 23
cell culture, 20
cell cycle, 161
cell death, 20, 128, 166, 169
cell differentiation, 162
cell line, 20, 21, 108, 113, 115, 126, 161, 164, 165, 166, 170
cell lines, 20, 161, 164, 165
cell membranes, 21, 23, 50, 163
cell metabolism, 100
cell surface, 19, 98, 164
cell-penetrating peptides, 100
ceramic, 172, 253
Ceramics, 174
cervical cancer, xiii, 131, 156, 163, 168, 175, 272, 274, 327
challenges, xi, 129, 130, 150, 177, 179, 196, 206, 208, 236, 325
charge density, 72
chelates, 100, 115, 116
chemical, x, xi, 2, 3, 8, 9, 10, 32, 47, 48, 49, 50, 54, 68, 71, 72, 75, 99, 108, 111, 115, 140, 143, 151, 152, 154, 158, 162, 177, 178, 179, 185, 191, 192, 195, 200, 204, 206, 216, 236, 250, 251, 253, 254, 262
chemical bonds, 108
chemical deposition, 195
chemical interaction, 250, 252
chemical properties, 99, 115, 143, 185
chemical reactions, x, 47, 48
chemical reactivity, 216
chemical stability, xi, 9, 177, 216
chemical vapor deposition, 32, 192, 206
chemiluminescence, 2, 34
chemiluminescence (CL), 2
chemotherapeutic agent, 107, 126, 156
Chemotherapeutics, 134, 325
chemotherapy, 155, 169, 205, 256
Chicago, 268
children, 265
China, 1, 175
chitosan, 27, 28, 29
chlorination, 221
chlorine, 68, 79, 86, 88
chloroambucil, 112
chloroform, 223
CHO cells, 160
cholera, 108
cholesterol, 28, 30
chromatography, 89
circulation, 98, 117, 119, 120, 122, 123, 124, 129, 155
classes, 48, 115, 248, 253
cleavage, 103, 108
clinical application, 19, 98, 112, 254
clinical diagnosis, 113
clusters, 11, 180, 205, 218, 231, 232, 235, 236, 239
CO2, 52, 91
coatings, 117, 179, 181, 190, 202, 216, 236, 246, 252
cobalt, 10, 24
collagen, 109, 196, 259, 260
collisions, 60
colon, 21
color, 26, 128, 227, 260, 286
colored dissolved organic carbon (CDOM), 48
combustion, 219
commercial, xii, xiii, 12, 54, 248, 249, 261, 272, 273, 274, 294
communities, 267
community, xi, 215, 216
compatibility, 2, 161, 178, 250, 257, 295
competition, 67
complementary DNA, 25
complexity, 219, 239
complications, 100, 114
composite resin, 262, 268
composites, xii, 13, 181, 201, 246, 247, 260, 261, 262, 263, 268
composition, ix, 1, 2, 35, 59, 162, 179, 181, 188, 190, 203, 206, 260, 289
compounds, 10, 48, 49, 51, 82, 88, 95, 172, 231, 232, 273
computer, 55, 56, 80, 300, 301

computer simulations, 55, 56, 80
condensation, 3, 141, 142, 143, 144, 145, 146, 163, 179, 181, 193, 201, 202, 216, 224, 225, 226, 232
conductivity, 28
configuration, 49, 54, 306, 307, 308, 310, 312
confinement, 188, 189
conjugation, xii, 15, 16, 17, 20, 23, 24, 27, 30, 31, 33, 98, 135, 199, 271, 273
connectivity, 149
constituents, 50, 87
construction, 256
contaminant, x, 47, 48, 49, 225
contaminated water, 50
contamination, 18
contour, 260
COOH, 33, 117, 119, 121, 156, 165
cooling, 26, 225, 229, 290
cooling process, 26, 225
cooperation, 295
coordination, 108, 188, 190, 194, 207
copolymer, 189, 267
copolymerization, 259, 260
copolymers, 141, 142, 185, 188, 203, 258
copper, 206
coronary heart disease, 265
correlation, 26, 92, 157, 164
cosmetic, xii, 215, 246
cost, xi, xii, 27, 35, 114, 156, 177, 178, 181, 200, 208, 257, 271, 272
co-structure directing agent (CSDA), 143
covalent bond, 6, 24, 190, 273
covalent bonding, 273
covering, 190
CPT, 110, 127, 156
cracks, 226
CRP, 186
crystalline, 10, 50, 139, 141, 165, 168, 175, 193, 231
crystallinity, 188, 190
crystals, 93, 151, 168, 178, 179, 188, 192
culture, 20, 165
current limit, 258
cycles, 181, 224, 290
cycling, 205
cyclodextrins, 109
cyclodextrins (CD), 109
cysteine, 109, 135, 325
cytochrome, 102
cytometry, 23, 109, 162
cytoplasm, 101, 102, 162, 163
cytotoxicity, xi, 20, 21, 109, 118, 126, 127, 131, 155, 165, 166, 167, 170, 171, 172, 173, 174, 175, 177, 326

D

data analysis, 290
database, 289
decay, 52, 53, 54, 55, 56, 61, 62, 63, 65, 67, 69, 70, 71, 72, 73, 74, 75, 76, 77, 81, 82, 83, 84, 94, 205, 281
decomposition, 117, 143, 182, 183, 255
defect formation, 94
defect site, 200, 258
defects, 68, 75, 77, 86, 186, 200, 205, 260
degradation, ix, x, 47, 48, 49, 87, 89, 101, 114, 124, 129, 149, 181, 253, 254, 258, 267
degradation rate, 125
denaturation, 157, 290
dendritic cell, 174
dental resins, 263
Department of Commerce, 95
Department of Energy, 315
deposition, xi, 31, 32, 177, 181, 182, 189, 190, 191, 192, 193, 195, 202, 206, 207, 311
depth, 236, 268
derivatives, 59, 102, 135, 259
desorption, 18, 50, 92, 147
destruction, 131
detectable, 116, 125, 273, 288
detection, xiii, 2, 4, 11, 13, 19, 23, 24, 25, 26, 27, 28, 29, 31, 32, 33, 34, 35, 65, 69, 98, 99, 113, 131, 136, 145, 157, 159, 172, 192, 196, 221, 272, 274, 290, 291, 293, 294, 295, 296, 300
detection techniques, 4, 294
detonation, 205
deviation, 310
diabetes, 252, 265
dialysis, 19, 143
diamonds, 320
diffraction, 141, 193, 230, 284, 300, 317, 318, 323
diffuse reflectance, 92
diffusion, 60, 72, 73, 77, 78, 85, 95, 184, 188, 224, 230, 235, 253, 255
diffusion process, 95
diffusivity, 261
dimensionality, 68, 94
dimerization, 153
dimethacrylate, 261
direct measure, 300
discs, 260
diseases, 98, 252, 254, 274
dispersion, xiii, 10, 25, 114, 186, 187, 190, 225, 236, 247, 250, 252, 295, 299, 300, 304, 310, 312, 323
dispersity, 161
displacement, 191, 192
disposition, 15, 117

dissociation, 16, 65, 72
distilled water, 289
distribution, 6, 7, 8, 113, 118, 122, 137, 146, 155, 160, 181, 284, 295, 304, 305, 306, 307, 309, 310, 312, 316, 318, 319
distribution function, 305, 309, 310
divergence, 262
diversity, 2, 129, 253
DMF, 204
DNA, vii, viii, ix, xiii, 2, 15, 18, 19, 20, 23, 24, 25, 26, 100, 105, 107, 108, 110, 113, 129, 132, 134, 136, 159, 163, 174, 175, 183, 221, 271, 272, 274, 288, 289, 290, 291, 292, 293, 294, 295, 296, 297, 315, 316, 318, 322, 323, 326, 327
DNase, 105, 110
DOI, 266, 268, 297
dopamine, 159
doping, xiii, 272, 297
dosage, 100, 253, 266
DRS, 87
drug carriers, 107, 108
drug delivery, ix, x, xi, xii, 21, 97, 99, 101, 102, 107, 108, 112, 125, 126, 127, 129, 131, 133, 134, 135, 137, 139, 140, 147, 149, 151, 152, 155, 156, 158, 160, 162, 167, 169, 170, 171, 173, 174, 181, 187, 195, 245, 252, 253, 254, 255, 263, 264, 265, 266, 324, 325
drug interaction, 151, 152
drug release, 98, 102, 112, 133, 140, 149, 152, 153, 155, 156, 158, 169, 252, 253, 254, 266, 326
drug resistance, 155
drug therapy, 254
drugs, 14, 98, 99, 101, 102, 107, 111, 127, 133, 151, 153, 155, 156, 158, 171, 205, 253, 255, 264
drying, 7, 140
ductility, 247
durability, 116, 125
dyes, 4, 23, 27, 111, 140, 144, 219, 236, 273, 280, 287, 292, 293, 294
dynamic systems, 222

E

editors, 267
egg, 184
elaboration, xi, 215, 239
elastomers, 247
electric field, 252, 299, 300, 303, 306, 308, 310, 312
electrical breakdown, 305
electrical properties, 199
electrochemical behavior, 28
electrochemical impedance, 33
electrochemiluminescence (ECL), 2
electrochemistry, 157
electrode surface, 6, 28, 29, 32, 35
electrodes, 30, 299
electrolyte, 60, 72, 90
electromagnetic, 13, 15
electron, 5, 28, 29, 49, 73, 79, 88, 100, 107, 144, 154, 157, 203, 204, 222, 232, 236, 300
electron microscopy, 5, 100, 107, 144, 222
electrophoresis, 33, 290
electroplating, 12
ELISA, 16
embolism, 123
emission, xii, 4, 5, 6, 14, 15, 20, 21, 33, 52, 53, 55, 56, 57, 58, 59, 60, 63, 99, 114, 122, 124, 144, 231, 234, 235, 236, 238, 271, 279, 280, 281, 282, 286, 287, 294
emitters, 236
emulsion polymerization, 143, 147, 181, 207, 246
encapsulation, ix, xi, 1, 3, 4, 6, 14, 15, 16, 29, 32, 147, 152, 158, 163, 215, 216, 217, 218, 219, 220, 225, 228, 231, 232, 235, 236, 239, 265
encoding, 33, 258
endothelial cells, 109, 166, 173
energy, 7, 14, 59, 68, 69, 72, 85, 93, 99, 133, 202, 208, 236, 250, 301, 303, 307, 311
energy transfer, 7, 14
engineering, xii, 178, 245, 246, 257, 258, 259, 262, 263, 264, 267, 273, 299
entrapment, 15, 16, 27, 109, 152, 254
environment, x, xiii, 3, 28, 48, 49, 50, 57, 86, 108, 111, 115, 144, 145, 155, 181, 200, 203, 208, 222, 230, 272, 273, 277
environmental care, 246
enzymatic activity, 101, 102, 147, 316
enzyme, 16, 18, 27, 28, 29, 30, 34, 147, 148, 157, 158, 316
enzyme immobilization, 147, 148
enzyme sensor, 30
enzyme-linked immunosorbent assay, 16
enzymes, 30, 101, 107, 110, 147, 157, 167
EPA, 163
ephemeral blood circulation, 129
epithelial cells, 170
EPR, 95, 126
equilibrium, 55, 72, 76, 83
ester, 18, 23, 105, 111, 152, 163, 200, 259, 275, 277
etching, 187, 188, 196, 202, 206, 208, 218
ethanol, 3, 12, 28, 60, 72, 74, 75, 144, 145, 180, 224, 225, 232, 248, 274, 275, 276, 277, 279, 280, 281, 285, 287, 288
ethylene, 141, 143, 187, 189, 193, 252
ethylene glycol, 143, 193
ethylene oxide, 141, 189, 252

europium, 26, 33
evaporation, 180
evidence, 20, 49, 72, 86, 90, 116, 125
evolution, 61, 228
excitation, xii, 6, 7, 33, 57, 59, 63, 68, 111, 114, 231, 234, 235, 236, 238, 271, 279, 281, 282, 283, 284, 285, 293, 294
exclusion, 4
excretion, 114, 117, 124, 127, 129, 136
experimental condition, 62, 71, 76, 79, 319
expertise, 295
exploitation, 8, 135
exposure, 5, 91, 111, 112, 166, 167
external environment, 273
external magnetic fields, 25
extinction, 256
extracellular matrix, 109
extraction, 19, 89, 185, 272, 311

F

fabrication, xi, 4, 5, 6, 8, 14, 27, 29, 30, 35, 177, 178, 179, 181, 182, 183, 185, 190, 191, 193, 195, 197, 201, 203, 206, 207, 208, 247, 254, 258
Fabrication, 179
FDA, 114
feces, 118, 127
ferrite, 11, 14, 229, 236, 239
fibers, 184, 206, 258, 260, 263
fibroblasts, 19
fibrosis, 21, 22, 170, 171, 259
fidelity, 182
fillers, xii, 205, 245, 247, 260, 261, 263
films, 13, 29, 31, 143, 169, 179, 180, 181, 226, 228, 246, 256
filtration, 3, 19, 276
financial, 130, 324
fingerprints, 136
first generation, 98
FITC conjugated MSNs (FMSN), 155
fixation, 257, 259
flame, 94, 248
flexibility, 57, 223, 247, 255
flocculation, xiii, 299
flotation, 311
Flow cytometry, 109
fluid, 56, 149, 162, 267, 300, 312
fluorescein 5-isothiocyanate (FITC), 5
fluorescence, xii, 4, 6, 7, 8, 14, 20, 21, 22, 23, 24, 25, 26, 34, 102, 108, 109, 111, 116, 118, 122, 124, 125, 126, 127, 128, 137, 145, 146, 158, 159, 161, 163, 164, 271, 294, 319, 322, 323, 324
fluorescent dyes, 23, 140, 144, 294
fluorimeter, 323, 324
fluorophores, 4, 6, 30, 100, 102, 273, 274, 275, 280, 281, 295
FMC, 28
foams, 170
folate, 20, 127, 162, 188
folic acid, 20, 127, 188
food, xiii, 127, 246, 272
force, xiii, 299, 300, 301, 302, 303, 304, 306, 310, 311, 312, 320
formation, x, 4, 7, 9, 10, 11, 12, 13, 23, 25, 31, 32, 47, 48, 49, 52, 57, 63, 67, 68, 71, 72, 76, 77, 79, 86, 87, 91, 94, 117, 141, 144, 145, 168, 182, 185, 192, 202, 203, 207, 226, 248, 249, 259, 267, 268, 284, 299, 304, 306, 307, 308, 310, 311, 312
France, 211, 215, 271, 295
free energy, 301, 311
free radicals, 48, 86
FTIR, 50
fullerene, 200, 205
functionalization, ix, x, xi, 1, 2, 3, 26, 32, 33, 51, 97, 113, 124, 142, 143, 146, 147, 148, 151, 152, 156, 168, 177, 200, 206, 216, 221, 255, 276, 277, 294, 295
funding, 170
furan, 141

G

gadolinium, 23, 115, 136
gastrointestinal tract, 120
gate-keeping, 140
GCE, 31
gel, 3, 6, 7, 10, 15, 16, 27, 28, 29, 32, 33, 50, 90, 91, 134, 140, 145, 156, 181, 190, 192, 193, 195, 196, 200, 202, 203, 204, 205, 207, 209, 216, 224, 246, 247, 248, 259, 260, 266, 267, 290, 326
gene therapy, 253
genes, 20, 158
genetic screening, 27
genome, 20
geometry, 149, 199
Georgia, 41
Germany, 264
glass transition, 186
glasses, xii, 205, 246, 259, 267
glioma, 163, 175
gluconic acid-modified insulin (G-Ins), 154
glucose, 15, 28, 29, 30, 154, 155, 157, 175, 266
glutamate, 17, 30, 147
glutamic acid, 159
glutathione, 108
glycine, 289

glycol, 17, 143, 146, 147, 193, 261
gold nanoparticles, 92, 99, 111, 136, 157, 175, 190, 219
governments, 246
grain size, 246
grants, 209
graph, 71, 291
graphene sheet, 32, 204
graphite, 33, 199
greed, 82
group size, 223
growth, 4, 12, 94, 109, 116, 125, 162, 163, 167, 179, 180, 191, 192, 195, 201, 203, 207, 219, 220, 239, 246, 251, 257, 258, 259, 260, 287
growth factor, 258
guanine, 32

H

habitat, 230
half-life, 98, 117, 123, 124
halogen, 268
halogens, 231, 233
hardness, 263, 264
H-bonding, 50
HE, 94
health, 165, 208, 254, 274
heart disease, 252, 265
heart valves, 257
hemisphere, 300, 301, 304
hemoglobin, 29
hepatic fibrosis, 21, 22, 171
hepatitis, 33, 34
heptane, 223, 225
herbicide, 87
heterogeneity, 54
high strength, 258, 263, 264
histology, 116
history, 139, 257
HIV, 25
HLA, 104
homeostasis, 109
homogeneity, 10, 11
homopolymers, 185
hormone, 265
hormones, 253
host, xi, 153, 177
HRTEM, 227, 228
human, 19, 20, 21, 23, 29, 30, 31, 32, 33, 34, 110, 111, 116, 125, 127, 131, 136, 137, 155, 156, 161, 162, 163, 164, 165, 166, 167, 169, 170, 171, 172, 173, 174, 175, 208, 235, 254, 259, 327
human body, 235, 259
human health, 208, 254
human leukemia cells, 19
humidity, 289
Hunter, 122
hybrid, xi, 25, 27, 29, 146, 158, 169, 177, 178, 179, 180, 185, 186, 187, 188, 189, 190, 191, 193, 195, 199, 201, 202, 203, 204, 205, 206, 208, 239, 248, 259, 260, 268
hybridization, 23, 24, 25, 26, 290, 291
hydrazine, 107
hydrogels, 253, 259
hydrogen, x, 28, 29, 47, 48, 59, 82, 86, 87, 89, 90, 92, 93, 115, 141, 142, 248, 249, 252, 263
hydrogen abstraction, 92, 93
hydrogen bonds, 249, 252
hydrogen peroxide, x, 28, 29, 47, 48, 89
hydrogenation, 191, 193, 219
hydrolysis, 3, 5, 108, 141, 142, 145, 146, 179, 182, 216, 224, 225, 232, 248
hydrophilicity, 143, 146
hydrophobicity, 7, 143, 146, 251, 252
hydrosphere, 49
hydroxide, 3, 142, 145, 146, 220, 287
hydroxyapatite, 27, 259
hydroxyethyl methacrylate, 267, 268
hydroxyl, x, 18, 47, 48, 49, 61, 63, 71, 75, 77, 87, 93, 164, 178, 181, 193, 201, 203, 204, 251, 273
hydroxyl groups, 181, 193, 201, 203, 251
hyperthermia, 99, 151, 235
hypothesis, xiv, 316

I

ibuprofen, 22, 149, 150, 152, 153
ideal, 10, 101, 102, 114, 116, 182, 199, 255, 273
identification, 19, 274
illumination, 94
images, 5, 109, 113, 114, 116, 122, 123, 126, 128, 144, 163, 164, 165, 180, 182, 184, 187, 189, 197, 198, 204, 232, 236, 238, 277, 283, 284, 285
immobilization, 2, 15, 17, 27, 28, 30, 31, 34, 67, 93, 146, 147, 148, 157, 190, 253, 290
immune response, 114, 160
immunoglobulin, 19, 30
implants, 259
impregnation, 140
improvements, 263, 295
in vitro, xi, 11, 20, 23, 99, 102, 109, 110, 112, 113, 115, 116, 125, 126, 129, 139, 157, 158, 163, 173, 174, 175, 257, 268
in vivo, x, xi, 7, 8, 20, 23, 30, 35, 98, 99, 101, 102, 107, 111, 112, 113, 114, 116, 117, 122, 123, 124,

125, 126, 129, 130, 135, 136, 137, 139, 155, 157, 166, 167, 169, 173, 267, 272
incidence, 191
incubation time, 21
indium, 26
induction, 161
industries, 246, 252
infancy, 27, 35, 110, 125
infection, 127
inflammation, 108, 124, 170
inflammatory responses, 166, 173
influenza, 34
infrared spectroscopy, 50
inhibition, 155, 156, 163, 166
initiation, 262
injury, 119, 123, 170, 257
inorganic fillers, 261, 263
insulin, 154, 265
integration, 258
integrity, 290
interface, 49, 50, 86, 90, 93, 182, 206, 217, 222, 223, 230
interference, 30, 114
intermolecular interactions, 151
internalization, 116, 125, 155, 161, 163, 164
internalizing, 116
intestinal tract, 124
intestine, 122, 127
intravenously, 115, 126, 137
inversion, 223, 225
investment, 257
ionization potentials, 92
ions, 6, 14, 23, 32, 49, 71, 75, 77, 83, 93, 104, 108, 115, 180, 190, 191, 193, 203
Iowa, 315, 323, 324
Iran, 245
iron, 10, 25, 31, 91, 99, 101, 113, 115, 116, 125, 126, 128, 170, 181, 220, 236
iron oxide nanoparticles (IONPs), 99
irradiation, x, xiii, 6, 34, 47, 101, 107, 111, 112, 192, 204, 235, 251, 315, 316, 323
isomerization, 108
isomers, 65
isotherms, 147, 318, 319, 323
isotope, 93
issues, 98, 99, 113, 208, 227, 273
Italy, 271, 324

J

Japan, 241, 312
Jordan, 264, 312

K

keratinocytes, 170
ketones, 49, 88
kidney, 114, 117, 119, 121, 122, 124, 127, 165, 166, 175
kidneys, 116, 118, 122, 123, 256
kill, 167
kinetics, x, 4, 26, 48, 49, 50, 52, 56, 62, 68, 72, 82, 83, 88, 92, 93, 98, 149, 162, 320
Korea, 177, 209

L

labeling, xii, 6, 17, 20, 21, 23, 24, 27, 108, 125, 136, 137, 189, 271, 272, 290, 291, 293, 294, 295
lack of control, 252
lactate dehydrogenase, 147, 166
lactic acid, 132, 158, 258
lanthanide, 6, 14, 33, 219
lasers, 262
leaching, 158, 320, 324
lead, 2, 3, 16, 26, 63, 77, 99, 151, 168, 186, 202, 223, 249, 250, 252, 257, 284, 322
leakage, 6
lending, 247
leukemia, 19, 22
life sciences, 257
lifetime, 54, 67, 277, 281, 283
ligand, 14, 17, 98, 190, 194, 207, 208
light, ix, 5, 6, 7, 21, 31, 47, 48, 49, 54, 68, 71, 82, 94, 99, 102, 103, 105, 111, 180, 222, 226, 238, 256, 262, 268, 275, 284, 300, 304
light scattering, 21, 300, 304
linear dependence, 76, 77
linear polymers, 202, 203
liposomes, 98, 130, 255
liquid chromatography, 89
liquid crystals, 168, 188
lithium, 205
lithography, 180
liver, 23, 105, 108, 110, 114, 115, 116, 117, 119, 121, 122, 123, 124, 127
liver cancer, 23, 110
localization, 122, 171, 180
low temperatures, 3
lubricants, 205
luminescence, 6, 14, 59, 92, 94, 161, 219, 231, 235, 236, 273, 274, 275, 277, 280, 283, 286, 288
luminescence efficiency, 274
Luo, 41, 134, 210
lymph, 145
lymph node, 145

M

macromolecules, 6, 67, 251, 266, 316
macrophages, 118, 122, 123
magnet, 13, 24, 34, 236
magnetic field, 13, 20, 25, 102, 103, 111, 113, 236, 238, 252, 306, 312, 313
magnetic materials, 23, 112
magnetic particles, ix, 1, 3, 4, 306
magnetic properties, xii, 9, 115, 215, 219, 230, 235, 239, 241, 246
magnetic resonance, 21, 23, 51, 99, 113, 129, 131, 137, 143, 151
magnetic resonance imaging, 23, 99, 113, 129, 131, 151
magnetic resonance imaging (MRI), 23, 99, 113, 151
magnetic resonance spectroscopy, 51, 99
magnetism, 219
magnetization, 11, 161, 228, 229, 236
magnitude, 11, 79, 188, 294
majority, 108
mammalian cells, 154
mammalian tissues, 257
manganese, 20
manipulation, 13, 221, 246
manufacturing, 254
mass, 32, 51, 52, 69, 155, 184, 227, 320
mast cells, 19
materials science, 258
matrix, xi, xii, 4, 6, 16, 28, 31, 49, 57, 62, 63, 65, 82, 91, 109, 140, 144, 149, 150, 152, 157, 177, 190, 199, 216, 217, 218, 219, 224, 232, 235, 236, 248, 250, 251, 252, 253, 260, 261, 263, 264, 271, 273, 274, 277, 280
matrix condition, 49
matrixes, 56
matter, x, 47, 48, 86, 122, 183
measurement, 30, 34, 52, 278, 280, 299, 300, 301, 303, 304, 305, 306, 310, 311
measurements, 20, 26, 52, 65, 67, 122, 123, 229, 279, 281, 300, 301, 304, 311, 318, 319
mechanical properties, xii, 202, 246, 252, 258, 259, 260, 261, 263, 264
media, xiii, 2, 10, 140, 141, 194, 208, 299
medical, 3, 23, 27, 140, 160, 174, 245, 257, 259, 263
medicine, xii, 245
melanoma, 126, 163
melting, xiv, 26, 110, 188, 263, 289, 316, 317, 318, 322
melting temperature, xiv, 110, 188, 289, 316, 317, 318, 322
membranes, 21, 23, 50, 161, 163, 167, 180, 188, 276
memory, 97, 315
mentor, 97, 315
mercaptoethanol (ME), 155, 158
Mercury, 91
mesenchymal stem cells, 116, 161, 162, 164, 169, 171
mesoporous materials, 148, 150, 151, 152, 168, 170, 323
messenger RNA, 163
metabolic pathways, 259
metabolism, 100
metabolites, 99
metal ion, 108, 203
metal ions, 108, 203
metal nanoparticles, xi, 177, 178, 179, 190, 191, 192, 193, 195, 200, 201, 208
metal oxides, 247
metalloenzymes, 29
metallurgy, 258
metals, 191, 247
meter, 300
methanol, 67, 141, 186, 193
methodology, 12, 300, 310
methyl groups, 54
methyl methacrylate, 186
mice, 108, 116, 117, 119, 122, 123, 126, 127, 129, 137, 166
microarray detection, 27
microarray technology, ix, xiii, 24, 272, 273, 274
microcrystalline, 92
microdialysis, 28, 30
microemulsion, xi, 4, 5, 7, 8, 10, 12, 13, 14, 16, 23, 27, 30, 31, 34, 147, 168, 180, 205, 215, 217, 218, 219, 220, 221, 222, 223, 224, 225, 226, 227, 228, 232, 235, 239, 248, 273, 294
microemulsion system, 4, 7, 8, 16
micrometer, 171, 183
microorganisms, 88, 289
microscope, 116, 161, 162, 163, 164, 236, 238, 277, 300, 311
microscopy, 19, 22, 23, 100, 102, 107, 155, 162, 222, 232, 236
microspheres, 11, 21, 174, 182, 192
microstructure, 149, 218, 236
migration, 162
mineralization, 267
miniaturization, 27
mission, 59, 63
mitochondria, 166
mixing, 13, 30, 247, 249, 260, 261
model system, 189
models, 102, 114, 117, 124
modifications, xiii, 15, 178, 179, 272, 273, 274
modulus, 261, 263

molar ratios, 146, 189
mole, 73, 82
molecular oxygen, x, 47, 48, 88
molecular structure, 186, 246
molecular targeting, 114
molecular weight, 10, 140, 141, 185, 186, 188, 276
molybdenum, 231
monoclonal antibody, 31
monolayer, 25, 118, 204, 206
monomers, 219, 224, 251, 262
Moon, 40, 125, 132, 137, 241
morphine, 98
morphology, x, 8, 25, 97, 99, 100, 129, 142, 143, 146, 149, 160, 165, 168, 173, 185, 217, 246, 255, 268, 274, 275, 277
motif, 110, 133, 325
motivation, 216
MRI, 23, 99, 113, 114, 116, 118, 125, 136, 137, 151, 187, 235
mRNA, 155
MSN drug delivery system, 112
multilayer films, 13, 29
myelin, 189
myoglobin, 29

N

Na^+, 90
NaCl, 25, 78, 79, 80, 289, 319, 323
Nanocarriers, 133, 325
nanocomposites, 14, 181, 197, 201, 247, 248, 249, 250, 251, 252, 259, 260, 263, 264, 267, 268
nanocrystals, xi, 6, 7, 14, 25, 112, 194, 195, 198, 215, 217, 219, 220, 225, 227, 228, 229, 235, 236, 239, 273
nanodevices, x, 98, 101, 246
nanofibers, 203, 204, 263
nanomaterials, xi, xii, 2, 12, 29, 35, 50, 91, 99, 110, 129, 168, 169, 174, 177, 178, 179, 185, 186, 190, 192, 199, 205, 208, 216, 245, 246, 263, 271, 272, 295
nanomedicine, 100, 125
nanometers, 218, 220, 262, 274, 277, 287, 294
nanometric range, 239
nanoreactors, 145, 195, 196, 217, 222
nanorods, 13, 14, 25, 31, 132
nanostructured materials, 7, 130, 190
nanostructures, xi, 12, 13, 14, 177, 178, 179, 180, 183, 185, 187, 188, 190, 191, 192, 193, 194, 195, 196, 197, 198, 199, 202, 205, 206, 207, 208, 255
Nanostructures, 27, 179, 181, 183, 185, 189, 192, 193, 199, 204, 206, 295
nanotechnology, x, xii, 2, 97, 113, 117, 130, 170, 199, 239, 245, 246, 255, 258, 262, 263, 264, 268
nanotube, 33, 200, 246
nanowires, 178, 179, 180, 192
National Bureau of Standards, 95
natural polymers, 258
NCA, 197
near-infrared (NIR), 6, 13, 107, 111
necrosis, 118
negative effects, 205
nervous system, 167
neuroblastoma, 20, 167
neurotransmitter, 153
neurotransmitters, 132, 155, 159, 172
neutral, 16, 30, 55, 80, 141, 159, 164, 236
NH2, 20, 120, 156, 165
NIR, 6, 13, 14, 99, 105, 107, 111, 114, 122, 125, 235, 256
nitric oxide, 95, 166
nitrogen, 51, 90, 170, 318, 319, 323
nitroxide, 186
NMR, 51, 90, 143, 168
nonionic surfactants, 140
non-polar, 145, 311
normal distribution, 310
NPS, 69, 70, 71, 72, 73, 74
nuclear magnetic resonance (NMR)., 143
nucleation, 4, 179, 192, 203, 260, 287
nuclei, 115, 128, 160, 161
nucleic acid, xiii, 3, 25, 131, 163, 272, 274
nucleotides, 289
nucleus, 164

O

observed behavior, 57
octane, 223
OH, 49, 51, 59, 73, 76, 85, 87, 94, 117, 119, 120, 121, 141, 146, 191, 231, 232, 233, 234, 235, 249, 260
oil, xi, 4, 27, 143, 145, 146, 147, 162, 180, 182, 215, 217, 219, 220, 221, 222, 223, 224, 225, 232, 239, 311, 312
oleic acid, 220, 252
oligomers, 110
one dimension, 248
open spaces, 2
opportunities, xi, 2, 130, 215, 257, 272, 325
optical microscopy, 19
optical properties, xi, xiii, 99, 136, 199, 215, 272, 274, 280, 284, 287
optimization, 275, 287, 295
optoelectronics, 189

ores, 113
organ, 118, 124, 192, 257
organelles, 113
organic compounds, 49, 51
organic matter, x, 47, 48, 86
organic polymers, 255, 260
organic solvents, 200
Organically modified silica (ORMOSIL), 143, 164
organism, 129
organs, 108, 116, 117, 124, 126, 127
ovarian cancer, 155
overlap, 86, 294
ox, 200
oxidation, 48, 49, 79, 82, 87, 88, 89, 193, 227
oxidative damage, 200
oxide nanoparticles, 91, 99
oxygen, x, 4, 7, 21, 47, 48, 50, 73, 87, 88, 90, 93, 166, 170, 200, 204, 231, 235, 248
ozone, 89

P

paclitaxel, 102, 111, 133, 155, 163
palladium, 219
pancreatic cancer, 155, 163, 164
pancreatic cancer cells (PANC-1), 155
parallel, xiii, 184, 185, 272, 274, 303, 312
parity, 64
particle morphology, 142, 143, 146, 160
pathogenesis, 113
pathogens, 274
pathology, 107
pathways, 67, 127, 259
PCR, 290, 291
peptide, 2, 100, 172
percolation, 199
permission, 5, 9, 11, 17, 18, 22, 24, 34, 116, 121, 123, 128, 141, 144, 148, 150, 153, 154, 159, 160, 165, 180, 182, 184, 187, 189, 191, 195, 197, 198, 201, 204, 207, 221, 226, 227, 228, 229, 230, 233, 234, 237, 239
permit, 192
peroxide, x, 28, 29, 47, 48, 87, 89, 186
pH, xiii, 8, 15, 17, 70, 71, 72, 73, 74, 75, 76, 77, 78, 79, 80, 81, 82, 83, 84, 85, 86, 89, 101, 102, 103, 104, 107, 112, 124, 132, 133, 134, 135, 144, 156, 157, 158, 182, 188, 189, 203, 220, 232, 236, 248, 252, 253, 266, 289, 304, 315, 316, 318, 319, 323, 324, 325
pharmaceutical, 101, 130, 146, 175, 253, 254
pharmacokinetics, 98, 119, 129
phase inversion, 225
phenol, 88
phosphate, 16, 22, 25, 32, 49, 53, 57, 60, 63, 68, 82, 86, 88, 89, 93, 158, 260, 289
phospholipids, 15, 117, 129
phosphorescence, 52, 54, 57, 58, 59, 63, 65, 67, 68, 86, 92
phosphorescence decay, 52, 54, 63
photobleaching, xii, 5, 144, 271, 273
photocatalysts, 14
photodegradation, xii, 144, 271
photographs, 204, 304
photoluminescence, xii, 6, 8, 215, 222, 235, 279, 281, 282, 283, 293
photolysis, ix, 47, 48, 52, 61, 64, 68, 71, 78, 79, 80, 82, 83, 84, 86, 87, 92, 93, 94
photonics, xii, 189, 215, 216
photooxidation, 15
photopolymerization, 262
phycoerythrin, 27
physical and mechanical properties, 261, 264
physical interaction, 251
physical properties, 252, 255, 262, 268
physicochemical properties, 35, 144, 162
plants, 132, 174
plasma membrane, 164
plasmid, 20, 25
plastics, 205, 258
platform, x, 21, 33, 97, 98, 100, 101, 102, 109, 113, 114, 115, 116, 117, 125, 126, 129, 206, 255, 317, 320, 322
platinum, 15, 28, 219
playing, 225
PM, 87
PMMA, 186
polar, 50, 145, 146, 204, 251, 260, 311
polarity, 50
polarizability, 227
polarization, 51, 90
pollutants, 89
poly(methyl methacrylate), 186
polyamine, 5
polycondensation, 194
polydispersity, 186, 188
polyesters, 258, 259
polyether, 203
polymer, xi, 12, 21, 100, 175, 177, 178, 179, 181, 185, 186, 187, 188, 189, 190, 194, 195, 203, 208, 247, 248, 249, 250, 251, 252, 253, 254, 259, 260, 263, 266, 267, 268
polymer chains, 185, 251, 253
polymer composites, 247
polymer films, 181
polymer matrix, 248, 250, 251
polymer nanocomposites, 247

polymer networks, 259
polymer structure, 186
polymeric matrices, 254
polymerization, xii, 12, 161, 182, 185, 186, 187, 188, 190, 207, 246, 247, 251, 260, 262, 268
polymers, x, xiii, 8, 97, 98, 100, 101, 163, 178, 181, 186, 188, 200, 202, 203, 221, 251, 254, 255, 258, 259, 260, 268, 315, 316
polymorphism, 24
polypeptides, 196
polystyrene, 186, 188, 273
population, 90
pore openings, xiii, 315, 317
porosity, 149, 157, 207, 218, 323
porous materials, 140
positron, 122
positron emission tomography, 122
precipitation, 49, 143, 190, 191, 225, 231, 232, 246, 248
preparation, ix, xi, xii, 3, 4, 5, 6, 8, 10, 16, 27, 33, 139, 142, 143, 147, 177, 180, 181, 187, 200, 216, 217, 219, 220, 235, 239, 245, 247, 249, 253, 259, 260, 263, 275, 323
preservation, 230
principles, 135, 257, 327
probability, 307
probe, 21, 24, 26, 31, 32, 48, 91, 124, 126, 189, 289
prodrugs, 109
pro-inflammatory, 166, 173
proliferation, 108, 110, 111, 113, 155, 156, 161, 162, 167, 258
propagation, 52, 114
propane, 261
proportionality, 55
prostate specific antigen, 31
prostheses, 257
protection, 111, 282
protein immobilization, 146
proteins, 2, 3, 15, 18, 19, 23, 26, 31, 32, 33, 101, 108, 125, 154, 173, 221, 255, 272
proteomics, 27
protons, 90, 115
pulmonary embolism, 123
purification, 3, 23, 143, 181, 323
PVP, 6, 12, 13, 191, 194
pyrite, 311
pyrolytic graphite, 33

Q

quality of life, 257
quantification, xiii, 27, 272, 274
quantum confinement, 189
quantum dot, ix, xiii, 1, 99, 100, 109, 113, 130, 135, 178, 219, 236, 272, 273, 274, 288, 290, 292, 293, 294
Quantum dots (QDs), 2
quantum yields, 6, 99, 273
quartz, 280
quaternary ammonium, 140, 161, 162
quinones, 49

R

radiation, 26, 48, 63, 87, 89, 94, 111, 191
radical polymerization, 186
radical reactions, 93, 94
radicals, ix, x, 47, 48, 49, 50, 52, 63, 64, 65, 67, 68, 69, 71, 73, 74, 75, 76, 77, 79, 80, 81, 82, 83, 84, 85, 86, 87, 88, 89, 92, 93, 94, 95
radius, 51, 60, 72, 301
Raman spectroscopy, 11, 222
reactant, 60, 72, 77, 146
reactants, 68, 74, 208, 225, 248
reaction mechanism, 50, 53, 55
reaction rate, 68, 77, 78
reaction time, 145, 224
reactions, ix, x, 19, 47, 48, 49, 54, 55, 60, 67, 68, 70, 72, 73, 74, 75, 76, 79, 80, 81, 86, 87, 89, 90, 93, 94, 95, 142, 146, 157, 191, 193, 197, 208, 219, 288
reactive oxygen, 21, 50, 166
reactive sites, 73, 75
reactivity, ix, 50, 52, 67, 72, 74, 75, 79, 88, 94, 216
reagents, 13, 35, 131, 143, 146, 274, 276, 283, 284, 287
real time, 117
reality, 296
receptors, 21, 98, 127, 162
recognition, 16, 17, 19, 24, 31, 35, 110, 134, 159, 296, 326
recombination, 67, 75, 83, 93
recommendations, iv
recovery, 24, 311
red blood cells, 161
red shift, 50
reform, 141
refractive index, 227
regeneration, 35, 152, 174, 258, 260
regression, 53, 57, 62, 69, 70, 82, 83, 92
regression analysis, 57, 62, 69, 70, 82, 83
reinforcement, 180, 181, 239, 259
relative toxicity, 223
relaxation, 115, 230, 267
relaxation rate, 115
relaxation times, 115

relevance, 272
repair, 99, 152
repulsion, 111, 185
requirements, 111, 151, 158, 251, 252, 255, 257
RES, 116
researchers, 3, 139, 150, 299
residuals, 64, 65
residues, 18, 23
resins, 261, 262, 263
resistance, 8, 33, 155, 185, 226, 261
resolution, 54, 113, 114, 284
respiration, 166, 174
response, 10, 15, 19, 21, 27, 28, 29, 31, 33, 114, 118, 119, 123, 157, 160, 166, 252, 258
restorative dentistry, 268
restorative material, 268
restorative materials, 268
rhodium, 219
riboflavin, 88
rights, iv
rings, 202
risk, 91, 275, 289
RNA, 23, 25, 136, 221, 318
rods, 20, 142, 183, 184, 185
room temperature, 14, 29, 59, 63, 186, 203, 275, 277, 289, 323
routes, 3, 123, 129, 140, 185, 205, 259
Royal Society, 237, 239
rubbers, 205
rules, 140
ruthenium, 6, 14

S

safety, 117, 208, 254
salt concentration, 71
SARS, 24
saturation, 11, 280, 281
scanning electron microscopy, 144, 222
scatter, 222, 226, 256
scattering, 13, 21, 90, 189, 256, 300, 304
scavengers, 75
science, 170, 206, 258, 260, 263, 266, 269
scope, xiv, 275, 316, 318
sedimentation, 180, 192
sediments, 50
seed, 180, 191
seeding, 257
selectivity, 17, 24, 27, 35, 148, 193, 262
self-assembly, 15, 21, 180, 205
semiconductor, 99, 273
semiconductors, 247
sensing, 8, 21, 136, 157, 183, 266
sensitivity, 2, 24, 26, 27, 28, 29, 30, 31, 32, 34, 35, 111, 113, 115, 157, 273, 293, 294, 295
sensors, 5, 27, 99, 146, 157
serum, 15, 16, 29, 31, 33
serum albumin, 15
shape, xi, xii, 57, 100, 139, 160, 162, 163, 165, 171, 173, 190, 215, 216, 222, 223, 245, 257, 277, 303
shock, 225
showing, 17, 116, 128, 189, 232, 235, 239, 280, 281, 288
Si3N4, 311
side effects, 98, 107, 122, 123, 155, 208
signal transduction, 4, 19
signals, 13, 29, 34, 35, 57, 61, 63, 68, 171, 234, 238
signal-to-noise ratio, 28
silane, 9, 12, 17, 19, 27, 30, 115, 145, 169, 178, 202, 205, 216
silanol groups, 49, 50, 51, 73, 78, 85, 86, 146, 152, 181, 249, 268
silica alkoxide precursor, 3
silicon, 49, 54, 90, 124, 143, 145, 179, 180, 261
silver, 11, 12, 13, 21, 22, 31, 191, 219
simulation, 79, 312
simulations, 53, 55, 56, 68, 79, 80, 312
SiO2, 7, 8, 9, 10, 11, 12, 13, 14, 15, 19, 20, 21, 22, 24, 26, 28, 29, 30, 31, 33, 34, 49, 51, 59, 68, 79, 91, 92, 94, 95, 143, 175, 183, 196, 198, 201, 219, 222, 226, 227, 228, 229, 231, 232, 233, 234, 235, 236, 237, 238, 239, 247, 248, 251, 252, 256, 259, 261, 267, 275, 293
siRNA, 155, 163, 169, 175
SO42-, 49
society, 168
sodium, 93, 142, 143, 194, 195, 200, 216, 223, 246, 289
sodium dodecyl sulfate (SDS), 223
sodium hydroxide, 142
soft lithography, 180
software, 289
sol-gel, 6, 7, 15, 16, 27, 29, 32, 91, 134, 140, 145, 156, 181, 190, 192, 193, 195, 196, 200, 202, 203, 204, 205, 207, 216, 224, 246, 247, 248, 326
solid matrix, 56
solid phase, 89
solid state, 231, 235
solid tumors, 126
solubility, 145, 199, 205, 254, 273
solution, 8, 10, 12, 15, 17, 26, 32, 34, 54, 56, 60, 67, 69, 72, 77, 80, 86, 88, 92, 93, 102, 109, 115, 140, 143, 144, 146, 181, 183, 189, 194, 196, 200, 204, 217, 220, 224, 231, 235, 236, 238, 247, 248, 257, 275, 276, 277, 280, 281, 282, 283, 284, 287, 288, 289, 290, 295, 300, 303, 304, 305, 319, 320, 323

solvents, 67, 142, 143, 183, 186, 199, 200, 203, 226, 300
sorption, 318, 319, 323
sorption isotherms, 318, 319, 323
Spain, 42
species, ix, x, 21, 47, 48, 49, 50, 54, 57, 60, 61, 62, 63, 64, 65, 66, 69, 71, 77, 82, 87, 90, 93, 141, 142, 152, 166, 170, 182, 192, 251
specific surface, x, 2, 48, 50, 183, 185, 199, 205, 216
spectroscopy, 11, 33, 51, 99, 111, 124, 155, 222, 236, 304, 318, 319, 322, 323
spin, 180, 230, 289, 290
spindle, 10
spleen, 114, 116, 118, 119, 122, 123, 124, 127, 155
sponge, 141, 142
SSA, 51, 52
stability, xi, 2, 9, 20, 27, 28, 29, 32, 143, 145, 157, 173, 177, 183, 185, 189, 202, 208, 216, 218, 222, 225, 232, 235, 236, 247, 273, 295
stabilization, 95
stabilizers, 26
standard deviation, 69, 72
state, 27, 29, 50, 53, 54, 59, 60, 62, 63, 86, 92, 110, 115, 143, 225, 231, 235, 277, 304
steel, 257
stem cells, 113, 115, 116, 125, 136, 137, 161, 162, 164, 169, 171
steroids, 253
stimulus, 108, 112
Stöber-based protocol, 3
stomach, 122, 127
storage, 11, 151, 153, 189, 205
stress, 166, 173, 175, 299
stretching, 59
striatum, 30
structural relaxation, 267
structure, xi, xii, 2, 3, 6, 11, 12, 14, 59, 88, 98, 100, 141, 142, 143, 148, 156, 171, 179, 183, 185, 190, 195, 203, 215, 227, 228, 230, 232, 239, 240, 246, 249, 251, 257, 260, 263, 267, 268, 271, 272, 304, 317, 318
styrene, 186, 187, 188
substitutes, 257
substrate, 2, 25, 28, 191, 192, 206, 226, 227
substrates, 11, 12, 26, 28, 34, 50, 72, 79, 93, 178, 179, 192, 196, 206, 239, 260
succinimidyl esters, 18, 23
sulfate, 49, 68, 72, 75, 82, 86, 89, 93, 94, 200, 223
sulfur, 93, 95
sulfuric acid, 94
Sun, 36, 39, 40, 41, 42, 43, 44, 45, 122, 131, 137, 173, 210, 211, 242, 264, 268
supplier, 51, 300
surface area, x, xi, 2, 34, 48, 50, 51, 77, 100, 114, 139, 141, 142, 148, 150, 157, 161, 166, 167, 183, 185, 199, 205, 206, 216, 248, 255, 263, 316, 318, 323
surface chemistry, 11, 26, 50, 90, 162, 183, 246, 258
surface modification, ix, 1, 2, 4, 9, 12, 15, 51, 147, 148, 178, 179, 187, 203, 250, 260, 273
surface properties, 98, 146, 153, 157, 160, 183, 199, 255
surface reactions, 68, 70, 73, 191
surface tension, 207
surfactant, 4, 9, 10, 11, 13, 140, 141, 142, 145, 146, 148, 156, 160, 167, 170, 171, 181, 183, 193, 200, 202, 205, 217, 222, 223, 224, 225, 232, 251, 255, 256, 311
surfactants, 140, 141, 143, 150, 156, 167, 168, 172, 175, 194, 200, 202, 207, 223, 251, 294
surgical removal, 259
survival, 20, 162
susceptibility, 230
suspensions, ix, x, xiii, 48, 52, 53, 54, 57, 62, 63, 64, 65, 70, 72, 76, 77, 78, 79, 82, 83, 84, 85, 86, 225, 244, 299, 311, 312
swelling, 253, 273
symmetry, 12, 149
sympathetic nervous system, 167
syndrome, 24
synthesis, xi, xii, xiii, 2, 3, 6, 7, 9, 10, 11, 12, 13, 14, 20, 21, 22, 23, 26, 31, 33, 67, 109, 115, 126, 131, 140, 141, 142, 143, 145, 146, 147, 154, 156, 160, 161, 168, 171, 175, 179, 180, 186, 190, 202, 205, 206, 207, 208, 215, 217, 219, 222, 224, 232, 235, 246, 248, 268, 272, 273, 274, 277, 280, 281, 282, 283, 284, 287, 294, 295, 315, 316, 317, 318, 324

T

Taiwan, 130
target, x, 17, 19, 21, 23, 24, 25, 26, 31, 34, 47, 48, 100, 103, 107, 109, 111, 113, 127, 129, 157, 158, 252, 253, 255, 264
techniques, xi, xiii, 2, 3, 4, 7, 10, 19, 21, 23, 113, 118, 146, 153, 180, 181, 186, 202, 208, 215, 225, 235, 236, 247, 248, 260, 294, 299, 300
technology, ix, xiii, 24, 25, 27, 170, 175, 182, 246, 263, 272, 273, 274
TEM, 5, 60, 107, 117, 123, 147, 148, 163, 164, 184, 187, 189, 197, 198, 204, 208, 222, 228, 229, 236, 237, 304
temperature, xiii, 3, 14, 26, 29, 57, 59, 63, 85, 102, 103, 107, 110, 157, 181, 186, 188, 192, 203, 208, 225, 228, 229, 231, 248, 252, 268, 275, 277, 289, 307, 315, 316, 317, 318, 320, 321, 322, 323

temperature dependence, 229
tension, 207
TEOS, 3, 5, 8, 12, 142, 143, 144, 145, 180, 181, 189, 193, 200, 201, 202, 205, 207, 216, 217, 220, 224, 225, 232, 275, 276, 283, 284, 287, 322
tetraethoxysilane, 3, 142, 145, 201
tetrahydrofuran, 181
tetrahydrofurane, 192
tetramethylrhodamine (TMR), 5
tetramethylrhodamine isothiocyanate (TRITC), 6
TGA, 51, 52
therapeutic agents, 98, 99, 100, 102, 109
therapeutic effects, 112, 127, 254
therapeutics, 112, 113, 130
therapy, 99, 108, 130, 133, 140, 151, 155, 156, 235, 253, 254, 255, 264
thermal degradation, 181
thermal energy, 99
thermal properties, 252
thermal stability, 2, 143, 157, 247
thermogravimetric analysis, 51
thermogravimetry, 52
thermolysis, 67, 93
thermosets, 247
thin films, 143, 180, 226, 228, 256
thrombosis, 123
thyroid, 252, 265
time periods, 124
tin, 26
tin oxide, 26
tissue, xii, 99, 107, 111, 112, 113, 114, 118, 122, 124, 126, 128, 135, 137, 162, 174, 236, 245, 246, 256, 257, 258, 259, 260, 261, 263, 264, 267
titania, 32, 182
titanium, 206
TMR-dextran (TMR-Dex), 5
toluene, 223
tooth, 257, 260
toxic effect, 108, 112, 167
toxic waste, 259
toxicity, 2, 7, 8, 9, 20, 23, 122, 123, 124, 125, 127, 137, 160, 165, 167, 170, 223, 225, 236, 253, 254, 255, 261, 294
toxicology, 117, 123, 165
toxin, 108
TPA, 5, 31
trafficking, 116, 162, 168
transduction, 4, 19
transfection, 20, 131, 173, 174, 324
transformation, 182, 194
transition metal, 192
transition temperature, 230
translation, 117
transmission, 5, 107, 180, 191, 222, 232, 236, 285, 300
transmission electron microscopy, 5, 107, 222
transmission electron microscopy (TEM), 5, 107, 222
transparency, 113, 157, 222, 300
transplantation, 257
transport, 3, 20, 102, 122, 126, 204
transportation, 184
treatment, ix, xii, 8, 25, 47, 48, 89, 98, 130, 135, 140, 151, 152, 155, 156, 181, 188, 189, 200, 201, 202, 236, 245, 250, 251, 256, 257
triggers, xiii, 101, 104, 107, 129, 315, 316
tri-n-propylamine (TPA), 5
trypsin, 105
tumor, 20, 108, 126, 127, 128, 135, 155, 161, 188
tungsten, 206
twins, 205
tyrosine, 159
Tyrosine, 88, 89

U

U.S. Department of Commerce, 95
UK, 139
ultrasound, 34, 102, 103, 106, 135, 193, 252
uniform, xi, 6, 11, 14, 19, 25, 31, 137, 140, 142, 145, 147, 148, 161, 177, 180, 181, 183, 184, 187, 189, 191, 194, 201, 202, 203, 205
unimolecular radical decay pathways, 67
unique features, 148, 151, 157
uric acid, 30
urinary bladder, 117, 119, 121
urine, 117, 118, 124, 127
USA, 97, 266, 315
USSR, 89
UV, xii, xiii, 48, 62, 65, 82, 86, 89, 105, 111, 204, 215, 222, 227, 228, 231, 235, 236, 239, 262, 279, 293, 315, 316, 318

V

vacancies, 200
valve, 110
vapor, 32, 180, 192, 200, 206, 248
vapor-liquid-solid, 180
variations, 107, 196, 275, 276, 281, 283
vector, 169
vehicles, x, 97, 102, 127, 167, 253, 255
vein, 115, 116
versatility, x, 98, 101, 108, 255, 273
vertebrae, 259
viruses, 108

viscosity, 261
visualization, 125, 126
vitamin B1, 265
VLS, 180
voiding, 259
volatility, 261

W

Wales, 200
Washington, 94, 95
waste, 259
water, ix, x, xi, 3, 4, 6, 7, 8, 16, 17, 20, 27, 47, 48, 49, 50, 52, 54, 57, 62, 70, 75, 76, 86, 87, 89, 90, 93, 115, 143, 145, 146, 156, 179, 182, 183, 186, 191, 192, 193, 200, 202, 205, 206, 215, 216, 217, 221, 222, 224, 225, 232, 235, 239, 249, 254, 259, 267, 273, 274, 275, 276, 289, 295
water solubilization, 3
water-in-oil (W/O), 4
wavelengths, 57, 62, 64, 70, 99, 114, 222, 256, 290, 293
wear, 261
web, 88
weight ratio, 184
welding, 256
wells, 290
wettability, 152
windows, 149, 151
wires, xi, 177, 206
workers, 10, 13, 16, 20, 24, 26, 101, 102, 115, 123, 125, 141, 142, 143, 144, 149, 151, 152, 153, 205, 251
worldwide, xiii, 246, 272, 274

X

xenografts, 127, 155
X-ray diffraction, 230, 317, 318
X-ray diffraction (XRD), 318
XRD, 318

Y

yeast, 318
yield, 8, 13, 53, 56, 59, 61, 67, 69, 73, 77, 82, 83, 86, 94, 186, 196, 204, 206, 207, 208, 299
yolk, 218

Z

zeolites, 67, 93, 170
zinc, 113, 229
zirconia, 261
zirconium, 261
ZnO, 7, 20